TUM School of Engineering and Design

Aging aware operation of lithium-ion based battery energy storage systems

Nils Collath, M.Sc.

Vollständiger Abdruck der von der TUM School of Engineering and Design der Technischen Universität München zur Erlangung des akademischen Grades eines

Doktors der Ingenieurwissenschaften (Dr.-Ing.)

genehmigten Dissertation.

Vorsitz:		Prof. Dr. rer. nat. Thomas Hamacher
Prüfende der Dissertation:	1.	Prof. Dr.-Ing. Andreas Jossen
	2.	Prof. Dr. rer. pol. Christoph Goebel
	3.	Prof. Dr.-Ing. Thilo Bocklisch

Die Dissertation wurde am 07.05.2024 bei der Technischen Universität München eingereicht und durch die TUM School of Engineering and Design am 05.03.2025 angenommen.

Abstract

The amount of globally installed stationary battery energy storage systems (BESSs) has been increasing steadily in recent years. Following economy-of-scale induced cost reductions and technological advancements, lithium-ion batteries have emerged as the most frequently used technology for new installations. However, lithium-ion batteries are subject to degradation due to various cell-internal aging mechanisms, which affect the lifespan and profitability of BESSs. Since the degradation rate depends on stress factors such as the state of charge and the charge rate, it can be directly influenced with the operation strategy. This publication-based thesis focuses on developing methods and providing guidelines for the aging aware operation of BESSs to prolong the lifespan of lithium-ion cells, increase the long-term profitability of BESSs, and thereby enable a more resource-efficient energy storage sector. First, a comprehensive review of the state of the art in the field of aging aware operation of BESSs is presented. Following that, a Python-based model predictive control framework is proposed for designing and benchmarking aging aware operation strategies. Using this framework, the significant increase in profitability that can be achieved by accounting for aging stress factors as part of the operation strategy and by determining the optimal aging cost is quantified. In addition, an aging aware operation strategy for peak shaving applications that accounts for the uncertainty of load forecasts is developed. Uncertainty is also investigated in the context of degradation modeling uncertainty and its impact on the techno-economic assessment of BESSs. Lastly, a physicochemical aging model is developed and parameterized to investigate the nonlinear aging phase with its increased degradation rate in typical stationary applications. It is shown that by adapting the operating conditions of a BESS towards the end-of-life, the nonlinear aging phase can be delayed, and the generated profit can be significantly increased.

Zusammenfassung

Die Anzahl der weltweit installierten stationären Batteriespeichersysteme (battery energy storage systems, BESS) hat in den letzten Jahren stetig zugenommen. Durch technologische Fortschritte und Kostensenkungen haben sich Lithium-Ionen-Batterien dabei als die am häufigsten genutzte Batterietechnologie hervorgetan. Allerdings unterliegen Lithium-Ionen-Batterien einer Vielzahl an zellinternen Alterungsmechanismen, die sich auf die Lebensdauer und Profitabilität von BESS auswirken. Da das Alterungsverhalten von Stressfaktoren wie dem Ladezustand und der Laderate abhängt, kann die Degradationsrate jedoch direkt durch die Betriebsstrategie beeinflusst werden. In dieser publikationsbasierten Dissertation werden Methoden und Richtlinien für den alterungsoptimierten Betrieb von BESS entwickelt, um die Lebensdauer der genutzten Lithium-Ionen-Zellen zu verlängern sowie die langfristige Profitabilität von BESS zu erhöhen, und dadurch eine ressourcenschonendere Energiespeicherung zu ermöglichen. Zunächst wird ein umfassender Überblick zum Stand der Technik präsentiert. Anschließend wird eine auf Python basierende Simulationsumgebung vorgestellt, die es ermöglicht, verschiedene alterungsoptimierte Betriebsstrategien zu vergleichen und zu bewerten. Mit Hilfe der Simulationsumgebung wird der signifikante Profitabilitätsanstieg quantifiziert, welcher durch die Berücksichtigung von Alterungsstressfaktoren in der Betriebsstrategie sowie durch die Ableitung der optimalen Alterungskosten erzielbar ist. Darüber hinaus wird eine alterungsoptimierte Betriebsstrategie für die Anwendung Peak Shaving entwickelt, die die Unsicherheit von Lastprognosen berücksichtigt. Unsicherheit wird auch im Zusammenhang mit Modellierungsfehlern bei der Alterungsmodellierung und ihren Auswirkungen auf die techno-ökonomische Bewertung von BESS betrachtet. Des Weiteren wird ein physikochemisches Alterungsmodell entwickelt und parametrisiert, um die nichtlineare Alterungsphase mit ihrer erhöhten Degradationsrate in typischen stationären Anwendungen zu untersuchen. Es wird gezeigt, dass durch eine Anpassung der Betriebsbedingungen eines BESS gegen Ende der Lebensdauer die nichtlineare Alterungsphase hinausgezögert und der in der Anwendung erwirtschaftete Profit erheblich gesteigert werden kann.

Contents

List of publications

Peer-reviewed journal paper contributions (lead author)

a Collath, N.; Winner, H.; Frank, A.; Durdel, A.; Jossen, A.: *Suitability of late-life lithium-ion cells for battery energy storage systems*, in: *Journal of Energy Storage* 87, p. 111508, doi.org/10.1016/j.est.2024.111508, 2024

b Collath, N.; Cornejo, M.; Engwerth, V.; Hesse, H.; Jossen, A.: *Increasing the lifetime profitability of battery energy storage systems through aging aware operation*, in: *Applied Energy* 348, p. 121531, doi.org/10.1016/j.apenergy.2023.121531, 2023

c Collath, N., Tepe, B.; Englberger, S.; Jossen, A.; Hesse, H.: *Aging aware operation of lithium-ion battery energy storage systems: A review*, in: *Journal of Energy Storage* 55, p. 105634, doi.org/10.1016/j.est.2022.105634, 2022

Peer-reviewed conference paper contributions (lead author)

a Collath, N.; Gasper, P.; Jossen, A.; Smith, K.; Hesse, H.: *The Economic Impact of Battery Degradation Modelling Uncertainty*, in: *2022 IEEE Power & Energy Society General Meeting (PESGM)*, doi.org/10.1109/PESGM48719.2022.9916844, 2022

b Collath, N.; Englberger, S.; Jossen, A.; Hesse, H.: *Reduction of battery energy storage degradation in peak shaving operation through load forecast dependent energy management*, in: *NEIS 2020; Conference on Sustainable Energy Supply and Energy Storage Systems*, ISBN: 978-3-8007-5359-8, 2020

Non-peer-reviewed paper contributions (lead author)

a Tepe, B.; Collath, N.; Hesse, H.; Rosenthal, M.; Windelen, U.: *Stationäre Batteriespeicher in Deutschland: Aktuelle Entwicklungen und Trends in 2021*, in: *Energiewirtschaftliche Tagesfragen* 71.3, pp. 23-27, https://mediatum.ub.tum.de/doc/1601843, shared lead-authorship, 2022

Self-written sections of lead author contributions are partially contained in this doctoral thesis without further reference in the text.

Peer-reviewed journal paper contributions (co-author)

a Gasper, P.; Collath, N.; Hesse, H.; Jossen, A.; Smith, K.: *Machine-Learning Assisted Identification of Accurate Battery Lifetime Models with Uncertainty*, in: *J. Electrochem. Soc.* 169.8, p. 80518 doi.org/10.1149/1945-7111/ac86a8, 2022

b Philipp, M.; Collath, N.; Roth, S.; Theumer, P.; Will-Ehlers, G.; Kellermann, M.; Hesse, H.: *Batteriespeicherlösungen zur energiewirtschaftlichen Optimierung von Industriebetrieben*, in: *Zeitschrift für wirtschaftlichen Fabrikbetrieb* 117.5, pp. 305-311, doi.org/10.1515/zwf-2022-1059, 2022 c Möller, M.; Kucevic, D.; Collath, N.; Parlikar, A.; Dotzauer, P.; Tepe, B.; Englberger, S.; Jossen, A.; Hesse, H.: *SimSES: A holistic simulation framework for modeling and analyzing stationary energy storage systems*, in: *Journal of Energy Storage* 49, p. 103743, `doi.org/10.1016/j.est.2021.103743`, 2022

d Kucevic, D.; Semmelmann, L.; Collath, N.; Jossen, A.; Hesse, H.: *Peak Shaving with Battery Energy Storage Systems in Distribution Grids: A Novel Approach to Reduce Local and Global Peak Loads*, in: *Electricity* 2.4, pp. 573-589, `doi.org/10.3390/electricity2040033`, 2021

Peer-reviewed conference paper contributions (co-author)

a Parlikar, A.; Collath, N.; Tepe, B.; Hesse, H.; Jossen, A.: *The Lifetime Carbon Footprint of Lithium-Ion Battery Systems in Exemplary Applications*, in: *15th International Conference on Applied Energy*, `EnerarXiv`, 2023

Selection of conference contributions

a Collath, N.; Cornejo, M.; Engwerth, V.; Holger, H., Jossen, A.: *Aging aware operation of battery energy storage systems: Prolonged lifetime, enhanced profitability and improved resource efficiency*, in: *15th International Conference on Applied Energy*, Doha, Presentation, 2023

b Collath, N.; Tepe, B.; Englberger, S.; Hesse, H.; Jossen, A.: *Aging aware operation of lithium-ion battery energy storage systems*, in: *Advanced Battery Power 2023*, Aachen, Presentation, 2023

c Collath, N., Tepe, B.; Englberger, S.; Hesse, H.; Jossen, A.: *Aging aware operation of lithium-ion battery energy storage systems*, in: *Batterieforum Deutschland 2023*, Berlin, Poster, 2023

d Collath, N.; Gasper, P.; Jossen, A.; Smith, K.; Hesse, H.: *The Economic Impact of Battery Degradation Modelling Uncertainty*, in: *IEEE Power and Energy Society General Meeting 2022*, Denver, Poster, 2022

e Collath, N.; Hesse, H.; Jossen, A.: *Degradation Models for Lithium-Ion Batteries and their Impact on Stationary Energy Storage System Operation*, in: *Advanced Battery Power 2021*, Remote, Poster, 2021

f Collath, N.; Parlikar, A.; Hesse, H.; Jossen A.: *Dynamic Modelling and Control of Stationary Battery Energy Storage System Thermal Behavior*, in: *IRES 2021: 15th International Renewable Energy Storage Conference*, Remote, Poster, 2021

g Collath, N.; Englberger, S.; Jossen, A.; Hesse, H.: *Reduction of Battery Energy Storage Degradation in Peak Shaving Operation through Load Forecast Dependent Energy Management*, in: *NEIS 2020: Conference on Sustainable Energy Supply and Energy Storage Systems*, Hamburg, Presentation, 2020

Abbreviations

Please note that the list below is based on the main part of this thesis and does not fully cover the abbreviations used in the individual publications of this thesis.

AC	alternating current
aFRR	automatic Frequency Restoration Reserve
BESS	battery energy storage system
BMS	battery management system
BTM	behind-the-meter
CESA	Continental Europe Synchronous Area
CP	constant power
$\mathrm{C}^{\mathrm{rate}}$	charge-discharge rate
CV	constant voltage
DC	direct current
DOC	depth of cycle
EMS	energy management system
ENTSO-E	European Network of Transmission System Operators for Electricity
EOL	end-of-life
EPEX	European Power Exchange
EV	electric vehicle
FCR	Frequency Containment Reserve
FEC	full equivalent cycle
FTM	front-of-the-meter
Gr	graphite
HVAC	heating, ventilation, and air conditioning
KWKG	combined heat and power act (Kraft-Wärme-Kopplungsgesetz)
LAM	loss of active material
$\mathrm{LAM}_{\mathrm{NE}}$	loss of active material on the negative electrode
$\mathrm{LAM}_{\mathrm{PE}}$	loss of active material on the positive electrode
LFP	lithium iron phosphate
LLI	loss of lithium inventory

LMO	lithium manganese oxide
mFRR	manual Frequency Restoration Reserve
MILP	mixed integer linear program
MPC	model predictive control
NCA	lithium nickel cobalt aluminium oxide
NMC	lithium nickel manganese cobalt oxide
NPV	net present value
OCV	open-circuit voltage
P2D	pseudo-two-dimensional
PV	photovoltaic
PyBaMM	Python Battery Mathematical Modelling
RI	resistance increase
SEI	solid electrolyte interphase
SimSES	Simulation Tool for Stationary Energy Storage Systems
SOC	state of charge
SOH	state of health
SOS	special ordered set
SPM	single particle model
StromNEV	ordinance on grid charges (Stromnetzentgeltverordnung)
TMS	thermal management system
TSO	transmission system operator
V2G	vehicle-to-grid

Formula symbols

Please note that the list below is based on the main part of this thesis and does not fully cover the symbols used in the individual publications of this thesis.

α^{cyc}	Relative cyclic capacity loss per full equivalent cycle
Δf	Frequency deviation in Hz
Δfec_t	Number of FECs at timestep t
Δsoh_t	SOH loss at timestep t
Δt	Optimization timestep length in h
η	Efficiency
$\lambda^{\text{cal}}_{t,i}$	SOS-type 2 variable for linearization of calendar aging at timestep t and point i
a_k	Slope of line k for linearized convex calendar aging function
b_k	Y-intercept of line k for linearized convex calendar aging function
c^{aging}	Aging cost per unit of capacity loss for the optimization model in EUR/kWh
$\mathbb{C}^{\text{aging}}_t$	Total aging cost at timestep t in EUR
c^{id}_t	Electricity price on the intraday electricity market at timestep t in EUR/kWh
C^{rate}	Charge-discharge rate in 1/h
DOC	Depth of cycle
E^{n}	Nominal battery capacity at the beginning of life in kW h
E^{batt}	Remaining rated energy after accounting for degradation in kW h
f	Frequency in Hz
FEC	Full equivalent cycle
FEC^{EOL}	Totals FECs until end-of-life is assumed
I	Current in A
I	Index set of points for the linearized non-convex calendar aging function, $i \in I$
K	Index set of lines for the linearized convex calendar aging function, $k \in K$
$k^{1,\text{ACDC}}$	AC/DC converter efficiency curve fitting factor 1
$k^{2,\text{ACDC}}$	AC/DC converter efficiency curve fitting factor 2
p	Power in kW
$P^{\text{AC,max}}$	Maximum charge and discharge power in kW
$p^{\text{BESS,target}}$	Target charge power of the BESS in kW

$p^{\mathrm{DC,delivered}}$	DC power delivered in kW
$p^{\mathrm{DC,target}}$	DC power target in kW
p^{load}	Load in kW
P^{n}	Nominal power in kW
P^{peak}	Peak shaving limit in kW
P^{PQ}	Prequalified power for FCR in kW
p^{PV}	PV generation in kW
$\mathbb{P}_t$	Profit gained at timestep t in EUR
p_t^{ch}	Charge power at timestep t in kW
p_t^{dis}	Discharge power at timestep t in kW
$q^{\mathrm{loss,cal}}$	Relative calendar capacity loss
$q_t^{\mathrm{loss,cal}}$	Relative calendar capacity loss at timestep t
$q^{\mathrm{loss,cyc}}$	Relative cyclic capacity loss
$q_t^{\mathrm{loss,cyc}}$	Relative cyclic capacity loss at timestep t
$q^{\mathrm{loss,total}}$	Total relative capacity loss
r	r-axis or r-dimension (pseudo-dimension) for physicochemical model in m
R^{i}	Internal resistance in Ω
$r^{\mathrm{inc,cal}}$	Relative calendar resistance increase
$r^{\mathrm{inc,cyc}}$	Relative cyclic resistance increase
$r^{\mathrm{inc,total}}$	Total relative resistance increase
SOC	State of charge
$\overline{\mathrm{SOC}}$	Average state of charge
$\mathrm{SOC}^{\mathrm{start}}$	State of charge at the beginning of the optimization horizon
soc_t	State of charge at timestep t
$\mathrm{SOH}^{\mathrm{EOL}}$	State of health at which end-of-life is assumed
T	Index set of timesteps for the current optimization horizon, $t \in T$
T^{cell}	Cell temperature in K
t	Time in s
U^{OCV}	Open circuit voltage in V
U^{T}	Terminal voltage in V
x	x-axis or x-dimension for physicochemical model in m
X_i^{cal}	x-value of the linearized non-convex calendar aging function at point i
x_t^{ch}	Binary variable for charging (1) or discharging (0) at timestep t
Y_i^{cal}	y-value of the linearized non-convex calendar aging function at point i

1 Introduction

1.1 Background and motivation

Renewable energy sources have gained significant traction in the past decades with the paradigm shift towards a sustainable electricity supply. Hydroelectric power has already been in use for over a century [1]. However, in the last decades, the share of photovoltaic (PV) and wind energy in the global electricity mix has increased significantly. While the global electricity production for 2000 was estimated at 17.51 % hydroelectric, 0.21 % wind, and less than 0.01 % PV, for 2022 these shares were estimated at 15.17 %, 7.50 %, and 4.52 %, respectively [2]. When accounting for other renewable electricity sources such as bioenergy, the total percentage of renewable energy in the world's electricity mix increased from 19.07 % in 2000 to 29.91 % in 2022 [2]. The United Nations's sustainable development goals from 2015 list a substantial increase of the share of renewable energy in the global energy mix as a target for 2030 [3]. The European Union agreed on the more quantifiable goal of 42.5 % renewable energy generation by 2030 over all energy sectors [4]. However, integrating wind and PV into the electricity grid creates new but manageable challenges due to their volatility and intermittency of supply [5]. In this context, stationary battery energy storage systems (BESSs) can stabilize the grid and balance out the intermittency of the supply of wind and PV energy to further advance the integration of renewable energy sources [6, 7].

The globally installed capacity of BESSs has been increasing steadily in recent years [8, 9]. While estimates and forecasts for the currently installed capacity and future growth vary, the agreed-upon trajectory in the vast majority of reports and studies is strongly upwards [10–12]. The market research organization BloombergNEF estimated the globally installed capacity of BESSs at the end of 2021 at 56 GWh and forecasted this number to grow to 1143 GWh until 2030 [10]. BESSs are used for various applications which are often categorized based on their location in the electricity grid. In behind-the-meter applications such as peak shaving [13] or as home storage systems [14], they create cost savings for the electricity consumer. In front-of-the-meter applications such as frequency containment reserve [15] or energy arbitrage [16], BESSs generate revenue on the respective electricity markets. If operated directly by a grid operator, they can relieve the existing transmission lines, thereby allowing to defer lengthy grid reinforcement [17]. Lastly, in off-grid and microgrid settings, a BESS combined with renewable energy sources can be a cost-competitive option over relying solely on diesel generators [18].

While lead-acid batteries were the battery technology of choice for many early BESSs [19], lithium-ion batteries have been the most commonly used technology for new BESS installations for a number of years [9, 11]. Lithium-ion batteries promise high cycle life and high energy efficiency compared to other battery technologies and have been subject to economies of scale-induced cost reductions over the past years [20]. Out of the 23.9 GWh of operational large-scale BESSs in the United States of America which were part of a survey by the U.S. Energy Information Administration in 2022, 99.5 % were lithium-ion based [21]. Out of the total BESS capacity installed in Germany between 2013 and 2019, 87 % was estimated to be lithium-ion based [22].

Like other battery types as well, lithium-ion batteries are subject to degradation over their lifetime. Multiple cell internal aging mechanisms, such as the loss of cyclable lithium to the growth of the solid electrolyte interphase (SEI) layer or active material loss from particle cracking, lead to, among others, a decrease in cell capacity and an increase of the cell resistance [23–25]. On a system level, battery aging manifests itself in decreasing usable capacity and power for the intended application and increasing charge/discharge losses over the lifetime of a BESS [26, 27]. In addition, it is often assumed that after a certain extent of degradation, the battery cells reach their end-of-life (EOL). A common assumption is that the EOL of the cells is reached once the remaining capacity is at 70 % [28] or 80 % [15, 29, 30] of the initial capacity. The physical rationale behind this assumption is that lithium-ion cells can show a rapid increase in their degradation rate past this point, which is often referred to as an aging knee or nonlinear aging [24, 31]. Manufacturers often provide warranties that cover cells that fall below this range of remaining capacity within the warranty period [32].

It is well understood and validated through cell aging studies that the rate of degradation depends on stress factors such as the temperature (T^{cell}), charge-discharge rate (C^{rate}), state of charge (SOC), and the depth of cycle (DOC) [33–38]. It has also been shown that the operating conditions influence the onset of the nonlinear aging phase towards the EOL [39, 40]. Accounting for these stress factors as part of the operation strategy is referred to as aging aware operation in this thesis. Compared to other applications of lithium-ion cells, such as electric vehicles (EVs) or consumer goods, the stationary applications that BESSs are used for have several key differentiating properties in terms of battery degradation and the potential for aging aware operation:

- The cycle life requirements for many stationary applications exceed those of many EVs, especially privately used ones: For residential storage systems used for self-consumption increase and large-scale storage systems used for frequency containment reserve, Kucevic et al. identified a yearly number of FECs in the range of 200 to 300 full equivalent cycles (FECs) per year, depending on system sizing [41]. For privately used EVs, between 25 and 64 FECs per year were simulated by Tepe et al. [42]. With regards to calendar life, large-scale BESSs are typically planned as long-term assets of up to decades, as opposed to short-lived consumer goods such as cellphones and laptops.
- A primary objective of the owner or operator in most stationary BESS applications is either a form of revenue generation, like is the case for energy arbitrage or frequency containment reserve, or cost reduction, such as for peak shaving or home storage systems. This provides an incentive to directly account for degradation effects as part of the operation strategy and to thereby optimize the long-term profitability of BESSs.
- Stationary applications have long been envisioned as a second-life usage scenario for decommissioned batteries from EVs [43, 44]. While the future economic viability of this concept remains uncertain today, detailed modeling and mitigation of degradation effects have been described as one of the key areas that require more investigation to enable the profitability of second-life applications [45, 46].

To summarize, aging aware operation promises longer lifetimes for lithium-ion cells, higher long-term profitability of BESSs, and can be seen as an accelerator for successfully adopting second-life EV batteries in stationary applications. In addition, while lithium-ion cell costs have decreased from an estimated 535 $/kWh in 2013 to 107 $/kWh in 2023 [47], the carbon footprint of cell production and the environmental impact of mining for the required resources remains a concern [48]. In this context, the aging aware operation of BESSs can contribute to a more resource-efficient energy storage sector.

1.2 Scope and outline of this work

This publication-based thesis focuses on developing methods and providing guidelines for the aging aware operation of BESSs to prolong the lifespan of lithium-ion cells, increase the long-term profitability of BESSs, and thereby enable a more resource-efficient energy storage sector. In particular, contributions are made to the below four key areas:

- *Comprehensive review:* There is a significant amount of individual contributions in the field of aging aware operation of BESSs, which mostly propose operation strategies for individual applications with varying considered aging mechanisms. A comprehensive review can make the topic accessible and actionable to a large audience and highlight gaps for future research.
- *Framework for designing aging aware operation strategies:* Since the existing literature focuses on operation strategies for individual applications, a framework for designing and benchmarking aging aware operation strategies can create comparability and simplify the validation process. Furthermore, additional lifetime benefit is created by deriving the *optimal aging cost* with the here developed framework as opposed to the prevalent assumption of basing aging cost on battery or BESS investment cost.
- *Consideration of uncertainty:* While perfect foresight of future time series, e.g., electric load forecasts, is a frequent assumption and deterministic aging models are often used in the existing literature, real-world applications are subject to uncertainty in both.
- *Nonlinear aging behavior towards the EOL:* The nonlinear aging behavior of lithium-ion cells has, to the knowledge of the author, not yet been considered in any previously existing publications in the field of aging aware operation, but is gaining increasing importance with the ever-growing and aging fleet of globally installed BESSs.

Figure 1.1 summarizes the overall structure of this work. Following this introduction, Chapter 2 describes the concepts and methods relevant to this thesis as well as the existing scientific literature of the field. The individual publications which are part of this work are then presented in the subsequent chapters.

Chapter 3 presents the first publication of this work: *Aging aware operation of lithium-ion battery energy storage systems: A review*. In this publication, a literature review is performed that focuses on the aging of lithium-ion batteries, degradation modeling approaches, and conclusions on both for the aging aware operation of BESSs. Furthermore, the plentiful literature in the field of aging aware operation of BESSs is summarized and categorized. Lastly, a case study is conducted to identify the most relevant aging stress factors in different stationary energy storage applications.

In Chapter 4, an open-source model predictive control (MPC) framework for designing and benchmarking aging aware operation strategies is presented, as part of the publication *Increasing the lifetime profitability of battery energy storage systems through aging aware operation*. With this framework, it is shown how the lifetime profit of BESSs can be increased by accounting for aging stress factors as part of the operation strategy and by determining the *optimal aging cost*.

Chapter 5 focusses on uncertainty in two areas which are relevant for the aging aware operation of BESSs. First, an aging aware operation strategy for peak shaving that accounts for uncertainty in load forecasts is presented in the publication *Reduction of battery energy storage degradation in peak shaving operation through load forecast dependent energy management* in Chapter 5.1. Following that, the impact of uncertainty in degradation modeling on the techno-economic assessment of BESSs is investigated in the publication *The economic impact of battery degradation modeling uncertainty* in Chapter 5.2.

In Chapter 6, the aging behavior and techno-economic performance of lithium-ion cells towards their EOL is investigated as part of the publication *Suitability of late-life lithium-ion cells for battery energy storage systems*. For that purpose, a physicochemical battery aging model is developed to model the nonlinear aging phase with its increased degradation rate in typical stationary applications.

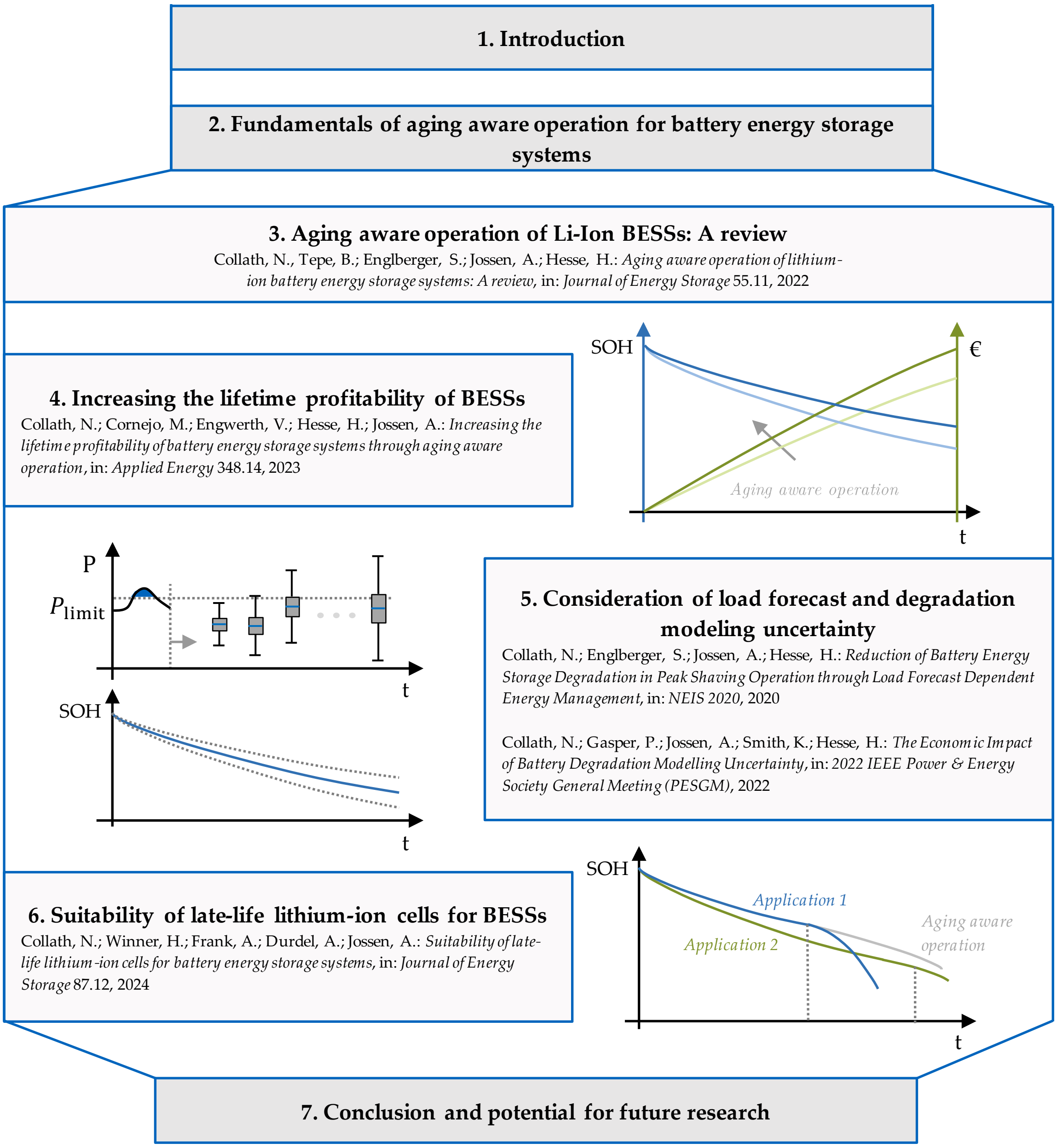

Collath, N., Tepe, B.; Englberger, S.; Jossen, A.; Hesse, H.: *Aging aware operation of lithium-ion battery energy storage systems: A review*, in: *Journal of Energy Storage* 55.11, 2022

Collath, N.; Cornejo, M.; Engwerth, V.; Hesse, H.; Jossen, A.: *Increasing the lifetime profitability of battery energy storage systems through aging aware operation*, in: *Applied Energy* 348.14, 2023

Collath, N.; Englberger, S.; Jossen, A.; Hesse, H.: *Reduction of Battery Energy Storage Degradation in Peak Shaving Operation through Load Forecast Dependent Energy Management*, in: *NEIS 2020*, 2020

Collath, N.; Gasper, P.; Jossen, A.; Smith, K.; Hesse, H.: *The Economic Impact of Battery Degradation Modelling Uncertainty*, in: *2022 IEEE Power & Energy Society General Meeting (PESGM)*, 2022

Collath, N.; Winner, H.; Frank, A.; Durdel, A.; Jossen, A.: *Suitability of late-life lithium-ion cells for battery energy storage systems*, in: *Journal of Energy Storage* 87.12, 2024

Figure 1.1: Graphical overview of this thesis.

Lastly, the thesis is concluded, and areas for future research are derived in Chapter 7. The Appendix further includes two co-authored publications, which present relevant foundations to the main chapters of this thesis. The open-source Simulation Tool for Stationary Energy Storage Systems (SimSES), which is used as part of the simulation toolchains in the above publications and further developed throughout this thesis, is presented in *SimSES: A holistic simulation framework for modeling and analyzing stationary energy storage systems* in Appendix A. Furthermore, the development and parameterization of the aging model that is used in Chapter 5.2 is presented in the publication *Machine-learning assisted identification of accurate battery lifetime models with uncertainty* in Appendix B.

2 Fundamentals of aging aware operation of battery energy storage systems

2.1 Stationary energy storage applications

Applications for stationary energy storage systems are frequently categorized into front-of-the-meter (FTM), behind-the-meter (BTM), and microgrid applications based on their point of effect in the electricity grid [18]. Table 2.1 summarizes key applications of BESSs.

Table 2.1: Key applications for BESSs, adapted and based on [18, 20].

Type	Application	Financial incentive
Front-of-the-meter (FTM)	Energy arbitrage	Profit through arbitrage trading on wholesale energy markets, e.g., the European Power Exchange (EPEX)
	Balancing power	Remuneration through the respective balancing power markets, e.g., Frequency Containment Reserve in Germany or Firm Frequency Response in the United Kingdom
	Transmission & distribution system	Investment deferral or replacement of traditional grid expansion
	Colocation with renewables	Time arbitrage, correction of forecast errors, or ramp control
Behind-the-meter (BTM)	Self-consumption increase of PV energy	Reduced electricity cost
	Peak shaving	Reduced demand charges
	Time-of-use	Reduced electricity cost
Microgrid	Off-grid operation with renewable energy sources	Potential for lower cost compared to diesel generators
	Backup power	Provision of backup power for critical loads
Combined applications	Multi-use, vehicle-to-grid (V2G), and aggregation concepts	Additional profit compared to serving only a single application

FTM applications serve the electricity grid in front of the electricity meter, i.e., upstream of household or industrial sites [49]. **Energy arbitrage** refers to using a BESS to trade electricity in the wholesale electricity markets, such as the EPEX, and generating a profit by buying at low and selling at high prices. When providing **balancing power**, a BESS is discharged if the grid frequency is below a certain frequency threshold and charged if it is above the threshold to stabilize the grid frequency and balance out electricity generation and consumption. In many liberalized electricity markets, public auctions determine which individual assets provide this service at what price [50]. Examples are the auction for Frequency Containment Reserve in Germany [51] and Firm Frequency Response in the United Kingdom [52]. In **transmission & distribution system** applications, BESSs may be operated by network operators directly to relieve congested lines or reduce peak loads [53, 54]. This, in turn, allows to defer or replace investments for traditional grid reinforcements, such as new transmission lines, switchgear, and transformers [17]. **Colocation with renewables** refers to applications in which BESSs are located on the same site as renewable energy resources to perform time arbitrage and ramp control or to balance out forecast errors of the generated electricity [18].

BTM applications serve households or industrial sites behind the electricity meter [55]. By charging a BESS when the generated PV power exceeds the electrical load and discharging it when the load exceeds the generated PV power, a **self-consumption increase of PV energy** can be achieved. If the remuneration for PV energy is lower than the cost of electricity from the grid, this increase in self-consumption results in overall reduced electricity cost [56]. In multiple electricity markets, industrial electricity consumers are subjected not only to a price for the amount of electrical energy consumed but also to demand charges for the maximum power peak generated in a given time period [55]. Through **peak shaving**, i.e., discharging a BESS during power peaks and charging it again afterward, the power peak and thereby the demand charges can be reduced [57, 58]. For electricity consumers with **time-of-use** pricing, using a BESS to shift electricity consumption to times with low electricity prices can further reduce overall electricity cost [55].

In **microgrid** applications, BESSs form or support a local grid separate from the public electricity grid [18]. In **off-grid operation with renewable energy sources**, such as PV systems, BESSs can be a cost-competitive option compared to solely relying on diesel generators, especially in locations with high fuel cost [59, 60]. Furthermore, BESSs can provide **backup power** to critical loads, such as data centers, during outages of the public electricity grid [61].

Combined applications refers to different concepts of serving more than one application. The term **multi-use** is frequently used to describe using a single BESS for multiple FTM applications, BTM applications, or a combination of both, which generally promises higher profits than serving only a single application [62, 63]. In **V2G**, controlled charging and discharging of electric vehicles is used to serve grid-related applications, such as providing balancing power [64]. **Aggregation** of multiple BESSs to a virtual power plant with generators and loads may be used for a more economic dispatch as well [65].

Electricity markets are designed markets resulting from regulatory processes, with different market designs in different countries and regions [66]. Therefore, the relevant BESS applications and their constraints vary geographically [18]. Additional geographical factors such as the PV generation potential or the strength of the existing electricity grid further affect the local prevalence of individual BESS applications [18]. In this thesis, the German electricity market and its local constraints serve as a basis for the techno-economic analyses of aging aware operation in different BESS applications. Due to their prevalence in Germany, four applications are repeatedly investigated in the individual publications of this thesis: energy arbitrage, balancing power, peak shaving, and self-consumption increase. These applications are described in detail in the following, along with their Germany-specific constraints.

2.1.1 Energy arbitrage

The EPEX SPOT is Europe's largest electrical power exchange, offering day-ahead and intraday trading. In 2021, a total of 498 TWh of electricity was traded on the day-ahead market and 123 TWh on the intraday market [67]. The day-ahead market is organized as a blind auction, closing daily at noon at 12:00 CET on the day before delivery [67]. Hourly contracts for each hour of the following day can be traded, as well as different variations of blocks that cover multiple hours [67]. For 2021 in Germany, an average price of 96.8 EUR/MWh was reached in the day-ahead auction with a minimum price of -69.0 EUR/MWh on the 22nd of May at 13:00 and a maximum price of 620.0 EUR/MWh on the 21st of December at 17:00 [68]. The intraday continuous market opens at 15:00 CET the day before delivery and offers hourly, half-hourly, and 15-minute contracts [67]. A trade is executed as soon as two orders match in the EPEX order book, and orders can be placed up until 5 min before delivery [67]. Due to the nature of this continuous trading, an individual price exists for each trade. EPEX publishes different price indices, such as the ID-1 price index, which is the average price of all trades executed within 1 hr before delivery [69]. In 2021 in Germany, the average ID-1 price for 15-minute-contracts was at 97.1 EUR/MWh, with a minimum of -122.9 EUR/MWh on the 9th of May at 13:00 and a maximum of 942.4 EUR/MWh on the 14th of August at 19:45 [68]. In addition to the continuous trading, an intraday auction allows bids to be placed for 15-minute contracts and closes daily at 15:00 CET for the following day [67].

BESSs can be used to buy electricity at low prices and sell it at high prices, thereby performing energy arbitrage. If a given trade is compensated before delivery, e.g. buying 1 MWh at 08:30 for delivery at 14:00 on the intraday market and then selling 1 MWh again at 09:30 for delivery at 14:00, a profit may even be generated without having to charge or discharge the BESS [70]. Due to the different available products, markets, and timelines, there is a large degree of flexibility for the operator to find the optimal charge-discharge schedule. Generally, higher profits can be achieved by using all available markets, i.e., the day-ahead auction, intraday continuous markets, and the intraday auction, when performing energy arbitrage with a BESS [71]. Consideration of efficiency and battery aging is particularly relevant in this application. Higher energetic losses will translate directly into reduced profits as additional energy must be procured to cover these losses [72, 73]. Compared to other stationary applications, energy arbitrage has higher charge-discharge rates, resulting in high energetic losses on a battery cell level [74]. From a battery aging perspective, higher profit can be reached by conducting more charge-discharge cycles in a given year, but this will also cause increased aging and a premature EOL of the cells [70]. Depending on the operator, the resulting charge-discharge schedule of a BESS used for energy arbitrage can result from a human trader, different optimization approaches for automated trading, or a combination of both.

Multiple publications provide advanced optimization methods that consider the uncertainty of future prices and participation in multiple markets, such as by Finnah et al. [75] and Löhndorf et al. [76], but do not explicitly account for battery aging. In this thesis, energy arbitrage is modeled through optimization with a mixed integer linear program (MILP) with perfect foresight of the 15 min ID-1 intraday continuous price in Chapter 4 and Chapter 6. The focus in those chapters lies on methods and guidelines for aging aware operation that can be transferred to other trading algorithms as well.

2.1.2 Balancing power

With the Continental Europe Synchronous Area (CESA), continental Europe has the world's largest synchronous electrical grid by connected electrical power [77]. The cooperation of the individual transmission system operators (TSOs) of this synchronous grid area is managed through the European Network of Transmission System Operators for Electricity (ENTSO-E) [77]. The ENTSO-E describes balancing as all actions and processes through which TSOs maintain the system frequency within a predefined stability range [78]. Due to historical developments and different approaches, the processes and products to balance the system can vary between different TSOs [78].

In Germany, which is part of the CESA, balancing the electricity grid is managed by its four TSOs: 50Hertz, Amprion, Tennet, and TransnetBW [51]. The balancing market is structured into three products with different time scales and constraints for participation: FCR, automatic Frequency Restoration Reserve (aFRR), and manual Frequency Restoration Reserve (mFRR). Frequency Containment Reserve (FCR) needs to be fully available after 30 s and is provided for up to 15 min. It is provided by all participating assets based on on-site frequency measurements [51]. After 5 min, it is replaced by aFRR, which is automatically activated by the responsible TSO through communication interfaces to the participating assets [51]. mFRR is then manually managed by the responsible TSO and fully activated after 12.5 min [51].

Out of these three balancing products, BESSs are most commonly used to provide FCR [79]. FCR is awarded through a public auction with 4 hr time blocks and 1 MW minimum bid sizes in which all prequalified assets can participate. Based on the publicly available auction results, the average price for a 4 hr time block was 68.80 EUR/MWh in 2021 [51]. If awarded, the respective assets must provide FCR for the 4 hr time block by following the requirements outlined in the prequalification conditions. At its core, the target charge power $p^{\text{BESS,target}}$ of a BESS providing FCR has to follow a droop curve based on the difference between the measured frequency f and the target frequency of 50 Hz, $\Delta f = f - 50\,\text{Hz}$, and the prequalified power P^{PQ} [51]:

$$p^{\text{BESS,target}} = \begin{cases} P^{\text{PQ}} \cdot \frac{\Delta f}{0.2\,\text{Hz}} & , |\Delta f| \leq 0.2\,\text{Hz} \\ P^{\text{PQ}} & , \Delta f > 0.2\,\text{Hz} \\ -P^{\text{PQ}} & , \Delta f < -0.2\,\text{Hz} \end{cases} \tag{2.1}$$

While conventional generators such as coal or gas power plants have few limitations in following this droop curve indefinitely, managing the SOC is of specific relevance for BESSs [79]. Through storage management activities, the operator has to ensure that the BESS is in a SOC range in alignment with the prequalification requirements to provide FCR when required [80]. For that purpose, scheduled charge and discharge transactions through trading electricity on the respective markets can be used [80]. However, it is often profitable for the operator to first use the so-called degrees of freedom that the prequalification conditions provide to keep the SOC close to its intended setpoint before using scheduled transactions [79]. These degrees of freedom are a deadband of 10 mHz around 50 Hz, in which Equation 2.1 does not need to but can be followed, the possibility to overfulfill the target power from Equation 2.1 by up to 20 %, and the option to provide FCR faster than the required linear ramp of full provision after 30 s [79, 80]. Furthermore, the German TSOs have specific requirements for sizing energy storage resources for FCR provision. These requirements consider the energy required for delivering the prequalified power for the required 15 min, the energy required from a previous activation, delayed effects of SOC management, and additional capacity for reserve operation [80]. Based on the present prequalification conditions, this results in a minimum of 0.91 MWh required energy capacity per 1 MW prequalified power [80].

Due to the strict requirements that are outlined in the prequalification conditions, FCR provides less flexibility with regard to the operation strategy than performing energy arbitrage. Individual scientific publications however investigate how to optimally use the degrees of freedom and scheduled transactions for managing the SOC, such as by Thien et al. [79], Zeh et al. [81], and Marchgraber et al. [82]. In this thesis, FCR in Germany is used as a reference application in both Chapter 3 and Chapter 5.2, as implemented in SimSES [83]. Two degrees of freedom, i.e., the deadband of 10 mHz around 50 Hz and the option of 20 % overfullfillment, are considered as part of the operation strategy, as well as storage management through trading on the the intraday market.

2.1.3 Peak shaving

The electricity cost for industrial consumers in Germany consists of multiple components: cost for procuring electricity from the energy provider, grid fees, and electricity tax [84]. In addition, multiple levies resulting from subsidies further increase the cost, namely the combined heat and power act (Kraft-Wärme-Kopplungsgesetz) (KWKG) levy, §19 ordinance on grid charges (Stromnetzentgeltverordnung) (StromNEV) levy, the offshore grid levy, and the levy for curtailable loads [84]. However, the largest cost components are the cost of procuring electricity from energy providers and grid fees [84]. The cost structure for grid fees generally has two components: a fee for each unit of energy used from the grid plus a demand charge for the highest load peak caused in a given billing period [85]. The cost structure further depends on the hours-of-use, defined as the yearly electricity consumption divided by the maximum load peak [85]. For Munich in 2024, the grid operator set the yearly demand charges at 193.62 EUR/kW/a on the low voltage grid and 153.88 EUR/kW/a on the medium voltage grid for consumers with more than 2500 hours-of-use [86]. By comparison, for Hamburg in 2024, these yearly demand charges were set significantly lower, with 61.60 EUR/kW/a on the low voltage grid and 59.67 EUR/kW/a on the medium voltage grid [87].

By reducing the maximum load peak in a given billing period through peak shaving with a BESS, i.e., discharging the BESS during load peaks and charging it afterward, the demand charges and thereby the overall electricity cost can be reduced [88]. Two corner cases can make peak shaving with a BESS even more profitable: *intensive grid usage* and *atypical grid usage* [88].
Under §19 StromNEV [85], grid operators have to offer electricity consumers customized grid fees if they have more than 7000 hours-of-use a year and a yearly electricity consumption of more than 10 GWh, which is referred to as *intensive grid usage* [88]. These customized grid fees can be up to 80-90 % lower than the public grid fees of that grid operator [85]. Depending on the load profile, a BESS may be used to smooth the load, reach the 7000 hours-of-use, and make the electricity consumer eligible for customized grid feeds under the intensive grid usage ruling [88].
Atypical grid usage refers to shifting the load towards time periods of overall low grid usage. Each distribution grid operator defines high load time periods during which high grid usage is expected in the following year, e.g., between 16:30 and 19:00 during winter months [88]. If an industrial electricity consumer classifies for atypical grid usage, demand charges are calculated only based on the highest load peak within these time periods, which can lead to a significant demand charge reduction [88]. To classify, the highest load peak during the high load time periods needs to be 20 % below the highest load peak outside of the high load time periods [88]. If the BESS is then only required to perform peak shaving during high load time periods, it may be used for other applications such as providing FCR outside of those time periods [88].

The charge-discharge profile of the BESS in a simple peak shaving operation strategy results from the difference between the set power limit for peak shaving P^{peak} and the site load p^{load}:

$$p^{\text{BESS,target}} = P^{\text{peak}} - p^{\text{load}} \tag{2.2}$$

Following this power target, the BESS will discharge during a load peak that exceeds P^{peak} until it is fully discharged and charge after the load peak until it is fully charged again or another load peak occurs. To determine the optimal peak shaving limit P^{peak} and for sizing the BESS, optimization approaches or heuristics may be used [13, 58]. Many scientific publications however assume perfect foresight of the future load, when deriving the peak shaving limit, e.g., [58, 89, 90]. In Chapter 5.1, an aging aware operation strategy for peak shaving is proposed that includes a method for handling load forecast uncertainty. Furthermore, peak shaving in Germany without intensive and atypical grid usage is used as a reference application to assess the battery aging behavior and the relevance of individual aging stress factors in Chapter 3 and Chapter 5.2.

2.1.4 Self-consumption increase

Germany is Europe's largest market for home storage systems [91]. An estimated 59 % of the total 2.3 GWh of home storage systems installed in Europe in 2021 were installed in Germany [91]. In combination with a PV system, the financial benefit for households lies in the difference between electricity cost and the PV feed-in tariff. The average electricity cost for households in Germany in 2022 was 38.57 ct/kWh [84]. On the other hand, the feed-in tariff for PV systems smaller than 10 kW peak constructed in January 2022, was at 6.83 ct/kWh [92]. For every kilowatt-hour of PV-generated electricity that can be used to cover the household load directly instead of being fed into the grid, a cost-benefit of 31.74 ct is generated for the household. A BESS can be used to charge in times of excess PV power and discharge when the household load exceeds the generated PV power, which is referred to as self-consumption increase. For a so-called *greedy* [41] operation strategy, the target BESS charge power is the difference between the generated PV power p^{PV} and the household load p^{load}:

$$p^{\text{BESS,target}} = p^{\text{PV}} - p^{\text{load}} \tag{2.3}$$

With this operation strategy, the BESS will charge until it is fully charged if the generated PV power is larger than the load and discharge until it is fully discharged when the household load is larger than the generated PV power. Instead of this greedy operation strategy, forecast-based operation strategies have been proposed to reduce battery aging in this application, i.e., by charging the BESS during the day only up to the energy that is expected to be needed at night [93]. Other authors proposed forecast-based operation strategies with the intention of limiting the power peaks that are generated by PV power that is being fed back into the distribution grid [94].

Early publications from the years 2014-2016 can be found that focus on the optimal sizing [95, 96] and the general techno-economic assessment [56] of home storage systems for self-consumption increase in Germany. Since then, the installed capacity of home storage systems in Germany has increased significantly which highlights their attractiveness and technological maturity. While at the end of 2016, only 367 MWh of home storage systems were registered in Germany, this number increased to 5.5 GWh by the end of 2022 [9]. Larger BESSs for self-consumption increase could also be used by industrial consumers with on-site PV systems. However, since the difference between electricity cost and the PV feed-in tariff is significantly smaller for industrial electricity consumers than for private households, self-consumption increase with BESSs is less attractive for industrial electricity consumers [97].

In this thesis, self-consumption increase with a representative home storage system serves as a reference application in Chapter 3, Chapter 5.2, and Chapter 6. In these chapters, the application is investigated with a focus on battery aging and its stress factors.

2.2 Battery energy storage systems

In this chapter, the structure and components of a BESS as well as developments in those are first described in Chapter 2.2.1, before the modeling approach used in this thesis is presented in Chapter 2.2.2.

2.2.1 Structure and components

BESSs vary in their physical layout and design. Existing installations range from small-scale home storage systems with only a few kilowatt-hours of capacity to large-scale, highly modular systems with up to gigawatt-hours of capacity on a single site. The average size of home storage systems that were installed in Germany in 2022 was at 5.3 kW nominal power and 8.8 kWh nominal energy [9]. In the same year, a total of 434 MW and 467 MWh of large-scale BESSs was installed in Germany with widely varying sizes of the individual sites [9]. Internationally, by the end of 2017, the *Hornsdale Power Reserve* in South-Australia was reported as the largest BESS at the time with a nameplate rating of 100 MW and 129 MWh [98]. At the end of 2023, the largest BESS, the *Moss Landing Energy Storage Facility* in California, was more than one order of magnitude larger in terms of storage capacity, with a nameplate rating of 750 MW and 3 GWh [99].

Figure 2.1 shows a schematic overview of a BESS with its key components. The core component of every BESS are the **battery modules**, consisting of individual battery cells. Multiple battery cells are connected in series and parallel to increase the voltage level and achieve the desired capacity. For lithium-ion cells, different typical form factors exist, i.e., prismatic, cylindrical, and pouch bag cells [100]. Typical cell chemistries are lithium iron phosphate (LFP), lithium nickel manganese cobalt oxide (NMC), and lithium nickel cobalt aluminium oxide (NCA), which specify the employed cathode material type [101]. Lithium-ion cells and especially their aging behavior are described in more detail in Chapter 2.3.

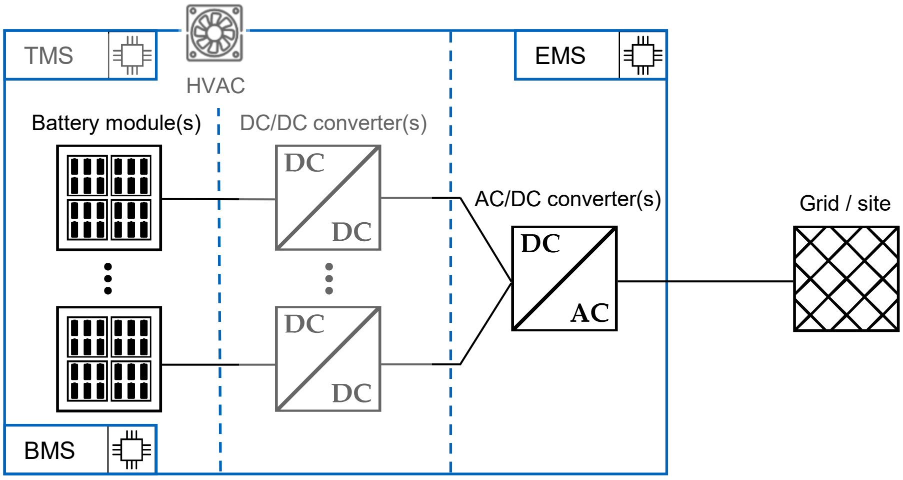

Figure 2.1: Schematic representation of a BESS with its key components. Every grid-connected BESS consists of, at a minimum, the battery module(s), AC/DC converter(s), a BMS, and an EMS. Other components are optional and dependent on system design, i.e., DC/DC converter(s), a TMS, and HVAC.

The **AC/DC converters** convert the direct current (DC) voltage provided by the battery modules to the required alternating current (AC) voltage at the grid connection point. They further control the power flow from and to the battery modules. If connected to the public grid, the AC/DC converters have to comply with the grid code of the local distribution network operator, which often entails requirements such as low-voltage fault ride-through capabilities and delivering a specific power factor [102, 103]. Multiple suitable converter topologies have been proposed for energy storage applications in the scientific literature, which Pires et al. categorized into standard, multilevel, and multiport technologies [104]. In the review by Wang et al. of commissioned BESSs, all listed sites used the topologies of either two-level converters or three-level converters [105]. In comparison, advanced converter topologies such as the modular multilevel converter promise higher efficiency and modularity [105, 106].

The **energy management system (EMS)** processes the charge-discharge signals for the BESS and serves as a communication interface for remote control and monitoring of the system. Its implementation is application and design-specific. For a home storage system used for self-consumption increase, the EMS will typically, among others, process the measurements from electricity meters at the PV system and the household electrical distribution panel, calculate the power target as in Equation 2.3, and pass it on the power electronics.

The **battery management system (BMS)** measures the relevant data points of the battery modules, e.g., temperatures, voltages, and currents, and ensures the safe operation of the modules [107]. Through communication of the BMS with the power electronics, safety-critical over-discharging and over-charging of the battery modules has to be prevented [107–109]. Furthermore, the BMS is used for state estimation of the battery modules, e.g., to estimate the SOC and state of health (SOH) [110]. While this state estimation may be performed onboard, cloud-based methods for state estimation have recently received increased attention in the literature, with the advantage of being able to rely on higher computational power and larger data-storage capabilities while allowing to aggregate data from multiple BESSs [110, 111]. Some BMS functions may be expanded by a central EMS, e.g., calculating a site-wide SOC or determining the site-wide maximum charge and discharge power based on the values from the individual BMSs of multiple battery modules. Lastly, SOC balancing of cells connected in series is another critical function of the BMS. Cells connected in series deviate in their SOC due to manufacturing inconsistencies, inhomogeneous temperature distributions, or different SOH values, which leads to the cell with the lowest SOC or highest SOC limiting the accessible discharge or charge capacity of the entire serial connected string [112]. SOC balancing may be performed through passive methods, i.e., dissipating energy from the cells that are at a high SOC through bleed resistors, or active methods, i.e., charging the cells that are at a low SOC with energy from the cells which are at a high SOC [112].

In addition to the above, some components are optional and dependent on system design, such as the **thermal management system (TMS)** and **heating, ventilation, and air conditioning (HVAC)** system. While small home storage systems often do not include active temperature management of the battery modules, large-scale BESSs typically do [113]. The temperature of lithium-ion cells significantly impacts their performance, with the optimal temperature range typically stated between 15°C and 35°C [114]. High temperatures cause increased cell degradation from SEI growth and increase the risk of thermal runaway [113, 114]. Low temperatures will lead to a higher cell resistance, lower efficiency, and an increased risk of lithium plating [113, 114]. During operation, the battery modules can generate significant excess heat from cell internal losses, which needs to be dissipated [115, 116]. Furthermore, the AC/DC converters require active cooling [115]. In particularly cold climates, active heating of the battery modules may further be required [117]. Heat exchange with the battery modules can then be performed through air cooling or liquid cooling [118].

Furthermore, **DC/DC converters** may be used as part of a BESS to step up the DC voltage and to connect multiple battery modules on one DC-bus before connecting to an AC/DC converter. While more power electronic equipment is required with this approach, it promises higher modularity and the ability to operate the individual battery modules independently of each other [105].

Lastly, the term *balance of system equipment* summarizes the additional equipment required for a BESS installation, such as enclosures for the battery modules and converters, electrical wiring, and control circuits [101]. Transformers are typically required as well to connect from the AC/DC converters to medium voltage or high voltage grids for larger BESSs. However, transformer-less concepts have been proposed in the scientific literature, such as the cascaded H-bridge converter, which can generate a sufficiently high voltage to connect to a medium voltage grid without an additional transformer [103].

For a representative lithium-ion BESS in the United States of America with a rating of 60 MW and 120 MWh installed in 2021, Augustine et al. estimated the total cost at 428 $/kWh [101]. Out of this, 50.2 % are attributed to the battery modules, 8.6 % to the central AC/DC converters, 12.9 % to the balance of system equipment, 9.1 % to the construction and related overhead cost, and lastly, 19.2 % to project development cost and profit, as well as sales tax [101].

2.2.2 Modeling of battery energy storage systems

Different software tools can be found for the technical and economic modeling of BESSs. These tools typically model the individual components of a BESSs with varying degrees of complexity as well as the interaction of these components. Some tools provide functionalities to model different energy storage applications and perform techno-economic analyses of BESSs in these applications. Examples are the Storage Value Estimation Tool (StorageVET) by the Electric Power Research Institute [119] and System Advisor Model (SAM) by the National Renewable Energy Laboratory [120]. In this thesis, the open-source SimSES, distributed by the Chair of Electrical Energy Storage Technology at the Technical University of Munich, is used and further developed [83]. SimSES is described in detail in the associated co-authored publication in Appendix A.

The primary components modeled in SimSES in this thesis are the AC/DC converters, the lithium-ion cells, the BMS, and the EMS. DC/DC converters are not modeled for the representative BESSs that are used in the individual publications of this thesis. Furthermore, the TMS and HVAC are not modeled, and instead, a representative constant cell temperature of 25°C is assumed.

The efficiency of AC/DC converters is a function of the requested power. Characteristically, the efficiency is especially low for small requested power values and shows a maximum at a requested power value below its nominal power [105]. In SimSES, this is modeled through efficiency curves. In the case studies of this thesis, the AC/DC converter in the publication by Notton et al. of ”type 2” is used with the below efficiency curve [121]:

$$\eta = \frac{\frac{p}{P^{\mathrm{n}}}}{\frac{p}{P^{\mathrm{n}}} + k^{1,\mathrm{ACDC}} + k^{2,\mathrm{ACDC}} \cdot \left(\frac{p}{P^{\mathrm{n}}}\right)^2} \tag{2.4}$$

Here, p is the requested power, P^{n} is the nominal power of the AC/DC converter, and $k^{1,\mathrm{ACDC}}$ and $k^{2,\mathrm{ACDC}}$ are fitting factors.

For the lithium-ion cells, two modeling approaches are used in this thesis: First, equivalent-circuit models combined with semi-empirical degradation models, and second, a physicochemical cell and degradation model. Both approaches will be described in Chapter 2.3.3. The BMS in SimSES is linked to the cell model and ensures that the critical cell parameters of maximum charge and discharge current and maximum and minimum voltage remain in the permissible range by limiting the requested charge and discharge signals as required.

The EMS in SimSES calculates the target power of the BESS $p_{\mathrm{BESS,target}}$ for each timestep for the selected application. The self-consumption increase, peak shaving, and FCR application investigated in this thesis are all modeled in SimSES directly, including the newly developed aging aware peak shaving strategy in Chapter 5.1. For the energy arbitrage application, the MPC framework developed in Chapter 4 is used, which determines the power target based on different optimization models but uses SimSES as an external package to model the system response for the next timestep.

2.3 Lithium-ion cells

Lithium-ion cells are composed of multiple layers of material wound up or stacked in a cell enclosure [122]. The electrolyte-filled layered structure of a typical cell consists of the anode current collector, the anode active material, the separator, the cathode active material, and the cathode current collector. The performance and aging behavior of a lithium-ion cell are strongly influenced by the anode active material, the cathode active material, the electrolyte, and the resulting interactions of those components [24, 123].

The most common materials for the cathode active material of lithium-ion cells that are used in BESSs are the three metal oxides NMC, NCA, and LFP [101]. While many existing BESSs have battery modules based on NMC cells, LFP cells are now more frequently used for new BESS installations [101]. The anode is often made out of graphite, however, commercial cells with silicon-graphite composite anodes are increasingly found [24]. The electrolyte usually consists of lithium salts, e.g., lithium hexafluorophosphate ($\mathrm{LiPF_6}$), in a carbonate solvent, such as mixtures of ethylene carbonate, dimethyl carbonate, propylene carbonate, diethyl carbonate, and/or ethyl methyl carbonate [124]. Different additives may be added to the electrolyte that can positively affect the cell lifetime [125].

Here, the aging behavior of lithium-ion cells is described Chapter 2.3.1 and Chapter 2.3.2. Following that, the cell and degradation modeling approaches used in this thesis are presented in Chapter 2.3.3.

2.3.1 Aging mechanisms and stress factors

Aging mechanisms of lithium-ion cells are often grouped based on their effect on the core components of a cell into four aging modes: loss of lithium inventory (LLI), loss of active material on the negative electrode ($\mathrm{LAM_{NE}}$), loss of active material on the positive electrode ($\mathrm{LAM_{PE}}$), and resistance increase (RI) [24, 25, 126]. LLI refers to the loss of previously cyclable lithium to side reactions, which reduces the available cell capacity [24, 25, 126]. Aging mechanisms that lead to RI increase the cell resistance or impedance, which decreases the available charge and discharge power in high and low SOC ranges, respectively, and increases energetic losses [24, 25]. $\mathrm{LAM_{NE}}$ and $\mathrm{LAM_{PE}}$ refer to the active material of the anode and the cathode not being available for the insertion of lithium anymore, which can reduce the available cell capacity as well [24, 25, 126]. Some authors propose additional degradation modes to summarize the effects of aging mechanisms, such as the loss of electrolyte [24] and stoichiometric drift [25].

Section 2 of the publication presented in Chapter 3 explains the relevant aging mechanisms of commonly used lithium-ion cells and their stress factors in detail. Here, a summary is provided. Figure 2.2 provides a schematic overview of the predominant aging mechanisms in lithium-ion cells with graphite anodes and metal oxide cathodes. On the anode, these mechanisms are SEI growth, lithium plating & dendrite growth, and particle cracking & graphite exfoliation. On the cathode, the predominant aging mechanisms depend on the used material [25]. For the commonly used metal oxides of NMC, NCA, and LFP, these mechanisms can be summarized as particle cracking, structural disordering, transition metal dissolution, and formation of the cathode electrolyte interface [24, 127]. Table 2.2 briefly describes these aging mechanisms on the anode and cathode and their impact. Further possible aging mechanisms not explained in detail here include electrolyte decomposition and loss, phase change to the cathode lattice, binder decomposition, and current collector corrosion [25, 126, 128].

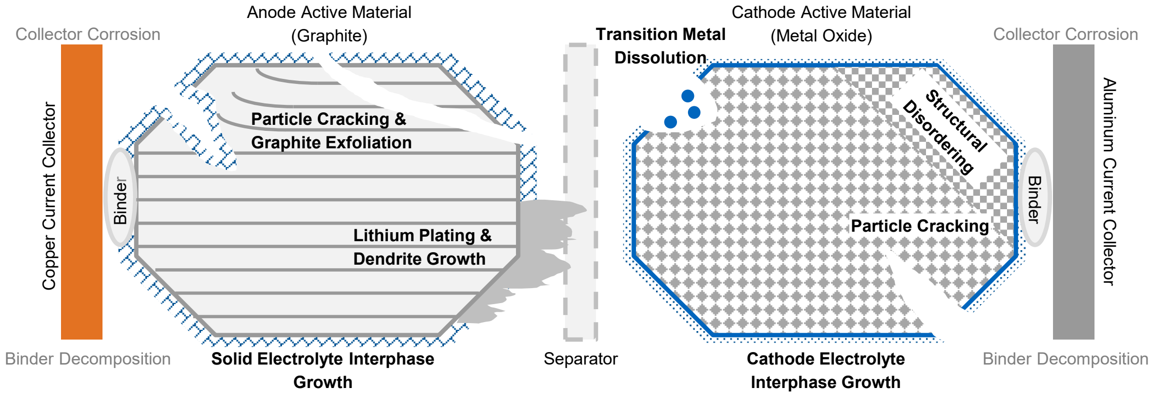

Figure 2.2: Schematic illustration of the predominant aging mechanisms in lithium-ion cells with graphite-based anodes and metal oxide cathodes [31].

The rate at which the above aging mechanisms progress depends on multiple factors, which include the active material type, material quality, production quality, and cell design parameters, such as the electrode thickness and the selected electrolyte additives [24]. Most notably, the degradation rate depends on the operating conditions and can, therefore, be directly affected through the operation strategy. Figure 2.3 depicts the relevant stress factors that affect calendar and cyclic aging in the main operation phase. A distinction is made with regards to the nonlinear aging behavior that can occur towards the EOL and is described in Chapter 2.3.2.

Calendar aging refers to those aging mechanisms that occur regardless of the battery being cycled or not, such as the continued growth of the SEI [31]. Calendar aging progresses with time and faster at high cell temperatures T^{cell} and a high SOC [34, 35].
Cyclic aging refers to those aging mechanisms that occur as a consequence of cycling a battery cell, such as particle cracking, solid electrolyte interphase re-formation at newly exposed anode surface areas, and lithium plating [31]. Cyclic aging progresses with the growing number of charge/discharge cycles, or FECs, and tends to accelerate when cycling at a high C^{rate} [38, 129] and a high DOC [130–132]. In addition, both high and low cell temperatures [129, 133] and cycling a battery cell in particularly straining SOC ranges that lead to high volume expansion of the anode material [34, 131, 134] can accelerate cyclic aging. Furthermore, the operating voltage window of a battery cell influences its

Table 2.2: Predominant anode and cathode aging mechanisms. Summarized from [31].

	Mechanism	Impact	Description
Anode	SEI growth	LLI, RI	• Passivation layer forming on the anode surface through reduction of the electrolyte. • Grows over lifetime and consumes lithium.
	Lithium plating	LLI	• Metallic lithium forming on the anode surface instead of intercalating into the anode. • Partially reversible through lithium stripping. • Dendrite growth may lead to internal shorts.
	Particle cracking & graphite exfoliation	$\mathrm{LAM_{NE}}$, LLI	• Caused by volume change, solvent co-intercalation, or gas-evolution. • Leads to electric contact loss ($\mathrm{LAM_{NE}}$), trapped lithium (LLI), and additional SEI forming at newly exposed anode surface area.
Cathode	Particle cracking	$\mathrm{LAM_{PE}}$, LLI	• Caused among others by volume change during cycling.
	Structural disordering	$\mathrm{LAM_{PE}}$, RI	• $\mathrm{Li^+}$ ions exchanging spots with transition metal ions in the cathode material.
	Cathode electrolyte interface growth	$\mathrm{LAM_{PE}}$, RI	• Formation of a passivation layer on the cathode surface, similar to the SEI but typically thinner.
	Transition metal dissolution	$\mathrm{LAM_{PE}}$	• Dissolution of transition metals from the cathode, which can migrate to the anode and cause additional SEI growth.

degradation rate. A high charge cut-off voltage [135, 136] and a low discharge cut-off voltage [135, 137] can lead to a significantly higher degradation rate.

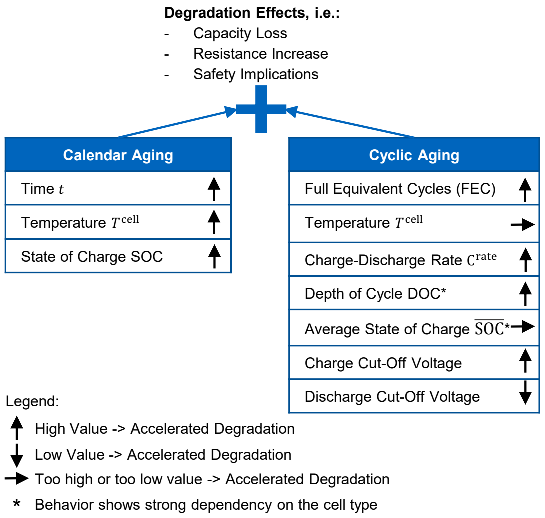

Figure 2.3: Relevant aging stress factors during the main operation phase and their effect [31].

However, calendar and cyclic aging stress factors are not independent of each other. The chronological order in which a cell is subjected to stress factors can affect its aging trajectory, which has been referred to as path-dependence [138–140]. Nevertheless, structuring stress factors into calendar and cyclic aging is a valuable concept for BESS operation, which is used as an underlying structure for many aging models [141, 142].

2.3.2 Aging over a cell's lifecycle and nonlinear aging

The possible dominant aging mechanisms vary over a lithium-ion cell's lifecycle as summarized in Figure 2.4. The initial SEI is formed during cell formation as one of the most costly manufacturing steps [143, 144], during which a significant amount of cyclable lithium is consumed. In the main operation phase, the SEI continues to grow, both over time and accelerated through cracking from volume expansion and contraction of the anode [31]. At the same time, particle cracking and contact loss from volume expansion lead to loss of active material (LAM) on both the anode and the cathode, and cathode structural disordering and transition metal dissolution may take place [31]. After extended periods of operation, lithium-ion cells often show a steep increase in their degradation rate. This is named the nonlinear aging phase by multiple authors [39, 145–147] and the onset of this phase is frequently labeled a *capacity knee* due to its form [148]. The rapidly decreasing capacity can coincide with a rapidly increasing cell resistance, i.e., a *resistance elbow* [148]. In their recent review, Attia et al. grouped the aging mechanisms and their interactions that can cause nonlinear aging into six *aging pathways*: lithium plating, electrode saturation, electrolyte and additive depletion, mechanical deformation, percolation-limited connectivity, and resistance growth, which are summarized in the following [148].

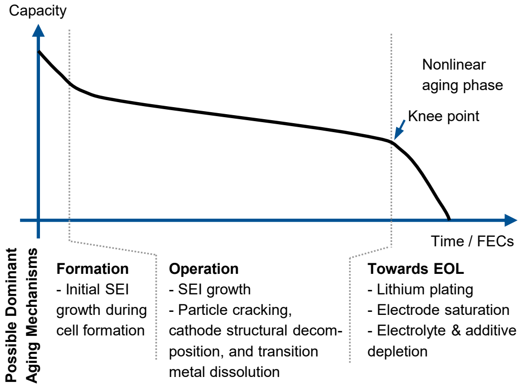

Figure 2.4: Schematic depiction of capacity loss and possible dominant aging mechanisms over a cell's life cycle for graphite anodes and metal oxide cathodes. Adapted from [31].

Lithium plating can occur on the anode when charging a lithium-ion cell at high currents, low temperatures, high SOC values, or a combination of all, with the specific limits being highly dependent on the cell design [148]. Lithium plating of pristine cells and its prevention is primarily a concern for fast-charging applications, e.g., for EVs [149]. Typical stationary BESS applications subject the cells to significantly lower charge rates than those that are used for EV fast charging [31, 53]. However, for BESSs, lithium plating of pristine cells can still be a concern in regions where cold climates lead to low cell temperatures [117, 150]. This must be prevented by derating the permissible charge power with the BMS for low cell temperatures combined with an appropriate TMS to heat the cells.

For aged lithium-ion cells, lithium plating can occur as a consequence of $\mathrm{LAM_{NE}}$ in two ways: First, lithium plating can occur if, due to excessive $\mathrm{LAM_{NE}}$, the negative electrode becomes the limiting component during charging and cannot accommodate the remaining lithium inventory anymore [151, 152]. This will lead to a steep increase in the degradation rate, which results in a capacity knee once the

anode becomes the limiting component [151, 152]. Second, the local current density of the remaining anode active material increases if $\mathrm{LAM_{NE}}$ takes place, which leads to lithium plating already occurring for lower cell charge currents and higher temperatures [148]. This can show as a capacity knee once significant lithium plating occurred during standard operating conditions [148].
In addition, lithium plating may occur in aged lithium-ion cells as a consequence of extensive SEI growth, which then leads to a self-reinforcing process of lithium plating [39, 145, 146]. The SEI reduces the anode's charge-transfer kinetics and can induce pore clogging, which is hypothesized to cause lithium plating even for moderate charging conditions in aged cells [39, 145, 146]. If the plated lithium is isolated by the formation of additional SEI around it, this leads to a further deterioration of the anode's charge-transfer kinetics and more pore clogging, which promotes additional lithium plating [145, 146].

Electrode saturation of the anode or the cathode can lead to a nonlinear aging trajectory as well [148]. As mentioned above, if the anode cannot accommodate the remaining lithium inventory due to excessive $\mathrm{LAM_{NE}}$, this can lead to lithium plating. For this to occur, $\mathrm{LAM_{NE}}$ needs to outpace LLI. Therefore, this trajectory is more likely when cycling at low temperatures since only slow LLI from SEI growth is expected for low temperatures, for poorly manufactured graphite anodes, and for graphite anodes with significant silicon content [148]. Similarly, a nonlinear aging trajectory may be observed once the cathode becomes the limiting component after extended cycling if $\mathrm{LAM_{PE}}$ outpaces LLI [148, 153, 154].

Electrolyte and additive depletion may lead to nonlinear aging by causing either LAM or lithium plating [148]. Consumption of the electrolyte and its additives can be driven by side reactions such as SEI growth or local gas generation [148]. Fang et al. proposed that local electrolyte dry-out can cause a positive feedback loop of LAM. The current density of the remaining active material increases after the electrolyte dry-out induced local LAM, which leads to further electrolyte consumption and additional LAM [155]. Sieg et al. showed that lower electrolyte contents can reduce the fast charging capability, which would result in an earlier onset of lithium plating [156]. In addition, multiple studies have shown that the depletion of the additive fluoroethylene carbonate can lead to a nonlinear aging trajectory for cells with silicon-containing anodes [157, 158].

The additional pathways proposed by Attia et al. are **mechanical deformation**, in which mechanical effects such as macro-scale deformation or micro-scale particle cracking lead to a positive feedback loop of LAM, **percolation limited connectivity**, a theory in which small connectivity changes of the porous electrode material may lead to significant LAM, and **resistance growth**, in which after a certain point resistance growth leads to a significant reduction of the available constant current discharge capacity based on the form of the open-circuit voltage (OCV) curve [148].

It should be noted that these pathways are not independent. Multiple pathways may occur simultaneously, or one pathway might accelerate another. For example, $\mathrm{LAM_{NE}}$ from electrolyte depletion, mechanical information, or percolation limited connectivity will lead to earlier saturation of the anode and to higher local current densities in the remaining anode active material, which both make the occurrence of lithium plating more likely.

Furthermore, lithium-ion cells, even of the same cell type and cycled under the same conditions, show a large degree of variance in the onset point of nonlinear aging [159, 160]. For the operation of BESSs, it is relevant by how far the nonlinear aging characteristics depend on the operating conditions. The summary of stress factors in Figure 2.3 for the main operation phase was primarily based on conclusions from the significant amount of cell aging studies that do not consider or observe nonlinear aging within their aging studies, e.g., well-cited studies by Schmalstieg et al. [34], Sarasketa-Zabala et al. [35, 36], Naumann et al. [37, 38], or Schimpe et al. [129]. The stress factors that influence the nonlinear aging phase have been less exhaustively investigated in the existing literature. Table 2.3 summarizes existing publications that observed nonlinear aging grouped by the stress factors that were shown to accelerate nonlinear aging.

Table 2.3: Summary of publications studying the effect of different stress factors on nonlinear aging. Based on [148].

Stress factor	**Nonlinear aging acceleration**	**Proposed mechanisms**	**Cell type and source**
Charge rate	high charge rate	Li plating	LFP/Gr [150], NCA/Gr [161, 162], NMC/Gr [163, 164]
		Li plating & SEI growth	LFP/Gr [160, 165], NMC/Gr [39, 138]
Discharge rate	low discharge rate	Li plating & SEI growth	NMC/Gr [39, 138], NCA/Gr [146]
	high discharge rate	SEI growth	LFP/Gr [166]
Voltage limits	high voltage	Electrolyte oxidation	NMC/Gr [167, 168]
	high DOC	Li plating	NMC/Gr [33, 39, 169], NMC+LMO/Gr [170], LFP/Gr [150]
		SEI growth	LFP/Gr [171]
	high $\overline{\mathrm{SOC}}$	Li plating	NMC+LMO/Gr [170]
	low $\overline{\mathrm{SOC}}$	SEI growth	NMC+NCA/Gr [172]
Temperature	T^{cell} above or below 35°C	Li plating & SEI growth	NMC/Gr [39]
		Li plating	NMC/Gr [164]
	T^{cell} above or below 25°C	Li plating & SEI growth	NMC+LMO/Gr [133]
	High T^{cell}	LAM	LFP/Gr [173]
	Low T^{cell}	Li plating	NMC/Gr and NMC+LMO/Gr [174]

All listed publications agree that high **charge rates** accelerate nonlinear aging. Schuster et al. observed that changing the charge rate from 1C to C/2 can extend the area of linear aging for the investigated NMC/Gr cells [39]. A reduction to C/5 resulted in no observed nonlinear aging. Other studies with NMC/Gr [138, 163, 164], LFP/Gr [150, 160, 165] and NCA/Gr [161, 162] cells confirm that lower charge rates can delay or prevent the onset of nonlinear aging. Lithium plating or lithium plating combined with SEI growth is hypothesized to lead to the observed behavior in all these studies.
The **discharge rate** has also been investigated as a stress factor of nonlinear aging, with inconsistent conclusions in the existing literature. While cells discharged at 0.5C and 1C showed a similar nonlinear aging trajectory, a discharge rate of 2C led to no nonlinear aging phase occurring in a study by Schuster et al. [39]. Similarly, Keil et al. [138] and Atalay et al. [146] observed that a higher discharge rate can delay the onset of nonlinear aging. On the other hand, Omar et al. observed an earlier onset of the nonlinear aging phase with higher discharge rates [166].
Voltage limits have been investigated in multiple variations in the existing literature as a stress factor for nonlinear aging. Aiken et al. observed nonlinear aging for NMC/Gr cells stored post-charging for 24 h at a charge cut-off voltage of 4.4 V compared to no observed nonlinear aging for cells stored

with a charge cut-off voltage 4.3 V [167]. In a study by Ma et al., varying the charge cut-off voltage of NMC/Gr cells between 4.1 V, 4.2 V, and 4.3 V impacted the onset of nonlinear aging as well. The cells with lower charge cut-off voltages exhibited the transition to nonlinear aging later or not at all [168]. In both studies, electrolyte oxidation was proposed to cause the observed behavior. In addition, multiple publications agree that a higher DOC generally accelerates the onset of nonlinear aging [33, 39, 150, 169–171]. For example, the NMC/Gr cells investigated by Ecker et al. showed a nonlinear aging phase when cycled at a DOC of 100 %, 80 %, and, 50 % around a $\overline{\text{SOC}}$ of 50 %, with an onset of the nonlinear aging phase after fewer FECs for larger DOC values. On the other hand, the cells cycled with a DOC of 20 %, 10 %, and 5 % around a $\overline{\text{SOC}}$ of 50 % showed no nonlinear aging phase [33]. For the NMC/Gr cells investigated by Schuster et al., a narrower operating voltage window (Δ1.2 V compared to Δ1.3 V) led to more FECs being completed before the onset of nonlinear aging and to the nonlinear aging phase starting at a lower remaining capacity [39]. Regarding the $\overline{\text{SOC}}$ as a stress factor for nonlinear aging, different results are found. Zhu et al. observed a nonlinear aging phase for NMC+NCA/Gr cells that were cycled at low SOC ranges, i.e., 5-25 %, 5-45 %, and 5-65 % SOC [172]. No nonlinear aging phase was observed in higher SOC ranges with the same DOC, e.g., 75-95 %, 55-95 %, and 35-95 % SOC [172]. Ma et al. observed an earlier onset of nonlinear aging when cycling in a SOC range of 60-100 % compared to 20-60 % [170].
Regarding the **temperature**, both too-high and too-low temperatures have been observed to accelerate nonlinear aging [39, 133, 164, 173, 174]. Schuster et al. and Zhang et al. found an earlier onset of nonlinear aging for temperature test points exceeding 35°C and less than 35°C [39, 164]. In a study by Waldmann et al., the optimal temperature with the slowest degradation behavior was at 25°C [133].

The operating conditions in the aforementioned publications are different between groups of cells but constant for each group of cells throughout the respective aging experiments. In his thesis, Schuster investigated adapting the operating conditions after the onset of nonlinear aging [40]. The voltage window, charge rate, and discharge rate were reduced past this point. It was concluded that the resulting capacity fade, while not as steeply nonlinear as before this adaption of operating conditions, is still more rapid than before the onset of nonlinear aging [40, Figure 31]. To the author's knowledge, no further publications investigate how adapting the operating conditions during an aging study affects the nonlinear aging phase. This will be investigated as part of Chapter 6.

2.3.3 Cell and degradation modeling

Two approaches are used in this thesis to model lithium-ion cells and their aging behavior. First, equivalent circuit models combined with semi-empirical aging models are employed in all publications from Chapter 3 to 6. Second, a physicochemical battery cell and aging model is developed in Chapter 6, specifically to model the nonlinear aging behavior towards the EOL. Both approaches are illustrated in Figure 2.5.

Equivalent circuit models are a widely used approach to model the behavior of lithium-ion cells [175]. These models typically consist of a voltage source that represents the OCV U^{OCV} of the battery for different SOC values as well as one resistance R^{i} and multiple RC circuits, to model the transient behavior of the terminal voltage U^{T} under load [176]. This type of equivalent circuit model is often called the *Thevenin model* [176], which can, for example, be parameterized through electrochemical impedance spectroscopy measurements [177]. Additional components such as inductors, constant phase elements, or Warburg impedances may be used as part of equivalent circuit models to achieve a better fit of the dynamic cell behavior [177].

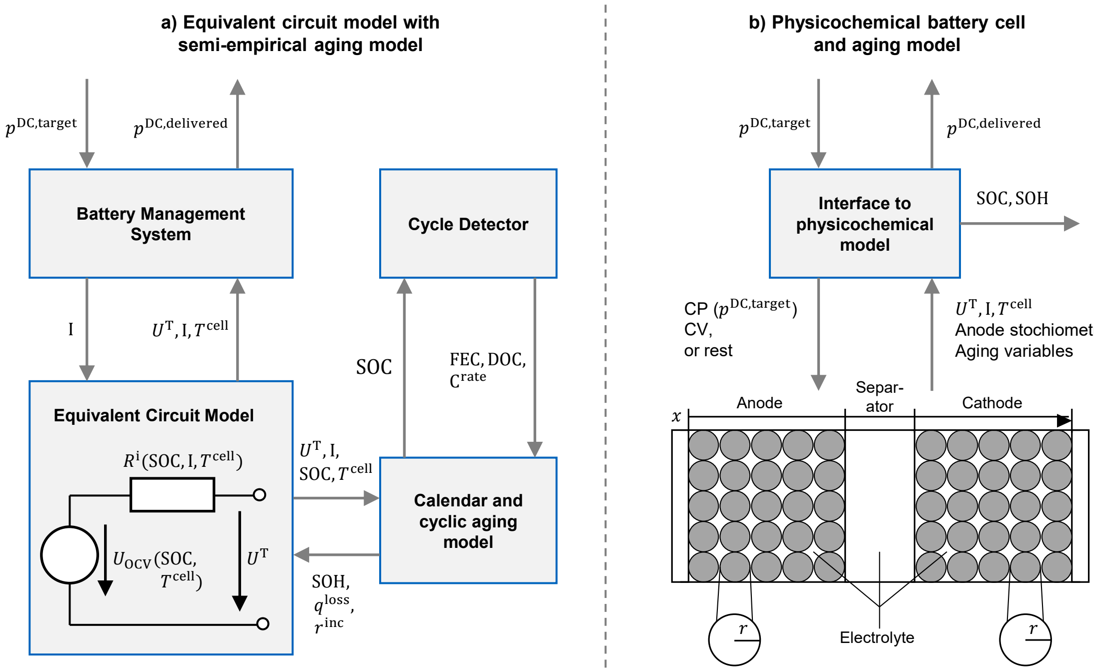

Figure 2.5: Schematic overview of the two lithium-ion cell modeling approaches used in this work as part of SimSES: a) Equivalent circuit models combined with semi-empirical degradation models, b) A physicochemical battery cell and aging model. The models receive a DC power target $p^{DC,target}$ from the upstream power electronics and return the delivered DC power $p^{DC,delivered}$, while logging relevant variables such as the current I, terminal voltage U^{T}, SOC, and SOH.

SimSES focuses on long-term system-level analyses and previously only provided simplified equivalent circuit models as highlighted in the left of Figure 2.5. These equivalent circuit models consist of a resistance based on 10 s DC pulse resistance measurements at different SOC values, currents I, and temperatures T^{cell}. While this approach is a simplification, it has been validated to deliver sufficient accuracy compared to measured BESS efficiency data by Schimpe et al. [115].

The equivalent circuit models are combined with semi-empirical degradation models. Semi-empirical degradation models are typically fitted to data from cell aging studies, in which a limited number of cells have been stored and cycled under accelerated aging conditions and different stress factors [31]. The prefix *semi-empirical* stems from these models relying on physics-inspired equations. A common approach is to model the total capacity loss [34–38, 129, 130, 178] and resistance increase [34, 37, 38] as a superposition of calendar and cyclic components:

$$q^{\mathrm{loss,total}} = q^{\mathrm{loss,cal}}(t, \mathrm{SOC}, T^{\mathrm{cell}}) + q^{\mathrm{loss,cyc}}(\mathrm{FEC}, \mathrm{C}^{\mathrm{rate}}, T^{\mathrm{cell}}, \overline{\mathrm{SOC}}, \mathrm{DOC}) \tag{2.5}$$

$$r^{\mathrm{inc,total}} = r^{\mathrm{inc,cal}}(t, \mathrm{SOC}, T^{\mathrm{cell}}) + r^{\mathrm{inc,cyc}}(\mathrm{FEC}, \mathrm{C}^{\mathrm{rate}}, T^{\mathrm{cell}}, \overline{\mathrm{SOC}}, \mathrm{DOC}) \tag{2.6}$$

Here, $q^{\mathrm{loss,total}}$ refers to the total capacity loss while $q^{\mathrm{loss,cal}}$ and $q^{\mathrm{loss,cyc}}$ refer to the calendar and cyclic components of capacity loss. Analogously, $r^{\mathrm{inc,total}}$, $r^{\mathrm{inc,cal}}$, and $r^{\mathrm{inc,cyc}}$ refer to the total, calendar, and cyclic relative resistance increase. Gasper et al. compiled an overview of algebraic functions that are commonly used to model calendar [142] and cyclic capacity loss [141]. For example, a square root dependence of calendar aging on time is frequently found, which can be traced back to approximating SEI growth as a diffusion-limited process [179]. In addition, the Arrhenius equation is often used to describe the temperature dependence of calendar aging [37, 129, 180–183], while Tafel-like equations may be used to describe the SOC or voltage dependence [129, 142, 182].

To apply cyclic aging models to load profiles with varying stress factors, a definition is needed of when one cycle ends and another starts to be able to determine the DOC, $\mathrm{C}^{\mathrm{rate}}$, and $\overline{\mathrm{SOC}}$ of that cycle. Naumann et al. and He et al. used a half-cycle counting algorithm in which a cycle is evaluated after every change of charge-discharge direction [38, 184]. After such a cycle is detected, the DOC and $\mathrm{C}^{\mathrm{rate}}$ are determined and the cyclic capacity loss is calculated. Another algorithm used for cycle counting is the rainflow-counting algorithm, which is commonly employed in material fatigue analysis [185, 186]. The algorithm sequences a data series of local maxima and minima into cycle loops and thereby allows the identification of individual half and full cycles, as well as their DOC, and $\mathrm{C}^{\mathrm{rate}}$ in a SOC profile [187, 188].

To validate the developed aging ware operation strategies and investigate the aging behavior in different stationary applications, the semi-empirical calendar [37] and cyclic [38] degradation models for LFP cells developed by Naumann et al. and implemented in SimSES are used in Chapter 3, 4, 5.1, and 5.2. In addition, the model by Schmalstieg et al. for NMC cells [34] is used as a reference in Chapter 3. Furthermore, the model developed by Gasper et al. [142] is presented in Appendix B and used in Chapter 5.2. For all the above, a half-cycle detector is used to identify individual cycles and calculate the relevant stress factors for cyclic aging. In Chapter 6, equivalent circuit models of a small cylindrical lithium-ion cell and a larger prismatic lithium-ion cell are used, which are derived from electrical cell characterizations without a coupled degradation model.

Physicochemical battery models typically consist of sets of differential equations that aim to describe the internal processes of the cell in addition to its external behavior. A common physicochemical modeling approach is the pseudo-two-dimensional (P2D) Newmann model [189, 190]. Its equations describe the internal processes of lithium-ion cells, such as the diffusion and migration of lithium-ions inside the electrolyte and active material as well as the charge transfer from the liquid to the solid phase [189, 190]. The name *P2D* refers to the x dimension, i.e., the through-plane dimension from anode to cathode, and r, i.e., the pseudo-dimension for the active material particles, compare Figure 2.5. With the standard P2D model, the in-plane dimensions are not modeled, but the area-specific current densities are scaled with the electrode area to achieve the quantities for the full cell. However, multiple P2D models can be coupled to, for example, investigate the current distribution in in-plane direction for different current collector designs [191, 192]. Next to aiding cell design, further practical applications of P2D models include deriving fast-charging profiles that avoid lithium plating based on modeling the minimum anode potential [191, 192].

In addition, multiple physicochemical modeling approaches can be found for modeling battery aging. For example, Ning et al. [193] and later publications by Pinson et al. [194] and Li et al. [195] provide models for the SEI growth on the anode. These publications use the single particle model (SPM), a reduction of the P2D model, which includes only one spherical particle for each electrode and no explicit electrolyte model. To model LAM, Sulzer et al. [154] described the change of the available active material fraction as a function of the hydrostatic particle stress, a simplification of previous models used by Reniers et al. [196] and Laresgoiti et al. [197]. In their review, Reniers et al. provided an overview and comparison of multiple physicochemical aging models that were published at the time [196]. Furthermore, O'Kane et al. recently proposed a combined modeling approach that

models the interactions of multiple previously published physicochemical models for individual aging mechanisms [198].
Most relevantly for this thesis, different physicochemical modeling approaches can be found in the literature that describe the nonlinear aging behavior toward the EOL. Multiple models can be found for the lithium plating pathway described in Chapter 2.3.2: Yang et al. proposed a model that includes SEI growth and lithium plating to describe nonlinear capacity fade towards the EOL [145]. Atalay et al. used a similar approach with SEI growth and lithium plating to describe the nonlinear capacity fade but with a multi-layer SEI model [146]. The model by Keil et al. encompasses SEI formation, SEI reformation resulting from particle cracking, as well as both lithium plating and lithium stripping [147]. All three aging models use the P2D Newman as a basis. Other contributions model the nonlinear capacity fade through $\mathrm{LAM_{NE}}$ from particle cracking [196] or $\mathrm{LAM_{PE}}$ from cathode dissolution [153] outpacing the SEI-induced LLI after extended cycling, i.e., the electrode saturation pathway. Park et al. published a model that describes nonlinear aging as per the electrolyte depletion pathway [199].
Based on the significant amount LLI observed for the cells under investigation, a physicochemical aging model following the lithium plating pathway and building on top of a P2D model is developed in Chapter 6. This physicochemical aging model is implemented in the open-source modeling environment Python Battery Mathematical Modelling (PyBaMM) [200] and linked to SimSES as indicated in the right of Figure 2.5. The interface in SimSES translates the power targets into constant power (CP), constant voltage (CV), or rest experiments for the physicochemical model. The interface then logs the relevant variables of the physicochemical model, such as the average terminal voltage and the average current, and aging variables, such as the amount of LLI, $\mathrm{LAM_{NE}}$, and $\mathrm{LAM_{PE}}$. Furthermore, the SOC is estimated based on the anode stoichiometry, and the SOH is determined in periodic intervals through virtual checkup experiments of the physicochemical model. The underlying code is open-source [201], and the physicochemical model and the interface are described in detail in Chapter 6.

For both modeling approaches, inhomogeneities, such as varying initial capacity or varying internal resistance between individual lithium-ion cells, are not modeled as part of this thesis. In SimSES, a lumped model is used in which the voltage and current are scaled based on the number of required serial and parallel connected cells to achieve the specified nominal energy for the full BESS [83].

2.4 Operation strategies

Several aspects must be considered for the optimal operation of energy storage systems: the system design and constraints, the application to be served, and technical properties, such as the degradation behavior and efficiency. The process of deriving the charge and discharge signals under consideration of technical constraints and economic benefit is referred to with multiple terms in the literature: energy management [29], scheduling [202], control [28], dispatch [72] or operation [203]. In this thesis, the overall approach is referred to as the operation strategy, and the specific methods used to derive the charge and discharge signals as scheduling methods. Chapter 2.4.1 provides an overview of scheduling methods, emphasizing the specific methods used in this thesis, and Chapter 2.4.2 summarizes methods that enable the aging aware operation of BESSs.

2.4.1 Scheduling methods

For the classification of scheduling methods, a first differentiation is made between rule-based operation strategies and optimization-based operation strategies [31]. Rule-based operation strategies are simple heuristics, such as discharging a BESS during load peaks for peak shaving up to a specific peak shaving limit and charging it again after the load peak until it is fully charged, as presented in Chapter 2.1.3. Another example is the greedy operation strategy for self-consumption increase with a home storage system presented in Chapter 2.1.4. In contrast, optimization-based operation strategies generally aim to determine the optimum of an objective function, sometimes called a fitting or reward function. Weitzel et al. grouped the scheduling methods for optimization-based operation strategies into three categories: exact solution approaches (e.g., linear programming), heuristics (e.g., reinforcement learning), and meta-heuristics (e.g., particle swarm optimization) [204].

Exact solution approaches are the most commonly used category of scheduling methods in the field of optimal operation of energy storage systems as concluded by Weitzel et al. [204]. As the name suggests, exact solution approaches generally allow finding the global optimum for a given optimization problem. This group of scheduling methods includes linear, quadratic, and nonlinear optimization problems, often with extensions to mixed integer problems. For example, a MILP is an optimization problem that includes a linear objective function and linear constraints with integer as well as continuous decision variables. Analogously, a mixed integer quadratic program refers to an optimization problem with a quadratic objective function and integer as well as continuous decision variables. As MILPs are the most commonly used scheduling method [204] and will be used in Chapter 4 and 6 of this thesis as well, a generic example for the operation of a BESS with a MILP is given below. A short overview of the other two categories of scheduling methods, i.e., heuristics and meta-heuristics, is provided as part of section 4 in Chapter 3.

$$\text{max.} \quad \sum_{t \in T} \mathbb{P}_t \tag{2.7}$$

$$\text{s.t.} \quad soc_t = soc_{t-1} + \frac{\Delta t}{E^{\text{batt}}} \cdot (p_t^{\text{ch}} \eta - \frac{1}{\eta} p_t^{\text{dis}}) \qquad \forall\, t \in T \backslash \{0\} \tag{2.8}$$

$$soc_{t=0} = \text{SOC}^{\text{start}} + \frac{\Delta t}{E^{\text{batt}}} \cdot (p_{t=0}^{\text{ch}} \eta - \frac{1}{\eta} p_{t=0}^{\text{dis}}) \tag{2.9}$$

$$0 \leq p_t^{\text{ch}} \leq P^{\text{AC,max}} \cdot x_t^{\text{ch}} \qquad \forall\, t \in T \tag{2.10}$$

$$0 \leq p_t^{\text{dis}} \leq P^{\text{AC,max}} \cdot (1 - x_t^{\text{ch}}) \qquad \forall\, t \in T \tag{2.11}$$

$$0 \leq soc_t \leq 1 \qquad \forall\, t \in T \tag{2.12}$$

$$x_t^{\text{ch}} \in \{0, 1\} \qquad \forall\, t \in T \tag{2.13}$$

$$p_t^{\text{ch}}, p_t^{\text{dis}}, soc_t \in \mathbb{R} \qquad \forall\, t \in T \tag{2.14}$$

Here, Equation 2.7 maximizes the sum of the profit gained in the respective application $\mathbb{P}_t$ for every timestep t as part of the optimization horizon T. Equation 2.8 combined with 2.9 is a simple modeling approach for the energy-based soc_t while considering a here constant charge and discharge efficiency η. $\text{SOC}^{\text{start}}$, E^{batt}, and Δt are the SOC at the beginning of the optimization horizon, the remaining rated energy of the BESS after accounting for degradation, and the optimization timestep width, respectively. p_t^{ch} and p_t^{dis} are the resulting charge and discharge power for every timestep. Equation 2.10 to 2.12 denote the upper and lower limits for the continuous decision variables soc_t, p_t^{ch}, and p_t^{dis} with $P^{\mathrm{AC,max}}$ being the maximum charge and discharge power of the BESS. The integer decision variable x_t^{ch} ensures that in every timestep, the optimal solution only includes charging or discharging, not both simultaneously. An example of the objective function in the case of performing energy arbitrage is given below:

$$\mathbb{P}_t = \sum_{t \in T} \left((p_t^{\mathrm{dis}} - p_t^{\mathrm{ch}}) \cdot \Delta t \cdot c_t^{\mathrm{id}} \right) \tag{2.15}$$

Here, the profit is generated by charging during low and discharging during high electricity prices c_t^{id} on the intraday market. Note that the charge and discharge efficiency is already considered through Equation 2.8 and 2.9. Similar but often more elaborate than this illustrative example, MILPs have been formulated for a variety of other applications, such as peak shaving with BESSs by Hou et al. [205] and operating BESSs combined with diesel generators in a microgrid by Weitzel et al. [29]. Different open-source and commercial solvers are available for solving such optimization problems. The commercial solver by Gurobi is used in the later parts of this thesis [206]. When it comes to the mathematical algorithms behind these solvers, the *Simplex algorithm* is frequently used for linear programs combined with methods such as *Branch and Bound* to solve MILPs [207]. Notably, in the simplified example above, using Equation 2.15 as the objective function would allow the reduction of the problem from a MILP to a linear program by omitting the binary variable x_t^{ch}, since the optimal solution would necessarily be to either charge or discharge the BESS at any given timestep t [70].

The above modeling approach in Equation 2.8 and 2.9 is a simplification of the actual behavior of a BESS that is often referred to as a *bucket model* [196], *power-energy model* [208], or *energy reservoir model* [209]. It neglects multiple effects that are relevant for operating a BESS, such as that the discharge power may be limited in high SOC ranges while charging and in low SOC ranges while discharging based on the operating voltage window of the battery cells [209]. Another relevant effect not represented by this model is that losses on a battery cell level are higher in lower SOC ranges, since more current is required to deliver the same requested power due to the lower OCV [210]. In addition, the AC/DC converter has varying efficiencies for different power ranges and usually especially low efficiency values in low power ranges [121].

To include more accurate BESS models as part of the scheduling method, different approaches are found in the literature. First, one may update the mathematical formulation of the BESS to a more accurate model, e.g., by including an equivalent circuit model as part of the optimization problem. This, however, makes the optimization problem nonlinear such that standard MILP solvers will not be able to solve it [208]. Instead, to find the exact solution, more computationally expensive solvers, such as *IPOPT*, must be employed to solve the resulting nonlinear optimization problem [208, 211]. Reniers et al. compared the performance of three different BESS optimization model types for an energy arbitrage application: a bucket model, an equivalent circuit model, and a SPM. While for the bucket model, a standard linear solver was sufficient, the nonlinear solver used for the equivalent circuit model required 1000 times more computation time than the solver for the bucket model, and the nonlinear solver used for the SPM resulted in another increase of the computation time by a factor of 10 compared to the equivalent circuit model [212]. The resulting optimization problems become even more complex and computationally expensive in the case of a mixed integer nonlinear problem [213], i.e., when integer variables are required as part of the nonlinear problem, which is often the case for modeling multi-use applications of BESSs [63].

Instead of aiming for an exact solution approach, meta-heuristics such as particle swarm optimization or heuristics such as reinforcement learning may be used at the risk of finding a local and not a global optimum [204]. Furthermore, these scheduling methods come with their own specific limitations. For example, the reinforcement learning agent by Cao et al. was trained on an equivalent circuit model, including a semi-empirical degradation model, and is reported to be highly computationally efficient after the initial training is completed [214]. However, the modeled action space for charging and discharging the BESS only includes discrete values, i.e., a charge or discharge power of 0, $0.5P^{\mathrm{AC,max}}$, or $1P^{\mathrm{AC,max}}$ [214], which is a crude simplification.
In order to combine more elaborate BESS models with the simplicity and computational efficiency of linear programming and MILPs, linearization techniques have been frequently used in existing literature. For example, Hesse et al. [215] and Kumtepeli et al. [210] each used linearization techniques to model the efficiency and aging behavior of BESSs as part of a MILP. Nevertheless, these linearizations are a simplification and come with inherit linearization errors [204].

With a variety of different scheduling methods for BESS operation available to solve the same problem, i.e., when to optimally charge and discharge a BESS in given stationary applications, accessible frameworks to benchmark the performance of different methods can create comparability. In addition, many publications treat the results of the scheduling methods as the ground truth for the subsequent evaluation, despite the simplified modeling of the BESS that was required to solve the optimization problem [27, 204, 215]. A potential solution is the concept of MPC, which was developed in the 1970s in the process control industry [216]. The basic principle is to build a model for the predicted behavior of a system, to represent the required behavior of the system using a cost function, and to minimize this cost function to produce the actual command to the system [216]. Updated measurements from the system then act as input for the optimization of the following step [216]. If the output of optimization-based scheduling methods is used to operate a real BESS, this falls under the loose definition of MPC. This concept can also be applied to benchmarking and comparing different scheduling methods through pure simulation. In Chapter 4, an MPC framework is proposed specifically for aging aware operation strategies. The basic principle is to implement a second, more accurate BESS model that validates the scheduling method's output and is not constrained to the simplified modeling approaches that common scheduling methods require.

Lastly, different approaches for handling uncertainty can be found as part of scheduling methods. In the example of Equation 2.15, knowledge of the future electricity price time series for the full optimization horizon is assumed. Perfect foresight of the price may be the case for time-of-use electricity pricing but not when trading electricity on an exchange such as the EPEX. Instead, different electricity price forecasting methods may be used, a research field for which a significant body of scientific literature can be found [217, 218]. Lago et al. grouped electricity forecasting methods into statistical and deep learning approaches in their review [217]. In terms of the output of the forecasts, Weron et al. differentiated between point forecasts, which provide one value for the electricity price for a given timestep, and probabilistic forecasts, which provide prediction intervals or prediction densities [218]. Point forecasts, e.g. for the day-ahead auction of the following day, could be implemented as part of Equation 2.15 to solve the scheduling problem as a MILP. However, a better result can often be expected when accounting for the uncertainty of the actual outcome and the inherent errors of the forecast as part of the scheduling method [204]. Stochastic dynamic programming, for example, performs a full enumeration of every scenario, e.g., different electricity price scenarios from probabilistic forecasts, which, however, leads to a high computational effort [204]. Robust optimization, on the other hand, aims to find the optimal solution for the worst-case scenario, which can, however, lead to an over-conservative solution [204]. In Chapter 4 and 6, perfect foresight of the ID-1 electricity price index is assumed to create a generic energy arbitrage application that showcases the different aging aware operation strategies. This is considered to be a conservative assumption in terms of the calculated profit despite assuming perfect foresight since, for real-time bidding, one may achieve higher sell and lower buy prices than the ID-1 price and may place additional bids that are compensated before execution by the BESS, which can generate additional profit [70]. This was also confirmed when comparing the simulated energy arbitrage profit to data reported from industry partners in the field of BESS operation. Furthermore, in Chapter 5.1, a rule-based aging aware operation strategy for peak shaving applications is proposed that includes a method for managing the uncertainty of load forecasts.

2.4.2 Aging aware operation

A significant number of individual contributions can be found that focus on the aging aware operation of BESSs. This body of literature is reviewed and categorized in detail in Chapter 3. Here, a brief summary of the different methods is provided. Furthermore, a generic example for aging aware operation is presented that builds on top of the exemplary MILP for operating a BESS from Equation 2.7 to 2.13 and showcases the linearization method used in Chapter 4.

Figure 2.6 shows the categorization of different methods for the aging aware operation of BESSs. A first differentiation is made based on the scheduling method. Rule-based scheduling methods generally use rule-based methods to incorporate degradation into the operation strategy. For example, Angenendt et al. proposed an operation strategy for home storage systems in which the BESS is charged during the day only up to the energy level that is expected to be needed at night, based on load forecasts [93]. Thereby, the average SOC and calendar aging are reduced [93].

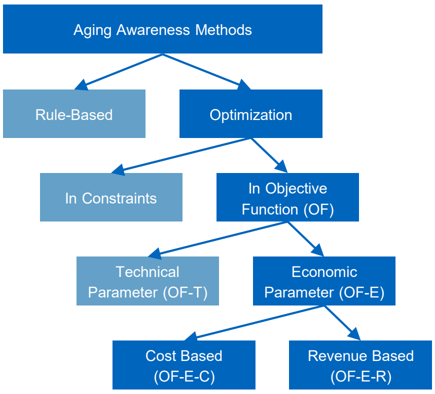

Figure 2.6: Classification of different methods for the aging aware operation of BESSs [31].

However, most publications in the field of aging aware operation use optimization-based scheduling methods [31]. One method to enable aging aware operation as part of an optimization-based scheduling method is through additional fixed constraints [27, 62, 219, 220]. For example, the effect of limiting the DOC in different SOC ranges was studied by Perez et al. in a multi-use application with energy arbitrage and balancing power [220]. It was found that for the optimal SOC range, the annual average gross revenue was reduced by 18 %, but the BESS lifespan was expected to double [220]. More commonly, degradation effects are considered as part of the objective function, either as a technical parameter or as an economic parameter [31]. With regards to technical parameters, the capacity loss or SOH reduction can be added to the objective function with scaling factors that are to be set by the operator [203, 221]. In the context of economic parameters, a monetary value can be assigned to the degradation effects, i.e., the capacity loss or decreasing SOH, and added to the remaining objective function, which describes the profit gained in the given application. For revenue-based economic parameters, this is a form of expected future revenue. For example, Liu et al. included a degradation-dependent future resale value of the battery in their objective function [222]. Abdulla et al. used the cumulative past savings that were generated by the BESS to determine a monetary value for capacity loss and included this value in their objective function [223].

The most commonly found method for aging aware operation in the existing literature is to define a cost-based economic parameter, i.e., *aging cost*, and include it as part of the objective function [31]. This allows to link the short-term scheduling problem to long-term degradation effects:

$$\max \sum_{t \in T} \left(\mathbb{P}_t - \mathbb{C}_t^{\text{aging}} \right) \tag{2.16}$$

Here, $\mathbb{C}_t^{\text{aging}}$ is the total aging cost for timestep $t \in T$. The total aging cost $\mathbb{C}_t^{\text{aging}}$ is then either calculated based on each percentage point of SOH loss in each time step Δsoh_t as in Equation 2.17 [15, 28, 30, 72, 204] or based on the number of FECs in each time step Δfec_t as in Equation 2.18 [62, 63, 224–226].

$$\mathbb{C}_t^{\text{aging}} = \frac{c^{\text{aging}} \cdot E^{\text{n}}}{1 - \text{SOH}^{\text{EOL}}} \cdot \Delta soh_t \tag{2.17}$$

$$\mathbb{C}_t^{\text{aging}} = \frac{c^{\text{aging}} \cdot E^{\text{n}}}{\text{FEC}^{\text{EOL}}} \cdot \Delta fec_t \tag{2.18}$$

Here, SOH^{EOL} and FEC^{EOL} represent the SOH threshold and number of FECs after which the EOL of the battery is reached. E^{n} is the nominal battery capacity at the beginning of life in kWh. The aging cost c^{aging} in EUR per kWh is then typically set to a cost value that relates to the battery system, such as the full storage system investment cost [63, 204, 226], battery investment cost [187, 205, 227], battery replacement cost [28, 30, 228], battery cell replacement cost [15, 224], or generic battery cost [72, 214, 225]. In Chapter 4, it is shown that increased lifetime profit can be achieved by determining the *optimal aging cost* based on the application and BESS characteristics opposed to this prevalent approach. For illustrating the later used linearization techniques, it is assumed that the FEC dependence of cyclic aging and the SOC dependence of calendar aging is aimed to be added to a MILP through aging cost, such as in the below optimization problem:

$$\max. \quad \sum_{t \in T} \left(\mathbb{P}_t - \mathbb{C}_t^{\text{aging}} \right) \tag{2.19}$$

$$\text{s.t.} \quad \mathbb{C}_t^{\text{aging}} = \frac{c^{\text{aging}} \cdot E^{\text{n}}}{1 - \text{SOH}^{\text{EOL}}} \cdot \Delta soh_t \qquad \forall\, t \in T \tag{2.20}$$

$$\Delta soh_t = q_t^{\text{loss,cal}} + q_t^{\text{loss,cyc}} \qquad \forall\, t \in T \tag{2.21}$$

$$q_t^{\text{loss,cyc}} = \alpha^{\text{cyc}} \cdot \frac{(p_t^{\text{ch}} + p_t^{\text{dis}}) * \Delta t}{2 \cdot E^{\text{n}}} \qquad \forall\, t \in T \tag{2.22}$$

$$\Delta soh_t, q_t^{\text{loss,cyc}}, q_t^{\text{loss,cal}}, \mathbb{C}_t^{\text{aging}} \in \mathbb{R} \qquad \forall\, t \in T \tag{2.23}$$

Here, $q_t^{\text{loss,cal}}$ and $q_t^{\text{loss,cyc}}$ denote the relative calendar and cyclic capacity loss. $q_t^{\text{loss,cyc}}$ is defined as in Equation 2.22 with α^{cyc} denoting the relative capacity loss per completed FEC. The previously introduced Equation 2.8 to 2.14 may be used as additional constraints to describe the BESS as a bucket model. For convex functions, the SOC dependence of the calendar capacity loss may be represented through sets of individual lines as additional constraints:

$$q_t^{\text{loss,cal}} \geq a_k \cdot soc_t + b_k \qquad \forall\, t \in T, \forall\, k \in K \tag{2.24}$$

The index set K denotes the lines used for the linearization with their slopes a_k, y-intercepts b_k, and $k \in K$. Since the aging cost is part of the objective function, the optimal solution will include a $q_t^{\text{loss,cal}}$ value that lies on the applicable line for the present SOC value, as indicated in the left subplot of Figure 2.7. The more individual lines $k \in K$ are used, the lower the linearization error that can be achieved, i.e., the difference between the original convex function and the sets of lines used to approximate it [29]. This approach, however, only works for convex functions. Many degradation models include non-convex functions, such as the cubic dependence of calendar capacity loss on the SOC in the model by Naumann et al. [37]. For non-convex functions, special ordered sets (SOSs) of type 2 may be used for linearization [229]. A SOS of type 2 is a set of continuous variables, which are often denoted λ, out of which a maximum of two variables can be nonzero and those two variables need to be consecutive in their ordering [229]. While these SOS type 2 variables are continuous, they nevertheless require a MILP solver [206]. Linearization of a non-convex calendar capacity loss function that depends on the SOC may be performed as below with SOS type 2 variables:

$$\sum_{i \in I} \lambda_{t,i}^{\text{cal}} \cdot X_i^{\text{cal}} = soc_t \qquad \forall\, t \in T \tag{2.25}$$

$$\sum_{i \in I} \lambda_{t,i}^{\text{cal}} \cdot Y_i^{\text{cal}} = q_t^{\text{loss,cal}} \qquad \forall\, t \in T \tag{2.26}$$

$$\sum_{i \in I} \lambda_{t,i}^{\text{cal}} = 1 \qquad \forall\, t \in T \tag{2.27}$$

$$0 \leq \lambda_{t,i}^{\text{cal}} \leq 1, \lambda_{t,i}^{\text{cal}} \in \mathbb{R} \qquad \forall\, t \in T, \forall\, i \in I \tag{2.28}$$

$\lambda_{t,i}^{\text{cal}}$ with $t \in T$ and $i \in I$ are continuous variables that are used to represent the linearized calendar aging function in the optimization model. The set of variables $\lambda_{t,i}^{\text{cal}}$ with $i \in I$ is implemented as one SOS of type 2 for each $t \in T$. X_i^{cal} represents the linearization points for the SOC and Y_i^{cal} the linearization points for the associated calendar capacity loss at that SOC, as indicated in the right subplot of Figure 2.7. The index set I denotes the total set of linearization points used with $i \in I$.

For example, let us assume the SOC dependence of calendar aging is linearized in eleven individual points over the SOC range from 0 to 1: $\{X_0^{\text{cal}} = 0, X_1^{\text{cal}} = 0.1, ..., X_{10}^{\text{cal}} = 1.0\}$, compare Equation 2.25. The associated calendar capacity loss values for these SOC values are denoted as Y_i^{cal}: $\{Y_0^{\text{cal}}, Y_1^{\text{cal}}, ..., Y_{10}^{\text{cal}}\}$, compare Equation 2.26. Equation 2.27 ensures that the sum of those two consecutive values of $\lambda_{t,i}^{\text{cal}}$ which are nonzero is equal to 1. Let us further assume that the solution to the scheduling problem in timestep t' yields a SOC value of $soc_{t'} = 0.125$. To satisfy Equation 2.25 and 2.27, the resulting values for the SOS type 2 variables in timestep t' then have to be $\lambda_{t',1} = 0.75$, $\lambda_{t',2} = 0.25$, and $\lambda_{t',i} = 0 \;\; \forall\, i \in \{0, 3, 4, ..., 10\}$. This then yields the respective calendar capacity loss at timestep t' as a linear interpolation of two linearization points from Equation 2.26: $q_{t'}^{\text{loss,cal}} = 0.75 \cdot Y_1^{\text{cal}} + 0.25 \cdot Y_2^{\text{cal}}$.

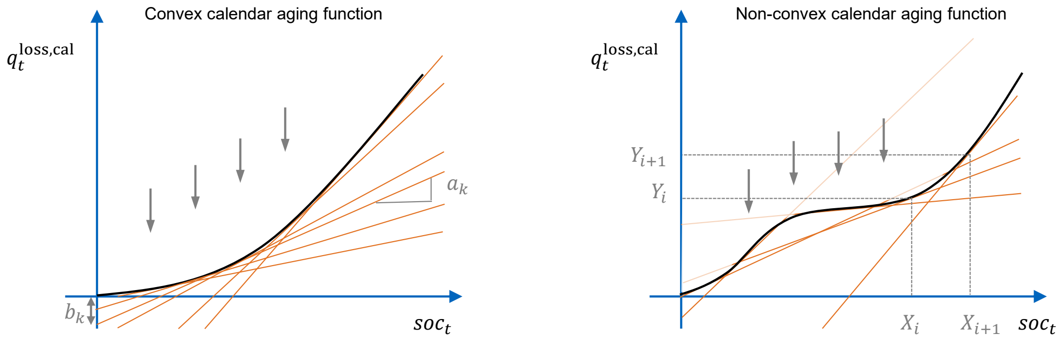

Figure 2.7: Left: Convex calendar aging function, which can be linearized through a set of lines with slope a_k and y-intercept b_k for each line $k \in K$. Right: Non-convex calendar aging function which can be linearized using a SOS of type 2 and the linearization points X_i and Y_i for each $i \in I$.

Similar to this example, SOSs of type 2 are used in Chapter 4 to linearize the calendar and cyclic aging functions.

3 Aging aware operation of lithium-ion battery energy storage systems: A review

In this chapter, the peer-reviewed journal publication *Aging aware operation of lithium-ion battery energy storage systems: A review* is presented. A significant amount of literature can be found on the aging behavior of lithium-ion batteries, aging stress factors, and degradation modeling approaches. In addition, multiple publications propose methods for the aging aware operation of BESSs, typically focused on one specific cell type and application. This review provides an overview of relevant aging mechanisms, their stress factors, and degradation modeling approaches. The key aspects of those topics for the aging aware operation of BESSs are derived. Following that, the existing literature in the field of aging aware operations of BESSs is summarized and categorized. Lastly, in a case study using the in-house developed and open-source SimSES, the most relevant aging stress factors are investigated for typical stationary applications. The highlights of this review paper are summarized below:

- **Aging mechanisms and stress factors**: An overview of the relevant aging mechanisms for typical lithium-ion cells with graphite anodes and metal-oxide cathodes (NMC, NCA, and LFP), is provided. The relevant aging mechanisms on the anode include SEI growth, particle cracking & graphite exfoliation, and lithium plating & dendrite growth. On the cathode, the relevant aging mechanisms are transition metal dissolution, particle cracking, cathode electrolyte interphase growth, and structural disordering. The aging stress factors are structured into calendar aging stress factors, i.e., time, temperature, and SOC, and cyclic aging stress factors, i.e., FECs, temperature, $\mathrm{C}^{\mathrm{rate}}$, DOC, $\overline{\mathrm{SOC}}$, and the operating voltage window.
- **Degradation modeling:** Degradation models are categorized into empirical, semi-empirical, and physicochemical degradation models. The different modeling approaches are compared, examples are provided, and requirements are defined for degradation models that are meant to be used for the aging aware operation of BESSs.
- **Aging aware operation:** First, the different categories of scheduling methods are presented, i.e., heuristics, meta-heuristics, and exact solution approaches. Furthermore, typical BESS applications are briefly summarized. Using the above categories of aging stress factors, degradation models, scheduling methods, and applications, the existing literature in the field of aging aware operation is summarized in a comprehensive tabular form. In addition, different methods for accounting for aging as part of the operation strategy are defined based on the literature.
- **Case study:** Using SimSES [83], see Appendix A, the most relevant aging stress factors are identified and quantified for the three exemplary BESS applications of self-consumption increase with a home storage system, FCR, and peak shaving. The adapted version of SimSES, as well as the simulation results, are available open-source[1] [230].

The literature shows that most publications in the field of aging aware operation rely on semi-empirical degradation models and consider only a subset of the calendar and cyclic aging stress factors. In addition, MILPs are a frequently used scheduling method in this field. To account for aging as part

---

[1] Code and simulation results are publicly available: https://doi.org/10.14459/2022mp1652796

of the operating strategy, defining aging cost was found to be the most commonly used method. The case study shows that a) in FCR, attention should be paid to the low DOC and C^{rate} when selecting a degradation model; b) in self-consumption increase, the high DOC and C^{rate} significantly affect cyclic aging; c) in peak shaving operation, the SOC is the most relevant stress factor and leads to significant calendar aging.

This comprehensive review was aimed at summarizing the state of the art and distributing this knowledge to a large audience in both industry and academia. In addition, the findings served as a starting point for the novel contributions of the four additional research papers of this thesis.

CRediT author statement:

- **Nils Collath:** Conceptualization, Investigation, Methodology, Project administration, Software, Visualization, Writing – original draft, Writing – review & editing
- **Benedikt Tepe:** Investigation, Visualization, Writing – original draft, Writing – review & editing, Software
- **Stefan Englberger:** Writing – original draft, Writing – review & editing
- **Andreas Jossen:** Funding acquisition, Writing – review & editing
- **Holger Hesse:** Supervision, Writing – original draft, Writing – review & editing

Aging aware operation of lithium-ion battery energy storage systems: A review

Nils Collath, Benedikt Tepe, Stefan Englberger, Andreas Jossen, Holger Hesse

Journal of Energy Storage 55, p. 105634, 2022

Permanent weblink:
https://doi.org/10.1016/j.est.2022.105634

Journal of Energy Storage 55 (2022) 105634

Contents lists available at ScienceDirect

Journal of Energy Storage

journal homepage: www.elsevier.com/locate/est

Review Article

Aging aware operation of lithium-ion battery energy storage systems: A review

Nils Collath [a,*], Benedikt Tepe [a], Stefan Englberger [a], Andreas Jossen [a], Holger Hesse [a,b]

[a] Technical University of Munich, TUM School of Engineering and Design, Department of Energy and Process Engineering, Institute for Electrical Energy Storage Technology, Arcisstr. 21, 80333 Munich, Germany
[b] Kempten University of Applied Sciences, Bahnhofstr. 61, 87435 Kempten, Germany

ARTICLE INFO

Dataset link: https://doi.org/10.14459/2022mp1652796

Keywords:
Battery energy storage system
Lithium-ion
Degradation model
Aging
Operation
Optimization

ABSTRACT

The amount of deployed battery energy storage systems (BESS) has been increasing steadily in recent years. For newly commissioned systems, lithium-ion batteries have emerged as the most frequently used technology due to their decreasing cost, high efficiency, and high cycle life. As a result of a multitude of cell internal aging mechanisms, lithium-ion batteries are subject to degradation. The effects of degradation, in particular decreasing capacity, increasing resistance, and safety implications, can have significant impact on the economics of a BESS. Influenced by aging stress factors such as the state of charge, charge–discharge rate, cycle count, and temperature, the extent of degradation is directly affected by the operating conditions. Significant amount of literature can be found that focuses on aging aware operation of BESSs. In this review, we provide an overview of relevant aging mechanisms as well as degradation modeling approaches, and deduce the key aspects from the state of the art in those topics for BESS operation. Following that, we review and categorize methods that aim to increase BESS lifetime by accounting for battery degradation effects in the operation strategy. The literature shows that using empirical or semi-empirical degradation models as well as the exact solution approach of mixed integer linear programming are particularly common for that purpose, as is the method of defining aging costs for the objective function. Furthermore, through a simulation case study, we identify the most relevant stress factors that influence degradation for the key applications of self consumption increase, peak shaving, and frequency containment reserve.

1. Introduction

The installed capacity of BESSs has been increasing steadily over the last years. These systems are used for a variety of stationary applications that are commonly categorized by their location in the electricity grid into behind-the-meter, front-of-the-meter, and off-grid applications [1,2]. In behind-the-meter applications such as peak shaving or as home storage systems, BESSs provide cost savings for the electricity consumer. For front-of-the-meter applications, like energy arbitrage or balancing power provision, revenue generation in the respective energy and power markets is the primary motive for installation of a BESS. Lastly, in off-grid/microgrid applications, BESSs combined with renewable energy sources can be a cost competitive option over solely relying on diesel generators [1]. For the year of 2020, the International Energy Agency estimated the globally installed power of BESSs to 17 GW [3]. While estimates and forecasts for the currently installed capacity and future growth vary, the agreed upon trajectory in the vast majority of reports and studies is strongly upwards [4–6]. This growth in battery energy storage systems is fueled by technology advances and cost reductions for lithium-ion cells, which are now the predominant battery technology used for new installations [5,6].

Despite cell cost reductions, batteries remain the primary cost component for BESSs [7]. Due to a multitude of cell internal aging mechanisms, lithium-ion cells are subject to degradation, which manifests itself in capacity loss, cell resistance increase, as well as safety implications. These degradation effects, most notably capacity loss, can have a significant impact on the profitability of a BESS [8,9]. Aging mechanisms for lithium-ion cells have received significant attention in scientific literature, with multiple reviews available on this subject [10–13]. It is well known and validated through cell aging studies that the rate of degradation depends on external stress factors such as the temperature (T), DOC, SOC, and the C_{rate} [14–19].

With the increasing adoption of electric vehicles (EVs), multiple reviews can be found that focus on the effects of battery degradation specifically for EVs [20,21]. Woody et al. compiled guidelines to extend

---

[*] Corresponding author.
E-mail address: nils.collath@tum.de (N. Collath).

https://doi.org/10.1016/j.est.2022.105634
Received 23 April 2022; Received in revised form 1 August 2022; Accepted 3 September 2022

Abbreviations

BESS	Battery energy storage system
BP	Balancing power
C_{rate}	Charge-discharge rate
DOC	Depth of cycle
DP	Dynamic programming
E	Exact solution approaches
EA	Energy arbitrage
EOL	End-of-life
EV	Electric vehicle
FCR	Frequency containment reserve
FEC	Full equivalent cycle
H	Heuristics
LAM_{NE}	Loss of active material on the negative electrode
LAM_{PE}	Loss of active material on the positive electrode
LFP	Lithium iron phosphate
LLI	Loss of lithium inventory
MH	Meta-heuristics
MILP	Mixed integer linear programming
NCA	Lithium nickel cobalt aluminum oxide
NLP	Nonlinear programming
NMC	Lithium nickel manganese cobalt oxide
PS	Peak shaving
PSO	Particle swarm optimization
PV	Photovoltaic
RI	Resistance increase
SCI	Self consumption increase
SEI	Solid electrolyte interphase
SimSES	Simulation Tool for Stationary Energy Storage Systems
SOC	State of charge
SPM	Single particle model
V2G	vehicle-to-grid

the service life for lithium-ion batteries used in EVs, laptops, powertools, and cellphones [22]. Compared to these applications, BESSs and their operation have several key differentiating properties with regards to battery degradation:

- The primary objective in most stationary BESS applications is either a form of revenue generation, like it is the case for energy arbitrage or balancing power provision, or cost reduction, such as for peak shaving or home storage systems [23,24]. This provides an incentive to directly account for the costs related to battery degradation in the operation strategy of BESS through appropriate models. For applications such as cellphones or EVs, there tend to be higher availability requirements, caused by consumer needs for telecommunication or motion, respectively [22].
- The cycle life requirements for many stationary applications significantly exceed those of electric vehicles, especially privately used ones: For residential storage systems used for self-consumption increase and large-scale storage systems used for frequency containment reserve, Kucevic et al. identified a yearly number of FECs in the range of 200 to 300 FECs per year, depending on system sizing [25]. In terms of calendar life, large-scale BESSs are typically planned as long-term assets of up to decades, opposed to short lived consumer goods such as cellphones and laptops.

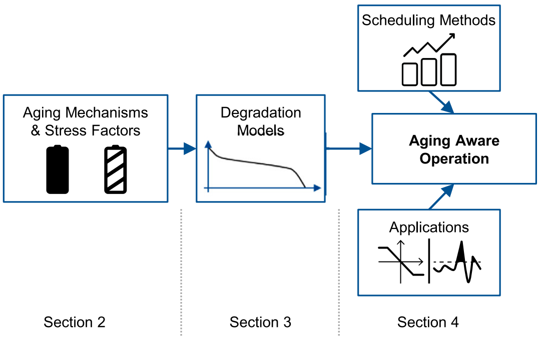

Fig. 1. Schematic overview of this contribution's structure.

- Stationary applications have long been envisioned as a second-life option for decommissioned batteries from EVs [26,27]. While the future economic viability of this concept still remains uncertain today, detailed modeling and mitigation of degradation effects have been described as one of the key areas that require more investigation to enable the profitability of second-life applications [28,29].

Multiple degradation modeling approaches exist to quantify the effects of aging mechanisms and their stress factors [30–32]. These approaches range from data-based empirical models to semi-empirical models with physics-inspired equations, up to detailed physicochemical models, which model individual aging mechanisms through sets of differential equations. All of these bring their own benefits and drawbacks for usage in BESS operation.

A significant number of individual contributions can be found on the topic of BESS operation. The objective commonly is to determine an economically beneficial charge–discharge schedule for one or multiple applications of BESSs. This is done through scheduling methods that can be categorized into exact solution approaches (e.g. mixed-integer linear programming), heuristics (e.g. fuzzy logic) and meta-heuristics (e.g. particle swarm optimization). A review on these methods for BESSs has been published by Weitzel et al. in 2018 [23]. They show that in the contributions published up until then, battery degradation is often either neglected or simplified with constant factors. 25 out of the 202 reviewed studies therein include degradation models [23]. However, especially in more recent years, a number of contributions have integrated more detailed degradation models into scheduling methods [33–38]. Applications of BESSs often overlap with those envisioned for V2G and therefore employ similar scheduling methods. In the field of V2G, Yang et al. reviewed scheduling methods with no particular focus on battery degradation [39]. Ahmadian et al. reviewed degradation models for V2G applications without investigating scheduling methods [32]. An overview of related reviews in the field of aging mechanisms, degradation modeling, and battery operation can be found in Table 1.

In this comprehensive review, we bridge the gap between aging mechanisms, their stress factors and degradation models on the one side, as well as aging aware BESS operation on the other side. We do so by deducing the key aspects for BESS operation from the state of the art in aging mechanisms and degradation modeling (cf. Fig. 1). We start by providing an overview of relevant aging mechanisms and their stress factors for the most commonly used cell types for stationary applications in Section 2. Following that, Section 3 focuses on relevant degradation model types from literature. At the end of both Sections 2 and 3, we deduce the key takeaways of aging mechanisms, stress factors and degradation models for BESS operation. Section 4 categorizes methods for internalizing degradation effects into operation strategies

Table 1
Selected reviews in the field of lithium-ion aging mechanisms, degradation modeling and battery operation.

Topic	Reference	Focus
Aging mechanisms	Edge et al. (2021) [10]	Aging mechanisms in lithium-ion cells
	Han et al. (2019) [20]	Aging mechanisms in automotive lithium-ion battery systems
	Vetter et al. (2005) [12]	Aging mechanisms in lithium-ion cells
Degradation modeling	Li et al. (2019) [30]	State of Health estimation and prediction
	Reniers et al. (2019) [31]	Physicochemical degradation models
	Ahmadian et al. (2018) [32]	Degradation models for V2G applications
	Pelletier et al. (2017) [21]	Degradation models for EVs
Battery operation	Woody et al. (2020) [22]	Strategies to limit battery degradation
	Weitzel et al. (2018) [23]	Scheduling methods for BESSs
	Yang et al. (2015) [39]	Scheduling methods for V2G

based on a comprehensive review of existing literature. In addition, we reveal the most relevant stress factors to consider for key BESS applications through a simulation case study.

2. Aging mechanisms and stress factors

This section provides an overview of the predominant aging mechanisms and their stress factors for commonly used lithium-ion batteries in BESSs.

2.1. Aging mechanisms

Lithium-ion batteries are composed of multiple layers of material wound up or stacked into a cell enclosure [40]. The electrolyte-filled, layered structure of a typical lithium-ion battery consists of: current collectors, the anode and cathode active material, and a separator. Both performance and degradation behavior are strongly influenced by the composition of the anode active material, the cathode active material, the electrolyte, and the resulting interactions of those materials [11,12,20].

Aging mechanisms are commonly grouped into the following four aging modes, based on their effect on the cell: loss of lithium inventory (LLI), loss of active material on the positive electrode ($\mathrm{LAM_{PE}}$), loss of active material on the negative electrode ($\mathrm{LAM_{NE}}$), and resistance increase (RI). LLI describes the loss of lithium ions through parasitic reactions, which can lead to a reduction of the available cell capacity [10,20,41]. $\mathrm{LAM_{PE}}$ or $\mathrm{LAM_{NE}}$ refer to active material being no longer available for the insertion of lithium on the cathode or anode, respectively [10,20,41]. These aging modes lead to both capacity and power fade. RI refers to aging mechanisms that cause an increase of the cell resistance or impedance and thereby lead to a decrease of the available power [10,20]. Notably, RI also leads to a reduction in usable capacity if the charge and discharge cut-off voltage stay constant [20]. Some authors propose further modes to summarize the effects of aging mechanisms, such as loss of electrolyte [20] and stoichiometric drift [10].

In the following, we confine ourselves to provide a short overview of the most predominant aging mechanisms, as illustrated in Fig. 2, and their effect on the most commonly referenced aging modes: LLI, $\mathrm{LAM_{PE}}$, $\mathrm{LAM_{NE}}$, and RI. Furthermore, we focus on three common cell types. That is, battery cells with graphite-based anodes and one of the following cathode active materials: lithium nickel manganese cobalt oxide (NMC), lithium nickel cobalt aluminum oxide (NCA) or lithium iron phosphate (LFP).

2.1.1. Anode aging mechanisms

Growth of the solid electrolyte interphase (SEI) on the anode surface has been identified as a key aging mechanism for capacity and power fade [10,12]. Graphite from the anode will react with electrolyte and lithium to form this solid passivation layer [12]. The SEI is initially formed within the first few cycles, usually during cell formation by the manufacturer [20]. The resulting passivation layer is aimed to be ionically conducting and electrically insulting [42]. It thereby should allow Li ions to pass through it, while protecting the anode from co-intercalation of solvent molecules and further decomposition of the electrolyte [42]. However, the SEI will continue to grow over a cell's life cycle [13,20]. Solvent molecules may still diffuse through existing SEI, volume change during cycling can lead to cracking and expose additional anode surface area for SEI growth, and side reaction products such as dissolved transition metals from the cathode or plated lithium can form additional SEI [10]. This continued growth of the SEI leads to the aging modes of both LLI and RI [10,20].

Volume change during cycling, solvent co-intercalation, or gas evolution inside the graphite can lead to particle cracking & graphite exfoliation [12]. This in turn can lead to electric contact loss of the active material and thereby induce $\mathrm{LAM_{NE}}$ [10,20]. If the anode material loses contact while being lithiated, the lithium will be trapped in the material which induces LLI in addition to $\mathrm{LAM_{NE}}$ [10]. Furthermore, additional SEI can form on the newly exposed anode surface area [10].

Lithium plating is a side reaction in which metallic lithium forms on the anode surface instead of intercalating into it [10,12]. This can especially occur through overcharging the cell or while charging at high currents or low temperatures [10,12]. During rest periods and through discharging the reaction is partially reversible, which is referred to as lithium stripping [43,44]. On the other hand, part of the metallic lithium may be enclosed by newly formed SEI, resulting in irreversible LLI [43]. Notably, dendrite growth as a consequence of lithium plating is a significant safety concern, as the dendrites can pierce the separator, short circuit the cell, and induce thermal runaway [45].

Further aging mechanisms on the anode, which are not discussed in detail here, include decomposition of the binder, as well as current collector corrosion [41,46].

2.1.2. Cathode aging mechanisms

Aging mechanisms on the cathode are highly dependent on the cathode material [10]. For most metal oxides, the predominant mechanisms on the cathode side are particle cracking, structural decomposition, transition metal dissolution, and formation of the cathode electrolyte interface [20,47].

Same as the anode, the cathode material is subject to volume change during charge and discharge, which can lead to particle cracking and thereby induce $\mathrm{LAM_{PE}}$ [10,41]. Also, if the cathode active material loses contact while being lithiated, this will lead to LLI in addition to $\mathrm{LAM_{PE}}$ due to trapped lithium [10]. Structural disordering describes a reaction in which $\mathrm{Li^+}$ ions exchange spots with transition metal ions inside the lattice, which can induce $\mathrm{LAM_{PE}}$ and RI [10,12,20]. Similar to the SEI, a cathode electrolyte interface forms through reaction of the cathode with the electrolyte. While this passivation layer is usually thinner than the SEI, it nevertheless induces RI and $\mathrm{LAM_{PE}}$ [10,20]. Lastly, transition metal dissolution from the cathode into the electrolyte can lead to $\mathrm{LAM_{PE}}$ as well [20,30]. The dissolved metal is known to then move to the anode and further accelerate SEI growth there [12].

Further reported degradation mechanisms on the cathode include electrolyte decomposition and loss, phase change to the lattice, binder decomposition, and current collector corrosion [10,46].

For NMC cathodes, transition metal dissolution and structural disordering have been reported as a prime concern due to the similar radii

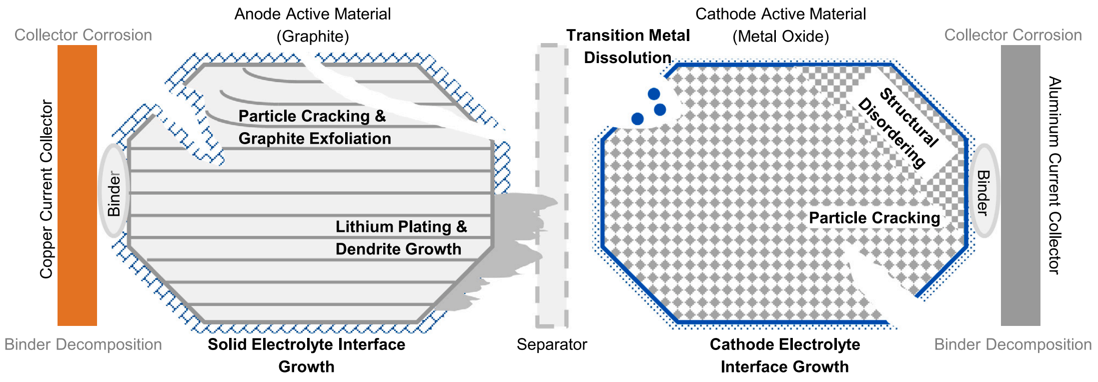

Fig. 2. Schematic illustration of predominant aging mechanisms in common lithium-ion batteries with graphite based anodes and metal oxide cathodes, based on [10,12,41].

of Li^+ and Ni^{2-} [12,48]. The degradation behavior of NMC cathodes is also influenced by their stoichiometry. To both increase energy density and reduce cobalt usage, NMC materials with higher nickel content, such as (NMC)-811, are receiving increased attention. This increase of Ni in the cathode mix shows disadvantageous effects on cycle stability, due to among other the before-mentioned cation mixing of Li^+ and Ni^{2-} as well as increased microcrack formation of (NMC)-811 compared to for example (NMC)-111 [11]. For lithium nickel cobalt aluminum oxide (NCA) cathodes, particle cracking has been reported as a main concern for cycle stability [48]. While cycle life also depends on cell design and cycle conditions, commercial LFP cells tend to show higher cycle stability than their NMC and NCA counterparts [49].

2.2. *Aging stress factors*

The aging behavior of lithium-ion cells is influenced by a multitude of factors. In the following, we will examine those external stress factors that can be influenced through appropriate operation strategies for BESSs. It should be noted that production quality and cell design parameters, such as the electrode thickness and choice of electrolyte additives, have a significant effect on the aging behavior of lithium-ion cells as well [20], but cannot be influenced in the operation phase of a BESS. Furthermore, extreme stress conditions outside of standard operating conditions can lead to catastrophic failure and thermal runaway, such as high temperature, high charge–discharge rates as well as overcharge and over-discharge of cells [50,51]. Such operating conditions should be prevented by appropriate design and battery management systems.

While the effects of aging mechanisms are commonly grouped into the four previously introduced aging modes (i.e. LLI, LAM_{PE}, LAM_{NE}, RI), a useful framework for BESS operation is the concept of calendar and cyclic aging, as depicted in Fig. 3. Cyclic aging refers to degradation effects that occur as a consequence of cycling the battery, i.e. charging and discharging. Calendar aging describes aging effects that occur regardless of cycling and especially during storage or idle time.

2.2.1. *Calendar aging*

Calendar aging is primarily influenced by time, temperature and the state of charge of the battery cells:

Time t: While not directly controllable during operation, side reactions such as SEI growth and binder decomposition will progress over time even without cycling the battery.

Temperature T: During storage, a higher temperature will lead to a higher reaction rate of the relevant side reactions, especially SEI growth, and therefore accelerate cell degradation [12].

State of Charge SOC: A high SOC comes with a low anode and high cathode potential. The low anode potential is known to accelerate SEI growth, therefore a high SOC will accelerate cell degradation [12,20]. Likewise, the high cathode potential can lead to increased transition metal dissolution due to oxidation of the lattice oxygen in NMC cathodes [10]. A calendar aging study conducted by Keil et al. with commercial NMC, NCA and LFP cells, all with graphite anodes, showed the lowest capacity loss for those cells that were stored at 0% SOC for all three cathode materials [52]. Instead of the normalized SOC, the cell terminal voltage V_{cell} may sometimes be used as an equivalent stress factor in degradation models [15]. For extended storage times, a direct relation from SOC to V_{cell} is given through the open circuit voltage curve.

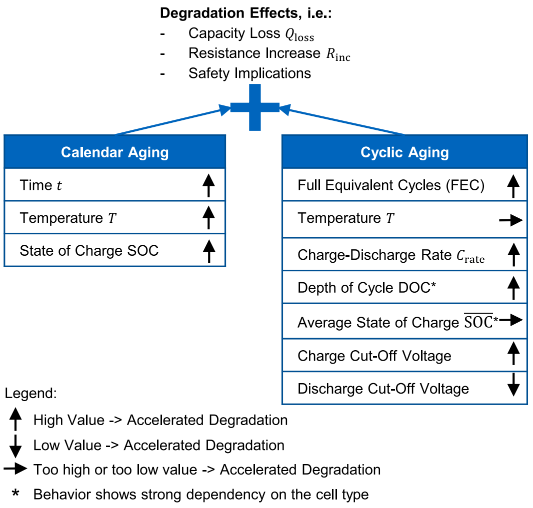

Fig. 3. Relevant stress factors during operation of a BESS and their effect.

2.2.2. *Cyclic aging*

Multiple stress factors impact the extent of cyclic aging: Next to temperature, the cycling parameters charge–discharge rate C_{rate}, average state of charge $\overline{SOC}$, and depth of cycle DOC determine the extent of cyclic aging. These cycling parameters are illustrated in Fig. 4. Furthermore, the operating voltage window, determined by the charge and discharge cut-off voltage have known impact on cyclic aging.

Full Equivalent Cycles FEC: The majority of aging mechanisms are either directly caused or accelerated by charging and discharging the

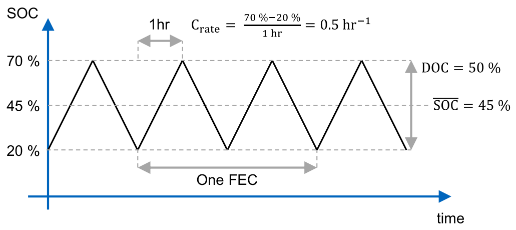

Fig. 4. Visualization of normalized battery cell cycling parameters: Here, an exemplary cell is cycled at a depth of cycle DOC of 50% around an average state of charge $\overline{\mathrm{SOC}}$ of 45% at a charge–discharge rate C_{rate} of 0.5 h^{-1}. A total of two full equivalent cycles FECs are displayed.

cell: particle cracking & graphite exfoliation, lithium plating & dendrite growth, structural decomposition, transition metal dissolution, as well as additional SEI growth induced by the aforementioned mechanisms. The amount of cycling is commonly stated in full equivalent cycles (FECs), by scaling the total charge throughput Q with the battery capacity C_{batt} in Ah:

$$Q = \int_0^t |I(t')|\, dt' \tag{1}$$

$$\mathrm{FEC} = \frac{Q}{2 * C_{batt}} \tag{2}$$

Here, I is the charge–discharge current. For C_{batt}, multiple definitions exist, as either the nominal battery capacity at the beginning of life or the present, degraded battery capacity may be used.

Temperature T: Especially while charging, low temperatures can lead to lithium plating on the graphite anode and thereby accelerate degradation [12,53]. On the other hand, the additional SEI growth caused by volume expansion, particle cracking and graphite exfoliation, as well as transition metal dissolution are further accelerated when cycling at high temperatures [53,54]. With low temperatures causing lithium plating and high temperatures accelerating SEI growth and transition metal dissolution, the temperature of a lithium-ion based BESS should ideally be neither too high nor too low [53,54]. It should be noted that a low operating temperature also negatively affects the available cell capacity as well as the cell resistance and thereby energetic efficiency. A range of 15 to 35 °C is often stated for the optimal operating temperature of lithium-ion cells [55].

Charge-Discharge Rate C_{rate}: To normalize for the battery capacity C_{batt}, the charge–discharge rate C_{rate} in h^{-1} is often given instead of the charge–discharge current I:

$$C_{rate} = \frac{I}{C_{batt}} \tag{3}$$

A high C_{rate} will accelerate particle cracking & graphite exfoliation as well as additional SEI formation [10,56]. Charging and discharging a cell for the same amount of FECs, but with a higher C_{rate}, can therefore accelerate capacity loss and resistance increase, as it was shown in a cyclic aging study by Naumann et al. with LFP-graphite cells [19]. It should be noted that a high C_{rate} will also cause the cell to generate more heat and increase its temperature, making it challenging to distinctly separate individual stress factors. In a study conducted by Barcellona et al. cells were kept in a temperature range of 20 to 30 ° C through active cooling with Peltier cells [57]. For the investigated lithium cobalt oxide cells with graphite anodes, the impact of the C_{rate} on capacity loss was found to be negligible for moderate charge–discharge rates [57]. Especially in combination with low temperatures or at a high SOC, lithium plating & dendrite formation on the anode may occur when charging with a high C_{rate} [12]. Fast charging with a high C_{rate} is especially required for EV and consumer electronic applications. During fast charging, the combination of inhomogeneous temperature distribution in the cell, lithium plating risk, and mechanical stress is the main concern for cell aging [58]. Notably though, typical stationary BESS applications require a lower C_{rate} in both charge and discharge direction [25].

Average State of Charge $\overline{\mathrm{SOC}}$: The average state of charge $\overline{\mathrm{SOC}}$ around which a cell is cycled is known to influence cyclic aging as well. In an aging study by Schmalstieg et al. NMC-graphite cells were cycled with a fixed DOC of 10% in different SOC ranges. After normalizing for the effects of SOC on calendar aging, the lowest cyclic aging was found in the range of 45 to 55% SOC, at $\overline{\mathrm{SOC}} = 50\%$, and the highest in the range of 90 to 100% SOC, at $\overline{\mathrm{SOC}} = 95\%$. In an experimental study focusing on this stress factor, Gantenbein et al. attributed the impact of SOC ranges to different stages of lithiation of the graphite anode [59]. The graphite anode will expand in volume when charging and retract when discharging [59,60]. Volume expansion and retraction of the graphite anode is especially pronounced when transitioning between these lithiation stages [60]. Cycling between lithiation stages is therefore expected to cause increased particle fraction and formation of new SEI [59]. The average cell terminal voltage $\overline{V_{cell}}$ may be used to quantify this stress factor in degradation models as well [15].

Depth of Cycle DOC: The DOC is sometimes also referred to as depth of discharge (DOD or ΔDOD) or cycle depth in literature. It refers to the difference in SOC levels between which a cell is cycled, as illustrated in Fig. 4. The general tendency of higher capacity loss with higher DOC has been attributed to increased cracking and new SEI Formation as a consequence of volume expansion in the graphite anode, especially when crossing the anode's phase change regions [59,61]. While in general a higher DOC will increase capacity loss, exceptions are found in empirical aging studies. In a study conducted by Ecker et al. with commercial NMC-graphite cells, the general trend showed a higher capacity loss with increasing DOC, for the same $\overline{\mathrm{SOC}}$ and number of FECs [62]. An exception being that after 750 FECs, cycling between 85% and 75%, at DOC = 10%, showed less degradation than between 82.5% and 77.5%, at DOC = 5% [62]. In another aging study with commercial LFP-graphite cells by Naumann et al. higher DOCs lead to higher capacity loss after extended cycling as well [19]. An exception being that for low DOCs, a capacity recovery effect was observed: After an initial accelerated capacity loss for lower DOCs such as 10% and 20% compared to higher DOCs of 80% and 100%, part of that capacity loss for low DOCs is regained following further cycling [19]. This effect was later attributed to non-uniform lithium distribution after extended shallow cycling at low DOC [63].

Charge and Discharge Cut-Off Voltage: The usable and nominal capacity and thereby the definition of the SOC are dependent on the set operating voltage limits of a cell, i.e. the charge and discharge cut-off voltage. A high charge cut-off voltage can lead to over-delithiation of the cathode material and thereby accelerate structural disordering on the cathode [30]. Furthermore, over-lithiation of the anode can lead to lithium plating and dendrite formation [12]. Low discharge cut-off voltages can lead to corrosion of the anode's copper current collector [30]. The operating voltage window should therefore be set such that the cells deliver a high nominal capacity while retaining high cycle life. Juarez-Robles et al. observed more than double the cycle life at a 20% reduction in usable capacity by limiting the manufacturer's recommended safe discharge and charge cut-off voltage from [2.7 V, 4.2 V] to [2.9 V, 4.0 V] for a commercial NCA-graphite cell [64]. In a similar setup of commercial cells with NCA cathodes and graphite/silicon composite anodes, Bazlen et al. found that by decreasing the charge cut-off voltage from 4.2 V to 4.1 V cathode aging effects can be reduced [65]. Increasing the discharge cut-off voltage from 2.5 V to 3.1 V, reduced anode aging, which was attributed to less volume change of the graphite/silicon anode [65].

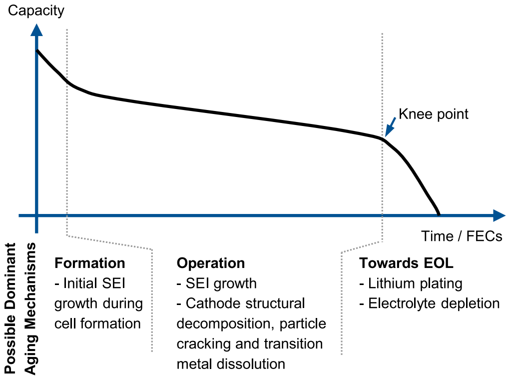

Fig. 5. Schematic depiction of capacity loss and possible dominant aging mechanisms over a cell's life cycle for graphite anodes and metal oxide cathodes. Based on [20,66].

2.3. Key aspects of aging mechanisms and stress factors for BESS operation

The previous sections provided an overview of the relevant aging mechanisms and their stress factors in common lithium-ion batteries with graphite based anodes and metal oxide cathodes. The specific degradation behavior is dependent on cell design, electrolyte additives and the cathode material, but the primary aging mechanisms and their stress factors remain the same across LFP, NMC and NCA.

Past studies have shown that over a cell's life cycle the dominant aging mechanisms vary as highlighted in Fig. 5. The initial formation of the SEI is mostly completed during production as one of the costliest manufacturing steps [67,68]. During the main operation phase, degradation for standard operating conditions is to a large extent driven by SEI growth combined with the cathode aging mechanisms [20,69,70]. Once the SEI has grown extensively, a self-reinforcing process of lithium plating may lead to rapid capacity loss [69,70]. The SEI growth leads to a reduction of the anode's ionic kinetics that can induce lithium plating even during standard operating conditions. If the plated lithium is isolated by formation of additional SEI around the lithium, this will lead to further deterioration of the anode's ionic kinetics and in turn promote further lithium plating [69,70]. Extensive loss of non-lithiated anode active material can also induce lithium plating and thereby rapid capacity loss. This is due to over-lithiation of the anode during charging, as the remaining anode active material may be unable to accommodate all remaining lithium [71]. Electrolyte depletion has been reported to cause significant loss of active material and thereby rapid capacity loss as well after extended operation [66,72]. The onset of this phase of rapid degradation is often referred to as an aging knee point, with a review of possible mechanisms leading to this knee point having been compiled by Attia et al. [73]. Notably, in a cell aging study by Johnen et al. the phase of rapid capacity loss was followed by another phase of slow degradation for low remaining capacity between 20% and 30% of the initial capacity [74].

Typically, the cell end-of-life (EOL) is defined before this region of rapid degradation between 70% and 80% remaining capacity [74,75]. This range is also commonly found in manufacturer warranties [76]. Instead of a fixed figure for the remaining capacity, application specific profitability criteria have been proposed to determine the EOL for BESSs, which may result in a system being operated up to lower remaining capacity [33,75]. It should be considered though that operating cells with low remaining capacity can negatively affect cell safety, especially in the presence of lithium plating [77–79].

While the specific degradation behavior is cell dependent, general conclusions can be drawn on how to extend BESS lifetime. During idle time, SOC and T should be kept low. During charging and discharging, capacity loss can be reduced by keeping the temperature T in a medium range, by avoiding phase change regions of the anode with $\overline{\mathrm{SOC}}$, and by cycling at low DOC and $\mathrm{C}_{\mathrm{rate}}$.

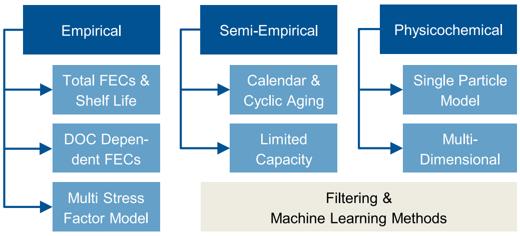

Fig. 6. Classification of degradation models.

3. Degradation models

Degradation models quantify the effects of aging mechanisms as a function of a cell's properties and usage profile. As we will show in Section 4, most publications in the field of BESS operation investigate capacity loss as the primary effect of battery degradation, due to its detrimental effect on the remaining useful life and the profitability of a BESS. We therefore focus on models that describe capacity loss. Depending on a degradation model's use-case, other effects may be relevant as well such as resistance increase to quantify power fade or the extent of cell internal lithium plating to assess safety risks.

3.1. Model types

Degradation models can loosely be categorized into empirical, semi-empirical and physicochemical models with further sub-categorization as shown in Fig. 6.

3.1.1. Empirical models

Empirical models are fit to cell aging data, without inherent modeling of the underlying physical aging mechanisms. Varying degrees of complexity for such models can be found.

The most simple form of an empirical model is the assumption that battery life is limited by a total amount of usable FECs in combination with a shelf life (e.g. 1500 FECs and 10 years). If either the total amount of FECs or shelf life is reached, the battery is assumed to have reached its EOL [80]. Though simple, this model does not account for any of the stress factors from Section 2.2.

DOC dependent total FEC models account for the fact that a small amount of cycles at high DOC tend to cause more battery degradation than the equivalent amount of cycles at a low DOC. This type of model has been employed by multiple authors for BESS operation [80–83].

Multi stress factor empirical models link any number of additional stress factors to capacity loss. For example, Padmanabhan et al. used a model that accounts for both the DOC and $\mathrm{C}_{\mathrm{rate}}$ dependence of capacity loss [84]. Fig. 7 provides a visualization of a degradation model from Maheshwari et al. with dependence on DOC, $\overline{\mathrm{SOC}}$ and $\mathrm{C}_{\mathrm{rate}}$ [85].

3.1.2. Semi-empirical models

Semi-empirical models typically rely on data from cell aging studies, in which a limited number of cells has been cycled and stored under accelerated aging conditions. For model fitting, they use functions that describe the underlying aging mechanisms. Multiple frequently used models use a superposition approach of calendar and cyclic loss to describe the total capacity loss, as indicated in Eq. (4) [15–19,54,86,87].

$$\begin{aligned} Q_{\mathrm{loss}}^{\mathrm{total}} = {} & Q_{\mathrm{loss}}^{\mathrm{cal}}(t, \mathrm{SOC}, T) + \\ & Q_{\mathrm{loss}}^{\mathrm{cyc}}(\mathrm{FEC}, \mathrm{C}_{\mathrm{rate}}, T, \overline{\mathrm{SOC}}, \mathrm{DOC}) \end{aligned} \tag{4}$$

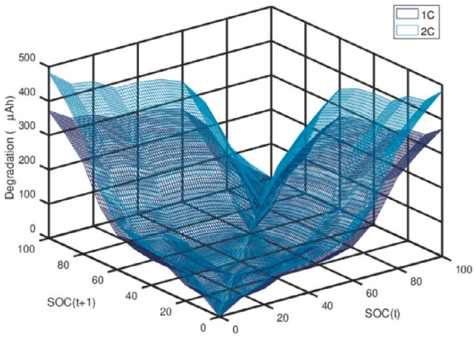

Fig. 7. Multi stress factor empirical model for a NMC cell, as depicted in Maheshwari et al. [85].

Here, $Q_{\text{loss}}^{\text{total}}$ refers to the total capacity loss while $Q_{\text{loss}}^{\text{cal}}$ and $Q_{\text{loss}}^{\text{cyc}}$ refer to the calendar and cyclic components of capacity loss, respectively. Table 2 provides an overview of selected semi-empirical degradation models.

Calendar Aging: For the calendar capacity loss $Q_{\text{loss}}^{\text{cal}}$, the selected models show a degree of uniformity: The common assumption of a square root dependency of $Q_{\text{loss}}^{\text{cal}}$ on time can be traced back to approximating SEI growth as a diffusion limited process for graphite electrodes [56]. More general power law and logarithmic expressions are also used for the time dependency of calendar aging by some authors [15,88]. The Arrhenius equation describes the exponential temperature dependency of reaction rates and is commonly referenced for modeling temperature dependent calendar aging [18,54,89–92]. Eq. (5) shows an adapted version of the Arrhenius equation as it can be used for fitting to aging test data [88,93].

$$\alpha_T = \gamma_1 * e^{-\frac{\gamma_2}{R}*\left(\frac{1}{T}-\frac{1}{T_{ref}}\right)} \tag{5}$$

α_T refers to the stress factor and γ_1 and γ_2 are fitting parameters, analogously to Table 2. R is the gas constant and T_{ref} the reference temperature for data fitting.

The Tafel equation describes the overpotential of an electrochemical reaction as a function of current density. Under the assumption that SEI growth is driven by over-potential, multiple authors use Tafel-like equations to describe the effect of SOC on calendar aging [54,88,91], see Eq. (6).

$$\alpha_{\text{SOC}} = \gamma_1 * e^{-\frac{\gamma_2 * F}{R} * \frac{U_{\text{a,ref}}-U_a(\text{SOC})}{T_{\text{ref}}}} \tag{6}$$

α_{SOC} is the stress factor, F is Faraday's constant and U_a the anode to reference potential. Simplified exponential expressions of the above dependency of α_{SOC} on SOC are used in the Saraketa-Zabala et al. and Guenther et al. models from Table 2 [16,86].

Cyclic Aging: The highlighted cyclic aging models show notably less uniformity in both model structure and the considered stress factors than the calendar aging models. Generally, cyclic aging models tend to use either cumulative charge throughput Q [15,17,92] or the total number of FECs [19,54,94] to represent battery cycling. On the other hand, the model of Guenther et al. relies on summation after every cycle to account for both the effect of cycling and the DOC of each cycle [86]. While most cyclic aging models tend to consider the DOC dependence, only some include further stress factors. Schmalstieg et al. also accounted for the average cell voltage during cycling V_{cell} [15]. Naumann et al. included the charge–discharge rate C_{rate} dependency in addition to the DOC in their model [19]. While not part of Table 2, Schimpe et al. published a cyclic aging model that also accounts for temperature dependence [54].

Smith et al. took a different approach to semi-empirical degradation modeling [95], labeled **Limited Capacity** in Fig. 6. Their model computes the available remaining capacity as the minimum of lithium inventory limited capacity, negative electrode limited capacity and positive electrode limited capacity. All three components are then described as physics inspired algebraic equations and fitted to aging test data [95].

3.1.3. Physicochemical models

Physicochemical models describe cell internal degradation mechanisms through sets of differential equations. Compared to empirical and semi-empirical models they are often considered computationally expensive, but promise extrapolation outside of the experimental data sets if parameterized accurately [88,96]. Generally, physicochemical models focus on individual degradation mechanisms such as SEI growth or particle cracking [31]. A detailed overview of published physicochemical degradation models and the considered mechanisms for each model has been compiled by Reniers et al. [31].

As a reduced order physicochemical model, single particle models (SPMs) provide a trade-off between computational efficiency and accuracy [97]. Under the assumption of uniform current distribution as well as same size spherical particles in both electrodes, each electrode is approximated as a single, spherical particle [97]. Ning et al. provided a SPM to describe SEI growth at the negative electrode under consideration of external stress factors [98]. At the core of the degradation model, the capacity loss caused by SEI growth is described by the current density of the solvent reduction side reaction, as shown in Eq. (7).

$$\frac{\partial Q_{\text{loss}}^{\text{SEI}}(t)}{\partial t} = i_{\text{s}}(t) * A_{\text{n}} \tag{7}$$

With $Q_{\text{loss}}^{\text{SEI}}$ being the capacity loss caused by SEI growth, i_{s} the side reaction current density and A_{n} the surface area of the negative electrode. Further differential equations then describe the side reaction current density as a function of over-potential in a Tafel-like equation [98]. Other authors use similar SPM formulations with notable examples provided in the following [97,99]. For increased accuracy, Pinson et al. added a one-dimensional porous electrode model to their SPM that accounts for spatial in-homogeneity of the SEI [99]. Li et al. developed a SPM that in addition to SEI growth considers crack propagation due to volume change [97]. Some more complex degradation models build on top of a modeling framework that is often referred to as the pseudo two-dimensional (P2D) Newman model [100,101]. Aswhin et al. proposed an SEI growth model based on the P2D Newman model [102]. Yang et al. developed a model that in addition to SEI growth, accounts for lithium-plating in order to represent the fast, nonlinear capacity loss towards the EOL [70]. Similarly, the model by Keil et al. represents SEI formation, SEI re-formation due to particle cracking, as well as lithium plating and lithium stripping [103].

3.1.4. Filtering and machine learning methods

Filtering and machine learning methods for capacity degradation modeling typically use online data of the system of interest. A review of methods in this field has been compiled by Li et al. [30]. Bayesian filters such as Kalman filters and particle filters allow to estimate and update the fitting parameters of degradation models during the operation phase [30,104]. Machine learning methods, such as artificial neural networks and support vector machines, rely on training data to tune the models before being applied to online data of the system of interest [105,106]. While filtering and machine learning methods are frequently proposed for the online estimation of the state of health [107] or remaining useful life of lithium-ion cells [108,109], none of the investigated publications in the field of BESS scheduling use such methods for degradation modeling. Especially machine learning methods, such as neural networks, tend to not provide a direct algebraic link between external stress factors and capacity loss, which makes them challenging to integrate into scheduling methods.

Table 2
Algebraic form of selected semi-empirical degradation models. α_i and β_i refer to the algebraic form of the calendar and cyclic stress factors, respectively. The index denotes the specific stress factor. γ_i refers to a fitting parameter that is determined based on accelerated cell aging tests in the respective studies.

		Schmalstieg (NMC) [15]	Naumann (LFP) [18,19]	Sarasketa-Zabala (LFP) [16,17]	Guenther (generic cell) [86]
$Q_{\text{loss}}^{\text{cal}}$	=	$\alpha_T * \alpha_{V_{\text{cell}}} * t^{0.75}$	$\alpha_T * \alpha_{\text{SOC}} * t^{0.5}$	$\alpha_T * \alpha_{\text{SOC}} * t^{0.5}$	$\alpha_T * \alpha_{\text{SOC}} * t^{0.5}$
α_T	=	$\gamma_1 * e^{-\frac{\gamma_2}{T}}$	$\gamma_1 * e^{-\gamma_2 * (\frac{1}{T} - \frac{1}{T_{\text{ref}}})}$	$\gamma_1 * e^{-\frac{\gamma_2}{T}}$	$\gamma_1 * e^{\frac{T - T_{\text{ref}}}{\gamma_2}}$
$\alpha_{\text{SOC},V_{\text{cell}}}$	=	$(\gamma_1 * V_{\text{cell}} - \gamma_2)$	$\gamma_1 * (\text{SOC} - 0.5)^3 + \gamma_2$	$\gamma_1 * e^{\gamma_2 * \text{SOC}}$	$e^{\frac{\text{SOC} - \text{SOC}_{\text{ref}}}{\gamma}}$
$Q_{\text{loss}}^{\text{cyc}}$	=	$(\beta_{V_{\text{cell}}} + \beta_{\text{DOC}} + \gamma) * Q^{0.5}$	$\beta_{\text{C-rate}} * \beta_{\text{DOC}} * \text{FEC}^{0.5}$	$\beta_{\text{DOC}} * Q^{\gamma}$	$\sum_{n=0}^{N} \beta_{\text{DOC,n}}$
$\beta_{\overline{\text{SOC}},\overline{V_{\text{cell}}}}$	=	$\gamma_1 * (\overline{V_{\text{cell}}} - \gamma_2)^2$	–	–	–
β_{DOC}	=	$\gamma * \text{DOC}$	$\gamma_1 * (\text{DOC} - 0.6)^3 + \gamma_2$	$10\% \leq \text{DOC} \leq 50\%$: $\gamma_1 * \text{DOC}^2 + \gamma_2 * \text{DOC} + \gamma_3$ Else: $\gamma_4 * e^{\gamma_5 * \text{DOC}} + \gamma_6 * e^{\gamma_7 * \text{DOC}}$	$\gamma_1 * \text{DOC}^3 + \gamma_2 * \text{DOC}^2 + \gamma_3 * \text{DOC}$
$\beta_{\text{C-rate}}$	=	–	$\gamma_1 * \text{C}_{\text{rate}} + \gamma_2$	–	–

Table 3
Assessment of different degradation model types for BESS operation.

Model type	Advantages	Disadvantages
Empirical	• high computational efficiency • can include all aging effects represented in the data	• strong reliance on aging data • limited extrapolation capacity
Semi-empirical	• high computational efficiency • minor extrapolation capacity	• strong reliance on aging data
Physicochemical	• high extrapolation capacity for the modeled mechanisms • model provides multiple cell parameters in addition to capacity loss	• high parameterization effort • computationally expensive

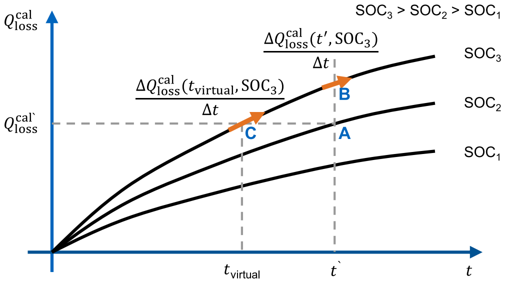

Fig. 8. Qualitative depiction of deriving the virtual time and the related degradation rate for changing from storage SOC_2 to storage SOC_3.

3.2. Key aspects of degradation models for BESS operation

Table 3 summarizes the key advantages and disadvantages of the different degradation model types for BESS operation. Empirical models provide no modeling of the underlying aging mechanisms and therefore solely rely on aging data. Physicochemical models model the underlying mechanisms in detail through sets of differential equation, require less aging test data, but in exchange bring a high parameterization effort with them. If the modeled aging mechanisms do not fundamentally change in the investigated time frame, a certain degree of extrapolation capacity can be assumed outside of the validation period with physicochemical models [88]. Semi-empirical models attempt to offer a trade-off between both physicochemical and empirical modeling approaches.

3.2.1. Varying stress factors and model discretization

Both empirical and semi-empirical models are typically fit to data from cell aging studies. These studies are run with multiple cells that are subjected to varying stress factors. While the stress factors such as temperature or charge–discharge rate vary from cell to cell, stress factors are usually kept constant for a given cell throughout the duration of the study, e.g. one cell stored at 25 °C and others at 35 °C and 45 °C [15,54]. Check-up tests are run after a specific amount of time or cycles for the cells to determine the remaining capacity and other relevant parameters such as the cell impedance. The models are then fit to the resulting data set. Contrary to this, outside-the-lab applications subject the cells to varying external stress factors [25,110]. Some studies age individual cells with varying stress factors to validate the resulting model [17–19]. This model validation at varying stress factors is of importance, since aging mechanisms may show path dependence, i.e. dependence on the order in which a cell has been subjected to different calendar and cyclic stress factors [111,112].

To apply a degradation model with a continuous function, such as $Q_{\text{loss}}^{\text{cal}} = \alpha_T * \alpha_{\text{SOC}} * t^{0.5}$ from Table 2 to varying stress factors, methods for discretization are needed in order to determine the degradation rate for each calculation step. Multiple authors propose to determine the present degradation rate based on the past capacity loss, rather than the past time or energy throughput [16,18,90]. This concept is highlighted in Fig. 8. Assume a cell has been stored at SOC_2 for a specific amount of time t' and accrued a calendar capacity loss of $Q_{\text{loss}}^{\text{cal}\prime}$, see point **A** in Fig. 8. The SOC is then increased to SOC_3, with $\text{SOC}_3 > \text{SOC}_2$. Instead of using the degradation rate at t' for the following calculation time step (point **B**), the higher degradation rate at t_{virtual} is applied (point **C**). The virtual time t_{virtual} refers to the time that had needed to pass for the cell to reach the capacity loss in point **C**. It is calculated by forming the inverse of the capacity loss function, cf. Eq. (8):

$$t_{\text{virtual}} = Q_{loss}^{cal\ -1}(Q_{loss}^{cal\prime}, \text{SOC}_2) \tag{8}$$

The physical rationale behind this concept is that the SEI growth rate is more correlated to the present thickness of the SEI, which manifests itself in capacity loss, than to the amount of time that has passed.

The same principle can be applied to cyclic aging as well, by calculating a virtual number of FECs or charge throughput [19]. Discretization of cyclic aging brings additional complexity though: cycle counting. While calendar aging can be evaluated after every timestep, computing cyclic capacity loss requires a definition of when a cycle is completed. A full charge–discharge cycle from 0% to 100% back to 0% SOC should be computed as one FEC at 100% DOC instead of ten cycles at 10% DOC. Naumann et al. as well as He et al. employ a half cycle counting algorithm in which a cycle is evaluated after every change of charge–discharge direction [19,80]. After such a cycle is detected, DOC and C_{rate} are determined and the cyclic capacity loss is calculated. Another algorithm used for cycle counting is the rainflow-counting algorithm, which is commonly employed in material fatigue analysis [113,114]. It sequences a data series of local maxima and minima into cycle loops and thereby allows to identify individual cycles, their DOC, and C_{rate} in a SOC profile [82,115].

3.2.2. Model requirements and examples

This section provided an overview of common degradation models and in doing so highlighted the significant variety in modeling approaches. To use degradation models for scheduling purposes, we identify four main requirements:

- **Modeling of varying stress factors:** To apply a model to real life use cases, it should include a validated method to represent varying stress factors.
- **Modeling of application relevant stress factors:** The stress factors that are relevant for a given application, should be represented in the model. For the semi-empirical models highlighted in Table 2, all consider the dependence of cyclic aging on DOC, but only some the dependence on C_{rate} and $\overline{SOC}$.
- **Validity for operation range and conditions:** A degradation model that is intended to be used for a given application should be validated for that application's operation range. For example, if an application shows a large amount of cycles at low DOC and high C_{rate}, this should be part of the test conditions through suitable design of experiment.
- **Sufficient computational efficiency:** Sufficient computational efficiency is needed to include degradation models in common scheduling methods.

Individual contributions can be found that aim to provide models specifically for use in battery operation and scheduling [87,114,116,117]. Muenzel et al. proposed a cycle life model that accounts for the cyclic stress factors of C_{rate}, DOC, T, $\overline{SOC}$ and uses the rainflow algorithm for cycle counting [114]. Shi et al. only consider DOC as a stress factor for cyclic aging, but prove convexity of their resulting model which is beneficial for a number of scheduling methods [116].

4. Aging aware operation

In this section, we move from degradation models to aging aware operation strategies. The process of deriving a schedule of charge and discharge signals for a BESS under consideration of technical constraints and economic benefit is referred to with multiple terms in literature: energy management [23], scheduling [39], control [37], dispatch [118] or operation [85]. In the following, we will refer to this general process as scheduling and provide an overview of scheduling methods in Section 4.1. In Section 4.2 we provide a tabular review of contributions that account for battery degradation during scheduling and perform a taxonomy of "aging awareness methods", meaning methods for how to internalize battery degradation into the scheduling method. In Section 4.3 we investigate through time-series simulations which aging stress factors are particularly relevant for selected applications of BESSs.

Fig. 9 summarizes selected key applications of BESSs, which are referenced again in later subsections. **SCI** is often a primary application for residential storage systems and refers to increasing one's own consumption of self generated renewable energy, mostly photovoltaic (PV), by charging energy into the BESS instead of feeding it into the grid in times of excess PV generation. Since electricity costs often exceed remuneration for feeding PV generated electricity into the grid, a net benefit is gained by using the energy from the BESS, once the household load exceeds PV generation again [119]. **Peak shaving (PS)** means smoothing a load profile by discharging the BESS into the load peak and thereby reducing demand charges for an industrial electricity consumer [33]. **Energy arbitrage (EA)** is the process of buying electricity at low prices and selling it at high prices on the respective energy markets. **Balancing power (BP)** describes a grid service in which a BESS provides its power capability to charge during grid over-frequency and discharge during under-frequency, in order to stabilize the electricity grid [36]. Remuneration is handled on the respective power markets, such as the central European auction for frequency containment reserve (FCR) or firm frequency response (FFR) in the United Kingdom. **Microgrid** refers to applications in which a BESS is used to form a microgrid in partial or full independence from larger national electricity grids [82]. In **multi-use** applications, a BESS is used for not one, but multiple of the aforementioned applications by either running them sequentially one after another or in parallel [2]. Lastly, **vehicle-to-grid (V2G)** is the concept of using electric vehicles to fulfill any of the aforementioned applications, including multi-use, through controlled or bi-directional charging [120]. Further applications of BESSs include the provision of backup power, time arbitrage for time-of-use tariffs, as well as transmission & distribution grid upgrade deferral [1].

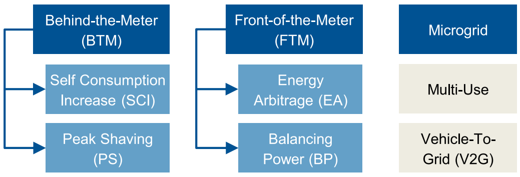

Fig. 9. Overview of key BESS applications. Multi-use and V2G are overarching concepts that can include BTM, FTM or microgrid applications.

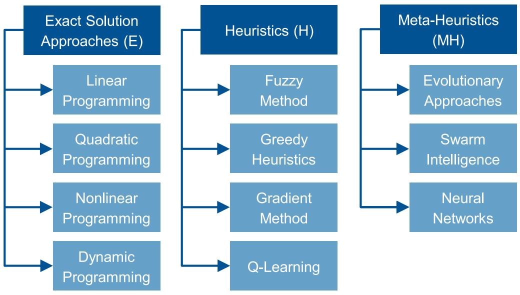

Fig. 10. Non-exhaustive overview of optimization based scheduling methods and their classification.

4.1. Scheduling methods

To operate an energy storage system as optimally as possible, several aspects must be taken into account. In addition to the design of the storage system and the definition of the applications to be served, system constraints, operating expenses, degradation and efficiency have to be considered [85]. In terms of scheduling methods, a distinction is made between rule-based and optimized operation strategies. Rule-based methods offer the advantage of relatively low computational complexity, e.g. discharging a BESS during load peaks in PS operation up to a peak shaving limit and charging it again after the load peak. Optimization based scheduling methods, on the other hand, aim to determine the optimum of an objective function, which is also referred to as the fitting or reward function. Based on literature, optimized operation strategies can be divided into three categories of algorithms: **exact solution approaches (E)**, **heuristics (H)**, and **meta-heuristics (MH)** (cf. Fig. 10) [23].

4.1.1. Exact solution approaches

The most common group of algorithms for optimization based BESS scheduling is exact solution approaches [23]. As the name suggests, this group of algorithms generally has the property of finding the optimal solution to a given optimization problem. It includes linear, nonlinear, and quadratic problems. Often, these standard categories also include extensions with mixed integer problems. A mixed integer linear programming (MILP) problem is an optimization problem that includes a linear objective function and linear constraints with integer as well as continuous decision variables. Analogously, mixed integer quadratic programming refers to a problem with a quadratic objective function and integer as well as continuous decision variables. In addition to the standard solution approaches for these problem types, such as the simplex algorithm and branch and bound methods, there are decomposition based methods, such as dynamic programming (DP), which are especially used for sequential decisions [121]. While they allow to find the global optimum to a problem, exact solution approaches have the disadvantage that solving them can be computationally expensive. Especially nonlinear programming (NLP) approaches with multiple decision variables can be elaborate and time consuming to solve, which can explain why the faster linear approaches are more frequent in the field of time-series optimization and energy storage [23]. In order to include nonlinear relationships, such as efficiency curves or aging models in a linear scheduling method, linearization approaches are commonly used [33,85]. It should be underlined though, that linearization of models will introduce errors and thereby decrease accuracy [122].

4.1.2. Heuristics

The second group of optimization based scheduling methods are heuristics, which include algorithms, such as the fuzzy method, greedy heuristic, gradient method, and reinforcement learning [23]. Compared to exact solution approaches, heuristics are fast, but have the disadvantage that they can get stuck in local optima [123]. Because of their advantage of relatively fast computing times, heuristics are able to bundle complex nonlinear relationships in an optimization problem. In the work by Cao et al. the reinforcement learning method was used to control an energy storage system during arbitrage trading, while considering battery degradation, charge–discharge efficiency, and market price prediction [38].

4.1.3. Meta-heuristics

In contrast to heuristic approaches, meta-heuristics can be described as heuristics that are allowed a step-wise worsening of the optimization objective, with the intention to avoid local optima [23]. Well-known representatives of meta-heuristics are methods such as evolutionary approaches, swarm intelligence, and neural networks. In Engels et al. a genetic algorithm is presented to determine the optimal scheduling of a large-scale storage system in the German frequency containment reserve market [36]. Comparing this algorithm with other gradient-free global optimization algorithms, the authors found that the chosen differential evolution method converges relatively fast towards the optimization bounds, while allowing the co-optimization of the degradation costs [36]. Other promising candidates for meta-heuristics are swarm intelligence-based search techniques. Hossain et al. and Li et al. used particle swarm optimization (PSO) in the context of microgrid communities and bi-directional electric vehicles, respectively [82,120]. In both approaches, the degradation is actively considered in the fitness functions of the optimization method and the degradation model was implemented with a rain-flow algorithm to determine the energy throughput at the mobile and stationary energy storage systems [82, 120]. Liu et al. used a electrothermal-aging model for their optimization problem, that captures the nonlinear electrical, thermal, and degradation dynamics of a lithium-ion battery and solve it using the NSGA-II algorithm [35]. Here, it was found that the chosen genetic algorithm is a viable candidate to determine the optimal operation strategy, allowing the modeling of nonlinear processes as well as hard constraints in the optimization algorithm [35].

4.1.4. Aging aware scheduling example

In general, it can be said that the more detailed the degradation model is, the more complex it is to find a suitable scheduling method. As the literature review shows that degradation aware scheduling methods are largely implemented with MILP algorithms (cf. Tables 4–7 in the following subsection), an example is provided in the following.

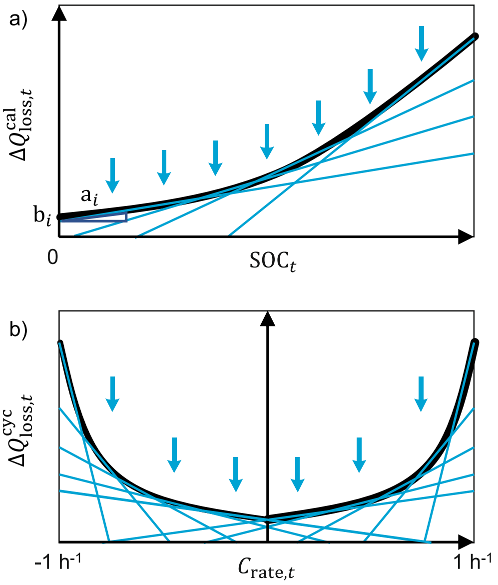

Fig. 11. Exemplary dependency between SOC, $\mathrm{C}_{\mathrm{rate}}$ and the respective degradation cost. The blue lines depict the linearization and the blue arrows illustrate the minimization of aging costs. (For interpretation of the references to color in this figure legend, the reader is referred to the web version of this article.)

Eq. (9) shows an exemplary objective function, which maximizes the profit $\mathbb{P}$ of the system while accounting for the cost of degradation $\mathbb{C}^{\mathrm{aging}}$. In order to limit the solution space of the optimization problem, constraints must be defined (cf. Eqs. (10)–(12)). As shown in Eq. (10), the cost of battery cell degradation at time step t is composed of the capacity loss change from calendar $\Delta Q^{\mathrm{cal}}_{\mathrm{loss}}$ and cyclic $\Delta Q^{\mathrm{cyc}}_{\mathrm{loss}}$ aging, multiplied by the specific aging cost per unit of capacity loss c_{aging}. Further constraints, which are not detailed here, then model how the profit $\mathbb{P}_t$ relates to the charge–discharge rate $\mathrm{C}_{\mathrm{rate},t}$ in the given application and how SOC_t changes based on $\mathrm{C}_{\mathrm{rate},t}$.

$$\max \sum_{t\in T} \left(\mathbb{P}_t(\mathrm{C}_{\mathrm{rate},t}) - \mathbb{C}^{\mathrm{aging}}_t\right) \tag{9}$$

$$\begin{aligned}\mathbb{C}^{\mathrm{aging}}_t &= (\Delta Q^{\mathrm{cal}}_{\mathrm{loss},t}\left(\mathrm{SOC}_t\right)\\ &\quad +\Delta Q^{\mathrm{cyc}}_{\mathrm{loss},t}\left(\mathrm{C}_{\mathrm{rate},t}\right)) * c_{\mathrm{aging}} \qquad \forall t\in T\end{aligned} \tag{10}$$

$$Q^{\mathrm{cal}}_{\mathrm{loss},t} \geq a_i\cdot \mathrm{SOC}_t + b_i \qquad \forall i\in I, \forall t\in T \tag{11}$$

$$Q^{\mathrm{cyc}}_{\mathrm{loss},t} \geq c_j\cdot \mathrm{C}_{\mathrm{rate},t} + d_j \qquad \forall j\in J, \forall t\in T \tag{12}$$

This generic example includes a simplified degradation model with two calendar aging stress factors, t and SOC, and two cyclic aging stress factors, FEC and $\mathrm{C}_{\mathrm{rate}}$. As discussed in Section 2.2, the usable capacity of lithium-ion cells usually degrades faster at high SOCs. For approximation purposes, the SOC-related stress behavior can be mathematically described with a respective function (cf. thick black line in Fig. 11a). To include this nonlinear degradation behavior in a MILP, linearization techniques are required. By applying the method of linearization, the nonlinear behavior can be step-wise linearized. As shown in Fig. 11a, the nonlinear function is partitioned into $i \in I$ linear functions with slope a_i and y-axis intercept b_i (cf. Eq. (11)). With battery degradation cost $\mathbb{C}^{\mathrm{aging}}_t$ included as a penalty factor in the objective function (cf. Eq. (9)), the solver will account for and

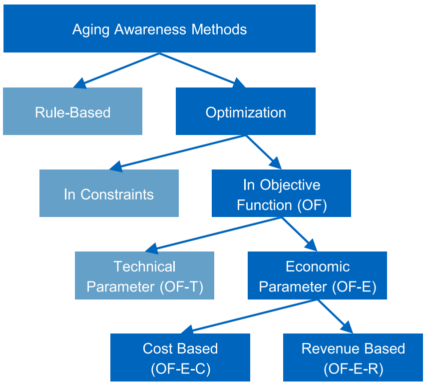

Fig. 12. Categorization of aging awareness methods.

reduce this stress factor (cf. blue arrows in Fig. 11a) and thus avoid higher SOC levels. Analogously, one can also apply linearizations for the C_{rate} in order to approximate this nonlinear stress characteristic that leads to higher degradation costs for increased C_{rate} values (cf. Fig. 11b). In Eq. (12), c_j and d_j respectively represent the slope and y-axis intercept for the set of linear functions $j \in J$ for the $C_{rate,t}$ stress factor. Note that a higher $C_{rate,t}$ will also lead to a larger number of FECs for that timestep. This means that both cyclic aging stress factors, FEC and C_{rate}, can be represented by one set of linear functions, as illustrated by the steep increase of $Q^{cyc}_{loss,t}$ in both charge and discharge direction in Fig. 11b.

4.2. Aging awareness methods

Tables 4 to 7 summarize existing publications in the field of aging aware BESS operation. Next to the scheduling method, application, aging model, and stress factors, the method used to account for battery degradation in the operation strategy is highlighted. A variety of such methods, that we refer to as aging awareness methods, can be found in literature and categorized as in Fig. 12. In summary, these aging awareness methods might negatively effect short-term profitability, but are expected increase long-term profitability by extending the BESS lifetime.

Rule-based approach: We make the first differentiation with regards to the scheduling methods themselves. Rule-based scheduling methods employ rule-based methods as well to limit degradation, while optimization based scheduling strategies provide a wider range of methods. As for rule-based aging awareness methods, Angenendt et al. proposed a forecast based method [119]. Here, a residential storage system is charged up only to the energy level during the day that is forecasted to be needed at night. Thereby the average SOC and calendar aging are reduced. A decrease in levelized cost of electricity of up to 12% is reported as a result [119].

Optimization approach: The majority of scheduling methods are optimization based. The target is to minimize or maximize an objective function through either exact solution approaches, heuristics or metaheuristics. For those scheduling methods, aging awareness may be induced through constraints, through the objective function or through both.

In Constraints: By setting fixed constraints for the aging stress factors in an optimization problem, the extent of degradation can be reduced. Li et al. limited the C_{rate} through fixed constraints for the charge and discharge power and induce upper and lower limits for the SOC range [120]. Wankmuller et al. limited the SOC range to 60% of the original battery capacity and investigate the techno-economic impact of different limits for the C_{rate} as part of their analysis [124]. Shi et al. limited the usable SOC range to 70% of the original battery capacity [116]. It should be noted that introducing limits for the SOC in an optimization problem will affect the maximum DOC as well. The effects of limiting DOC in different SOC ranges were studied by Perez et al. in a multi-use balancing power and energy arbitrage application [125]. It was found that for the optimal SOC range, the annual average gross revenue is reduced by 18%, but the BESS lifespan is expected to double [125].

A different kind of aging aware constraints was used by Cardoso et al. [126]. Here, an energy throughput limit for the BESS was introduced, which is calculated based on a semi-empirical aging model with the target lifetime and tolerable capacity loss before EOL as inputs [126]. Notably, Cardoso et al. considered both scheduling and system sizing in their optimization framework [126].

Objective Function (OF): Instead of solely relying on constraints, the majority of investigated studies account for degradation directly in the objective function with a penalty factor, as either a Technical Parameter (OF-T) or Economic Parameter (OF-E).

Technical Parameter (OF-T): Multi-objective approaches allow to include technical parameters in the objective function alongside economic parameters for the profit gained in an application. Li et al. directly optimized the sum of all cycles and half-cycles in the objective function for the investigated V2G application [120]. Maheshwari et al. proposed an optimization framework that includes a detailed empirical degradation model for energy arbitrage applications [85]. They used a multi-objective approach, in which revenue and degradation are linked through a weighting factor that should be chosen by the operator. With a lower weighting factor, battery degradation decreases, but so does the short-term revenue that is gained through energy arbitrage [85]. Analogously, with the multi-objective approach by Li et al. the annual cashflow for a residential BESS in their case study decreases from 318 € to 312 €, but the expected lifetime increases from 12 to 15 years [127].

Economic Parameter (OF-E): A significantly larger subset of publications are using a form of economic parameter to link battery degradation with the profit that is generated from the primary applications of the BESS. This is done by either directly assigning a monetary value to degradation in the form of aging cost or by formulating future profit as a function of the expected battery lifetime.

Cost Based (OF-E-C): Two definitions are especially common for aging cost $\mathbb{C}^{aging}$, which are given in Eqs. (13) and (14).

$$\mathbb{C}^{aging}_{SOH} = \frac{c_{battery} * E_n}{1 - SOH_{EOL}} * \Delta SOH \tag{13}$$

In Eq. (13), the aging cost $\mathbb{C}^{aging}_{SOH}$ is calculated based on the specific battery cost $c_{battery}$, the nominal battery capacity at the beginning of life E_n in Wh, the SOH threshold for the end of life SOH_{EOL} and the decrease in SOH (ΔSOH), as proposed by multiple authors [34,36,118,122,128]. In this context, $c_{battery}$ is often chosen as the installation or replacement cost for the full BESS or for just the battery cells. For SOH_{EOL}, 70% [34] or 80% [36,118,122,128] are typical assumptions. As in the example from Section 4.1.4, $\mathbb{C}^{aging}_{SOH}$ is then added to the objective function and ΔSOH is linked to the degradation model through constraints.

$$\mathbb{C}^{aging}_{FEC} = \frac{c_{battery} * E_n}{FEC_{EOL}} * \Delta FEC \tag{14}$$

In Eq. (14), the expected number of full equivalent cycles until EOL FEC_{EOL} and the increase in full equivalent cycles ΔFEC are used to calculate the aging cost $\mathbb{C}^{aging}_{FEC}$, as also proposed by multiple authors [2,83,84,116,129]. Here, FEC_{EOL} can be constant or linked to the degradation model, the latter often making the model nonlinear.

With such aging cost in the objective function, Englberger et al. reported a system lifetime increase from 2.4 to 8.6 years and a profitability index increase over its lifetime from 0.06 to 1.24 [2], for the investigated multi-use application. Weitzel et al. reported a lifetime

Table 4
Scheduling methods that are using technical parameters (OF-T) or reward based economic parameters (OF-E-R) within the objective function.

Reference	Aging awareness method[a]	Aging model types[b]	FEC	DOC	C_{rate}	$\overline{SOC}$	T_{cyc}	t	SOC	T_{cal}	Scheduling method	Applications
Li [127]	**OF-T:** Calendar capacity loss in OF, linked to economic benefit through weighting factors	Semi-Empirical [86]						×	×	×	E: DP	SCI
Maheshwari [85]	**OF-T:** Cyclic capacity loss in OF, linked to economic benefit through weighting factors	Empirical [94]	×	×	×	×					E: MILP	EA
He [80]	**OF-E-R:** Profit maximization based on expected lifetime in days times projected profit per day	Empirical	×	×				×			E: NLP	EA & BP
Abdulla [130]	**OF-E-R:** Penalty factor based on the cumulative degradation and expected lifetime cost savings generated through the BESS	Empirical [114]	×	×	×	×		×			E: DP	SCI
Liu [35]	**OF-E-R:** Penalty factor based on the expected cycles until EOL and battery resale value	Semi-Empirical [117]	×	×	×	×	×				MH: NSGA-II	V2G

[a] Aging Awareness Method Abbreviations: Technical Parameter in Objective Function (OF-T), Cost Based Economic Parameter in Objective Function (OF-E-C), Revenue Based Economic Parameter in Objective Function (OF-E-R).

[b] For each aging model, the cyclic (FEC, DOC, C_{rate}, $\overline{SOC}$, T_{cyc}) and calendar (t, SOC, T_{cal}) stress factors are marked by "×" if they are internalized into the listed scheduling method.

increase from 6.9 to 12 years in the investigated microgrid application by adding aging cost to the objective function [122].

As Eqs. (13) and (14) show, the assumption for the EOL criterion significantly influences the aging cost and thereby the optimized operation strategy. Hou et al. investigated in more detail the affect of the EOL criterion and propose an alternative efficiency-based criterion in their optimization model [33].

Instead of deriving the aging cost directly from battery cost as in Eqs. (13) and (14), Wankmuller et al. investigated the impact of varying aging cost values through parameter variation in a MILP [124]. They concluded that a penalty factor of 100 $ per kWh of capacity loss leads to the highest total profit in the investigated energy arbitrage application over the BESS lifetime, when assuming EOL at either 80% remaining capacity or after 10 years of operation. It is worth pointing out that 100 $ per kWh of capacity loss is significantly lower than the commonly assumed costs for battery replacement or installation $c_{battery}$ in other published aging aware operation strategies, in the range of 250 to 500 € per kWh [36,118].

Revenue Based (OF-C-R): While cost based methods include some form of aging cost as a penalty factor, revenue based methods create a link between revenue and degradation behavior in the objective function. Liu et al. added the degradation dependent future resale value of the battery to the objective function [35]. Abdulla et al. used cumulative past savings that were generated by the BESS to determine a monetary value for capacity loss [130]. They also investigated the influence of the forecasting errors on their stochastic DP. Intuitively, the revenue generated in the application is higher with the simplified assumption of perfect foresight than with their multiple linear regression forecast for power demand and power generation. The lifetime increases from their reference case of basic set point control (4 years predicted lifetime) to stochastic DP (11 years predicted lifetime) was reported to be the same though for both perfect foresight and the multiple linear regression forecast [130]. Lastly, He et al. multiplied the projected daily revenue with the expected lifetime in days, based on an empirical degradation model, as part of a nonlinear programming approach [80]. Here, with consideration of battery cycle life, daily revenue decreased by 19.2%, but the expected lifetime increases from 6.3 to 10 years [80].

4.3. Application specific relevance of stress factors

In this section, the relevance of calendar and cyclic stress factors for different applications is investigated. For that purpose, we use the inhouse developed open-source Simulation Tool for Stationary Energy Storage Systems (**SimSES**) [143]. **SimSES** can be used to conduct time-series simulations for energy storage systems in various applications. A variety of battery storage technologies and peripheral components are available. The simulation tool allows a detailed techno-economic analysis following the simulation. This includes an analysis of calendar and cyclic capacity loss, which is in focus here.

For this review, BESSs with NMC and LFP lithium-ion batteries are simulated in the previously introduced applications FCR, SCI and PS. The cell and aging model of the NMC type battery are based on the work of Schmalstieg et al. [15] and those of the LFP battery are based on Naumann et al. [18,19] (cf. Table 2 for the degradation models). For each application, input profiles are used: a grid frequency profile for FCR, a household load profile and a PV generation profile for SCI and an industrial load profile for PS. The BESSs are dimensioned analogously to Kucevic et al. [25]. For the power electronics, the model of an AC/DC converter measured by Notton et al. is used [140]. In addition, 25 ° C is chosen as fixed cell temperature to ensure comparability between the three applications, irrespective of the thermal design of each system. The simulation parameters are summarized in Table 8.

First, we investigate the distribution of calendar and cyclic stress factors for the three applications (FCR, SCI, PS) and their effect on cell degradation for the two investigated degradation models (LFP Naumann and NMC Schmalstieg): Fig. 13 shows the resulting calendar and cyclic stress factors. FCR is characterized by an average SOC around 50% with a large amount of cycles at low DOC and C_{rate}, following the BESS response to the fluctuating grid frequency. In SCI, the BESS spends a large amount of time at 100% SOC after being fully charged by the PV system and 0% SOC after discharging all its energy to cover the household load, once the household load exceeds PV production again. Compared to the other two applications, SCI requires more cycles at a higher DOC and C_{rate}. Lastly, in PS the BESS is fully charged in anticipation of a possible load peak for the majority of time, while being subjected to few cycles.

Table 5
Scheduling methods that are using cost based economic parameters within objective function (OF-E-C) Part I.

Reference	Aging awareness method	Aging model types	FEC	DOC	C_{rate}	$\overline{\text{SOC}}$	T_{cyc}	t	SOC	T_{cal}	Scheduling Method	Applications
Kazemi [81]	**OF-E-C:** Aging cost per day based on battery cost divided by the expected lifetime in days	Empirical	×	×							E: Benders Decomposition	EA & BP
Engels [36]	**OF-E-C:** Aging cost based on capacity loss times battery cost, assuming EOL at 80%	Semi-Empirical [15]	×	×		×		×	×	×	MH: Differential Evolution Algorithm	BP
Hesse [118]	**OF-E-C:** Aging cost based on capacity loss times battery cost, assuming EOL at 80%	Semi-Empirical [54]	×		×			×	×		E: MILP	EA & BP
Weitzel [122]	**OF-E-C:** Aging cost based on capacity loss times BESS investment cost, assuming EOL at 80%	Semi-Empirical [16,17]	×	×				×	×		E: MILP	Microgrid
Kruger [128]	**OF-E-C:** Aging cost based on future discounted replacement cost, assuming EOL at 80%	Semi-Empirical [90]	×		×			×	×		E: MILP	SCI
Cao [38]	**OF-E-C:** Aging cost based on capacity loss times battery cost	Semi-Empirical [87]	×	×		×	×	×	×	×	H: Reinforcement Learning	EA
Cai [34]	**OF-E-C:** Aging cost based on capacity loss times battery cost, assuming EOL at 70%	Physicochemical[a] [131]	×	×	×			×	×		E: NLP (Convex)	SCI
Reniers [37]	**OF-E-C:** Aging cost based on capacity loss times different penalty factors in € per kWh capacity loss	x: Empirical y: Semi-Empirical [15] z: Physicochemical[b]	xyz	yz	yz	z	z	yz	yz	yz	E: Linear & Nonlinear Programming	EA

[a] The physicochemical model in [34] considers SEI growth and active material loss. It is linearized and not directly embedded in the optimization problem.
[b] While the physicochemical model in [37] is dependent on all mentioned stress factors, the only aging mechanisms modeled is SEI growth.

Table 6
Scheduling methods that are using cost based economic parameters within objective function (OF-E-C) Part II.

Reference	Aging awareness method	Aging model types	FEC	DOC	C_{rate}	$\overline{\text{SOC}}$	T_{cyc}	t	SOC	T_{cal}	Scheduling Method	Applications
Hossain [82]	**OF-E-C:** Aging cost based on relative amount of used cycles times investment cost	Empirical	×	×							MH: PSO	Microgrid
Shi [83]	**OF-E-C:** Aging cost based on relative amount of used cycles times replacement cost	Empirical	×	×							E: NLP (Convex)	BP
Padmanabhan [84]	**OF-E-C:** Aging cost based on relative amount of used cycles times battery cost	Empirical [132]	×	×	×						E: MILP	EA & BP
Kim [129]	**OF-E-C:** Aging cost based on relative amount of used cycles times installation cost	Empirical [133]	×	×		×					E: DP	Generic
Englberger [2]	**OF-E-C:** Aging cost based on relative amount of used cycles times investment cost	Semi-Empirical [15]	×	(×)[a]		(×)		(×)	(×)	(×)	E: MILP	Multi-Use
Hou [33]	**OF-E-C:** Aging cost based on relative amount of used cycles times investment cost, efficiency based criterion for EOL	Semi-Empirical [15]	×	×							E: MILP	PS
Zia [134]	**OF-E-C:** Aging cost based on investment cost, O&M cost and battery residual value, divided by scaling factors to account for degradation	Empirical	×	×			×				E: NLP	Microgrid

[a] For stress factor entries marked with "(×)" instead of "×", the stress factors are not directly integrated into the scheduling method, but used for validation of the scheduling results in a separate model.

Fig. 14 shows the resulting calendar and cyclic capacity loss in the respective applications for the LFP Naumann and NMC Schmalstieg models after 5 years. It can be seen that the LFP model has a higher cycle stability than the NMC model, while the NMC model shows less calendar aging than the LFP model. In the FCR application, the calendar capacity loss predominates for the LFP battery due to the small DOCs and C_{rate}. For the NMC battery, the calendar aging also predominates slightly. SCI is the application with the largest cyclic capacity loss for both models. The extremely high cyclic capacity loss for the NMC model can be explained through the stress factor $\beta_{\overline{V}_{\text{cell}}} = \gamma_1 * (\overline{V}_{\text{cell}} - \gamma_2)^2$ (cf. Table 2): in the SCI application a large amount of FECs are conducted at high or low cell voltage, with the battery being

Table 7
Scheduling methods that employ a rule-based aging awareness method or that are using constraints within the optimization problem.

Reference	Aging awareness method	Aging model types	FEC	DOC	C_{rate}	$\overline{SOC}$	T_{cyc}	t	SOC	T_{cal}	Scheduling Method	Applications
Angenendt [119]	**Rule-based:** Reduction of average SOC through load forecasting	Semi-Empirical [135]	(×)	(×)		(×)		(×)	(×)	(×)	Rule-based	SCI
Perez [125]	**In Constraints:** Varying upper and lower limits for the usable SOC range	Empirical [136]	(×)	×	(×)						E: MILP	EA & BP
Cardoso [126]	**In Constraints:** Limit for the energy throughput based on the target lifetime and the expected operating temperature	Semi-Empirical [137]	×		(×)			×		(×)	E: MILP	Microgrid
Li [120]	**In Constraints:** upper and lower limits for SOC and C_{rate} **OF-T:** Minimization of total FECs	Empirical	×		×	×					MH: PSO	V2G
Wankmuller [124]	**In Constraints:** upper and lower limits for SOC and C_{rate} **OF-E-C:** Aging cost as penalty factor with optimal value as subject the investigation	Empirical [138,139]	×								E: MILP	EA
Shi [116]	**In Constraints:** upper and lower limits for SOC **OF-E-C:** Aging cost as penalty factor based on battery cost and cycles until EOL	Empirical	×	×							E: NLP (Convex)	Multi-Use

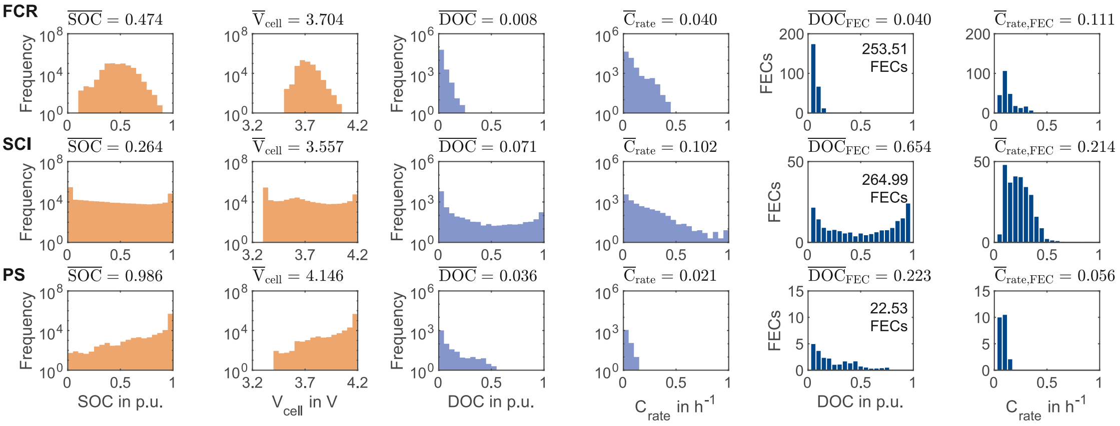

Fig. 13. Distribution and averages of calendar and cyclic stress factors for the three investigated applications (1 year simulation): frequency containment reserve (FCR - top), self consumption increase (SCI - mid), and peak shaving (PS - bottom), based on a one year simulation with the NMC Schmalstieg [15] model at 60 s timesteps. The left two columns (orange) show the frequency of the calendar stress factors, the mid two columns the frequency of the cyclic stress factors (light blue) and the right two columns (dark blue) show the amount of FECs conducted with the cyclic stress factors. Note the logarithmic y-axis for the left four columns of plots. (For interpretation of the references to color in this figure legend, the reader is referred to the web version of this article.)

either empty or full the majority of time, leading to high values for this stress factor with $\gamma_2 = 3.725$ V. Lastly, for the PS application, calendar capacity loss dominates for both models due to the high average SOC / V_{cell} and low amount of FECs.

Often, only a subset of all stress factors are tested in an aging study (cf. Table 2). For example, Schmalstieg et al. cycled all cells at C_{rate} of 1 h^{-1} [15]. While the model by Naumann et al. includes variations in C_{rate}, it does not account for the cyclic stress factor of $\overline{SOC}$ [19]. An even smaller subset of stress factors is considered in most scheduling methods (cf. Tables 4–7). In order to give an estimate of the expected modeling errors due to neglect of individual stress factors in the cell aging study or scheduling method, a series of case studies is conducted hereafter: As a reference case, the NMC Schmalstieg and LFP Naumann models are simulated with all stress factors for FCR, SCI and PS over five years. In the second case, simulations are carried out where for each run one of the stress factors is set to a fixed value that is typically used in an aging study if the dependence of that stress factor is not explicitly modeled. The other stress factors are explicitly calculated as per the aging models. Here, we assume for the LFP Naumann model a DOC of 5%, a C_{rate} of 1 h^{-1} and a SOC of 50%. For the NMC Schmalstieg model, we assume a DOC of 5% as well as a V_{cell} and $\overline{V_{cell}}$ of 3.7136 V, which equals a SOC of 50% as per its open circuit voltage curve. This scenario is referred to as **"typical in aging study"** in the following. In the third case, in each simulation an average value for the respective stress factor is assumed, in order to elaborate if doing so is a valid

Table 8
Application-specific data and profiles for the case study.

Application	FCR	SCI	PS
Storage capacity	1.6 MWh	5 kWh	100 kWh
Rated power	1.6 MW	5 kW	40 kW
AC/DC Conv.	Notton [140]	Notton [140]	Notton [140]
Profiles (1 year)	Frequency profile [141]	PV profile [25], household load profile (profile 28 in [142])	Industry load profile (cluster 2 in [25])
Cell/Degradation Models	3 Ah LFP/Naumann et al. [18,19] 2.15 Ah NMC/Schmalstieg et al. [15]		

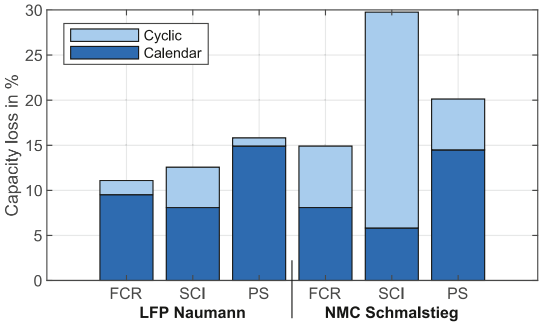

Fig. 14. Capacity loss over five years of the LFP Naumann model (left) and the NMC Schmalstieg model (right) in the BESS applications frequency containment reserve (FCR), self consumption increase (SCI) and peak shaving (PS), split into calendar and cyclic capacity loss. This case is the "standard aging model" in the following figures.

option over internalizing each stress factor into a scheduling method. This case is referred to as **"average in application"** in the following. The average values are determined based on one year simulations, analogously to Fig. 13, e.g. 7.1% for the DOC in the SCI application with the NMC Schmalstieg model. The results of the capacity loss for the BESS with the LFP Naumann model in the use cases for the SCI application are shown in Fig. 15. An example: in Fig. 15b, calculating the cyclic capacity loss using a constant C_{rate} of $1\,h^{-1}$ (scenario T-C_{rate}) leads to an overestimation of the cyclic capacity loss, while the usage of the average C_{rate} in this application replicates the real cyclic capacity loss well (scenario A-C_{rate}).

In the following, we analyze the deviations of the cases from the standard aging model calculation for the LFP Naumann and NMC Schmalstieg models in the three applications (cf. Fig. 16).

In the FCR application with many small cycles around an SOC of about 50%, the assumption of typical values from aging studies or application specific averages for the SOC or V_{cell} only lead to minor deviations compared to the use of the respective exact values from the reference case. The assumption of fixed values for the C_{rate} and DOC leads to slight deviations, which, however, are in the range of less than one percentage point.

The SCI application shows the greatest deviations overall. The values of the stress factors are widely scattered in this application: The BESS sees time-of-day and seasonal variations in SOC and very small, as well as very large, DOCs. In addition, SOCs and DOCs are also very dependent on the dimensioning of the PV system, the BESS, and the load curve. The largest deviations in the results are found when the average or typical value for the DOC or the typical value for the C_{rate} are used instead of the exact values. This is mainly due to the large variation in DOC in this application.

A BESS in PS application is often in the high SOC range and runs few cycles. As a result, calendar aging is particularly relevant in this application (see Fig. 14). If a fixed SOC of 50% or the corresponding V_{cell} is used here, this leads to large deviations in the capacity loss results. In contrast, using the PS average SOC of around 98% leads to very small deviations, as the SOC of the BESS is often in this range. Average or typical values can also be used for the C_{rate} and DOC, but this leads to small deviations, especially for the NMC Schmalstieg model.

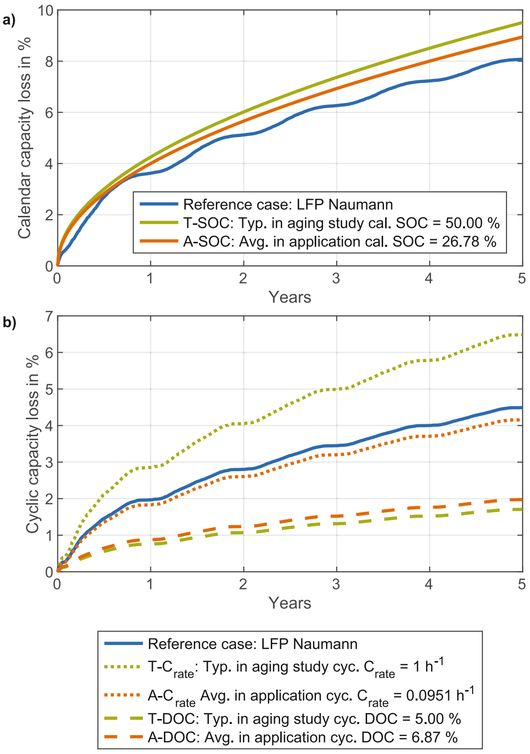

Fig. 15. Calendar capacity loss (a) and cyclic capacity loss (b) for a BESS with the LFP Naumann model in the SCI application over 5 years. The green curves show the results when using typical values from aging studies for the stress factors (SOC = 50%, $C_{rate} = 1\,h^{-1}$ and DOC = 5%). The orange curves show the results when using the application-specific averages (SOC = 26.78%, $C_{rate} = 0.0951\,h^{-1}$ and DOC = 6.87%). (For interpretation of the references to color in this figure legend, the reader is referred to the web version of this article.)

Overall, the evaluation and variation of the stress factors in the applications shows that (a) in FCR, the use of average values for the stress factors leads to only small deviations, attention should be paid though to the low DOC and C_{rate} when selecting a degradation model; (b) in SCI, DOC and C_{rate} are especially relevant; (c) in PS, SOC is the most relevant stress factor, but due to the small variation in operation, an average value may be used without major deviations in the resulting capacity loss.

5. Summary and outlook

This contribution summarizes aging mechanisms, aging stress factors, and degradation modeling approaches for common lithium-ion cell types that are used in BESSs. Furthermore, we review and categorize methods that aim to increase BESS lifetime by accounting for battery degradation effects in the operation strategy. SEI growth on the anode alongside multiple cathode aging mechanisms are the predominant aging mechanisms during the main operation phase. Towards the EOL, cells often show rapid capacity loss, which can be caused

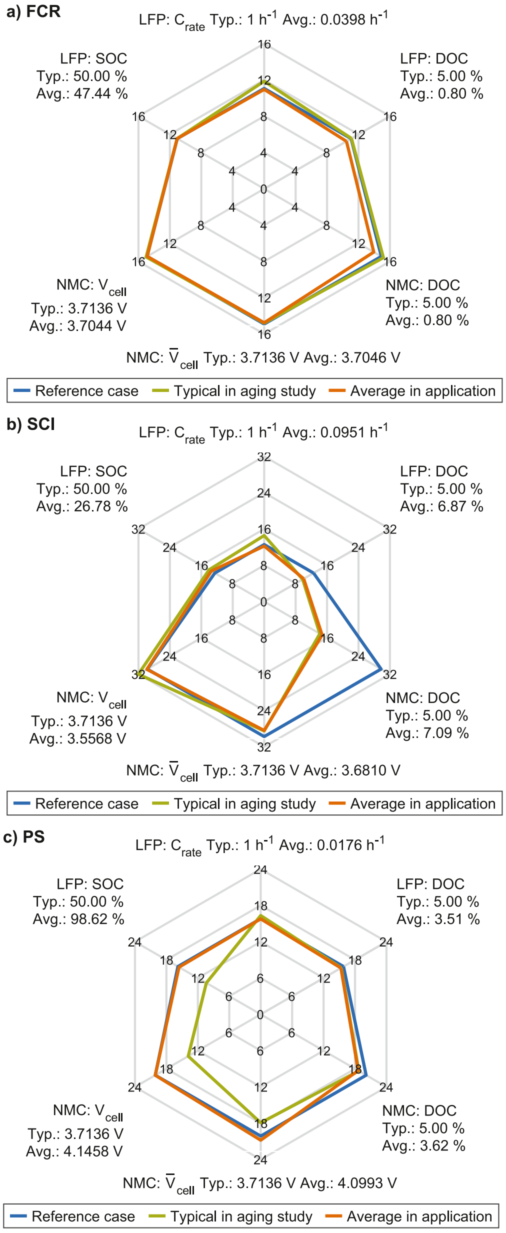

Fig. 16. Spider diagrams of the relative capacity loss for varying the different stress factor scenarios in the applications frequency containment reserve (a), self consumption increase (b) and peak shaving (c). The relative capacity loss is shown after 5 years of simulation time. The top three categories represent the LFP stress factors, the bottom three categories represent the NMC ones. The diagrams show the relative capacity loss using the reference aging model (blue), using typical values from aging studies (green) and using the average values for each application (orange). (For interpretation of the references to color in this figure legend, the reader is referred to the web version of this article.)

by lithium plating or electrolyte depletion. Since the extend of aging depends on external calendar and cyclic stress factors, the degradation behavior can be directly influenced through the operation strategy.

To quantify the resulting capacity loss, empirical, semi-empirical, and physicochemical modeling approaches exist. Present publications in the field of BESS scheduling primarily rely on empirical and semi-empirical modeling approaches, that usually include only a subset of the calendar and cyclic stress factors.

To determine an optimal operation strategy, different scheduling method find use: exact solution approaches, heuristics, and meta-heuristics. The exact solution approach of mixed integer linear programming is particularly frequently used in existing publications. The approaches that are used to account for battery degradation in the scheduling method can be categorized into different aging awareness methods. Most publications rely on a cost based penalty factor for battery degradation, i.e. "aging cost", that is linked to the economic profit from the BESS application as part of the objective function. The case study in Section 4.3 highlights the difference in aging stress factors for key applications of BESSs and shows the importance of making sure that the key stress factors of an application are represented in the degradation model and considered in the scheduling method.

A number of challenges in the field aging aware operation of BESSs remain open and provide opportunity for future research:

- The degradation models that are used for BESS operation usually do not consider the rapid capacity decrease and change in dominant aging mechanisms towards the EOL. Adapting the charge and discharge cut-off voltage or limiting the C_{rate} further towards the EOL may enable further extension of BESS lifetime.
- Machine learning and filtering methods provide an opportunity to improve aging aware operation strategies over the BESS lifetime. This may be done by adapting the degradation models that are used for scheduling based on field data.
- Capacity loss is usually modeled as part of the scheduling method as the primary effect of battery degradation. Accounting for the resistance increase as well may lead to performance improvements.
- While uncertainty in forecasts for price, load, or PV production are considered in some contributions and addressed through methods such as stochastic programming, the uncertainty in degradation modeling is not considered. Accounting for degradation modeling uncertainty may lead to different optimal strategies for risk-seeking and risk-averse BESS operators.
- Aging costs are often chosen based on the battery installation or replacement cost, to link the short-term scheduling problem to long-term degradation effects. Depending on the system operator's objective (e.g. maximum profit until EOL at 80% remaining capacity, maximum profit in the next five years, or maximum profit with system replacements for the indefinite future), a different definition of aging cost may lead to the actual optimal long-term result.

Finally, field data from the increasingly growing and aging fleet of globally installed BESSs is likely to lead to further insights into aging aware operation.

CRediT authorship contribution statement

Nils Collath: Conceptualization, Methodology, Writing – original draft, Writing – review & editing, Software, Project administration, Visualization, Investigation. **Benedikt Tepe:** Writing – original draft, Writing – review & editing, Software, Visualization, Investigation. **Stefan Englberger:** Writing – original draft, Writing – review & editing. **Andreas Jossen:** Writing – review & editing, Funding acquisition. **Holger Hesse:** Writing – original draft, Writing – review & editing, Supervision.

Declaration of competing interest

The authors declare that they have no known competing financial interests or personal relationships that could have appeared to influence the work reported in this paper.

Data availability

The adapted version of the open-source software **SimSES** that was used in Section 4.3 and the simulation are available online, hosted by the Technical University of Munich [144]: https://doi.org/10.14459/2022mp1652796

Funding and acknowledgment

This research is funded by the Bavarian Research Foundation via the research project SmartB4P, Germany (reference number AZ-1376-19) as well as by the German Federal Ministry of Education and Research (BMBF) via the research project greenBattNutzung (grant number 03XP0302D). The project greenBattNutzung is overseen by Project Management Juelich (PtJ).

References

[1] M. Killer, M. Farrokhseresht, N.G. Paterakis, Implementation of large-scale Li-ion battery energy storage systems within the EMEA region, Appl. Energy 260 (2020) 114166, http://dx.doi.org/10.1016/j.apenergy.2019.114166.

[2] S. Englberger, A. Jossen, H. Hesse, Unlocking the potential of battery storage with the dynamic stacking of multiple applications, Cell Rep. Phys. Sci. 1 (11) (2020) 100238, http://dx.doi.org/10.1016/j.xcrp.2020.100238.

[3] International Energy Agency, Energy storage: tracking report - november 2021, 2021, URL https://www.iea.org/reports/energy-storage.

[4] International Renewable Energy Agency, Electricity storage and renewables: Costs and markets to 2030, 2017, URL https://www.irena.org/publications/2017/Oct/Electricity-storage-and-renewables-costs-and-markets.

[5] J. Figgener, P. Stenzel, K.-P. Kairies, J. Linßen, D. Haberschusz, O. Wessels, G. Angenendt, M. Robinius, D. Stolten, D.U. Sauer, The development of stationary battery storage systems in Germany – A market review, J. Energy Storage 29 (2020) 101153, http://dx.doi.org/10.1016/j.est.2019.101153.

[6] U.S. Energy Information Administration, Battery storage in the United States: An update on market trends, 2020, URL https://www.eia.gov/analysis/studies/electricity/batterystorage/.

[7] K. Mongrid, Viswanathan Vilayanur, J. Alam, C. Vartanian, V. Sprenkle, 2020 Grid energy storage technology cost and performance assessment, 2020, URL https://www.energy.gov/energy-storage-grand-challenge/downloads/2020-grid-energy-storage-technology-cost-and-performance.

[8] K. Uddin, R. Gough, J. Radcliffe, J. Marco, P. Jennings, Techno-economic analysis of the viability of residential photovoltaic systems using lithium-ion batteries for energy storage in the United Kingdom, Appl. Energy 206 (10) (2017) 12–21, http://dx.doi.org/10.1016/j.apenergy.2017.08.170.

[9] M. Astaneh, R. Roshandel, R. Dufo-López, J.L. Bernal-Agustín, A novel framework for optimization of size and control strategy of lithium-ion battery based off-grid renewable energy systems, Energy Convers. Manage. 175 (Part 1) (2018) 99–111, http://dx.doi.org/10.1016/j.enconman.2018.08.107.

[10] J.S. Edge, S. O'Kane, R. Prosser, N.D. Kirkaldy, A.N. Patel, A. Hales, A. Ghosh, W. Ai, J. Chen, J. Yang, S. Li, M.-C. Pang, L. Bravo Diaz, A. Tomaszewska, M.W. Marzook, K.N. Radhakrishnan, H. Wang, Y. Patel, B. Wu, G.J. Offer, Lithium ion battery degradation: what you need to know, Phys. Chem. Chem. Phys.: PCCP 23 (14) (2021) 8200–8221, http://dx.doi.org/10.1039/d1cp00359c.

[11] J.P. Pender, G. Jha, D.H. Youn, J.M. Ziegler, I. Andoni, E.J. Choi, A. Heller, B.S. Dunn, P.S. Weiss, R.M. Penner, C.B. Mullins, Electrode degradation in lithium-ion batteries, ACS Nano 14 (2) (2020) 1243–1295, http://dx.doi.org/10.1021/acsnano.9b04365.

[12] J. Vetter, P. Novák, M.R. Wagner, C. Veit, K.-C. Möller, J.O. Besenhard, M. Winter, M. Wohlfahrt-Mehrens, C. Vogler, A. Hammouche, Ageing mechanisms in lithium-ion batteries, J. Power Sources 147 (2005) 269–281, http://dx.doi.org/10.1016/j.jpowsour.2005.01.006.

[13] P. Arora, R.E. White, Capacity fade mechanisms and side reactions in lithium–Ion batteries, J. Electrochem. Soc. 145 (1998) 3647–3667, http://dx.doi.org/10.1149/1.1838857.

[14] M. Ecker, J.B. Gerschler, J. Vogel, S. Käbitz, F. Hust, P. Dechent, D.U. Sauer, Development of a lifetime prediction model for lithium-ion batteries, ecker.2based on extended accelerated aging test data, J. Power Sources 215 (2012) 248–257, http://dx.doi.org/10.1016/j.jpowsour.2012.05.012.

[15] J. Schmalstieg, S. Käbitz, M. Ecker, D.U. Sauer, A holistic aging model for Li(NiMnCo)O2 based 18650 lithium-ion batteries, J. Power Sources 257 (2014) 325–334, http://dx.doi.org/10.1016/j.jpowsour.2014.02.012.

[16] E. Sarasketa-Zabala, I. Gandiaga, L.M. Rodriguez-Martinez, I. Villarreal, Calendar ageing analysis of a LiFePO4/graphite cell with dynamic model validations: Towards realistic lifetime predictions, J. Power Sources 272 (2014) 45–57, http://dx.doi.org/10.1016/j.jpowsour.2014.08.051.

[17] E. Sarasketa-Zabala, I. Gandiaga, E. Martinez-Laserna, L.M. Rodriguez-Martinez, I. Villarreal, Cycle ageing analysis of a LiFePO4/graphite cell with dynamic model validations: Towards realistic lifetime predictions, J. Power Sources 275 (2015) 573–587, http://dx.doi.org/10.1016/j.jpowsour.2014.10.153.

[18] M. Naumann, M. Schimpe, P. Keil, H.C. Hesse, A. Jossen, Analysis and modeling of calendar aging of a commercial LiFePO4/graphite cell, J. Energy Storage 17 (2018) 153–169, http://dx.doi.org/10.1016/j.est.2018.01.019.

[19] M. Naumann, F.B. Spingler, A. Jossen, Analysis and modeling of cycle aging of a commercial LiFePO4/graphite cell, J. Power Sources 451 (2020) 227666, http://dx.doi.org/10.1016/j.jpowsour.2019.227666.

[20] X. Han, L. Lu, Y. Zheng, X. Feng, Z. Li, J. Li, M. Ouyang, A review on the key issues of the lithium ion battery degradation among the whole life cycle, ETransportation (2019) http://dx.doi.org/10.1016/j.etran.2019.100005.

[21] S. Pelletier, O. Jabali, G. Laporte, M. Veneroni, Battery degradation and behaviour for electric vehicles: Review and numerical analyses of several models, Transp. Res. B 103 (2017) 158–187, http://dx.doi.org/10.1016/j.trb.2017.01.020.

[22] M. Woody, M. Arbabzadeh, G.M. Lewis, G.A. Keoleian, A. Stefanopoulou, Strategies to limit degradation and maximize Li-ion battery service lifetime - critical review and guidance for stakeholders, J. Energy Storage 28 (2020) http://dx.doi.org/10.1016/j.est.2020.101231.

[23] T. Weitzel, C.H. Glock, Energy management for stationary electric energy storage systems: A systematic literature review, European J. Oper. Res. 264 (2) (2018) 582–606, http://dx.doi.org/10.1016/j.ejor.2017.06.052.

[24] H. Hesse, M. Schimpe, D. Kucevic, A. Jossen, Lithium-ion battery storage for the grid—A review of stationary battery storage system design tailored for applications in modern power grids, Energies 10 (12) (2017) 2107, http://dx.doi.org/10.3390/en10122107.

[25] D. Kucevic, B. Tepe, S. Englberger, A. Parlikar, M. Mühlbauer, O. Bohlen, A. Jossen, H. Hesse, Standard battery energy storage system profiles: Analysis of various applications for stationary energy storage systems using a holistic simulation framework, J. Energy Storage 28 (2020) 101077, http://dx.doi.org/10.1016/j.est.2019.101077.

[26] N. Pinsky, L. Gaillac, A. Mendoza, J. Argueta, T. Knipe, Performance of advanced electric vehicle batteries in stationary applications, in: 24th Annual International Telecommunications Energy Conference, IEEE, 2002, pp. 366–372, http://dx.doi.org/10.1109/INTLEC.2002.1048682.

[27] J. Neubauer, A. Pesaran, The ability of battery second use strategies to impact plug-in electric vehicle prices and serve utility energy storage applications, J. Power Sources 196 (23) (2011) 10351–10358, http://dx.doi.org/10.1016/j.jpowsour.2011.06.053.

[28] E. Martinez-Laserna, I. Gandiaga, E. Sarasketa-Zabala, J. Badeda, D.-I. Stroe, M. Swierczynski, A. Goikoetxea, Battery second life: Hype, hope or reality? A critical review of the state of the art, Renew. Sustain. Energy Rev. 93 (April) (2018) 701–718, http://dx.doi.org/10.1016/j.rser.2018.04.035.

[29] L.C. Casals, B. Amante García, C. Canal, Second life batteries lifespan: Rest of useful life and environmental analysis, J. Environ. Manag. 232 (2019) 354–363, http://dx.doi.org/10.1016/j.jenvman.2018.11.046.

[30] Y. Li, K. Liu, A.M. Foley, A. Zülke, M. Berecibar, E. Nanini-Maury, J. van Mierlo, H.E. Hoster, Data-driven health estimation and lifetime prediction of lithium-ion batteries: A review, Renew. Sustain. Energy Rev. 113 (2019) 109254, http://dx.doi.org/10.1016/j.rser.2019.109254.

[31] J. Reniers, G. Mulder, D. Howey, Review and performance comparison of mechanical-chemical degradation models for lithium-ion batteries, J. Electrochem. Soc. 166 (14) (2019) A3189–A3200, http://dx.doi.org/10.1149/2.0281914jes.

[32] A. Ahmadian, M. Sedghi, A. Elkamel, M. Fowler, M. Aliakbar Golkar, Plug-in electric vehicle batteries degradation modeling for smart grid studies: Review, assessment and conceptual framework, Renew. Sustain. Energy Rev. 81 (2018) 2609–2624, http://dx.doi.org/10.1016/j.rser.2017.06.067.

[33] Q. Hou, Y. Yu, E. Du, H. He, N. Zhang, C. Kang, G. Liu, H. Zhu, Embedding scrapping criterion and degradation model in optimal operation of peak-shaving lithium-ion battery energy storage, Appl. Energy 278 (2020) 115601, http://dx.doi.org/10.1016/j.apenergy.2020.115601.

[34] J. Cai, H. Zhang, X. Jin, Aging-aware predictive control of PV-battery assets in buildings, Appl. Energy 236 (2019) 478–488, http://dx.doi.org/10.1016/j.apenergy.2018.12.003.

[35] K. Liu, X. Hu, Z. Yang, Y. Xie, S. Feng, Lithium-ion battery charging management considering economic costs of electrical energy loss and battery degradation, Energy Convers. Manage. 195 (2019) 167–179, http://dx.doi.org/10.1016/j.enconman.2019.04.065.

[36] J. Engels, B. Claessens, G. Deconinck, Techno-economic analysis and optimal control of battery storage for frequency control services, applied to the German market, Appl. Energy 242 (2019) 1036–1049, http://dx.doi.org/10.1016/j.apenergy.2019.03.128.

[37] J.M. Reniers, G. Mulder, S. Ober-Blöbaum, D.A. Howey, Improving optimal control of grid-connected lithium-ion batteries through more accurate battery and degradation modelling, J. Power Sources 379 (2018) 91–102, http://dx.doi.org/10.1016/j.jpowsour.2018.01.004.

[38] J. Cao, D. Harrold, Z. Fan, T. Morstyn, D. Healey, K. Li, Deep reinforcement learning-based energy storage arbitrage with accurate lithium-ion battery degradation model, IEEE Trans. Smart Grid 11 (5) (2020) 4513–4521, http://dx.doi.org/10.1109/TSG.2020.2986333.

[39] Z. Yang, K. Li, A. Foley, Computational scheduling methods for integrating plug-in electric vehicles with power systems: A review, Renew. Sustain. Energy Rev. 51 (2015) 396–416, http://dx.doi.org/10.1016/j.rser.2015.06.007.

[40] A. Väyrynen, J. Salminen, Lithium ion battery production, J. Chem. Thermodyn. 46 (2012) 80–85, http://dx.doi.org/10.1016/j.jct.2011.09.005.

[41] C.R. Birkl, M.R. Roberts, E. McTurk, P.G. Bruce, D.A. Howey, Degradation diagnostics for lithium ion cells, J. Power Sources 341 (2017) 373–386, http://dx.doi.org/10.1016/j.jpowsour.2016.12.011.

[42] Y. Chu, Y. Shen, F. Guo, X. Zhao, Q. Dong, Q. Zhang, W. Li, H. Chen, Z. Luo, L. Chen, Advanced characterizations of solid electrolyte interphases in lithium-ion batteries, Electrochem. Energy Rev. 3 (1) (2020) 187–219, http://dx.doi.org/10.1007/s41918-019-00058-y.

[43] C. von Lüders, J. Keil, M. Webersberger, A. Jossen, Modeling of lithium plating and lithium stripping in lithium-ion batteries, J. Power Sources 414 (2019) 41–47, http://dx.doi.org/10.1016/j.jpowsour.2018.12.084.

[44] S. Hein, T. Danner, A. Latz, An electrochemical model of lithium plating and stripping in lithium ion batteries, ACS Appl. Energy Mater. 3 (9) (2020) 8519–8531, http://dx.doi.org/10.1021/acsaem.0c01155.

[45] Y. Chen, Y. Kang, Y. Zhao, L. Wang, J. Liu, Y. Li, Z. Liang, X. He, X. Li, N. Tavajohi, B. Li, A review of lithium-ion battery safety concerns: The issues, strategies, and testing standards, J. Energy Chem. 59 (2021) 83–99, http://dx.doi.org/10.1016/j.jechem.2020.10.017.

[46] L. Guo, D.B. Thornton, M.A. Koronfel, I.E.L. Stephens, M.P. Ryan, Degradation in lithium ion battery current collectors, J. Phys.: Energy 3 (3) (2021) 032015, http://dx.doi.org/10.1088/2515-7655/ac0c04.

[47] R. Xiong, Y. Pan, W. Shen, H. Li, F. Sun, Lithium-ion battery aging mechanisms and diagnosis method for automotive applications: Recent advances and perspectives, Renew. Sustain. Energy Rev. 131 (2020) 110048, http://dx.doi.org/10.1016/j.rser.2020.110048.

[48] S.-T. Myung, F. Maglia, K.-J. Park, C.S. Yoon, P. Lamp, S.-J. Kim, Y.-K. Sun, Nickel-rich layered cathode materials for automotive lithium-ion batteries: Achievements and perspectives, ACS Energy Lett. 2 (1) (2017) 196–223, http://dx.doi.org/10.1021/acsenergylett.6b00594.

[49] Y. Preger, H.M. Barkholtz, A. Fresquez, D.L. Campbell, B.W. Juba, J. Romàn-Kustas, S.R. Ferreira, B. Chalamala, Degradation of commercial lithium-ion cells as a function of chemistry and cycling conditions, J. Electrochem. Soc. 167 (2020) 120532, http://dx.doi.org/10.1149/1945-7111/abae37.

[50] E. Cabrera-Castillo, F. Niedermeier, A. Jossen, Calculation of the state of safety (SOS) for lithium ion batteries, J. Power Sources 324 (2016) 509–520, http://dx.doi.org/10.1016/j.jpowsour.2016.05.068.

[51] D. Ouyang, M. Chen, J. Liu, R. Wei, J. Weng, J. Wang, Investigation of a commercial lithium-ion battery under overcharge/over-discharge failure conditions, RSC Adv. 8 (58) (2018) 33414–33424, http://dx.doi.org/10.1039/C8RA05564E.

[52] P. Keil, S.F. Schuster, J. Wilhelm, J. Travi, A. Hauser, R.C. Karl, A. Jossen, Calendar aging of lithium-ion batteries: I. Impact of the graphie anode on capacity fade, J. Electrochem. Soc. 163 (9) (2016) A1872–A1880, http://dx.doi.org/10.1149/2.0411609jes.

[53] T. Waldmann, M. Wilka, M. Kasper, M. Fleischhammer, M. Wohlfahrt-Mehrens, Temperature dependent ageing mechanisms in lithium-ion batteries – A post-mortem study, J. Power Sources 262 (2014) 129–135, http://dx.doi.org/10.1016/j.jpowsour.2014.03.112.

[54] M. Schimpe, M.E.v. Kuepach, M. Naumann, H. Hesse, K. Smith, A. Jossen, Comprehensive modeling of temperature-dependent degradation mechanisms in lithium iron phosphate batteries, J. Electrochem. Soc. 165 (2) (2018) A181–A193, http://dx.doi.org/10.1149/2.1181714jes.

[55] J. Wang, W. Huang, A. Pei, Y. Li, F. Shi, X. Yu, Y. Cui, Improving cyclability of Li metal batteries at elevated temperatures and its origin revealed by cryo-electron microscopy, Nature Energy 4 (8) (2019) 664–670, http://dx.doi.org/10.1038/s41560-019-0413-3.

[56] P.M. Attia, W.C. Chueh, S.J. Harris, Revisiting the t0.5 dependence of SEI growth, J. Electrochem. Soc. 167 (9) (2020) 090535, http://dx.doi.org/10.1149/1945-7111/ab8ce4.

[57] S. Barcellona, L. Piegari, Effect of current on cycle aging of lithium ion batteries, J. Energy Storage 29 (2020) 101310, http://dx.doi.org/10.1016/j.est.2020.101310.

[58] A. Tomaszewska, Z. Chu, X. Feng, S. O'Kane, X. Liu, J. Chen, C. Ji, E. Endler, R. Li, L. Liu, Y. Li, S. Zheng, S. Vetterlein, M. Gao, J. Du, M. Parkes, M. Ouyang, M. Marinescu, G. Offer, B. Wu, Lithium-ion battery fast charging: A review, ETransportation 1 (15) (2019) 100011, http://dx.doi.org/10.1016/j.etran.2019.100011.

[59] S. Gantenbein, M. Schönleber, M. Weiss, E. Ivers-Tiffée, Capacity fade in lithium-ion batteries and cyclic aging over various state-of-charge ranges, Sustainability 11 (23) (2019) 6697, http://dx.doi.org/10.3390/su11236697.

[60] S. Schweidler, L. de Biasi, A. Schiele, P. Hartmann, T. Brezesinski, J. Janek, Volume changes of graphite anodes revisited: A combined operando X-ray diffraction and in situ pressure analysis study, J. Phys. Chem. C 122 (16) (2018) 8829–8835, http://dx.doi.org/10.1021/acs.jpcc.8b01873.

[61] R.D. Deshpande, K. Uddin, Physics inspired model for estimating 'cycles to failure' as a function of depth of discharge for lithium ion batteries, J. Energy Storage 33 (2) (2021) 101932, http://dx.doi.org/10.1016/j.est.2020.101932.

[62] M. Ecker, N. Nieto, S. Käbitz, J. Schmalstieg, H. Blanke, A. Warnecke, D.U. Sauer, Calendar and cycle life study of Li(NiMnCo)O2-based 18650 lithium-ion batteries, J. Power Sources 248 (9) (2014) 839–851, http://dx.doi.org/10.1016/j.jpowsour.2013.09.143.

[63] F.B. Spingler, M. Naumann, A. Jossen, Capacity recovery effect in commercial LiFePO4 / graphite cells, J. Electrochem. Soc. 167 (4) (2020) 040526, http://dx.doi.org/10.1149/1945-7111/ab7900.

[64] D. Juarez-Robles, J.A. Jeevarajan, P.P. Mukherjee, Degradation-safety analytics in lithium-ion cells: Part I. Aging under charge/discharge cycling, J. Electrochem. Soc. 167 (16) (2020) 160510, http://dx.doi.org/10.1149/1945-7111/abc8c0.

[65] S. Bazlen, P. Heugel, O. von Kessel, W. Commerell, J. Tübke, Influence of charging protocols on the charging capability and aging of lithium-ion cells with silicon-containing anodes, J. Energy Storage 49 (23) (2022) 104044, http://dx.doi.org/10.1016/j.est.2022.104044.

[66] J. Park, W.A. Appiah, S. Byun, D. Jin, M.-H. Ryou, Y.M. Lee, Semi-empirical long-term cycle life model coupled with an electrolyte depletion function for large-format graphite/LiFePO 4 lithium-ion batteries, J. Power Sources 365 (2017) 257–265, http://dx.doi.org/10.1016/j.jpowsour.2017.08.094.

[67] A. Kwade, W. Haselrieder, R. Leithoff, A. Modlinger, F. Dietrich, K. Droeder, Current status and challenges for automotive battery production technologies, Nature Energy 3 (4) (2018) 290–300, http://dx.doi.org/10.1038/s41560-018-0130-3.

[68] S.J. An, J. Li, Z. Du, C. Daniel, D.L. Wood, Fast formation cycling for lithium ion batteries, J. Power Sources 342 (2017) 846–852, http://dx.doi.org/10.1016/j.jpowsour.2017.01.011.

[69] S.F. Schuster, T. Bach, E. Fleder, J. Müller, M. Brand, G. Sextl, A. Jossen, Nonlinear aging characteristics of lithium-ion cells under different operational conditions, J. Energy Storage 1 (2015) 44–53, http://dx.doi.org/10.1016/j.est.2015.05.003.

[70] X.-G. Yang, Y. Leng, G. Zhang, S. Ge, C.-Y. Wang, Modeling of lithium plating induced aging of lithium-ion batteries: Transition from linear to nonlinear aging, J. Power Sources 360 (2017) 28–40, http://dx.doi.org/10.1016/j.jpowsour.2017.05.110.

[71] D. Anseán, M. Dubarry, A. Devie, B.Y. Liaw, V.M. García, J.C. Viera, M. González, Operando lithium plating quantification and early detection of a commercial LiFePO4 cell cycled under dynamic driving schedule, J. Power Sources 356 (2) (2017) 36–46, http://dx.doi.org/10.1016/j.jpowsour.2017.04.072.

[72] C. Kupper, B. Weißhar, S. Rißmann, W.G. Bessler, End-of-life prediction of a lithium-ion battery cell based on mechanistic aging models of the graphite electrode, J. Electrochem. Soc. 165 (14) (2018) A3468–A3480, http://dx.doi.org/10.1149/2.0941814jes.

[73] P.M. Attia, A. Bills, F. Brosa Planella, P. Dechent, G. dos Reis, M. Dubarry, P. Gasper, R. Gilchrist, S. Greenbank, D. Howey, O. Liu, E. Khoo, Y. Preger, A. Soni, S. Sripad, A.G. Stefanopoulou, V. Sulzer, Review—"knees" in lithium-ion battery aging trajectories, Journal of the Electrochemical Society 169 (6) (2022) 060517, http://dx.doi.org/10.1149/1945-7111/ac6d13.

[74] M. Johnen, S. Pitzen, U. Kamps, M. Kateri, P. Dechent, D.U. Sauer, Modeling long-term capacity degradation of lithium-ion batteries, J. Energy Storage 34 (9) (2021) 102011, http://dx.doi.org/10.1016/j.est.2020.102011.

[75] G. He, R. Ciez, P. Moutis, S. Kar, J.F. Whitacre, The economic end of life of electrochemical energy storage, Appl. Energy 273 (2020) 115151, http://dx.doi.org/10.1016/j.apenergy.2020.115151.

[76] P. Fermín-Cueto, E. McTurk, M. Allerhand, E. Medina-Lopez, M.F. Anjos, J. Sylvester, G. dos Reis, Identification and machine learning prediction of knee-point and knee-onset in capacity degradation curves of lithium-ion cells, Energy AI 1 (5) (2020) 100006, http://dx.doi.org/10.1016/j.egyai.2020.100006.

[77] D. Ren, H. Hsu, R. Li, X. Feng, D. Guo, X. Han, L. Lu, X. He, S. Gao, J. Hou, Y. Li, Y. Wang, M. Ouyang, A comparative investigation of aging effects on thermal runaway behavior of lithium-ion batteries, ETransportation 2 (2019) 100034, http://dx.doi.org/10.1016/j.etran.2019.100034.

[78] Y. Li, X. Feng, D. Ren, M. Ouyang, L. Lu, X. Han, Thermal runaway triggered by plated lithium on the anode after fast charging, ACS Appl. Mater. Interfaces 11 (50) (2019) 46839–46850, http://dx.doi.org/10.1021/acsami.9b16589.

[79] L. Feng, L. Jiang, J. Liu, Z. Wang, Z. Wei, Q. Wang, Dynamic overcharge investigations of lithium ion batteries with different state of health, J. Power Sources 507 (6) (2021) 230262, http://dx.doi.org/10.1016/j.jpowsour.2021.230262.

[80] G. He, Q. Chen, C. Kang, P. Pinson, Q. Xia, Optimal bidding strategy of battery storage in power markets considering performance-based regulation and battery cycle life, IEEE Trans. Smart Grid 7 (5) (2016) 2359–2367, http://dx.doi.org/10.1109/TSG.2015.2424314.

[81] M. Kazemi, H. Zareipour, Long-term scheduling of battery storage systems in energy and regulation markets considering battery's lifespan, IEEE Trans. Smart Grid 9 (6) (2018) 6840–6849, http://dx.doi.org/10.1109/TSG.2017.2724919.

[82] M.A. Hossain, H.R. Pota, S. Squartini, F. Zaman, J.M. Guerrero, Energy scheduling of community microgrid with battery cost using particle swarm optimisation, Appl. Energy 254 (9) (2019) 113723, http://dx.doi.org/10.1016/j.apenergy.2019.113723.

[83] Y. Shi, B. Xu, Y. Tan, D. Kirschen, B. Zhang, Optimal battery control under cycle aging mechanisms in pay for performance settings, IEEE Trans. Automat. Control 64 (6) (2019) 2324–2339, http://dx.doi.org/10.1109/TAC.2018.2867507.

[84] N. Padmanabhan, M. Ahmed, K. Bhattacharya, Battery energy storage systems in energy and reserve markets, IEEE Trans. Power Syst. 35 (1) (2020) 215–226, http://dx.doi.org/10.1109/TPWRS.2019.2936131.

[85] A. Maheshwari, N.G. Paterakis, M. Santarelli, M. Gibescu, Optimizing the operation of energy storage using a non-linear lithium-ion battery degradation model, Appl. Energy 261 (4) (2020) 114360, http://dx.doi.org/10.1016/j.apenergy.2019.114360.

[86] C. Guenther, B. Schott, W. Hennings, P. Waldowski, M.A. Danzer, Model-based investigation of electric vehicle battery aging by means of vehicle-to-grid scenario simulations, J. Power Sources 239 (2013) 604–610, http://dx.doi.org/10.1016/j.jpowsour.2013.02.041.

[87] B. Xu, A. Oudalov, A. Ulbig, G. Andersson, D.S. Kirschen, Modeling of lithium-ion battery degradation for cell life assessment, IEEE Trans. Smart Grid 9 (2) (2018) 1131–1140, http://dx.doi.org/10.1109/TSG.2016.2578950.

[88] P. Gasper, K. Gering, E. Dufek, K. Smith, Challenging practices of algebraic battery life models through statistical validation and model identification via machine-learning, J. Electrochem. Soc. 168 (2021) 020502, http://dx.doi.org/10.1149/1945-7111/abdde1.

[89] M. Broussley, S. Herreyre, P. Biensan, P. Kasztejna, K. Nechev, R.J. Staniewicz, Aging mechanism in Li ion cells and calendar life predictions, J. Power Sources 97–98 (2001) 13–21, http://dx.doi.org/10.1016/S0378-7753(01)00722-4.

[90] S. Grolleau, A. Delaille, H. Gualous, P. Gyan, R. Revel, J. Bernard, E. Redondo-Iglesias, J. Peter, Calendar aging of commercial graphite/LiFePO4 cell – predicting capacity fade under time dependent storage conditions, J. Power Sources 255 (2014) 450–458, http://dx.doi.org/10.1016/j.jpowsour.2013.11.098.

[91] S. Khaleghi Rahimian, M.M. Forouzan, S. Han, Y. Tang, A generalized physics-based calendar life model for Li-ion cells, Electrochim. Acta 348 (2020) 136343, http://dx.doi.org/10.1016/j.electacta.2020.136343.

[92] J. Wang, P. Liu, J. Hicks-Garner, E. Sherman, S. Soukiazian, M. Verbrugge, H. Tataria, J. Musser, P. Finamore, Cycle-life model for graphite-LiFePO4 cells, J. Power Sources 196 (8) (2011) 3942–3948, http://dx.doi.org/10.1016/j.jpowsour.2010.11.134.

[93] K.J. Laidler, The development of the arrhenius equation, J. Chem. Educ. 61 (1984) 494–498, http://dx.doi.org/10.1021/ed061p494.

[94] A. Maheshwari, M. Heck, M. Santarelli, Cycle aging studies of lithium nickel manganese cobalt oxide-based batteries using electrochemical impedance spectroscopy, Electrochim. Acta 273 (1) (2018) 335–348, http://dx.doi.org/10.1016/j.electacta.2018.04.045.

[95] K. Smith, A. Saxon, M. Keyser, B. Lundstrom, Z. Cao, A. Roc, Life prediction model for grid-connected Li-ion battery energy storage system, in: 2017 American Control Conference (ACC), IEEE, 2017, pp. 4062–4068, http://dx.doi.org/10.23919/ACC.2017.7963578.

[96] X. Jin, A. Vora, V. Hoshing, T. Saha, G. Shaver, O. Wasynczuk, S. Varigonda, Applicability of available Li-ion battery degradation models for system and control algorithm design, Control Eng. Pract. 71 (8) (2018) 1–9, http://dx.doi.org/10.1016/j.conengprac.2017.10.002.

[97] J. Li, K. Adewuyi, N. Lotfi, R.G. Landers, J. Park, A single particle model with chemical/mechanical degradation physics for lithium ion battery state of health (SOH) estimation, Appl. Energy 212 (4) (2018) 1178–1190, http://dx.doi.org/10.1016/j.apenergy.2018.01.011.

[98] G. Ning, B.N. Popov, Cycle life modeling of lithium-ion batteries, J. Electrochem. Soc. 151 (10) (2004) A1584–A1591, http://dx.doi.org/10.1149/1.1787631.

[99] M.B. Pinson, M.Z. Bazant, Theory of SEI formation in rechargeable batteries: Capacity fade, accelerated aging and lifetime prediction, J. Electrochem. Soc. 160 (2) (2013) A243–A250, http://dx.doi.org/10.1149/2.044302jes.

[100] M. Doyle, T.F. Fuller, J. Newman, Modeling of galvanostatic charge and discharge of the lithium/polymer/insertion cell, J. Electrochem. Soc. 140 (1993) 1526–1533, http://dx.doi.org/10.1149/1.2221597.

[101] M. Doyle, J. Newman, Modeling the performance of rechargeable lithium-based cells: design correlations for limiting cases, J. Power Sources (1995) 45–51, http://dx.doi.org/10.1016/0378-7753(94)02038-5.

[102] T.R. Ashwin, Y.M. Chung, J. Wang, Capacity fade modelling of lithium-ion battery under cyclic loading conditions, J. Power Sources 328 (2016) 586–598, http://dx.doi.org/10.1016/j.jpowsour.2016.08.054.

[103] J. Keil, A. Jossen, Electrochemical modeling of linear and nonlinear aging of lithium-ion cells, J. Electrochem. Soc. 167 (11) (2020) 110535, http://dx.doi.org/10.1149/1945-7111/aba44f.

[104] C. Hu, H. Ye, G. Jain, C. Schmidt, Remaining useful life assessment of lithium-ion batteries in implantable medical devices, J. Power Sources 375 (2018) 118–130, http://dx.doi.org/10.1016/j.jpowsour.2017.11.056.

[105] M. Lucu, E. Martinez-Laserna, I. Gandiaga, K. Liu, H. Camblong, W.D. Widanage, J. Marco, Data-driven nonparametric Li-ion battery ageing model aiming at learning from real operation data - part B: Cycling operation, J. Energy Storage 30 (3) (2020) 101410, http://dx.doi.org/10.1016/j.est.2020.101410.

[106] Kristen A. Severson, Peter M. Attia, Norman Jin, Nicholas Perkins, Benben Jiang, Zi Yang, Michael H. Chen, Muratahan Aykol, Patrick K. Herring, Dimitrios Fraggedakis, Martin Z. Bazant, Stephen J. Harris, William C. Chueh, Richard D. Braatz, Data-driven prediction of battery cycle life before capacity degradation, Nature Energy 4 (2019) 383–391, http://dx.doi.org/10.1038/s41560-019-0356-8.

[107] Z. Deng, X. Lin, J. Cai, X. Hu, Battery health estimation with degradation pattern recognition and transfer learning, J. Power Sources 525 (2022) 231027, http://dx.doi.org/10.1016/j.jpowsour.2022.231027.

[108] W. Li, N. Sengupta, P. Dechent, D. Howey, A. Annaswamy, D.U. Sauer, One-shot battery degradation trajectory prediction with deep learning, J. Power Sources 506 (1) (2021) 230024, http://dx.doi.org/10.1016/j.jpowsour.2021.230024.

[109] X. Tang, K. Liu, X. Wang, F. Gao, J. Macro, W.D. Widanage, Model migration neural network for predicting battery aging trajectories, IEEE Trans. Transp. Electrif. 6 (2) (2020) 363–374, http://dx.doi.org/10.1109/TTE.2020.2979547.

[110] M. Dubarry, A. Devie, K. Stein, M. Tun, M. Matsuura, R. Rocheleau, Battery energy storage system battery durability and reliability under electric utility grid operations: Analysis of 3 years of real usage, J. Power Sources 338 (2) (2017) 65–73, http://dx.doi.org/10.1016/j.jpowsour.2016.11.034.

[111] T. Raj, A.A. Wang, C.W. Monroe, D.A. Howey, Investigation of path–dependent degradation in lithium–Ion batteries**, Batter. Supercaps 3 (12) (2020) 1377–1385, http://dx.doi.org/10.1002/batt.202000160.

[112] G. Baure, A. Devie, M. Dubarry, Battery durability and reliability under electric utility grid operations: Path dependence of battery degradation, J. Electrochem. Soc. (2019) A1991–A2001.

[113] B. Xu, J. Zhao, T. Zheng, E. Litvinov, D.S. Kirschen, Factoring the cycle aging cost of batteries participating in electricity markets, IEEE Trans. Power Syst. 33 (2) (2018) 2248–2259, http://dx.doi.org/10.1109/TPWRS.2017.2733339.

[114] V. Muenzel, J. de Hoog, M. Brazil, A. Vishwanath, S. Kalyanaraman, A multi-factor battery cycle life prediction methodology for optimal battery management, in: S. Kalyanaraman, D.P. Seetharam, R. Shorey, S. Ramchurn, M. Srivastava (Eds.), Proceedings of the 2015 ACM Sixth International Conference on Future Energy Systems, ACM, New York, NY, USA, 2015, pp. 57–66, http://dx.doi.org/10.1145/2768510.2768532.

[115] A. Nuhic, T. Terzimehic, T. Soczka-Guth, M. Buchholz, K. Dietmayer, Health diagnosis and remaining useful life prognostics of lithium-ion batteries using data-driven methods, J. Power Sources 239 (3) (2013) 680–688, http://dx.doi.org/10.1016/j.jpowsour.2012.11.146.

[116] Y. Shi, B. Xu, Di Wang, B. Zhang, Using battery storage for peak shaving and frequency regulation: Joint optimization for superlinear gains, IEEE Trans. Power Syst. 33 (3) (2018) 2882–2894, http://dx.doi.org/10.1109/TPWRS.2017.2749512.

[117] G. Suri, S. Onori, A control-oriented cycle-life model for hybrid electric vehicle lithium-ion batteries, Energy 96 (2) (2016) 644–653, http://dx.doi.org/10.1016/j.energy.2015.11.075.

[118] H. Hesse, V. Kumtepeli, M. Schimpe, J. Reniers, D. Howey, A. Tripathi, Y. Wang, A. Jossen, Ageing and efficiency aware battery dispatch for arbitrage markets using mixed integer linear programming, Energies 12 (6) (2019) 999, http://dx.doi.org/10.3390/en12060999.

[119] G. Angenendt, S. Zurmühlen, H. Axelsen, D.U. Sauer, Comparison of different operation strategies for PV battery home storage systems including forecast-based operation strategies, Appl. Energy 229 (1) (2018) 884–899, http://dx.doi.org/10.1016/j.apenergy.2018.08.058.

[120] S. Li, J. Li, C. Su, Q. Yang, Optimization of bi-directional V2G behavior with active battery anti-aging scheduling, IEEE Access 8 (2020) 11186–11196, http://dx.doi.org/10.1109/ACCESS.2020.2964699.

[121] Mónica Aguado, Elixabete Ayerbe, Cristina Azcárate, Rosa Blanco, Raquel Garde, Fermín Mallor, David M. Rivas, Economical assessment of a wind–hydrogen energy system using WindHyGen® software, Int. J. Hydrogen Energy 34 (7) (2009) 2845–2854, http://dx.doi.org/10.1016/j.ijhydene.2008.12.098.

[122] T. Weitzel, M. Schneider, C.H. Glock, F. Löber, S. Rinderknecht, Operating a storage-augmented hybrid microgrid considering battery aging costs, J. Cleaner Prod. 188 (7) (2018) 638–654, http://dx.doi.org/10.1016/j.jclepro.2018.03.296.

[123] W.B. Powell, Approximate Dynamic Programming: Solving the Curses of Dimensionality, Vol. 703, John Wiley & Sons, 2011.

[124] F. Wankmüller, P.R. Thimmapuram, K.G. Gallagher, A. Botterud, Impact of battery degradation on energy arbitrage revenue of grid-level energy storage, J. Energy Storage 10 (2017) 56–66, http://dx.doi.org/10.1016/j.est.2016.12.004.

[125] A. Perez, R. Moreno, R. Moreira, M. Orchard, G. Strbac, Effect of battery degradation on multi-service portfolios of energy storage, IEEE Trans. Sustain. Energy 7 (4) (2016) 1718–1729, http://dx.doi.org/10.1109/TSTE.2016.2589943.

[126] G. Cardoso, T. Brouhard, N. DeForest, D. Wang, M. Heleno, L. Kotzur, Battery aging in multi-energy microgrid design using mixed integer linear programming, Appl. Energy 231 (2018) 1059–1069, http://dx.doi.org/10.1016/j.apenergy.2018.09.185.

[127] J. Li, M.A. Danzer, Optimal charge control strategies for stationary photovoltaic battery systems, J. Power Sources 258 (2014) 365–373, http://dx.doi.org/10.1016/j.jpowsour.2014.02.066.

[128] E. Kruger, Q.T. Tran, Minimal aging operating strategies for battery energy storage systems in photovoltaic applications, in: 2016 IEEE PES Innovative Smart Grid Technologies Conference Europe (ISGT-Europe), IEEE, 2016, pp. 1–6, http://dx.doi.org/10.1109/ISGTEurope.2016.7856325.

[129] W.-W. Kim, J.-S. Shin, S.-Y. Kim, J.-O. Kim, Operation scheduling for an energy storage system considering reliability and aging, Energy 141 (2017) 389–397, http://dx.doi.org/10.1016/j.energy.2017.09.091.

[130] K. Abdulla, J. de Hoog, V. Muenzel, F. Suits, K. Steer, A. Wirth, S. Halgamuge, Optimal operation of energy storage systems considering forecasts and battery degradation, IEEE Trans. Smart Grid 9 (3) (2016) 2086–2096, http://dx.doi.org/10.1109/TSG.2016.2606490.

[131] X. Jin, A. Vora, V. Hoshing, T. Saha, G. Shaver, R.E. García, O. Wasynczuk, S. Varigonda, Physically-based reduced-order capacity loss model for graphite anodes in Li-ion battery cells, J. Power Sources 342 (9) (2017) 750–761, http://dx.doi.org/10.1016/j.jpowsour.2016.12.099.

[132] M.A. Ortega-Vazquez, Optimal scheduling of electric vehicle charging and vehicle–to–grid services at household level including battery degradation and price uncertainty, IET Gener. Transm. Distrib. 8 (6) (2014) 1007–1016, http://dx.doi.org/10.1049/iet-gtd.2013.0624.

[133] X. Qing, X. Lin, Y. Wang, M. Pedram, D. Shin, N. Chang, State of health aware charge management in hybrid electrical energy storage systems, in: 2012 Design, Automation & Test in Europe Conference & Exhibition (DATE), IEEE, 2012, pp. 1060–1065, http://dx.doi.org/10.1109/DATE.2012.6176652.

[134] M.F. Zia, E. Elbouchikhi, M. Benbouzid, Optimal operational planning of scalable DC microgrid with demand response, islanding, and battery degradation cost considerations, Appl. Energy 237 (2019) 695–707, http://dx.doi.org/10.1016/j.apenergy.2019.01.040.

[135] D. Magnor, Globale Optimierung Netzgekoppelter PV-Batteriesysteme Unter Besonderer Berücksichtigung der Batteriealterung (Ph.D. thesis), 2017, http://dx.doi.org/10.18154/RWTH-2017-06592.

[136] B.E. Olivares, M.A. Cerda Munoz, M.E. Orchard, J.F. Silva, Particle-filtering-based prognosis framework for energy storage devices with a statistical characterization of state-of-health regeneration phenomena, IEEE Trans. Instrum. Meas. 62 (2) (2013) 364–376, http://dx.doi.org/10.1109/TIM.2012.2215142.

[137] D. Wang, J. Coignard, T. Zeng, C. Zhang, S. Saxena, Quantifying electric vehicle battery degradation from driving vs. vehicle-to-grid services, J. Power Sources 332 (2016) 193–203, http://dx.doi.org/10.1016/j.jpowsour.2016.09.116.

[138] S.B. Peterson, J. Apt, J.F. Whitacre, Lithium-ion battery cell degradation resulting from realistic vehicle and vehicle-to-grid utilization, J. Power Sources 195 (8) (2010) 2385–2392, http://dx.doi.org/10.1016/j.jpowsour.2009.10.010.

[139] S. Watanabe, M. Kinoshita, T. Hosokawa, K. Morigaki, K. Nakura, Capacity fade of LiAlyNi1−x−yCoxO2 cathode for lithium-ion batteries during accelerated calendar and cycle life tests (surface analysis of LiAlyNi1−x−yCoxO2 cathode after cycle tests in restricted depth of discharge ranges), J. Power Sources 258 (2014) 210–217, http://dx.doi.org/10.1016/j.jpowsour.2014.02.018.

[140] G. Notton, V. Lazarov, L. Stoyanov, Optimal sizing of a grid-connected PV system for various PV module technologies and inclinations, inverter efficiency characteristics and locations, Renew. Energy 35 (2) (2010) 541–554, http://dx.doi.org/10.1016/j.renene.2009.07.013.

[141] 50Hertz Transmission GmbH, Archiv netzfrequenz (in German): Daten der ENTSO-E netzfrequenz, 2019, URL https://www.50hertz.com/de/Transparenz/Kennzahlen/Regelenergie/ArchivNetzfrequenz.

[142] T. Tjaden, J. Bergner, J. Weniger, V. Quaschning, Repräsentative elektrische lastprofile für wohngebäude in deutschland auf 1-sekündiger datenbasis (in German), 2015, URL https://pvspeicher.htw-berlin.de/veroeffentlichungen/daten/.

[143] M. Möller, D. Kucevic, N. Collath, A. Parlikar, P. Dotzauer, B. Tepe, S. Englberger, A. Jossen, H. Hesse, SimSES: A holistic simulation framework for modeling and analyzing stationary energy storage systems, J. Energy Storage 49 (11) (2022) 103743, http://dx.doi.org/10.1016/j.est.2021.103743.

[144] N. Collath, B. Tepe, S. Englberger, A. Jossen, H. Holger, Battery degradation in BESS use-cases with varying degradation models and stress factor assumptions, 2022, http://dx.doi.org/10.14459/2022mp1652796.

4 Increasing the lifetime profitability of battery energy storage systems through aging aware operation

This chapter presents the peer-reviewed journal publication *Increasing the lifetime profitability of battery energy storage systems through aging aware operation.* As detailed in Chapter 3, different approaches are found in the literature for modeling battery degradation as part of optimization problems for the aging aware operation of BESSs. The different degradation modeling approaches vary in complexity and in the solution methods that are required for solving the resulting optimization problem. This publication proposes a MPC framework for designing aging aware operation strategies and for benchmarking different aging aware operation strategies against each other. As part of the publication, it is shown that an increase of the lifetime profitability can be achieved by determining the *optimal aging cost* with the MPC framework as opposed to the approach commonly used in the literature of basing aging cost on the battery or BESS investment cost.

The basic principle of the MPC framework is to use a detailed system model, or *digital twin*, of a BESS as a benchmark for comparing the effect of different operation strategies. Here, SimSES [83], which is described in Appendix A, is used as a detailed system model. The MPC framework includes different pre-configured optimization models for the aging aware operation of BESSs. It passes the power target for the next timesteps to SimSES after solving the selected optimization model. Following that, the detailed system model is run in SimSES, and the relevant MPC variables, such as the SOC and SOH, are passed back to the MPC framework, which subsequently solves the optimization model for the next optimization horizon. The code of the MPC framework and the configuration files that were used to generate the results which are presented in the paper are available open source[2] [231].

Using the MPC framework, the application of energy arbitrage on the intraday market of the EPEX electricity exchange is investigated using a representative BESS with LFP cells. Three different degrees of complexity for modeling battery aging as part of the MILP optimization model are compared:

- *Energy throughput:* This approach only accounts for the FEC dependence of cyclic aging.
- *Energy throughput and calendar degradation model:* Here, a linearized calendar degradation model of the LFP cells is integrated into the MILP, in addition to the energy throughput model. The linearized calendar aging model accounts for the SOC dependence of calendar aging.
- *Cyclic and calendar degradation model:* Here, linearized calendar and cyclic degradation models of the LFP cells are integrated into the MILP. Thereby, the SOC dependence of calendar aging and the FEC, C^{rate}, and DOC dependence of cyclic aging are accounted for.

For each of the three model types, the *optimal aging cost* for achieving the maximum lifetime profit over a representative twelve-year timeframe is determined. If the aging costs are set too low, the BESS reaches its EOL of 80 % SOH prematurely. If the aging costs are too high, additional profit could have been generated in the investigated timeframe. Further analyses show that when accounting for

---

[2] The code and configuration files that were used to generate the results are publicly available: https://gitlab.lrz.de/open-ees-ses/aging-aware-MPC

the interest rate and maximizing the lifetime net present value (NPV) instead of the lifetime profit, the optimal lifespan can be determined with the MPC framework as well, instead of investigating a representative timeframe over which the profit is meant to be maximized.

Comparing the three optimization model types with their respective optimal aging cost shows that the lifetime profit from energy arbitrage can be increased by 24.9 % by using the linearized calendar degradation model and by 29.3 % by using both the linearized calendar and cyclic degradation model, compared to the energy throughput-based aging cost model. The more detailed degradation models allow the BESS to more accurately avoid those energy arbitrage opportunities that promise high arbitrage profit but also cause significant battery degradation. The significant increase in lifetime profit underlines the benefit that can be gained through aging aware operation.
By examining price data from 2019 to 2022, the case study further demonstrates that the recent increases in prices and price fluctuations on wholesale electricity markets have led to a substantial increase in the lifetime profit that can be achieved with BESSs through energy arbitrage.

In summary, this contribution provides an easy-to-adopt framework for designing and validating aging aware operation strategies. In addition, the monetary benefit of including aging stress factors in optimization models is quantified and the benefit of determining the optimal aging cost is highlighted. Finally, the code is released open-source to make the methods used accessible to a broad audience.

Author contribution

- **Nils Collath:** Conceptualization, Investigation, Methodology, Project administration, Software, Visualization, Writing – original draft, Writing – review & editing
- **Martin Cornejo:** Software, Writing – review & editing
- **Veronika Engwerth:** Methodology, Writing – review & editing
- **Holger Hesse:** Methodology, Writing – review & editing
- **Andreas Jossen:** Funding acquisition, Supervision, Writing – review & editing

Increasing the lifetime profitability of battery energy storage systems through aging aware operation

Nils Collath, Martin Cornejo, Veronika Engwerth, Holger Hesse, Andreas Jossen

Applied Energy 348, p. 121531, 2023

Permanent weblink:
https://doi.org/10.1016/j.apenergy.2023.121531

Applied Energy 348 (2023) 121531

Contents lists available at ScienceDirect

Applied Energy

journal homepage: www.elsevier.com/locate/apenergy

Increasing the lifetime profitability of battery energy storage systems through aging aware operation

Nils Collath [a,*], Martin Cornejo [a], Veronika Engwerth [a], Holger Hesse [b], Andreas Jossen [a]

[a] *Technical University of Munich, TUM School of Engineering and Design, Department of Energy and Process Engineering, Chair of Electrical Energy Storage Technology, Arcisstr. 21, 80333 Munich, Germany*
[b] *Kempten University of Applied Sciences, Bahnhofstr. 61, 87435 Kempten, Germany*

ARTICLE INFO

Keywords:
Battery energy storage system
Lithium-ion
Degradation model
Aging cost
Intraday trading
Energy arbitrage

ABSTRACT

Lithium-ion cells are subject to degradation due to a multitude of cell-internal aging effects, which can significantly influence the economics of battery energy storage systems (BESS). Since the rate of degradation depends on external stress factors such as the state-of-charge, charge/discharge-rate, and depth of cycle, it can be directly influenced through the operation strategy. In this contribution, we propose a model predictive control (MPC) framework for designing aging aware operation strategies. By simulating the entire BESS lifetime on a digital twin, different aging aware optimization models can be benchmarked and the optimal value for aging cost can be determined. In a case study, the application of generating profit through arbitrage trading on the EPEX SPOT intraday electricity market is investigated. For that, a linearized model for the calendar and cyclic capacity loss of a lithium iron phosphate cell is presented. The results show that using the MPC framework to determine the optimal aging cost can significantly increase the lifetime profitability of a BESS, compared to the prevalent approach of selecting aging cost based on the cost of the battery system. Furthermore, the lifetime profit from energy arbitrage can be increased by an additional 24.9% when using the linearized calendar degradation model and by 29.3% when using both the linearized calendar and cyclic degradation model, compared to an energy throughput based aging cost model. By examining price data from 2019 to 2022, the case study demonstrates that the recent increases in prices and price fluctuations on wholesale electricity markets have led to a substantial increase of the achievable lifetime profit.

1. Introduction

Stationary battery energy storage system (BESS) are used for a variety of applications and the globally installed capacity has increased steadily in recent years [1,2]. In behind-the-meter applications such as increasing photovoltaic self-consumption or optimizing electricity tariffs through peak shaving, BESSs generate cost savings for the end-user. In front-of-the-meter applications such as frequency regulation and energy arbitrage, operators generate revenue by marketing BESSs in the respective energy and power markets. Lastly, in microgrids using a BESS with a renewable energy source can be a cost-competitive option over relying on diesel generators [3].

Following the cost reductions and technological advances of recent years, lithium-ion cells are now the predominant battery technology for BESS installations [1,4]. However, like other battery types as well, lithium-ion batteries are subject to degradation due to a multitude of cell internal aging mechanisms. This leads, among others, to a decrease in cell capacity and an increase of the cell's internal resistance. Multiple reviews are available that focus on the aging mechanisms in lithium-ion cells [5–7].

On a system level, battery aging manifests itself in decreasing usable capacity and increasing charge/discharge losses over a BESS lifetime [8,9]. This in turn directly affects the economic viability of a BESS, as less profit from the application can be generated in later years compared to the beginning of life [10,11]. Furthermore, it is often assumed that after a certain extent of battery aging, the BESS will reach its end-of-life (EOL). A common assumption is to set the EOL to the point at which a certain level of remaining capacity, often named state of health [.] (SOH), is reached, for example at a SOH of 70% [12] or 80% [13–15] of the initial battery capacity. The physical rationale behind this assumption is that many lithium-ion cells show a rapid increase in their degradation rate following this SOH range, which is referred to as an aging knee or nonlinear aging [16,17]. In addition, manufacturers often provide warranties that cover batteries

---

[*] Corresponding author at: Technical University of Munich, TUM School of Engineering and Design, Department of Energy and Process Engineering, Chair of Electrical Energy Storage Technology, Arcisstr. 21, 80333 Munich, Germany.
E-mail address: nils.collath@tum.de (N. Collath).

https://doi.org/10.1016/j.apenergy.2023.121531
Received 4 April 2023; Received in revised form 13 June 2023; Accepted 25 June 2023

Abbreviations

BESS	battery energy storage system
C_{rate}	charge-discharge rate
DOC	depth of cycle
EOL	end-of-life
FEC	full equivalent cycle
LFP	lithium iron phosphate
MILP	mixed integer linear programming
MPC	model predictive control
NPV	net present value
SimSES	Simulation Tool for Stationary Energy Storage Systems
SOC	state of charge
SOH	state of health [.]

General parameters

$\mathbb{C}^{aging}$	Total aging cost over the full optimization horizon [EUR]
$\mathbb{C}^{aging,cyc,cal}$	Total aging cost over the full optimization horizon for aging cost model (iii) [EUR]
$\mathbb{C}^{aging,FEC}$	Total aging cost over the full optimization horizon for aging cost model (i) [EUR]
$\mathbb{C}^{aging,FEC,cal}$	Total aging cost over the full optimization horizon for aging cost model (ii) [EUR]
$\mathbb{C}_t^{aging}$	Total aging cost in timestep t [EUR]
ΔFEC_t	Number of FECs in timestep t [.]
i	Interest rate [.]
$\mathbb{P}_m^{arb}$	Profit gained from energy arbitrage in year m [EUR]
$\mathbb{P}_t$	Profit gained in the respective application in timestep t [EUR]
SOH	state of health [.]

Optimization constants

η	Charge/discharge efficiency of the BESS assumed for the optimization model [.]
c^{aging}	Aging cost per unit of capacity loss for the optimization model [EUR/kWh]
c_t^{id}	Electricity price on the intraday electricity market in timestep t [EUR/kWh]
E^{batt}	Remaining rated energy after accounting for degradation [kWh]
E^n	Nominal battery capacity at the beginning of life [kWh]
$P^{AC,max}$	Maximum charge and discharge power of the BESS [kW]
$Q^{loss,cal}$	Total calendar capacity loss at the beginning of the optimization horizon [.]
$Q^{loss,cyc}$	Total cyclic capacity loss at the beginning of the optimization horizon [.]
X_i^{cal}	x-values of the linearized calendar aging function in point i [.]
X_j^{cyc}	x-values of the linearized cyclic aging function in point j [kWh]
Z_i^{cal}	z-values of the linearized calendar aging function in point i [.]
Z_j^{cyc}	z-values of the linearized cyclic aging function in point j [.]
Δt	Optimization timestep length [h]
FEC^{EOL}	Totals FECs until end-of-life is assumed [.]
SOC^{start}	SOC at the beginning of the optimization horizon [.]
SOH^{EOL}	SOH at which end-of-life is assumed [.]

Optimization index sets

H	Index set of timeblocks for the linearized cyclic aging model, $h \in H$
I	Index set of points for the linearized calendar aging model, $i \in I$
J	Index set of points for the linearized cyclic aging model, $j \in J$
T	Index set of timesteps for the current optimization horizon, $t \in T$
T_h	Index set of all timesteps in timeblock h, $t \in T_h$

Optimization decision variables

$\lambda_{t,i}^{cal}$	SOS-type 2 variables for linearization of calendar aging [.]
$\lambda_{h,j}^{cyc,ch}$	SOS-type 2 variables for linearization of cyclic aging in charge direction [.]
$\lambda_{h,j}^{cyc,dis}$	SOS-type 2 variables for linearization of cyclic aging in discharge direction [.]
e_h^{ch}	Energy throughput in charge direction in timeblock h [kWh]
e_h^{dis}	Energy throughput in discharge direction in timeblock h [kWh]
p_t^{ch}	Charge power of the BESS in timestep t [kW]
p_t^{dis}	Discharge power of the BESS in timestep t [kW]
$q_t^{loss,cal}$	Calendar capacity loss in timestep t [.]
$q_h^{loss,cyc,ch}$	Cyclic capacity loss in charge direction in timeblock h [.]
$q_h^{loss,cyc,dis}$	Cyclic capacity loss in discharge direction in timeblock h [.]
soc_t	BESS state-of-charge at timestep t [.]

dropping below a specified SOH threshold within the warranty period [18], which is why these thresholds can act as a reference for the techno-economic assessment and operation of BESSs.

The rate of battery aging itself depends on multiple external stress factors [19], which enables the operator to influence the aging behavior through the operating conditions. For the purpose of BESS operation, battery aging can be grouped into calendar and cyclic aging. Calendar aging refers to those mechanisms that occur regardless of the battery being cycled or not, for example the continued growth of the solid electrolyte interphase [19]. Calendar aging generally progresses faster at a high storage temperature and a high state of charge (SOC) [20,21]. Cyclic aging refers to those aging mechanisms that occur as a consequence of cycling the battery cells, such as particle cracking, solid electrolyte interphase re-formation at newly exposed anode surface areas, and lithium plating [19]. Cyclic aging progresses with the growing number of charge/discharge cycles and tends to accelerate when cycling at a high charge-discharge rate (C_{rate}) and a high depth of cycle (DOC) [22,23]. In addition, both high and low temperatures [23] and cycling a battery in particularly straining SOC ranges can accelerate cyclic aging [20].

Operating a BESS under consideration of the relevant stress factors provides an opportunity to slow down battery aging. Aging aware operation therefore promises higher profits over the BESS lifetime and more resource-efficient use of the battery cells. In this contribution, we propose a model predictive control (MPC) framework for aging aware operation of BESSs. The MPC framework allows benchmarking the performance of different aging aware optimization models on a digital twin of a BESS. Thereby, the operation strategy can be designed and validated before being deployed on the real-world BESS. While we focus on the application of energy arbitrage, the framework is transferable to other applications as well. In the following two subsections of this introduction, we will first present the literature review before describing the structure and highlighting the main contributions of this work.

1.1. Literature review

The process of deriving a series of charge and discharge signals for a BESS under consideration of technical constraints and economic benefit is referred to with different terms in the literature: operation strategy [24], energy management [25], scheduling [26], control [27], or dispatch [28]. We here refer to this process as an operation strategy in the following. A distinction is then made between simple, rule-based operation strategies and optimization-based operation strategies, which also differ in how battery aging can be incorporated, i.e. how the operation strategy can be made "aging aware" [10]. Examples of rule-based, aging aware operation strategies are variable limits for the maximum $\mathrm{C}_{\mathrm{rate}}$ of the BESS [29], or forecast-based rules such as to only charge a home-storage system with the amount of surplus photovoltaic energy during the day, that is forecasted to be needed during the night, thereby reducing calendar aging [24].

Optimization-based operation strategies generally aim to find an optimum to an objective function, which is also referred to as a fitting or reward function for some methods. The methods used to determine the optimum can be classified into exact solution approaches (e.g. linear programming), heuristics (e.g. reinforcement learning), and meta-heuristics (e.g. particle swarm optimization) [25]. A particularly common approach for considering battery aging in an optimization-based operation strategy is to define a monetary value that represents the effects of battery aging, i.e. aging cost [19]. This approach allows to link the short-term scheduling problem to long-term degradation effects:

$$\max \sum_{t\in T} \left(\mathbb{P}_t - \mathbb{C}_t^{\text{aging}}\right) \tag{1}$$

Here, $\mathbb{P}_t$ is the profit gained in the respective application for timestep $t \in T$ and $\mathbb{C}_t^{\text{aging}}$ the total aging cost for timestep $t \in T$. The total aging cost $\mathbb{C}_t^{\text{aging}}$ is then either calculated based on each percentage point of SOH loss in each time step $\Delta\mathrm{SOH}_t$ as in Eq. (2) [12–15,28] or based on the number of full equivalent cycles (FECs) in each time step $\Delta\mathrm{FEC}_t$ as in Eq. (3) [30–34].

$$\mathbb{C}_t^{\text{aging,SOH}_t} = \frac{c^{\text{aging}} \cdot E^{\mathrm{n}}}{1 - \mathrm{SOH}^{\mathrm{EOL}}} \cdot \Delta\mathrm{SOH}_t \tag{2}$$

$$\mathbb{C}_t^{\text{aging,FEC}} = \frac{c^{\text{aging}} \cdot E^{\mathrm{n}}}{\mathrm{FEC}^{\mathrm{EOL}}} \cdot \Delta\mathrm{FEC}_t \tag{3}$$

Here, $\mathrm{SOH}^{\mathrm{EOL}}$ and $\mathrm{FEC}^{\mathrm{EOL}}$ represent the SOH threshold and number of FECs after which the EOL of the battery is reached. E^n is the nominal battery capacity at the beginning of life in kWh. The aging cost c^{aging} in EUR per kWh is then typically set to a cost value that relates to the battery system, such as the full storage system investment cost [14,33,34], battery investment cost [11,35,36], battery replacement cost [12,15,37], battery cell replacement cost [13,30], or generic battery cost [28,31,38].

This common practice of setting the value of aging cost c^{aging} equal to battery system cost has a shortcoming: The profit generated in a given application, e.g. performing energy arbitrage through an electricity exchange, is generated after the BESS has been installed and has no dependence on the original system cost. Instead, c^{aging} can be seen as a penalty factor for operating a BESS. As we will show, by using the proposed MPC framework to determine the optimal value for c^{aging} based on the application and battery aging behavior, a higher lifetime profitability can be achieved.

Furthermore, different approaches are found in the literature for modeling battery aging as part of the optimization problem. The different degradation modeling approaches vary in their degree of complexity and the solution methods required to solve the resulting optimization problem. In relation to Eqs. (2) and (3), these degradation models are additional constraints that define how $\Delta\mathrm{SOH}_t$ and $\mathrm{FEC}^{\mathrm{EOL}}$ are calculated based on the operating conditions.

Table 1 shows an overview of related publications that propose aging aware operations strategies for energy arbitrage with BESSs. Hesse et al. [28] and Kumtepeli et al. [39] both used semi-empirical degradation models as part of their mixed integer linear programming (MILP) optimization, the originally nonlinear, calendar and cyclic degradation models were linearized in order to be solved in the MILPs. Englberger et al. used an MPC approach, in which no other stress factors than the charge throughput are considered in the optimization model, but a separate nonlinear, semi-empirical degradation model is run to validate the optimization results and update the SOH [34]. Cao et al. used a reinforcement learning approach in which a reinforcement learning agent is trained on both predictions and a nonlinear battery model that accounts for calendar and cyclic capacity loss [38]. Reniers et al. compared three different degradation models with a sliding horizon optimization over a one-year timeframe, the most complex model being a single particle physicochemical model, which required a complex gradient-based nonlinear solution approach to solve [27].

Optimization models for BESS operation can get complex and timely to solve even without incorporating battery aging, for example when using stochastic programming to consider forecast uncertainty or when optimizing for multi-use applications, in which multiple applications are served by the same BESS [40]. The question that remains is what benefit can be gained by using more complex degradation models as part of the optimization model when considering the entire BESS lifetime. This requires the determination of the lifetime optimal aging cost of each model for a fair comparison. Maheshwari et al. used different weighting factors which are to be set by the operator to link aging cost to the profit from the application and investigated only a 1-week timeframe [41]. He et al. notably proposed an optimization model that determines the optimal aging cost value [42]. The optimization model however, includes a simplified aging model that only accounts for the DOC dependence of cyclic aging.

In contrast to previous contributions, the MPC framework proposed here allows the comparison of different optimization models on a digital twin of a BESS. By finding the optimal aging cost value c^{aging} for each optimization model and by considering the entire BESS lifetime, the optimal lifetime profit of different aging aware operation strategies can be quantified. Thereby, the proposed MPC framework can be used to benchmark different aging aware operation strategies on a digital twin, before deploying the optimal strategy on the real-world BESS.

1.2. Structure and main contributions

In the following sections, we first describe the proposed MPC framework. In addition, the electricity price time series used for the case study, the different aging aware optimization models, and the software that is used as a digital twin of the BESS are presented. In the subsequent case study, the application of energy arbitrage on the intraday electricity market is investigated. We thereby showcase the functionality of the MPC framework and investigate the increase in lifetime profitability that can be achieved by determining the optimal aging cost value and by using different degrees of complexity for modeling battery aging as part of the optimization model. We summarize our main contributions as follows:

- Open-source MPC framework for designing aging aware operation strategies on a digital twin of a BESS

Table 1
Publications that propose aging aware operation strategies for energy arbitrage with BESSs, compared to this contribution.

Reference	Stress factors considered in optimization model	Optimal aging cost	Investigated timeframe	MPC approach
Kazemi[a] [37]	$Q^{\mathrm{loss,cyc}}(\mathrm{FEC},\mathrm{DOC})$	no (c^{aging}: replacement cost)	1 day	no
Hesse [28]	$Q^{\mathrm{loss,cal}}(t,\mathrm{SOC})$; $Q^{\mathrm{loss,cyc}}(\mathrm{FEC},\mathrm{C_{rate}})$	no (c^{aging}: battery cost)	1 month	no
Reniers [27]	Various (physicochemical model)	no (c^{aging}: battery cost)	1 week	no
Cao[a] [38]	$Q^{\mathrm{loss,cal}}(t,\mathrm{SOC},T)$; $Q^{\mathrm{loss,cyc}}(\mathrm{FEC},\mathrm{DOC},\overline{\mathrm{SOC}},T)$[a]	no (c^{aging}: battery cost)	1 year	no
Maheshwari [41]	$Q^{\mathrm{loss,cyc}}(\mathrm{FEC},\mathrm{DOC},\overline{\mathrm{SOC}},\mathrm{C_{rate}})$	no (c^{aging}: weighting factors)	7 days	no
Wankmuller [9]	$Q^{\mathrm{loss,cyc}}(\mathrm{FEC})$	no (c^{aging}: different values)	10 years	no
He [42]	$Q^{\mathrm{loss,cyc}}(\mathrm{FEC},\mathrm{DOC})$	**yes**	**full lifetime**	no
Englberger[a] [34]	$Q^{\mathrm{loss,cyc}}(\mathrm{FEC})$	no (c^{aging}: battery cost)	**full lifetime**	partially
Kumtepeli [39]	$Q^{\mathrm{loss,cal}}(t,\mathrm{SOC},T)$; $Q^{\mathrm{loss,cyc}}(\mathrm{FEC},\mathrm{C_{rate}},T)$	no (c^{aging}: battery cost)	1 year	**yes**
This contribution	$Q^{\mathrm{loss,cal}}(t,\mathrm{SOC})$; $Q^{\mathrm{loss,cyc}}(\mathrm{FEC},\mathrm{DOC},\mathrm{C_{rate}})$	**yes**	**full lifetime**	**yes**

[a] Kazemi et al. consider frequency regulation in addition to energy arbitrage while Englberger et al. consider energy arbitrage, frequency regulation and peak shaving. In Cao et al. the stress factors are not explicitly considered in the operation strategy, but the reinforcement learning agent is trained on a battery model that considers these stated stress factors.

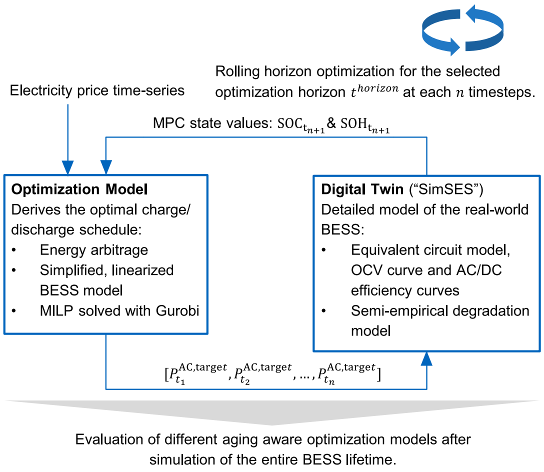

Fig. 1. Depiction of the proposed MPC framework for designing and validating aging aware operation strategies. Our implementation of the MPC framework is available open-source under [43].

- Linearized lithium iron phosphate (LFP) cell degradation models, suitable for MILP
- Increased lifetime profitability through determining the *optimal aging cost*, thereby optimizing both short-term profit and long-term degradation effects
- Quantification of the increase in lifetime profitability through aging aware operation with different levels of degradation model complexity
- Analysis of factors influencing the *optimal aging cost*: interest rate, EOL-criterion, and intraday electricity price (2019 to 2022)
- A formulation for aging cost that accounts for the interest rate

2. Model predictive control framework for designing aging aware operation strategies

The proposed MPC framework is shown in Fig. 1. The digital twin is a detailed model of the investigated BESS and should represent the real-world BESS and its expected aging behavior accurately. We use the in-house developed, open-source Simulation Tool for Stationary Energy Storage Systems (**SimSES**) as the digital twin, which is described in detail in [44]. Optimization models have limitations in their complexity determined by the optimization method that is used. For example, linear programming requires a linear objective function and constraints, while quadratic programming also allows quadratic objective functions. Generally, the optimization model will therefore incorporate a simplified storage model, which in turn is a simplified version of the digital twin.

The optimization model is solved for the selected optimization horizon t^{horizon} with a time resolution of Δt, after which the resulting power targets $P^{\mathrm{AC,target}}$ for the next n timesteps are simulated with the digital twin. For $n = 1$, the optimization model is solved at every timestep and only the power target for the next timestep is passed to the simulation model before the next optimization is called. The relevant MPC state values, that represent the new BESS state after these n timesteps, are handed back to the optimization model to solve the next optimization horizon. Thereby the more accurate digital twin is used to validate the operation strategy derived through the optimization model. Also, this framework mirrors the real-world application, where the operation strategy would be run in a similar MPC approach on a real BESS instead of the digital twin.

The relevant MPC state values of the digital twin used in this contribution are the SOC and the capacity-based SOH, but further values could be used for the optimization model such as the system temperature. Our implementation of the proposed MPC framework is available open-source [43] and designed in a modular way, such that different use cases or optimization formulations can be added and investigated. Here, we focus on the application of energy arbitrage on the European intraday spot market. In the following, we will first describe the electricity price time series, before presenting the digital twin model and the investigated optimization models.

2.1. Price time series

We investigate the application of generating profit through arbitrage trading on the intraday electricity market. For that, we use data from the largest European intraday power exchange, the EPEX SPOT, with price data obtained from [45]. The intraday electricity prices are shown in Fig. 2. Price data from the year 2021 serves as the base scenario in the later case study. Since the intraday market is designed to offer continuous trading, not one fixed price exists for a given delivery period. The ID-1 price index is the weighted price average off all trades executed within 1 h before delivery [46]. Because this index represents the potential to market flexibility without inflating optimistic price assumptions, it has been used as a benchmark in previous publications to develop and test energy arbitrage strategies [47] and is also adopted for the later case study presented here. While the average ID-1 price for the year 2021 is at 97.15 EUR/MWh, individual price peaks of up to 942.35 EUR/MWh and down to −122.92 EUR/MWh are found in the data.

2.2. Digital twin

SimSES allows to conduct time series based simulations for stationary energy storage systems and includes equivalent circuit models and degradation models for different battery systems [44]. It also includes models for periphery components such as the AC/DC converter. For

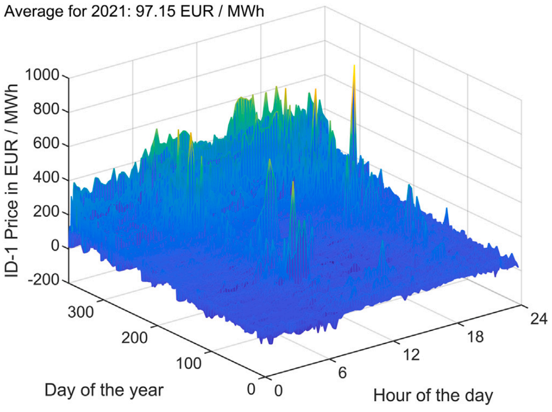

Fig. 2. 15 min Intraday ID-1 electricity prices for the year 2021 with data obtained from [45].

Table 2
Key parameters for the digital twin in **SimSES**.

Parameter	Value
Cell type	Sony/Murata LFP-graphite
Degradation model	Semi-empirical by Naumann et al. [48,49]
AC/DC converter	Notton et al. [50]
System sizing	1 MW, 1.2 MWh

the cell model, we use a model of a Sony/Murata LFP graphite cell for which a semi-empirical degradation model by Naumann et al. has been incorporated into **SimSES** [48,49]. For the AC/DC converter, an efficiency curve by Notton et al. is used [50]. Table 2 summarizes the key parameters.

2.3. Optimization models

We investigate the increase in lifetime profitability achieved through different degrees of complexity for modeling battery aging as part of the optimization model. All three optimization model types are formulated as either linear programs or mixed integer linear programs and structured as follows:

$$\max \sum_{t\in T}\left((p_t^{\text{dis}}-p_t^{\text{ch}})\cdot \Delta t\cdot c_t^{\text{id}}\right)-\mathbb{C}^{\text{aging}} \tag{4}$$

The first part of the equation is the profit generated on the intraday market. Here, p_t^{dis} and p_t^{ch} are the discharged and charged power of the BESS and c_t^{id} the electricity price on the intraday electricity market at time t. Δt is the optimization timestep, which is set to 15 min. $\mathbb{C}^{\text{aging}}$ is the total aging cost over the optimization horizon. In addition to the objective function, the constraints below ensure energy conservation and provide upper and lower limits for the three sets of continuous decision variables, p_t^{dis}, p_t^{ch}, and soc_t with $t\in T$:

$$soc_t = soc_{t-1}+\frac{\Delta t}{E^{\text{batt}}}\cdot\left(p_t^{\text{ch}}\eta-\frac{1}{\eta}p_t^{\text{dis}}\right)\quad \forall\, t\in T\backslash\{0\} \tag{5}$$

$$soc_{t=0}=\text{SOC}^{\text{start}}+\frac{\Delta t}{E^{\text{batt}}}\cdot\left(p_{t=0}^{\text{ch}}\eta-\frac{1}{\eta}p_{t=0}^{\text{dis}}\right) \tag{6}$$

$$0\le p_t^{\text{ch}}, p_t^{\text{dis}}\le P^{\text{AC,max}}\quad \forall\, t\in T \tag{7}$$

$$0\le soc_t\le 1\quad \forall\, t\in T \tag{8}$$

$\text{SOC}^{\text{start}}$ and E^{batt} are the SOC at the beginning of the optimization horizon and the remaining rated energy of the BESS after accounting for degradation, respectively. $P^{\text{AC,max}}$ is the maximum charge and discharge power of 1 MW. soc_t is the energy based state of charge of the BESS at every time step and η the fixed charge/discharge efficiency.

Notably, one could use a linearized model for the efficiency that follows the BESS efficiency curve [14,28] instead of a constant for η We found good results with a constant efficiency factor of $\eta = 0.9$ and focus here on modeling of battery aging in the optimization model. However, the system model in **SimSES** as part of the MPC framework models power losses in both the battery cells through the battery cell internal resistance and the AC/DC converter through an efficiency curve.

For the total aging cost $\mathbb{C}^{\text{aging}}$, we investigate different models with increasing complexity that are described in the following subsections.

2.3.1. Aging cost model (i) - Energy throughput

This aging cost model defines aging cost based on the energy throughput of the BESS and the expected amount of FECs the system can endure before reaching its EOL. This model does not explicitly consider any other stress factors of either calendar or cyclic aging. The aging cost $\mathbb{C}^{\text{aging,FEC}}$ are defined as follows:

$$\begin{aligned}\mathbb{C}^{\text{aging,FEC}} &= \sum_{t\in T}\frac{(p_t^{\text{ch}}+p_t^{\text{dis}})\cdot\Delta t}{E^{\text{n}}\cdot 2}\cdot\frac{E^{\text{n}}\cdot c^{\text{aging}}}{\text{FEC}^{\text{EOL}}}\\ &= \sum_{t\in T}\frac{(p_t^{\text{ch}}+p_t^{\text{dis}})\cdot\Delta t\cdot c^{\text{aging}}}{2\cdot\text{FEC}^{\text{EOL}}}\end{aligned} \tag{9}$$

The first part of the top equation denotes the change in FECs, based on the charge and discharge power, p_t^{ch} and p_t^{dis}, in the given timestep, the timestep width Δt and the rated energy of the BESS at the beginning of life E^n. The second part expresses the aging cost per FEC, based on the aging cost per kWh c^{aging} and the expected number of cycles until EOL FEC^{EOL}.

We here set $\text{FEC}^{\text{EOL}} = 6000$, as the 80% SOH limit is reached after 6000 FECs for the majority of cycling conditions in the LFP cell aging study [49]. How to determine the optimal value for the aging cost c^{aging} will be investigated in the later case study. This aging cost model equals the common definition from Eq. (3), with a fixed value for FEC^{EOL}.

2.3.2. Aging cost model (ii) — Energy throughput and calendar degradation model

In addition to the energy throughput model, a linearized version of the calendar degradation model from Naumann et al. [48] is implemented in the optimization model. Thereby, this aging cost model with the aging cost $\mathbb{C}^{\text{aging,FEC,cal}}$ accounts for the SOC dependence of calendar aging in the optimization:

$$\begin{aligned}\mathbb{C}^{\text{aging,FEC,cal}} =&\, \mathbb{C}^{\text{aging,FEC}}\\ &+\sum_{t\in T}\frac{E^{\text{batt}}}{1-\text{SOH}^{\text{EOL}}}\cdot c^{\text{aging}}\cdot q_t^{\text{loss,cal}}\end{aligned} \tag{10}$$

$\mathbb{C}^{\text{aging,FEC}}$ is the definition of energy throughput based aging cost from Eq. (9). SOH^{EOL} is the SOH threshold at which the EOL is defined and $q_t^{\text{loss,cal}}$ is the projected calendar capacity loss in the given timestep in per unit as a continuous decision variable.

The calendar degradation model from Naumann et al. [48] is linearized as detailed in Appendix A such that it can be solved as part of a MILP. The resulting linearization is depicted in Fig. 3 and implemented in the optimization model as below:

$$\sum_{i\in I}\lambda_{t,i}^{\text{cal}}\cdot X_i^{\text{cal}} = soc_t\quad \forall\, t\in T \tag{11}$$

$$\sum_{i\in I}\lambda_{t,i}^{\text{cal}}\cdot Z_i^{\text{cal}} = q_t^{\text{loss,cal}}\quad \forall\, t\in T \tag{12}$$

$$\sum_{i\in I}\lambda_{t,i}^{\text{cal}} = 1\quad \forall\, t\in T \tag{13}$$

I is the set of points used for the linearization of the calendar aging function. X_i^{cal} with $i\in I$ are the x-values of the linearization from Fig. 3, representing the SOC. Z_i^{cal} with $i\in I$ are the z-values of the linearization from Fig. 3, meaning the calendar capacity loss in a given

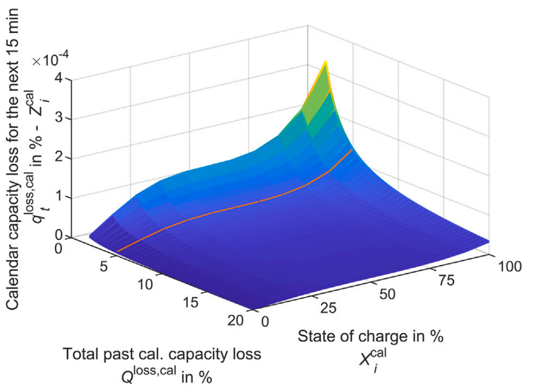

Fig. 3. Linearized calendar degradation model. A set of 10 lines is used to represent the SOC dependency of calendar aging. To account for the dependence of future degradation on the total past capacity loss $Q^{\text{loss,cal}}$, a lookup table with 229 sets of these 10 lines is used, such that the correct set of lines can be chosen at the beginning of the optimization horizon based on $Q^{\text{loss,cal}}$. However, $Q^{\text{loss,cal}} = 5\%$ (marked in orange) serves as the base scenario for the optimization.

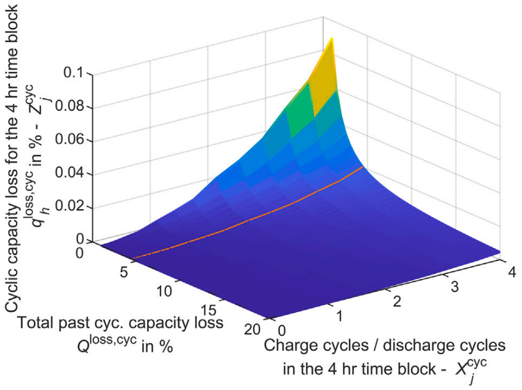

Fig. 4. Linearized cyclic degradation model. A set of 27 lines is used to represent the amount of cyclic degradation for a given 4 h time block, based on the number of charge cycles or discharge cycles in that time block. To account for the dependence of future degradation on the past total cyclic capacity loss $Q^{\text{loss,cyc}}$, a lookup table with 229 sets of these 27 lines is used, such that the correct set of lines can be chosen at the beginning of each optimization based $Q^{\text{loss,cyc}}$. However, $Q^{\text{loss,cyc}} = 5\%$ (marked in orange) serves as the base scenario for the optimization.

15 min timestep for the respective SOC. $\lambda^{\text{cal}}_{t,i}$ $\lambda^{\text{cal}}_{t,i}$ with $t \in T$ and $i \in I$ each are continuous variables that are used to represent the linearized calendar aging function in the optimization model. The set of variables $\lambda^{\text{cal}}_{t,i}$ with $i \in I$ is implemented as one special ordered set of type 2 for each $t \in T$. This means that at most two variables of each set can be nonzero, and they must be consecutive in their ordering. In addition, the following constraints for the decision variable $q_t^{\text{loss,cal}}$ and $\lambda^{\text{cal}}_{t,i}$ are implemented:

$$0 \leq q_t^{\text{loss,cal}} \quad \forall\, t \in T \tag{14}$$

$$0 \leq \lambda^{\text{cal}}_{t,i} \leq 1 \quad \forall\, t \in T,\ \forall\, i \in I \tag{15}$$

As Fig. 3 shows, calendar aging has a square root dependence on past capacity loss due to the $\sqrt{t}$ dependence of the original calendar aging function. Multiple other calendar degradation models have this sublinear dependency of calendar capacity loss on time as well [51], which some authors also implement in the optimization model [13]. However, as we will show in the case study, implementing this dependency in the optimization would lead to sub-optimal lifetime profit of the BESS, as calendar aging cost would be significantly higher in earlier than in later years of operation. Therefore, we choose the linearization at $Q^{\text{loss,cal}} = 5\%$ as the base scenario in the later case study, which is marked with an orange line in Fig. 3.

2.3.3. Aging cost model (iii) — Cyclic and calendar degradation model

Here, the calendar degradation model [48] and cyclic degradation model [49] are both linearized and implemented in the optimization model. The aging cost model thereby accounts for the stress factors of both calendar and cyclic aging. The linearization is described in detail in Appendix A. The resulting definition for the aging cost $\mathbb{C}^{\text{aging,cyc,cal}}$ is as follows:

$$\begin{aligned}\mathbb{C}^{\text{aging,cyc,cal}} = & \frac{E^{\text{batt}}}{1 - \text{SOH}^{\text{EOL}}} \cdot c^{\text{aging}} \cdot \Big(\sum_{t \in T} q_t^{\text{loss,cal}} \\ & + \sum_{h \in H} (q_h^{\text{loss,cyc,ch}} + q_h^{\text{loss,cyc,dis}}) \Big)\end{aligned} \tag{16}$$

The objective function includes the calendar aging cost from Eq. (10) of the previous subsection. The previous constraints Eqs. (13) to (14) are included in this model as well.

The linearized cyclic degradation model is split in the cyclic capacity loss in charge and cyclic capacity loss in discharge direction, i.e. $q_h^{\text{loss,cyc,ch}}$ and $q_h^{\text{loss,cyc,dis}}$. As described in Appendix A, cyclic aging is calculated separately for every 4 h time horizon h in the optimization horizon $h \in H$. This means for a 12 h optimization horizon, H would be an index set of three elements. For each of these 4 h time blocks, the total energy throughput in charge direction e_h^{ch} and discharge direction e_h^{dis} are calculated:

$$\sum_{t \in T_h} p_t^{\text{ch}} \cdot \Delta t = e_h^{\text{ch}} \quad \forall\, h \in H \tag{17}$$

$$\sum_{t \in T_h} p_t^{\text{dis}} \cdot \Delta t = e_h^{\text{dis}} \quad \forall\, h \in H \tag{18}$$

Here, T_h is the set of all timesteps in each of the 4 h time blocks. Based on this energy throughput, the cyclic aging for each 4 h time block is calculated with the linearized cyclic degradation model, analogously to the calendar degradation model from the previous subsection:

$$\sum_{j \in J} \lambda^{\text{cyc,ch}}_{h,j} \cdot X_j^{\text{cyc}} = e_h^{\text{ch}} \quad \forall\, h \in H \tag{19}$$

$$\sum_{j \in J} \lambda^{\text{cyc,dis}}_{h,j} \cdot X_j^{\text{cyc}} = e_h^{\text{dis}} \quad \forall\, h \in H \tag{20}$$

$$\sum_{j \in J} \lambda^{\text{cyc,ch}}_{h,j} \cdot Z_i^{\text{cyc}} = q_h^{\text{loss,cyc,ch}} \quad \forall\, h \in H \tag{21}$$

$$\sum_{j \in J} \lambda^{\text{cyc,dis}}_{h,j} \cdot Z_i^{\text{cyc}} = q_h^{\text{loss,cyc,dis}} \quad \forall\, h \in H \tag{22}$$

$$\sum_{j \in J} \lambda^{\text{cyc,ch}}_{h,j} = 1 \quad \forall\, h \in H \tag{23}$$

$$\sum_{j \in J} \lambda^{\text{cyc,dis}}_{h,j} = 1 \quad \forall\, h \in H \tag{24}$$

J is the set of points used for the linearization of the cyclic aging function. X_j^{cyc} with $j \in J$ are the x-values of the linearization from Fig. 4, representing the energy throughput for a 4 h time block. Z_j^{cyc} are the z-values of the linearization from Fig. 4, meaning the cyclic capacity loss for a 4 h time block in p.u. for the respective energy throughput. The sets of continuous variables $\lambda^{\text{cyc,ch}}_{h,j}$ and $\lambda^{\text{cyc,dis}}_{h,j}$ with $j \in J$ are implemented as special ordered sets of type 2 for each $h \in H$. In addition, the following constraints for the continuous decision variables $\lambda^{\text{cyc,ch}}_{h,j}$, $\lambda^{\text{cyc,dis}}_{h,j}$, $q_h^{\text{loss,cyc,ch}}$, $q_h^{\text{loss,cyc,dis}}$, e_h^{ch} and e_h^{dis} are implemented:

$$0 \leq \lambda^{\text{cyc,ch}}_{h,j}, \lambda^{\text{cyc,dis}}_{h,j} \leq 1 \quad \forall\, h \in H,\ \forall\, j \in J \tag{25}$$

$$0 \le q_h^{\text{loss,cyc,ch}}, q_h^{\text{loss,cyc,dis}}, e_h^{\text{ch}}, e_h^{\text{dis}} \quad \forall\, h \in H \tag{26}$$

Analogously to the calendar degradation model, the cyclic degradation model has a square root dependence on past cyclic capacity loss due to the square root dependence of the original cyclic aging function on the number of FECs, see Fig. 4. As we will highlight in the case study, implementing this sublinear relationship in the optimization model would lead to sub-optimal lifetime profit of the BESS as well, since the cyclic aging cost would be significantly higher in earlier than in later years of operation. Therefore, we choose the linearization at $Q^{\text{loss,cyc}} = 5\%$ as the base scenario in the later case study, which is marked with an orange line in Fig. 4.

3. Simulation case study

In this chapter, we present and discuss the simulation results with the proposed MPC simulation framework. Section 3.1 shows the dependence of the lifetime cumulative arbitrage profit on the selection of the aging cost c^{aging} and highlights the increase in lifetime profitability that can be achieved by finding the optimal value for c^{aging}, i.e. the *optimal aging cost*. In Section 3.2, we investigate the benefits of the different aging cost model types. In Section 3.3, we show that the interest rate, EOL criterion, and the price time series all affect the *optimal aging cost*. Furthermore, Section 3.3 will highlight that the common practice of defining battery aging cost based on the cost of the battery system (c.f. Section 1.1) leads to reduced lifetime arbitrage profit, as opposed to using the here proposed MPC simulation framework to find the *optimal aging cost*. Section 3.4 proposes a novel definition of aging cost that promises higher economic return by accounting for the interest rate.

In the following, the optimization models use a time horizon t^{horizon} of 12 hr, with a timestep Δt of 15 min. For aging cost model type (i), the optimization is called every 30 min ($n = 2$) and for aging cost model type (ii) and type (iii) every 60 min ($n = 4$). The digital twin in **SimSES** in all cases runs on a 3 min time resolution. The commercial solver Gurobi Optimizer is used for solving the optimization models. Note that the resulting optimization problem for cost model type (i) is a linear program, while the special ordered sets in aging cost model type (ii) and (iii) require a MILP solver. The simulations for the case study were run on a workstation with an Intel Xeon W-2265 CPU and 96 GB RAM with multiple simulations in parallel. Running one year of simulation with the complete MPC framework took on average 23.4 min with aging cost model type (i), 73.6 min with model type (ii), and 308.7 min with model type (iii). Fig. 5 shows one exemplary day of operation with the three different aging cost models. In general, the profit in the energy arbitrage application is generated by charging at low prices and discharging at high prices. However, the different implementations of aging costs lead to different schedules. Aging cost model type (i) has aging costs that only depend on the energy throughput and do not explicitly consider any other aging stress factors, which results in the BESS charging up early at a low ID-1 price. Implementing the SOC dependence of calendar aging for model type (ii) results in the BESS charging later and discharging earlier to keep the SOC low. The added dependence of cyclic aging on DOC and C_{rate} for model type (iii) entices more shallow cycles at low DOC and C_{rate}, such as for the small price changes at 00:45 and 17:00 in Fig. 5.

3.1. Increased lifetime profit through the optimal choice of aging cost

To investigate the effect of aging cost c^{aging} on the lifetime profit from energy arbitrage, multiple 12-year simulations with different aging cost values were conducted. Fig. 6 shows the resulting cumulative profit and number of FECs for aging cost model (i), i.e. the energy throughput model. The cumulative profit includes the gains and losses from energy arbitrage, but no BESS investment cost. It therefore reflects the profit gained in the application, which after installation of the BESS is independent of the initial investment cost. The 12-year time horizon is chosen arbitrarily to reflect an investor's goal of achieving maximum profit over a fixed timeframe of interest, and will be varied in the later subsections.

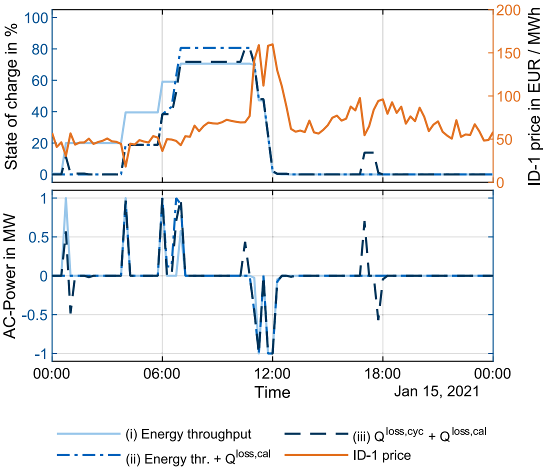

Fig. 5. One exemplary day of operation with the three different aging cost models.

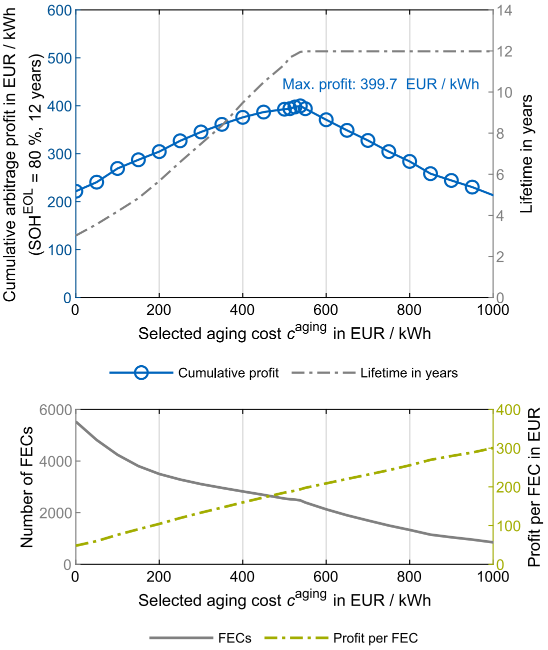

Fig. 6. Top: Cumulative profit from energy arbitrage and lifetime in years after 12 years of operation for different aging cost values. The profit is stated in EUR/kWh with regards to the initial nominal capacity ($E^{\text{n}} = 1.2\,\text{MWh}$). Here, aging cost model (i) is used, i.e. the energy throughput model. The maximum cumulative profit is obtained if aging costs are defined such that the EOL criterion is reached at the end of the investigated 12-year horizon and an *optimal aging cost* of $c^{\text{aging}} = 538$ EUR/kWh. Bottom: FECs and profit per FEC for the different aging cost values.

The top of Fig. 6 shows the benefit of finding the *optimal aging cost*. If c^{aging} is chosen lower than optimal, the high amount of cycling will cause the BESS to degrade quickly and reach its EOL before the end of the 12-year time horizon. With aging cost of 0 EUR/kWh, the BESS reaches its EOL at 80% SOH after 3.0 years and 5525.7 FECs, while obtaining a cumulative profit of 265.9 kEUR, or 221.6 EUR/kWh with regards to the initial nominal capacity of 1.2 MWh. If c^{aging} is chosen higher than optimal, the low amount of cycling will cause the BESS to forego energy arbitrage opportunities, leading to lower profit over the 12-year time horizon. With aging cost of 1000 EUR/kWh, the BESS obtains a cumulative profit of 256.1 kEUR or 213.4 EUR/kWh through energy arbitrage after only 852.8 FECs over the 12 years, while still having a remaining SOH of 86.7%. The highest cumulative profit is obtained if aging cost are chosen such that the EOL threshold of 80% remaining capacity is reached at the end of the investigated 12-year time horizon. With the *optimal aging cost* of $c^{\text{aging}} = 538$ EUR/kWh, the BESS generates a cumulative profit from energy arbitrage of 479.7 kEUR or 399.7 EUR/kWh, while reaching its EOL at the end of the 12-year time horizon after 2476.7 FECs.

The bottom part of Fig. 6 highlights the diminishing marginal return of additional cycles. When setting the aging cost to a high value, only the most profitable energy arbitrage opportunities are part of the optimization model's solution, resulting in a profit per FEC of 300.3 EUR for aging cost of 1000 EUR/kWh. On the other side, low aging cost lead to a high amount of cycles and even less profitable energy arbitrage opportunities being part the optimization model's solution, with a profit per FEC of 48.1 EUR for aging cost of 0 EUR/kWh.

3.2. *Increased lifetime profit through advanced aging cost models*

In this section, we investigate the benefit of the previously presented aging cost models. The top of Fig. 7 shows the cumulative profit after 12 years for all three previously introduced aging cost models with increasing complexity. In all three cases, the digital twin in **SimSES** as well as the price time series remain the same and only the optimization model formulation changes. Since the modeling approach differs between the aging cost models, different *optimal aging cost* lead to the maximum arbitrage profit when considering the entire BESS lifetime: $c^{\text{aging}} = 538$ EUR/kWh for model type (i) with only energy throughput being considered, $c^{\text{aging}} = 275$ EUR/kWh for model type (ii) with energy throughput and the linearized calendar degradation model, and $c^{\text{aging}} = 350$ EUR/kWh for model type (iii) with the linearized calendar and linearized cyclic degradation model. The bottom of Fig. 7 depicts the development of the SOH and arbitrage profit for the identified optima over time. The results show that the more complex aging cost models allow to generate more profit, while being subjected to similar SOH trajectories, resulting in 80% SOH at the end of the investigated 12-year time horizon. Compared to aging cost model (i), the maximum profit from energy arbitrage is 24.9% higher with aging cost model (ii) and 29.3% with aging cost model (iii).

The analysis of the relevant aging stress factors in Fig. 8 highlights how this increase in cumulative profit is achieved. Including the linearized calendar and cyclic aging cost models in the optimization model, leads to an improved aging aware operation strategy. In summary, the detailed aging cost models in the optimization model entice the BESS to avoid those energy arbitrage opportunities that promise high arbitrage profit but would also cause high battery degradation. This in turn enables the BESS to complete more FECs that are less profitable but also less straining for the battery and thereby achieve a higher profit over its total lifetime.

With the linearized calendar degradation model in aging cost model (ii), the BESS is able to complete 4378.6 FECs over the 12-year time horizon before reaching its end of life, compared to 2477.8 FECs for aging cost model (i). The lower average SOC reduces calendar aging and the coincidentally slightly lower average C_{rate} and DOC cyclic aging, thereby enabling this increase in FECs before the end of life. However, the average cumulative profit per FEC decreases from 193.6 EUR with aging cost model (i) to 136.8 EUR with aging cost model (ii). This highlights that the BESS engages in more, but on average less profitable energy arbitrage opportunities with aging cost model (ii).

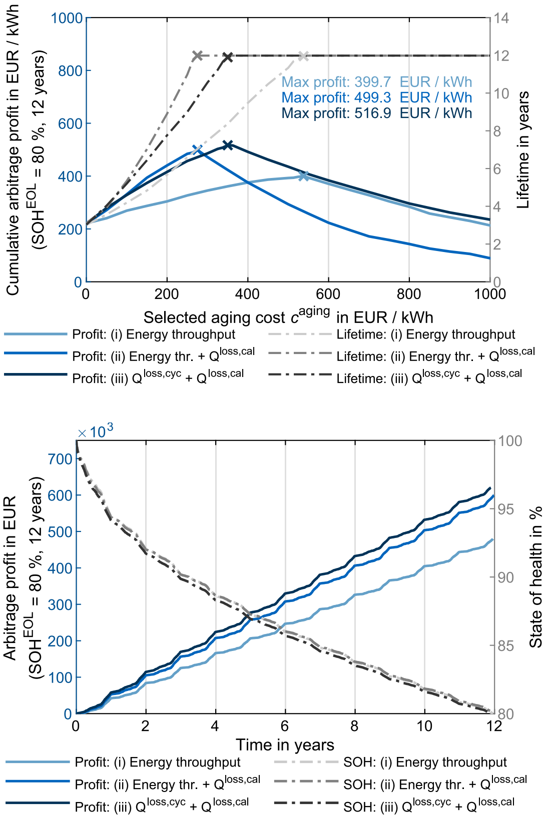

Fig. 7. Top: Cumulative profit from energy arbitrage after 12 years of operation for different aging cost values. All three aging cost models with increasing complexity are depicted here: (i) Energy throughput model, (ii) Energy throughput and calendar degradation model, (iii) Cyclic and calendar degradation model. Bottom: Arbitrage profit and SOH over time for the *optimal aging cost*: (i) $c^{\text{aging}} = 538$ EUR/kWh, (ii) $c^{\text{aging}} = 275$ EUR/kWh, (iii) $c^{\text{aging}} = 350$ EUR/kWh.

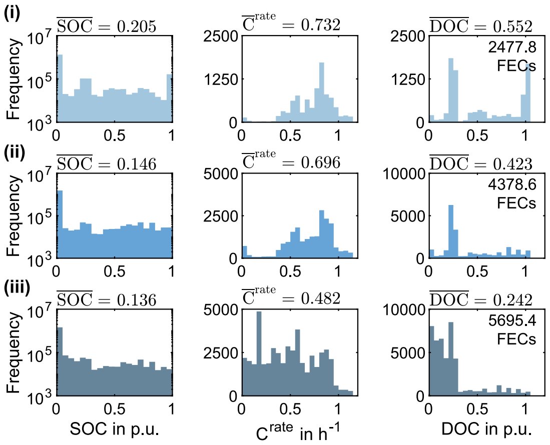

Fig. 8. Distribution of the calendar aging stress factor SOC and the cyclic aging stress factors C_{rate} and DOC for the three different aging cost models (i), (ii) and (iii) with the *optimal aging cost* from Fig. 7.

With the additional linearized cyclic degradation model in aging cost model (iii), the average SOC, C_{rate} and DOC are further reduced. Analogously to model type (ii), the largest reduction of stress factors for model type (iii) is seen in the cyclic aging stress factors C_{rate} and DOC as expected, but a slight reduction in the average SOC is seen as well. The 5695.4 FECs until the end of life translates to an average profit per FEC of 108.9 EUR.

3.3. Impact of interest rate, end-of-life threshold and price profile

After the previous sections have focused on the cumulative profit as the main financial indicator, we now investigate the net present value (NPV) of future profit. The NPV is a common financial metric to assess investment options. It discounts future profit and thereby considers that profit in earlier years is more valuable than in later years of an investment, since the earlier profit can be invested elsewhere and generate return. The NPV here is calculated as follows:

$$\mathrm{NPV} = \sum_{m=0}^{M} \frac{\mathbb{P}^{\mathrm{arb}}_{m}}{(1+\mathrm{i})^{m}} \tag{27}$$

Here, $\mathbb{P}^{\mathrm{arb}}_{m}$ is the cumulative profit from energy arbitrage in year m and i the interest rate.

The top of Fig. 9 shows the NPV of arbitrage profit for different aging cost values and interest rates. Furthermore, the lifetime in years is given until the EOL criterion of 80% SOH is reached for each aging cost value. Aging cost model type (i) is used here which only considers the energy throughput. The time horizon here is increased to 20 years to investigate the influence of the interest rate i on the optimal lifetime.

With an interest rate of i = 0%, the NPV simply equals the cumulative profit from energy arbitrage from the previous sections. With i = 0% and the *optimal aging cost* of 825 EUR/kWh, a cumulative profit of 444.5 EUR/kWh is reached after 20.0 years, at an average yearly profit of 26.7 kEUR. While for the 12-year time horizon with *optimal aging cost* of 538 EUR/kWh, a cumulative profit of 399.7 EUR/kWh is reached, at an average yearly profit of 40.0 kEUR. Prolonging the investigated horizon from 12 to 20 years and extending the BESS lifetime by increasing the aging cost, therefore does not lead to a proportional increase in the cumulative profit.

In the previous sections, the optimal cumulative profit was nevertheless reached when the aging cost are chosen such that the EOL is reached at the end of the investigated time horizon, i.e. 12 years. By using the NPV as the main financial metric, this relationship changes. The higher the interest rate, the lower the value of future profit. Therefore, for high interest rates, the optimal aging cost and resulting lifetime decrease, as it is beneficial to generate a higher profit in early years and forego additional profit in later years. For an interest rate of i = 7.5%, the optimal NPV of 265.9 EUR/kWh is reached if aging cost are set to 250 EUR/kWh, which results in a BESS lifetime of 8.7 years. The interest rate can therefore be the starting point for designing an aging aware operation strategy, by choosing the aging cost value that yields the optimal NPV and the resulting BESS lifetime for the relevant interest rate.

The bottom of Fig. 9 shows how different thresholds for the EOL affect the *optimal aging cost*. In general, the higher the SOH limit for the EOL threshold, the higher the aging cost should be chosen, as low aging cost would lead to a particularly early EOL in that case. The results highlight the importance of the EOL assumption for the assessment of the expected lifetime profit. The degradation model used here was validated until around 80% SOH [48,49]. Insights into the aging behavior towards the EOL, such as when an aging knee [16] can be expected, would be of use twofold. First, a more accurate assessment of the expected lifetime profit can be obtained in the planning phase of a BESS project. Second, if the aging behavior towards the EOL is known, the aging cost can be set accordingly to optimize the lifetime profit for the operation phase of a BESS project. Instead of having all information available at the beginning of a BESS project, one may choose though to update the aging aware operation strategy, i.e. the chosen value for the aging cost or the aging cost model itself, once more information becomes available through the analysis of field data over the years of operation.

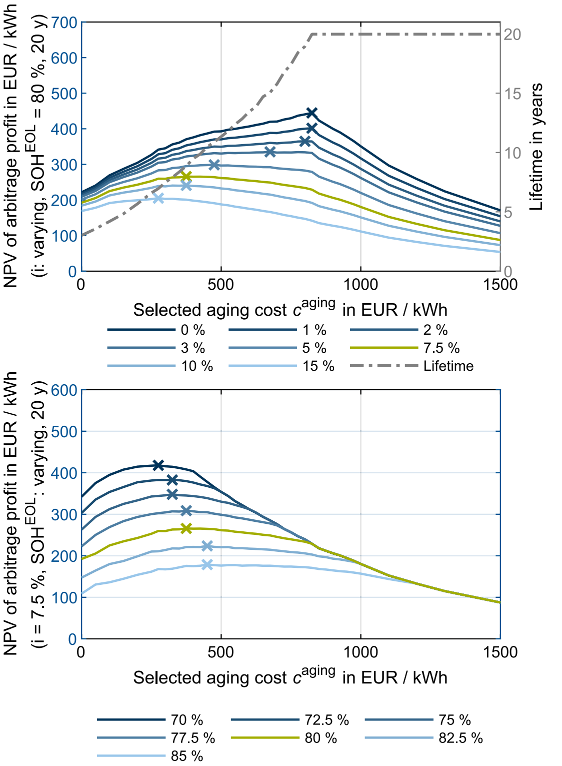

Fig. 9. NPV of arbitrage profit after 20 years of operation for different aging cost values. Aging cost model (i) was used here. The top figure shows the impact of the interest rate on the optimal definition of aging cost, while assuming a constant EOL threshold at $\mathrm{SOH}^{\mathrm{EOL}} = 80\%$. The bottom figure shows the impact of the EOL threshold while assuming a constant interest rate of i = 7.5%.

After previously using ID-1 price data from the year 2021, Fig. 10 now shows the NPV for different aging cost values with ID-1 prices from the years 2019 to 2022. The price data was obtained from [45] as well. Table 3 summarizes the optimal values when either aiming to maximize the lifetime NPV with an interest rate of i = 7.5% or maximizing profit over a 12 year horizon. Most noticeably, the maximum lifetime NPV and profit significantly increase from 2019 to 2022. The higher maximum lifetime NPV is a consequence of the increasing electricity prices and higher electricity price volatility as shown by the mean and standard deviation of the ID-1 price index in Table 3. In addition, the more profitable energy arbitrage opportunities also lead to a higher aging cost value yielding the optimal lifetime profit. With price data from the year 2019, c^{aging} = 225 EUR/kWh leads to the optimal lifetime NPV of 109.7 EUR/kWh, while with price data from the year 2022, c^{aging} = 1150 EUR/kWh leads to the optimal lifetime NPV of 571.0 EUR/kWh.

For the investigations here, price data from the respective year was looped over the full time horizon. However, the dependence of the optimal aging cost on the price profile shows that the lifetime profitability in real applications can be increased by using a realistic prognosis of long-term future price data or by re-determining the optimal value for c^{aging} regularly over the years that a BESS is operated.

Table 3
Mean and standard deviation (SD) of the ID-1 prices for 2019 to 2022 and key simulation results (aging cost model type (i) and SOH^{EOL} = 80%) with those price profiles: *optimal aging cost* and resulting lifetime to achieve a maximum NPV (i = 7.5%), as well as *optimal aging cost* to achieve maximum profit over 12 years.

Year	Mean ID-1 €/MWh	SD ID-1 €/kWh	Max. NPV with i = 7.5%			Max. profit over 12 years	
			c^{aging} €/MWh	Max. NPV €/kWh	Lifetime years	c^{aging} €/kWh	Max. profit €/kWh
2019	37.6	22.6	225	109.7	11.9	225	168.4
2020	31.7	32.4	250	148.2	10.3	288	226.8
2021	97.2	78.4	400	265.4	9.5	538	399.8
2022	236.1	156.2	1150	571.0	11.5	1225	872.0

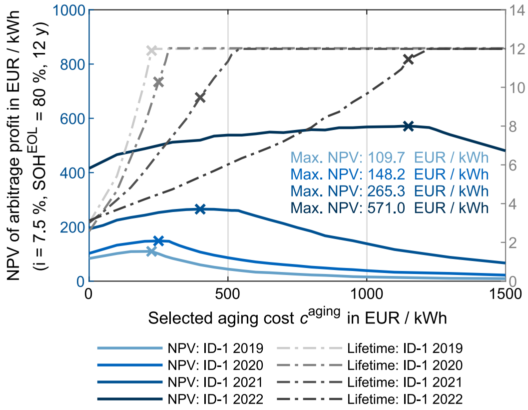

Fig. 10. NPV of arbitrage profit and lifetime after 12 years of operation for different aging cost values. Aging cost model (i) was used here. The results are depicted for the ID-1 price profiles of the years 2019 to 2022. A constant EOL threshold at SOH^{EOL} = 80% as well as an interest rate of i = 7.5% are considered for all simulations.

The results of this subsection and the previous subsection highlight that the *optimal aging cost* depends on the application (e.g. the interest rate of concern and the price profile), the aging characteristics of the BESS and the selected aging cost model. Therefore, the standard approach from literature to choose the aging cost c^{aging} based on the battery system cost (c.f. Section 1.1) leads to non-optimal lifetime profit. For example, in literature for the year 2022 values in the range of 340 to 580 USD/kWh are stated as BESS investment cost [52]. In this case study however, the *optimal aging cost* range between 225 EUR/kWh and 1225 EUR/kWh. Instead of setting the aging cost equal to the battery system cost, the here proposed MPC framework may be used to compare different optimization models and determine the *optimal aging cost* for the investigated application, thereby increasing the lifetime profitability of the BESS.

3.4. Impact of scaling aging cost and increasing lifetime profitability by accounting for the interest rate

As indicated in Section 2.3.2 and Section 2.3.3, implementing the square root dependency of calendar capacity loss on time and square root dependency of cyclic capacity loss on the number of FECs, would lead to detrimental behavior in terms of the lifetime profitability. This is highlighted in Fig. 11, which shows three different adaptions of aging cost model type (iii). The first version in light gray and light blue is with the non-scaled aging cost, which refers to including the square root dependency of cyclic and calendar capacity loss on the number of FECs and time. The second version in gray and blue is with the scaled model, which means that the linearized degradation model at $Q^{loss,cal}$ = 5% and $Q^{loss,cyc}$ = 5% is used for the optimization model, regardless of the actual total past calendar capacity loss $Q^{loss,cal}$ and total past cyclic capacity loss $Q^{loss,cyc}$ of the digital twin. This is the scenario of using the orange lines from Fig. 3 and Fig. 4, instead of

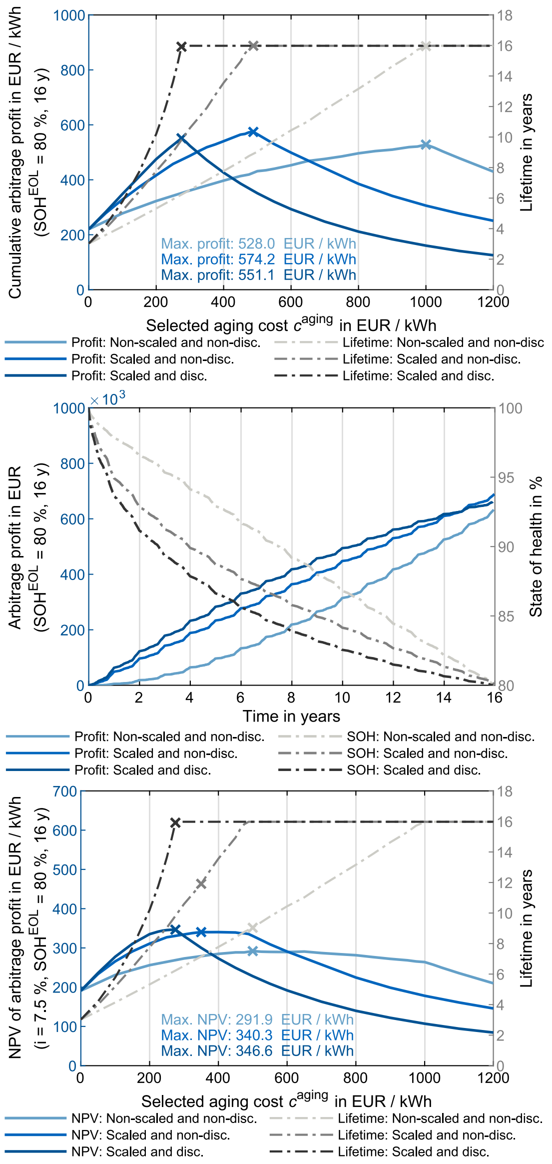

Fig. 11. Top: Cumulative arbitrage profit after 16 years of operation for different aging cost values. Here, three different adaptions for the aging cost model (iii) are investigated: non-scaled and non-discounted, scaled and non-discounted, as well as scaled and discounted. Mid: Cumulative arbitrage profit and state of health over time for the *optimal aging cost* from the top figure. Bottom: NPV of arbitrage profit for the three different adaptions of aging cost model (iii).

selecting the respective set of linearization points based on $Q^{\text{loss,cal}}$ and $Q^{\text{loss,cyc}}$ at the beginning of each optimization. It can be seen that the scaled aging cost has a beneficial effect on both the 16-year maximum cumulative profit (top plot) and the NPV (bottom plot). The maximum cumulative arbitrage profit is 8.7% higher and the maximum NPV of arbitrage profit is 16.6% higher, compared to the non-scaled scenario.

The middle plot of Fig. 11 highlights why this is the case. The square root dependency leads to over-proportionally high aging cost in the first few years, resulting in a low amount of cycling and arbitrage profit in the early years (light blue and light gray line). With non-scaled aging cost, a profit of 5.4 kEUR is achieved in year 1 and 48.9 kEUR in year 10. This higher profit in later years is subject to a higher discount rate and therefore less beneficial for the NPV, c.f. Eq. (27). With the scaled aging cost (blue and gray lines), the magnitude of aging cost remains the same throughout the years, while the impact of the stress factors SOC, C_{rate} and DOC is still considered in the aging cost model. As a result, there is a more consistent level of profit over time. In addition, the previous trend reverses, since the lower usable capacity and the higher losses due to the increasing cell resistance, cause slightly lower profits in later years. With scaled aging cost, a profit of 49.1 kEUR is achieved in year 1 and 41.7 kEUR in year 10.

The third adaption of aging cost model (iii) aims to further utilize the fact that earlier profit is more valuable in terms of the NPV. The aging cost formulation inside the optimization model is adapted as follows:

$$c^{\text{aging}'} = c^{\text{aging}} * (1 + i)^{m} \tag{28}$$

With i being the interest rate that is used for the project evaluation, here i = 7.5% and m the current fractional year since the start of the simulation horizon. Thereby, aging cost at the end of the 16-year simulation horizon are 3.18 times higher than at the beginning, leading to more profit in earlier than in later years. By both scaling and discounting the aging cost, the maximum cumulative arbitrage profit is 4.4% higher and the maximum NPV of the arbitrage profit is 18.7% higher than for the non-scaled and non-discounted scenario. A profit of 63.3 kEUR is achieved in year 1 and 36.7 kEUR in year 10.

In summary, scaling the aging cost to $Q^{\text{loss,cal}} = 5\%$ and $Q^{\text{loss,cyc}} = 5\%$ in the scenario investigated here has a beneficial effect on both the cumulative profit from energy arbitrage and its NPV. Further discounting the aging cost leads to a lower cumulative profit but an even higher NPV, compared to only scaling the aging cost, since more profit is generated in earlier years.

4. Conclusions

With the steadily growing amount of globally installed BESSs, aging aware operation of these systems becomes increasingly relevant. Operating a BESS under consideration of the relevant aging stress factors promises higher profits over its lifetime and more resource-efficient use of battery cells. For designing and benchmarking aging aware operation strategies, this work presents a model predictive control framework. By simulating the entire lifetime on a digital twin of the BESS, different aging aware optimization models can be compared before the optimal operation strategy is deployed to the real-world BESS. This work focuses on the application of generating profit through arbitrage trading on the EPEX Spot intraday electricity market. For that purpose, a linearized MILP ready model for the calendar and cyclic capacity loss of a LFP battery cell is presented. The proposed MPC framework is made available open-source [43] and designed in a modular way, such that different use cases and optimization formulations may be added and investigated. In contrast to previous contributions, we investigate the entire lifetime with the MPC framework, which allows to quantify the effect of aging aware operation on the lifetime profitability of BESSs, including the benefit of different degrees of complexity for modeling battery aging. Furthermore, the effect of aging cost c^{aging} on lifetime profitability is investigated in detail and the MPC framework is used to determine the *optimal aging cost*.

The results show that over the same investigated 12-year time horizon, the lifetime profit from energy arbitrage can be increased by 24.9% with the linearized calendar degradation model and by 29.3% with the linearized calendar and cyclic degradation model as part of the optimization model formulation, compared to only assuming energy throughput based aging cost. The linearized degradation models entice the BESS to avoid those energy arbitrage opportunities that promise high arbitrage profit but would also cause high battery degradation. This in turn enables the BESS to complete more total FECs over its lifetime and thereby achieve the before-mentioned higher lifetime profit. The results further show that the selection of the aging cost c^{aging} significantly impacts the lifetime profit and NPV. By determining the *optimal aging cost* through parameter variation with the MPC framework, the lifetime profit and NPV can be significantly increased. Most notably, the standard practice from the literature of choosing c^{aging} based on the battery system cost would lead to sub-optimal lifetime profit. Instead, the *optimal aging cost* is dependent on the aging behavior of the system, the aging cost model used in the optimization, the price profile, EOL-criterion, as well as the interest rate of concern. Scaling the degradation model and discounting the aging cost to obtain higher profit in earlier years of operation can further increase the lifetime profitability, especially when using the NPV as the financial metric of concern. In addition, the case study with price data from 2019 to 2022 shows, that the recent increases in wholesale electricity prices and wholesale electricity price volatility directly translate into a substantial increase of the achievable lifetime profit with BESSs used for arbitrage trading.

For this work, some uncertainties and limitations are considered. In the case study, price data from the respective year was looped over the full time horizon and a degradation model was used, which does account for accelerated capacity fade towards the end-of-life. As the dependence of the optimal aging aware operation strategy on the price profile and battery aging behavior highlights, the operation strategy should be reevaluated periodically by rerunning the MPC framework, once up-to-date price forecasts and additional insights into the BESS aging behavior from field data become available throughout the course of the BESS lifetime. Furthermore, the energy arbitrage application was modeled in a simplified way for the case study. Perfect foresight of the ID-1 price was assumed, which we believe to be a conservative assumption. For real-time bidding, one may achieve higher sell and lower buy prices than the ID-1 price and may place additional bids that are compensated before execution by the BESS, which can generate additional profit. On the other hand, the profit from energy arbitrage stated here does not account for market access cost, taxes, or labor costs. In addition, using the proposed framework requires the availability of a suitable degradation model, which cell manufacturers often do not provide. However, there are some third-party providers who offer degradation prognosis for BESSs. Finally, while this contribution focuses on the impact of aging aware operation on lifetime profitability, it can be worthwhile to also quantify the ecological benefit of a widespread adoption of aging aware operation.

Funding and acknowledgment

This research is funded by the German Federal Ministry of Education and Research (BMBF) via the research project greenBattNutzung (grant number 03XP0302D) and the German Federal Ministry for Economic Affairs and Climate Action (BMWK) via the research project StorageMultiApp (grant number 03EI6081B). The projects greenBattNutzung and StorageMultiApp are both overseen by Project Management Juelich (PtJ).

CRediT authorship contribution statement

Nils Collath: Conceptualization, Investigation, Methodology, Project administration, Software, Visualization, Writing – original draft, Writing – review & editing. **Martin Cornejo:** Software, Writing – review & editing. **Veronika Engwerth:** Methodology, Writing – review & editing. **Holger Hesse:** Methodology, Writing – review & editing. **Andreas Jossen:** Funding acquisition, Supervision, Writing – review & editing.

Declaration of competing interest

The authors declare that they have no known competing financial interests or personal relationships that could have appeared to influence the work reported in this paper.

Data availability

The code for the MPC framework is available open-source under [43].

Appendix A. Degradation model linearization

The degradation model by Naumann et al. describes the total capacity loss Q^{loss} as the sum of calendar capacity loss $Q^{\text{loss,cal}}$ and cyclic capacity loss $Q^{\text{loss,cyc}}$ [48,49]:

$$Q^{\text{loss}} = q^{\text{loss,cal}}(t, \text{SOC}, T) + q^{\text{loss,cyc}}(\text{FEC}, C^{\text{rate}}, \text{DOC}) \tag{29}$$

$$Q^{\text{loss,cal}} = k_{\text{ref,T}} \cdot (c_1(\text{SOC} - 0.5)^3 + d_1) \cdot \sqrt{t} \tag{30}$$

$$Q^{\text{loss,cyc}} = (a_2 C^{\text{rate}} + b_2) \cdot (c_2(\text{DOC} - 0.6)^3 + d_2) \cdot \sqrt{\text{FEC}} \tag{31}$$

Here, t, SOC, T refer to the time, state of charge, and temperature, respectively. FEC, C^{rate} and DOC refer to the number of full equivalent cycles, the charge–discharge rate, and the depth of cycle. In Eq. (30), $k_{\text{ref,T}}$, c_1 and d_1 are fitting parameters of the calendar degradation model. In Eq. (31), a_2, b_2, c_2 and d_2 are the fitting parameters of the cyclic model.

Notably, $k_{\text{ref,T}}$ in the original model by Naumann et al. describes the dependence of calendar capacity loss on temperature with an Arrhenius equation [48]. The battery cell temperature inside a BESS depends highly on the thermal design and the heating/cooling system and control [53]. To compare the different optimization models investigated here, we make the simplification of assuming a constant cell temperature of 25 °C for both the digital twin and the optimization model. This turns $k_{\text{ref,T}}$ into a constant for the purpose of this work.

A.1. Calendar aging

To adapt Eq. (30) to varying external stress factors, the concept of virtual time t^{virtual} from [48] is implemented in **SimSES** as well. t^{virtual} is the time that would have needed to pass to reach the total past calendar capacity loss under the present stress factors and can be calculated by solving Eq. (30) for t:

$$t^{\text{virtual}} = \left(\frac{Q^{\text{loss,cal}}}{k_{\text{ref,T}} \cdot (c_1 \cdot (\text{SOC} - 0.5)^3 + d_1)}\right)^2 \tag{32}$$

The additional calendar capacity loss in the current timestep $\Delta q^{\text{loss,cal}}$ can then be calculated as follows:

$$\Delta q^{\text{loss,cal}} = k_{\text{ref,T}} \cdot (c_1(\text{SOC} - 0.5)^3 + d_1) \cdot \sqrt{t^{\text{virtual}} + \Delta t} - Q^{\text{loss,cal}} \tag{33}$$

To solve this nonlinear degradation model in a MILP, it needs to be linearized. Eq. (33) has a dependence on both the past capacity loss $Q^{\text{loss,cal}}$ as well as on SOC. $Q^{\text{loss,cal}}$ only shows minor change over the short-term optimization horizon and can therefore be assumed as a constant for each optimization horizon. However, due to the square root dependency of calendar capacity loss on time, $\Delta q^{\text{loss,cal}}$ is significantly higher for low values of $Q^{\text{loss,cal}}$ than for high values of $Q^{\text{loss,cal}}$. Therefore, we performed linearizations of the SOC for 229 different values of $Q^{\text{loss,cal}}$, as depicted in Fig. 3. The cubic dependence of $\Delta q^{\text{loss,cal}}$ on SOC is represented by a resulting set of 10 lines for each of the 229 linearization points for $Q^{\text{loss,cal}}$. For each optimization, the corresponding set of SOC linearization points is chosen based on the total capacity loss $Q^{\text{loss,cal}}$ at the beginning of the optimization horizon. Through this method, an average relative error of less than +/−4% is achieved over all $Q^{\text{loss,cal}}$ ranges.

A.2. Cyclic aging

Analogously to the approach for calendar aging, the concept of virtual full equivalent cycles $\text{FEC}^{\text{virtual}}$ is used to apply Eq. (31) to varying external stress factors:

$$\text{FEC}^{\text{virtual}} = \left(\frac{Q^{\text{loss,cyc}}}{(a_2 C^{\text{rate}} + b_2) \cdot (c_2(\text{DOC} - 0.6)^3 + d_2)}\right)^2 \tag{34}$$

The additional degradation after a cycle is then calculated as follows:

$$\Delta q^{\text{loss,cyc}} = (a_2 C^{\text{rate}} + b_2) \cdot (c_2(\text{DOC} - 0.6)^3 + d_2) \cdot \sqrt{\text{FEC}^{\text{virtual}} + \Delta\text{FEC}} - Q^{\text{loss,cyc}} \tag{35}$$

In **SimSES**, a half-cycle counter is used which checks after every simulation steps if the charge–discharge direction has changed and then evaluates Eq. (35) with the DOC and C^{rate} from the last half-cycle. This nonlinear model requires linearization as well in order to be represented as part of a MILP. $\text{FEC}^{\text{virtual}}$ and C^{rate} are directly related for fixed timesteps and can be expressed through the energy throughput for those timesteps. However, determining the DOC would require the implementation of half-cycle counting in the scheduling method based on integer variables. Furthermore, the dependency of $\Delta q^{\text{loss,cyc}}$ on two multiplied decision variables, i.e. C^{rate} and DOC, would make the model inherently nonlinear. We therefore introduce the following simplification to linearize this cyclic degradation model: We subdivide the optimization horizon into 4 h time blocks. For each 4 h time block, the DOC is expressed through the energy throughput as well. If the DOC exceeds an increment of 100% for a given 4 h time block in either charge or discharge direction, this is evaluated as one half-cycle plus the remaining DOC as a partial cycle.

Analogously to calendar aging, $\Delta q^{\text{loss,cyc}}$ is significantly higher for low values of $Q^{\text{loss,cyc}}$ than for high values of $Q^{\text{loss,cyc}}$, due to the square root dependency of cyclic capacity loss on the number of FECs. We therefore perform the above linearization of C^{rate} and DOC in 229 points of $Q^{\text{loss,cyc}}$. Applying this principle to Eq. (35), leads to the linearized capacity loss from Fig. 4.

References

[1] Figgener J, Hecht C, Haberschusz D, Bors J, Spreuer KG, Kairies K-P, Stenzel P, Sauer DU. The development of battery storage systems in Germany: A market review (status 2023). 2022, URL http://arxiv.org/pdf/2203.06762v3.

[2] USDepartment of Energy. Energy storage grand challenge: Energy storage market report. 2020, URL https://www.energy.gov/energy-storage-grand-challenge/downloads/energy-storage-market-report-2020.

[3] Killer M, Farrokhseresht M, Paterakis NG. Implementation of large-scale Li-ion battery energy storage systems within the EMEA region. Appl Energy 2020;260:114166. http://dx.doi.org/10.1016/j.apenergy.2019.114166.

[4] USEnergy Information Administration. Battery storage in the United States: An update on market trends. 2020, URL https://www.eia.gov/analysis/studies/electricity/batterystorage/,

[5] Vetter J, Novák P, Wagner MR, Veit C, Möller K-C, Besenhard JO, Winter M, Wohlfahrt-Mehrens M, Vogler C, Hammouche A. Ageing mechanisms in lithium-ion batteries. J Power Sources 2005;147:269–81. http://dx.doi.org/10.1016/j.jpowsour.2005.01.006.

[6] Han X, Lu L, Zheng Y, Feng X, Li Z, Li J, Ouyang M. A review on the key issues of the lithium ion battery degradation among the whole life cycle. ETransportation 2019. http://dx.doi.org/10.1016/j.etran.2019.100005.

[7] Edge JS, O'Kane S, Prosser R, Kirkaldy ND, Patel AN, Hales A, Ghosh A, Ai W, Chen J, Yang J, Li S, Pang M-C, Bravo Diaz L, Tomaszewska A, Marzook MW, Radhakrishnan KN, Wang H, Patel Y, Wu B, Offer GJ. Lithium ion battery degradation: what you need to know. Phys Chem Chem Phys PCCP 2021;23(14):8200–21. http://dx.doi.org/10.1039/d1cp00359c.

[8] Uddin K, Gough R, Radcliffe J, Marco J, Jennings P. Techno-economic analysis of the viability of residential photovoltaic systems using lithium-ion batteries for energy storage in the United Kingdom. Appl Energy 2017;206(10):12–21. http://dx.doi.org/10.1016/j.apenergy.2017.08.170.

[9] Wankmüller F, Thimmapuram PR, Gallagher KG, Botterud A. Impact of battery degradation on energy arbitrage revenue of grid-level energy storage. J Energy Storage 2017;10(11):56–66. http://dx.doi.org/10.1016/j.est.2016.12.004.

[10] Collath N, Gasper P, Jossen A, Smith K, Hesse H. The economic impact of battery degradation modelling uncertainty. In: IEEE, editor. 2022 IEEE Power & Energy Society General Meeting. PESGM, 2022, http://dx.doi.org/10.1109/PESGM48719.2022.9916844.

[11] Hou Q, Yu Y, Du E, He H, Zhang N, Kang C, Liu G, Zhu H. Embedding scrapping criterion and degradation model in optimal operation of peak-shaving lithium-ion battery energy storage. Appl Energy 2020;278:115601. http://dx.doi.org/10.1016/j.apenergy.2020.115601.

[12] Cai J, Zhang H, Jin X. Aging-aware predictive control of PV-battery assets in buildings. Appl Energy 2019;236:478–88. http://dx.doi.org/10.1016/j.apenergy.2018.12.003.

[13] Engels J, Claessens B, Deconinck G. Techno-economic analysis and optimal control of battery storage for frequency control services, applied to the german market. Appl Energy 2019;242:1036–49. http://dx.doi.org/10.1016/j.apenergy.2019.03.128.

[14] Weitzel T, Schneider M, Glock CH, Löber F, Rinderknecht S. Operating a storage-augmented hybrid microgrid considering battery aging costs. J Clean Prod 2018;188(7):638–54. http://dx.doi.org/10.1016/j.jclepro.2018.03.296.

[15] Kruger E, Tran QT. Minimal aging operating strategies for battery energy storage systems in photovoltaic applications. In: 2016 IEEE PES Innovative Smart Grid Technologies Conference Europe (ISGT-Europe). IEEE; 2016, p. 1–6. http://dx.doi.org/10.1109/ISGTEurope.2016.7856325.

[16] Attia PM, Bills A, Brosa Planella F, Dechent P, dos Reis G, Dubarry M, Gasper P, Gilchrist R, Greenbank S, Howey D, Liu O, Khoo E, Preger Y, Soni A, Sripad S, Stefanopoulou AG, Sulzer V. Review—"Knees" in lithium-ion battery aging trajectories. J Electrochem Soc 2022;169(6):060517. http://dx.doi.org/10.1149/1945-7111/ac6d13.

[17] Keil J, Jossen A. Electrochemical modeling of linear and nonlinear aging of lithium-ion cells. J Electrochem Soc 2020;167(11):110535. http://dx.doi.org/10.1149/1945-7111/aba44f.

[18] Fermín-Cueto P, McTurk E, Allerhand M, Medina-Lopez E, Anjos MF, Sylvester J, dos Reis G. Identification and machine learning prediction of knee-point and knee-onset in capacity degradation curves of lithium-ion cells. Energy AI 2020;1(5):100006. http://dx.doi.org/10.1016/j.egyai.2020.100006.

[19] Collath N, Tepe B, Englberger S, Jossen A, Hesse H. Aging aware operation of lithium-ion battery energy storage systems: A review. J Energy Storage 2022;55(11):105634. http://dx.doi.org/10.1016/j.est.2022.105634.

[20] Schmalstieg J, Käbitz S, Ecker M, Sauer DU. A holistic aging model for Li(NiMnCo)O2 based 18650 lithium-ion batteries. J Power Sources 2014;257:325–34. http://dx.doi.org/10.1016/j.jpowsour.2014.02.012.

[21] Sarasketa-Zabala E, Gandiaga I, Rodriguez-Martinez LM, Villarreal I. Calendar ageing analysis of a LiFePO4/graphite cell with dynamic model validations: Towards realistic lifetime predictions. J Power Sources 2014;272:45–57. http://dx.doi.org/10.1016/j.jpowsour.2014.08.051.

[22] Guenther C, Schott B, Hennings W, Waldowski P, Danzer MA. Model-based investigation of electric vehicle battery aging by means of vehicle-to-grid scenario simulations. J Power Sources 2013;239:604–10. http://dx.doi.org/10.1016/j.jpowsour.2013.02.041.

[23] Schimpe M, Kuepach MEv, Naumann M, Hesse H, Smith K, Jossen A. Comprehensive modeling of temperature-dependent degradation mechanisms in lithium iron phosphate batteries. J Electrochem Soc 2018;165(2):A181–93. http://dx.doi.org/10.1149/2.1181714jes.

[24] Angenendt G, Zurmühlen S, Axelsen H, Sauer DU. Comparison of different operation strategies for PV battery home storage systems including forecast-based operation strategies. Appl Energy 2018;229(1):884–99. http://dx.doi.org/10.1016/j.apenergy.2018.08.058.

[25] Weitzel T, Glock CH. Energy management for stationary electric energy storage systems: A systematic literature review. European J Oper Res 2018;264(2):582–606. http://dx.doi.org/10.1016/j.ejor.2017.06.052.

[26] Yang Z, Li K, Foley A. Computational scheduling methods for integrating plug-in electric vehicles with power systems: A review. Renew Sustain Energy Rev 2015;51:396–416. http://dx.doi.org/10.1016/j.rser.2015.06.007.

[27] Reniers JM, Mulder G, Ober-Blöbaum S, Howey DA. Improving optimal control of grid-connected lithium-ion batteries through more accurate battery and degradation modelling. J Power Sources 2018;379:91–102. http://dx.doi.org/10.1016/j.jpowsour.2018.01.004.

[28] Hesse H, Kumtepeli V, Schimpe M, Reniers J, Howey D, Tripathi A, Wang Y, Jossen A. Ageing and efficiency aware battery dispatch for arbitrage markets using mixed integer linear programming. Energies 2019;12(6):999. http://dx.doi.org/10.3390/en12060999.

[29] Schimpe M, Barreras J, Wu B, Offer GJ. Battery degradation-aware current derating: An effective method to prolong lifetime and ease thermal management. J Electrochem Soc 2021;168. http://dx.doi.org/10.1149/1945-7111/ac0553.

[30] Shi Y, Xu B, Tan Y, Kirschen D, Zhang B. Optimal battery control under cycle aging mechanisms in pay for performance settings. IEEE Trans Automat Control 2019;64(6):2324–39. http://dx.doi.org/10.1109/TAC.2018.2867507.

[31] Padmanabhan N, Ahmed M, Bhattacharya K. Battery energy storage systems in energy and reserve markets. IEEE Trans Power Syst 2020;35(1):215–26. http://dx.doi.org/10.1109/TPWRS.2019.2936131.

[32] Shi Y, Xu B, Wang D, Zhang B. Using battery storage for peak shaving and frequency regulation: Joint optimization for superlinear gains. IEEE Trans Power Syst 2018;33(3):2882–94. http://dx.doi.org/10.1109/TPWRS.2017.2749512.

[33] Kim W-W, Shin J-S, Kim S-Y, Kim J-O. Operation scheduling for an energy storage system considering reliability and aging. Energy 2017;141:389–97. http://dx.doi.org/10.1016/j.energy.2017.09.091.

[34] Englberger S, Jossen A, Hesse H. Unlocking the potential of battery storage with the dynamic stacking of multiple applications. Cell Rep Phys Sci 2020;1(11):100238. http://dx.doi.org/10.1016/j.xcrp.2020.100238.

[35] Hossain MA, Pota HR, Squartini S, Zaman F, Guerrero JM. Energy scheduling of community microgrid with battery cost using particle swarm optimisation. Appl Energy 2019;254(9):113723. http://dx.doi.org/10.1016/j.apenergy.2019.113723.

[36] Zia MF, Elbouchikhi E, Benbouzid M. Optimal operational planning of scalable DC microgrid with demand response, islanding, and battery degradation cost considerations. Appl Energy 2019;237:695–707. http://dx.doi.org/10.1016/j.apenergy.2019.01.040.

[37] Kazemi M, Zareipour H. Long-term scheduling of battery storage systems in energy and regulation markets considering battery's lifespan. IEEE Trans Smart Grid 2018;9(6):6840–9. http://dx.doi.org/10.1109/TSG.2017.2724919.

[38] Cao J, Harrold D, Fan Z, Morstyn T, Healey D, Li K. Deep reinforcement learning-based energy storage arbitrage with accurate lithium-ion battery degradation model. IEEE Trans Smart Grid 2020;11(5):4513–21. http://dx.doi.org/10.1109/TSG.2020.2986333.

[39] Kumtepeli V, Hesse HC, Schimpe M, Tripathi A, Wang Y, Jossen A. Energy arbitrage optimization with battery storage: 3D-MILP for electro-thermal performance and semi-empirical aging models. IEEE Access 2020;8:204325–41. http://dx.doi.org/10.1109/ACCESS.2020.3035504.

[40] Steriotis K, Sepetanc K, Smpoukis K, Efthymiopoulos N, Makris P, Varvarigos E, Pandzic H. Stacked revenues maximization of distributed battery storage units via emerging flexibility markets. IEEE Trans Sustain Energy 2022;13(1):464–78. http://dx.doi.org/10.1109/TSTE.2021.3117313.

[41] Maheshwari A, Paterakis NG, Santarelli M, Gibescu M. Optimizing the operation of energy storage using a non-linear lithium-ion battery degradation model. Appl Energy 2020;261(4):114360. http://dx.doi.org/10.1016/j.apenergy.2019.114360.

[42] He G, Ciez R, Moutis P, Kar S, Whitacre JF. The economic end of life of electrochemical energy storage. Appl Energy 2020;273:115151. http://dx.doi.org/10.1016/j.apenergy.2020.115151.

[43] Collath N. Aging_aware_MPC: Chair of electrical energy storage technology. 2023, URL https://gitlab.lrz.de/open-ees-ses/aging-aware-MPC.

[44] Möller M, Kucevic D, Collath N, Parlikar A, Dotzauer P, Tepe B, Englberger S, Jossen A, Hesse H. Simses: A holistic simulation framework for modeling and analyzing stationary energy storage systems. J Energy Storage 2022;49(11):103743. http://dx.doi.org/10.1016/j.est.2021.103743.

[45] Fraunhofer Institute for Solar Energy Systems. Energy charts. 2022, URL https://www.energy-charts.info/?l=en&c=DE.

[46] EPEX Spot. EPEX spot indices. 2023, URL https://www.epexspot.com/en/indices.

[47] Draheim P, Schlachter U, Wigger H, Worschech A, Brand U, Diekmann T, Schuldt F, Hanke B, von Maydell K, Vogt T. Business case analysis of hybrid systems consisting of battery storage and power-to-heat on the German energy market. Utilities Policy 2020;67(2):101110. http://dx.doi.org/10.1016/j.jup.2020.101110.

[48] Naumann M, Schimpe M, Keil P, Hesse HC, Jossen A. Analysis and modeling of calendar aging of a commercial LiFePO4/graphite cell. J Energy Storage 2018;17:153–69. http://dx.doi.org/10.1016/j.est.2018.01.019.

[49] Naumann M, Spingler FB, Jossen A. Analysis and modeling of cycle aging of a commercial LiFePO4/graphite cell. J Power Sources 2020;451:227666. http://dx.doi.org/10.1016/j.jpowsour.2019.227666.

[50] Notton G, Lazarov V, Stoyanov L. Optimal sizing of a grid-connected PV system for various PV module technologies and inclinations, inverter efficiency characteristics and locations. Renew Energy 2010;35(2):541–54. http://dx.doi.org/10.1016/j.renene.2009.07.013.

[51] Gasper P, Gering K, Dufek E, Smith K. Challenging practices of algebraic battery life models through statistical validation and model identification via machine-learning. J Electrochem Soc 2021;168:020502. http://dx.doi.org/10.1149/1945-7111/abdde1.

[52] Kucevic D, Meißner R, Jossen A, Hesse H. Battery energy storage systems as an alternative to conventional grid reinforcement. In: Energy proceedings, vol. 24. 2021, http://dx.doi.org/10.46855/energy-proceedings-9834.

[53] Schimpe M, Naumann M, Truong N, Hesse HC, Santhanagopalan S, Saxon A, Jossen A. Energy efficiency evaluation of a stationary lithium-ion battery container storage system via electro-thermal modeling and detailed component analysis. Appl Energy 2018;210(4):211–29. http://dx.doi.org/10.1016/j.apenergy.2017.10.129.

5 Consideration of load forecast and degradation modeling uncertainty

Here, two peer-reviewed conference publications are presented that address uncertainty in the context of aging aware operation.

5.1 Reduction of battery energy storage degradation in peak shaving operation through load forecast dependent energy management

This chapter presents the peer-reviewed conference publication titled *Reduction of battery energy storage degradation in peak shaving operation through load forecast dependent energy management*. The basic peak shaving strategy, presented in Chapter 2.1.3, is to discharge while the load is larger than a given peak shaving limit and to charge again after the load peak until the BESS is fully charged. As the case study in Chapter 3 highlighted, this leads to a high average SOC and, thereby, significant calendar aging.

In this paper, an aging aware operation strategy is proposed to reduce calendar aging in peak shaving applications. The underlying principle is to use load forecasts to charge up the BESS sufficiently early before a load peak with the energy that is forecasted to be needed during the load peak. The challenge lies in the inherent errors of the load forecasts. If a load peak is not successfully reduced, this impacts the cost savings of the whole billing period, i.e., the whole month or year. The adaptive rule-based operation strategy proposed in this paper uses the past performance of load forecasts to calculate the average forecast error and its standard deviation. Based on these values, safety margins are calculated for the required energy level of the BESS at a given time.

The performance of the proposed operation strategy is investigated for a representative one-year industrial load profile that was provided by a research project partner. An artificial neural network was trained with a one-year data set of load values from the previous year to generate the load forecasts. The *proposed* strategy is compared to a *naive* peak shaving strategy and a scenario in which *perfect foresight* of the future load profile is assumed. The naive operation strategy used as a reference here equals the basic peak operation strategy presented in Chapter 2.1.3. As part of the case study for validating the proposed operation strategy, five consecutive years of peak shaving are simulated for a representatively sized BESS with LFP cells in SimSES [83], see Appendix A. After five years, remaining capacity-based SOH values of 92.8 %, 89.7 %, and 84.8 % are observed for the perfect-foresight, the proposed, and the naive peak shaving operation strategies. All operation strategies successfully reduce the load peaks in the first year. The results highlight the extended lifetime that can be achieved with the aging aware operation strategy proposed in this contribution. In addition, multiple parameter variations are conducted to investigate the impact of the tuning parameters of the proposed operation strategy, e.g., the confidence interval, on its performance.

Notably, with its novel method for handling forecast errors, the proposed operation strategy can be applied in combination with any load forecasting method. Easier to forecast load profiles, such as scheduled production lines, cumulated profiles of multiple consumers, or improvements in load forecasting methods themselves, would allow reduced safety margins of the required energy for peak shaving. Thereby, a further reduction of the capacity fade could be achieved, as highlighted by the perfect foresight scenario in the case study.

In summary, a rule-based, aging aware operation strategy for peak shaving applications is proposed in this publication and validated through a simulative case study. Compared to previous publications in the field, an adaptive method for handling load forecast errors has been developed as part of the operation strategy.

CRediT author statement:

- **Nils Collath:** Conceptualization, Formal analysis, Investigation, Methodology, Project administration, Software, Visualization, Writing – original draft, Writing – review & editing
- **Stefan Englberger:** Methodology, Writing – original draft, Writing – review & editing
- **Andreas Jossen:** Funding acquisition, Writing – review & editing
- **Holger Hesse:** Supervision, Writing – review & editing

Reduction of Battery Energy Storage Degradation in Peak Shaving Operation through Load Forecast Dependent Energy Management

Nils Collath, Stefan Englberger, Andreas Jossen, Holger Hesse

NEIS 2020; Conference on Sustainable Energy Supply and Energy Storage Systems, 2020

This paper was peer-reviewed and presented at the 2020 Conference on Sustainable Energy Supply and Energy Storage Systems (NEIS).

Permanent weblink:
https://ieeexplore.ieee.org/document/9273426

Reduction of Battery Energy Storage Degradation in Peak Shaving Operation through Load Forecast Dependent Energy Management

Nils Collath[1,*], Stefan Englberger[1], Andreas Jossen[1], and Holger Hesse[1]
[1]Institute for Electrical Energy Storage Technology, Technical University of Munich (TUM)
[*]nils.collath@tum.de

Abstract

One application for the increasing number of battery energy storage systems is the reduction of demand charges for industrial consumers through peak shaving. Commonly used lithium-ion batteries are subject to degradation due to a multitude of cell-internal aging processes that can have significant impact on the economics of a system. In this contribution, we propose a rule-based operation strategy to reduce battery degradation during peak shaving through the use of load forecasting. Since load forecasting methods include significant inaccuracies, the operation strategy focuses on means to handle forecast errors. The performance of this operation strategy is assessed through time series based simulations and comparison with reference scenarios. A state of health of 89.7 % is remaining with the proposed strategy after five operating years. This is a reduction of capacity loss of 4.9 % percentage points compared to an often implemented naive peak shaving strategy with 84.8 % remaining state of health, while achieving the same performance in terms of reducing load peaks successfully.

Keywords – *battery energy storage system, lithium-ion, peak shaving, degradation, aging, load forecasting*

1 Introduction

The installed capacity of battery energy storage systems (BESS), especially lithium-ion based systems, has been increasing steadily over the last years. Among other applications, battery energy storage systems are used to reduce demand charges for industrial-scale consumers through peak shaving. Next to a price for the consumed energy, industrial electricity consumers in most regions are subject to a demand charge based on the highest power demand in a given billing period. By discharging an energy storage system when the power demand exceeds a power threshold and charging when it subceeds this threshold, the peak power for a given billing period and thereby demand charges can be reduced. Depending on the load profile and demand charge structure, peak shaving alone can lead to a positive business case for battery energy storage systems [1].

The benefits for the grid operator in consumer-side, behind-the-meter peak shaving lie in improved power quality, system-efficiency and ultimately cost reductions [2]. Furthermore, peak shaving with BESSs, is envisioned as a potential means for reducing the peak load through congested lines in the electricity grid and therefore allow for a deferral of investments in upgraded transmission and distribution equipment [3].

Battery degradation can have a significant impact on the economics of a BESS that is used for peak shaving [4]. In this contribution, we propose a novel rule-based operation strategy that relies on load forecasts and related error handling in order to reduce battery degradation in peak shaving operation for lithium-ion batteries.

1.1 Battery Degradation

Lithium-ion batteries are subject to degradation due to a multitude of cell-internal aging processes. Existing semi-empirical modelling approaches for cell degradation describe the overall capacity loss as a superposition of calendar and cyclic aging [5]. While cyclic aging is particularly sensible to the energy throughput and the charge/discharge rates, calendar aging shows strong dependence on temperature and battery state of charge (SOC). For most types of lithium-ion batteries, high temperatures and a high SOC will result in significantly higher calendar aging [6]. The impact of cell aging with particular focus on stationary storage systems has been part of recent studies which showed that an application specific assessment is needed to optimally deal with stress factors and resulting degradation [7]. For residential storage systems that are used for buffering surplus photovoltaic generation behind the meter, various simulations and field studies were undertaken to analyze the impact of degradation [8]. Utility-scale battery storage systems have taken a significant market share for the provision of frequency control reserve. Their economic feasibility in the context of battery degradation has also been subject of recent contributions [9]. Cycle duty is particularly high in this ancillary service application, but the depth of discharge remains low and the rest-state state of charge resides at close to mid level. A battery chemistry that copes well with this duty pattern needs to be selected in order to allow for an adequate lifetime and a positive business case.

However, a recent market review underlines the importance of industrial peak shaving applications as being the fastest growing market segment in Germany [10]. For peak shav-

ISBN 978-3-8007-5359-8

ing, calendar aging mechanisms are especially of concern. With common peak shaving control strategies, the battery cells are kept at high SOC for extended periods of time in order to be able to discharge during the next upcoming peak. The high SOC accelerates decomposition of the electrolyte as well as growth of the solid electrolyte interface and thereby causes an increase in cell impedance and a reduction of the usable cell capacity [5].

1.2 Load Forecasting

Driven by increasing competition and renewable integration, load forecasting in the energy market is becoming an increasingly important issue [11]. For energy storage systems, probabilistic load forecasting algorithms can be used to facilitate efficient system operation. To ensure that high power peaks are reduced successfully by an energy storage system in peak shaving operation, it is essential to know which peak loads can be expected in subsequent hours. Here, not only the height of the power peak, but particularly also its energy content plays a crucial role, as a shortage of stored energy during peak shaving will result in partial or complete failure of the load peak reduction [12]. In existing literature, possible algorithms for load prediction have already been identified [11]. In addition to time series analysis and regression algorithms, more mathematically complex methods are frequently used. Following the progress in more powerful hardware and ongoing research in artificial intelligence, approaches such as support vector machines and artificial neural networks are becoming increasingly popular in the field of load forecasting [11]. Nevertheless, short-term load forecasting methods are subject to significant forecast errors, especially when applied to load profiles of individual consumers instead of cumulative loads at grid or substation level [13].

1.3 Focus of this Contribution

A number of contributions can be found on the operation of BESSs for peak shaving. Existing contributions tend to either neglect the aspect of calendar aging, assume perfect foresight of load-profiles or do not include means for the handling of forecast errors.
Martins et al. considered both calendar and cyclic battery aging for BESS sizing by using linear optimization [4]. They assume perfect foresight of the underlying load profile though. Shi et al. introduce a stochastic joint programming approach to optimize BESS operation for both peak shaving and frequency response simultaneously, using load forecasts [14]. The considered degradation model does not account for calendar aging, which as highlighted in this contribution is the primary aging driver in peak shaving operation. Abdulla et al. use a stochastic dynamic programming approach to optimize BESS operation for a residential application, considering load forecasts and degradation [15]. Papadopoulos et al. conclude that up until today the forecast accuracy is not sufficient for the given peak shaving application. Degradation or means for error handling are not considered here [16].
The focus of this contribution therefore lies on the development and assessment of a peak shaving operation strategy that allows reducing calendar aging for BESSs under consideration of load forecast inherent forecast errors.

2 Methodology

A peak shaving operation strategy is developed that aims to reduce the average SOC of a BESSs over its lifetime and thereby calendar aging. Using load forecasts, the required peak shaving energy for a given future time horizon is determined under consideration of sufficient confidence intervals. The BESS will then only charge up to the energy level that is required for peak shaving for the next forecast horizon. The effects of this operation strategy on system performance and battery degradation are analyzed using time series based simulations with the open-source software SimSES [17].

2.1 Operation Strategy

The underlying principal of the operation strategy is to determine the energy E_{peak} that is required for peak shaving for a predetermined forecast horizon N, based on load forecasts. In order to account for forecast inaccuracy, past values of the distribution of forecast errors are used to calculate E_{peak} as the upper limit of a confidence interval.
While studies have shown that using more elaborate probability density functions for modelling load forecast errors can lead to accuracy improvements, a Gaussian distribution is expected to be sufficient for this investigation [18]. With a Gaussian distribution of forecast errors, the power for the upper limit of the confidence interval P^n_{conf} for step n can be calculated as:

$$P^n_{\text{conf}} = P^n_{\text{pred}} - \mu^n_{\text{pred,error}} + k_\sigma * \sigma^n_{\text{pred,error}} \tag{1}$$

Whereat P^n_{pred} is the predicted load power, $\mu^n_{\text{pred,error}}$ the mean value of forecast errors and $\sigma^n_{\text{pred,error}}$ the standard deviation of forecast errors for the forecast step n. The factor k_σ is derived from the Gaussian distribution for the respective confidence interval probability, as shown in **Table 1**. **Figure 1** depicts the concept of using confidence intervals around multi-step forecasts with a receding horizon.

Table 1 Factor k_σ for a given confidence interval probability following a Gaussian distribution

Probability	k_σ
99.95%	3.291
99.5%	2.576
97.5%	1.960
95.0%	1.645
75.0%	0.675

The energy that is required for peak shaving under consideration of the described confidence intervals, E_{peak}, is then calculated as follows:

$$E_{\text{peak}} = E^N_{\text{peak}} = \sum_{n=1}^{N} \Delta t * f(P^n_{\text{conf}} - P_{\text{limit}}) \tag{2}$$

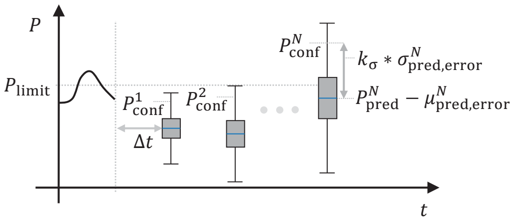

Figure 1 Forecast steps and confidence interval limits for a peak shaving scenario as indicated through box plots.

With $E^n_{\text{peak}} \geq 0$ for every $n \in \{1,..,N\}$ of the sum to allow for sufficient peak shaving energy for every future forecast step. Here, Δt is the forecast period and P_{limit} the peak shaving limit. The function $f(x)$ limits the difference to the maximum discharge and charge energy P_{max} and $-P_{\text{max}}$, respectively:

$$f(x) = \begin{cases} -P_{\text{max}}, & x \leq -P_{\text{max}} \\ x, & -P_{\text{max}} < x \leq P_{\text{max}} \\ P_{\text{max}}, & P_{\text{max}} < x \end{cases} \tag{3}$$

Based on the calculation of the peak shaving energy E_{peak}, the proposed operation strategy is summarized in **Figure 2**. After every passed forecast period Δt, a new load forecast is received. Based on the past error values for previous forecasts, $\sigma^n_{\text{pred,error}}$ and $\mu^n_{\text{pred,error}}$ are calculated for each forecast step $n \in \{1,..,N\}$. The peak shaving energy E_{peak} is calculated with the aforementioned method for the next N forecast steps.

Based on E_{peak}, the logic for determining the battery power P_{batt} resembles a naive peak shaving strategy. If the net load P_{net}, calculated from the current load at the grid connection point P_{load} and the peak shaving limit P_{limit}, is positive, the BESS will discharge according to the difference in order to reduce the peak, which is represented as Case I in **Figure 2**. If the net load is negative, the BESS will charge if the current stored energy is smaller than the required energy for peak shaving E_{peak} (Case II). The current stored energy is calculated from the BESS capacity E_{cap}, the current state of charge SOC and includes a state of charge margin SOC_m. Following the above-mentioned logic, the BESS would discharge only during a power peak, which may lead to an SOC that is higher than required to fulfill the E_{peak} requirement for extended periods of time. As a countermeasure, an active discharge of the BESS is introduced after the BESS has been idle for longer than the specified active discharge delay $t_{\text{discharge}}$ (Case III). If none of the other cases holds true, the BESS will stay idle (Case IV). While the active discharge after extended idle time can be expected to decrease the average SOC and therefore reduce calendar aging, it increases the total number of cycles and thereby cyclic aging as well as energy losses.

2.2 Modelling Framework

Using the open source software SimSES, time series simulations are carried out for the validation of the proposed operation strategy [17]. A summary of the key parameters that are used for the simulation is given in **Table 2**. All cell and degradation models for the lithium iron phosphate (LFP) cells are based on in-house laboratory measurements at the Institute for Electrical Energy Storage Technology [19, 20]. The inverter efficiency model is parametrized according to Notton et al. [21]. Simulations are carried out with a time resolution of 15 minutes and the forecast period is set to $\Delta t = 15$ min as well. The load profile that is used is the measured load of an industrial consumer for one year of operation and is repeated for simulations that exceed one year.

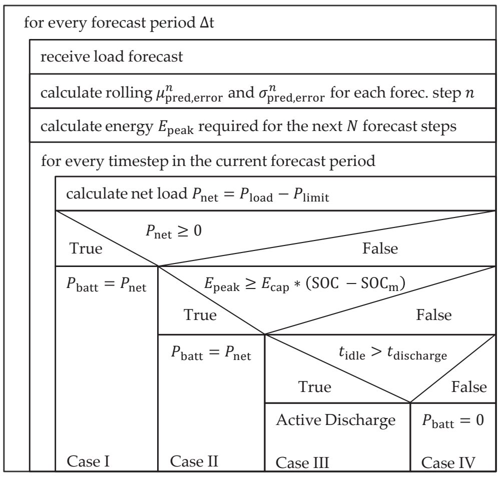

Figure 2 Structogram for the proposed peak shaving operation strategy.

The proposed operation strategy provides a total of six degrees of freedom: the SOC margin SOC_m, the peak shaving limit P_{limit}, the timeframe for calculating the rolling horizon mean $\mu^n_{\text{pred,error}}$ as well as variance $\sigma^n_{\text{pred,error}}$ of the forecast errors, the number of forecast steps N, the confidence interval factor k_σ, and the threshold for active discharge $t_{\text{discharge}}$. Determining the peak shaving limit P_{limit} is considered out of the scope of this investigation. It has been set to a fixed $P_{\text{limit}} = 5.95$ MW for all simulations, based on the highest peak that can be shaved with the given profile and BESS. The SOC margin is set to $\text{SOC}_\text{m} = 0.1$ and the horizon for calculating the mean and variance of the forecast error is set to one week of past data, resulting in 672 individual values. The effect of the configuration parameters k_σ, N, and $t_{\text{discharge}}$ on system performance will be investigated in more detail.

Table 2 Key parameters of the BESS and load profile

Parameter	Value
BESS power / energy	1000 kW / 1370 kWh
Cell chemistry	lithium iron phosphate
Load peak power / yearly demand	6.62 MW / 25 GWh

2.3 Load Forecasting Method

An artificial neural network is used for multi-step time series forecasting in this work. Due to existing frameworks for neural networks, the forecast data is processed using the Matlab Deep Learning toolbox. To analyze the effect of different forecast horizons, the data is generated using forecast horizons from 15 minutes up to 4 hours. With a sample time of 15 minutes, 16 unique forecast values are generated for each time step of the one year load profile. The artificial neural network was trained with a one-year data set of load values from the previous year. For the load forecast, data in the form of ambient temperature, solar irradiation, day of the week, and time is included in the model.
To ensure comparability with existing literature, the following metrics are used to evaluate the forecast quality [22]: mean absolute error (MAE) and root mean squared error (RMSE). Both, MAE and RMSE show lower values and therefore higher model accuracy for shorter forecast horizons. As the forecast horizon increases from 15 minutes to 4 hours, the values for MAE and RMSE also increase from 2.4 % to 13.6 % and 3.7 % to 17.9 %, respectively.

3 Simulation Results

In this chapter, the simulation results are presented and discussed. Two reference scenarios are considered for the proposed operation strategy:

- Naive scenario: The naive peak shaving scenario assumes that no load forecast is available. Therefore, the BESS will charge up to full SOC whenever the load P_{load} is below the peak shaving limit P_{limit}.
- Perfect foresight scenario: This scenario uses the here proposed operation strategy, but assumes perfect foresight of the load profile for the next twelve hours.

In **Figure 3**, peak shaving operation for six exemplary days is depicted, which include a total of four power peaks that exceed the peak shaving limit. While all strategies successfully reduce the load peaks by discharging the BESS, the SOC management inbetween power peaks is vastly different. Load forecasts combined with the proposed operation strategy allow for a lower average SOC than in the naive scenario, only outmatched by the improbable scenario of perfect foresight. Here, $N = 6$ forecast steps, an active discharge delay of $t_{\text{discharge}} = 2$ days, and a confidence interval of 97.5 % ($k_\sigma = 1.960$) were chosen.
Figure 4 shows the effect of the lower average SOC on the state of health (SOH) of the BESS. While the naive scenario leads to a capacity loss of 15.2 % over five years, the proposed method only causes a capacity loss of 10.3 % in the described scenario, a reduction of 4.9 percentage points. The degradation model yielded a distribution of 15.0 % to 0.2 % capacity loss due to calendar aging and cyclic aging, respectively. With the proposed operation strategy this distribution is at 9.8 % to 0.5 %. This highlights that calendar aging can be seen as the dominant aging mechanism in peak shaving operation due to the usually low cycle numbers, but high average SOC. Over the five year time frame the used load profile includes a total of 198 peaks above the specified peak shaving threshold P_{limit} of 5.95 MW, which for the perfect foresight scenario as well as with the proposed operation strategy are all successfully shaved. On the other hand, with the naive strategy a total of eight peaks were not successfully shaved in the last two years of operation. Closer investigation shows that this is due to the higher degradation in the naive scenario that leads to the BESS not having enough remaining capacity to reduce all load peaks successfully for the given peak shaving limit after extended operating time.

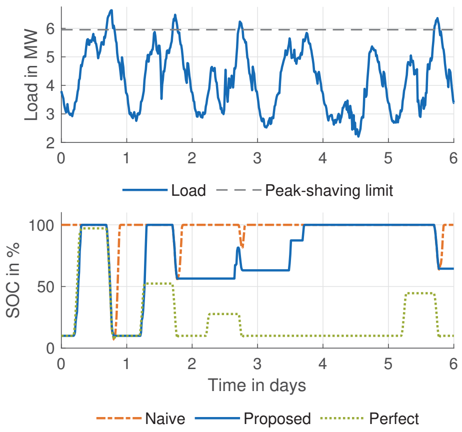

Figure 3 Load and state of charge (SOC) for peak shaving operation over six exemplary days.

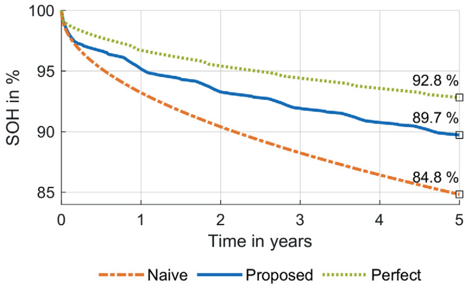

Figure 4 State of health (SOH) development for peak shaving operation over five years.

The effects of a variation from the above base case scenario on the proposed operation strategy are investigated in the following. **Figure 5** highlights the effect of the number of forecast steps N that are considered. The average SOC in the plot is the average of all SOC values over the five year period. In general, a higher number of forecast steps leads to higher values of the determined peak shaving energy E_{peak}, which as depicted leads to a higher average SOC and therefore increased degradation. On the other hand, a smaller forecast horizon increases the amount of missed peaks, meaning load peaks that can not be sufficiently reduced by the BESS, due to not enough energy being available for the discharge in the instance of the peak. The variation of the confidence interval in **Figure 6** shows the same results in terms of a trade-off between a high probability of successfully reducing all power peaks on the one side and BESS degradation on the other side. It should be noted that a high confidence interval (99.5 % or 99.95 %), as seen in **Figure 6**, or a large number of forecast steps ($N = 8$), as seen in **Figure 5**, lead to BESS degradation to an extend that yet again not all peaks are successfully shaved in the last two years of operation.

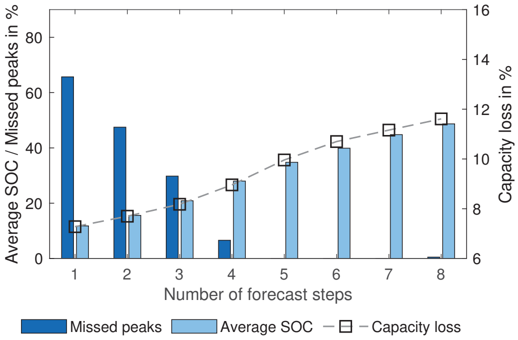

Figure 5 Effects of a variation of the forecast horizon N on system performance.

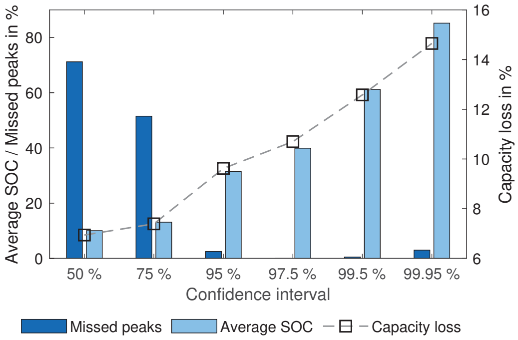

Figure 6 Effects of a variation of the confidence interval and k_σ on system performance.

As previously mentioned, a trade-off between calendar aging on the one side and cyclic aging as well as energy losses on the other side can be expected when varying the active discharge delay $t_{\text{discharge}}$. For a lower $t_{\text{discharge}}$, the stored energy will on average be closer to the calculated peak shaving energy E_{peak}, which in turn requires more cycles. This is confirmed by the results in **Figure 7**. Furthermore, **Figure 7** highlights that calendar aging is the dominant aging mechanism for the here proposed peak shaving operation strategy as well, even for low values of the active discharge delay. Taking into account the cost for both energy losses and capacity fade, a parameterization of $t_{\text{discharge}} = 1$ day is most economical. This is assuming electricity costs of 0.1844 €/kWh for an industrial consumer, a battery pack price of 236 €/kWh, and end-of-life at 80 % SOH [23, 24].

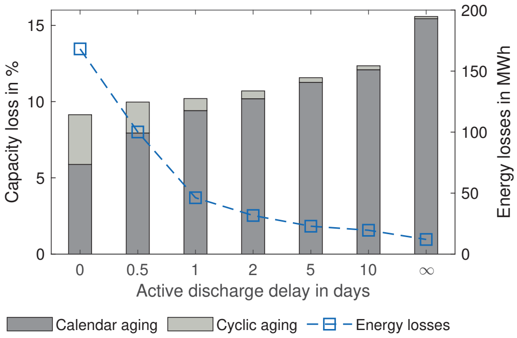

Figure 7 Effects of a variation of the active discharge delay $t_{\text{discharge}}$ on system performance.

4 Conclusion

With the proposed operation strategy, a significant reduction of cell degradation can be observed compared to a naive peak shaving strategy. The operation strategy primarily relies on load forecast dependent SOC management in order to decrease calendar aging. As part of the operation strategy, error handling is especially important due to the imperfectness of load forecasts.

For the chosen parameterization, all peaks are successfully shaved. The parameter variation though highlights the trade-off between battery degradation and the risk of missing load peaks. Missing individual load peaks, especially for industrial demand charge tariffs can significantly affect the BESSs economic benefit for the entire month or year depending on the tariff. Notably, higher degradation as seen for the naive scenario and more conservative parameterizations of the proposed strategy also leads to missing power peaks in later operating years. Though this may be solved be adapting the peak shaving limit upwards with increasing battery degradation.

Finally, it should be noted that the method for handling forecast errors causes the performance of the proposed operation strategy to directly scale with the quality of the load forecast. Easier to forecast load profiles, i.e. scheduled production lines, cumulated profiles of multiple consumers, or improvements in load forecasting methods would therefore allow to further reduce battery degradation in peak shaving operation.

5 Acknowledgement

The authors would like to thank the Bavarian Research Foundation for their financial support via the project SmartB4P, reference number AZ-1376-19.

6 References

[1] C. Rahmann, B. Mac-Clure, V. Vittal, and F. Valencia, “Break-even points of battery energy storage systems for peak shaving applications,” *Energies*, vol. 10, no. 7, 2017.

[2] M. Uddin, M. F. Romlie, M. F. Abdullah, S. Abd Halim, A. H. Abu Bakar, and T. Chia Kwang, “A review on peak load shaving strategies,” *Renewable and Sustainable Energy Reviews*, vol. 82, pp. 3323–3332, 2018.

[3] M. Resch, J. Bühler, M. Klausen, and A. Sumper, “Impact of operation strategies of large scale battery systems on distribution grid planning in germany,” *Renewable and Sustainable Energy Reviews*, vol. 74, pp. 1042–1063, 2017.

[4] R. Martins, H. Hesse, J. Jungbauer, T. Vorbuchner, and P. Musilek, “Optimal component sizing for peak shaving in battery energy storage system for industrial applications,” *Energies*, vol. 11, no. 8, 2018.

[5] Y. Li, K. Liu, A. M. Foley, A. Zülke, M. Berecibar, E. Nanini-Maury, J. van Mierlo, and H. E. Hoster, “Data-driven health estimation and lifetime prediction of lithium-ion batteries: A review,” *Renewable and Sustainable Energy Reviews*, vol. 113, 2019.

[6] P. Keil, S. F. Schuster, J. Wilhelm, J. Travi, A. Hauser, R. C. Karl, and A. Jossen, “Calendar aging of lithium-ion batteries,” *Journal of The Electrochemical Society*, vol. 163, pp. A1872–A1880, 2016.

[7] H. Hesse, M. Schimpe, D. Kucevic, and A. Jossen, “Lithium-ion battery storage for the grid—a review of stationary battery storage system design tailored for applications in modern power grids,” *Energies*, vol. 10, no. 12, p. 2107, 2017.

[8] K. Uddin, R. Gough, J. Radcliffe, J. Marco, and P. Jennings, “Techno-economic analysis of the viability of residential photovoltaic systems using lithium-ion batteries for energy storage in the united kingdom,” *Applied Energy*, vol. 206, pp. 12–21, 2017.

[9] J. Fleer, S. Zurmühlen, J. Badeda, P. Stenzel, J.-F. Hake, and D. U. Sauer, “Model-based economic assessment of stationary battery systems providing primary control reserve,” *Energy Procedia*, vol. 99, pp. 11–24, 2016.

[10] J. Figgener, P. Stenzel, K.-P. Kairies, J. Linßen, D. Haberschusz, O. Wessels, G. Angenendt, M. Robinius, D. Stolten, and D. U. Sauer, “The development of stationary battery storage systems in germany – a market review,” *Journal of Energy Storage*, vol. 29, 2020.

[11] T. Hong and S. Fan, “Probabilistic electric load forecasting: A tutorial review,” *International Journal of Forecasting*, vol. 32, no. 3, pp. 914–938, 2016.

[12] A. Oudalov and R. Cherkaoui, “Sizing and optimal operation of battery energy storage system for peak shaving application,” in *IEEE Lausanne Power Tech, 2007*. Piscataway, NJ: IEEE Service Center, 2007.

[13] P. Mirowski, S. Chen, T. Kam Ho, and C.-N. Yu, “Demand forecasting in smart grids,” *Bell Labs Technical Journal*, vol. 18, no. 4, pp. 135–158, 2014.

[14] Y. Shi, B. Xu, Di Wang, and B. Zhang, “Using battery storage for peak shaving and frequency regulation: Joint optimization for superlinear gains,” *IEEE Transactions on Power Systems*, vol. 33, no. 3, pp. 2882–2894, 2018.

[15] K. Abdulla, J. de Hoog, V. Muenzel, F. Suits, K. Steer, A. Wirth, and S. Halgamuge, “Optimal operation of energy storage systems considering forecasts and battery degradation,” *IEEE Transactions on Smart Grid*, vol. 9, no. 3, pp. 2086–2096, 2016.

[16] V. Papadopoulos, T. Delerue, J. van Ryckeghem, and J. Desmet, “Assessing the impact of load forecasting accuracy on battery dispatching strategies with respect to peak shaving and time-of-use (tou) applications for industrial consumers,” in *2017 52nd International Universities Power Engineering Conference (UPEC)*. Piscataway, NJ: IEEE, 2017.

[17] M. Naumann, F. B. Spingler, and A. Jossen, “Analysis and modeling of cycle aging of a commercial lifepo4/graphite cell,” *Journal of Power Sources*, vol. 451, 2020.

[18] B.-M. Hodge, D. Lew, and M. Milligan, “Short-term load forecast error distributions and implications for renewable integration studies,” in *2013 IEEE Green Technologies Conference (GreenTech)*. IEEE, 2013, pp. 435–442.

[19] M. Naumann, M. Schimpe, P. Keil, H. C. Hesse, and A. Jossen, “Analysis and modeling of calendar aging of a commercial lifepo4/graphite cell,” *Journal of Energy Storage*, vol. 17, pp. 153–169, 2018.

[20] M. Naumann and C. Nam Truong, “Simses - software for techno-economic simulation of stationary energy storage systems,” 2020. [Online]. Available: www.simses.org

[21] G. Notton, V. Lazarov, and L. Stoyanov, “Optimal sizing of a grid-connected pv system for various pv module technologies and inclinations, inverter efficiency characteristics and locations,” *Renewable Energy*, vol. 35, no. 2, pp. 541–554, 2010.

[22] H. Hahn, S. Meyer-Nieberg, and S. Pickl, “Electric load forecasting methods: Tools for decision making,” *European Journal of Operational Research*, vol. 199, no. 3, pp. 902–907, 2009.

[23] BDEW, “Electricity prices for the industry (incl. tax),” 2019. [Online]. Available: https://www.bdew.de/service/daten-und-grafiken/strompreis-fuer-die-industrie/

[24] D. Frankel, S. Kane, and C. Tryggestad, “The new rules of competition in energy storage,” 2018. [Online]. Available: https://www.mckinsey.com/industries/electric-power-and-natural-gas/our-insights/the-new-rules-of-competition-in-energy-storage

5.2 The economic impact of battery degradation modeling uncertainty

This chapter presents the peer-reviewed conference publication titled *The economic impact of battery degradation modeling uncertainty*. Degradation models are typically fitted to data from cell-aging studies and the resulting models include inherent errors and uncertainty. This publication investigates for the first time how these degradation modeling uncertainties affect the techno-economic assessment of typical stationary applications. This work stems from a research collaboration and builds on top of the degradation models that were derived in the accompanying paper *Machine-learning assisted identification of accurate battery lifetime models with uncertainty*, see Appendix B.

Three representative BESSs with LFP cells are modeled in the applications of self-consumption increase, peak shaving, and FCR. Two degradation models are compared for the same LFP cell, the *expert-identified* model published by Naumann et al. [37, 38] and the *machine learning-assisted* model, which is detailed in Appendix B. Confidence intervals for the respective degradation models are derived through bootstrap resampling, i.e., randomly redrawing samples from the original set of tested battery cells. The large sets of resampled parameters fits for the two degradation models are implemented in SimSES [83], see Appendix A. The adapted version of SimSES as well as the simulation results are available open-source[3] [232].
For each simulated timestep, one thousand resampled parameter sets for the capacity loss model are simulated, and the respective confidence interval of capacity loss is selected from an ordered list of all simulated capacity loss models. The NPV, i.e., the future discounted cashflow generated in the three applications, is used as the main metric for comparison alongside the SOH trajectory. The results show that the spread of NPV confidence intervals can be reduced in all investigated applications by employing a degradation model with higher parameter fit quality, in this case by choosing the *machine learning-assisted* over the *expert-identified* degradation model. Furthermore, it is shown that the consideration of degradation modeling uncertainty is especially crucial when: (i) The cash flow highly depends on the available battery capacity; (ii) A fixed, e.g., warranty mandated, state of health limit is assumed as the threshold for EOL of the BESS; (iii) Long evaluation periods and low discount rates are the focus of the economic evaluation.

In summary, the developed method for model identification detailed in Appendix B allows the automated identification of algebraic formulations and their parameter fits for degradation models, while also quantifying the model uncertainty. The case study here highlights the impact that degradation model uncertainty can have on the techno-economic assessment of typical BESS applications.

CRediT author statement:

- **Nils Collath:** Conceptualization, Investigation, Methodology, Project administration, Software, Visualization, Writing – original draft, Writing – review & editing
- **Paul Gasper:** Methodology, Writing – original draft, Writing – review & editing
- **Andreas Jossen:** Funding acquisition, Writing – review & editing
- **Kandler Smith:** Funding acquisition, Supervision, Writing – review & editing
- **Holger Hesse:** Supervision, Writing – review & editing

---

[3] Code and simulation results are publicly available: https://doi.org/10.14459/2021mp1633017

The Economic Impact of Battery Degradation Modelling Uncertainty

Nils Collath, Paul Gasper, Andreas Jossen, Kandler Smith, Holger Hesse

2022 IEEE Power & Energy Society General Meeting (PESGM), 2022

This paper was peer-reviewed and presented at the 2022 IEEE Power & Energy Society General Meeting.

Permanent weblink:
https://doi.org/10.1109/PESGM48719.2022.9916844

The Economic Impact of Battery Degradation Modelling Uncertainty

1st Nils Collath
Technical University of Munich
Munich, Germany
nils.collath@tum.de

2nd Paul Gasper
National Renewable Energy Laboratory
Denver, USA
paul.gasper@nrel.gov

3rd Andreas Jossen
Technical University of Munich
Munich, Germany
andreas.jossen@tum.de

4th Kandler Smith
National Renewable Energy Laboratory
Denver, USA
kandler.smith@nrel.gov

5th Holger Hesse
Technical University of Munich
Munich, Germany
holger.hesse@tum.de

***Abstract*—Battery energy storage systems (BESS) are used for a variety of applications, with their economic benefit often being the decisive factor for deployment. A multitude of physico-chemical aging mechanisms lead to capacity fade over a BESS life cycle. The models that are used to describe this capacity fade are prone to inherent model errors. Through a holistic techno-economic modelling approach, we investigate the impact of battery degradation modelling uncertainty on the economic benefit of representative BESS applications. Here, it is shown how improved parameter fit quality can reduce the resulting economic uncertainty. Furthermore, we highlight that the consideration of degradation modelling uncertainty is especially crucial when: (i) the cash flow highly depends on the available battery capacity, (ii) a fixed, e.g. warranty mandated, state of health limit acts as the threshold for battery end-of-life, (iii) long evaluation periods and low discount rates are the focus of economic evaluation.**

***Index Terms*—battery energy storage system, degradation, aging, techno-economic analysis, lithium-ion**

I. INTRODUCTION

The installed capacity of Battery Energy Storage Systems (BESS) has been increasing steadily over the past years. These systems are used for a variety of applications, which are commonly categorized into three groups: behind-the-meter, front-of-the-meter and off-grid applications [1]. For behind-the-meter applications, such as peak shaving or home storage systems, electricity cost reductions are a primary motive for the installation of a BESS. Front-of-the-meter applications allow revenue generation through participation in energy and power markets, such as the European frequency containment reserve market. Lastly, in off-grid applications, BESS based microgrids can be a cost competitive option over solely relying on diesel generators [1]. While lead-acid batteries used to be the technology of choice for BESSs, lithium-ion batteries are now the predominant technology for new installations, following economies-of-scale induced cost and performance advances in recent years [2]. Over the life cycle of a lithium-ion battery, a multitude of cell internal aging mechanisms lead to degradation, which manifest itself in an increase of cell resistance, safety implications, and capacity fade.

Multiple authors have published methods to account for degradation effects in operating strategies and thereby allow a more economic dispatch of BESSs [3], [4]. Other authors performed techno-economic analyses under consideration of battery degradation for individual BESS applications [5], [6]. Typically, researchers rely on degradation models that are fit to data from a cell aging study, in which a limited amount of cells has been cycled and stored under accelerated aging conditions [3]–[6]. Metrics such as the coefficient of determination (R^2) or mean average error (MAE) are commonly used to describe the fit quality of the resulting model to the underlying test data [7]–[9]. While these inherent model errors may be referenced, they are not propagated to the system lifetime analysis, which raises the question by how far the uncertainty of degradation models impacts the techno-economic analyses that they are being used for. To the knowledge of the authors, no existing work in the field of BESS techno-economic analyses and scheduling methods accounts for the modelling uncertainty associated with degradation models.

In this contribution, we determine confidence intervals for semi-empirical degradation models of lithium-ion cells and embed them into a time-series based simulation environment. Through a techno-economic analysis, we highlight the impact of battery degradation modelling uncertainty on the economic evaluation of BESSs for three common applications: Self Consumption Increase (SCI) with home storage systems, Peak Shaving (PS) and Frequency Containment Reserve (FCR). We focus on investigating how the net present value (NPV)

The authors would like to thank the Bavarian Research Foundation for their financial support via the project SmartB4P, reference number AZ-1376-19. Paul Gasper and Kandler Smith are supported by the National Renewable Energy Laboratory which is operated by Alliance for Sustainable Energy, LLC, for the U.S. Department of Energy under Contract No. DE-AC36-08GO28308, and acknowledge support from the Assistant Secretary for Energy Efficiency and Renewable Energy, Office of Vehicle Technologies of the U.S. Department of Energy. The views expressed in the article do not necessarily represent the views of the DOE or the U.S. Government. The U.S. Government retains and the publisher, by accepting the article for publication, acknowledges that the U.S. Government retains a nonexclusive, paid-up, irrevocable, worldwide license to publish or reproduce the published form of this work, or allow others to do so, for U.S. Government purposes.

978-1-6654-0823-3/22/$31.00 ©2022 IEEE

of future income relates to the confidence intervals of the underlying degradation models.

II. METHODOLOGY

A. Degradation Models

We investigate two different degradation models, fit to the same degradation data set of lithium iron phosphate (LFP) cells that has previously been published in [8], [9]. Both models fall into the category of semi-empirical degradation models, with calendar and cyclic capacity loss components:

$$\mathrm{Q}_{\mathrm{loss}}^{\mathrm{total}} = \mathrm{Q}_{\mathrm{loss}}^{\mathrm{cyc}}(\mathrm{FEC}, \mathrm{DOC}, C_{\mathrm{rate}}) + \mathrm{Q}_{\mathrm{loss}}^{\mathrm{cal}}(t, \mathrm{SOC}) \tag{1}$$

In (1), $\mathrm{Q}_{\mathrm{loss}}^{\mathrm{cyc}}$ is the cyclic degradation, depending on the number of full equivalent cycles (FEC), the depth of cycle between individual cycles DOC as well as the C-rate during charge and discharge C_{rate}. $\mathrm{Q}_{\mathrm{loss}}^{\mathrm{cal}}$ refers to the calendar degradation depending on time t and the state of charge SOC. The first degradation model uses the same, expert-identified, algebraic structure as in the original data publication of Naumann et al. [8], [9]. The second degradation model uses an algebraic structure that has been identified by a machine learning (ML) assisted method that was previously published in [7] and is described in detail in [10]. The resulting equations that describe both models can be found in the Appendix. The MAE of the ML-assisted modelling approach over both cyclic and calendar aging data (0.79 %) is less than half of the MAE of the expert-identified modeling approach (1.66 %) [10].
Uncertainty of the degradation models is estimated utilizing a bootstrap resampling approach. For each iteration of bootstrap resampling, the aging data from various test conditions (e.g. DOC, SOC) are randomly resampled with replacement. The model parameters are then optimized on these randomly resampled sets, resulting in different optimal values for each fitting parameter for every set. For the ML-assisted model, both the calendar and cyclic capacity loss models are optimized on the resampled data simultaneously. For the expert-identified model proposed by Naumann et al. [8], [9], where calendar and cyclic degradation models are optimized separately, the bootstrap resampling procedure is modified to reflect this dependence: First, the calendar aging data is randomly resampled with replacement, and the calendar aging model parameters optimized. Afterwards, the cyclic fade data is randomly resampled with replacement, and the cyclic fade model parameters are optimized. For extrapolating uncertainty to new use-cases or into the future, the degradation model is evaluated using both the best-fit parameter values, which have been optimized to all available aging data, as well as the M bootstrapped parameter values, as reported in Fig. 1.

B. Simulation Environment

We adapt the open-source simulation software SimSES to conduct time-series simulations and perform the techno-economic analysis [11], [12]. In order to account for the uncertainty of the degradation model parameter fits, we adapt the simulation environment as highlighted in Fig. 1: The degradation models have access to a sufficiently large number of bootstrapped parameter sets for the expert-identified and ML-assisted model. Here, we use $\mathrm{M} = 1000$ parameter sets. The relevant stress factors are passed to the degradation model at every time step. A half cycle counting algorithm is used to determine DOC and C_{rate}. Following that, the calendar capacity loss and cyclic capacity loss are calculated for every parameter set, with the cyclic degradation only being calculated after a half cycle has been detected. We employ the concept of virtual time and virtual FECs to discretize the models [9]. The applicable incremental capacity loss for the investigated confidence interval is then chosen from the list sorted in ascending order, e.g. element 250 for the lower limit of the 50 % confidence interval with 1000 parameter sets. The adapted software was made available open-source under [11].

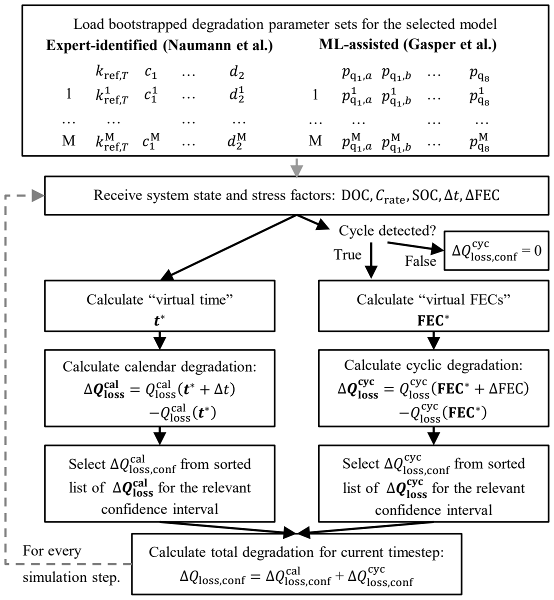

Fig. 1. Overview of how capacity loss for the selected confidence interval $\Delta Q_{\mathrm{loss,conf}}$ is calculated. The aging models are detailed in the Appendix. The adapted open-source software was made available under [11].

C. Use-Cases

The application specific system sizing for SimSES, as well as the input profiles are based on Kucevic et al. [13]. SCI refers to a home storage system, using a household load profile and a photovoltaic (PV) generation profile for the Munich area as input. PS refers to reducing load peaks with a BESS for an industrial-scale consumer with the respective load profile. FCR refers to the operation of a BESS on the central European FCR market, using a frequency profile as input to determine the battery charge and discharge pattern. The key technical simulation parameters are summarized in Table I.

978-1-6654-0823-3/22/$31.00 ©2022 IEEE

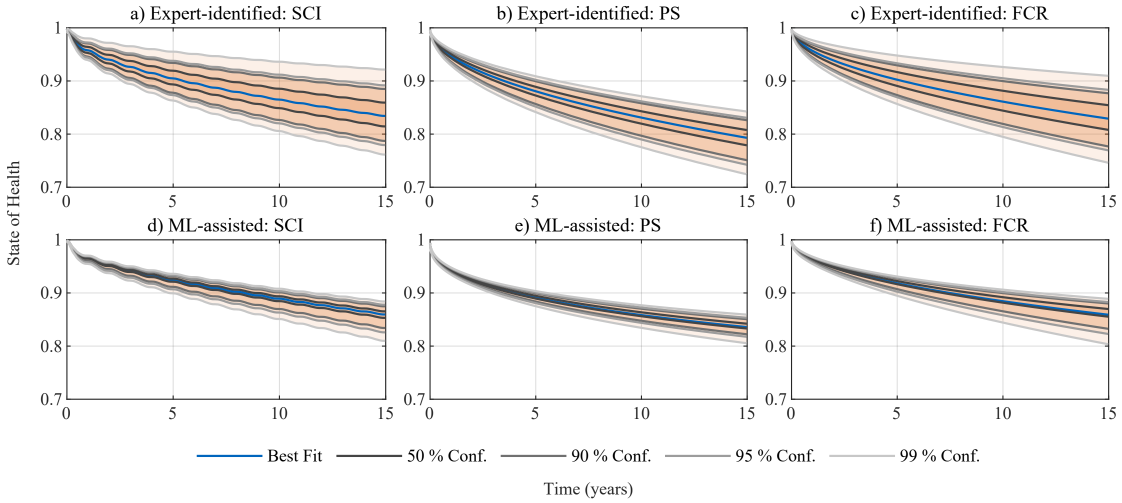

Fig. 2. State of Health (relative remaining capacity) and its confidence intervals for the investigated degradation models (expert-identified & ML-assisted) as well as the three applications (SCI, PS & FCR). Visualized from simulation results that are made available under [11].

TABLE I
TECHNICAL SIMULATION PARAMETERS

	SCI	PS	FCR
Energy	5 kWh	100 kWh	1.6 MWh
Power	5 kW	40 kW	1.6 MW
Cell Model	LFP 3 Ah: Expert-identified vs. ML-assisted		
Input Profiles (time series)	PV generation, household load	industrial load	grid frequency

TABLE II
ECONOMIC EVALUATION PARAMETERS

Application	Parameter	Value
SCI	feed-in tarrif	0.0816 EUR / kWh
SCI & PS	electricity cost	0.3167 EUR / kWh
PS	demand charge	97.80 EUR / (kW * a)
FCR	daily revenue	0.3 EUR / (kW * d)
FCR	IDM electricity price	0.04 EUR / kWh

D. *Economic Evaluation*

For the economic evaluation, we use the NPV of future income as the key performance indicator (2). Here, i is the discount rate and $\mathrm{CF_n}$ the application specific cash flow for the year n. The constant price assumptions are shown in Table II. For SCI, the economic benefit for the end-user is gained through electricity bill savings. As electricity costs tend to be higher than the PV feed-in tariff, a net benefit is gained for the end-user through self use of PV generated electricity. The cash flow for this application therefore is calculated by deducting the energy cost that occur with a BESS $\mathrm{EC_n^{BESS}}$ from the energy cost that were to occur without a BESS $\mathrm{EC_n}$, as in (3). Next to the cost for the consumed energy, industrial-scale electricity consumers in Germany are subject to demand charges, based on the highest 15 min averaged power demand in a given year. In (4), $\mathrm{DC_n^{BESS}}$ and $\mathrm{DC_n}$ denote the demand charges that occur with and without a BESS, respectively. Lastly, the cash flow for FCR is equal to the generated revenue on the FCR market $\mathrm{R_n^{FCR}}$ in the respective year, plus the revenue $\mathrm{R_n^{IDM}}$ and minus the cost $\mathrm{C_n^{IDM}}$ for the total of traded kWh of electricity on the intraday market (IDM), to keep the BESS in its mandated SOC range (5).

$$\mathrm{NPV} = \sum_{\mathrm{n}=1}^{\mathrm{N}} \frac{\mathrm{CF_n}}{(1+\mathrm{i})^{\mathrm{n}}} \tag{2}$$

$$\mathrm{CF_n^{SCI}} = \mathrm{EC_n} - \mathrm{EC_n^{BESS}} \tag{3}$$

$$\mathrm{CF_n^{PS}} = \mathrm{DC_n} - \mathrm{DC_n^{BESS}} + \mathrm{EC_n} - \mathrm{EC_n^{BESS}} \tag{4}$$

$$\mathrm{CF_n^{FCR}} = \mathrm{R_n^{FCR}} + \mathrm{R_n^{IDM}} - \mathrm{C_n^{IDM}} \tag{5}$$

III. TECHNO-ECONOMIC ANALYSIS

All time-series simulations are conducted with the aforementioned method for 15 years with 60 sec timesteps. The full simulation results are available under [11].

A. *Application Specific Capacity Loss*

Fig. 2 shows the state of health (SOH) for all three applications and the two different degradation models. Generally, the ML-assisted model yields narrower confidence intervals for all applications due to the improved parameter fit quality. The FCR application is characterized by a large amount of cycles with small DOC. PS shows few cycles, a high average SOC and therefore a high share of calendar degradation. SCI shows a large amount of cycles with a generally larger DOC than FCR. Notably, seasonality as a consequence of varying solar irradiation and a varying load profile shows in the degradation behavior, in the form of ripples with a higher degradation gradient during summer time.

978-1-6654-0823-3/22/$31.00 ©2022 IEEE

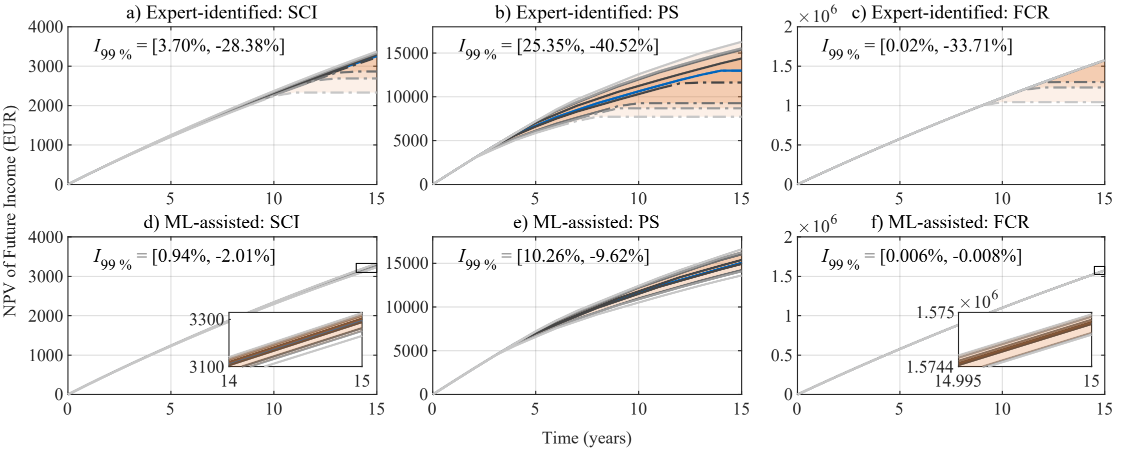

Fig. 3. NPV and confidence intervals for the investigated degradation models and applications. We assume a base discount rate of $i = 2$ % as well as a EOL threshold at 80 % SOH. Both are varied in the following figures. Same confidence intervals as in Fig. 2, with dashed lines once the EOL threshold is reached. $I_{99\%}$ is the interval of percentage deviations of the upper and lower bounds of the 99% confidence intervals of the NPV from the "best fit" scenario.

B. *Application Specific Net Present Value*

The NPV from Fig. 3 shows a larger degree of variance between applications and degradation models than the SOH. Here, we assume a warranty mandated threshold of 80% SOH for the end-of-life (EOL) criterion and a discount rate of 2 % as the base scenario. Both will be varied in the following subchapters. There are two ways in which uncertainty in degradation modelling has an impact on the economic evaluation: First, the reduced capacity can impede the BESS ability to perform its destined application. Second, if the BESS reaches its end-of-life (EOL) at 80% SOH before the end of the evaluation period, a cash flow of 0 EUR is assumed moving forward, causing an even more significant spread in NPV confidence intervals.

For SCI in Fig. 3a, the NPV confidence intervals slightly widen over the years, as every year less PV energy can be stored by the BESS, leading to a higher electricity bill for the household. The more significant change occurs, once the upper bound of the 99 % degradation confidence interval reaches EOL in year 11, leading to reduced cash flow that year and no cash flow moving forward. With the ML-assisted model in Fig. 3d, the confidence intervals are narrower and none reach EOL in the evaluation period, leading to a negligible spread of the NPV. In the case of PS (Fig. 3b & 3e), the impact of degradation uncertainty is more severe even before the EOL threshold. The BESS does not have sufficient capacity left to reduce the largest load peak of the year completely, leading to a noticeable NPV reduction in that case and wider NPV confidence intervals. With a suitable forecasting strategy and SOH awareness in place, the peak shaving limit would likely be adapted upwards in real world use, slightly reducing this effect. For FCR (Fig. 3c & 3f), the influence of degradation in this scenario is negligible until the system reaches its EOL. The small spread before EOL is caused by different purchase quantities of energy on the intraday market to bring the BESS back into its mandated SOC range for FCR. As long as the BESS capacity loss does not limit its minimum bid size of 1 MW for the European market, the financial impact will be negligible.

C. *Impact of the EOL Criterion*

Assuming a constant EOL at 80 % SOH in the previous section, we now vary this parameter. Here, we only consider the SCI application with the expert-identified degradation model. As Fig. 4a shows, the EOL has a significant impact on the confidence intervals of the NPV. Only a small NPV spread shows around 75 % SOH, since for none of the investigated confidence intervals EOL is reached within the 15 year timeframe. The NPV spread then widens with an increasing SOH threshold, as the upper bounds of the degradation confidence intervals reach the EOL criterion before the end of the 15 year timeframe, while the lower bounds do not. For very low EOL thresholds, such as 95 % SOH, the NPV confidence intervals narrow again, as in each scenario EOL is reached for all confidence intervals before a significant difference in NPV has developed.

D. *Impact of the Discount Rate*

Here, we vary the discount rate, which is one of the key metrics when assessing investment options. Generally, a higher discount rate will reduce the value of future cash flow for the investor. This also shows in Fig. 4b. An increased discount rate will not only reduce the NPV for all confidence intervals, but also the width of the confidence intervals themselves. As cash flow in years further down the evaluation is discounted more than the upcoming ones, the cash flow for those confidence in-

978-1-6654-0823-3/22/$31.00 ©2022 IEEE

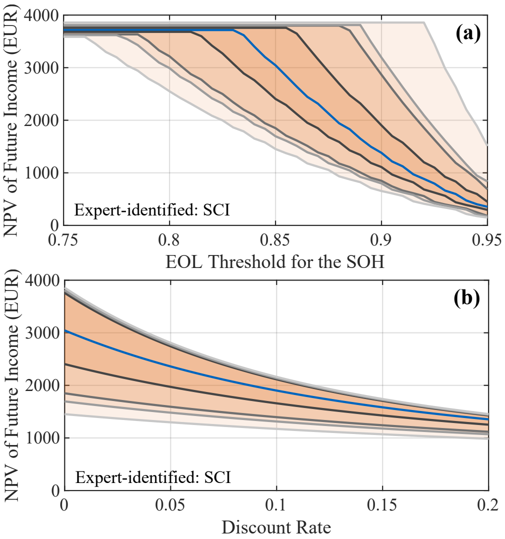

Fig. 4. Impact of the EOL criterion (a) and the discount rate (b) on the NPV over 15 years for SCI with the expert-identified degradation model. Same confidence intervals as in Fig. 2.

tervals that reach EOL later, is discounted over-proportionally, which leads to narrower confidence intervals.

IV. CONCLUSION

The holistic techno-economic modelling approach of this contribution allows to characterize the economic impact of degradation modelling uncertainty for different applications of BESSs. The results show that the spread of NPV confidence intervals can be reduced in all investigated use-cases by employing a degradation model with higher parameter fit quality, in this case by choosing the ML-assisted over the expert-identified degradation model. Furthermore, we conclude that there are three cases in which considering degradation model uncertainty is especially crucial for valid techno-economic analyses: First, when investigating applications in which the revenue is significantly affected by the reduced capacity, as it is the case for PS in this contribution. Second, when using fixed SOH thresholds as an EOL criterion, since the outer degradation confidence intervals may reach EOL significantly faster than the "best fit" scenario. Finally, when performing analyses over a long time horizon with a low discount rate, as the degradation confidence intervals widen over time and the dampening effect of the discount rate for cash flow in later years is then reduced.

REFERENCES

[1] M. Killer, M. Farrokhseresht, and N. G. Paterakis, "Implementation of large-scale li-ion battery energy storage systems within the emea region," *Applied Energy*, vol. 260, p. 114166, 2020.

[2] J. Figgener, P. Stenzel, K.-P. Kairies, J. Linßen, D. Haberschusz, O. Wessels, G. Angenendt, M. Robinius, D. Stolten, and D. U. Sauer, "The development of stationary battery storage systems in germany – a market review," *Journal of Energy Storage*, vol. 29, p. 101153, 2020.

[3] A. Maheshwari, N. G. Paterakis, M. Santarelli, and M. Gibescu, "Optimizing the operation of energy storage using a non-linear lithium-ion battery degradation model," *Applied Energy*, vol. 261, no. 4, 2020.

[4] K. Abdulla, J. de Hoog, V. Muenzel, F. Suits, K. Steer, A. Wirth, and S. Halgamuge, "Optimal operation of energy storage systems considering forecasts and battery degradation," *IEEE Transactions on Smart Grid*, vol. 9, no. 3, pp. 2086–2096, 2016.

[5] F. Wankmüller, P. R. Thimmapuram, K. G. Gallagher, and A. Botterud, "Impact of battery degradation on energy arbitrage revenue of grid-level energy storage," *Journal of Energy Storage*, vol. 10, no. 11, 2017.

[6] K. Uddin, R. Gough, J. Radcliffe, J. Marco, and P. Jennings, "Techno-economic analysis of the viability of residential photovoltaic systems using lithium-ion batteries for energy storage in the united kingdom," *Applied Energy*, vol. 206, no. 10, pp. 12–21, 2017.

[7] P. Gasper, K. Gering, E. Dufek, and K. Smith, "Challenging practices of algebraic battery life models through statistical validation and model identification via machine-learning," *Journal of the Electrochemical Society*, vol. 168, no. 2, p. 020502, 2021.

[8] M. Naumann, M. Schimpe, P. Keil, H. C. Hesse, and A. Jossen, "Analysis and modeling of calendar aging of a commercial lifepo4/graphite cell," *Journal of Energy Storage*, vol. 17, pp. 153–169, 2018.

[9] M. Naumann, F. B. Spingler, and A. Jossen, "Analysis and modeling of cycle aging of a commercial lifepo4/graphite cell," *Journal of Power Sources*, vol. 451, p. 227666, 2020.

[10] P. Gasper, N. Collath, H. Hesse, A. Jossen, and K. Smith, "Machine-learning battery lifetime equations with uncertainty for simulating extended aging and real-world use," *unpublished*.

[11] N. Collath, P. Gasper, A. Jossen, K. Smith, and H. Hesse, "Techno-economic analysis results of bess use-cases considering battery degradation model confidence intervals," 2021. [Online]. Available: https://doi.org/10.14459/2021mp1633017

[12] M. Naumann and C. Nam Truong, "Simses - software for techno-economic simulation of stationary energy storage systems," 2021. [Online]. Available: www.simses.org

[13] D. Kucevic, B. Tepe, S. Englberger, A. Parlikar, M. Mühlbauer, O. Bohlen, A. Jossen, and H. Hesse, "Standard battery energy storage system profiles: Analysis of various applications for stationary energy storage systems using a holistic simulation framework," *Journal of Energy Storage*, vol. 28, p. 101077, 2020.

APPENDIX

Model I - Naumann et al. (Expert-identified) [8], [9]:

In (6), $k_{\mathrm{ref,T}}$, c_1 and d_1 are fitting parameters of the calendar degradation model. In (7), a_2,b_2,c_2 and d_2 are the fitting parameters of the cyclic model.

$$\mathrm{Q}^{\mathrm{cal}}_{\mathrm{loss}} = k_{\mathrm{ref,T}} * (c_1 * (\mathrm{SOC} - 0.5)^3 + d_1) * \sqrt{t} \tag{6}$$

$$\mathrm{Q}^{\mathrm{cyc}}_{\mathrm{loss}} = (a_2 * C_{\mathrm{rate}} + b_2) * (c_2 * (\mathrm{DOC} - 0.6)^3 + d_2) * \sqrt{\mathrm{FEC}} \tag{7}$$

Model II - Gasper et al. (ML-assisted) [7], [10]:

In (8), q_2 is a fitting parameter while q_1 and q_3 are defined as described in (9) and (10). $p_{q_1,a}$, $p_{q_1,b}$, $p_{q_1,c}$, $p_{q_3,a}$, $p_{q_3,b}$, $p_{q_3,c}$, $p_{q_3,d}$ and $p_{q_3,e}$ are the fitting parameters for this part of the calendar degradation model. U_a is the anode-to-reference potential, dependent on the SOC, using the same relationship as in [7], [10]. In (11), p_{q_5}, $p_{q_7,a}$, $p_{q_7,b}$ and $p_{q_7,c}$ are the fitting parameters for the cyclic degradation model.

$$\mathrm{Q}^{\mathrm{cal}}_{\mathrm{loss}} = 2q_1 * (\frac{1}{2} - \frac{1}{1 + \exp((q_2 * t)^{q_3})}) \tag{8}$$

$$q_1 = p_{q_1,a} * \exp(p_{q_1,b} * \frac{\sqrt{U_a}}{T^2}) * \exp(p_{q_1,c} * \frac{\sqrt{U_a}}{T}) \tag{9}$$

$$\begin{aligned} q_3 = p_{q_3,a} * \exp(p_{q_3,b} * \frac{U_a^{1/3}}{T^4}) * \exp(p_{q_3,c} * T^3 * U_a^{1/4}) \\ * \exp(p_{q_3,d} * \frac{U_a^{1/3}}{T^3}) * \exp(p_{q_3,e} * T^2 * U_a^{1/4}) \end{aligned} \tag{10}$$

$$\begin{aligned} \mathrm{Q}^{\mathrm{cyc}}_{\mathrm{loss}} = (p_{q_7,a} + p_{q_7,b} * \mathrm{DOC} + p_{q_7,c} \\ * \exp(\mathrm{DOC}^2 * C^3_{\mathrm{rate}}))^{q_8} * \mathrm{FEC}^{q_8} \end{aligned} \tag{11}$$

To ensure comparability between application profiles, we here assume a constant 25°C cell temperature in both models. Variable temperature modelling would affect the amount of calendar degradation, depending on the local climatic conditions and the BESS thermal design.

978-1-6654-0823-3/22/$31.00 ©2022 IEEE

6 Suitability of late-life lithium-ion cells for battery energy storage systems

This chapter presents the peer-reviewed journal publication *Suitability of late-life lithium-ion cells for battery energy storage systems*. Here, the performance of already significantly degraded lithium-ion cells, labelled late-life cells, is investigated in stationary energy storage applications in two ways. First, a representative prismatic cell, which is known to be used in multiple operational BESSs, is compared to a cylindrical cell that is primarily intended for EV applications, but can be envisioned in stationary second-life applications. This comparison is performed for typical stationary applications at different but constant SOH values in SimSES [83], see Appendix A. Second, a novel physicochemical aging model is developed based on a small-scale experimental aging study for the cylindrical cell and coupled to SimSES to investigate the nonlinear aging phase with its increased degradation rate. With this physicochemical aging model and supported by the aging study it is shown that through adapting the operating conditions of a BESS towards the EOL, the nonlinear aging phase can be delayed, the lifetime prolonged, and the generated profit significantly increased.

The publication first presents the two representative stationary applications that are used for the later case study: energy arbitrage with a large-scale storage system and self-consumption increase with a home storage system. For the energy arbitrage application, the MPC framework from Chapter 4 is used. Afterward, an electrical cell characterization is performed for the two investigated cell types: a 94 Ah prismatic cell, presumably with an NMC cathode and graphite anode, which is known to be used in multiple operational BESSs, and a 4.8 Ah cylindrical cell, presumably with an NMC cathode and silicon-graphite anode, which is primarily intended for EV applications. Overall, the 94 Ah prismatic cell shows a larger nominal power range and higher roundtrip efficiency. Equivalent circuit models are derived for both cells and implemented in SimSES. For the 4.8 Ah cylindrical cell, a physicochemical aging model is developed which captures the nonlinear aging behavior that is observed in the associated small-scale aging study. The model includes the aging mechanisms of SEI growth, both continuous over time and accelerated from anode expansion, lithium plating, and LAM induced from particle stress on both anode and cathode. LLI from lithium that is trapped in lost active material is also modelled on both electrodes. The aging model builds on top of a previously parameterized P2D model of the cylindrical cell. While most parameters of the aging model are physics-inspired and taken from the literature, the remaining parameters are determined based on a small-scale aging study. Notably, the aging study shows that lithium-ion cells can transition back out of the nonlinear aging phase towards a significantly reduced aging rate through adapted operating conditions, namely a reduced charging rate and operating voltage window. The physicochemical aging model is implemented in the open-source software PyBaMM [200] and an interface from SimSES to PyBaMM is developed to investigate the nonlinear aging behavior for the two exemplary stationary applications. The interface includes an SOC estimator for the P2D model, which estimates the SOC based on the anode stoichiometry. Furthermore, the interface conducts regular virtual checkup capacity tests to determine the SOH of the physicochemical battery and aging model. The entire simulation toolchain used for the case study is available open-source[4] [201].

In the first part of the case study, the performance of the 4.8 Ah cylindrical cell is compared to the 94 Ah prismatic cell at different, but static SOH values, using the equivalent circuit models in SimSES. The results show that the profit generated in the energy arbitrage application is more affected by the reduced SOH than in the self-consumption increase application. Furthermore, the 94 Ah prismatic cell has a higher profit potential in both applications over all SOH ranges than the 4.8 Ah cylindrical cell. However, this difference is more pronounced for the energy arbitrage application as well. For example, in the energy arbitrage application, at 100 % SOH, the profit potential of the cylindrical cell is 5.2 % lower and at 60 % SOH 10.3 % lower than the profit potential of the prismatic cell. For the self-consumption increase application, these differences in profit potential between the two cells are only 0.6 % at 100 % SOH and 0.7 % at 60 % SOH.

The second part of the case study presents the simulation results with the novel physicochemical aging model and the SimSES to PyBaMM link. The results show that the battery cells enter the nonlinear aging phase significantly earlier when they are used in the energy arbitrage application compared to the self-consumption increase application. While the self-consumption increase application comes with a faster initial capacity fade due to accelerated SEI growth at high SOC ranges, the higher charge rates in the energy arbitrage application lead to an earlier onset of lithium plating and thereby earlier nonlinear aging. However, by reducing charge rate and operating voltage window below 80 % SOH, the onset of nonlinear aging is delayed, the lifetime is significantly prolonged, and the obtainable NPV over the investigated ten-year timeframe in the energy arbitrage application increases by 39.8 %.

To conclude, the comparison of the two cell types highlights the performance differences between EV cells, which are often envisioned for stationary second-life applications, and BESS cells, which are specifically intended for stationary applications. While the differences in profit potential are marginal for the self-consumption increase application, they are noticeable for the energy arbitrage application and should be considered when selecting cells for a BESS.

Furthermore, the physicochemical aging model with its link to SimSES allows to model the nonlinear aging phase in different stationary applications. The case study that was performed with the physicochemical aging model highlights the benefit of considering and delaying nonlinear aging as part of a holistic aging aware operation strategy for BESSs.

CRediT author statement:

- **Nils Collath:** Conceptualization, Investigation, Formal analysis, Methodology, Project administration, Software, Visualization, Writing - original draft, Writing - review & editing
- **Henry Winner:** Investigation, Writing - original draft, Writing - review & editing
- **Alexander Frank:** Investigation, Writing - original draft, Writing - review & editing
- **Axel Durdel:** Investigation, Writing - original draft, Writing - review & editing
- **Andreas Jossen:** Funding acquisition, Supervision, Writing - review & editing

---

[4] The code and configuration files that were used to generate the results are publicly available: https://gitlab.lrz.de/open-ees-ses/late-life-bess-toolchain

Suitability of late-life lithium-ion cells for battery energy storage systems

Nils Collath, Henry Winner, Alexander Frank, Axel Durdel, Andreas Jossen

Journal of Energy Storage 87, p. 111508, 2024

Permanent weblink:
https://doi.org/10.1016/j.est.2024.111508

Journal of Energy Storage 87 (2024) 111508

Contents lists available at ScienceDirect

Journal of Energy Storage

journal homepage: www.elsevier.com/locate/est

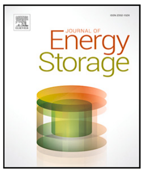

Research papers

Suitability of late-life lithium-ion cells for battery energy storage systems

Nils Collath *, Henry Winner, Alexander Frank, Axel Durdel, Andreas Jossen

Technical University of Munich, TUM School of Engineering and Design, Department of Energy and Process Engineering, Chair of Electrical Energy Storage Technology, Arcisstr. 21, 80333 Munich, Germany

ARTICLE INFO

Keywords:
Physicochemical aging model
Nonlinear aging
Lithium plating
Degradation model
Energy arbitrage
Home storage system

ABSTRACT

The globally installed capacity of battery energy storage systems (BESSs) has increased steadily in recent years. Lithium-ion cells have become the predominant technology for BESSs due to their decreasing cost, increasing cycle life, and high efficiency. However, the cells are subject to degradation due to a multitude of cell internal aging mechanisms, which result in reduced capacity, efficiency, and usable nominal power range over a BESS life cycle. Towards their end-of-life, the cells often show a steep increase in their degradation rate, called nonlinear aging. This work investigates how these "late-life" lithium-ion cells perform in typical BESS applications. We show how decreased capacity, efficiency, and nominal power range impact the profitability of a home storage system for self-consumption increase (SCI) and a large-scale storage system for energy arbitrage (EA). A physicochemical aging model, which accounts for lithium-plating-induced nonlinear aging, is developed and parameterized based on an experimental cell aging study. The aging study and model show that cells that have entered the nonlinear aging phase can transition back to a significantly reduced degradation rate through adapted operating conditions, namely a reduced charging rate and operating voltage window. The case study highlights that the battery cells enter the nonlinear aging phase significantly earlier when used for the EA application compared to the SCI application. However, by adapting the operating conditions below 80% state of health, the obtainable net present value over the investigated ten-year timeframe in the EA application increases by 39.8%, and the lifetime is significantly prolonged.

1. Introduction

Stationary battery energy storage systems (BESSs) are used for a variety of applications. In behind-the-meter applications such as peak shaving or as home storage systems, they create cost savings for the operator. In front-of-the-meter applications such as frequency containment reserve or energy arbitrage, they generate revenue on the respective electricity markets, or support existing transmission lines and allow deferring lengthy grid reinforcement if operated directly by a grid operator. Lastly, in off-grid and microgrid settings, a BESS combined with renewable energy sources can be a cost-competitive option over relying solely on diesel generators [1]. Following recent years' cost reductions and technological advances, lithium-ion cells are now the most frequently used battery technology for new BESS installations [2,3]. Nevertheless, lithium-ion cells are subject to degradation due to a multitude of cell-internal aging mechanisms, with multiple reviews being available specifically on this topic [4–6].

The globally installed capacity of BESSs has been increasing steadily [7]. In the data collected by Figgener et al. the oldest lithium-ion based BESSs registered in Germany date back to 2012 [3,8]. At the same time, stationary applications have long been envisioned as a potential second-use scenario for retired electric vehicle (EV) batteries [9,10]. This highlights that a large amount of "late-life" lithium-ion cells will be operated in stationary energy storage applications in the already existing, growing, and aging fleet of BESSs, likely amended by second-life EV batteries.

Aging mechanisms for lithium-ion cells are often grouped based on their effect on core components of the cell into the degradation modes loss of lithium inventory (LLI), loss of active material on the negative electrode (LAM_{NE}), and loss of active material on the positive electrode (LAM_{PE}) [11]. Throughout the course of a cell's life cycle, the dominant aging mechanisms that cause these degradation modes change [12]: During cell production, an initial solid electrolyte interphase (SEI) is formed on the anode surface, which passivates the electrode but also leads to LLI [12]. In the main operation phase, this SEI keeps growing and consumes more lithium [12]. Particle cracking and graphite exfoliation on the anode lead to LAM_{NE}, which also exposes additional anode surface area for further SEI growth [12]. Particle cracking, transition metal dissolution, and structural dissolution cause LAM_{PE} on the cathode [12]. Further mechanisms, such as the growth of a passivating layer

---

* Corresponding author.
E-mail address: nils.collath@tum.de (N. Collath).

https://doi.org/10.1016/j.est.2024.111508
Received 3 January 2024; Received in revised form 14 March 2024; Accepted 26 March 2024

Abbreviations

BESS	Battery energy storage system
C_{rate}	Charge-discharge rate
CC	Constant current
CP	Constant power
CV	Constant voltage
DMA	Degradation mode analysis
DOC	Depth of cycle
EA	Energy arbitrage
EC	Ethylene dicarbonate
EOL	End-of-life
EV	Electric vehicle
FEC	Full equivalent cycle
LAM	Loss of active material
LAM_{NE}	Loss of active material on the negative electrode
LAM_{PE}	Loss of active material on the positive electrode
LFP	Lithium iron phosphate oxide
LLI	Loss of lithium inventory
MPC	Model predictive control
MRE	Mean relative error
NMC	Lithium nickel manganese cobalt oxide
NPV	Net present value
OCV	Open-circuit voltage
P2D	Pseudo-two-dimensional
PV	Photovoltaic
PyBaMM	Python Battery Mathematical Modelling
RMSE	Root-mean-square error
SCI	Self-consumption increase
SEI	Solid electrolyte interphase
SimSES	Simulation Tool for Stationary Energy Storage Systems
SOC	State of charge
SOH	State of health

General parameters

I	Cell current, A
i	Interest rate, –
n	Fractional years, –
$p_{\mathrm{BESS,target}}$	Charge power target of the BESS, W
p_{load}	Household load, W
$p_{\mathrm{loss,hyst}}$	Cell hysteresis losses, W
$p_{\mathrm{loss,R}}$	Cell resistance losses, W
p_{pv}	Generated PV power, W
$\mathbb{P}_t$	Profit gained in the respective application in timestep t, EUR
R_{i}	Cell resistance, Ω
T	Cell temperature, K
U_{hyst}	Cell hysteresis voltage, V
U_{max}	Charge cut-off voltage, V
U_{min}	Discharge cut-off voltage, V
U_{OCV}	Cell open-circuit voltage, V
U_{T}	Cell terminal voltage, V

Optimization – constants

η_{eff}	Charge and discharge efficiency of the BESS assumed for the optimization model, –
c^{penalty}	Penalty cost, EUR / kW h
c_t^{id}	Electricity price on the intraday electricity market in timestep t, EUR / kW h
E^{batt}	Remaining rated energy after accounting for degradation, kW h
$P^{\mathrm{AC,max}}$	Maximum charge and discharge power of the BESS, kW
$\mathrm{SOC}^{\mathrm{start}}$	SOC at the beginning of the optimization horizon, –
Δt	Optimization timestep length, h

Optimization – index sets

T	Index set of timesteps for the current optimization horizon with $t \in T$

Optimization – decision variables

p_t^{ch}	Charge power of the BESS in timestep t, kW
p_t^{dis}	Discharge power of the BESS in timestep t, kW
soc_t	BESS state of charge at timestep t, –

Physicochemical model – symbols

α	Charge transfer coefficient, –
β_{brug}	Bruggeman coefficient, –
β	LAM constant proportional term, $\mathrm{s^{-1}}$
c	Concentration, $\mathrm{mol\,m^{-3}}$
χ	Stoichiometry, –
D	Diffusivity, $\mathrm{m^2\,s^{-1}}$
$\frac{d\ln f_{\pm}}{d\ln c_1(x,t)}$	Activity, –
E	Young's modulus, Pa
E_{eq}	Equilibrium potential, V
ε	Volume fraction, –
η	Overpotential, V
$\mathcal{F}$	Faraday's constant, 96,485 $\mathrm{A\,s\,mol^{-1}}$
f_{exp}	Graphite expansion gradient, –
$\gamma_{\mathrm{pl,1}}$	Plating tangens hyperbolicus stretch, $\mathrm{V^{-1}}$
$\gamma_{\mathrm{pl,2}}$	Plating tangens hyperbolicus shift, V
γ_{SEI}	SEI on cracks scaling factor, –
i	Current density, $\mathrm{A\,m^{-2}}$
i_0	Exchange current density, $\mathrm{A\,m^{-2}}$
$i_{\mathrm{pl,0}}$	Plating exchange current density, $\mathrm{A\,m^{-2}}$
j_n	Pore-wall flux, $\mathrm{mol\,m^{-2}\,s^{-1}}$
k	Reaction rate constant, $\mathrm{m\,s^{-1}}$
k_{SEI}	SEI kinetic rate constant, $\mathrm{m\,s^{-1}}$
κ	Conductivity, $\mathrm{S\,m^{-1}}$
L	Through-plane thickness, m
m	LAM constant exponential term, –
Ω	Partial molar volume, $\mathrm{m^3\,mol^{-1}}$
φ	Electrical potential, V
r	r-axis or r-dimension (pseudo-dimension), m
$\mathcal{R}$	Universal gas constant, 8.314 $\mathrm{J\,mol^{-1}\,K^{-1}}$
R_{p}	Particle radius, m
R_{SEI}	SEI resistivity, Ω m
σ_{h}	Hydrostatic particle stress, Pa
σ_{yield}	Yield strength, Pa
T	Temperature, K
t	Time, s

t_{+}^{0}	Transference number, –
U_{SEI}	SEI open-circuit potential, V
ν	Poisson's ratio, –
x	x-axis or x-dimension, m
$z_{\mathrm{Li-SEI}}$	Ratio of lithium moles to SEI moles, –

Physicochemical model – subscripts and superscripts

a	Anodic
AM	Active material
app	Applied
c	Cathodic
EC	Ethylene carbonate
eff	Effective
l	Liquid phase
max	Maximum
pl	Plating
ref	Reference
s	Solid phase
SEI	Solid electrolyte interface
surf	Surface
tot	Total

on the cathode or interactions between individual mechanisms, may lead to additional degradation [6]. Towards the end of their life cycle, lithium-ion cells often show a steep increase in the degradation rate, referred to as an aging knee or nonlinear aging. Possible mechanisms for this behavior include lithium-plating and electrolyte depletion, with a review on this topic available by Attia et al. [13].

From a system perspective, these aging mechanisms reduce efficiency and available capacity [14,15]. This, in turn, has a negative impact on the economic viability of a BESS, i.e., the cost-savings or generated revenue from the intended application [16]. In addition, the end-of-life of a BESS is often assumed to be around the point of 70% [17] or 80% [18–20] remaining capacity, since past this point, the before-mentioned nonlinear aging is often observed [13,21]. Many manufacturers offer warranties covering their batteries until this range of remaining capacity [22].

In this work, a performance comparison and profit potential assessment of lithium-ion cells at different state of health (SOH) values are performed for the two stationary applications of energy arbitrage (EA) with a large-scale storage system and self-consumption increase (SCI) with a home-storage system. In addition, a physicochemical aging model is developed and parameterized to describe the nonlinear aging behavior of lithium-ion cells in these stationary applications and, for the first time, show that adapting the operating conditions towards the end-of-life (EOL) can delay the onset of nonlinear aging and significantly increase the profitability of BESSs.

1.1. Literature review

Battery degradation and its effects have been modeled in multiple publications that relate to the techno-economic assessment of BESSs. The degradation models used for that purpose can be categorized into empirical, semi-empirical, and physicochemical models [12]. Empirical degradation models are fit to cell aging data without inherent modeling of the underlying aging mechanisms. Semi-empirical models rely on physics-inspired equations, such as the Arrhenius and Tafel equation for fitting the model to cell aging data. Lastly, physicochemical models typically consist of sets of differential equations that aim to describe the internal processes of the cell in addition to its external behavior.

Uddin et al. for example, investigated the techno-economic viability of home storage systems in the United Kingdom using an empirical degradation model [15]. Casals et al. used an empirical degradation model to estimate the remaining lifetimes of BESSs in different second-life applications [9]. Next to techno-economic assessments, a significant body of literature can be found on the aging aware operation of BESSs, with a recent review available on this topic [12]. The degradation models used for that purpose are also usually empirical, e.g., in [23–25], or semi-empirical models, e.g., in [26–28].

The prevalent empirical and semi-empirical degradation modeling approaches do not consider the changing dominant aging mechanisms that lead to the nonlinear aging phase with its increased degradation rate, which is especially of concern for late-life lithium-ion cells. The challenge of creating an empirical or semi-empirical model for the nonlinear aging phase is twofold: First, even cells of the same type show variance in terms of the onset point of nonlinear aging [29], which further depends on the operating conditions [30]. Second, to get to the nonlinear aging phase, extended prior cycling of the cells is required. Both effects combined would result in large test matrices and long experiments to generate a statistically relevant empirical or semi-empirical degradation model that describes nonlinear aging.

A possible solution for accounting for the nonlinear aging phase is to use physicochemical models which model the underlying aging mechanisms that lead to nonlinear aging. Attia et al. identified multiple "pathways" that can lead to nonlinear aging behavior in their review [13]: lithium plating, electrolyte and additive depletion, mechanical deformation, electrode saturation, percolation-limited connectivity, and resistance growth. While identified as individual pathways, electrolyte and additive depletion, mechanical deformation, and electrode saturation may also lead to lithium plating as a consequence [13]. Multiple models can be found in the existing literature that describe lithium plating over a cell's lifetime [21,31,32]. Yang et al. proposed a model that includes SEI growth and lithium-plating to describe nonlinear capacity fade towards the EOL [31]. Atalay et al. used a similar approach with SEI growth and lithium plating to describe the nonlinear capacity fade but with a multi-layer SEI model [32]. Keil et al.'s physicochemical aging model encompasses SEI formation, SEI re-formation resulting from particle cracking, as well as both lithium plating and lithium stripping [21]. All three of the above aging models use the pseudo-two-dimensional (P2D) Newman model [33,34] as a basis. Kindermann et al. proposed a model that follows the electrode saturation pathway, in which $\mathrm{LAM_{PE}}$ from cathode dissolution [35] outpaces the SEI-induced LLI after extended cycling. Fang et al. provided a model for the electrolyte depletion pathway, in which local electrolyte dry-out causes a positive feedback loop of $\mathrm{LAM_{NE}}$ [36]. The degradation mode analysis of the later presented experimental study shows significantly more LLI than $\mathrm{LAM_{PE}}$ and $\mathrm{LAM_{NE}}$ after the onset of nonlinear aging, as the following subsection will highlight. Therefore, lithium plating is assumed to be the main mechanism leading to nonlinear aging in this contribution.

The physicochemical aging model, as part of the larger open-source simulation toolchain presented in this work, for the first time, allows the investigation of lithium-plating induced nonlinear aging in typical BESS applications.

In addition to modeling nonlinear aging, multiple publications include experimental studies that investigate nonlinear aging at different operating conditions.

The operating voltage window has been investigated in multiple variations in the existing literature as a stress factor for nonlinear aging: For the lithium nickel manganese cobalt oxide (NMC) cells investigated by Schuster et al. a narrower operating voltage window ($\Delta 1.2\,\mathrm{V}$ instead of $\Delta 1.3\,\mathrm{V}$) led to more full equivalent cycles (FECs) being completed before the onset of nonlinear aging and the nonlinear aging phase starting at lower remaining capacity values [30]. Similarly, the NMC cells investigated by Ecker et al. showed later or no onset of nonlinear aging for shallower depth of cycle (DOC) ranges [37]. Cells cycled at 50% DOC exhibited nonlinear aging, while cells cycled at 20%

DOC did not [37]. In a study by Ma et al. varying the charge cut-off voltage of NMC cells between 4.1 V, 4.2 V, and 4.3 V impacted the onset of nonlinear aging as well. The cells with a lower cut-off voltage exhibited the transition to nonlinear aging later or not at all [38]. Further studies confirm that a smaller operating voltage window tends to be beneficial for delaying nonlinear aging for NMC [39,40] and lithium iron phosphate oxide (LFP) cells [41,42].

Another operating condition that has been studied as a stress factor for accelerating nonlinear aging is the charge rate. Schuster et al. showed that changing the charge rate from 1C to C/2 can extend the area of linear aging. A reduction to C/5 even resulted in no nonlinear aging behavior [30]. Other studies for NMC [43,44] and LFP [45,46] cells confirm that lower charge rates generally delay the onset of nonlinear aging. The mentioned publications attribute this behavior to increased lithium plating at high charge rates.

Besides the charge rate, the discharge rate has also been studied as an influencing factor of nonlinear aging, with inconsistent conclusions in the existing literature. Schuster et al. changed the discharge rate from 1C to C/2 and observed no significant impact on battery lifetime [30]. Keil et al. [44] and Atalay et al. [32] showed that an increased discharge rate could delay the onset of nonlinear aging. On the other hand, Omar et al. observed earlier nonlinear aging with higher discharge rates [47].

The operating conditions in the aforementioned aging studies are different between sets of cells but constant for each set of cells throughout the respective studies. In his dissertation, Schuster investigated a change in operating conditions after the onset of nonlinear aging [48]. The voltage window, charge rate, and discharge rate were reduced past this point. It was concluded that the resulting capacity fade, while not as steeply nonlinear as before this adaption of operating conditions, is still more rapid than before the onset of nonlinear aging [48, Figure 31]. To the authors' knowledge, no further studies investigate how adapting the operating conditions during an aging study affects nonlinear aging.

In this work, it is shown for the first time that by adapting the operating condition, the lithium-ion cells can transition to a significantly reduced degradation rate. The case study with the developed physicochemical aging model further shows that these adapted operating conditions can lead to significantly increased profitability when implemented on a BESS.

1.2. Structure and main contributions

In Section 2, we first describe the investigated two stationary applications and the simulation tool that is used for modeling the BESS. Following that, we present the results of the cell characterization study from which equivalent circuit models are derived for a 4.8 Ah cylindrical cell, primarily intended for EV applications, and a 94 Ah prismatic cell, which is used for BESS applications and serves as a reference scenario in the latter case study. We further present the aging study, physicochemical aging model, and its parameterization for the 4.8 Ah cylindrical cell and show that the cells can transition back out of nonlinear aging by adapting the operating conditions. Section 3 presents the techno-economic simulation results with the full simulation framework, including the profit potential of both cells at different SOH values in the two stationary applications as well the aging behavior and achievable net present value (NPV) over the full lifetime with the cylindrical cell. We summarize our main contributions as follows:

- Performance comparison and evaluation of the profit potential of late-life lithium-ion cells at different SOH for a reference BESS cell and EV cell in two stationary applications.
- Development and parameterization of a physicochemical aging model that includes lithium-plating induced nonlinear aging towards the end-of-life.
- Experimental results supported by the physicochemical aging model show how lithium-ion cells can transition back out of the nonlinear aging phase through adapted operating conditions.
- Investigation of the nonlinear aging behavior and the achievable lifetime NPV in different stationary applications.
- Open-source availability of the entire simulation toolchain.

2. Methodology and model parameterization

Fig. 1 provides an overview of the methodology used in this work. For modeling the BESS with all relevant components, we use our in-house developed and open source Simulation Tool for Stationary Energy Storage Systems (SimSES) [49], which allows to conduct time series based simulations for stationary energy storage systems. Section 2.1 briefly describes the two investigated stationary applications, i.e., a home storage system used for SCI and a large-scale BESS used to perform EA on the intraday electricity market. To investigate the profit potential of late-life lithium-ion cells at different SOH values and to compare the performance of the cylindrical cell to the prismatic cell, equivalent circuit models are added to SimSES based on electrical parameterization as described in Section 2.2 for both cells. To investigate the aging behavior over time and the lifetime NPV in the two stationary applications, a physicochemical aging model is developed and parameterized based on a cell aging study, as described in Section 2.3 for the cylindrical cell. The physicochemical cell and aging model is implemented in the open source tool Python Battery Mathematical Modelling (PyBaMM) [50] and an interface that links the two simulation tools, SimSES and PyBaMM, is developed in this work.

2.1. Applications

The key parameters of the two stationary applications, SCI with a home storage system and EA with a large-scale BESS, are summarized in Table 1.

Germany is Europe's largest market for home-storage systems [52] and serves as a basis for modeling this application. The system power rating for the home storage application is set to 5.3 kW and the energy rating to 8.8 kWh, which is the mean system size of home storage systems installed in Germany in the year 2022 [53]. The operation strategy is a "greedy" self-consumption increase strategy, in which the BESS charges until it is fully charged if the generated photovoltaic (PV) power p_{pv} exceeds the household load p_{load} and discharges until it is fully discharged if the household load exceeds the generated PV power. The charge power target of the BESS $p_{\mathrm{BESS,target}}$ for each timestep therefore is the difference between both:

$$p_{\mathrm{BESS,target}} = p_{\mathrm{PV}} - p_{\mathrm{load}} \tag{1}$$

This application and the resulting charge–discharge profile for a representative BESS have been described in detail by Kucevic et al. [54]. For the PV generation profile, a one-year time-series measured in Munich is used [54] and the household load time-series is taken from [55]. The profit in this application is calculated from the yearly electricity cost of the household with a BESS subtracted by the electricity cost of the same household without a BESS. The cost for electricity consumed from the grid is set to 38.57 ct/kWh, based on the average electricity cost in Germany in 2022 [56]. PV generated electricity that is fed into the grid by the household is remunerated with the applicable feed-in tariff of 6.83 ct/kWh for PV systems constructed in January 2022 [57].

The large-scale BESS for EA is also sized based on average values for Germany. In 2022, 467 MWh and 434 MW of large-scale BESSs were installed in Germany, according to data by Figgener et al. [53]. Since the scale of individual installations varies widely, we assume a representative BESS with 1 MW rated power and 1.076 MWh storage capacity-based on the average power-to-energy ratio of the systems installed in 2022 [53]. Profit is generated through arbitrage trading on the European intraday continuous electricity market. The data basis

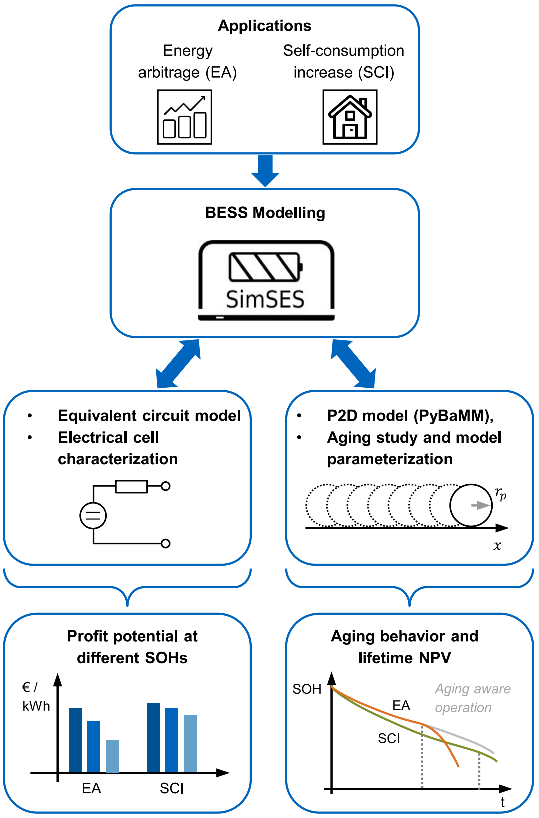

Fig. 1. Overview of the methodology used in this work. The simulation toolchain is available open-source [51].

Table 1
Key parameters of the two applications modeled in this work.

System	Large-scale BESS - EA	Home storage system - SCI
Storage capacity	1.076 MW h	8.8 kW h
Rated power	1.0 MW	5.3 kW
AC/DC conv.	Notton [58]	Notton [58]
Application	Energy arbitrage (EPEX intraday continuous)	Self-consumption increase
Operation strategy	Linear program with model predictive control framework [59]	“Greedy” charge–discharge logic
Profiles (1 year)	ID-1 electricity price for 2022 [60]	PV profile [54] with 9.05 $\mathrm{kW_P}$, household load profile (profile 28 in [55]) with 5.047 MWh yearly consumption
Price data	See profiles	Electricity price: 38.57 ct/kWh [56], PV feed-in tariff: 6.83 ct/kWh [57]
Battery cells	I. 4.8 Ah cylindrical 21 700, presumably NMC/silicon-graphite; II. 94 Ah prismatic, presumably NMC/graphite (as reference)	

for this application is the price time-series of the ID-1 index for 15 min contracts on the largest European electricity exchange, the EPEX Spot, for the year 2022 [60]. The ID-1 index is the weighted price average of all trades executed within 1 h before delivery [61].

For the operation strategy, we use the model predictive control (MPC) framework that was introduced and described in detail in our previous work [28,59]. An optimization model is solved every 1 h of the simulation period, with the assumption of perfect foresight of the ID-1 price (15 min time-resolution) for the next 12 h. Following that, the optimized charge–discharge schedule is simulated in SimSES for the next 1 h and the relevant MPC variables (new simulated SOH and SOC) are passed to the optimization model, which is then called again to determine the next charge–discharge-schedule. The base optimization model from our previous work is used, which does not explicitly consider any aging stress factors other than the number of FECs [28] through the penalty cost c^{penalty}:

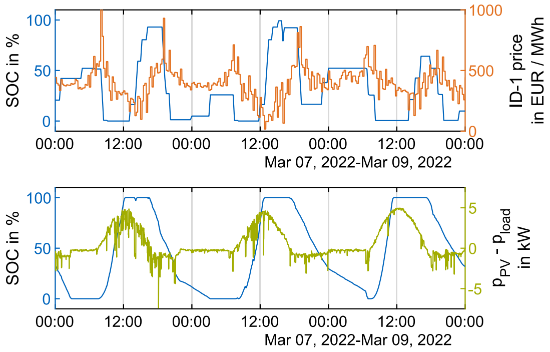

Fig. 2. Battery SOC over three exemplary days for energy arbitrage with the ID-1 electricity price (top) and self-consumption increase with the difference between PV generation and household load (bottom).

$$\max \sum_{t\in T} \left(\Delta t (p_t^{\text{dis}} - p_t^{\text{ch}}) \cdot c_t^{\text{id}} - \Delta t (p_t^{\text{ch}} + p_t^{\text{dis}}) \cdot c^{\text{penalty}} \right) \tag{2}$$

The first part of the equation is the profit generated on the intraday market. Here, p_t^{dis} and p_t^{ch} are the discharged and charged power of the BESS and c_t^{id} the electricity price on the intraday electricity market at time $t \in T$, with T being the index set of timesteps in the optimization horizon. Δt is the time resolution of the price profile, i.e., 15 min. The penalty cost c^{penalty} ensures that only sufficiently profitable arbitrage opportunities are part of the optimal solution, thereby preventing a premature EOL of the BESS from excessive cycling and aging. As a reference, we set the penalty cost to $c^{\text{penalty}} = 0.09375$ EUR/kWh, which yielded the optimal result in our previous work for the energy arbitrage application with 2022 price data and the same optimization model [28]. In addition to the objective function, the constraints below ensure energy conservation and provide upper and lower limits for the three sets of continuous decision variables, p_t^{dis}, p_t^{ch}, and soc_t with $t \in T$:

$$soc_t = soc_{t-1} + \frac{\Delta t}{E^{\text{batt}}} \cdot (p_t^{\text{ch}} \eta_{\text{eff}} - \frac{1}{\eta_{\text{eff}}} p_t^{\text{dis}}) \quad \forall\, t \in T \backslash \{0\} \tag{3}$$

$$soc_{t=0} = \text{SOC}^{\text{start}} + \frac{\Delta t}{E^{\text{batt}}} \cdot (p_{t=0}^{\text{ch}} \eta_{\text{eff}} - \frac{1}{\eta_{\text{eff}}} p_{t=0}^{\text{dis}}) \tag{4}$$

$$0 \le p_t^{\text{dis}} \le P^{\text{AC,max}} \quad \forall\, t \in T \tag{5}$$

$$0 \le p_t^{\text{ch}} \le P^{\text{AC,max}} \quad \forall\, t \in T \tag{6}$$

$$0 \le soc_t \le 1 \quad \forall\, t \in T \tag{7}$$

$\text{SOC}^{\text{start}}$ and E^{batt} are the SOC at the beginning of the optimization horizon and the remaining rated energy of the BESS after accounting for degradation. $P^{\text{AC,max}}$ is the maximum charge and discharge power of 1 MW and soc_t is the state of charge of the BESS at each time step. η_{eff} is the charge and discharge efficiency, which is assumed constant and symmetrical ($\eta_{\text{eff}} = 0.9$) in the optimization model but variable and modeled in detail with converter and battery cell models in SimSES as part of the here used MPC approach [28].

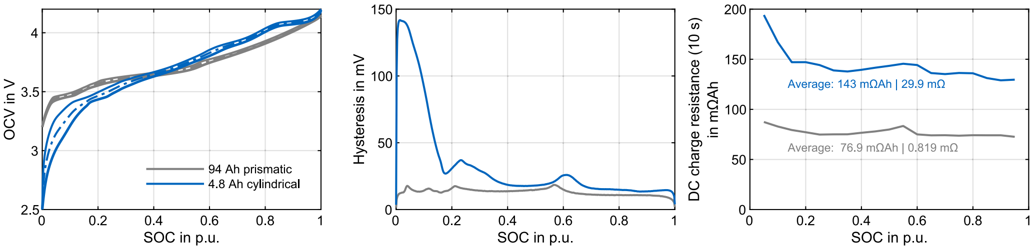

Fig. 3. Measured open-circuit voltage (OCV), hysteresis behavior, and charge resistance of the 94 Ah prismatic cell (used for BESS applications) and the 4.8 Ah cylindrical cell (primarily intended for EV applications) at 25 °C. For the OCV, the measured voltage in charge direction (top solid line), discharge direction (bottom solid line), and average (middle dashed-dotted line) are shown. The hysteresis is calculated as the difference between the charge and discharge OCV curves. The charge resistance is shown normalized by the nominal cell capacities.

Fig. 2 shows the resulting SOC for three exemplary days for the two applications. The battery cell models are described in the following subsections.

2.2. Electrical cell characterization and equivalent circuit model

Two commercial lithium-ion cell types are electrically characterized and equivalent circuit models are derived in this subsection as a foundation for the case study in Section 3.1. The first cell is a cylindrical battery cell with a nominal capacity of 4.8 Ah, presumably with an NMC cathode and a silicon-graphite anode, which is primarily intended for EV applications. EV cells may be removed from their primary application after extended operation time and then used in stationary second-life applications, in varying conditions and at different SOHs. However, one might alternatively consider purchasing a battery cell specifically intended for stationary applications instead of a second-life EV cell. For that purpose, we compare the first cell with a commercial prismatic cell with a nominal capacity of 94 Ah, an NMC cathode and presumably a pure graphite anode that is known to be used in multiple existing large-scale BESS installations.

In Fig. 3, key characteristics of the two cell types are compared with the detailed testing conditions described in Appendix A.1. The cylindrical cells show a significantly larger hysteresis behavior, especially in low SOC ranges, which is expected for the silicon-graphite anode material [62]. In addition, the OCV of the cylindrical cell is higher and flatter for high SOC values. The absolute resistance of the cylindrical cells (29.9 mΩ average over the measured SOC range) is expectedly higher than for the larger, prismatic cell (0.819 mΩ). For a valid comparison, the measured resistance values are multiplied by the nominal cell capacity. Normalized by multiplying with the nominal cell capacity, the resistance of the cylindrical cell (143 mΩ A h), is significantly larger than it is for the prismatic cell as well (76.9 mΩ A h).

These characteristics translate into performance differences, which are relevant from a system perspective and displayed in Fig. 4 with the detailed testing conditions described in Appendix A.2. The larger cell resistance and larger internal resistance translate into lower energy efficiency, as seen in the top of Fig. 4. While the energy efficiency of the cylindrical cell is already lower at low C-rates due to its stronger hysteresis behavior, the differences become even more pronounced at higher C-rates due to the additional larger cell resistance. This would lead to higher energy losses and costs for the BESS operator.

The control signal in most stationary applications is a power target for the BESS, which is determined by the operation strategy and then passed by the energy management system to the converters, which control the power flow to and from the upstream AC-grid. Therefore, the power capability of a lithium-ion cell is of relevance in terms of which BESS applications it is suited for.

As seen in the bottom of Fig. 4, the higher OCV for high SOC ranges of the cylindrical cell, combined with its larger internal resistance, translate to a reduced power capability, especially in charge direction.

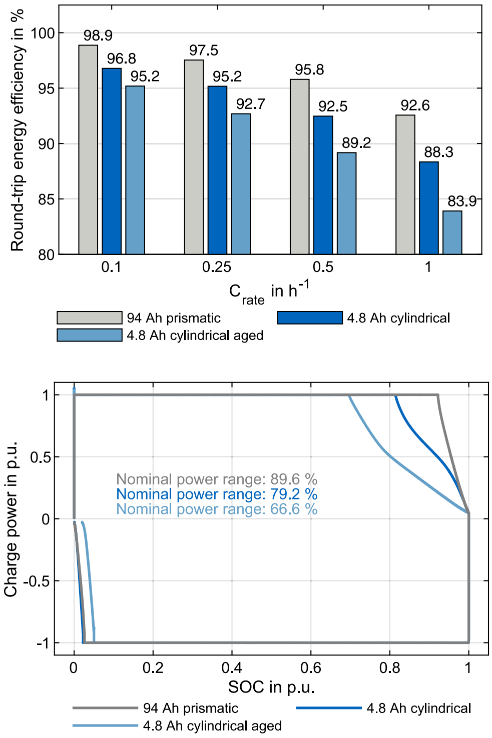

Fig. 4. Measured round-trip energy efficiency (top) from a CC charge followed by a CC discharge at different C-rates (C_{rate}). Nominal power range (bottom) from a CPCV charge followed by a CPCV discharge with charge power stated in per unit of the nominal charge power, i.e., 345.9 W for the prismatic and 17.472 W for the cylindrical cell. Both at 25 °C.

Here, the cells were charged with a CPCV-charge protocol, followed by a CPCV-discharge protocol. The target power for the constant power charge and discharge phases was set to the respective nominal power of the cells, i.e., the nominal capacity multiplied by the nominal voltage; 345.9 W for the prismatic and 17.472 W for the cylindrical cell. Based on this test, we calculate the *nominal power range* of the cells as the percentage of the SOC range, in which the cells can deliver their nominal power in both charge and discharge direction. This nominal power range is significantly higher for the prismatic cell (89.6%) than for the cylindrical cell (79.2%).

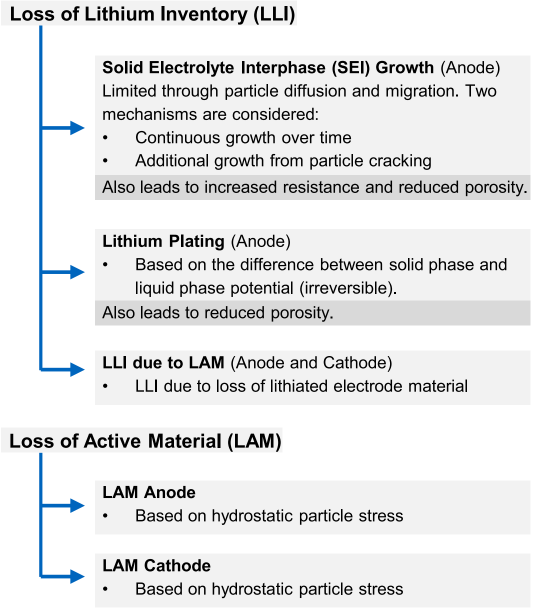

Fig. 5. Considered aging mechanisms in the physicochemical aging model grouped by the resulting degradation modes. While the LAM models were readily available in PyBaMM and only the parameterization was changed, the lithium plating and SEI growth models were adapted to the proposed modeling approach of this work.

In addition to the results with the previously uncycled cylindrical cells, the measured efficiency and nominal power range are also depicted for the 4.8 Ah cylindrical cells that were previously subjected to an accelerated aging study. At the point of the efficiency and nominal power measurements, these cells were subjected to 1200 cycles and had an average remaining discharge capacity of 3.54 Ah, which corresponds to a capacity-based SOH of 73.8%. The details of this aging study are presented in Section 2.3. As shown in Fig. 4, the efficiency of the aged cylindrical cells deteriorates. The energy efficiency is significantly worse than for the new cells, especially at high C-rates. In addition, the nominal power range of the aged cell is reduced to 66.6%.

To investigate how these cell performance differences impact BESS level performance and profitability, equivalent circuit models are derived for both cells and added to SimSES. An extension to the SimSES equivalent circuit model was implemented to account for the hysteresis voltage and the associated energy losses:

$$\begin{aligned} U_{\mathrm{T}} = U_{\mathrm{OCV}}(\mathrm{SOC},T) + I \cdot R_{\mathrm{i}}(\mathrm{SOC},I,T) \\ + \operatorname{sign}(I) \cdot \tfrac{1}{2} U_{\mathrm{hyst}}(\mathrm{SOC},T) \end{aligned} \tag{8}$$

Here, U_{T} is the cell terminal voltage, U_{OCV} the OCV, U_{hyst} the hysteresis voltage, I the cell charge current, R_{i} the cell internal resistance, and T the cell temperature. For U_{OCV}, U_{hyst}, and R_{i}, the measured data from Fig. 3 is used and was added to SimSES. For U_{OCV}, the average of the charge OCV and discharge OCV is used, and for U_{hyst}, the difference of both. For R_{i}, the 10 s DC-charge resistance at the respective SOC is used for $I > 0$, and the 10 s DC-discharge resistance for $I < 0$. Furthermore, the OCV, hysteresis voltage, and internal resistance were all recorded for different temperatures (15 °C, 25 °C, and 35 °C). However, the cell temperature highly depends on the BESS thermal design and the climatic conditions of its location. Therefore, all later simulations will be conducted at an assumed constant cell temperature of 25 °C. While modeling the cell resistance through the 10 s DC resistance is a simplification, this approach has been validated to deliver sufficient accuracy compared to measured BESS efficiency data by Schimpe et al. [63]. This modeling approach results in the following two energy loss components for the BESS on a cell level, with $p_{\mathrm{loss,R}}$ describing the resistance-based losses on a cell level and $p_{\mathrm{loss,hyst}}$ the hysteresis-based losses:

$$p_{\mathrm{loss,R}} = R_{\mathrm{i}}(\mathrm{SOC},I,T) \cdot I^2 \tag{9}$$

$$p_{\mathrm{loss,hyst}} = |I| \cdot \tfrac{1}{2} U_{\mathrm{hyst}}(\mathrm{SOC},T) \tag{10}$$

This modeling approach will be used in the first part of the simulation case study, i.e. Section 3.1, to assess the profit potential of the two cell types in different stationary applications. However, a more complex physicochemical modeling approach is required to model the aging behavior over time and derive the achievable lifetime profit under consideration of nonlinear cell aging.

2.3. *Physicochemical aging model*

The physicochemical aging model that is used in this work builds on top of a P2D model for the 4.8 Ah cylindrical cell. The P2D model that serves as a basis and its parameterization are described in Appendix B. Section 2.3.1 first describes the structure of the physicochemical aging model and the associated equations. The model parameterization, based on a small-scale aging study, is then presented in Section 2.3.2. In Section 2.3.3, we show that past the onset of nonlinear aging, the cells can be transitioned back to a reduced aging rate by adapting the operating conditions, which is supported by the physicochemical aging model as well. Lastly, in Section 2.3.4, the link between the two modeling tools PyBaMM and SimSES is described.

2.3.1. *Aging model description*

Fig. 5 provides an overview of the aging model proposed in this work. It considers the key degradation modes that have been used by multiple authors to summarize the effect of the underlying aging mechanisms on the behavior of a lithium-ion cell: LLI, $\mathrm{LAM_{NE}}$, and $\mathrm{LAM_{PE}}$ [5,11,64]. The aging mechanisms and equations are described in the following.

Loss of active material: During cycling, both the anode and cathode are subject to volume change and mechanical stress due to the intercalation and de-intercalation of lithium in the anode and the reaction of lithium with the transition metal oxide in the cathode [4,6]. This can lead to particle cracking, making part of the active material unavailable, thereby causing $\mathrm{LAM_{NE}}$ and $\mathrm{LAM_{PE}}$ [4,6]. If part of the active material becomes inactive while it is lithiated, the lithium inside becomes trapped, such that the loss of active material leads to LLI as well [6]. On the anode, graphite exfoliation may lead to further $\mathrm{LAM_{NE}}$ [6], and on the cathode transition metal dissolution and structural disordering to further $\mathrm{LAM_{PE}}$ [5]. For this aging model, we focus on the main mechanisms of mechanical stress-induced $\mathrm{LAM_{NE}}$ and $\mathrm{LAM_{PE}}$ and the resulting LLI from lost lithiated active material. The model by Sulzer et al. [65] is used, which is readily available in PyBaMM and is a simplification of the models used by Reniers et al. [66] and Laresgoiti et al. [67]. The model describes the change of the available active material fraction $\varepsilon_{\mathrm{AM}}$ as a function of the hydrostatic particle stress σ_{h}:

$$\frac{\partial \varepsilon_{\mathrm{AM}}(x,t)}{\partial t} = \begin{cases} \beta \left(\frac{\sigma_{\mathrm{h}}(x,t)}{\sigma_{\mathrm{yield}}} \right)^m & , \sigma_{\mathrm{h}} \geq 0 \\ 0 & , \sigma_{\mathrm{h}} < 0 \end{cases} \tag{11}$$

Here, σ_{yield} is the critical yield strength, and β and m are fitting parameters. The hydrostatic stress is then calculated from concentration differences within the particle:

$$\sigma_h = \frac{2\Omega E}{3(1-\nu)} \left(\frac{1}{R_{\mathrm{p}}^3} \int_0^{R_{\mathrm{p}}} c_{\mathrm{s}}(x,r,t) r^2 dr - \frac{c_{\mathrm{s,surf}}(x,t)}{3} \right) \tag{12}$$

$$c_{\mathrm{s,surf}}(x,t) = c_{\mathrm{s}}(x, r = R_{\mathrm{p}}, t) \tag{13}$$

Here, E, ν, and Ω are the material-specific Young's modulus, Poisson's ratio, and partial molar volume for either anode or cathode. $c_{\mathrm{s,surf}}$ is the lithium concentration at the spherical particle surface $r = R_{\mathrm{p}}$. This simplification of the stress model from [66,67] assumes maximum stress at the particle surface and zero stress at the beginning of a cycle [65]. As we will use the model in the later case study for realistic application profiles with frequently changing charge–discharge directions, zero stress at the beginning of a cycle is not a valid assumption. We, therefore, make the further simplification of setting the fitting parameter $m = 1$ to have a linear relationship rather than a polynomial one that would require a cycle-counting algorithm, such as the rainflow algorithm [68], as part of the model. The resulting model is used do describe the loss of active material on both the anode and cathode.

The additional LLI from the loss of active material is already inherently considered as part of Eq. (11), since the lost active material fraction and its lithium concentration will not be available in the following timesteps.

SEI growth: Growth of the SEI on the anode surface has frequently been stated as a key aging mechanism of lithium-ion cells with graphite [4,6] and silicon-graphite blend anodes [69]. The growth of this passivation layer consumes lithium, leading to LLI and an increased cell impedance [4,6]. SEI growth is generally known to progress over time and at an accelerated rate if the cell is stored at high temperatures or SOC [12]. Additionally, cycling the cell has been shown to accelerate it further, as SEI forms at the anode surface area that is newly exposed from particle cracking [12]. Multiple approaches for physicochemical SEI modeling can be found in the existing literature. We use the model from Yang et al. [31] and combine it with a modeling approach by Kindermann et al. [35] to account for additional SEI from particle cracking. The main equation of the basic SEI model is stated below:

$$i_{\mathrm{SEI,b}}(x,t) = -\frac{\mathcal{F} \cdot c_{\mathrm{EC}}}{\frac{1}{k_{\mathrm{SEI}} \cdot \exp\left(\frac{-\alpha_{\mathrm{SEI}} \mathcal{F} \eta_{\mathrm{SEI}}(x,t)}{\mathcal{R} T}\right)} + \frac{L_{\mathrm{SEI}}(x,t)}{D_{\mathrm{EC}}}} \tag{14}$$

Here, $i_{\mathrm{SEI,b}}$ is the interfacial current density of the basic SEI reaction, not yet accounting for particle cracking. $\mathcal{F}$, $\mathcal{R}$, and T are the Faraday constant, ideal gas constant, and the temperature. c_{EC} and D_{EC} are the bulk concentration of ethylene dicarbonate (EC) in the electrolyte and the diffusion constant of EC through existing SEI. These stem from the simplified assumption that the SEI is made solely of lithium ethylene dicarbonate $(\mathrm{CH_2OCO_2LI})_2$, generated by the reaction of EC with Li^+ ions [31]. L_{SEI} is the thickness of the existing SEI, k_{SEI} the SEI kinetic rate constant, and η_{SEI} the driving overpotential of the reaction-limited SEI component. If the left term of the denominator in Eq. (14) is larger, the SEI growth is reaction-limited. If the right term is larger, it is diffusion-limited [65]. η_{SEI} is defined as below:

$$\eta_{\mathrm{SEI}}(x,t) = \varphi_{\mathrm{s}}(x,t) - \varphi_{\mathrm{l}}(x,t) - \mathcal{F} j_n(x,t) R_{\mathrm{SEI}} L_{\mathrm{SEI}}(x,t) - U_{\mathrm{SEI}} \tag{15}$$

j_n is the pore-wall flux, U_{SEI} the equilibrium potential of the SEI formation reaction and R_{SEI} the resistivity of the SEI. To account for accelerated SEI growth from cycling and particle cracking, the approach from Kindermann et al. is utilized, which includes additional SEI growth proportional to the charge–discharge current I and the anode volume expansion [35]. Through that, we derive the following equation for the total SEI growth:

$$i_{\mathrm{SEI}}(x,t) = i_{\mathrm{SEI,b}}(x,t) \cdot \left(1 + \gamma_{\mathrm{SEI}} \cdot \frac{|I(t)|}{I_{\mathrm{C/100}}} \cdot f_{\mathrm{exp}}(x,t)\right) \tag{16}$$

Here, f_{exp} is the gradient of the graphite expansion curve as shown in Fig. 6, $\frac{|I(t)|}{I_{\mathrm{C/100}}}$ scales the cracking to different charge–discharge rates, γ_{SEI} is an empirical fitting factor. i_{SEI} is the total SEI interfacial current density. Thereby, the SEI has one component, primarily driven by time, and one component, driven by time but accelerated through cycling-induced volume expansion. Both components use the same underlying diffusion and reaction-limited SEI model, while the fitting factor γ_{SEI} determines the share of each component. The change of the SEI thickness L_{SEI} is then defined as below:

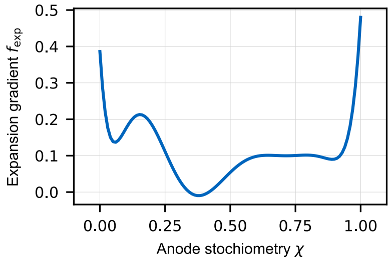

Fig. 6. Expansion gradient f_{exp} for different anode lithiation degrees, derived from [70].

$$\frac{\partial L_{\mathrm{SEI}}(x,t)}{\partial t} = \frac{\Omega_{\mathrm{SEI}} \cdot i_{\mathrm{SEI}}(x,t)}{z_{\mathrm{Li-SEI}} \cdot \mathcal{F}} \tag{17}$$

Here, Ω_{SEI} is the partial molar volume of the SEI and $z_{\mathrm{Li-SEI}}$ is the ratio of lithium to SEI moles with $z_{\mathrm{Li-SEI}} = 2$ for the lithium ethylene dicarbonate reaction.

Lithium plating: As mentioned in Section 1.1, different pathways that can lead to a nonlinear aging trajectory have been defined in the review by Attia et al. many of which can lead to lithium plating eventually [13]. In addition, the degradation mode analysis of our test data for the 4.8 Ah cylindrical cell showed significantly more LLI than $\mathrm{LAM_{PE}}$ and $\mathrm{LAM_{NE}}$ after the onset of nonlinear aging, as the following subsection will highlight. Therefore, lithium plating is assumed as the driving mechanism for the nonlinear aging trajectory, similarly as in the models by Keil et al. [21], Atalay et al. [32], and Yang et al. [31], and modeled as below:

$$\begin{aligned} i_{\mathrm{pl}}(x,t) = &- i_{\mathrm{pl,0}} \exp\left(-\frac{\alpha_{\mathrm{pl}} \mathcal{F} \eta_{\mathrm{pl}}(x,t)}{\mathcal{R} T}\right) \\ &\cdot \frac{\tanh(\gamma_{\mathrm{pl,1}}(\eta_{\mathrm{pl}}(x,t) - \gamma_{\mathrm{pl,2}})) + 1}{2} \end{aligned} \tag{18}$$

$$\eta_{\mathrm{pl}}(x,t) = \varphi_s(x,t) - \varphi_l(x,t) - \mathcal{F} j_n(x,t) R_{\mathrm{SEI}} L_{\mathrm{SEI}}(x,t) \tag{19}$$

$$\frac{\partial L_{\mathrm{pl}}(x,t)}{\partial t} = \frac{\Omega_{\mathrm{pl}} \cdot i_{\mathrm{pl}}(x,t)}{\mathcal{F}} \tag{20}$$

The first part of Eq. (18) is the lithium plating reaction, as described in Yang et al. [31]. As in [31,32], lithium plating is assumed to be irreversible, and stripping of plated lithium is neglected. In Eq. (18), i_{pl} is the current density of the lithium plating reaction, $i_{\mathrm{pl,0}}$ the plating exchange current density, and η_{pl} is the driving overpotential of the plating reaction. By itself, this equation leads to plating already for $\eta_{\mathrm{pl}} > 0$. Therefore, we introduce a hyperbolic tangent to ensure negligible plating below the threshold $\gamma_{\mathrm{pl,2}}$, while the transition width of this term from 0 to 1 is determined by $\gamma_{\mathrm{pl,1}}$. The lithium plating thickness L_{pl} is then calculated as in Eq. (20) with the molar volume of lithium Ω_{pl}.

Lastly, the aging model accounts for the porosity reduction in the anode through the built-up of both the SEI and plated lithium:

$$\varepsilon_{\mathrm{l}}(x,t) = \varepsilon_{\mathrm{l,0}} - \frac{3\varepsilon_{\mathrm{AM}}(x,t)}{R_{\mathrm{p}}} \cdot (L_{\mathrm{SEI}}(x,t) + L_{\mathrm{pl}}(x,t)) \tag{21}$$

Here, ε_{l} is the anode porosity and $\varepsilon_{\mathrm{l,0}}$ the initial anode porosity. The parameterization of the presented physicochemical aging model is described in the following subsection.

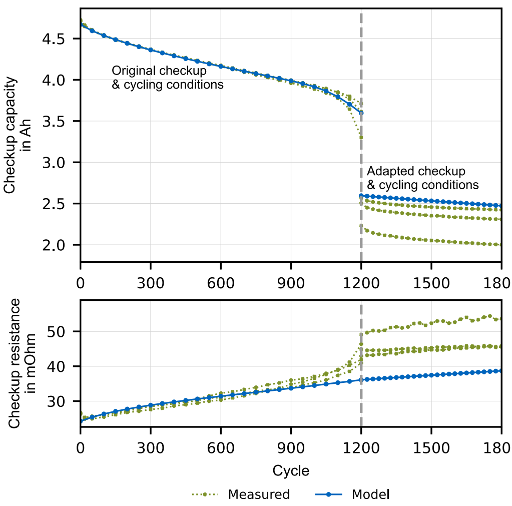

Fig. 7. Checkup capacity (top) and resistance (bottom) during the cell aging study with the 4.8 Ah cylindrical cell. The experimental checkup results for three cells are shown, as well as the checkup results with the physicochemical aging model. After 1200 cycles, the operating conditions were adapted as highlighted in Table 2 to prevent further nonlinear aging.

2.3.2. Aging model parameterization

While the majority of parameters required for the aging model are material-specific, such as Young's modulus E or the partial molar volume Ω, each modeled aging mechanism includes a limited amount of parameters that have to be empirically determined based on cell aging studies. For that purpose, a small-scale cell aging study was conducted with three of the 4.8 Ah cylindrical cells. The capacity loss and resistance increase of the cells are highlighted in Fig. 7, and the cycling and checkup conditions are summarized in Table 2. The model parameterization is performed based on the "original" operating conditions and presented here. The "adapted" operating conditions are detailed in the next subsection.

After initial characterization, 1200 cycles were performed within the manufacturer-specified operating limits of 2.5 V to 4.2 V. The cells were charged with a CCCV charge protocol at a C-rate of 1C in the CC phase and a cut-off current of C/5 for the CV phase. The tests were performed in a climate chamber at 25 °C with a 120 s break between each cycle. Capacity and resistance checkups were performed every 50 cycles. The capacity checkup protocol consisted of two cycles as follows: A CCCV charge phase, followed by a 60 min pause, and a CCCV discharge phase. The CC phases were conducted at a current of C/5, and the CV phases with a cutoff current of C/20. A 60 min pause was implemented between the two capacity checkup cycles. The capacity value depicted in Fig. 7 is the CCCV discharge capacity of the second capacity checkup cycle.

This capacity checkup was followed by a resistance checkup. For that, the cells were charged to a voltage of 3.6 V at a C-rate of C/2 and a CV cutoff at C/50. After a 120 min pause, 10 s charge and discharge pulses were conducted at 0.25C, then 0.5C and 0.75C with a 10 min pause after every pulse. The checkup resistance depicted in Fig. 7 is the average of all these 10 s DC pulse resistances.

The capacity loss behavior in Fig. 7 follows the same trend observed in many cell aging studies. Until approximately 1000 cycles, a sublinear capacity loss behavior is observed, with a higher capacity loss rate over the first few hundred cycles, which then slows down. Many authors attribute this sublinear aging behavior to SEI growth, which is assumed to progress slower the thicker the SEI is, with a frequently quoted $\sqrt{t}$-dependence [71,72]. Past approximately 1000 cycles, nonlinear aging behavior or an "aging knee" is observed, with a rapid increase of the capacity loss rate over the next 200 cycles. The aging study started with the cells being at an average SOH of 98.29%, based on their nominal capacity of 4.8 Ah. After the first 1000 cycles, the cells showed an average SOH of 81.49% and 73.80% after an additional 200 cycles. The average capacity loss rate between cycle 1000 and 1200 is 2.2 times higher than between cycle 0 and 1000, with a further accelerating trend. The resistance increase generally shows the same trend as the capacity loss behavior, with a sublinear resistance increase followed by an accelerated resistance increase rate or "resistance elbow" [13].

Table 2
Operating conditions during cycling and checkup for both the original and the adapted operating conditions.

Condition	Original ≤ 1200 cycles	Adapted > 1200 cycles
U_{max}	4.2 V	4.08 V
U_{min}	2.5 V	3.35 V
Cycling		
Charge	CC at 1C to U_{max}	CC at C/2 to U_{max}
	CV to C/5	
Discharge	CC at 1C to U_{min}	
Checkup interval	50 cycles	25 cycles
Capacity checkup		
Charge	CC at C/5 to U_{max} CV to C/20	
Discharge	CC at C/5 to U_{min} CV to C/20	
Resistance checkup		
DC pulse length	10 s	
DC pulse voltage	3.6 V	
DC pulse rate	±0.25C, ±0.50C, ±0.75C	

At the end of the cyclic aging study with the original operating conditions and after 9 months of storage time, a degradation mode analysis (DMA) of the cells was performed, as described by Dubarry et al. [73]. For that, the charge half-cell open-circuit potential curves from Fig. 15 were fitted to the charge OCV curves of the aged cells after the first 1200 cycles and compared to the charge OCV curves of those cells before the aging study. For the two cells with the least degradation, this led to the following values for the respective degradation modes: LLI = 20.0%, LAM_{NE} = 11.7%, and LAM_{PE} = 5.0%. The DMA did not yield conclusive results for the most strongly degraded cell.

Based on the capacity loss and resistance increase behavior of the cyclic aging study and the DMA, the physicochemical aging model is parameterized as follows with the parameterization summarized in Table 3: First, the constant proportional terms of the loss of active material (LAM) model, β_a and β_c, were fitted to the results of the DMA at the end of the aging study for LAM_{NE} and LAM_{PE} through parameter variation. For that purpose, the exact cycling and checkup schedule that the three cells of the aging study were subjected to was also simulated with the physicochemical aging model in PyBaMM. m_a and m_c are assumed to be equal to 1, as highlighted in the previous subsection. The remaining values of the LAM through the particle stress model are taken from the literature.

Following that, the key parameters of the basic SEI growth model, D_{EC} and k_{SEI}, were fitted such that the capacity checkups of the aging model fit the experimental data as in Fig. 7 until cycle 1000. The scaling factor γ_{SEI} was then fitted through parameter variation such that at the end of the first 1000 cycles, approximately three-quarters of the SEI growth is caused by the cyclic component of Eq. (16) from particle cracking and one-quarter is caused by pure calendar SEI growth, which is an assumption. The initial thickness $L_{SEI,0}$ and the resistivity R_{SEI} of the SEI were then set to match the resistance checkup data from the bottom of Fig. 7.

To parameterize the lithium-plating reaction, cycles 1000 to 1200 of the aging study were used. The fitting factor $\gamma_{pl,2}$ was set such that the onset of plating coincides with the measured data and $i_{pl,0}$ such that the accelerated degradation rate matches the measured data.

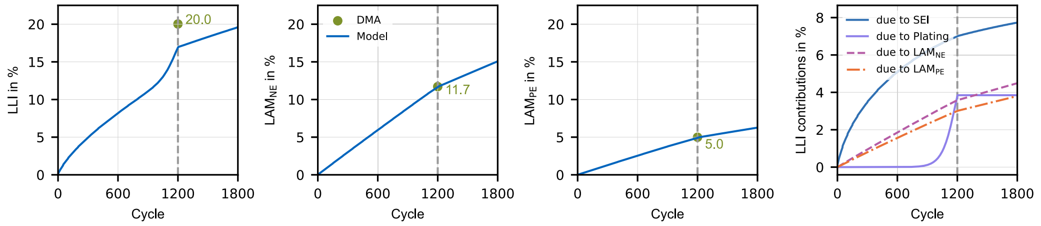

Fig. 8. Development of individual loss components with the physicochemical aging model. For the three degradation modes LLI, LAM$_{NE}$, and LAM$_{PE}$, the results of the DMA of the actual cells are shown in addition to the modeled behavior. The utmost right subplot shows the contributions of the four aging mechanisms to the total LLI.

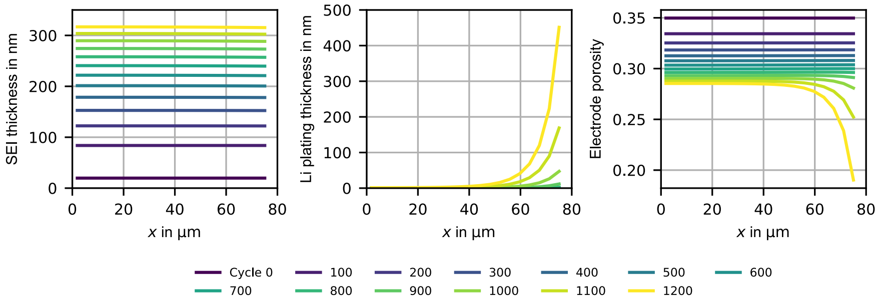

Fig. 9. Modeled SEI thickness, plated lithium thickness, and electrode porosity of the anode at different cycles of the aging study, with the current collector to the left at $x = 0$ and the separator to the right. While SEI growth is nearly homogeneous throughout the anode, lithium plating occurs predominantly close to the separator.

Table 3
Parameters of the physicochemical aging model.

	Unit	Value
Solid electrolyte interphase		
Partial molar volume Ω_{SEI}	$m^3\,mol^{-1}$	$7.545 \cdot 10^{-5}$ [32]
Transfer coefficient α_{SEI}	–	0.5 [74]
Open-circuit potential U_{SEI}	V	0.4 [32]
Lithium to SEI moles z_{Li-SEI}	–	2 [31]
EC initial concentration c_{EC}	$mol\,m^{-3}$	4541.0 [74]
Expansion gradient f_{exp}	–	Fig. 6 [70]
Cracks scaling factor γ_{SEI}	–	0.475[a]
EC diffusivity D_{EC}	$m^2\,s^{-1}$	$1 \cdot 10^{-20}$[b]
Kinetic rate constant k_{SEI}	$m\,s^{-1}$	$1 \cdot 10^{-15}$[b]
Resistivity R_{SEI}	$\Omega\,m$	80,000[b]
Initial thickness $L_{SEI,0}$	m	$1.875 \cdot 10^{-8}$[b]
Lithium plating		
Partial molar volume Ω_{pl}	$m^3\,mol^{-1}$	$1.3 \cdot 10^{-5}$ [31]
Transfer coefficient α_{pl}	–	0.5 [31]
Initial thickness $L_{pl,0}$	m	0[a]
tanh stretch $\gamma_{pl,1}$	V^{-1}	100[a]
tanh shift $\gamma_{pl,2}$	V	−0.08[b]
Exchange current density $i_{pl,0}$	$A\,m^{-2}$	0.09[b]
LAM **Anode**		
Partial molar volume Ω_a	$m^3\,mol^{-1}$	$3.1 \cdot 10^{-6}$ [70]
Young's modulus E_a	Pa	$1.5 \cdot 10^{10}$ [70]
Poisson's ratio ν_a	–	0.3 [70]
Critical stress $\sigma_{yield,a}$	Pa	$6 \cdot 10^{7}$ [75]
Constant exponential term m_a	–	1[a]
Constant proportional term β_a	s^{-1}	$1.564 \cdot 10^{-6}$[b]
LAM **Cathode**		
Partial molar volume Ω_c	$m^3\,mol^{-1}$	$1.25 \cdot 10^{-5}$ [76]
Young's modulus E_c	Pa	$3.75 \cdot 10^{11}$ [70]
Poisson's ratio ν_c	–	0.2 [70]
Critical stress $\sigma_{yield,c}$	Pa	$3.75 \cdot 10^{8}$ [75]
Constant exponential term m_c	–	1[a]
Constant proportional term β_c	s^{-1}	$1.514 \cdot 10^{-6}$[b]

[a] Assumption.

[b] Fitted.

The resulting model shows a good fit with the measured capacity checkup data, with a root-mean-square error (RMSE) of 0.014 Ah within the first 1000 cycles and 0.043 Ah within the first 1200 cycles, or a mean relative error (MRE) of 0.217% and 0.497%, respectively. The larger error metrics when considering the entire 1200 cycles are partially driven by the capacity loss behavior becoming less homogeneous towards the end as the onset of nonlinear aging varies between the cells. For the resistance increase, the overall quality of the fit is slightly worse with an RMSE of 1.071 mΩ within the first 1000 cycles or an MRE of 2.685%. The resistance increase model does currently not account for the resistance from additional SEI that might form around plated lithium [75] during the nonlinear aging phase, which could be a future addition to the model.

Fig. 8 shows the development of the individual loss components LLI, LAM$_{NE}$, and LAM$_{PE}$ in the three left subplots. The LAM$_{NE}$ and LAM$_{PE}$ aging models were fitted to match the DMA results that were obtained after the first 1200 cycles. However, the modeled LLI after the first 1200 cycles does not exactly match with the results of the DMA. A contributing factor to this deviation are the 9 months of storage time in between the first 1200 cycles and the recording the OCV that was used for the DMA. The utmost right subplot shows the individual aging mechanisms as part of the physicochemical aging model that lead to LLI. LLI from SEI growth shows the characteristic square root dependence as the cycles progress. The additional LLI caused by LAM shows a linear development over the cycles of the aging study. Lastly, the model shows significant LLI from lithium plating from approximately cycle 1000 onwards, which causes the nonlinear aging behavior or aging knee of the checkup capacity trajectory from Fig. 7.

Fig. 9 shows the SEI thickness, plated lithium thickness, and electrode porosity of the anode at different cycles of the aging study. While for the here proposed modeling approach SEI growth is nearly homogeneous through the anode, lithium plating predominantly occurs in proximity to the separator due to the lower plating potential η_{pl}. This also leads to lower electrode porosity close to the separator as the cycles progress. The SEI thickness of this model is in good agreement with existing literature, where SEI thickness ranges from 1.5 to 584 nm for SOH values in the range of 100–70%, as reviewed by Andriunas et al. [77].

2.3.3. Adapted operating conditions towards the end-of-life

After the first 1200 cycles, the operating conditions of the cells in the aging study were adapted based on the findings in the literature from Section 1.1, and the cycling was then continued. Table 2 provides an overview of the original and adapted operating conditions for both cycling and checkup.

The charge cut-off voltage U_{max} was lowered to 4.08 V, thereby removing 20% of the remaining capacity per the averaged charge OCV of the three aged cells. The discharge cut-off voltage U_{min} was increased to 3.35 V, thereby removing an additional 10% remaining capacity per the averaged discharge OCV. The total voltage window ΔV was thereby changed from 1.70 V to 0.73 V. This was done for both the cycling protocol and the checkup protocol. Next to its detrimental effect on nonlinear aging, further cycling at the original voltage window would not have been advisable due to another observed effect: Two out of the three cells showed abnormal heating during the CV phase at 4.2 V while performing the nominal power and efficiency checkups after the first 1200 cycles. Han et al. observed the same phenomenon in their study on aged cells [78]. They hypothesize that cell-internal shorts from lithium dendrites, which self-terminate over time, could be the reason for this behavior [78].

The CC charge rate for cycling was reduced from 1C to C/2. The charge and discharge rates for the capacity checkup protocol remained unchanged at C/5. The checkup interval was changed from every 50 cycles to every 25 cycles. All other conditions remained unchanged as described in 2.3.2. The CC discharge rate was kept unchanged as well since part of the existing literature points towards higher discharge rates being beneficial [32,44], while others saw none [30] or negative impact of higher discharge rates [47] on the nonlinear aging behavior.

Fig. 7 shows that with the adapted operating conditions, the cells transition back out of the previously nonlinear aging phase towards a highly reduced rate of capacity loss. The rate of capacity loss with the adapted operating conditions is not only smaller than in the nonlinear aging phase but also smaller than in the first cycles of the aging study. From cycle 0 to 600, the average checkup discharge capacity of the three cells decreased by 0.49 Ah, while from cycle 1200 to 1800 with the adapted operating conditions, the discharge capacity decreased by only 0.19 Ah. However, the usable capacity is reduced by the adapted voltage limits. At the last checkup with the original operating conditions, an average discharge capacity of 3.54 Ah was measured for the three cells, while the first checkup with the new operating conditions yielded an average discharge capacity of 2.43 Ah. The physicochemical battery model replicates this reduced aging rate, which stems from the lack of additional lithium plating, see Fig. 8, due to the reduced charge rate and lower charge cut-off voltage.

The resistance increase in the bottom of Fig. 7 proceeds significantly slower as well with the adapted operating conditions than in the nonlinear aging phase. While the aging model's trajectory captures this reduced resistance increase rate, there is an offset in the absolute values. This stems from the previously discussed fact that the physicochemical aging model does not consider the accelerated resistance increase during the nonlinear aging phase.

2.3.4. Interface between SimSES and PyBaMM

To allow for the simulation of the full BESS with the physicochemical aging model, the model was implemented in PyBaMM [50] and integrated into the SimSES [49] simulation framework. For that purpose, a PyBaMM interface was implemented as an additional technology package in the SimSES environment. This interface converts the power targets of the upstream converter modules in SimSES into constant power experiments for the battery cell in PyBaMM for the next timestep. If the minimum or maximum cell voltage is reached within the timestep, the constant power experiment is followed by a constant voltage experiment for the remaining time of that timestep. After the simulation of this timestep in PyBaMM, relevant variables are saved in the technology state data structure of SimSES and passed to the upstream components to update their state variables and determine the power target for the next timestep.

Within the interface, checkup experiments are conducted periodically to determine the SOH and allow for SOC estimation of the PyBaMM physicochemical battery model. The capacity checkup procedure from Table 2 with the original operating conditions is used for that purpose. For the EA and SCI applications in the case studies, additional aging is deactivated during these checkup cycles by setting β_{a}, β_{c}, D_{EC}, and $i_{\mathrm{pl,0}}$ to zero. The SOH is then calculated based on the CCCV discharge capacity. For the SOC, an estimation approach is required. The minimum average anode stoichiometry $\chi_{\mathrm{a}}^{\mathrm{min}}$ and maximum average anode stoichiometry $\chi_{\mathrm{a}}^{\mathrm{max}}$ are recorded during each capacity checkup cycle. After every timestep, the anode SOC is calculated based on the present average anode stoichiometry χ_{a}: $\mathrm{SOC} = (\chi_{\mathrm{a}} - \chi_{\mathrm{a}}^{\mathrm{min}})/(\chi_{\mathrm{a}}^{\mathrm{max}} - \chi_{\mathrm{a}}^{\mathrm{min}})$. This SOC value can then be used by the energy management system, such as the optimization model for intraday trading from Section 2.1, to determine the power targets for the next timesteps.

As for the other technologies implemented in SimSES, a lump modeling approach is used in which a single cell is modeled, and the output voltage and current are scaled accordingly to match the rated power and energy of the full BESS. While SimSES is run on a 15 min time resolution for the following case study, the solver in PyBaMM runs on a significantly higher resolution, based on the given accuracy specifications. Checkup cycles are run every 6 h to update the SOH and the anode stoichiometry values that are used for the SOC estimation.

3. Simulation case study

A simulation case study is conducted using the previously described simulation framework. In Section 3.1, we investigate the general performance of lithium-ion cells at different SOHs in the two applications of SCI with a home storage system and EA with a large-scale storage system by comparing the 4.8 Ah cylindrical cell with the 94 Ah prismatic cell. In Section 3.2, we use the physicochemical aging model that we developed for the 4.8 Ah cylindrical cell to investigate the aging behavior over time in the two stationary applications and show how the lifetime profit can be increased by adapting the operating conditions towards the EOL. The full toolchain used to conduct the simulations is available open-source [51].

3.1. Profit potential at different states of health

One-year simulations were conducted in SimSES at different fixed capacity-based SOH values with the equivalent circuit models described in Section 2.2. At the same time, for each SOH value, a resistance increase following the same trajectory as in the aging study from Fig. 7 is assumed. In the aging study, an average resistance increase of 62.45% was observed after 1200 cycles, with the capacity-based SOH reducing from 98.29% to 73.80%. This leads to the following linear interpolation for the assumed internal resistance increase r_{i} of the equivalent circuit model:

$$r_{\mathrm{i}} = \frac{62.45\%}{98.29\% - 73.80\%} \cdot (100\% - \mathrm{SOH}) \tag{22}$$

Fig. 10 shows key results of the simulations at different SOH values. The discharged energy over a given year expectedly decreases with reduced battery capacity. However, this relationship is not directly proportional, such that at low SOH, more cycles are completed when based on the remaining capacity. With the 4.8 Ah cylindrical cell and an SOH of 100%, 218.15 equivalent discharge cycles are completed in the given year in the EA application, and 202.92 equivalent discharge cycles in the self-consumption increase application. At an SOH of 60%, these numbers increase to 263.31 and 268.63 equivalent discharge cycles per year, based on the remaining capacity.

The difference in BESS round-trip efficiency between the two cells is larger for the EA application than for the SCI application, as the second column of Fig. 10 shows. At the same time, the round-trip efficiency of

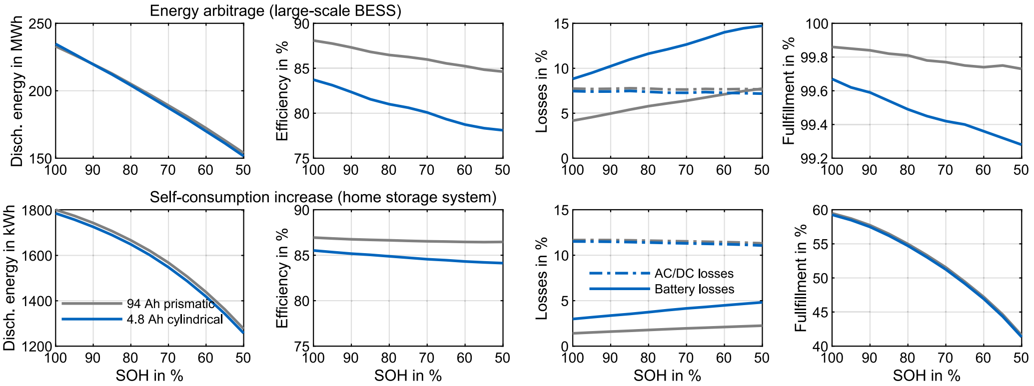

Fig. 10. Simulated performance parameters based on one-year simulations with the 94 Ah prismatic cell and 4.8 Ah cylindrical cell for the application of energy arbitrage (top row) and self-consumption increase (bottom row) at different fixed SOH values with no further degradation in the given year.

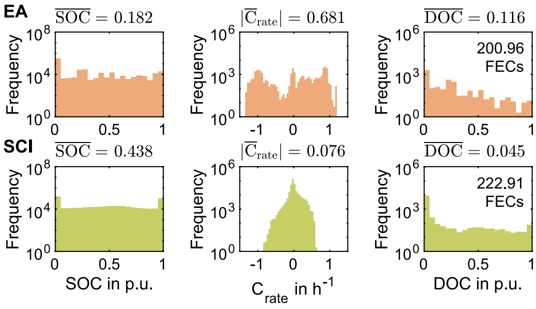

Fig. 11. Distribution of key aging stress factors in the two applications of energy arbitrage (EA) and self-consumption increase (SCI) based on the one-year simulations with the 4.8 Ah cylindrical cells at 100% SOH.

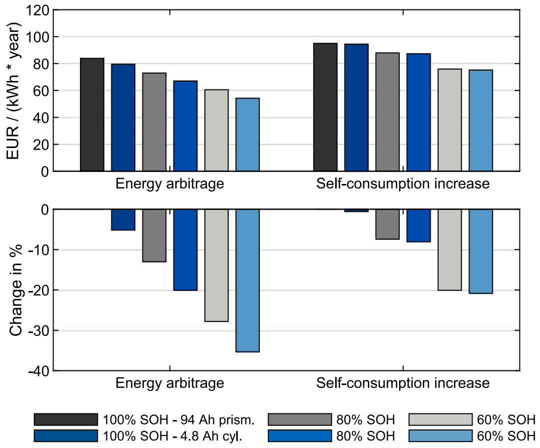

Fig. 12. Profit potential per year in EUR per kWh of the originally installed capacity at selected SOH values for the two applications (top). Change in percent from the reference scenario, i.e., the 94 Ah prismatic cell at 100% SOH (bottom).

the BESS with the 94 Ah prismatic cell is higher for the EA than for the SCI scenario (88.09% and 86.94% efficiency at 100% SOH), while with the 4.8 Ah cylindrical cell is lower (83.73% and 85.52% efficiency at 100% SOH). The causes for this become evident by looking at the distribution of C-rates in Fig. 11. First, the average C-rate in the EA application is higher, which leads to higher cell internal losses, especially for the 4.8 Ah cylindrical cell with its higher internal resistance. Therefore, the gap in round-trip efficiency between the two cells widens further with decreasing SOH and increasing cell resistance, especially in the EA application. Second, due to more charge/discharge events at a low C-rate, the SCI application has an overall worse AC/DC converter efficiency since the converter efficiency is particularly low at low power values [58]. This results in the BESS round-trip efficiency for the SCI application being driven more by the converter efficiency than the cell resistance, as the third column of plots in Fig. 10 confirms. For both applications, the C-rate from Fig. 11 is, on average, larger in discharge than in charge direction since due to the voltage drop over the internal cell resistance, higher currents are drawn from the cell to deliver a specified discharge power, compared to the same charge power. Similarly, higher currents are needed to deliver a specified discharge or charge power at low SOC values due to the lower OCV compared to at high SOC values. Both effects combined lead to maximum observed current-based C-rates in discharge direction, i.e., $1.32\,\mathrm{h}^{-1}$ for the EA and $0.85\,\mathrm{h}^{-1}$ for the SCI application, that significantly exceed the power-to-energy ratios calculated from the system nominal values, i.e., $0.93\,\mathrm{h}^{-1}$ for the EA and $0.60\,\mathrm{h}^{-1}$ for the SCI application.

Next to the efficiency, the fulfillment factor shows differences between the two cells and the two applications, as highlighted in the fourth column of Fig. 10. Fulfillment is here defined as the average ratio of requested power by the energy management system to the delivered power of the BESS. For the SCI application, the requested power is the difference between the household load and the generated PV power as in Eq. (1). This leads to overall low fulfillment, as the BESS cannot continue charging once it is full around noon or continue discharge once it has been emptied at night. For the EA application, the requested power is the output of the optimization model described in Eqs. (2) to (7). Since the optimization model is aware of the SOC limitations of the BESS, the fulfillment factor is higher overall. In both applications, a lower fulfillment factor is observed for the 4.8 Ah cylindrical cell compared to the 94 Ah prismatic cell due to its lower nominal power range that was shown in Fig. 4. This difference in fulfillment factor further increases with decreasing SOH.

These differences in the BESS round-trip efficiency and the fulfillment factor translate into different profit potentials, as shown in Fig. 12. With the 4.8 Ah cylindrical cell, a profit potential of 79.56 EUR per kWh nominal capacity and year is achieved for EA and 94.44 EUR per kWh nominal capacity and year for SCI at an SOH of 100%. Notably, the higher intraday electricity prices and price volatility led to significantly higher obtainable profit through EA in 2022 compared to previous years [28].

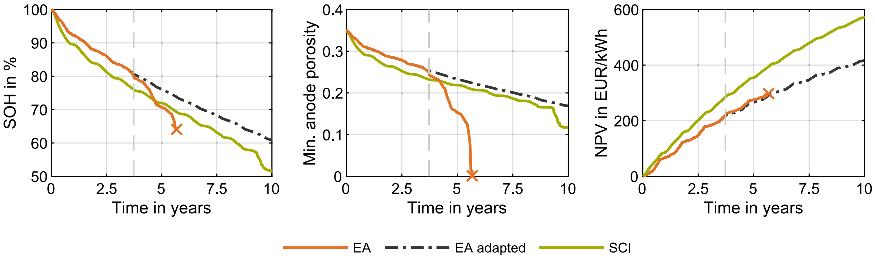

Fig. 13. Development of capacity-based SOH, minimum anode porosity, and NPV over a simulated ten-year period for the two applications of EA with a large-scale BESS and SCI with a home storage system. For the EA application, an additional scenario is shown in which the operating limits of the optimization algorithm are adapted following Table 2 once a remaining SOH of 80% is reached. EOL is assumed once the minimum anode porosity reaches zero, as is the case for the basic EA application after 5.7 years.

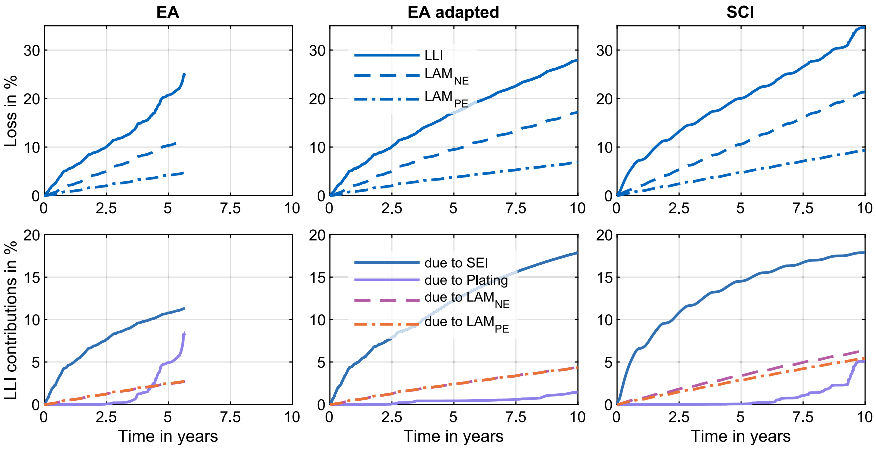

Fig. 14. Degradation modes (top) and individual mechanisms leading to LLI (bottom) over time for the EA application, the EA application with adapted operating conditions past 80% SOH, and the SCI application.

The results further show that the profit in EA has a stronger sensitivity on both the battery cell type and the SOH. In EA, the profit potential at 100% SOH is 5.17% lower with the cylindrical cell than with the prismatic cell. At 60% SOH, this gap widens to 10.30%. For the SCI application, these differences in profit potential between the two cells are only 0.59% and 0.72%. This can be explained by the stronger dependency of the overall BESS efficiency on the battery cell resistance in the EA application. Furthermore, the lower nominal power range impacts the EA application more than the SCI application. While for SCI, the home storage system will generally just charge up to full SOC slightly later in the day, for EA, the lower nominal power range leads to missing profitable arbitrage opportunities. Notably, the performance of the optimization model might be improved by accounting for the nominal power range through introducing SOC dependent power limits in Eqs. (5) and (6). For the cylindrical cell, the profit potential is 31.64% lower at 60% SOH than at 100% SOH in the EA application and 20.84% lower in the SCI application. This highlights the overall higher sensitivity of the profit in the EA application on the SOH compared to the SCI application.

3.2. Aging behavior over lifetime

In this subsection, the physicochemical aging model, implemented in PyBaMM, is used in conjunction with SimSES to perform 10-year simulations for the two applications of EA and SCI. Fig. 13 shows the development of the capacity-based SOH, the minimum anode porosity, and the NPV of the profit generated in the two applications, scaled with the nominal capacity at the beginning of life. The NPV is defined as below:

$$\mathrm{NPV} = \sum_{t=0}^{t_{\max}} \frac{\mathbb{P}_t}{(1+\mathrm{i})^{n(t)}} \tag{23}$$

Here, $\mathbb{P}_t$ is the profit generated from the given application in timestep t, $t_{\max}$ the last timestamp up until the evaluation point of the NPV, and $n(t)$ the fractional years since the beginning of the simulation. i is the interest rate which is set to $\mathrm{i} = 0.075$ for the purpose of this analysis, as in [28]. The EA and SCI applications show distinct differences in terms of the aging behavior of the battery cells: In SCI, the capacity loss proceeds faster in the first few years and is then outpaced by the capacity loss in the EA application. After 3 years of operation, the checkup cycles with the physicochemical battery model show a remaining capacity-based SOH of 83.61% for the EA application and 79.34% for the SCI application. Here, the EOL is assumed once the minimum anode porosity reduces to zero, resulting in pore clogging, similar to Yang et al. [31]. For the EA application, this point is reached after 5.7 years at an SOH of 64.10%. After the same period, the SOH is at 69.28% in the SCI application.

Fig. 14 provides insights into the aging mechanisms that lead to this behavior. In the SCI application, the LLI from SEI growth progresses faster. After 3 years of operation, 11.75% total LLI are observed in the EA application and 14.61% in the SCI application. The faster SEI growth in the SCI application stems from more time being spent at a high SOC, as the stress factor overview of Fig. 11 in the previous subsection showed. After about three years, lithium plating starts to occur in the EA application, leading to a steep increase in the capacity loss rate. As the stress factor analysis showed, the cells are subjected to higher charge rates in the EA application, which causes the earlier onset of lithium plating. The plated lithium leads to LLI and a steep reduction in the anode porosity close to the separator. Lithium plating is also observed for the SCI application after about 6 years of operation at a slower rate. After 5.7 years, when the EOL is reached for the EA application, a total of 24.98% LLI is observed for the EA application and 22.00% LLI for the SCI application. The aging mechanisms of $\mathrm{LAM_{NE}}$ and $\mathrm{LAM_{PE}}$ and their concurrent LLI show no significant differences between the two applications.

In addition to the two applications SCI and EA, which use the "original" operating conditions from Table 2, an additional scenario for the EA application is depicted in Figs. 13 and 14. For this "EA adapted" scenario, the operating limits of the optimization algorithm are adapted in accordance with Table 2, once a SOH of 80% is reached. Here, this is the case after 3.7 years of operation. The previous constraints from Eqs. (6) and (7) are adapted past this point as follows:

$$0 \leq p_t^{\mathrm{ch}} \leq \frac{1}{2} P^{\mathrm{AC,max}} \quad \forall\, t \in T \tag{24}$$

$$0.1 \leq soc_t \leq 0.8 \quad \forall\, t \in T \tag{25}$$

These adapted operating conditions lead to a reduction of the degradation rate. Most importantly, the reduced charge rate and lower maximum cell voltage delay any further significant lithium plating until after approximately 8.5 years of operation.

After the simulated 10-year time period, a NPV of 570.23 EUR per kWh of originally installed BESS capacity is reached in the SCI application. For the EA application with the original operating conditions, the EOL is reached after 5.7 years of operation after having obtained a NPV of 297.66 EUR per kWh. By adapting the operating conditions, a NPV of 416.22 EUR per kWh is achieved after ten years, a significant increase of 39.83%. Notably, the adapted operating conditions only marginally affect the generated profit between the time the adaption takes place after 3.7 years and the time the EOL is reached with the original operating conditions after 5.7 years. After 5.7 years, a NPV of 291.94 EUR per kWh is obtained with adapted operating conditions, which is a decrease of only 1.92% compared to the original EA application. While the reduced usable SOC range and charge power expectedly decrease the profit, this is counterbalanced by the fact that without the adaptions, the sharp decrease in SOH and efficiency would otherwise negatively affect the profitability.

4. Conclusion

With the steadily growing amount of globally installed BESSs and the increasing operation time of the installed systems, the performance of late-life lithium-ion cells becomes increasingly relevant. This includes how reduced capacity, nominal power range, and efficiency affect the profitability as well as the aging behavior of late-life cells in different applications. In this work, we investigate these effects with an open-source simulation toolchain for the two applications of energy arbitrage (EA) with a large-scale storage system and self-consumption increase (SCI) with a home storage system.

To investigate the impact of reduced capacity, efficiency, and nominal power range on profitability, equivalent circuit models were derived for the primary cell under investigation, a 4.8 Ah cylindrical cell, as well as for a 94 Ah prismatic cell as a reference. The simulations were then conducted using the in-house developed SimSES tool in conjunction with a previously published MPC framework to simulate the EA application. The results show that the profit generated in the EA application is more affected by cell aging than in the SCI application. Furthermore, the 94 Ah prismatic reference cell, which is used for BESS applications, shows higher profit potential in both applications than the 4.8 Ah cylindrical cell, which is primarily intended for EV applications. However, this difference is more pronounced for the EA than for the SCI application. In summary, the comparison of the two cell types highlights the performance differences between EV cells, which are often envisioned for stationary second-life applications, and BESS cells, which are specifically intended for stationary applications. While the differences in profit potential are marginal for the SCI application, they are noticeable for the EA application and should be considered when selecting cells for a BESS.

A physicochemical aging model was developed and parameterized based on a small-scale aging study for the 4.8 Ah cylindrical cell to model the aging behavior over time for the two applications. The model captures the aging mechanisms of particle cracking-induced loss of active material on the anode and cathode as well as SEI growth and lithium plating. The aging study shows that cells that have entered the accelerated nonlinear aging phase can transition back to a reduced degradation rate by adapting the operating conditions, which is supported by the developed physicochemical aging model. For the case study, the model was implemented in PyBaMM and linked to SimSES. While for the SCI application, the onset of lithium plating shows after approximately 6 years at a slow rate, for EA, this is already the case after 3 years at an accelerated aging rate leading to EOL after 5.7 years of the investigated 10-year time-horizon. We show that by adapting the operating conditions once a SOH of 80% is reached, the lifetime in the EA application can be extended to cover the whole 10-year time-horizon while obtaining an increase in the NPV of 39.83%. This highlights that adapting the operating conditions of late-life lithium-ion cells can significantly increase their lifetime and the generated profit.

For this work, some uncertainties and limitations are considered. The EA application was modeled in a simplified way since perfect foresight of the ID-1 price was assumed. We believe this to be a conservative assumption since, for real-time bidding, one may achieve higher sell and lower buy prices than the ID-1 price and may place additional bids that are compensated before execution by the BESS, which can generate additional profit [28]. Furthermore, cell-to-cell variations of the aging rate were neglected in the case study. In addition, only a small-scale aging study was used to parameterize the physicochemical aging model, a shortfall of many physicochemical aging models [21,31,35,75]. While the model generally represents the expected behavior of the underlying aging mechanisms well, larger studies should be conducted in the future with cells at different calendar and cycling aging conditions.

As for the outlook, the aging study conducted in this work showed that nonlinear aging can not only be delayed by adapting the operating conditions before its occurrence but that lithium-ion cells that have already entered the nonlinear aging phase can transition back to a significantly reduced degradation rate by adapting the operating conditions after extended cycling. This is a highly promising result since the operating conditions of a BESS could be adapted once nonlinear aging behavior is first observed through SOH estimation instead of adapting the operating conditions preemptively. This effect requires additional investigation with regard to the exact operating conditions that influence it. Here, only one set of adapted operating conditions was investigated, i.e., a reduced charge rate combined with a narrowed voltage window. To what extent this effect occurs for different types of lithium-ion cells should also be investigated further.

Using the physicochemical aging model, the case study highlighted the lifetime and profit increase that can be achieved by adapting the operating conditions of late-life lithium-ion cells. Here, a fixed SOH value was used as a threshold for adapting the operating conditions. An even higher increase in profitability may be achieved in future work through dynamic criteria that gradually reduce the charge rate and operating voltage window based on the SOH. In addition, the accuracy of the physicochemical aging model may be improved further by also accounting for the resistance increase during nonlinear aging, e.g., through additional SEI formed around plated lithium. In addition, the cell temperature was kept at a constant 25 °C in the aging study and was assumed to be constant in the model. If lithium plating is the expected mechanism that leads to nonlinear aging, operating late-life cells at slightly higher temperatures during charging could further extend their lifetime.

Finally, while this work proposes a method to extend the lifetime and increase the lifetime and generated profit of late-life lithium-ion cells, the method remains to be validated in the ever-growing and aging fleet of stationary battery energy storage systems.

CRediT authorship contribution statement

Nils Collath: Writing – review & editing, Writing – original draft, Visualization, Software, Project administration, Methodology, Investigation, Formal analysis, Conceptualization. **Henry Winner:** Writing – review & editing, Writing – original draft, Investigation. **Alexander Frank:** Writing – review & editing, Writing – original draft, Investigation. **Axel Durdel:** Writing – review & editing, Writing – original draft, Investigation. **Andreas Jossen:** Writing – review & editing, Supervision, Funding acquisition.

Declaration of competing interest

The authors declare that they have no known competing financial interests or personal relationships that could have appeared to influence the work reported in this paper.

Data availability

The simulation toolchain is available open-source in the link specified iin the document.

Funding and acknowledgment

This research is funded by the Federal Ministry for Economic Affairs and Climate Action (BMWK), Germany via the research project StorageMultiApp (grant number 03EI6081B) and the Federal Ministry of Education and Research (BMBF), Germany via the research project greenBattNutzung (grant number 03XP0302D). The projects StorageMultiApp and greenBattNutzung are both overseen by Project Management Juelich (PtJ). We further thank Alexander Unger for his contributions to parameterizing the basic P2D model used in this work.

Appendix A. Electrical cell characterization

The measurement conditions for the OCV, hysteresis, and charge resistance from Fig. 3 and the energy efficiency and nominal power range from Fig. 4 are briefly outlined here.

A.1. OCV, hysteresis, and charge resistance

The quasi-stationary OCV curves were measured at a C-rate of C/25 in the respective manufacturer-given operating voltage windows of the two cells: 3.2 V–4.15 V for the prismatic cell and 2.5 V–4.2 V for the cylindrical cell in first charge then discharge direction. The hysteresis voltage is the difference between the quasi-stationary OCV measurements in charge and discharge direction. The displayed resistance is the 10 s DC-charge resistance, measured at different SOC values and at a charge rate of 1C. For the cylindrical cells, the average of two cells is shown, while for the prismatic cells, only one cell had not seen any cycling yet and was therefore available for characterization. The average discharge capacity of the two cylindrical cells was measured at 4.688 Ah and for the prismatic cell at 95.45 Ah prior to the above measurements. These capacity values were determined from a 0.5C CC-discharge after a CCCV charge with 0.5C charge rate in the CC phase and 0.04C cutoff current in the CV phase. All data was recorded in climate chambers set to 25 °C. The results are depicted in Fig. 3.

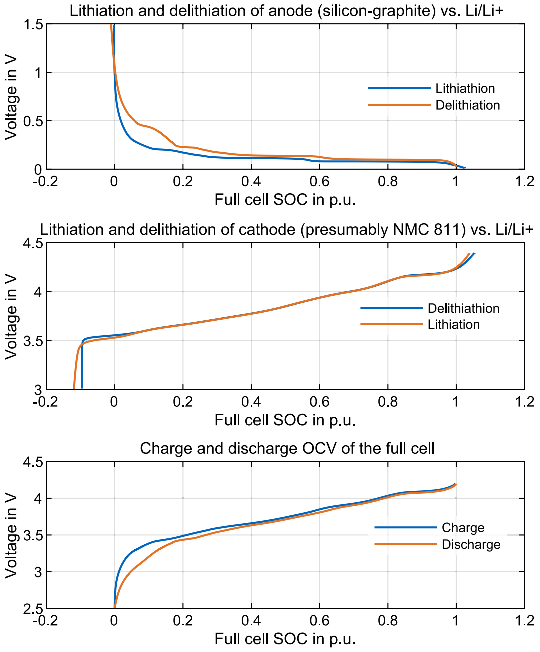

Fig. 15. Open-circuit voltages for the lithiation and delithiation direction for the anode material coin cell (top), lithiation and delithiation of the cathode material coin cell (mid), and charge and discharge direction of the full-cell (bottom). Measured at C/50 and 25 °C. The model in the main part of this work uses the charge direction curves of the full-cell, meaning the lithiation curve for the anode and the delithation curve for the cathode material.

A.2. Energy efficiency and nominal power range

The energy efficiency was measured with a CC-charge at different C-rates, followed by a CCCV-discharge at the same C-rates, within the manufacturer-specified voltage range. The CV-discharge phase was ended at a C-rate below 0.04C. The displayed energy efficiency in Fig. 4 is the measured discharge energy of the CCCV-discharge divided by the measured charge energy of the CC-charge.

For the nominal power range test, the cells were subjected to a CPCV charge phase followed by a 30 min pause and a CPCV discharge phase within their manufacturer-stated voltage ranges. In the constant power phases, the charge and discharge power were set to the nominal cell power, i.e., 345.9 W for the prismatic cell and 17.472 W for the cylindrical cell. The CV phases were both ended at a charge or discharge current below 0.04 C.

Both tests were conducted in a climate chamber set to 25 °C. For the efficiency plot, the average of two new cylindrical cells and three aged cylindrical cells is shown, while for the prismatic cell, only one new cell was available for characterization, and its results are depicted. The aged cylindrical cells are the three exact cells from Fig. 7 after 1200 cycles. For the usable power range plot, the charge–discharge behavior of one cell of each type is shown.

Appendix B. P2D model equations and parameterization

Parameterization of the P2D for the 4.8 Ah cylindrical cell was performed in-house using measurements. Literature data was used for all parameters that were not determined experimentally. Some parameters have been fitted while minimizing the error between simulation and measurements. The equations of the Newman-type model are outlined

Table 4
Equations for the P2D model. Here, ∇_x is the spatial gradient in the real dimension, i.e., along the through-plane direction of the cell stack, and ∇_r is the spatial gradient in the pseudo dimension, i.e., along the radius of the spherical active material particles. The additional equations of the physicochemical aging model are stated in Section 2.3.1.

Spatial gradients	$\nabla_x = \frac{\partial}{\partial x}, \qquad \nabla_r = \frac{\partial}{\partial r} \quad$ (r in spherical pseudo dimension)	(26)
Mass balance	$\frac{\partial \left(\varepsilon_1(x,t) \cdot c_1(x,t)\right)}{\partial t} = \nabla_x \cdot \left(D_1^{\mathrm{eff}}(x,t) \nabla_x c_1(x,t) + \frac{i_1(x,t)\left(1 - t_+^0\right)}{\mathcal{F}} \right)$	(27)
Mass balance	$\frac{\partial c_{\mathrm{s}}(x,t,r)}{\partial t} = \nabla_r \cdot \left(D_{\mathrm{s}} \nabla_r c_{\mathrm{s}}(x,t,r)\right) = \frac{1}{r^2} \frac{\partial}{\partial r} \left(D_{\mathrm{s}} r^2 \frac{\partial c_{\mathrm{s}}(x,t,r)}{\partial r} \right)$	(28)
Potentials	$\nabla_x \varphi_1(x,t) = -\frac{i_1(x,t)}{\kappa_1^{\mathrm{eff}}(x,t)} + \frac{2\mathcal{R}T}{\mathcal{F}} \left(1 - t_+^0\right) \left(1 + \frac{d \ln f_\pm}{d \ln c_1(x,t)}\right) \nabla_x \ln c_1(x,t)$	(29)
	$\nabla_x \varphi_{\mathrm{s}}(x,t) = -\frac{i_{\mathrm{s}}(x,t)}{\kappa_{\mathrm{s}}^{\mathrm{eff}}(x,t)} \quad$ with $\quad i_{\mathrm{app}}(t) = i_{\mathrm{s}}(x,t) + i_1(x,t) \quad \forall\, x, t$	(30)
Charge balance	$\nabla_x \cdot i_1(x,t) + \nabla_x \cdot i_{\mathrm{s}}(x,t) = 0$	(31)
	$\nabla_x \cdot i_{\mathrm{s}}(x,t) = \begin{cases} -\frac{3\varepsilon_{\mathrm{AM}}(x,t)}{R_{\mathrm{p}}} \left(\mathcal{F} j_n(x,t) + i_{\mathrm{SEI}}(x,t) + i_{\mathrm{pl}}(x,t)\right) & \text{anode domain} \\ -\frac{3\varepsilon_{\mathrm{AM}}(x,t)}{R_{\mathrm{p}}} \mathcal{F} j_n(x,t) & \text{cathode domain} \end{cases}$	(32)
Electrode kinetics	$j_n(x,t) = \frac{i_0(x,t)}{\mathcal{F}} \left(\exp\left(\frac{\alpha_{\mathrm{a}} \mathcal{F} \eta(x,t)}{\mathcal{R}T} \right) - \exp\left(-\frac{\alpha_{\mathrm{c}} \mathcal{F} \eta(x,t)}{\mathcal{R}T} \right) \right)$	(33)
	$\eta(x,t) = \varphi_{\mathrm{s}}(x,t) - \varphi_1(x,t) - \Delta\varphi_{\mathrm{SEI}}(x,t) - E_{\mathrm{eq}}(x,t)$	(34)
	$\Delta\varphi_{\mathrm{SEI}}(x,t) = \begin{cases} \mathcal{F} j_n(x,t) R_{\mathrm{SEI}} L_{\mathrm{SEI}}(x,t) & \text{anode domain} \\ 0 & \text{cathode domain} \end{cases}$	(35)
	$i_0(x,t) = \mathcal{F} k \left(c_{\mathrm{s,max}} - c_{\mathrm{s,surf}}\right)^{\alpha_{\mathrm{a}}} \left(c_{\mathrm{s,surf}}\right)^{\alpha_{\mathrm{c}}} \left(\frac{c_1}{c_{1,\mathrm{ref}}}\right)^{\alpha_{\mathrm{a}}}$	(36)
Effective transport parameters	$\kappa_{\mathrm{s}}^{\mathrm{eff}}(x,t) = \kappa_{\mathrm{s}} \cdot \varepsilon_{\mathrm{AM}}(x,t)^{\beta_{\mathrm{brug}}}, \quad \kappa_1^{\mathrm{eff}}(x,t) = \kappa_1(x,t) \cdot \varepsilon_1(x,t)^{\beta_{\mathrm{brug}}}, \quad D_1^{\mathrm{eff}}(x,t) = D_1(x,t) \cdot \varepsilon_1(x,t)^{\beta_{\mathrm{brug}}}$	(37)
Boundary conditions	$\nabla_x c_1(x,t)\Big\vert_{x=0 \;\wedge\; x=L_{\mathrm{tot}}} = 0$	(38)
	$\nabla_x \varphi_1(x,t)\Big\vert_{x=0 \;\wedge\; x=L_{\mathrm{tot}}} = 0$	(39)
	$\varphi_{\mathrm{s}}(x,t)\Big\vert_{x=0} = 0$	(40)
	$\nabla_x \varphi_{\mathrm{s}}(x,t)\Big\vert_{x=L_{\mathrm{tot}}} = -\frac{i_{\mathrm{app}}}{\kappa_{\mathrm{s}}^{\mathrm{eff}}}$	(41)
	$\nabla_r c_{\mathrm{s}}(x,t,r)\Big\vert_{r=0} = 0$	(42)
	$\nabla_r c_{\mathrm{s}}(x,t,r)\Big\vert_{r=R_{\mathrm{p}}} = -\frac{j_n}{D_{\mathrm{s}}}$	(43)

in Table 4 and the final parameters are summarized in Table 5. Superscripts indicate whether the respective parameter was measured directly, calculated from measurements, estimated, fitted, or taken from the literature. While the final simulations were conducted in PyBaMM, the simulations for parameterization were conducted using COMSOL Multiphysics.

The following briefly discusses the parameters from Table 5 that were not taken from the literature. We deliberately keep this section concise as the parameterization of the basic P2D model is not the focus of this work.

B.1. OCV measurements

A new cylindrical cell was opened to harvest electrode material and assemble anode and cathode half coin cells vs. Li metal. The disassembly, sample preparation, and coin cell assembly was performed in an argon-filled glovebox and the entire procedure is similar to what is described in the literature [84]. Quasi-OCV measurements at C/50 CC charge/discharge have been conducted to retrieve the OCV curve for the anode and cathode half-cells as well as for the cylindrical full-cell. The anode OCV was measured between 0.01 V and 1.5 V vs. Li metal, the cathode OCV between 3.0 V and 4.4 V vs. Li metal, and the full-cell OCV between 2.5 V and 4.2 V. All cells were placed inside a climate chamber at 25 °C. The half-cell OCVs are then scaled and shifted such that their superposition yields the measured full-cell curves, similarly as reported in the literature [85]. This reconstruction of the full-cell OCV results in Fig. 15 as well as the stoichiometric coefficients χ at 0 % and 100 % full-cell SOC in Table 5.

B.2. Particle radius

Additional samples from the opened cylindrical cell were used for scanning electron microscopy (SEM) imaging. Using a similar procedure as described by [86], the mean particle radius assuming spherical particles was retrieved.

B.3. Material composition

Simultaneously to SEM imaging, energy dispersive X-ray (EDX) spectroscopy was performed to obtain a quantitative elemental analysis. Based on the atomic ratio, it was determined that the cathode is an NMC with a high Ni content and the anode is a silicon-graphite mixture with a ratio of 98:2. The specific capacity of each electrode was calculated from these information. Using density values from the literature, the maximum solid-phase concentration was calculated.

B.4. Volume fractions

The porosity of the separator is assumed to be similar to that reported in the literature. The porosity values for the electrodes are visually estimated from SEM images by segmenting the solid material and the pore space. Segmenting the solid active material from the solid inactive material, however, was not possible. To still obtain a value for the active material volume fraction (contributing to the electrodes' capacities and thus to the balancing between anode and cathode), this value was fitted for both electrodes in such way that the RMSE between measurement and simulation at low currents is minimized.

Table 5
Parameterization of the P2D model for the 4.8 Ah cylindrical cell with NMC811 cathode (presumably) and SiC anode.

	Unit	Anode	Separator	Cathode
Geometry				
Thickness coating L	µm	77[e]	13.3[e]	61[e]
d_{50} Particle radius R_p	µm	6.0834[e]	–	4.642[e]
Active material width	mm	1079.5[e]	–	1079.5[e]
Active material height	mm	62.85[e]	–	62.85[e]
AM volume fraction ε_{AM}	–	0.49386[d]	–	0.70104[d]
Electrolyte volume fraction ε_l	–	0.35[c]	0.45 [79]	0.2[c]
Bruggeman coefficient β_{brug}	–	1.5 [79]	1.5 [79]	1.85 [79]
Thermodynamics				
Equilibrium potential E_{eq}	V	Fig. 15 (top)[e]	–	Fig. 15 (mid)[e]
Stoichiometry χ 100% SOC	–	0.93889[d]	–	0.08736[d]
0% SOC	–	0.03455[d]	–	0.95[d]
Max. concentration $c_{s,max}$	mol m^{-3}	37,295[b]	–	48,452[b]
Transport				
Solid diffusivity D_s	m^2 s^{-1}	$5 \cdot 10^{-13}$[d]	–	$4 \cdot 10^{-14}$ [80]
Electric conductivity κ_s	S m^{-1}	100 [81]	–	1.2 [82]
Kinetics				
Reaction rate constant k	m s^{-1}	$3 \cdot 10^{-11}$ [79]	–	$1 \cdot 10^{-11}$ [79]
Charge transfer coefficients α_a/α_c	–	0.5/0.5 [79]	–	0.5/0.5 [79]
Electrolyte				
Salt diffusivity D_l[a], [83]	m^2 s^{-1}	$10^{-4} \cdot 10^{-4.43-\frac{54}{T-229-5c_l}-0.22c_l}$		
Ionic conductivity κ_l[a], [83]	S m^{-1}	$0.1c_l(-10.5+0.668c_l+0.494c_l^2+0.074T-0.0178c_lT$ $-8.8610^{-4}c_l^2T-6.9610^{-5}T^2+2.810^{-5}c_lT^2)$		
Activity $\frac{d\ln f_\pm}{d\ln c_l(x,t)}$[a], [83]	–	$(0.601-0.24c_l^{0.5}+0.982(1-0.0052(T-294))c_l^{1.5})\cdot(1-t_+^0)^{-1}-1$		
Transference number t_+^0 [83]	–	0.38		
Reference concentration $c_{l,ref}$	mol m^{-3}	1.0		

[a] Analytic functions for the electrolyte are physically not interpretable. Input arguments are to be normalized (concentration c_l per mol L^{-1} and temperature T per K). The functions are only valid for $c_l \in$ [0 mol L^{-1}; ≤4 mol L^{-1}]. The output value is to be interpreted in the unit given in the table.
[b] Calculated.
[c] Estimated.
[d] Fitted.
[e] Measured.

B.5. Solid diffusion coefficient

Using measurement data at C-rates of 4C, the solid diffusion inside active material particles is considered to be limiting to the cell performance. Minimizing the RMSE between measurement and simulation in COMSOL Multiphysics by fitting the solid diffusion coefficient yields the final value listed in Table 5.

References

[1] M. Killer, M. Farrokhseresht, N.G. Paterakis, Implementation of large-scale li-ion battery energy storage systems within the EMEA region, Appl. Energy 260 (2020) 114166, http://dx.doi.org/10.1016/j.apenergy.2019.114166.

[2] H. Hesse, M. Schimpe, D. Kucevic, A. Jossen, Lithium-ion battery storage for the grid—A review of stationary battery storage system design tailored for applications in modern power grids, Energies 10 (12) (2017) 2107, http://dx.doi.org/10.3390/en10122107.

[3] J. Figgener, P. Stenzel, K.-P. Kairies, J. Linßen, D. Haberschusz, O. Wessels, G. Angenendt, M. Robinius, D. Stolten, D.U. Sauer, The development of stationary battery storage systems in Germany – A market review, J. Energy Storage 29 (2020) 101153, http://dx.doi.org/10.1016/j.est.2019.101153.

[4] J. Vetter, P. Novák, M.R. Wagner, C. Veit, K.-C. Möller, J.O. Besenhard, M. Winter, M. Wohlfahrt-Mehrens, C. Vogler, A. Hammouche, Ageing mechanisms in lithium-ion batteries, J. Power Sources 147 (2005) 269–281, http://dx.doi.org/10.1016/j.jpowsour.2005.01.006.

[5] X. Han, L. Lu, Y. Zheng, X. Feng, Z. Li, J. Li, M. Ouyang, A review on the key issues of the lithium ion battery degradation among the whole life cycle, eTransportation (2019) http://dx.doi.org/10.1016/j.etran.2019.100005.

[6] J.S. Edge, S. O'Kane, R. Prosser, N.D. Kirkaldy, A.N. Patel, A. Hales, A. Ghosh, W. Ai, J. Chen, J. Yang, S. Li, M.-C. Pang, L. Bravo Diaz, A. Tomaszewska, M.W. Marzook, K.N. Radhakrishnan, H. Wang, Y. Patel, B. Wu, G.J. Offer, Lithium ion battery degradation: what you need to know, Phys. Chem. Chem. Phys.: PCCP 23 (14) (2021) 8200–8221, http://dx.doi.org/10.1039/d1cp00359c.

[7] U.S. Department of Energy, Energy storage grand challenge: Energy storage market report, 2020, URL https://www.energy.gov/energy-storage-grand-challenge/downloads/energy-storage-market-report-2020.

[8] J. Figgener, C. Hecht, D. Haberschusz, J. Bors, K.G. Spreuer, K.-P. Kairies, P. Stenzel, D.U. Sauer, The development of battery storage systems in Germany: A market review (status 2023), 2022, URL http://arxiv.org/pdf/2203.06762v3.

[9] L.C. Casals, B. Amante García, C. Canal, Second life batteries lifespan: Rest of useful life and environmental analysis, J. Environ. Manag. 232 (2019) 354–363, http://dx.doi.org/10.1016/j.jenvman.2018.11.046.

[10] M. Shahjalal, P.K. Roy, T. Shams, A. Fly, J.I. Chowdhury, M.R. Ahmed, K. Liu, A review on second-life of li-ion batteries: prospects, challenges, and issues, Energy 241 (4) (2022) 122881, http://dx.doi.org/10.1016/j.energy.2021.122881.

[11] C.R. Birkl, M.R. Roberts, E. McTurk, P.G. Bruce, D.A. Howey, Degradation diagnostics for lithium ion cells, J. Power Sources 341 (2017) 373–386, http://dx.doi.org/10.1016/j.jpowsour.2016.12.011.

[12] N. Collath, B. Tepe, S. Englberger, A. Jossen, H. Hesse, Aging aware operation of lithium-ion battery energy storage systems: A review, J. Energy Storage 55 (11) (2022) 105634, http://dx.doi.org/10.1016/j.est.2022.105634.

[13] P.M. Attia, A. Bills, F. Brosa Planella, P. Dechent, G. dos Reis, M. Dubarry, P. Gasper, R. Gilchrist, S. Greenbank, D. Howey, O. Liu, E. Khoo, Y. Preger, A. Soni, S. Sripad, A.G. Stefanopoulou, V. Sulzer, Review—"Knees" in lithium-ion battery aging trajectories, J. Electrochem. Soc. 169 (6) (2022) 060517, http://dx.doi.org/10.1149/1945-7111/ac6d13.

[14] F. Wankmüller, P.R. Thimmapuram, K.G. Gallagher, A. Botterud, Impact of battery degradation on energy arbitrage revenue of grid-level energy storage, J. Energy Storage 10 (11) (2017) 56–66, http://dx.doi.org/10.1016/j.est.2016.12.004.

[15] K. Uddin, R. Gough, J. Radcliffe, J. Marco, P. Jennings, Techno-economic analysis of the viability of residential photovoltaic systems using lithium-ion batteries for energy storage in the united kingdom, Appl. Energy 206 (10) (2017) 12–21, http://dx.doi.org/10.1016/j.apenergy.2017.08.170.

[16] N. Collath, P. Gasper, A. Jossen, K. Smith, H. Hesse, The economic impact of battery degradation modelling uncertainty, in: 2022 IEEE Power & Energy Society General Meeting, PESGM, IEEE, 2022, pp. 1–5, http://dx.doi.org/10.1109/PESGM48719.2022.9916844.

[17] J. Cai, H. Zhang, X. Jin, Aging-aware predictive control of PV-battery assets in buildings, Appl. Energy 236 (2019) 478–488, http://dx.doi.org/10.1016/j.apenergy.2018.12.003.

[18] J. Engels, B. Claessens, G. Deconinck, Techno-economic analysis and optimal control of battery storage for frequency control services, applied to the german market, Appl. Energy 242 (2019) 1036–1049, http://dx.doi.org/10.1016/j.apenergy.2019.03.128.

[19] T. Weitzel, M. Schneider, C.H. Glock, F. Löber, S. Rinderknecht, Operating a storage-augmented hybrid microgrid considering battery aging costs, J. Clean. Prod. 188 (7) (2018) 638–654, http://dx.doi.org/10.1016/j.jclepro.2018.03.296.

[20] E. Kruger, Q.T. Tran, Minimal aging operating strategies for battery energy storage systems in photovoltaic applications, in: 2016 IEEE PES Innovative Smart Grid Technologies Conference Europe (ISGT-Europe), IEEE, 2016, pp. 1–6, http://dx.doi.org/10.1109/ISGTEurope.2016.7856325.

[21] J. Keil, A. Jossen, Electrochemical modeling of linear and nonlinear aging of lithium-ion cells, J. Electrochem. Soc. 167 (11) (2020) 110535, http://dx.doi.org/10.1149/1945-7111/aba44f.

[22] P. Fermín-Cueto, E. McTurk, M. Allerhand, E. Medina-Lopez, M.F. Anjos, J. Sylvester, G. dos Reis, Identification and machine learning prediction of knee-point and knee-onset in capacity degradation curves of lithium-ion cells, Energy AI 1 (5) (2020) 100006, http://dx.doi.org/10.1016/j.egyai.2020.100006.

[23] N. Padmanabhan, M. Ahmed, K. Bhattacharya, Battery energy storage systems in energy and reserve markets, IEEE Trans. Power Syst. 35 (1) (2020) 215–226, http://dx.doi.org/10.1109/TPWRS.2019.2936131.

[24] M. Kazemi, H. Zareipour, Long-term scheduling of battery storage systems in energy and regulation markets considering battery's lifespan, IEEE Trans. Smart Grid 9 (6) (2018) 6840–6849, http://dx.doi.org/10.1109/TSG.2017.2724919.

[25] Y. Shi, B. Xu, Y. Tan, D. Kirschen, B. Zhang, Optimal battery control under cycle aging mechanisms in pay for performance settings, IEEE Trans. Automat. Control 64 (6) (2019) 2324–2339, http://dx.doi.org/10.1109/TAC.2018.2867507.

[26] G. Angenendt, S. Zurmühlen, H. Axelsen, D.U. Sauer, Comparison of different operation strategies for PV battery home storage systems including forecast-based operation strategies, Appl. Energy 229 (1) (2018) 884–899, http://dx.doi.org/10.1016/j.apenergy.2018.08.058.

[27] G. Cardoso, T. Brouhard, N. DeForest, D. Wang, M. Heleno, L. Kotzur, Battery aging in multi-energy microgrid design using mixed integer linear programming, Appl. Energy 231 (2018) 1059–1069, http://dx.doi.org/10.1016/j.apenergy.2018.09.185.

[28] N. Collath, M. Cornejo, V. Engwerth, H. Hesse, A. Jossen, Increasing the lifetime profitability of battery energy storage systems through aging aware operation, Appl. Energy 348 (14) (2023) 121531, http://dx.doi.org/10.1016/j.apenergy.2023.121531.

[29] M. Johnen, S. Pitzen, U. Kamps, M. Kateri, P. Dechent, D.U. Sauer, Modeling long-term capacity degradation of lithium-ion batteries, J. Energy Storage 34 (9) (2021) 102011, http://dx.doi.org/10.1016/j.est.2020.102011.

[30] S.F. Schuster, T. Bach, E. Fleder, J. Müller, M. Brand, G. Sextl, A. Jossen, Nonlinear aging characteristics of lithium-ion cells under different operational conditions, J. Energy Storage 1 (2015) 44–53, http://dx.doi.org/10.1016/j.est.2015.05.003.

[31] X.-G. Yang, Y. Leng, G. Zhang, S. Ge, C.-Y. Wang, Modeling of lithium plating induced aging of lithium-ion batteries: Transition from linear to nonlinear aging, J. Power Sources 360 (2017) 28–40, http://dx.doi.org/10.1016/j.jpowsour.2017.05.110.

[32] S. Atalay, M. Sheikh, A. Mariani, Y. Merla, E. Bower, W.D. Widanage, Theory of battery ageing in a lithium-ion battery: Capacity fade, nonlinear ageing and lifetime prediction, J. Power Sources 478 (2020) 229026, http://dx.doi.org/10.1016/j.jpowsour.2020.229026.

[33] M. Doyle, T.F. Fuller, J. Newman, Modeling of galvanostatic charge and discharge of the lithium/polymer/insertion cell, J. Electrochem. Soc. 140 (1993) 1526–1533, http://dx.doi.org/10.1149/1.2221597.

[34] M. Doyle, J. Newman, Modeling the performance of rechargeable lithium-based cells: design correlations for limiting cases, J. Power Sources (1995) 45–51, http://dx.doi.org/10.1016/0378-7753(94)02038-5.

[35] F. Kindermann, J. Keil, A. Frank, A. Jossen, A SEI modeling approach distinguishing between capacity and power fade, J. Electrochem. Soc. 164 (12) (2017) E287–E293, http://dx.doi.org/10.1149/2.0321712jes.

[36] R. Fang, P. Dong, H. Ge, J. Fu, Z. Li, J. Zhang, Capacity plunge of lithium-ion batteries induced by electrolyte drying-out: Experimental and modeling study, J. Energy Storage 42 (1) (2021) 103013, http://dx.doi.org/10.1016/j.est.2021.103013.

[37] M. Ecker, N. Nieto, S. Käbitz, J. Schmalstieg, H. Blanke, A. Warnecke, D.U. Sauer, Calendar and cycle life study of Li(NiMnCo)O2-based 18650 lithium-ion batteries, J. Power Sources 248 (9) (2014) 839–851, http://dx.doi.org/10.1016/j.jpowsour.2013.09.143.

[38] Z. Ma, R. Yang, Z. Wang, A novel data-model fusion state-of-health estimation approach for lithium-ion batteries, Appl. Energy 237 (2019) 836–847, http://dx.doi.org/10.1016/j.apenergy.2018.12.071.

[39] X. Ma, J.E. Harlow, J. Li, L. Ma, D.S. Hall, S. Buteau, M. Genovese, M. Cormier, J.R. Dahn, Editors' choice—Hindering rollover failure of Li[Ni 0.5 Mn 0.3 Co 0.2]O 2 /graphite pouch cells during long-term cycling, J. Electrochem. Soc. 166 (4) (2019) A711–A724, http://dx.doi.org/10.1149/2.0801904jes.

[40] A. Pfrang, A. Kersys, A. Kriston, D.U. Sauer, C. Rahe, S. Käbitz, E. Figgemeier, Long-term cycling induced jelly roll deformation in commercial 18650 cells, J. Power Sources 392 (2018) 168–175, http://dx.doi.org/10.1016/j.jpowsour.2018.03.065.

[41] M. Petzl, M. Kasper, M.A. Danzer, Lithium plating in a commercial lithium-ion battery – A low-temperature aging study, J. Power Sources 275 (2015) 799–807, http://dx.doi.org/10.1016/j.jpowsour.2014.11.065.

[42] M. Klett, R. Eriksson, J. Groot, P. Svens, K. Ciosek Högström, R.W. Lindström, H. Berg, T. Gustafson, G. Lindbergh, K. Edström, Non-uniform aging of cycled commercial LiFePO4//graphite cylindrical cells revealed by post-mortem analysis, J. Power Sources 257 (2014) 126–137, http://dx.doi.org/10.1016/j.jpowsour.2014.01.105.

[43] S. Schindler, M. Bauer, H. Cheetamun, M.A. Danzer, Fast charging of lithium-ion cells: Identification of aging-minimal current profiles using a design of experiment approach and a mechanistic degradation analysis, J. Energy Storage 19 (2018) 364–378, http://dx.doi.org/10.1016/j.est.2018.08.002.

[44] J. Keil, N. Paul, V. Baran, P. Keil, R. Gilles, A. Jossen, Linear and nonlinear aging of lithium-ion cells investigated by electrochemical analysis and in-situ neutron diffraction, J. Electrochem. Soc. 166 (16) (2019) A3908–A3917, http://dx.doi.org/10.1149/2.1271915jes.

[45] M. Lewerenz, J. Münnix, J. Schmalstieg, S. Käbitz, M. Knips, D.U. Sauer, Systematic aging of commercial LiFePO 4 |graphite cylindrical cells including a theory explaining rise of capacity during aging, J. Power Sources 345 (2017) 254–263, http://dx.doi.org/10.1016/j.jpowsour.2017.01.133.

[46] K.A. Severson, P.M. Attia, N. Jin, N. Perkins, B. Jiang, Z. Yang, M.H. Chen, M. Aykol, P.K. Herring, D. Fraggedakis, M.Z. Bazant, S.J. Harris, W.C. Chueh, R.D. Braatz, Data-driven prediction of battery cycle life before capacity degradation, Nat. Energy 4 (2019) 383–391, http://dx.doi.org/10.1038/s41560-019-0356-8.

[47] N. Omar, M.A. Monem, Y. Firouz, J. Salminen, J. Smekens, O. Hegazy, H. Gaulous, G. Mulder, P. van den Bossche, T. Coosemans, J. van Mierlo, Lithium iron phosphate based battery – Assessment of the aging parameters and development of cycle life model, Appl. Energy 113 (2014) 1575–1585, http://dx.doi.org/10.1016/j.apenergy.2013.09.003.

[48] S.F. Schuster, Reuse of Automotive Lithium-Ion Batteries: An Assessment from the Cell Aging Perspective (Ph.D. thesis), Technical University of Munich, Munich, 2016, URL https://mediatum.ub.tum.de/?id=1311465.

[49] M. Möller, D. Kucevic, N. Collath, A. Parlikar, P. Dotzauer, B. Tepe, S. Englberger, A. Jossen, H. Hesse, Simses: A holistic simulation framework for modeling and analyzing stationary energy storage systems, J. Energy Storage 49 (11) (2022) 103743, http://dx.doi.org/10.1016/j.est.2021.103743.

[50] V. Sulzer, S.G. Marquis, R. Timms, M. Robinson, S.J. Chapman, Python battery mathematical modelling (PyBaMM), J. Open Res. Softw. 9 (1) (2021) 14, http://dx.doi.org/10.5334/jors.309.

[51] N. Collath, Late life BESS toolchain: Suitability of late-life lithium-ion cells for battery energy storage systems, 2023, URL https://gitlab.lrz.de/open-ees-ses/late-life-bess-toolchain.

[52] J. Christiansen, European market outlook for residential battery storage 2022–2026, 2022, URL https://www.solarpowereurope.org/insights/thematic-reports/european-market-outlook-for-residential-battery-storage-1.

[53] J. Figgener, C. Hecht, D. Haberschusz, J. Bors, K.G. Spreuer, K.-P. Kairies, P. Stenzel, D.U. Sauer, The development of battery storage systems in Germany: A market review (status 2023), 2023, URL http://arxiv.org/pdf/2203.06762v3.

[54] D. Kucevic, B. Tepe, S. Englberger, A. Parlikar, M. Mühlbauer, O. Bohlen, A. Jossen, H. Hesse, Standard battery energy storage system profiles: Analysis of various applications for stationary energy storage systems using a holistic simulation framework, J. Energy Storage 28 (2020) 101077, http://dx.doi.org/10.1016/j.est.2019.101077.

[55] T. Tjaden, J. Bergner, J. Weniger, V. Quaschning, Repräsentative elektrische lastprofile für wohngebäude in deutschland auf 1-sekündiger datenbasis (in german), 2015, URL https://pvspeicher.htw-berlin.de/veroeffentlichungen/daten/.

[56] BDEW, BDEW-strompreisanalyse juli 2023, 2023, URL https://www.bdew.de/service/daten-und-grafiken/bdew-strompreisanalyse/.

[57] Bundesnetzagentur, Archivierte EEG-vergütungssätze und datenmeldungen, 2023, URL https://www.bundesnetzagentur.de/DE/Fachthemen/ElektrizitaetundGas/ErneuerbareEnergien/EEG_Foerderung/Archiv_VergSaetze/start.html.

[58] G. Notton, V. Lazarov, L. Stoyanov, Optimal sizing of a grid-connected PV system for various PV module technologies and inclinations, inverter efficiency characteristics and locations, Renew. Energy 35 (2) (2010) 541–554, http://dx.doi.org/10.1016/j.renene.2009.07.013.

[59] N. Collath, Aging_aware_mpc: Aging aware MPC for battery energy storage systems, 2023, URL https://gitlab.lrz.de/open-ees-ses/aging-aware-MPC.

[60] Fraunhofer Institute for Solar Energy Systems, Energy charts, 2022, URL https://www.energy-charts.info/?l=en&c=DE.

[61] EPEX Spot, EPEX spot indices, 2023, URL https://www.epexspot.com/en/indices.

[62] W. Ai, N. Kirkaldy, Y. Jiang, G. Offer, H. Wang, B. Wu, A composite electrode model for lithium-ion batteries with silicon/graphite negative electrodes, J. Power Sources 527 (1) (2022) 231142, http://dx.doi.org/10.1016/j.jpowsour.2022.231142.

[63] M. Schimpe, M.E.v. Kuepach, M. Naumann, H. Hesse, K. Smith, A. Jossen, Comprehensive modeling of temperature-dependent degradation mechanisms in lithium iron phosphate batteries, J. Electrochem. Soc. 165 (2) (2018) A181–A193, http://dx.doi.org/10.1149/2.1181714jes.

[64] Y. Li, K. Liu, A.M. Foley, A. Zülke, M. Berecibar, E. Nanini-Maury, J. van Mierlo, H.E. Hoster, Data-driven health estimation and lifetime prediction of lithium-ion batteries: A review, Renew. Sustain. Energy Rev. 113 (2019) 109254, http://dx.doi.org/10.1016/j.rser.2019.109254.

[65] V. Sulzer, P. Mohtat, S. Pannala, J.B. Siegel, A.G. Stefanopoulou, Accelerated battery lifetime simulations using adaptive inter-cycle extrapolation algorithm, J. Electrochem. Soc. 168 (12) (2021) 120531, http://dx.doi.org/10.1149/1945-7111/ac3e48.

[66] J. Reniers, G. Mulder, D. Howey, Review and performance comparison of mechanical-chemical degradation models for lithium-ion batteries, J. Electrochem. Soc. 166 (14) (2019) A3189–A3200, http://dx.doi.org/10.1149/2.0281914jes.

[67] I. Laresgoiti, S. Käbitz, M. Ecker, D.U. Sauer, Modeling mechanical degradation in lithium ion batteries during cycling: Solid electrolyte interphase fracture, J. Power Sources 300 (3) (2015) 112–122, http://dx.doi.org/10.1016/j.jpowsour.2015.09.033.

[68] B. Xu, J. Zhao, T. Zheng, E. Litvinov, D.S. Kirschen, Factoring the cycle aging cost of batteries participating in electricity markets, IEEE Trans. Power Syst. 33 (2) (2018) 2248–2259, http://dx.doi.org/10.1109/TPWRS.2017.2733339.

[69] J. Bareño, I.A. Shkrob, J.A. Gilbert, M. Klett, D.P. Abraham, Capacity fade and its mitigation in li-ion cells with silicon-graphite electrodes, J. Phys. Chem. C 121 (38) (2017) 20640–20649, http://dx.doi.org/10.1021/acs.jpcc.7b06118.

[70] W. Ai, L. Kraft, J. Sturm, A. Jossen, B. Wu, Electrochemical thermal-mechanical modelling of stress inhomogeneity in lithium-ion pouch cells, J. Electrochem. Soc. (2020) http://dx.doi.org/10.1149/2.0122001JES.

[71] P.M. Attia, W.C. Chueh, S.J. Harris, Revisiting the t0.5 dependence of SEI growth, J. Electrochem. Soc. 167 (9) (2020) 090535, http://dx.doi.org/10.1149/1945-7111/ab8ce4.

[72] P. Gasper, N. Collath, H.C. Hesse, A. Jossen, K. Smith, Machine-learning assisted identification of accurate battery lifetime models with uncertainty, J. Electrochem. Soc. 169 (8) (2022) 080518, http://dx.doi.org/10.1149/1945-7111/ac86a8.

[73] M. Dubarry, C. Truchot, B.Y. Liaw, Synthesize battery degradation modes via a diagnostic and prognostic model, J. Power Sources 219 (2012) 204–216, http://dx.doi.org/10.1016/j.jpowsour.2012.07.016.

[74] M. Safari, M. Morcrette, A. Teyssot, C. Delacourt, Multimodal physics-based aging model for life prediction of li-ion batteries, J. Electrochem. Soc. 2009 (A145) (2009) http://dx.doi.org/10.1149/1.3043429.

[75] S.E.J. O'Kane, W. Ai, G. Madabattula, D. Alonso-Alvarez, R. Timms, V. Sulzer, J.S. Edge, B. Wu, G.J. Offer, M. Marinescu, Lithium-ion battery degradation: how to model it, Phys. Chem. Chem. Phys. : PCCP 24 (13) (2022) 7909–7922, http://dx.doi.org/10.1039/d2cp00417h.

[76] R. Xu, Y. Yang, F. Yin, P. Liu, P. Cloetens, Y. Liu, F. Lin, K. Zhao, Heterogeneous damage in li-ion batteries: Experimental analysis and theoretical modeling, J. Mech. Phys. Solids 129 (2019) 160–183, http://dx.doi.org/10.1016/j.jmps.2019.05.003.

[77] I. Andriunas, Z. Milojevic, N. Wade, P.K. Das, Impact of solid-electrolyte interphase layer thickness on lithium-ion battery cell surface temperature, J. Power Sources 525 (2022) 231126, http://dx.doi.org/10.1016/j.jpowsour.2022.231126.

[78] B. Han, J.R. Harding, J.K.S. Goodman, Z. Cai, Q.C. Horn, End-of-charge temperature rise and state-of-health evaluation of aged lithium-ion battery, Energies 16 (1) (2023) 405, http://dx.doi.org/10.3390/en16010405.

[79] J. Sturm, Everlasting electric vehicle enhanced range, lifetime and safety through ingenious battery management, 2018, http://dx.doi.org/10.3030/713771.

[80] M.A. Cabanero, N. Boaretta, M. Röder, J. Müller, J. Kallo, A. Latz, Direct determination of diffusion coefficients in commercial li-ion batteries, J. Electrochem. Soc. (2018) A847–A855, http://dx.doi.org/10.1149/2.0301805jes.

[81] H.-J. Noh, S. Youn, C.S. Yoon, Y.-K. Sun, Comparison of the structural and electrochemical properties of layered Li[NixCoyMnz]O2 (x=1/3, 0.5, 0.6, 0.7, 0.8 and 0.85) cathode material for lithium-ion batteries, J. Power Sources 233 (2013) 121–130, http://dx.doi.org/10.1016/j.jpowsour.2013.01.063.

[82] R. Amin, D.B. Ravnsbæk, Y.-M. Chiang, Characterization of electronic and ionic transport in Li 1-x Ni 0.8 Co 0.15 Al 0.05 O 2 (NCA), J. Electrochem. Soc. 162 (7) (2015) A1163–A1169, http://dx.doi.org/10.1149/2.0171507jes.

[83] L.O. Valoen, J.N. Reimers, Transport properties of LiPF6-based li-ion battery electrolytes, J. Electrochem. Soc. 152 (5) (2005) A882–A891, http://dx.doi.org/10.1149/1.1872737.

[84] J. Schmitt, M. Schindler, A. Jossen, Change in the half-cell open-circuit potential curves of silicon–graphite and nickel-rich lithium nickel manganese cobalt oxide during cycle aging, J. Power Sources 506 (1) (2021) 230240, http://dx.doi.org/10.1016/j.jpowsour.2021.230240.

[85] J. Sturm, A. Rheinfeld, I. Zilberman, F.B. Spingler, S. Kosch, F. Frie, A. Jossen, Modeling and simulation of inhomogeneities in a 18650 nickel-rich, silicon-graphite lithium-ion cell during fast charging, J. Power Sources 412 (13) (2019) 204–223, http://dx.doi.org/10.1016/j.jpowsour.2018.11.043.

[86] J. Wilhelm, S. Seidlmayer, S. Erhard, M. Hofmann, R. Gilles, A. Jossen, In situ neutron diffraction study of lithiation gradients in graphite anodes during discharge and relaxation, J. Electrochem. Soc. (2018) A1846–A1856, http://dx.doi.org/10.1149/2.1231809jes.

7 Conclusion and potential for future research

7.1 Conclusion

This work focuses on developing guidelines and methods for the aging aware operation of lithium-ion based BESSs. For that purpose, a first comprehensive review of the field is presented. Based on the gaps found in the literature, an MPC framework is proposed for designing and benchmarking aging aware operation strategies. Furthermore, an aging aware operation strategy for peak shaving that accounts for uncertainty in load forecasts is developed, and the impact of uncertainty in degradation modeling on techno-economic assessments of BESSs is investigated. Lastly, a physicochemical aging model is developed to investigate the nonlinear aging phase with its increased degradation rate in typical stationary BESS applications.

First, in Chapter 3, the relevant aging mechanisms for commonly used lithium-ion batteries are summarized from the literature, and the stress factors are categorized into calendar and cyclic aging stress factors. In addition, prevalent approaches for degradation modeling are presented. Furthermore, the existing literature in the field of aging aware operation is presented in a concise tabular form, and various categories of methods for aging aware operation are derived. The review shows that defining aging cost based on either the battery or the BESS investment cost and including them in the objective function is a widespread method. In addition, most publications in the field use MILPs as a scheduling method and rely on simplified semi-empirical degradation models that often only consider a subset of the total calendar and cyclic aging stress factors.

A case study is conducted as part of the review to investigate which stress factors affect the aging behavior the most in typical stationary applications and, therefore, should be considered for selecting a suitable degradation model and deriving aging aware operation strategies. This case study is performed with the open-source SimSES tool, which is further developed and used throughout the subsequent chapters of this thesis. SimSES is presented in Appendix A. For the peak shaving application, the high average SOC is the most relevant stress factor and leads to significant calendar aging. In the self-consumption increase application, the high DOC and C^{rate} significantly affect cyclic aging. This application further leads to high SOC values if the BESS is fully charged from the PV system around midday. For a BESS providing FCR, attention should be paid to the overall low DOC and C^{rate} when selecting a suitable degradation model for modelling this application.

Following this review, the MPC framework for designing and benchmarking aging aware operation strategies is presented in Chapter 4. The underlying principle is to use a detailed system model, or digital twin, to evaluate different operation strategies, especially different optimization model formulations, on the same reference. Optimization models are constrained in complexity by the solution methods that are used to solve them, e.g., MILP requiring linear or linearized objective functions and constraints. However, the more detailed system model of the digital twin is not subject to such constraints. Specifically, this allows quantifying the benefit of different levels of complexity for degradation modeling as part of the optimization model.

Here, SimSES is used as the system model, and different optimization models are derived and compared for the aging aware operation of a BESS for the application of energy arbitrage on the intraday market of the EPEX electricity exchange. For this investigation, a linearized calendar and a linearized cyclic degradation model for the investigated LFP cell are developed, which are solvable as part of a MILP. It is shown that a significant increase in lifetime profitability can be achieved by determining the optimal aging cost instead of the prevalent approach in the literature of determining the aging cost based on the battery or BESS investment cost. Furthermore, the lifetime profit from energy arbitrage can be increased by an additional 24.9 % over the same time period when using the linearized calendar degradation model and by 29.3 % when using both the linearized calendar and the linearized cyclic degradation model, compared to an energy throughput-based aging cost model. The more advanced optimization models lead to the BESS avoiding energy arbitrage opportunities that would be highly profitable in the short term but also lead to significant battery degradation and, therefore, an earlier EOL. Instead, more energy arbitrage opportunities are part of the optimal solution that, on average, are less profitable but also cause less battery degradation and, in total, lead to a higher lifetime profit in the long term. The significant increase in lifetime profit highlights the financial benefit of aging aware operation for BESS operators.

Chapter 5 deals with two types of uncertainty in the context of aging aware operation: uncertainty affecting the operation strategy, i.e., load forecast errors in this case, and uncertainty of degradation models. Chapter 5.1 proposes an adaptive rule-based aging aware operation strategy for peak shaving with BESSs. The underlying principle is to charge up the BESS sufficiently early before a load peak with the energy that is forecasted to be needed during the load peak, thereby reducing the average SOC and calendar aging effects. Load forecasts generated with an artificial neural network are used as input, and confidence intervals for the required energy are derived based on the past accuracy of the load forecasts. The developed operation strategy is compared to a scenario with perfect foresight and a basic peak shaving strategy. With the proposed operation strategy, the capacity loss is reduced by 32.2 % over the investigated five-year timeframe compared to the basic peak shaving strategy. When assuming perfect foresight of the load profile, the capacity loss can be reduced by 52.6 %. The significant reduction of capacity fade compared to the basic peak shaving strategy shows the potency of the proposed aging aware operation strategy. At the same time, the gap to the perfect foresight scenario highlights that the often-used assumption of perfect foresight would lead to overly optimistic results.

Chapter 5.2 builds on top of the modeling approach presented in Appendix B and investigates how uncertainty in degradation models affects techno-economic assessments of BESSs. Three representative BESSs with LFP cells are modeled for the applications of peak shaving, self-consumption increase, and FCR. The expert-identified degradation model is compared to the machine-learning assisted model using SimSES. The results show that the confidence intervals of the NPV can be reduced by employing the model with the higher parameter fit quality, i.e., the machine-learning assisted model. The results further show that considering degradation modeling uncertainty is especially important when, first, the generated profit highly depends on the available battery capacity. Second, when a fixed SOH limit acts as the threshold for the assumed EOL, e.g., at 80 % SOH, since due to the sublinear form of the degradation model slight errors can lead to significantly varying lifetime predictions. Third, when long evaluation periods and low interest rates are the focus of the analysis since the dampening effect of discounting the cash flow in later years is less pronounced for low interest rates.

Lastly, Chapter 6 investigates the performance of significantly aged cells, named late life cells, in typical stationary applications.

First, a prismatic cell, which is known to be used in multiple operational BESSs, is compared at varying

SOH values to a cylindrical cell that is primarily intended for EV applications but can be envisioned in stationary second-life applications. For that purpose, an electrical characterization of the cells is performed, and equivalent-circuit models are derived and implemented in SimSES. The prismatic cell shows a higher roundtrip efficiency and nominal power range, which translates into different profit potentials for the two investigated applications. As the case study shows, the profit generated in an energy arbitrage application is more affected by a reduced SOH than in a self-consumption increase application. Furthermore, the prismatic cell has a higher profit potential in both applications over all SOH ranges than the cylindrical cell. However, this difference is more pronounced for the energy arbitrage application as well. For example, in the energy arbitrage application, the profit potential of the cylindrical cell at 60 % SOH is 10.3 % lower than the profit potential of the prismatic cell. For the self-consumption increase application, this difference in profit potential between the two cells is only 0.7 % at 60 % SOH. While the differences in profit potential are marginal for the self-consumption increase application, they are noticeable for the energy arbitrage application. They should, therefore, be considered when selecting cells for a BESS.

Furthermore, for the cylindrical cells, a physicochemical aging model is developed and parameterized based on an experimental aging study to investigate the nonlinear aging phase with its increased degradation rate in typical stationary applications. The aging model includes the mechanisms of lithium plating, LAM from particle stress, and SEI growth, both continuous over time and accelerated through cycling the cell. The model is implemented in PyBaMM, and an interface is developed to link it to SimSES. Notably, the accompanying aging study reveals that cells that have entered the nonlinear aging phase can transition back to a significantly lower degradation rate through adapted operating conditions, namely a reduced charge rate and narrowed operating voltage window. The case study shows that while the cells initially degrade faster in the self-consumption increase application due to faster SEI growth, the higher charge rates in the energy arbitrage application lead to an earlier onset of lithium plating and, thereby, nonlinear aging. However, by adapting the operating conditions below 80 % SOH, the lifetime in the energy arbitrage application can be significantly prolonged, and the NPV over the investigated ten-year timeframe increases by 39.8 %. This highlights the benefit of considering and delaying nonlinear aging as part of a holistic aging aware operation strategy for BESSs, for which the here developed open-source simulation approach may serve as a foundation.

7.2 Potential for future research

While this thesis addresses several topics in the field of aging aware operation, the potential for future research arises in multiple areas.

The importance of understanding and delaying nonlinear aging effects towards the EOL is only going to increase now that the first BESSs have been operational for multiple years and with stationary applications still being envisioned as a second-life scenario for retired batteries from the increasing number of EVs. Therefore, especially the operating conditions that delay or prevent nonlinear aging require additional research. For example, the existing literature provides contradicting conclusions with regard to whether increasing the discharge rate accelerates or delays the onset of nonlinear aging. Similarly, contradicting results can be found with regards to cycling a lithium-ion cell in high compared to low SOC ranges. Furthermore, most existing studies that investigate the nonlinear aging behavior of lithium-ion cells only test individual cells, while in actual applications, multiple cells are connected to modules. Therefore, the effect of parallel and serial connections of cells to battery modules on the nonlinear aging behavior requires more investigation as well.

The small-scale aging study conducted in this thesis showed that nonlinear aging can not only be delayed by adapting the operating conditions before its occurrence, but lithium-ion cells that have already entered the nonlinear aging phase can transition back to a significantly reduced degradation rate by adapting the operating conditions after extended cycling. This was also supported by the developed physicochemical aging model. This is, in general, a highly promising result since the operating conditions of a BESS could simply be adapted once nonlinear aging behavior is first observed, which can then lead to a substantial lifetime extension. However, this effect requires additional investigation as well with regard to the exact operating conditions that influence it. Here, only one set of adapted operating conditions was investigated, i.e., a reduced charge rate combined with a narrowed voltage window. The cell temperature was kept at a constant 25 °C in the aging study and was assumed to be constant in the model as well. If lithium plating is the expected mechanism that leads to nonlinear aging, operating late-life cells at slightly higher temperatures during charging could further extend their lifetime. In addition, how far these results are transferable to different types of lithium-ion cells remains to be investigated as well.

In terms of aging aware operation in the nonlinear aging phase, adapted but constant new operating limits below 80 % SOH were proposed, which matched those from the cell aging study. This already resulted in a significant lifetime and profit increase for the investigated energy arbitrage application. While this is an easy-to-implement heuristic, better results could be achieved through dynamic criteria for gradually adapting, for example, the maximum charge rate and charge cut-off voltage based on the present SOH of the battery cell. This could be even further improved by modeling nonlinear aging and its stress factors inherently as part of the optimization problem with associated aging cost.

In this thesis, techno-economic analyses were conducted to investigate and quantify the benefit of aging aware operation, using metrics such as the generated profit in a given application and its NPV. The ecological benefit of aging aware operation remains to be quantified. This ecological benefit originates from the prolonged calendar life or additional FECs being delivered before the battery EOL is reached, both enabled through aging aware operation strategies. Such figures for the ecological benefit can provide an increased incentive for the widespread adoption of aging aware operation strategies.

Regarding the proposed MPC framework, the question arises of how accurate the modeling of the degradation behavior as part of the optimization model has to be in order to achieve the desired benefit. For example, instead of using sets of multiple lines to linearize the SOC dependence of calendar aging, a single line may already sufficiently entice the optimization to avoid high SOC ranges while making the optimization model less computationally expensive. The proposed MPC framework may serve as a basis for finding a trade-off between modeling accuracy and computationally efficiency for a given application. In the same context, there is a need for methods and tools that automatically transfer semi-empirical or even physicochemical degradation models to reduced-order models that can be solved with standard scheduling methods. This could include the linearization of the dependence of capacity loss on the relevant aging stress factors, which can then be solved as part of a MILP.

Using the extensive field data that BESS operators have gathered over the past years provides an opportunity to use data-driven methods for parameterizing degradation models, such as it is aimed for in the research project BattLifeBoost[5]. A fully integrated solution can even be envisioned, in which the degradation model is updated based on field data, and the relevant stress factors of the updated degradation model are automatically linearized and integrated into the optimization model that is used for the aging aware operation of the BESS.

---

[5] BattLifeBoost in the EnArgus databank: https://www.enargus.de/detail/?id=28619541

With the battery technology landscape still rapidly developing, the guidelines and methods developed in this thesis should be transferred to new battery technologies as they enter the market. This may include sodium-ion batteries or solid-state lithium batteries. For such new technologies, the aging stress factors are of interest. While multiple well-parameterized degradation models are available in the literature for commonly used NMC, NCA, and LFP cells, such models will be needed for the new battery technologies as well.

Lastly, the methods and guidelines developed in this thesis remain to be implemented in the constantly growing and aging fleet of lithium-ion based BESSs in order to increase the resource efficiency of energy storage.

References

[1] Allerhand, A.: *Hydroelectric Power: The First 30 Years [History]*. In: *IEEE Power and Energy Magazine* 18.5 (2020), pp. 76–87. ISSN: 1540-7977. DOI: 10.1109/MPE.2020.2999791 (see p. 1).

[2] Ember - Energy Institute Statistical Review of World Energy: *Electricity Mix - Our World in Data*. 2023. URL: https://ourworldindata.org/electricity-mix (visited on 11/16/2023) (see p. 1).

[3] United Nations: *Sustainable Development Goals*. 2015. URL: https://sdgs.un.org/goals/goal7#targets_and_indicators (visited on 11/16/2023) (see p. 1).

[4] European Commission: *European Green Deal: EU agrees stronger legislation to accelerate the rollout of renewable energy*. 2023. URL: https://ec.europa.eu/commission/presscorner/detail/en/IP_23_2061 (visited on 11/30/2023) (see p. 1).

[5] Sovacool, B. K.: *The intermittency of wind, solar, and renewable electricity generators: Technical barrier or rhetorical excuse?* In: *Utilities Policy* 17 (2009), pp. 288–296. ISSN: 0957-1787. DOI: 10.1016/j.jup.2008.07.001 (see p. 1).

[6] Zsiborács, H., Baranyai, N. H., Vincze, A., Zentkó, L., Birkner, Z., Máté, K., and Pintér, G.: *Intermittent Renewable Energy Sources: The Role of Energy Storage in the European Power System of 2040*. In: *Electronics* 8.7 (2019), p. 729. DOI: 10.3390/electronics8070729 (see p. 1).

[7] Agnew, S. and Dargusch, P.: *Effect of residential solar and storage on centralized electricity supply systems*. In: *Nature Climate Change* 5 (2015), pp. 315–318. ISSN: 1758-678X. DOI: 10.1038/nclimate2523 (see p. 1).

[8] U.S. Department of Energy: *Energy Storage Grand Challenge: Energy Storage Market Report*. 2020. URL: https://www.energy.gov/energy-storage-grand-challenge/downloads/energy-storage-market-report-2020 (see p. 1).

[9] Figgener, J., Hecht, C., Haberschusz, D., Bors, J., Spreuer, K. G., Kairies, K.-P., Stenzel, P., and Sauer, D. U.: *The development of battery storage systems in Germany: A market review (status 2023)*. 2023. URL: http://arxiv.org/pdf/2203.06762v3 (see pp. 1, 12, 13).

[10] BloombergNEF: *Global Energy Storage Market to Grow 15-Fold by 2030*. 2022. URL: https://about.bnef.com/blog/global-energy-storage-market-to-grow-15-fold-by-2030/ (see p. 1).

[11] U.S. Energy Information Administration: *Battery Storage in the United States: An Update on Market Trends*. Ed. by U.S. Department of Energy. 2020. URL: https://www.eia.gov/analysis/studies/electricity/batterystorage/ (visited on 01/23/2024) (see p. 1).

[12] International Renewable Energy Agency: *Electricity storage and renewables: Costs and markets to 2030*. 2017. URL: https://www.irena.org/publications/2017/Oct/Electricity-storage-and-renewables-costs-and-markets (see p. 1).

[13] Henni, S., Becker, J., Staudt, P., Vom Scheidt, F., and Weinhardt, C.: *Industrial peak shaving with battery storage using a probabilistic forecasting approach: Economic evaluation of risk attitude.* In: *Applied Energy* 327 (2022), p. 120088. ISSN: 0306-2619. DOI: `10.1016/j.apenergy.2022.120088` (see pp. 1, 12).

[14] Hesse, H., Martins, R., Musilek, P., Naumann, M., Truong, C., and Jossen, A.: *Economic Optimization of Component Sizing for Residential Battery Storage Systems.* In: *Energies* 10 (2017), p. 835. DOI: `10.3390/en10070835` (see p. 1).

[15] Engels, J., Claessens, B., and Deconinck, G.: *Techno-economic analysis and optimal control of battery storage for frequency control services, applied to the German market.* In: *Applied Energy* 242 (2019), pp. 1036–1049. ISSN: 0306-2619. DOI: `10.1016/j.apenergy.2019.03.128` (see pp. 1, 2, 30).

[16] Metz, D. and Saraiva, J. T.: *Use of battery storage systems for price arbitrage operations in the 15- and 60-min German intraday markets.* In: *Electric Power Systems Research* 160 (2018), pp. 27–36. ISSN: 0378-7796. DOI: `10.1016/j.epsr.2018.01.020` (see p. 1).

[17] Kucevic, D., Meißner, R., Jossen, A., and Hesse, H.: "Battery Energy Storage Systems as an Alternative to Conventional Grid Reinforcement." In: *Energy Proceedings*. 2021. DOI: `10.46855/energy-proceedings-9834` (see pp. 1, 8).

[18] Killer, M., Farrokhseresht, M., and Paterakis, N. G.: *Implementation of large-scale Li-ion battery energy storage systems within the EMEA region.* In: *Applied Energy* 260 (2020), p. 114166. ISSN: 0306-2619. DOI: `10.1016/j.apenergy.2019.114166` (see pp. 1, 7, 8).

[19] Kebede, A. A., Coosemans, T., Messagie, M., Jemal, T., Behabtu, H. A., van Mierlo, J., and Berecibar, M.: *Techno-economic analysis of lithium-ion and lead-acid batteries in stationary energy storage application.* In: *Journal of Energy Storage* 40 (2021), p. 102748. ISSN: 2352-152X. DOI: `10.1016/j.est.2021.102748` (see p. 1).

[20] Hesse, H., Schimpe, M., Kucevic, D., and Jossen, A.: *Lithium-Ion Battery Storage for the Grid—A Review of Stationary Battery Storage System Design Tailored for Applications in Modern Power Grids.* In: *Energies* 10 (2017), p. 2107. DOI: `10.3390/en10122107` (see pp. 1, 7).

[21] U.S. Energy Information Administration: *Form EIA-860 detailed data with previous form data.* 2022. URL: `https://www.eia.gov/electricity/data/eia860/` (visited on 11/30/2023) (see p. 1).

[22] Tepe, B., Collath, N., Hesse, H., Rosenthal, M., and Windelen, U.: *Stationäre Batteriespeicher in Deutschland: Aktuelle Entwicklungen und Trends in 2021.* In: *Energiewirtschaftliche Tagesfragen* 71.3 (2021), pp. 23–27. URL: `https://mediatum.ub.tum.de/doc/1601843` (see p. 1).

[23] Vetter, J. et al.: *Ageing mechanisms in lithium-ion batteries.* In: *Journal of Power Sources* 147 (2005), pp. 269–281. ISSN: 0378-7753. DOI: `10.1016/j.jpowsour.2005.01.006` (see p. 2).

[24] Han, X., Lu, L., Zheng, Y., Feng, X., Li, Z., Li, J., and Ouyang, M.: *A review on the key issues of the lithium ion battery degradation among the whole life cycle.* In: *eTransportation* 1 (2019). ISSN: 2590-1168. DOI: `10.1016/j.etran.2019.100005` (see pp. 2, 16, 17).

[25] Edge, J. S. et al.: *Lithium ion battery degradation: what you need to know.* In: *Physical chemistry chemical physics: PCCP* 23.14 (2021), pp. 8200–8221. DOI: `10.1039/d1cp00359c` (see pp. 2, 16, 17).

[26] Uddin, K., Gough, R., Radcliffe, J., Marco, J., and Jennings, P.: *Techno-economic analysis of the viability of residential photovoltaic systems using lithium-ion batteries for energy storage in the United Kingdom*. In: *Applied Energy* 206 (2017), pp. 12–21. ISSN: 0306-2619. DOI: `10.1016/j.apenergy.2017.08.170` (see p. 2).

[27] Wankmüller, F., Thimmapuram, P. R., Gallagher, K. G., and Botterud, A.: *Impact of battery degradation on energy arbitrage revenue of grid-level energy storage*. In: *Journal of Energy Storage* 10 (2017), pp. 56–66. ISSN: 2352-152X. DOI: `10.1016/j.est.2016.12.004` (see pp. 2, 28, 29).

[28] Cai, J., Zhang, H., and Jin, X.: *Aging-aware predictive control of PV-battery assets in buildings*. In: *Applied Energy* 236 (2019), pp. 478–488. ISSN: 0306-2619. DOI: `10.1016/j.apenergy.2018.12.003` (see pp. 2, 25, 30).

[29] Weitzel, T., Schneider, M., Glock, C. H., Löber, F., and Rinderknecht, S.: *Operating a storage-augmented hybrid microgrid considering battery aging costs*. In: *Journal of Cleaner Production* 188 (2018), pp. 638–654. ISSN: 0959-6526. DOI: `10.1016/j.jclepro.2018.03.296` (see pp. 2, 25, 27, 31).

[30] Kruger, E. and Tran, Q. T.: "Minimal aging operating strategies for battery energy storage systems in photovoltaic applications." In: *2016 IEEE PES Innovative Smart Grid Technologies Conference Europe (ISGT-Europe)*. IEEE, 2016, pp. 1–6. ISBN: 978-1-5090-3358-4. DOI: `10.1109/ISGTEurope.2016.7856325` (see pp. 2, 30).

[31] Collath, N., Tepe, B., Englberger, S., Jossen, A., and Hesse, H.: *Aging aware operation of lithium-ion battery energy storage systems: A review*. In: *Journal of Energy Storage* 55 (2022), p. 105634. ISSN: 2352-152X. DOI: `10.1016/j.est.2022.105634` (see pp. 2, 17–19, 23, 26, 29, 30).

[32] Fermín-Cueto, P., McTurk, E., Allerhand, M., Medina-Lopez, E., Anjos, M. F., Sylvester, J., and dos Reis, G.: *Identification and machine learning prediction of knee-point and knee-onset in capacity degradation curves of lithium-ion cells*. In: *Energy and AI* 1 (2020), p. 100006. ISSN: 2666-5468. DOI: `10.1016/j.egyai.2020.100006` (see p. 2).

[33] Ecker, M., Nieto, N., Käbitz, S., Schmalstieg, J., Blanke, H., Warnecke, A., and Sauer, D. U.: *Calendar and cycle life study of Li(NiMnCo)O2-based 18650 lithium-ion batteries*. In: *Journal of Power Sources* 248 (2014), pp. 839–851. ISSN: 0378-7753. DOI: `10.1016/j.jpowsour.2013.09.143` (see pp. 2, 21, 22).

[34] Schmalstieg, J., Käbitz, S., Ecker, M., and Sauer, D. U.: *A holistic aging model for Li(NiMnCo)O2 based 18650 lithium-ion batteries*. In: *Journal of Power Sources* 257 (2014), pp. 325–334. ISSN: 0378-7753. DOI: `10.1016/j.jpowsour.2014.02.012` (see pp. 2, 17, 21, 23, 24).

[35] Sarasketa-Zabala, E., Gandiaga, I., Rodriguez-Martinez, L. M., and Villarreal, I.: *Calendar ageing analysis of a LiFePO4/graphite cell with dynamic model validations: Towards realistic lifetime predictions*. In: *Journal of Power Sources* 272 (2014), pp. 45–57. ISSN: 0378-7753. DOI: `10.1016/j.jpowsour.2014.08.051` (see pp. 2, 17, 21, 23).

[36] Sarasketa-Zabala, E., Gandiaga, I., Martinez-Laserna, E., Rodriguez-Martinez, L. M., and Villarreal, I.: *Cycle ageing analysis of a LiFePO4/graphite cell with dynamic model validations: Towards realistic lifetime predictions*. In: *Journal of Power Sources* 275 (2015), pp. 573–587. ISSN: 0378-7753. DOI: `10.1016/j.jpowsour.2014.10.153` (see pp. 2, 21, 23).

[37] Naumann, M., Schimpe, M., Keil, P., Hesse, H. C., and Jossen, A.: *Analysis and modeling of calendar aging of a commercial LiFePO4/graphite cell.* In: *Journal of Energy Storage* 17 (2018), pp. 153–169. ISSN: 2352-152X. DOI: `10.1016/j.est.2018.01.019` (see pp. 2, 21, 23, 24, 31, 84).

[38] Naumann, M., Spingler, F. B., and Jossen, A.: *Analysis and modeling of cycle aging of a commercial LiFePO4/graphite cell.* In: *Journal of Power Sources* 451 (2020), p. 227666. ISSN: 0378-7753. DOI: `10.1016/j.jpowsour.2019.227666` (see pp. 2, 17, 21, 23, 24, 84).

[39] Schuster, S. F., Bach, T., Fleder, E., Müller, J., Brand, M., Sextl, G., and Jossen, A.: *Nonlinear aging characteristics of lithium-ion cells under different operational conditions.* In: *Journal of Energy Storage* 1 (2015), pp. 44–53. ISSN: 2352-152X. DOI: `10.1016/j.est.2015.05.003` (see pp. 2, 19–22).

[40] Schuster, S. F.: *Reuse of Automotive Lithium-Ion Batteries: An Assessment from the Cell Aging Perspective.* PhD Dissertation. Munich: Technical University of Munich, 2016. URL: `https://mediatum.ub.tum.de/?id=1311465` (visited on 11/22/2023) (see pp. 2, 22).

[41] Kucevic, D., Tepe, B., Englberger, S., Parlikar, A., Mühlbauer, M., Bohlen, O., Jossen, A., and Hesse, H.: *Standard battery energy storage system profiles: Analysis of various applications for stationary energy storage systems using a holistic simulation framework.* In: *Journal of Energy Storage* 28 (2020), p. 101077. ISSN: 2352-152X. DOI: `10.1016/j.est.2019.101077` (see pp. 2, 12).

[42] Tepe, B., Jablonski, S., Hesse, H., and Jossen, A.: *Lithium-ion battery utilization in various modes of e-transportation.* In: *eTransportation* 18 (2023), p. 100274. ISSN: 2590-1168. DOI: `10.1016/j.etran.2023.100274` (see p. 2).

[43] Pinsky, N., Gaillac, L., Mendoza, A., Argueta, J., and Knipe, T.: "Performance of advanced electric vehicle batteries in stationary applications." In: *24th Annual International Telecommunications Energy Conference.* IEEE, 2002, pp. 366–372. ISBN: 0-7803-7512-2. DOI: `10.1109/INTLEC.2002.1048682` (see p. 2).

[44] Neubauer, J. and Pesaran, A.: *The ability of battery second use strategies to impact plug-in electric vehicle prices and serve utility energy storage applications.* In: *Journal of Power Sources* 196 (2011), pp. 10351–10358. ISSN: 0378-7753. DOI: `10.1016/j.jpowsour.2011.06.053` (see p. 2).

[45] Martinez-Laserna, E., Gandiaga, I., Sarasketa-Zabala, E., Badeda, J., Stroe, D.-I., Swierczynski, M., and Goikoetxea, A.: *Battery second life: Hype, hope or reality? A critical review of the state of the art.* In: *Renewable and Sustainable Energy Reviews* 93 (2018), pp. 701–718. ISSN: 1364-0321. DOI: `10.1016/j.rser.2018.04.035` (see p. 2).

[46] Casals, L. C., Amante García, B., and Canal, C.: *Second life batteries lifespan: Rest of useful life and environmental analysis.* In: *Journal of environmental management* 232 (2019), pp. 354–363. DOI: `10.1016/j.jenvman.2018.11.046` (see p. 2).

[47] BloombergNEF: *Lithium-Ion Battery Pack Prices Hit Record Low of $139/kWh.* 2023. URL: `https://about.bnef.com/blog/lithium-ion-battery-pack-prices-hit-record-low-of-139-kwh/` (see p. 2).

[48] Peters, J. F., Baumann, M., Zimmermann, B., Braun, J., and Weil, M.: *The environmental impact of Li-Ion batteries and the role of key parameters – A review.* In: *Renewable and Sustainable Energy Reviews* 67 (2017), pp. 491–506. ISSN: 1364-0321. DOI: 10.1016/j.rser.2016.08.039 (see p. 2).

[49] Kebede, A. A., Kalogiannis, T., van Mierlo, J., and Berecibar, M.: *A comprehensive review of stationary energy storage devices for large scale renewable energy sources grid integration.* In: *Renewable and Sustainable Energy Reviews* 159 (2022), p. 112213. ISSN: 1364-0321. DOI: 10.1016/j.rser.2022.112213 (see p. 7).

[50] Ocker, F., Braun, S., and Will, C.: "Design of European balancing power markets." In: *2016 13th International Conference on the European Energy Market (EEM).* IEEE, 2016, pp. 1–6. ISBN: 978-1-5090-1298-5. DOI: 10.1109/EEM.2016.7521193 (see p. 8).

[51] regelleistung.net: *Balancing Market in Germany.* 2023. URL: https://www.regelleistung.net/en-us/General-info/What-is-control-energy-Prequalification (visited on 11/13/2023) (see pp. 8, 10).

[52] National Grid ESO: *Firm Frequency Response (FFR).* 2023. URL: https://www.nationalgrideso.com/industry-information/balancing-services/frequency-response-services/firm-frequency-response-ffr (visited on 12/13/2023) (see p. 8).

[53] Kucevic, D., Semmelmann, L., Collath, N., Jossen, A., and Hesse, H.: *Peak Shaving with Battery Energy Storage Systems in Distribution Grids: A Novel Approach to Reduce Local and Global Peak Loads.* In: *Electricity* 2 (2021), pp. 573–589. DOI: 10.3390/electricity2040033 (see pp. 8, 19).

[54] Prakash, K., Ali, M., Siddique, M. N. I., Chand, A. A., Kumar, N. M., Dong, D., and Pota, H. R.: *A review of battery energy storage systems for ancillary services in distribution grids: Current status, challenges and future directions.* In: *Frontiers in Energy Research* 10 (2022), p. 325. DOI: 10.3389/fenrg.2022.971704 (see p. 8).

[55] Rezaeimozafar, M., Monaghan, R. F., Barrett, E., and Duffy, M.: *A review of behind-the-meter energy storage systems in smart grids.* In: *Renewable and Sustainable Energy Reviews* 164 (2022), p. 112573. ISSN: 1364-0321. DOI: 10.1016/j.rser.2022.112573 (see p. 8).

[56] Truong, C., Naumann, M., Karl, R., Müller, M., Jossen, A., and Hesse, H.: *Economics of Residential Photovoltaic Battery Systems in Germany: The Case of Tesla's Powerwall.* In: *Batteries* 2.2 (2016), p. 14. DOI: 10.3390/batteries2020014 (see pp. 8, 12).

[57] Neubauer, J. and Simpson, M.: *Deployment of Behind-The-Meter Energy Storage for Demand Charge Reduction.* 2015. DOI: 10.2172/1168774 (see p. 8).

[58] Martins, R., Hesse, H., Jungbauer, J., Vorbuchner, T., and Musilek, P.: *Optimal Component Sizing for Peak Shaving in Battery Energy Storage System for Industrial Applications.* In: *Energies* 11.8 (2018), p. 2048. DOI: 10.3390/en11082048 (see pp. 8, 12).

[59] Cardoso, G., Brouhard, T., DeForest, N., Wang, D., Heleno, M., and Kotzur, L.: *Battery aging in multi-energy microgrid design using mixed integer linear programming.* In: *Applied Energy* 231 (2018), pp. 1059–1069. ISSN: 0306-2619. DOI: 10.1016/j.apenergy.2018.09.185 (see p. 8).

[60] Marqusee, J., Becker, W., and Ericson, S.: *Resilience and economics of microgrids with PV, battery storage, and networked diesel generators.* In: *Advances in Applied Energy* 3 (2021), p. 100049. ISSN: 2666-7924. DOI: 10.1016/j.adapen.2021.100049 (see p. 8).

[61] Cupelli, L., Schutz, T., Jahangiri, P., Fuchs, M., Monti, A., and Muller, D.: *Data Center Control Strategy for Participation in Demand Response Programs*. In: *IEEE Transactions on Industrial Informatics* 14.11 (2018), pp. 5087–5099. ISSN: 1551-3203. DOI: 10.1109/TII.2018.2806889 (see p. 8).

[62] Shi, Y., Xu, B., Di Wang, and Zhang, B.: *Using Battery Storage for Peak Shaving and Frequency Regulation: Joint Optimization for Superlinear Gains*. In: *IEEE Transactions on Power Systems* 33.3 (2018), pp. 2882–2894. ISSN: 0885-8950. DOI: 10.1109/TPWRS.2017.2749512 (see pp. 8, 29, 30).

[63] Englberger, S., Jossen, A., and Hesse, H.: *Unlocking the Potential of Battery Storage with the Dynamic Stacking of Multiple Applications*. In: *Cell Reports Physical Science* 1.11 (2020), p. 100238. ISSN: 2666-3864. DOI: 10.1016/j.xcrp.2020.100238 (see pp. 8, 27, 30).

[64] Englberger, S., Abo Gamra, K., Tepe, B., Schreiber, M., Jossen, A., and Hesse, H.: *Electric vehicle multi-use: Optimizing multiple value streams using mobile storage systems in a vehicle-to-grid context*. In: *Applied Energy* 304 (2021), p. 117862. ISSN: 0306-2619. DOI: 10.1016/j.apenergy.2021.117862. URL: https://www.sciencedirect.com/science/article/pii/S0306261921011843 (see p. 8).

[65] Loßner, M., Böttger, D., and Bruckner, T.: *Economic assessment of virtual power plants in the German energy market — A scenario-based and model-supported analysis*. In: *Energy Economics* 62 (2017), pp. 125–138. ISSN: 0140-9883. DOI: 10.1016/j.eneco.2016.12.008 (see p. 8).

[66] Cramton, P.: *Electricity market design*. In: *Oxford Review of Economic Policy* (2017). URL: https://www.jstor.org/stable/48539475 (see p. 8).

[67] EPEX Spot: *EPEX Spot Indices*. 2023. URL: https://www.epexspot.com/en/indices (visited on 02/23/2023) (see p. 9).

[68] Fraunhofer Institute for Solar Energy Systems: *Energy Charts*. 2022. URL: https://www.energy-charts.info/?l=en&c=DE (visited on 01/23/2023) (see p. 9).

[69] EPEX Spot: *Trading Products*. 2023. URL: https://www.epexspot.com/en/tradingproducts (visited on 12/19/2023) (see p. 9).

[70] Collath, N.: *Late Life BESS Toolchain*. Ed. by Chair of Electrical Energy Storage Technology. 2023. URL: https://gitlab.lrz.de/open-ees-ses/late-life-bess-toolchain (visited on 01/23/2024) (see pp. 9, 27, 29).

[71] Kern, T., Hinterstocker, and Roon, S. v.: "Rückwirkungen von Batterie-Vermarktungsoptionen." In: *11. Internationale Energiewirtschaftstagung an der TU Wien*. Ed. by TU Wien. 2019. URL: https://www.ffe.de/wp-content/uploads/2019/01/236_fullpaper_20190219_133648-1.pdf (visited on 12/19/2023) (see p. 9).

[72] Hesse, H., Kumtepeli, V., Schimpe, M., Reniers, J., Howey, D., Tripathi, A., Wang, Y., and Jossen, A.: *Ageing and Efficiency Aware Battery Dispatch for Arbitrage Markets Using Mixed Integer Linear Programming*. In: *Energies* 12.6 (2019), p. 999. DOI: 10.3390/en12060999 (see pp. 9, 25, 30).

[73] Schimpe, M., Truong, C. N., Naumann, M., Jossen, A., Hesse, H. C., Reniers, J. M., and Howey, D. A.: "Marginal Costs of Battery System Operation in Energy Arbitrage Based on Energy Losses and Cell Degradation." In: *2018 IEEE International Conference on Environment and Electrical Engineering and 2018 IEEE Industrial and Commercial Power Systems Europe (EEEIC / I&CPS Europe)*. IEEE, 2018. ISBN: 978-1-5386-5186-5. DOI: 10.1109/EEEIC.2018.8493717 (see p. 9).

[74] Collath, N., Winner, H., Frank, A., Durdel, A., and Jossen, A.: *Suitability of late-life lithium-ion cells for battery energy storage systems*. In: *Journal of Energy Storage* 87 (2024), p. 111508. ISSN: 2352-152X. DOI: 10.1016/j.est.2024.111508 (see p. 9).

[75] Finnah, B., Gönsch, J., and Ziel, F.: *Integrated day-ahead and intraday self-schedule bidding for energy storage systems using approximate dynamic programming*. In: *European Journal of Operational Research* 301 (2022), pp. 726–746. ISSN: 0377-2217. DOI: 10.1016/j.ejor.2021.11.010 (see p. 9).

[76] Löhndorf, N. and Wozabal, D.: *The Value of Coordination in Multimarket Bidding of Grid Energy Storage*. In: *Operations Research* 71.1 (2023). ISSN: 0030-364X. DOI: 10.1287/opre.2021.2247 (see p. 9).

[77] ENTSO-E: *Continental Europe successful synchronisation with Ukraine and Moldova power systems*. 2022. URL: https://www.entsoe.eu/news/2022/03/16/continental-europe-successful-synchronisation-with-ukraine-and-moldova-power-systems/ (visited on 12/18/2023) (see pp. 9, 10).

[78] ENTSO-E: *Electricity Balancing in Europe: An overview of the European balancing market and electricity balancing guidelines*. 2018. URL: https://www.entsoe.eu/news/2018/12/12/electricity-balancing-in-europe-entso-e-releases-an-overview-of-the-european-electricity-balancing-market-and-guideline/#:~:text=The%20Commission%20Regulation%20(EU)%202017,discrimination%2C%20transparency%20and%20integration%20in (visited on 12/18/2023) (see p. 10).

[79] Thien, T., Schweer, D., Vom Stein, D., Moser, A., and Sauer, D. U.: *Real-world operating strategy and sensitivity analysis of frequency containment reserve provision with battery energy storage systems in the german market*. In: *Journal of Energy Storage* 13 (2017), pp. 143–163. ISSN: 2352-152X. DOI: 10.1016/j.est.2017.06.012 (see pp. 10, 11).

[80] 50Hertz, Amprion, Tennet, and TransnetBW: *Prequalification Process for Balancing Service Providers (FCR, aFRR, mFRR) in Germany ("PQ conditions")*. 2023. URL: https://www.regelleistung.net/xspproxy/api/StaticFiles/Regelleistung/Infos_f%C3%BCr_Anbieter/Wie_werde_ich_Regelenergieanbieter_Pr%C3%A4qualifikation/Pr%C3%A4qualifikationsbedingungen_FCR_aFRR_mFRR/PQ-Bedingungen-03.06.2022(englisch).pdf (visited on 12/18/2023) (see p. 10).

[81] Zeh, A., Müller, M., Naumann, M., Hesse, H., Jossen, A., and Witzmann, R.: *Fundamentals of Using Battery Energy Storage Systems to Provide Primary Control Reserves in Germany*. In: *Batteries* 2.3 (2016), p. 29. DOI: 10.3390/batteries2030029 (see p. 11).

[82] Marchgraber, J., Gawlik, W., and Wailzer, G.: *Reducing SoC-Management and losses of battery energy storage systems during provision of frequency containment reserve*. In: *Journal of Energy Storage* 27 (2020), p. 101107. ISSN: 2352-152X. DOI: 10.1016/j.est.2019.101107 (see p. 11).

[83] Möller, M., Kucevic, D., Collath, N., Parlikar, A., Dotzauer, P., Tepe, B., Englberger, S., Jossen, A., and Hesse, H.: *SimSES: A holistic simulation framework for modeling and analyzing stationary energy storage systems.* In: *Journal of Energy Storage* 49 (2022), p. 103743. ISSN: 2352-152X. DOI: 10.1016/j.est.2021.103743 (see pp. 11, 15, 25, 33, 57, 75, 84, 91).

[84] BDEW: *BDEW-Strompreisanalyse Juli 2023.* 2023. URL: https://www.bdew.de/service/daten-und-grafiken/bdew-strompreisanalyse/ (see pp. 11, 12).

[85] Bundesministerium der Justiz: *Verordnung über die Entgelte für den Zugang zu Elektrizitätsversorgungsnetzen (Stromnetzentgeltverordnung - StromNEV).* 2023. URL: https://www.gesetze-im-internet.de/stromnev/__17.html#:~:text=%C2%A7%2017%20Ermittlung%20der%20Netzentgelte,und%20dem%20Ort%20der%20Entnahme. (visited on 12/20/2023) (see p. 11).

[86] SWM Infrastruktur GmbH & Co. KG: *Netzentgelte Strom 2024.* 2024. URL: https://www.swm-infrastruktur.de/strom/netzzugang/netznutzungsentgelte (visited on 02/09/2024) (see p. 11).

[87] Stromnetz Hamburg: *Neztentgelte.* 2024. URL: https://www.stromnetz-hamburg.de/fuer-partner/stromlieferanten/netzentgelte (visited on 02/09/2024) (see p. 11).

[88] Philipp, M., Collath, N., Roth, S., Theumer, P., Will-Ehlers, G., Kellermann, M., and Hesse, H.: *Batteriespeicherlösungen zur energiewirtschaftlichen Optimierung von Industriebetrieben.* In: *Zeitschrift für wirtschaftlichen Fabrikbetrieb* 117.5 (2022), pp. 305–311. DOI: 10.1515/zwf-2022-1059. URL: https://www.degruyter.com/document/doi/10.1515/zwf-2022-1059/html?lang=de (see p. 11).

[89] Lucas, A. and Chondrogiannis, S.: *Smart grid energy storage controller for frequency regulation and peak shaving, using a vanadium redox flow battery.* In: *International Journal of Electrical Power & Energy Systems* 80 (2016), pp. 26–36. ISSN: 0142-0615. DOI: 10.1016/j.ijepes.2016.01.025 (see p. 12).

[90] Oudalov, A., Cherkaoui, R., and Beguin, A.: "Sizing and Optimal Operation of Battery Energy Storage System for Peak Shaving Application." In: *IEEE Lausanne Power Tech.* Ed. by IEEE. 2007. DOI: 10.1109/PCT.2007.4538388. URL: http://ieeexplore.ieee.org/servlet/opac?punumber=4534843 (see p. 12).

[91] Christiansen, J.: *European Market Outlook for Residential Battery Storage 2022-2026.* Ed. by SolarPower Europe. 2022. URL: https://www.solarpowereurope.org/insights/thematic-reports/european-market-outlook-for-residential-battery-storage-1 (see p. 12).

[92] Bundesnetzagentur: *Archivierte EEG-Vergütungssätze und Datenmeldungen.* 2023. URL: https://www.bundesnetzagentur.de/DE/Fachthemen/ElektrizitaetundGas/ErneuerbareEnergien/EEG_Foerderung/Archiv_VergSaetze/start.html (visited on 12/20/2023) (see p. 12).

[93] Angenendt, G., Zurmühlen, S., Axelsen, H., and Sauer, D. U.: *Comparison of different operation strategies for PV battery home storage systems including forecast-based operation strategies.* In: *Applied Energy* 229 (2018), pp. 884–899. ISSN: 0306-2619. DOI: 10.1016/j.apenergy.2018.08.058 (see pp. 12, 29).

[94] Zeh, A. and Witzmann, R.: *Operational Strategies for Battery Storage Systems in Low-voltage Distribution Grids to Limit the Feed-in Power of Roof-mounted Solar Power Systems.* In: *Energy Procedia* 46 (2014), pp. 114–123. ISSN: 1876-6102. DOI: 10.1016/j.egypro.2014.01.164 (see p. 12).

[95] Hoppmann, J., Volland, J., Schmidt, T. S., and Hoffmann, V. H.: *The economic viability of battery storage for residential solar photovoltaic systems – A review and a simulation model.* In: *Renewable and Sustainable Energy Reviews* 39 (2014), pp. 1101–1118. ISSN: 1364-0321. DOI: `10.1016/j.rser.2014.07.068` (see p. 12).

[96] Weniger, J., Tjaden, T., and Quaschning, V.: *Sizing of Residential PV Battery Systems.* In: *Energy Procedia* 46 (2014), pp. 78–87. ISSN: 1876-6102. DOI: `10.1016/j.egypro.2014.01.160` (see p. 12).

[97] Merei, G., Moshövel, J., Magnor, D., and Sauer, D. U.: *Optimization of self-consumption and techno-economic analysis of PV-battery systems in commercial applications.* In: *Applied Energy* 168 (2016), pp. 171–178. ISSN: 0306-2619. DOI: `10.1016/j.apenergy.2016.01.083` (see p. 12).

[98] Neon: *Hornsdale Power Reserve - FAQs: When was the Hornsdale Power Reserve constructed?* 2024. URL: `https://hornsdalepowerreserve.com.au/faqs/` (visited on 01/04/2024) (see p. 13).

[99] Virstra Corp: *Vistra Completes Milestone Expansion of Flagship California Energy Storage System: 350 MW / 1,400 MWh addition is online and bolstering California grid reliability this summer.* 2023. URL: `https://investor.vistracorp.com/2023-08-01-Vistra-Completes-Milestone-Expansion-of-Flagship-California-Energy-Storage-System` (visited on 01/04/2024) (see p. 13).

[100] Saw, L. H., Ye, Y., and Tay, A. A.: *Integration issues of lithium-ion battery into electric vehicles battery pack.* In: *Journal of Cleaner Production* 113 (2016), pp. 1032–1045. ISSN: 0959-6526. DOI: `10.1016/j.jclepro.2015.11.011` (see p. 13).

[101] Augustine, C. and Blair, N.: *Storage Futures Study: Storage Technology Modeling Input Data Report.* Ed. by National Renewable Energy Lab. 2021. URL: `https://atb.nrel.gov/electricity/2022/utility-scale_battery_storage` (visited on 01/04/2024) (see pp. 13, 15, 16).

[102] VDE: *Technical Connection Rules for Medium-Voltage (VDE-AR-N 4110).* 2018. URL: `https://www.vde.com/en/fnn/topics/technical-connection-rules/tcr-for-medium-voltage` (visited on 01/05/2024) (see p. 14).

[103] Farivar, G. G. et al.: *Grid-Connected Energy Storage Systems: State-of-the-Art and Emerging Technologies.* In: *Proceedings of the IEEE* 111.4 (2023), pp. 397–420. ISSN: 0018-9219. DOI: `10.1109/JPROC.2022.3183289` (see pp. 14, 15).

[104] Fernão Pires, V., Romero-Cadaval, E., Vinnikov, D., Roasto, I., and Martins, J. F.: *Power converter interfaces for electrochemical energy storage systems – A review.* In: *Energy Conversion and Management* 86 (2014), pp. 453–475. ISSN: 0196-8904. DOI: `10.1016/j.enconman.2014.05.003` (see p. 14).

[105] Wang, G., Konstantinou, G., Townsend, C. D., Pou, J., Vazquez, S., Demetriades, G. D., and Agelidis, V. G.: *A Review of Power Electronics for Grid Connection of Utility-Scale Battery Energy Storage Systems.* In: *IEEE Transactions on Sustainable Energy* 7.4 (2016), pp. 1778–1790. ISSN: 1949-3029. DOI: `10.1109/TSTE.2016.2586941` (see pp. 14, 15).

[106] Wang, Y., Aksoz, A., Geury, T., Ozturk, S. B., Kivanc, O. C., and Hegazy, O.: *A Review of Modular Multilevel Converters for Stationary Applications.* In: *Applied Sciences* 10.21 (2020), p. 7719. DOI: `10.3390/app10217719` (see p. 14).

[107] Gabbar, H., Othman, A., and Abdussami, M.: *Review of Battery Management Systems (BMS) Development and Industrial Standards*. In: *Technologies* 9.2 (2021), p. 28. DOI: `10.3390/technologies9020028` (see p. 14).

[108] Cabrera-Castillo, E., Niedermeier, F., and Jossen, A.: *Calculation of the state of safety (SOS) for lithium ion batteries*. In: *Journal of Power Sources* 324 (2016), pp. 509–520. ISSN: 0378-7753. DOI: `10.1016/j.jpowsour.2016.05.068` (see p. 14).

[109] Ouyang, D., Chen, M., Liu, J., Wei, R., Weng, J., and Wang, J.: *Investigation of a commercial lithium-ion battery under overcharge/over-discharge failure conditions*. In: *RSC Advances* 8.58 (2018), pp. 33414–33424. DOI: `10.1039/C8RA05564E` (see p. 14).

[110] Wang, Y., Tian, J., Sun, Z., Wang, L., Xu, R., Li, M., and Chen, Z.: *A comprehensive review of battery modeling and state estimation approaches for advanced battery management systems*. In: *Renewable and Sustainable Energy Reviews* 131 (2020), p. 110015. ISSN: 1364-0321. DOI: `10.1016/j.rser.2020.110015` (see p. 14).

[111] Li, W., Rentemeister, M., Badeda, J., Jöst, D., Schulte, D., and Sauer, D. U.: *Digital twin for battery systems: Cloud battery management system with online state-of-charge and state-of-health estimation*. In: *Journal of Energy Storage* 30 (2020), p. 101557. ISSN: 2352-152X. DOI: `10.1016/j.est.2020.101557` (see p. 14).

[112] Turksoy, A., Teke, A., and Alkaya, A.: *A comprehensive overview of the dc-dc converter-based battery charge balancing methods in electric vehicles*. In: *Renewable and Sustainable Energy Reviews* 133 (2020), p. 110274. ISSN: 1364-0321. DOI: `10.1016/j.rser.2020.110274` (see p. 14).

[113] Reniers, J. M. and Howey, D. A.: *Digital twin of a MWh-scale grid battery system for efficiency and degradation analysis*. In: *Applied Energy* 336 (2023), p. 120774. ISSN: 0306-2619. DOI: `10.1016/j.apenergy.2023.120774` (see p. 14).

[114] Wang, J., Huang, W., Pei, A., Li, Y., Shi, F., Yu, X., and Cui, Y.: *Improving cyclability of Li metal batteries at elevated temperatures and its origin revealed by cryo-electron microscopy*. In: *Nature Energy* 4.8 (2019), pp. 664–670. DOI: `10.1038/s41560-019-0413-3` (see p. 14).

[115] Schimpe, M., Naumann, M., Truong, N., Hesse, H. C., Santhanagopalan, S., Saxon, A., and Jossen, A.: *Energy efficiency evaluation of a stationary lithium-ion battery container storage system via electro-thermal modeling and detailed component analysis*. In: *Applied Energy* 210 (2018), pp. 211–229. ISSN: 0306-2619. DOI: `10.1016/j.apenergy.2017.10.129` (see pp. 14, 23).

[116] Teichert, O., Müller, F., and Lienkamp, M.: *Techno-economic design of battery thermal management systems in different climates*. In: *Journal of Energy Storage* 48 (2022), p. 103832. ISSN: 2352-152X. DOI: `10.1016/j.est.2021.103832` (see p. 14).

[117] Olis, W., Rosewater, D., Nguyen, T., and Byrne, R. H.: *Impact of heating and cooling loads on battery energy storage system sizing in extreme cold climates*. In: *Energy* 278 (2023), p. 127878. ISSN: 0360-5442. DOI: `10.1016/j.energy.2023.127878` (see pp. 15, 19).

[118] Guo, Y., Qiu, Y., Lei, B., Wu, Y., Shi, Y., Cao, W., Liu, H., and Jiang, F.: *Modeling and analysis of liquid-cooling thermal management of an in-house developed 100 kW/500 kWh energy storage container consisting of lithium-ion batteries retired from electric vehicles*. In: *Applied Thermal Engineering* 232 (2023), p. 121111. ISSN: 1359-4311. DOI: `10.1016/j.applthermaleng.2023.121111` (see p. 15).

[119] Evans, M. et al.: *StoragetVET 2.0.* Ed. by Electric Power Research Institute. 2024. URL: `https://github.com/epri-dev/StorageVET` (visited on 01/04/2024) (see p. 15).

[120] National Renewable Energy Lab.: *System Advisor Model.* 2024. URL: `https://sam.nrel.gov/` (visited on 01/07/2024) (see p. 15).

[121] Notton, G., Lazarov, V., and Stoyanov, L.: *Optimal sizing of a grid-connected PV system for various PV module technologies and inclinations, inverter efficiency characteristics and locations.* In: *Renewable Energy* 35 (2010), pp. 541–554. ISSN: 0960-1481. DOI: `10.1016/j.renene.2009.07.013` (see pp. 15, 27).

[122] Väyrynen, A. and Salminen, J.: *Lithium ion battery production.* In: *The Journal of Chemical Thermodynamics* 46 (2012), pp. 80–85. ISSN: 0021-9614. DOI: `10.1016/j.jct.2011.09.005` (see p. 16).

[123] Pender, J. P. et al.: *Electrode Degradation in Lithium-Ion Batteries.* In: *ACS nano* 14.2 (2020), pp. 1243–1295. DOI: `10.1021/acsnano.9b04365` (see p. 16).

[124] Li, Q., Chen, J., Fan, L., Kong, X., and Lu, Y.: *Progress in electrolytes for rechargeable Li-based batteries and beyond.* In: *Green Energy & Environment* 1.1 (2016), pp. 18–42. ISSN: 2468-0257. DOI: `10.1016/j.gee.2016.04.006` (see p. 16).

[125] Haregewoin, A. M., Wotango, A. S., and Hwang, B.-J.: *Electrolyte additives for lithium ion battery electrodes: progress and perspectives.* In: *Energy Environ. Sci.* 9.6 (2016), pp. 1955–1988. ISSN: 1754-5692. DOI: `10.1039/C6EE00123H` (see p. 16).

[126] Birkl, C. R., Roberts, M. R., McTurk, E., Bruce, P. G., and Howey, D. A.: *Degradation diagnostics for lithium ion cells.* In: *Journal of Power Sources* 341 (2017), pp. 373–386. ISSN: 0378-7753. DOI: `10.1016/j.jpowsour.2016.12.011` (see pp. 16, 17).

[127] Xiong, R., Pan, Y., Shen, W., Li, H., and Sun, F.: *Lithium-ion battery aging mechanisms and diagnosis method for automotive applications: Recent advances and perspectives.* In: *Renewable and Sustainable Energy Reviews* 131 (2020), p. 110048. ISSN: 1364-0321. DOI: `10.1016/j.rser.2020.110048` (see p. 17).

[128] Guo, L., Thornton, D. B., Koronfel, M. A., Stephens, I. E. L., and Ryan, M. P.: *Degradation in lithium ion battery current collectors.* In: *Journal of Physics: Energy* 3.3 (2021), p. 032015. DOI: `10.1088/2515-7655/ac0c04` (see p. 17).

[129] Schimpe, M., Kuepach, M. E. v., Naumann, M., Hesse, H., Smith, K., and Jossen, A.: *Comprehensive Modeling of Temperature-Dependent Degradation Mechanisms in Lithium Iron Phosphate Batteries.* In: *Journal of The Electrochemical Society* 165.2 (2018), A181–A193. DOI: `10.1149/2.1181714jes` (see pp. 17, 21, 23, 24).

[130] Guenther, C., Schott, B., Hennings, W., Waldowski, P., and Danzer, M. A.: *Model-based investigation of electric vehicle battery aging by means of vehicle-to-grid scenario simulations.* In: *Journal of Power Sources* 239 (2013), pp. 604–610. ISSN: 0378-7753. DOI: `10.1016/j.jpowsour.2013.02.041` (see pp. 17, 23).

[131] Gantenbein, S., Schönleber, M., Weiss, M., and Ivers-Tiffée, E.: *Capacity Fade in Lithium-Ion Batteries and Cyclic Aging over Various State-of-Charge Ranges.* In: *Sustainability* 11.23 (2019), p. 6697. DOI: `10.3390/su11236697` (see p. 17).

[132] Deshpande, R. D. and Uddin, K.: *Physics inspired model for estimating 'cycles to failure' as a function of depth of discharge for lithium ion batteries.* In: *Journal of Energy Storage* 33 (2021), p. 101932. ISSN: 2352-152X. DOI: `10.1016/j.est.2020.101932` (see p. 17).

[133] Waldmann, T., Wilka, M., Kasper, M., Fleischhammer, M., and Wohlfahrt-Mehrens, M.: *Temperature dependent ageing mechanisms in Lithium-ion batteries – A Post-Mortem study.* In: *Journal of Power Sources* 262 (2014), pp. 129–135. ISSN: 0378-7753. DOI: 10.1016/j.jpowsour.2014.03.112 (see pp. 17, 21, 22).

[134] Schweidler, S., Biasi, L. de, Schiele, A., Hartmann, P., Brezesinski, T., and Janek, J.: *Volume Changes of Graphite Anodes Revisited: A Combined Operando X-ray Diffraction and In Situ Pressure Analysis Study.* In: *The Journal of Physical Chemistry C* 122.16 (2018), pp. 8829–8835. ISSN: 1932-7447. DOI: 10.1021/acs.jpcc.8b01873 (see p. 17).

[135] Juarez-Robles, D., Jeevarajan, J. A., and Mukherjee, P. P.: *Degradation-Safety Analytics in Lithium-Ion Cells: Part I. Aging under Charge/Discharge Cycling.* In: *Journal of the Electrochemical Society* 167.16 (2020), p. 160510. ISSN: 0013-4651. DOI: 10.1149/1945-7111/abc8c0 (see p. 18).

[136] Schindler, M., Sturm, J., Ludwig, S., Durdel, A., and Jossen, A.: *Comprehensive Analysis of the Aging Behavior of Nickel-Rich, Silicon-Graphite Lithium-Ion Cells Subject to Varying Temperature and Charging Profiles.* In: *Journal of the Electrochemical Society* 168.6 (2021), p. 060522. ISSN: 0013-4651. DOI: 10.1149/1945-7111/ac03f6 (see p. 18).

[137] Bazlen, S., Heugel, P., Kessel, O. von, Commerell, W., and Tübke, J.: *Influence of charging protocols on the charging capability and aging of lithium-ion cells with silicon-containing anodes.* In: *Journal of Energy Storage* 49 (2022), p. 104044. ISSN: 2352-152X. DOI: 10.1016/j.est.2022.104044 (see p. 18).

[138] Keil, J., Paul, N., Baran, V., Keil, P., Gilles, R., and Jossen, A.: *Linear and Nonlinear Aging of Lithium-Ion Cells Investigated by Electrochemical Analysis and In-Situ Neutron Diffraction.* In: *Journal of the Electrochemical Society* 166.16 (2019), A3908–A3917. ISSN: 0013-4651. DOI: 10.1149/2.1271915jes (see pp. 18, 21).

[139] Raj, T., Wang, A. A., Monroe, C. W., and Howey, D. A.: *Investigation of Path–Dependent Degradation in Lithium–Ion Batteries.* In: *Batteries & Supercaps* 3.12 (2020), pp. 1377–1385. ISSN: 2566-6223. DOI: 10.1002/batt.202000160 (see p. 18).

[140] Rogge, M. and Jossen, A.: *Path–Dependent Ageing of Lithium–ion Batteries and Implications on the Ageing Assessment of Accelerated Ageing Tests.* In: *Batteries & Supercaps* 7.1 (2024). ISSN: 2566-6223. DOI: 10.1002/batt.202300313 (see p. 18).

[141] Gasper, P., Collath, N., Hesse, H. C., Jossen, A., and Smith, K.: *Machine-Learning Assisted Identification of Accurate Battery Lifetime Models with Uncertainty.* In: *Journal of the Electrochemical Society* 169.8 (2022), p. 080518. ISSN: 0013-4651. DOI: 10.1149/1945-7111/ac86a8 (see pp. 19, 24).

[142] Gasper, P., Gering, K., Dufek, E., and Smith, K.: *Challenging Practices of Algebraic Battery Life Models through Statistical Validation and Model Identification via Machine-Learning.* In: *Journal of the Electrochemical Society* 168 (2021), p. 020502. ISSN: 0013-4651. DOI: 10.1149/1945-7111/abdde1 (see pp. 19, 24).

[143] Kwade, A., Haselrieder, W., Leithoff, R., Modlinger, A., Dietrich, F., and Droeder, K.: *Current status and challenges for automotive battery production technologies.* In: *Nature Energy* 3 (2018), pp. 290–300. DOI: 10.1038/s41560-018-0130-3 (see p. 19).

[144] An, S. J., Li, J., Du, Z., Daniel, C., and Wood, D. L.: *Fast formation cycling for lithium ion batteries.* In: *Journal of Power Sources* 342 (2017), pp. 846–852. ISSN: 0378-7753. DOI: `10.1016/j.jpowsour.2017.01.011` (see p. 19).

[145] Yang, X.-G., Leng, Y., Zhang, G., Ge, S., and Wang, C.-Y.: *Modeling of lithium plating induced aging of lithium-ion batteries: Transition from linear to nonlinear aging.* In: *Journal of Power Sources* 360 (2017), pp. 28–40. ISSN: 0378-7753. DOI: `10.1016/j.jpowsour.2017.05.110` (see pp. 19, 20, 25).

[146] Atalay, S., Sheikh, M., Mariani, A., Merla, Y., Bower, E., and Widanage, W. D.: *Theory of battery ageing in a lithium-ion battery: Capacity fade, nonlinear ageing and lifetime prediction.* In: *Journal of Power Sources* 478 (2020), p. 229026. ISSN: 0378-7753. DOI: `10.1016/j.jpowsour.2020.229026` (see pp. 19–21, 25).

[147] Keil, J. and Jossen, A.: *Electrochemical Modeling of Linear and Nonlinear Aging of Lithium-Ion Cells.* In: *Journal of the Electrochemical Society* 167.11 (2020), p. 110535. ISSN: 0013-4651. DOI: `10.1149/1945-7111/aba44f` (see pp. 19, 25).

[148] Attia, P. M. et al.: *Review—"Knees" in Lithium-Ion Battery Aging Trajectories.* In: *Journal of the Electrochemical Society* 169.6 (2022), p. 060517. ISSN: 0013-4651. DOI: `10.1149/1945-7111/ac6d13` (see pp. 19–21).

[149] Tomaszewska, A. et al.: *Lithium-ion battery fast charging: A review.* In: *eTransportation* 1 (2019), p. 100011. ISSN: 2590-1168. DOI: `10.1016/j.etran.2019.100011` (see p. 19).

[150] Petzl, M., Kasper, M., and Danzer, M. A.: *Lithium plating in a commercial lithium-ion battery – A low-temperature aging study.* In: *Journal of Power Sources* 275 (2015), pp. 799–807. ISSN: 0378-7753. DOI: `10.1016/j.jpowsour.2014.11.065` (see pp. 19, 21, 22).

[151] Dubarry, M., Baure, G., and Devie, A.: *Durability and Reliability of EV Batteries under Electric Utility Grid Operations: Path Dependence of Battery Degradation.* In: *Journal of the Electrochemical Society* 165.5 (2018), A773–A783. ISSN: 0013-4651. DOI: `10.1149/2.0421805jes` (see pp. 19, 20).

[152] Anseán, D., Dubarry, M., Devie, A., Liaw, B. Y., García, V. M., Viera, J. C., and González, M.: *Operando lithium plating quantification and early detection of a commercial LiFePO4 cell cycled under dynamic driving schedule.* In: *Journal of Power Sources* 356 (2017), pp. 36–46. ISSN: 0378-7753. DOI: `10.1016/j.jpowsour.2017.04.072` (see pp. 19, 20).

[153] Kindermann, F., Keil, J., Frank, A., and Jossen, A.: *A SEI Modeling Approach Distinguishing between Capacity and Power Fade.* In: *Journal of the Electrochemical Society* 164.12 (2017), E287–E293. ISSN: 0013-4651. DOI: `10.1149/2.0321712jes` (see pp. 20, 25).

[154] Sulzer, V., Mohtat, P., Pannala, S., Siegel, J. B., and Stefanopoulou, A. G.: *Accelerated Battery Lifetime Simulations Using Adaptive Inter-Cycle Extrapolation Algorithm.* In: *Journal of the Electrochemical Society* 168.12 (2021), p. 120531. ISSN: 0013-4651. DOI: `10.1149/1945-7111/ac3e48` (see pp. 20, 24).

[155] Fang, R., Dong, P., Ge, H., Fu, J., Li, Z., and Zhang, J.: *Capacity plunge of lithium-ion batteries induced by electrolyte drying-out: Experimental and Modeling Study.* In: *Journal of Energy Storage* 42 (2021), p. 103013. ISSN: 2352-152X. DOI: `10.1016/j.est.2021.103013` (see p. 20).

[156] Sieg, J., Schmid, A. U., Rau, L., Gesterkamp, A., Storch, M., Spier, B., Birke, K. P., and Sauer, D. U.: *Fast-charging capability of lithium-ion cells: Influence of electrode aging and electrolyte consumption.* In: *Applied Energy* 305 (2022), p. 117747. ISSN: 0306-2619. DOI: 10.1016/j.apenergy.2021.117747 (see p. 20).

[157] Petibon, R., Chevrier, V. L., Aiken, C. P., Hall, D. S., Hyatt, S. R., Shunmugasundaram, R., and Dahn, J. R.: *Studies of the Capacity Fade Mechanisms of LiCoO2/Si-Alloy: Graphite Cells.* In: *Journal of The Electrochemical Society* 163.7 (2016), A1146–A1156. DOI: 10.1149/2.0191607jes (see p. 20).

[158] Jung, R., Metzger, M., Haring, D., Solchenbach, S., Marino, C., Tsiouvaras, N., Stinner, C., and Gasteiger, H. A.: *Consumption of Fluoroethylene Carbonate (FEC) on Si-C Composite Electrodes for Li-Ion Batteries.* In: *Journal of the Electrochemical Society* 163.8 (2016), A1705–A1716. ISSN: 0013-4651. DOI: 10.1149/2.0951608jes (see p. 20).

[159] Johnen, M., Pitzen, S., Kamps, U., Kateri, M., Dechent, P., and Sauer, D. U.: *Modeling long-term capacity degradation of lithium-ion batteries.* In: *Journal of Energy Storage* 34 (2021), p. 102011. ISSN: 2352-152X. DOI: 10.1016/j.est.2020.102011 (see p. 20).

[160] Severson, K. A. et al.: *Data-driven prediction of battery cycle life before capacity degradation.* In: *Nature Energy* 4 (2019), pp. 383–391. DOI: 10.1038/s41560-019-0356-8 (see pp. 20, 21).

[161] Burns, J. C., Stevens, D. A., and Dahn, J. R.: *In-Situ Detection of Lithium Plating Using High Precision Coulometry.* In: *Journal of the Electrochemical Society* 162.6 (2015), A959–A964. ISSN: 0013-4651. DOI: 10.1149/2.0621506jes (see p. 21).

[162] Waldmann, T., Kasper, M., and Wohlfahrt-Mehrens, M.: *Optimization of Charging Strategy by Prevention of Lithium Deposition on Anodes in high-energy Lithium-ion Batteries – Electrochemical Experiments.* In: *Electrochimica Acta* 178 (2015), pp. 525–532. ISSN: 0013-4686. DOI: 10.1016/j.electacta.2015.08.056 (see p. 21).

[163] Schindler, S., Bauer, M., Cheetamun, H., and Danzer, M. A.: *Fast charging of lithium-ion cells: Identification of aging-minimal current profiles using a design of experiment approach and a mechanistic degradation analysis.* In: *Journal of Energy Storage* 19 (2018), pp. 364–378. ISSN: 2352-152X. DOI: 10.1016/j.est.2018.08.002 (see p. 21).

[164] Zhang, C., Wang, Y., Gao, Y., Wang, F., Mu, B., and Zhang, W.: *Accelerated fading recognition for lithium-ion batteries with Nickel-Cobalt-Manganese cathode using quantile regression method.* In: *Applied Energy* 256 (2019), p. 113841. ISSN: 0306-2619. DOI: 10.1016/j.apenergy.2019.113841 (see pp. 21, 22).

[165] Lewerenz, M., Münnix, J., Schmalstieg, J., Käbitz, S., Knips, M., and Sauer, D. U.: *Systematic aging of commercial LiFePO 4 |Graphite cylindrical cells including a theory explaining rise of capacity during aging.* In: *Journal of Power Sources* 345 (2017), pp. 254–263. ISSN: 0378-7753. DOI: 10.1016/j.jpowsour.2017.01.133 (see p. 21).

[166] Omar, N. et al.: *Lithium iron phosphate based battery – Assessment of the aging parameters and development of cycle life model.* In: *Applied Energy* 113 (2014), pp. 1575–1585. ISSN: 0306-2619. DOI: 10.1016/j.apenergy.2013.09.003 (see p. 21).

[167] Aiken, C. P., Harlow, J. E., Tingley, R., Hynes, T., Logan, E. R., Glazier, S. L., Keefe, A. S., and Dahn, J. R.: *Accelerated Failure in Li[Ni 0.5 Mn 0.3 Co 0.2]O 2 /Graphite Pouch Cells Due to Low LiPF 6 Concentration and Extended Time at High Voltage.* In: *Journal of the Electrochemical Society* 167.13 (2020), p. 130541. ISSN: 0013-4651. DOI: `10.1149/1945-7111/abbe5b` (see pp. 21, 22).

[168] Ma, X., Harlow, J. E., Li, J., Ma, L., Hall, D. S., Buteau, S., Genovese, M., Cormier, M., and Dahn, J. R.: *Editors' Choice—Hindering Rollover Failure of Li[Ni 0.5 Mn 0.3 Co 0.2]O 2 /Graphite Pouch Cells during Long-Term Cycling.* In: *Journal of the Electrochemical Society* 166.4 (2019), A711–A724. ISSN: 0013-4651. DOI: `10.1149/2.0801904jes` (see pp. 21, 22).

[169] Pfrang, A., Kersys, A., Kriston, A., Sauer, D. U., Rahe, C., Käbitz, S., and Figgemeier, E.: *Long-term cycling induced jelly roll deformation in commercial 18650 cells.* In: *Journal of Power Sources* 392 (2018), pp. 168–175. ISSN: 0378-7753. DOI: `10.1016/j.jpowsour.2018.03.065` (see pp. 21, 22).

[170] Ma, Z., Yang, R., and Wang, Z.: *A novel data-model fusion state-of-health estimation approach for lithium-ion batteries.* In: *Applied Energy* 237 (2019), pp. 836–847. ISSN: 0306-2619. DOI: `10.1016/j.apenergy.2018.12.071` (see pp. 21, 22).

[171] Klett, M. et al.: *Non-uniform aging of cycled commercial LiFePO4//graphite cylindrical cells revealed by post-mortem analysis.* In: *Journal of Power Sources* 257 (2014), pp. 126–137. ISSN: 0378-7753. DOI: `10.1016/j.jpowsour.2014.01.105` (see pp. 21, 22).

[172] Zhu, J. et al.: *Investigation of capacity fade for 18650-type lithium-ion batteries cycled in different state of charge (SoC) ranges.* In: *Journal of Power Sources* 489 (2021), p. 229422. ISSN: 0378-7753. DOI: `10.1016/j.jpowsour.2020.229422` (see pp. 21, 22).

[173] Safari, M. and Delacourt, C.: *Aging of a Commercial Graphite/LiFePO4 Cell.* In: *Journal of the Electrochemical Society* 158.10 (2011), A1123. ISSN: 0013-4651. DOI: `10.1149/1.3614529` (see pp. 21, 22).

[174] Coron, E., Geniès, S., Cugnet, M., and Thivel, P. X.: *Impact of Lithium-Ion Cell Condition on Its Second Life Viability.* In: *Journal of the Electrochemical Society* 167.11 (2020), p. 110556. ISSN: 0013-4651. DOI: `10.1149/1945-7111/aba703` (see pp. 21, 22).

[175] Tamilselvi, S. et al.: *A Review on Battery Modelling Techniques.* In: *Sustainability* 13.18 (2021), p. 10042. DOI: `10.3390/su131810042` (see p. 22).

[176] Deng, Z., Lin, X., Cai, J., and Hu, X.: *Battery health estimation with degradation pattern recognition and transfer learning.* In: *Journal of Power Sources* 525 (2022), p. 231027. ISSN: 0378-7753. DOI: `10.1016/j.jpowsour.2022.231027` (see p. 22).

[177] Vyroubal, P. and Kazda, T.: *Equivalent circuit model parameters extraction for lithium ion batteries using electrochemical impedance spectroscopy.* In: *Journal of Energy Storage* 15 (2018), pp. 23–31. ISSN: 2352-152X. DOI: `10.1016/j.est.2017.10.019` (see pp. 22, 23).

[178] Xu, B., Zhao, J., Zheng, T., Litvinov, E., and Kirschen, D. S.: *Factoring the Cycle Aging Cost of Batteries Participating in Electricity Markets.* In: *IEEE Transactions on Power Systems* 33.2 (2018), pp. 2248–2259. ISSN: 0885-8950. DOI: `10.1109/TPWRS.2017.2733339` (see p. 23).

[179] Attia, P. M., Chueh, W. C., and Harris, S. J.: *Revisiting the t0.5 Dependence of SEI Growth.* In: *Journal of the Electrochemical Society* 167.9 (2020), p. 090535. ISSN: 0013-4651. DOI: `10.1149/1945-7111/ab8ce4` (see p. 24).

[180] Broussley, M., Herreyre, S., Biensan, P., Kasztejna, P., Nechev, K., and Staniewicz, R. J.: *Aging mechanism in Li ion cells and calendar life predictions.* In: *Journal of Power Sources* 97-98 (2001), pp. 13–21. ISSN: 0378-7753. DOI: 10.1016/S0378-7753(01)00722-4 (see p. 24).

[181] Grolleau, S., Delaille, A., Gualous, H., Gyan, P., Revel, R., Bernard, J., Redondo-Iglesias, E., and Peter, J.: *Calendar aging of commercial graphite/LiFePO4 cell – Predicting capacity fade under time dependent storage conditions.* In: *Journal of Power Sources* 255 (2014), pp. 450–458. ISSN: 0378-7753. DOI: 10.1016/j.jpowsour.2013.11.098 (see p. 24).

[182] Khaleghi Rahimian, S., Forouzan, M. M., Han, S., and Tang, Y.: *A generalized physics-based calendar life model for Li-ion cells.* In: *Electrochimica Acta* 348 (2020), p. 136343. ISSN: 0013-4686. DOI: 10.1016/j.electacta.2020.136343 (see p. 24).

[183] Wang, J., Liu, P., Hicks-Garner, J., Sherman, E., Soukiazian, S., Verbrugge, M., Tataria, H., Musser, J., and Finamore, P.: *Cycle-life model for graphite-LiFePO4 cells.* In: *Journal of Power Sources* 196 (2011), pp. 3942–3948. ISSN: 0378-7753. DOI: 10.1016/j.jpowsour.2010.11.134 (see p. 24).

[184] He, G., Chen, Q., Kang, C., Pinson, P., and Xia, Q.: *Optimal Bidding Strategy of Battery Storage in Power Markets Considering Performance-Based Regulation and Battery Cycle Life.* In: *IEEE Transactions on Smart Grid* 7.5 (2016), pp. 2359–2367. ISSN: 1949-3053. DOI: 10.1109/TSG.2015.2424314 (see p. 24).

[185] Xu, B., Oudalov, A., Ulbig, A., Andersson, G., and Kirschen, D. S.: *Modeling of Lithium-Ion Battery Degradation for Cell Life Assessment.* In: *IEEE Transactions on Smart Grid* 9.2 (2018), pp. 1131–1140. ISSN: 1949-3053. DOI: 10.1109/TSG.2016.2578950 (see p. 24).

[186] Muenzel, V., Hoog, J. de, Brazil, M., Vishwanath, A., and Kalyanaraman, S.: "A Multi-Factor Battery Cycle Life Prediction Methodology for Optimal Battery Management." In: *Proceedings of the 2015 ACM Sixth International Conference on Future Energy Systems.* New York, NY, USA: ACM, 2015, pp. 57–66. ISBN: 9781450336093. DOI: 10.1145/2768510.2768532 (see p. 24).

[187] Hossain, M. A., Pota, H. R., Squartini, S., Zaman, F., and Guerrero, J. M.: *Energy scheduling of community microgrid with battery cost using particle swarm optimisation.* In: *Applied Energy* 254 (2019), p. 113723. ISSN: 0306-2619. DOI: 10.1016/j.apenergy.2019.113723 (see pp. 24, 30).

[188] Nuhic, A., Terzimehic, T., Soczka-Guth, T., Buchholz, M., and Dietmayer, K.: *Health diagnosis and remaining useful life prognostics of lithium-ion batteries using data-driven methods.* In: *Journal of Power Sources* 239 (2013), pp. 680–688. ISSN: 0378-7753. DOI: 10.1016/j.jpowsour.2012.11.146 (see p. 24).

[189] Doyle, M., Fuller, T. F., and Newman, J.: *Modeling of Galvanostatic Charge and Discharge of the Lithium/Polymer/Insertion Cell.* In: *Journal of The Electrochemical Society* 140 (1993), pp. 1526–1533. DOI: 10.1149/1.2221597 (see p. 24).

[190] Doyle, M. and Newman, J.: *Modeling the performance of rechargeable lithium-based cells: design correlations for limiting cases.* In: *Journal of Power Sources* (1995), pp. 45–51. ISSN: 0378-7753. DOI: 10.1016/0378-7753(94)02038-5 (see p. 24).

[191] Sturm, J., Rheinfeld, A., Zilberman, I., Spingler, F. B., Kosch, S., Frie, F., and Jossen, A.: *Modeling and simulation of inhomogeneities in a 18650 nickel-rich, silicon-graphite lithium-ion cell during fast charging.* In: *Journal of Power Sources* 412 (2019), pp. 204–223. ISSN: 0378-7753. DOI: 10.1016/j.jpowsour.2018.11.043 (see p. 24).

[192] Frank, A., Sturm, J., Steinhardt, M., Rheinfeld, A., and Jossen, A.: *Impact of Current Collector Design and Cooling Topology on Fast Charging of Cylindrical Lithium-Ion Batteries.* In: *ECS Advances* 1.4 (2022), p. 040502. DOI: `10.1149/2754-2734/ac97e0` (see p. 24).

[193] Ning, G. and Popov, B. N.: *Cycle Life Modeling of Lithium-Ion Batteries.* In: *Journal of The Electrochemical Society* 151.10 (2004), A1584–A1591. DOI: `10.1149/1.1787631` (see p. 24).

[194] Pinson, M. B. and Bazant, M. Z.: *Theory of SEI Formation in Rechargeable Batteries: Capacity Fade, Accelerated Aging and Lifetime Prediction.* In: *Journal of the Electrochemical Society* 160.2 (2013), A243–A250. ISSN: 0013-4651. DOI: `10.1149/2.044302jes` (see p. 24).

[195] Li, J., Adewuyi, K., Lotfi, N., Landers, R. G., and Park, J.: *A single particle model with chemical/mechanical degradation physics for lithium ion battery State of Health (SOH) estimation.* In: *Applied Energy* 212 (2018), pp. 1178–1190. ISSN: 0306-2619. DOI: `10.1016/j.apenergy.2018.01.011` (see p. 24).

[196] Reniers, J., Mulder, G., and Howey, D.: *Review and Performance Comparison of Mechanical-Chemical Degradation Models for Lithium-Ion Batteries.* In: *Journal of The Electrochemical Society* 166.14 (2019), A3189–A3200. DOI: `10.1149/2.0281914jes` (see pp. 24, 25, 27).

[197] Laresgoiti, I., Käbitz, S., Ecker, M., and Sauer, D. U.: *Modeling mechanical degradation in lithium ion batteries during cycling: Solid electrolyte interphase fracture.* In: *Journal of Power Sources* 300 (2015), pp. 112–122. ISSN: 0378-7753. DOI: `10.1016/j.jpowsour.2015.09.033` (see p. 24).

[198] O'Kane, S. E. J. et al.: *Lithium-ion battery degradation: how to model it.* In: *Physical chemistry chemical physics : PCCP* 24.13 (2022), pp. 7909–7922. DOI: `10.1039/d2cp00417h` (see p. 25).

[199] Park, J., Appiah, W. A., Byun, S., Jin, D., Ryou, M.-H., and Lee, Y. M.: *Semi-empirical long-term cycle life model coupled with an electrolyte depletion function for large-format graphite/LiFePO 4 lithium-ion batteries.* In: *Journal of Power Sources* 365 (2017), pp. 257–265. ISSN: 0378-7753. DOI: `10.1016/j.jpowsour.2017.08.094` (see p. 25).

[200] Sulzer, V., Marquis, S. G., Timms, R., Robinson, M., and Chapman, S. J.: *Python Battery Mathematical Modelling (PyBaMM).* In: *Journal of Open Research Software* 9.1 (2021), p. 14. DOI: `10.5334/jors.309` (see pp. 25, 91).

[201] Collath, N., Cornejo, M., Engwerth, V., Hesse, H., and Jossen, A.: *Increasing the lifetime profitability of battery energy storage systems through aging aware operation.* In: *Applied Energy* 348 (2023), p. 121531. ISSN: 0306-2619. DOI: `10.1016/j.apenergy.2023.121531` (see pp. 25, 92).

[202] Yang, Z., Li, K., and Foley, A.: *Computational scheduling methods for integrating plug-in electric vehicles with power systems: A review.* In: *Renewable and Sustainable Energy Reviews* 51 (2015), pp. 396–416. ISSN: 1364-0321. DOI: `10.1016/j.rser.2015.06.007` (see p. 25).

[203] Maheshwari, A., Paterakis, N. G., Santarelli, M., and Gibescu, M.: *Optimizing the operation of energy storage using a non-linear lithium-ion battery degradation model.* In: *Applied Energy* 261 (2020), p. 114360. ISSN: 0306-2619. DOI: `10.1016/j.apenergy.2019.114360` (see pp. 25, 30).

[204] Weitzel, T. and Glock, C. H.: *Energy management for stationary electric energy storage systems: A systematic literature review.* In: *European Journal of Operational Research* 264 (2018), pp. 582–606. ISSN: 0377-2217. DOI: `10.1016/j.ejor.2017.06.052` (see pp. 26, 28–30).

[205] Hou, Q., Yu, Y., Du, E., He, H., Zhang, N., Kang, C., Liu, G., and Zhu, H.: *Embedding scrapping criterion and degradation model in optimal operation of peak-shaving lithium-ion battery energy storage.* In: *Applied Energy* 278 (2020), p. 115601. ISSN: 0306-2619. DOI: 10.1016/j.apenergy.2020.115601 (see pp. 27, 30).

[206] Gurobi Optimization: *Gurobi.* 2024. URL: https://www.gurobi.com/ (visited on 01/15/2024) (see pp. 27, 31).

[207] Conforti, M., Cornuéjols Gérard, and Zambelli, G.: *Integer Programming.* Vol. 271. SpringerLink Bücher. Cham and s.l.: Springer International Publishing, 2014. ISBN: 978-3-319-11008-0. DOI: 10.1007/978-3-319-11008-0. URL: http://dx.doi.org/10.1007/978-3-319-11008-0 (see p. 27).

[208] Vykhodtsev, A. V., Jang, D., Wang, Q., Rosehart, W., and Zareipour, H.: *A review of modelling approaches to characterize lithium-ion battery energy storage systems in techno-economic analyses of power systems.* In: *Renewable and Sustainable Energy Reviews* 166 (2022), p. 112584. ISSN: 1364-0321. DOI: 10.1016/j.rser.2022.112584 (see p. 27).

[209] Rosewater, D. M., Copp, D. A., Nguyen, T. A., Byrne, R. H., and Santoso, S.: *Battery Energy Storage Models for Optimal Control.* In: *IEEE Access* 7 (2019), pp. 178357–178391. DOI: 10.1109/ACCESS.2019.2957698 (see p. 27).

[210] Kumtepeli, V., Hesse, H. C., Schimpe, M., Tripathi, A., Wang, Y., and Jossen, A.: *Energy Arbitrage Optimization With Battery Storage: 3D-MILP for Electro-Thermal Performance and Semi-Empirical Aging Models.* In: *IEEE Access* 8 (2020), pp. 204325–204341. DOI: 10.1109/ACCESS.2020.3035504 (see pp. 27, 28).

[211] Wächter, A. and Biegler, L. T.: *On the implementation of an interior-point filter line-search algorithm for large-scale nonlinear programming.* In: *Mathematical Programming* 106.1 (2006), pp. 25–57. ISSN: 0025-5610. DOI: 10.1007/s10107-004-0559-y (see p. 27).

[212] Reniers, J. M., Mulder, G., Ober-Blöbaum, S., and Howey, D. A.: *Improving optimal control of grid-connected lithium-ion batteries through more accurate battery and degradation modelling.* In: *Journal of Power Sources* 379 (2018), pp. 91–102. ISSN: 0378-7753. DOI: 10.1016/j.jpowsour.2018.01.004 (see p. 27).

[213] Lee, J., ed.: *Mixed Integer Nonlinear Programming.* Vol. 154. SpringerLink Bücher. New York, NY: Springer New York, 2012. ISBN: 978-1-4614-1927-3. DOI: 10.1007/978-1-4614-1927-3 (see p. 27).

[214] Cao, J., Harrold, D., Fan, Z., Morstyn, T., Healey, D., and Li, K.: *Deep Reinforcement Learning-Based Energy Storage Arbitrage With Accurate Lithium-Ion Battery Degradation Model.* In: *IEEE Transactions on Smart Grid* 11.5 (2020), pp. 4513–4521. ISSN: 1949-3053. DOI: 10.1109/TSG.2020.2986333 (see pp. 28, 30).

[215] Hesse, H., Kumtepeli, V., Schimpe, M., Reniers, J., Howey, D., Tripathi, A., Wang, Y., and Jossen, A.: *Ageing and Efficiency Aware Battery Dispatch for Arbitrage Markets Using Mixed Integer Linear Programming.* In: *Energies* 12.6 (2019), p. 999. DOI: 10.3390/en12060999 (see p. 28).

[216] Sultana, W. R., Sahoo, S. K., Sukchai, S., Yamuna, S., and Venkatesh, D.: *A review on state of art development of model predictive control for renewable energy applications.* In: *Renewable and Sustainable Energy Reviews* 76 (2017), pp. 391–406. ISSN: 1364-0321. DOI: 10.1016/j.rser.2017.03.058 (see p. 28).

[217] Lago, J., Marcjasz, G., Schutter, B. de, and Weron, R.: *Forecasting day-ahead electricity prices: A review of state-of-the-art algorithms, best practices and an open-access benchmark.* In: *Applied Energy* 293 (2021), p. 116983. ISSN: 0306-2619. DOI: `10.1016/j.apenergy.2021.116983` (see p. 28).

[218] Weron, R.: *Electricity price forecasting: A review of the state-of-the-art with a look into the future.* In: *International Journal of Forecasting* 30.4 (2014), pp. 1030–1081. ISSN: 0169-2070. DOI: `10.1016/j.ijforecast.2014.08.008` (see p. 28).

[219] Li, S., Li, J., Su, C., and Yang, Q.: *Optimization of Bi-Directional V2G Behavior With Active Battery Anti-Aging Scheduling.* In: *IEEE Access* 8 (2020), pp. 11186–11196. ISSN: 2169-3536. DOI: `10.1109/ACCESS.2020.2964699` (see p. 29).

[220] Perez, A., Moreno, R., Moreira, R., Orchard, M., and Strbac, G.: *Effect of Battery Degradation on Multi-Service Portfolios of Energy Storage.* In: *IEEE Transactions on Sustainable Energy* 7.4 (2016), pp. 1718–1729. ISSN: 1949-3029. DOI: `10.1109/TSTE.2016.2589943` (see p. 29).

[221] Li, J. and Danzer, M. A.: *Optimal charge control strategies for stationary photovoltaic battery systems.* In: *Journal of Power Sources* 258 (2014), pp. 365–373. ISSN: 0378-7753. DOI: `10.1016/j.jpowsour.2014.02.066` (see p. 30).

[222] Liu, K., Hu, X., Yang, Z., Xie, Y., and Feng, S.: *Lithium-ion battery charging management considering economic costs of electrical energy loss and battery degradation.* In: *Energy Conversion and Management* 195 (2019), pp. 167–179. ISSN: 0196-8904. DOI: `10.1016/j.enconman.2019.04.065` (see p. 30).

[223] Abdulla, K., Hoog, J. de, Muenzel, V., Suits, F., Steer, K., Wirth, A., and Halgamuge, S.: *Optimal Operation of Energy Storage Systems Considering Forecasts and Battery Degradation.* In: *IEEE Transactions on Smart Grid* 9.3 (2016), pp. 2086–2096. ISSN: 1949-3053. DOI: `10.1109/TSG.2016.2606490` (see p. 30).

[224] Shi, Y., Xu, B., Tan, Y., Kirschen, D., and Zhang, B.: *Optimal Battery Control Under Cycle Aging Mechanisms in Pay for Performance Settings.* In: *IEEE Transactions on Automatic Control* 64.6 (2019), pp. 2324–2339. ISSN: 0018-9286. DOI: `10.1109/TAC.2018.2867507` (see p. 30).

[225] Padmanabhan, N., Ahmed, M., and Bhattacharya, K.: *Battery Energy Storage Systems in Energy and Reserve Markets.* In: *IEEE Transactions on Power Systems* 35.1 (2020), pp. 215–226. ISSN: 0885-8950. DOI: `10.1109/TPWRS.2019.2936131` (see p. 30).

[226] Kim, W.-W., Shin, J.-S., Kim, S.-Y., and Kim, J.-O.: *Operation scheduling for an energy storage system considering reliability and aging.* In: *Energy* 141 (2017), pp. 389–397. ISSN: 0360-5442. DOI: `10.1016/j.energy.2017.09.091` (see p. 30).

[227] Zia, M. F., Elbouchikhi, E., and Benbouzid, M.: *Optimal operational planning of scalable DC microgrid with demand response, islanding, and battery degradation cost considerations.* In: *Applied Energy* 237 (2019), pp. 695–707. ISSN: 0306-2619. DOI: `10.1016/j.apenergy.2019.01.040` (see p. 30).

[228] Kazemi, M. and Zareipour, H.: *Long-Term Scheduling of Battery Storage Systems in Energy and Regulation Markets Considering Battery's Lifespan.* In: *IEEE Transactions on Smart Grid* 9.6 (2018), pp. 6840–6849. ISSN: 1949-3053. DOI: `10.1109/TSG.2017.2724919` (see p. 30).

[229] Kallrath, J.: *Gemischt-ganzzahlige Optimierung: Modellierung in der Praxis: Mit Fallstudien aus Chemie, Energiewirtschaft, Papierindustrie, Metallgewerbe, Produktion und Logistik.* 2., überarb. u. erw. Aufl. 2013. Springer eBook Collection. Wiesbaden: Springer Vieweg, 2013. ISBN: 978-3-658-00690-7. DOI: `10.1007/978-3-658-00690-7` (see p. 31).

[230] Collath, N., Tepe, B., Englberger, S., Jossen, A., and Holger, H.: *Battery degradation in BESS use-cases with varying degradation models and stress factor assumptions.* 2022. DOI: `10.14459/2022mp1652796`. URL: `https://doi.org/10.14459/2022mp1652796` (visited on 01/23/2024) (see p. 33).

[231] Collath, N.: *aging_aware_MPC: Aging aware MPC for battery energy storage systems.* Ed. by Chair of Electrical Energy Storage Technology. 2023. URL: `https://gitlab.lrz.de/open-ees-ses/aging-aware-MPC` (visited on 01/23/2024) (see p. 57).

[232] Collath, N., Gasper, P., Jossen, A., Smith, K., and Hesse, H.: *Techno-economic analysis results of BESS use-cases considering battery degradation model confidence intervals.* 2021. DOI: `10.14459/2021mp1633017`. URL: `https://doi.org/10.14459/2021mp1633017` (visited on 01/23/2024) (see p. 84).

Appendix

A SimSES: A holistic simulation framework for modeling and analyzing stationary energy storage systems

SimSES: A holistic simulation framework for modeling and analyzing stationary energy storage systems

Marc Möller, Daniel Kucevic, Nils Collath, Anupam Parlikar, Petra Dotzauer, Benedikt Tepe, Stefan Englberger, Andreas Jossen, Holger Hesse

Journal of Energy Storage 49, p. 103743, 2022

Permanent weblink:
https://doi.org/10.1016/j.est.2021.103743

Journal of Energy Storage 49 (2022) 103743

Contents lists available at ScienceDirect

Journal of Energy Storage

journal homepage: www.elsevier.com/locate/est

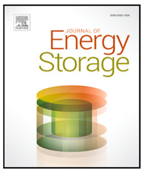

Research papers

SimSES: A holistic simulation framework for modeling and analyzing stationary energy storage systems

Marc Möller [a,*], Daniel Kucevic [a], Nils Collath [a], Anupam Parlikar [a], Petra Dotzauer [b], Benedikt Tepe [a], Stefan Englberger [a], Andreas Jossen [a], Holger Hesse [a]

[a] Institute for Electrical Energy Storage Technology, Technical University of Munich (TUM), Arcisstr. 21, 80333 Munich, Germany
[b] Bavarian Center for Applied Energy Research (ZAE Bayern), Department of Energy Storage, Walther-Meiner-Str. 6, 85748 Garching, Germany

ARTICLE INFO

Keywords:
Energy storage system simulation
Lithium-ion battery
Redox flow battery
Hydrogen technology
Storage system design
Stationary application

ABSTRACT

The increasing feed-in of intermittent renewable energy sources into the electricity grids worldwide is currently leading to technical challenges. Stationary energy storage systems provide a cost-effective and efficient solution in order to facilitate the growing penetration of renewable energy sources. Major technical and economical challenges for energy storage systems are related to lifetime, efficiency, and monetary returns. Holistic simulation tools are needed in order to address these challenges before investing in energy storage systems. One of these tools is SimSES, a holistic simulation framework specialized in evaluating energy storage technologies technically and economically. With a modular approach, SimSES covers various topologies, system components, and storage technologies embedded in an energy storage application. This contribution shows the capabilities and benefits of SimSES by providing in-depth knowledge of the implementations and models. Selected functionalities are demonstrated, with two use cases showing the easy-to-use simulation framework while providing detailed technical analysis for expert users. Hybrid energy storage systems consisting of lithium-ion and redox-flow batteries are investigated in a peak shaving application, while various system topologies are analyzed in a frequency containment reserve application. The results for the peak shaving case study show a benefit in favor of the hybrid system in terms of overall cost and degradation behavior in applications that have a comparatively low energy throughput during lifetime. In terms of system topology, a cascaded converter approach shows significant improvements in efficiency for the frequency containment reserve application.

1. Introduction

In former decades, the worldwide energy transition was predominantly driven by introducing more Renewable Energy Sources (RES) capacity to existing power networks, a process strongly supported by both globally declining cost for wind and solar power generation as well as through local legislation support, including subsidy schemes [1,2]. Following these early stage developments, the energy transition in various regions has now started to face new constraints and technical challenges, which demand other and often more site-specific solution approaches. Coupling of the power grid to both heating and electrified transport is certainly a key strategy to increase RES penetration on a global and nationwide level within the power system itself. At the same time, increasing the intermittence of supply that relies more on variable sources like solar and wind generation brings incorporation of grid-tied energy storage into discussion as a technically mature and potentially cost-competitive measure addressing volatility issues [3].

In order to categorize storage integration in power grids we may distinguish among Front-The-Meter (FTM) and Behind-the-Meter (BTM) applications [4]. FTM includes applications such as storage-assisted renewable energy time shift [5], wholesale energy arbitrage [6,7], and Frequency Containment Reserve (FCR) provision [8]. A more distributed and locally coordinated power supply is discussed in the context of BTM applications, e.g., Peak Shaving (PS) for industrial sites or at electric vehicle charging stations [9], or bill-saving at residential sites through Self-Consumption Increase (SCI) with local photovoltaic generation (residential battery storage) [10]. However, before taking a solid investment decision, it is crucial to analyze and optimize the technical parameters, storage dispatch control, as well as cost/revenue streams over the course of the entire project lifetime. Simulation and modeling tools in conjunction with sensitivity analyzes and optimization routines are commonly used to support these crucial steps in the planning and operational phase of grid-integrated storage projects.

---

[*] Corresponding author.
E-mail address: marc.moeller@tum.de (M. Möller).

https://doi.org/10.1016/j.est.2021.103743
Received 10 March 2021; Received in revised form 30 August 2021; Accepted 2 December 2021
Available online 24 February 2022

The Simulation Tool for Stationary Energy Storage Systems (**SimSES**) was developed to assist through the aforementioned tasks of storage system planning and operation. Through combining user-defined inputs with pre-parameterized component building blocks, as well as calculation methods and result analysis functions, a reserve is built for research, industry, and policy makers in equal measure to support deployment and enrollment of storage integration to the grid. The approach of **SimSES** is presented within this contribution.

In Section 2, comparable existing tools are reviewed and evaluated before the structure of **SimSES** is elaborated further in Section 3 as well as its detail models for storage technologies (Section 4) and its periphery (Section 5). Afterwards, in Section 6 two case studies are presented to show the capabilities of **SimSES** and concludes with a summary and outlook of further investigations in Section 7.

2. Literature review

Various authors have analyzed sizing and (economically) optimal operation of a specifically chosen storage system in a dedicated application setting, e.g., the usage of redox flow battery (RFB) for industrial PS applications [9] or the usage of lithium-ion battery (LIB) for SCI [11, 12]. Fewer studies exist comparing the suitability of different storage options for a given use case, e.g., refer to Toledo et al. [13] for a suitability comparison of different storage types for conducting residential self-consumption increase. Also, the profitability attainable across different applications was analyzed with a given technology to start off with, e.g., LIB in a wide range of application settings [14]. There is consensus that no uniform ideal candidate to meet all application-specific requirements exists within the storage technologies available to date [15]. In order to predict internal states of a storage system such as the State of Health (SOH) or the storage internal losses, it may become necessary to parameterize and simulate an adequately complex model of a storage system. Furthermore, simulations need to be fed with an operational concept that complies with the application constrains, and may deliver the compatibility of a given configuration as well as provide state predictions for the storage system. From an investor's perspective and ultimately for the most cost-effective integration of storage system to power grids with a high share of Variable Renewable Energy Sources (vRES), it is detrimental to conduct in-depth sensitivity and optimization studies relying on a full spectrum techno-economic model before subsequent tasks of project acquisition, realization, operation, and ultimately disposal are to be considered.

In the following, an overview of a selection of depicted tools for the techno-economic modeling of stationary storage in grid applications is provided. While Table 1 summarizes some of the main characteristics of these tools, it should be noted that this paper does not claim to provide a complete overview of all tools that may be relevant in the context matter.

GridLab-D,[1] developed and distributed via Pacific Northwest National Laboratory (*PNNL*), is a universal tool that allows modeling and analyzing multi-component power system networks. Its strength lies in the ability to simulate physical properties of various components through setting up and solving multiple differential equations, describing all sub-components in the modeling region. While the tool is certainly strong in modeling an entire micro-grid with its numerous grid states, it lacks detailed performance models for energy storage systems as well as application-specific parameterization and is therefore not applicable for detailed techno-economic analysis and optimization of storage project as it is focused in this work.

Other tools like **NAS Battery Simulator**,[2] **PNNL Flow Battery Calculator**,[3] and **H2FAST**,[4] are tools dedicated to specific storage types being sodium sulfur battery (NaS) redox flow, and electrolysis/hydrogen storage, respectively. These tools are developed for conducting rapid cost-revenue calculations for the specific technology of choice and offer limited user-specific input in terms of system parameterization and choice of application use case. Nevertheless, the aforementioned tools are confined to a dedicated storage system technology, rendering them less suitable for cross-technology comparisons. Furthermore, most tools of this kind are distributed as a proprietary code, matching only a dedicated commercial product well, and are not suitable for conducting sensitivity analyzes and adaption to envisioned new storage system control and operation.

More tailored simulations can be conducted using the tool **PerModAC** developed at htw Berlin [16]. Using this open-source software tool, performance and efficiency modeling of PV-coupled residential battery storage systems can be conducted. While the tool is extraordinarily strong in conducting battery storage product-specific performance and efficiency modeling, the model lacks the capabilities to analyze battery degradation. More importantly, the current version of this open-source tool is strictly confined to a specific residential BTM use case and cannot be used directly for cross-application assessments, as is desired for an investor's decision support.

Homer Pro and **Homer Grid** are more versatile modeling tools when it comes to comparing and optimizing the techno-economic performance of storage systems in (micro-)grids. The tools support various storage specific libraries and application-specific modeling capabilities, e.g., storage-supported renewable energy time shift in island grids as well as peak-shaving and solar-plus storage calculations in the current professional versions, and has been used in various scientific publications [17,18]. The software was developed by National Renewable Energy Laboratory (*NREL*), but the license for these tools are distributed solely via *Homerenergy* as a commercial product and cannot be extended/adapted according to the users' desire to address new application scenarios, specific personal needs, or local regulation frameworks. E.g., applications like the provision of frequency containment reserve and arbitrage marketing scenarios are not covered in the current version of the software tools.

Two other tools developed by *NREL* and Sandia National Laboratories (*SNL*) are worth looking at in more detail: **BLAST**[5] (Battery Lifetime Analysis and Simulation Tool) is a powerful software suite programmed using MATLAB® and it is distributed for both vehicle and stationary BTM applications. BLAST-BTM-Lite has powerful modeling capabilities for battery performance and lifetime calculations in stationary BTM applications and it includes both optimization and basic economic calculations. While it is highly recommended that this tool to be looked at closer by users interested in PV self-consumption and PS application, applications (only BTM) and storage systems to be analyzed (only conventional electro-chemical batteries) are clearly limited and confined. Furthermore, its original code structure lies hidden behind a graphical user interface and a proprietary executable file, making it unfeasible for the end-user to adapt parameters, e.g., sample time for peak shaving control.

The System Advisor Model[6] (**SAM**) tool builds up on a PV modeling framework originally set up by *SNL* and is now distributed via *NREL*. In its current version it allows coupling of battery storage with PV systems and incorporates financial models, e.g., for Power Purchase Agreement (PPA) calculations. More importantly, the user interface has been re-factored and is now distributed as an open-source software development kit for the Python programming language, allowing others to contribute with their individual extensions and developments. Nevertheless, on the technology side of its current version only batteries are supported and implemented (no other storage media).

---

[1] https://www.gridlabd.org/

[2] https://www.ngk-insulators.com/en/product/nas/simulator/

[3] https://github.com/PNNL-OE-Redox-Flow-Battery-Cost-Tool/PNNL-OE-Redox-Flow-Battery-Cost-Tool

[4] https://www.nrel.gov/hydrogen/h2fast.html

[5] https://www.nrel.gov/transportation/blast-btm-lite.html

[6] https://sam.nrel.gov/about-sam.html

Table 1
Overview of technical and economic modeling tools for energy storage in stationary applications.

Tool name	License type	Developer (primary)	Focus
GridLab-D	BSD open license	PNNL	Multi-domain state modeling for power distribution system simulation
NAS Battery Simulator	commercial	NGK-insulators	NGK product-tailored NaS battery simulation in peak shaving application
Flow Battery Calculator	open source	PNNL	Estimation tool of cost for redox flow batteries
H2FAST	open source (Excel sheet)	NREL	Economic assessment of hydrogen fuel stations
PerModAC	open source	htw	Performance and efficiency modeling of PV coupled residential battery storage systems
Homer Pro	commercial	Homerenergy (UL.com)	Residential/Microgrid modeling—multiple storage systems, multiple application scenarios
BLAST-BTM-Lite	commercial freeware (lite version)	NREL	Analysis and modeling of battery degradation
StorageVET	open source	EPRI	Optimization of size and financial evaluation of energy storage
SAM — System Advisor Model	BSD-3-clause	NREL	Modeling and analysis software for renewable energy projects
SimSES	BSD-3-clause	TUM	Physically motivated energy storage component, system and application behavior model

The storage value estimation tool[7] (**StorageVET**) developed mainly by the Electric Power Research Institute (*EPRI*) comes with a documentation, tutorial videos, and a user feedback forum. Since the release of version 2.0 the tool has been available as a Python package and most functional parts are licensed as 3-clause BSD open source. The tools allow conducting cost–benefit analysis and includes various application services like voltage support, retail demand charge reduction, frequency regulation, and even value stacking via aggregating multiple services to be served by one storage system. While the interface to the generation and storage technologies allows multiple options, at present only a very limited number of choices is available (PV/Internal Combustion Engine (ICE) and Battery/Compressed Air Energy Storage (CAES)). Furthermore, performance and degradation modeling is very limited, as it is based on an energy bucket model rather than analyzing the voltage and current specific phenomena of real world electro-chemical devices. Also, there is no thermal model included in the calculations, limiting the value of simulations for temperature sensible parameters like storage system efficiency (including Heating Ventilation Air Conditioning (HVAC) consumption) and storage aging.

Unlike the aforementioned tools, **SimSES** aims to bring together the model precision of tools like **SAM** and **PermodAC** and combine it with an interface to various applications and energy market scenarios. To do so, the model is distributed as open-source code on Gitlab[8] and Python Package Index[9] and builds up on a object-oriented approach programmed in Python language. Several modules are interlinked and interchangeable, and configuration files are used to select the setting of choice for typical time-series evaluations. The program as a whole, or parts of it, can also be integrated into simulation toolchains and modeling environments, making it feasible to be used in sensitivity and optimization studies and at the interface to a super-ordinate multi-instance controlling unit, as is further described in one of the case scenarios (Section 6.1). In order to allow the Energy Storage Systems (ESS) to react directly to states in a distribution grid, **SimSES** can be coupled to grid models, thus making it possible to have a power flow analysis and a detailed simulation of an ESS at the same time. **SimSES** stands out against above-mentionded tools, e.g., **Homer Pro** or **SAM**, by providing various detailed energy storage systems including validated and literature-based degradation models. Furthermore, a plethora of predefined storage-specific application Energy Management System (EMS) like ancillary services and energy trading are implemented and combined with suitable economic parameters, so that end-users are able to test a system of choice for a selected application use case. At the same time, the existent code framework is open-source accessible and open for future contributions from other developers worldwide.

3. Simulation framework for stationary energy storage systems

Stationary ESS may become a key component for future energy systems and incorporating various FTM and BTM applications supporting the electricity grid. Simulation tools are needed in order to provide advice for investment decisions and to analyze the impact of a stationary ESS. These tools should be able to model impact of applications on the health status of the ESS and its implications for prospective revenues.

While SimSES aims to allow for techno-economic cross-application and cross-technology comparisons, the tool is designed in a modular fashion and incorporates all technical components necessary for the grid connection of energy storage. Hence, **SimSES** does not only model various technologies, but also their thermal behavior, the corresponding power electronics, as well as the impact of different operating strategies. An integration into other energy simulation frameworks can be easily applied, as shown in project *openBEA*.[10]

The main task of **SimSES** is to determine the effects of the target power provided by the EMS regarding efficiency, temperature, and degradation of the ESS when applied to the storage system. Each implemented component is responsible for modeling its relevant principles. **SimSES** is divided into a simulation part for modeling the physical representation of the ESS and an evaluation part that provides technical and economic results as shown in Fig. 1. The figure also shows the basic working principle of **SimSES**: the time-series based simulation allocates an AC power target provided by the selected EMS to the storage system. After updating all models of the storage system, the current state regarding important variables such as SOC, temperature, SOH, and delivered power is transferred back to the operating strategy on which a new target power is calculated for the next time step.

In order to represent a storage system as a whole, various components need to be taken into account for a storage simulation. Besides the storage technology, power electronics is an important element. For instance, a simple Battery Energy Storage System (BESS) configuration consists of an Alternating Current to Direct Current (ACDC) converter connected to the grid and a battery. Additionally, stationary ESS are usually covered by a housing. These housings need to be thermally controlled in order to keep the ESS within its safety ranges. **SimSES** covers these possibilities with various configurable components and topologies.

More complex topologies can also include Direct Current to Direct Current (DCDC) converter or parallel connected ACDC converters, each connected to an ESS. Various ESS topologies are built with an AC connection to the grid or site location by connecting an ACDC converter to the storage system. However, in recent years Direct Current (DC)-coupled ESS has gained importance, especially in the residential

---

[7] https://www.storagevet.com/
[8] https://gitlab.lrz.de/open-ees-ses/simses
[9] https://pypi.org/project/simses/
[10] https://openbeaproject.wordpress.com/

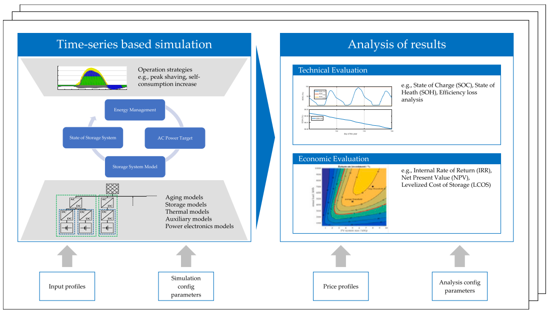

Fig. 1. Graphical overview of **SimSES** showing its simulation and analysis models, including the Energy Management System (EMS), storage system setup, technical and economical evaluation, and its necessary inputs. The state of a storage system includes the most important variables of the storage models, e.g., State of Charge (SOC), temperature, and State of Health (SOH).

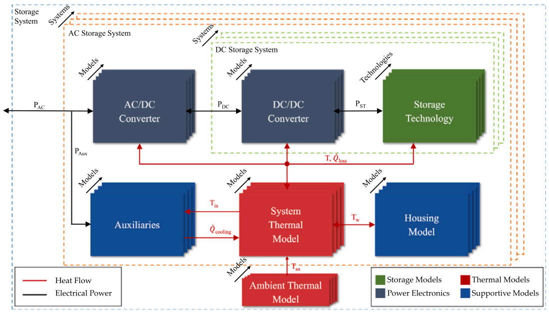

Fig. 2. Main component classes in **SimSES**: Interconnection of electrical and thermal models for ESS including the abstract AC and DC storage systems. Multiple model implementations exist for each component. Possible parallel connections of various AC and DC storage systems are indicated.

sector [19]. Hence, a state-of-the-art storage simulation framework needs to take varying topologies into account. **SimSES** considers these topologies by defining two abstract systems: AC and DC storage systems, which can also be combined in order to meet versatile topology configurations. Every AC storage system consists at least of an ACDC converter and a DC storage system. On the one hand, this allows the connection of several storage systems to the grid in parallel; on the other hand, this allows multiple DC-connected ESS within one storage system. Furthermore, the main ESS model is located inside the DC storage system behind a DCDC converter. These models are depicted in Fig. 2.

In the following sections, each of the **SimSES** packages as well as the underlying models and implementations are described in detail and shown in Fig. 3. *Storage Technology* and *System* provides models to represent physical models of storage system components while *Analysis* focuses on examining the simulation results regarding the technical and economical behavior of the simulated storage systems. All control algorithms and power flow management are handled within the *Logic* package.

Additional packages like *Commons*, *Simulation*, and *Data* deliver supportive functions for **SimSES**. *Config* is tasked to deliver functionality for the mentioned modular configuration of the ESS. In this package, software design patterns like the factory pattern are used to provide a wide range of configurable components [20]. Additionally, the structure allows the use of sensitivity analysis, e.g., by varying either different components or their dimensions. *Simulation* is another package that supports sensitivity analysis by allowing running multiple **SimSES** instances in parallel, therefore increasing simulation speed. For this purpose, Python's multiprocessing library is used. Further time series functions are implemented, like handling of profiles for power or price time series. These functions are used throughout **SimSES**, for example, by providing power profiles for the EMS. These supportive functions are covered within *Commons*, providing general functionality for time-series based simulations.

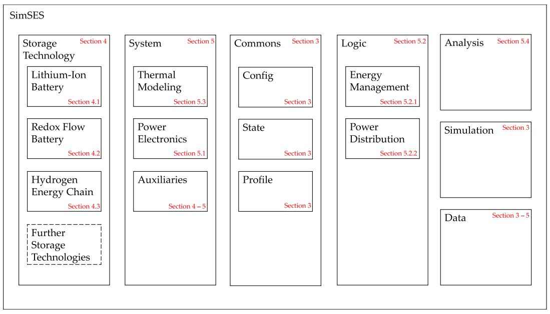

Fig. 3. Structure of **SimSES**: Packages are divided into *Storage Technology*, *System*, *Commons*, *Logic*, *Analysis*, *Simulation*, and *Data*. Within *Storage Technology*, the physical representation of each technology, namely LIB, RFB, and Hydrogen, is located. The *Commons* package delivers general functions for configuration and common features. The periphery is handled in the *System* package. Control algorithm and management is dealt with in the *Logic* package. *Analysis* focuses on the technical and economical evaluation of the simulation results. *Simulation* provides functions for simultaneous simulations, whereas *Data* stores all necessary information.

4. Storage technology models

Energy storage models represent the core of **SimSES**. In-depth models of various storage technologies are implemented, namely for LIB, RFB, and a hydrogen energy chain represented by electrolyzer, fuel cell and hydrogen storage. Each of these storage technologies have specific implementations regarding their physics and behavior. Due to the modularity of **SimSES**, further technologies can be implemented in future work.

4.1. Lithium-ion battery

ESSs based on LIB have evolved rapidly with a wide range of cell technologies and falling costs in recent years [11,21]. In **SimSES** LIBs are implemented as a distinct storage technology. The target power for this technology P_{st} depends on the storage structure and the power distributor as described in Section 5.

Four subcomponents are implemented in **SimSES** for behavior modeling of LIB. The **Equivalent Circuit Model (ECM)** is used to describe the electrical behavior of a specific cell type providing terminal voltage according to operational input data. The **Battery Management System (BMS)** monitors the cell operation conditions and updates values for the current. The electrical characteristics of LIBs in **SimSES** differ with chemistry and composition of constituent materials and may be fed with predefined manufacturer-specific datasets. Furthermore, various cell-specific degradation models can be selected in **SimSES**. The **aging** calculation is based on the cycle detector selected (e.g., half-cycle detector). These four main components are schematically illustrated in Fig. 4, and explained in detail in the following subsections.

4.1.1. Equivalent circuit model

To describe the electrical behavior, in **SimSES** the battery is implemented as a single-cell ECM. The currently implemented model includes an Open Circuit Voltage (OCV) and an internal resistance R_i, which is depicted in Fig. 4. According to Eq. (1), the terminal voltage

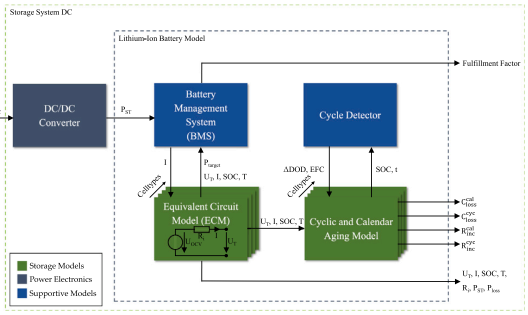

Fig. 4. Package structure of a lithium-ion battery. The battery package in **SimSES** includes four main components: a battery management system, a cell type including a equivalent circuit model, a degradation model, and a cycle detector.

U_T of each cell is calculated from the OCV and the voltage drop ΔU across R_i, due to the cell current I.

The OCVs of all currently implemented cell types are only dependent on the SOC but could be extended with further parameters like temperature and SOH. The internal resistance R_i of all currently implemented cell types takes the cell temperature T_{cell}, I, and the SOC into consideration. For both the SOC as well as R_i, the required data for different cell types are stored as look-up tables in **SimSES**. In between the available data points a linear interpolation is executed. Hence, the result quality relies on the number of data points. To improve performance, the interpolation of the SOC data was replaced by a fitted mathematical function, which is explained in Appendix A.

$$U_T = U_{OCV} - \Delta U = U_{OCV}\,(SOC) - I \cdot R_i\,\left(SOC, I, T_{cell}\right) \tag{1}$$

4.1.2. Battery management system

The BMS is linked to the ECM and is responsible for maintaining critical cell parameters within their permissible ranges. In addition to the target power P_{target}, voltage U_T, temperature T_{cell}, SOC, and current I are further input parameter for the BMS. According to the cell-specific parameters (e.g., maximum temperature), the BMS checks the input parameters and indicates whether they are within their limits. If limit violations occur, the current is restricted and returned to the ECM. The other parameters are recalculated accordingly and passed on to the aging models. The fulfillment factor indicates the share of the output power to the target power and will become sub-unity for simulations with boundary violations.

As seen in Eq. (1), the current I and the terminal voltage U_T are interdependent. Differential equations are necessary for calculating these values in the discrete time domain. To avoid these computationally intensive differential equations, an iteration loop is integrated in **SimSES**: the updated current I and terminal voltage U_T are iteratively derived through repetitive numerical approximation. This loop terminates after a predefined maximum number of iterations or as soon as the change in the current I or the terminal voltage U_T falls below a preset limit.

4.1.3. Lithium-ion battery cell types

The LIB cell forms the core of the BESS, and is essential for understanding the electrical and thermal characteristics of an entire system. For a more detailed discussion the reader is referred to [22,23] and for a description of current and future materials for LIBs as well as beyond lithium-based anode materials the reader is referred to [24]. In **SimSES**, three state-of-the-art technologies based on a Carbon-Graphite (C) anode and various cathode materials are currently implemented: two cells with a Nickel-Manganese-Cobalt-Oxide (NMC) cathode and one cell, each with a Lithium-Iron-Phosphate (LFP) and Nickel-Cobalt-Aluminum-Oxide (NCA) cathode, respectively. In addition, a generic cell with linear OCV is implemented in order to run simulations independent of the cell chemistry. Table 2 gives an overview of these cells, including their electrical attributes. The thermal parameters are summarized in Appendix B.

4.1.4. Lithium-ion battery degradation models

LIBs are subject to degradation due to multiple cell-internal aging processes, which can have significant impact on the economics of a BESS project [30]. In **SimSES**, degradation is modeled following a semi-empirical superposition approach of cyclic and calendar aging, as shown in Eqs. (2) and (3).

$$C^{total}_{loss} = C^{cal}_{loss} + C^{cyc}_{loss} \tag{2}$$

$$R^{total}_{inc} = R^{cal}_{inc} + R^{cyc}_{inc} \tag{3}$$

The resulting capacity loss C^{total}_{loss} and resistance increase R^{total}_{inc} are calculated through the addition of the respective calendar aging (C^{cal}_{loss}, R^{cal}_{inc}) and cyclic-aging components (C^{cyc}_{loss}, R^{cyc}_{inc}). Table 3 provides an overview of the primary LIB degradation models that are available in **SimSES** and their dependencies, as well as the sources on which these models are based. Here, t, SOC, T_{cell}, and U_T refer to the simulation time, state of charge, cell terminal voltage, and cell temperature, respectively. ΔDOD, EFC, Q, and $\overline{U_T}$ refer to the delta in depth of discharge for a cycle, the number of equivalent full cycles, the charge throughput, and the average cell terminal voltage over one equivalent cycle. The delta in depth of discharge (ΔDOD), as it is implemented here, is also referenced as depth of cycle or cycle depth in literature by some authors.

While calendar aging is computed once every simulation step, the model routine to calculate increase in cyclic aging is only triggered following the detection of half an equivalent cycle of charge throughput. This decreases the calculation time and allows determining the C-rate as well as DOC for that half equivalent cycle.

4.2. Redox flow battery

Large-scale storage systems are purportedly to be of rising concern in order to ease the growing penetration of RES. Hence, RFBs are of particular interest for multiple hour- and large-scale stationary ESSs because they can be easily and efficiently scaled according to the needs and become cost competitive at an energy range of multiple MWh [31]. To analyze their potential in different applications from small-scale (e.g., residential storage) to large-scale applications (e.g., industrial storage), they are integrated into **SimSES** as an additional storage technology. In an RFB, the liquid storage medium (electrolyte) is stored in external tanks. To charge and discharge the RFB, the electrolyte is pumped through a stack where the electrochemical reactions take place. The electrolyte divided in anolyte and catholyte solutions are separated by an ion-exchange membrane through which the charge carriers are transported. There are several known possible electrolyte combinations, e.g., all-vanadium or vanadium/bromine solutions [32]. As the energy conversion unit and the energy storage medium are decoupled, the power and energy of an RFB can be scaled separately [31,32].

Fig. 5 shows the structure of the main components modeled in **SimSES** to describe an RFB. The electrochemical model calculates the electrical operating parameters of a specific stack module dependent on the chemical composition of the selected electrolyte system. The control system checks whether the target parameters are within safe operating limits and returns the actual usable values. Different pumps and pump control algorithms can be configured. In the following, the model components are described in more detail.

Table 2
Lithium-ion battery cells currently implemented in **SimSES**, including their electrical parameters.

Manufacturer Model	Acronym in **SimSES**	Anode Cathode	Nom. voltage (V) Voltage range (V)	Capacity (Ah)	C_{rate} Ch. (1/h) C_{rate} Dch. (1/h)	Source
Sony[a] US26650FTC1	SonyLFP	Graphite $LiFePo_4$	3.2 2.0–3.6	3.0	1.0 6.6	[25,26]
Panasonic NCR18650PD	Panasonic- NCA	Graphite $LiNiCoAlO_2$	3.6 2.5–4.2	2.73	0.5 3.5	[27]
E-One Moli Energy IHR18650A	MolicelNMC	Graphite $LiNiCoMnO_2$	3.7 3.0–4.25	1.9	1.05 2.1	[28]
Sanyo UR18650E	SanyoNMC	Graphite $LiNiCoMnO_2$	3.6 2.5–4.2	2.05	1.0 3.0	[27,29]
Generic cell model	GenericCell	–	3.5 3.0–4.0	2.5	2.0 2.0	–

[a] Murata Manufacturing Co. acquired the Sony battery division in 2017.

Table 3
LIB-specific degradation models along with corresponding variable dependencies and literature sources.

Cell acronym	Calendar aging		Cyclic aging		Model based on
	C_{loss}^{cal}	R_{inc}^{cal}	C_{loss}^{cyc}	R_{inc}^{cyc}	
SonyLFP	t, SOC, T_{cell}	t, SOC, T_{cell}	EFC, ΔDOD, C-rate	EFC, ΔDOD, C-rate	[25,26]
PanasonicNCA	t, U_T, T_{cell}	t, SOC, T_{cell}	EFC, U_T, C-rate	EFC, U_T, C-rate	[27]
MolicelNMC	t, SOC, T_{cell}	t, SOC, T_{cell}	Q, ΔDOD, C-rate	Q, ΔDOD, C-rate	[28]
SanyoNMC	t, U_T, T_{cell}	t, U_T, T_{cell}	$Q, \Delta DOD, \overline{U_T}$	$Q, \Delta DOD, \overline{U_T}$	[29]
GenericCell	t	–	EFC	–	–

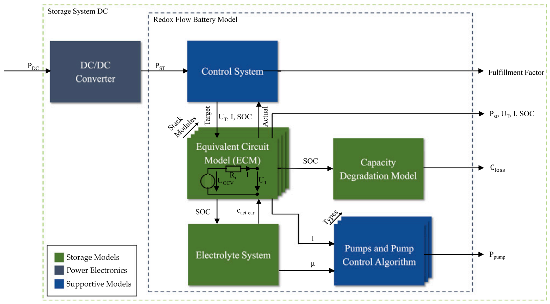

Fig. 5. Package structure for a redox flow battery (RFB). It contains an electrochemical model (equivalent circuit model) with specific parameters for different stack modules, an implemented control system, an electrolyte system, a degradation model, and pumps, with interchangeable control algorithms.

4.2.1. *Electrochemical model*

As with LIB, the currently implemented electrochemical model of an RFB is based on an equivalent circuit model (cf. Fig. 5). The terminal voltage U_T is directly calculated from the power applied to the RFB. Eq. (4) can be derived from Eq. (1) by using the relation between storage power P_{st}, terminal voltage U_T, and current I ($P_{st} = U_T \cdot I$). U_T is therefore calculated by P_{st}, the OCV, and the internal resistance R_i. Both OCV and R_i are dependent on the SOC and the electrolyte temperature in the stack module T_{stack}.

$$\begin{aligned} U_T &= 0.5 \cdot \left(U_{OCV} + \sqrt{U_{OCV}^2 + 4 \cdot R_i \cdot P_{st}} \right) \\ U_{OCV} &= f\left(SOC, T_{stack}\right) \\ R_i &= f\left(SOC, T_{stack}\right) \end{aligned} \tag{4}$$

Charge effects are taken into account by implementing a current for the charging losses $I_{char\text{-}loss}$ when calculating the change of the system SOC (SOC_{system}) via Eq. (5), considering the simulation time step Δt, the nominal voltage at the stack module U_{nom}, and the total energy of the electrolyte E_{total}. $I_{char\text{-}loss}$ includes coulombic losses due to self-discharge through the transport of reactants over the membrane and shunt currents. Shunt currents occur due to a connection of cells in the stack through an ionic conductive electrolyte distribution system. This creates a bypass current forced by the electric field due to the electrical series connection of the cells [33].

$$\Delta SOC_{system} = \frac{\left(I - I_{char\text{-}loss}\right) \cdot \Delta t \cdot U_{nom}}{E_{total}} \tag{5}$$

A control system is integrated in the electrochemical model, which checks whether U_T, I, and SOC are within safe operating limits. If the values are out of range, they will be adapted and the other parameters are recalculated accordingly.

Additionally, a capacity degradation model including the capacity losses C_{loss} due to hydrogen evolution is implemented in the RFB model. Further research is required to estimate a realistic hydrogen evolution current for industrial-sized stacks to predict the capacity reduction realistically over time. A current approach using experimental data of a laboratory cell from Schweiss et al. [34] overestimates the resulting capacity losses. Whitehead et al. [35] stated a capacity loss of less than 1% per year due to hydrogen evolution. Therefore, a hydrogen current of $5 \cdot 10^{-8}\ \frac{mA}{cm^2}$ is assumed, resulting in a capacity loss of about 1% per year for a system with an Energy-to-Power Ratio (EPR) of 1. As the EPR increases, the loss decreases accordingly.

4.2.2. *Stack module and electrolyte system*

The calculations in the electrochemical model are based on electrical and geometrical data for a stack. A stack consists of a fixed number of cells electrically connected in series. The data to consider the voltage, charge, and hydraulic losses of a stack can be obtained either from experimental data or from the literature values and models. Stacks can be electrically connected in parallel or in series to a stack module to increase power and voltage of the RFB system. In this configuration the electrolyte flows in parallel through all cells and stacks. The performance parameters of the stack are directly connected to the used electrolyte system. The currently in **SimSES** examined and implemented electrolyte is an all-Vanadium system, consisting of 1.6 mol/l Vanadium solved in an aqueous sulfuric acid (2 mol/l H_2SO_4) from GfE (Gesellschaft für Elektrometallurgie mbH). To reduce side reaction due to high potentials and to prevent performance penalties the electrolyte needs to operate in a limited SOC range. A typical usable SOC range for a RFB lies between 20 and 80% [36]. Based on this SOC

Table 4
Redox-flow battery stack types in **SimSES**.

Acronym in SimSES	Cell number	Cell area (cm^2)	Based on experimental data of	Model based on
CellDataStack5500W	40	2160	Appendix C	[37–39]
DummyStack3000W	20	1000	N/A	N/A
IndustrialStack1500W	18	551	Voltstorage GmbH	[37,38]

range the nominal power of a stack is calculated. An overview of the in **SimSES** implemented stacks is listed in Table 4. The name of the stack includes its nominal power. In addition, some modifications of the described stacks are included, which are up-scaled or simplified versions that are not included in the list.

4.2.3. Pumps and pump control algorithm

The pump control algorithm used to control the flow rate or pressure drop in the system is an important performance-determining factor that affects the operating losses. Two different algorithms to choose from are currently integrated: the constant and the stoichiometric flow rate. It is assumed that the pumps always stop during stand-by to reduce the operating losses. If flow rate $\dot{V}$ or pressure drop Δp is given, the other value is calculated via Eq. (6) from the specific hydraulic, viscosity-corrected resistance $R_{hydraulic,specific}$ and the viscosity μ of the anolyte or catholyte.

$$\Delta p = \dot{V} \cdot R_{hydraulic,specific} \cdot \mu \tag{6}$$

If the pump is operating with a constant flow rate, it must be ensured that the volume flow is sufficiently high so that the stack module is supplied with enough reactants at any time of operation (depending on SOC and I). This is checked by the control system integrated in the electrochemical model.

For the stoichiometric flow rate algorithm $\dot{V}$ is calculated according to Eq. (7) via the stoichiometric factor ν, the total concentration of the active charge carriers in the electrolyte $c_{act\text{-}car}$ (for the implemented Vanadium electrolyte it is 1.6 mol/l), the Faraday constant F, and the still available concentration of reactants in the electrolyte, which is described through the SOC for discharging and (SOC − 1) for charging. If, for example, the RFB is charging at SOC 70%, reactants that can be maximal charged in the Stack are 30% of the total concentration, therefore value is 0.3.

$$\begin{aligned} \dot{V} &= \frac{\nu \cdot I}{F \cdot c_{act\text{-}car} \cdot (SOC - 1)} \qquad \text{for} \quad P >= 0 \\ \dot{V} &= \frac{\nu \cdot I}{F \cdot c_{act\text{-}car} \cdot SOC} \qquad \text{for} \quad P < 0 \end{aligned} \tag{7}$$

The pump losses P_{pump} can be calculated with Δp, $\dot{V}$, and the pump efficiency η_{pump} of a specific pump that can be selected in **SimSES** via Eq. (8) [40].

$$P_{pump} = \frac{\dot{V} \cdot \Delta p}{\eta_{pump}} \tag{8}$$

4.3. Hydrogen energy chain: Electrolyzer, storage, and fuel cell

Hydrogen as an energy carrier is supposed to be one of the major contributors impacting future energy provision, storage, and distribution [41]. The abundance of chemically-bound hydrogen in the form of water as well as its very high-energy density is compelling for its deployment as an energy carrier for large-scale energy storage. However, the efficiency of splitting water into its separate components via electrochemical electrolysis and reverting the process through fuel cells or combustion power plants is comparatively low, in striking contrast to electrochemical storage like LIB [14,42]. As such, hydrogen is thought to complement rather than to compete with LIB and RFB. In order to understand the effects of a hydrogen-based energy chain on a system level including its periphery, models for *electrolyzers*, *fuel cells*, *hydrogen storage*, and its auxiliary components like pumps and compressors are integrated as models within **SimSES**. Within this section, implementations of the respective models are explained in detail.

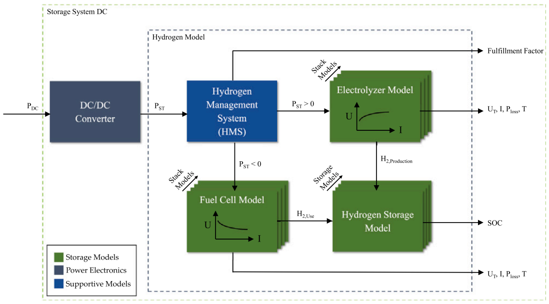

Fig. 6. Package structure for hydrogen in **SimSES** includes four main components: a *hydrogen management system*, an *electrolyzer*, a *fuel cell*, and a *storage model*.

The hydrogen package structure is displayed in Fig. 6, consisting of a *Hydrogen Management System (HMS)*, an *electrolyzer*, a *fuel cell*, and a H_2 *storage model*. The *HMS* supervises the whole hydrogen chain for valid ranges of temperature and SOC and reduces applied power if necessary. The storage model could be a gas pipe with an assumed infinite capacity or a hydrogen pressure tank with a predefined energy capacity. Depending on the pressure of the gas within the storage tank, the gas needs to be compressed to the desired pressure level. The *electrolyzer* and *fuel cell* models are explained in detail in the following sections. It is worth to mention that **SimSES** also allows a single-direction hydrogen energy chain by neglecting either the *electrolyzer* or the *fuel cell* component with special implementations. A summary of all currently implemented models is given in Table 5. Due to the modular structure of **SimSES**, additional models can be implemented in a future release accordingly.

4.3.1. Electrolyzer

A water electrolyzer splits water with the use of electricity into hydrogen and oxygen by passing ions through an electrolyte from one electrode to the other. The pressure and temperature-dependent polarization curve is based on the general equation of Nernst voltage U_{nernst} as well as overpotentials represented by ohmic η_{ohm}, activation η_{act}, and diffusion losses η_{diff} as shown in Eq. (9) [50]. In some implementations mass transport and membrane permeation are also considered.

$$U_{T,EL} = U_{nernst} + \eta_{ohm} + \eta_{act} + \eta_{diff} \tag{9}$$

Depending on the stack technology, e.g., alkaline or polymer electrolyte membranes (PEM), the *electrolyzer* is operated at different pressure and temperature levels, which is taken into consideration by varying polarization curves for each technology [50]. As shown in Fig. 7, the *electrolyzer* model is divided into its stack and corresponding degradation models, pressure and thermal models as well as necessary auxiliaries like a pump, water heater, and gas dryer. The electrical auxiliary power is calculated according to the hydrogen and oxygen generation pressures for the anode and cathode, as well as the stack temperature. A water pump regulates the humidification of the *electrolyzer*, whereas the generated hydrogen gas needs to be dried. These auxiliary models calculate the necessary electrical power in order to provide a temperature and mass equilibrium.

Table 5
Overview of implemented *electrolyzer*, *fuel cell* and *hydrogen storage* models in **SimSES**.

Technology	Acronym in SimSES	Type	Degradation effects	Based on experimental data of	Model based on
Electrolyzer	PemElectrolyzerMultiDimAnalytic	PEM	Resistance increase, Decrease of exchange current	Forschungszentrum Jülich	[43–45]
	PemElectrolyzer	PEM	N/A	N/A	[46]
	AlkalineElectrolyzer	Alkaline	N/A	Hydrogen Research Institute	[47,48]
Fuel Cell	PemFuelCell	PEM	N/A	N/A	[49]
	JupiterFuelCell	PEM	N/A	SFC Energy AG	–
Hydrogen Storage	PressureTank	Pressure Tank	N/A	N/A	–
	SimplePipeline	Pipeline	N/A	N/A	–

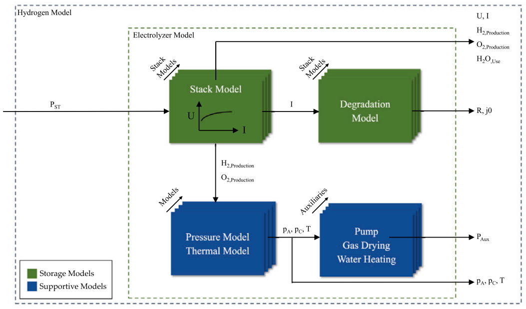

Fig. 7. Package structure for *electrolyzer* in **SimSES** includes a stack, pressure, thermal and degradation model as well as a pump and gas dryer.

Electrolyzer degradation is a field of ongoing research with controversy over underlying mechanisms and influencing factors [51,52]. However, active operation time and applied current density seem to be major impact factors for electrolyzer degradation. For instance, the implemented degradation for the Polymer Electrolyte Membrane (PEM) electrolyzer acquired from the work of Tjarks [43] is based on the findings of Rakousky et al. [44,45] considering a resistance increase and a decrease of the exchange current. Other implementations of electrolyzers are a PEM variant without degradation effects based on the work of Marangio et al. [46] and an alkaline version based on the work of Hammoudi et al. [47] and Henao et al. [48].

4.3.2. Fuel cell

As an opposite to *electrolyzers*, *fuel cells* combine hydrogen and oxygen to water while releasing usable energy in the form of electricity [42]. The terminal voltage is calculated by the Nernst voltage subtracted by the voltages due to ohmic, activation, and diffusion losses shown in Eq. (10).

$$U_{T,FC} = U_{nernst} - \eta_{ohm} - \eta_{akt} - \eta_{diff} \tag{10}$$

The *fuel cell* package has a structure that is similar to the *electrolyzer* package, with a stack, pressure, and thermal model. During operation, the water handling especially for PEM fuel cells is crucial and handled by water pumps. An implementation of a PEM fuel cell based on Feroldi et al. [49] as well as a model for the Jupiter PEM fuel cell of SFC Energy AG[11] including a thermal model is available in **SimSES**. However, the implementation of adequate degradation models within SimSES is a task for future action.

5. System periphery, management, and evaluation

Energy storage systems not only consist of the underlying storage technology but also the periphery like power electronic components and thermal behavior as well as an EMS. These elements are crucial for evaluating energy storage systems as a whole. In order to provide insights into the overall system behavior, **SimSES** not only models the periphery and the EMS, it also provides in-depth technical and economical analysis of the investigated ESS.

5.1. Power electronics

Besides the storage technology, the power electronic components play a crucial role in terms of system efficiency. Depending on topology and application, power electronics may contribute significantly to the overall system losses [53]. Hence, **SimSES** has to consider these electronic components for an accurate simulation of a storage system like ACDC and DCDC converters. An overview of the implemented models in **SimSES** is given in Table 6. Models of these converters are represented by power and voltage-dependent efficiency curves. In principle, the efficiency of a power electronics module is represented by a given storage power $P_{Storage}$ and the rated power of the power electronics component P_{Rated} as displayed in Eq. (11).

$$\eta_{PE} = f\left(P_{Storage}, P_{Rated}\right) \tag{11}$$

The power applied to the power electronic components is crucial for simulating the efficiency. When considering storage systems, it is possible that these systems do not fully deliver the requested power. These situations occur, for example, if the storage is outside of its temperature limits or the SOC is at its lower or upper limits. Hence, the power is adjusted compared to the target power of the EMS, which leads not only to non-fulfillment, but also to an altered efficiency.

5.2. Power control

Every power flow in an ESS has to be monitored and controlled. The power flow is dependent on the application and system topology. In **SimSES**, these two dependencies are handled separately with an EMS, respectively, Power Distribution Strategies (PDS). The EMS defines the target power for the ESS as a function of the application while the PDS allocates the target power to the configured subsystems. These control mechanisms are explained in detail in the following sections.

5.2.1. Energy management system

The EMS in an ESS is a system consisting of both hardware and software that allows the user to monitor and control the energy flows within an ESS. In **SimSES**, the function of the EMS is to calculate and supply a target power value for each simulation timestep (Δt) based on the selected operation strategy. This target power value can be dependent or independent of previous system states as well as interfere with various input profiles. In **SimSES** both stand-alone and stacked operation strategies can be simulated. Stacked operation strategies are sorted according to their user-associated priority level. Consequently, the individual stand-alone operating strategies are executed one after another depending on their priority. Additionally, time-discrete serial stacking is already available within **SimSES**. More complex multi-use strategies can be integrated as stand-alone strategies. At present, a handful of

---

[11] https://www.efoy-pro.com/efoy-pro/efoy-jupiter-2-5/

Table 6
Overview of implemented ACDC and DCDC converter models in **SimSES**.

Converter type	Acronym in SimSES	Based on experimental data of	Model based on
AC/DC	FixEfficiencyAcDcConverter	N/A	N/A
	NottonAcDcConverter	N/A	[54]
	Sinamics120AcDcConverter	Sinamics S120	[55]
	BonfiglioliAcDcConverter	Bonfiglioli RPS TL-4Q	Datasheet[a]
	SungrowAcDcConverter	Sungrow SC 1000 TL	Datasheet[b]
	M2bAcDcConverter	Stable Energy GmbH	[56]
DC/DC	FixEfficiencyDcDcConverter	N/A	N/A

[a] https://www.docsbonfiglioli.com.

[b] https://en.sungrowpower.com.

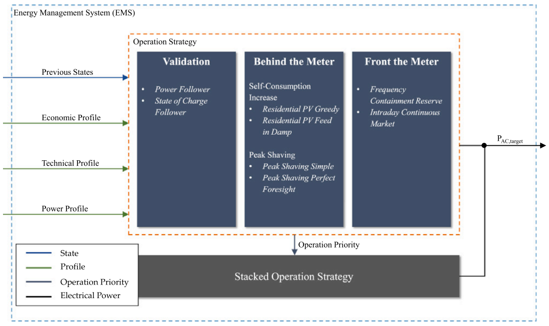

Fig. 8. Structure of the energy management system and overview of available operation strategies and their categorization in **SimSES**.

operation strategies are implemented in **SimSES**. An overview of these operation strategies and their categorization is depicted in Fig. 8.

The *power follower* strategy is a basic operation strategy which aims to get the storage system operation to replicate a given power profile. Similar to the aforementioned strategy, the *SOC follower* converts a given SOC profile to a power profile and attempts to make the storage system fulfill this calculated demand power at each timestep.

Based on the work of Zeh and Witzmann [57], two operation strategies for residential SCI in combination with Photovoltaic (PV) generation units have been implemented. The *residential PV greedy* operation strategy charges the ESS as fast as possible without consideration of the grid by meeting the residual load at all times. To reduce the maximum grid load the *residential PV feed in damp* operation strategy schedules the charging of the ESS according to a PV prediction. It attempts to provide a constant charging power and aims for a fully charged ESS at sundown.

Two strategies have currently been implemented for industrial consumers. The simple *Peak Shaving (PS)* strategy works as follows. As long as the target power is above a specified threshold, the additionally required power is provided by the ESS. In addition, the ESS will recharge itself if the power value is below the PS threshold [58] (used in the case study in Section 6.1). In order to reduce calendar aging for a lithium-ion based ESS, the *PS perfect foresight* strategy operates under the assumption of perfect foresight for the load profile. The ESS will only charge up to the energy that is required for the next load peak, right before the occurrence of that load peak [59].

The EMS strategy for providing *FCR* implemented in **SimSES** is based on the German regulatory framework [60,61]. The requested charging and discharging power is proportional to the frequency deviation. Below 49.8 Hz or above 50.2 Hz the output power is set to the prequalified power. Within the frequency dead band around 50 Hz with +/-10 mHz the output power is set to 0 W. The degree of freedom to exceed the output power by 20% is used, aiming to bring the SOC back to a predefined SOC set-point. The *IDM* operation strategy charges or discharges the ESS by trading energy on the electricity market, in particular on the IDM, if the SOC falls below a predefined lower limit or it exceeds an upper limit [62]. An example for a *FCR* and a *IDM* stacked operation strategy is provided in Section 6.2.

5.2.2. Power distribution strategies

For complex storage system topologies, the power needs to be distributed between the different subsystems of an ESS [63,64]. For this purpose, several power distribution logics are implemented in **SimSES**. These logics distribute the power to the corresponding storage systems, for instance, based on the respective SOH or SOC. In **SimSES**, the ESS is differentiated between an AC and DC storage system (see Section 3). For each node of parallel connected AC systems as well as DC systems, a power flow decision has to be made similar to Bauer [64]. Mühlbauer et al. [63] as well as Bauer [64] define PDS as a simple problem of a distribution factor α as shown in Eq. (12).

$$\mathrm{P_i} = \mathrm{P_{target}} \cdot \alpha_\mathrm{i}, \tag{12}$$

where $\mathrm{P_{target}}$ is the target power provided by the EMS, α_i the power distribution factor for system i, and $\mathrm{P_i}$ the corresponding power of system i on condition that the sum of all α_i equals one. In an optimal case the PDS takes the current limitations of the underlying storage technology for $\mathrm{P_i}$ into consideration in order to be able to fulfill the requested power, e.g., temperature limitations could lead to lower deliverable power. For each node, a PDS can be configured.

Mühlbauer et al. distinguish between static and dynamic categories for PDS while Bauer has more subtle definitions for a dynamical PDS approach with a fixed and variable sequence [63,64]. Bauer also mentions a PDS as an optimization problem currently not considered in **SimSES**. In the following, PDS implemented in **SimSES** are presented.

The most straightforward implementation of a PDS is an equal distribution of the power to all storage systems. This is a static PDS approach with a fixed power distribution factor. Other static PDS-like distribution based on the ESS capacity can be easily added to the PDS set of **SimSES**. In addition, a dynamic PDS is implemented by differentiating between charge and discharge distribution factors depending on the SOC of each system based on [63].

Due to the modularity of **SimSES**, multiple ESSs with different storage technologies can be combined with a hybrid ESS, e.g., a LIB and a RFB system. For this purpose, a novel PDS is introduced prioritizing configured storage technologies by base and peak loads, respectively. While the prioritized system stays within a defined SOC range, e.g., between 25 % and 75 %, it tries to fulfill the target power within its power limits. If either the SOC or the power limit is exceeded, the next highest prioritized system takes over. If the power target is not completely allocated, a second loop distributes the power independent from the defined SOC range. In addition, the logic balances the SOC of the configured ESS if one or more systems are outside of the defined SOC range while other systems are within those ranges. The algorithm also allows a two or one way balancing, e.g., if only the peak load system should be balanced by the base load system (used in the case studies in Section 6).

5.3. Thermal modeling

Performance, efficiency, and aging of all aforementioned storage processes depend not only on charge and discharge currents, but are also highly sensitive to thermal conditions. While for some small-scale storage realizations (e.g., residential battery storage) modeling electricity flows in a fixed temperature setting might be a solution of choice with sufficient accuracy for techno-economic simulations [65], larger storage systems along with investigations about storage efficiency particularly require detailed thermal models [53]. Utility-scale LIB stationary ESS are often designed as free-standing systems, which are installed outdoors and exposed to the environment. The use of standard shipping containers to install entire energy storage systems is the preferred option in the industry today to shield sensitive electric components from adverse environmental conditions. The benefits of such a configuration include modularity, scalability, ease of logistics, conformance with road-transport regulations, and the ability to plan and optimize land usage. Such containers are also specially fitted out with insulation to limit heat flow to/from the environment, and to present a stable operation temperature to the components inside.

Heat is generated in LIBs due to internal resistance to the passage of current during operation. Lithium-ion cell technology is particularly vulnerable to adverse changes in cell temperatures, and degrade faster when operated outside of their optimal temperature ranges. In particular, degradation may result from accelerated kinetics for unwanted side reactions at elevated temperatures resulting in a loss of capacity and an increase in the internal resistance. If the generated heat is not rejected to the environment at a rate greater than the rate of heat generation, overheating and—in extreme cases—a *thermal runaway* may occur. In contrast, for applications with relatively lower current rates (alike most stationary storage use cases), air cooling systems are deemed adequate to aid the heat rejection process to maintain the cell temperatures within the stipulated ranges. It is worth to mention in this context, that in the absence of cooling systems, the capabilities of the cells are severely limited, and under-utilized [66].

In summary, thermal modeling of energy storage systems is a crucial step of the system design process, especially due to the following factors:

- temperature-dependence of the energy conversion efficiency of LIB (dependent on the internal resistance) [67] and other storage technologies,
- temperature-dependence of the degradation mechanisms [68,69],
- dependence of the round-trip efficiency on the energy consumption of auxiliary components, such as the HVAC system [55] and
- operational hazards under extreme temperatures which are too low, or too high [70].

Thermal modeling in **SimSES** follows a zero-dimensional lumped-capacity approach, and consists of a number of component packages which run in tandem to emulate the thermal behavior of a system under the specified operating conditions. Zero-dimensional lumped-capacity approaches are widely used in the reviewed literature and found to be suitable for system models [55,71]. Each of these packages and their core features are presented in this section, along with how they fit into the larger picture within **SimSES** and its architecture. The thermal model and its associated components function at the AC storage system level in **SimSES**. **SimSES** currently supports a container-based housing solution with an air cooling system for LIB stationary ESS. An overview of these packages and their interplay is seen in Fig. 9.

5.3.1. Ambient thermal model

The primary function of the ambient thermal model is to account for the predominant environmental effects that play a role in the thermal behavior of the ESS. The ambient thermal model currently consists of an ambient temperature which supplies a value of ambient air temperature T_{aa} for each simulation timestep Δt at time t. The ambient temperature is available in two variants: a constant temperature model, which supplies a user-specified T_{aa} for each timestep, and a location-specific model, which, depending on the time of day and year, supplies a value of T_{aa} based on recorded temperature time-series data. The ambient temperature datasets currently present in SimSES have been generated with the help of the publicly available simulation tool *greenius*, developed by the German Aerospace Center (DLR) [72]. A solar irradiation model is also envisioned for a future release of SimSES as an extension of the ambient thermal model in order to be able to supply values of incident solar irradiation at a given location at time t to allow for better estimation of the heat load on an ESS. The ambient thermal model is understandably applicable to all AC storage system instances present in a given BESS configuration.

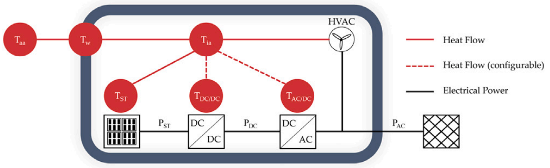

Fig. 9. **SimSES** is thermally interconnected with the thermal nodes of ambient air T_{aa}, wall T_w, inner air T_{ia}, and storage technology T_{ST}. The temperature conjunction of T_{ACDC} and T_{DCDC} can be switched off. The HVAC system controls T_{ia} of the storage system.

5.3.2. Housing model

The housing model emulates the physical attributes of the specified housing type. **SimSES** currently supports system simulations with a standard 20 foot shipping container as the housing. The walls are modeled with three layers of materials, including an insulating layer of Polyurethane (PU) between the outer and inner metal layers. The geometrical dimensions and physical and thermal properties of the walls of the shipping container can be adapted to suit any desired variant. The modular and extendable structure of **SimSES** ensures that the choice is not limited to the presently implemented model, but rather allows for other housing types or installation conditions to be modeled and included in simulations.

5.3.3. Heating, ventilation and air conditioning model

As the temperature inside the housing is to be maintained within a stipulated range to ensure safe and optimal operating conditions, a HVAC unit is necessary to correct temperature deviations. **SimSES** also supports inclusion and modeling of HVAC systems. Two basic HVAC models are currently implemented: one, which uses the internal air temperature T_{ia} deviation from its user-specified set-point to roughly estimate the amount of thermal power required to counter this deviation, and the other, which employs a Proportional-Integral-Derivative (PID) controller logic to arrive at a value of thermal power to counteract the deviation in T_{ia} from its set-point. The corresponding electrical power consumption $P_{electrical}$ of the HVAC, which is related to the thermal power P_{hvac} by the Coefficient of Performance (COP) (see Eq. (13)), is logged in the state of the AC storage system, and influences the round-trip efficiency of the ESS.

$$P_{electrical} = \frac{P_{hvac}}{COP} \tag{13}$$

5.3.4. System thermal model

The system thermal model is central to the thermal modeling process in **SimSES**, in that it emulates the physical phenomenon of heat transfer among the components of the ESS and its environment, as well as integrates the functioning of all aforementioned components. The system thermal model estimates the temperatures of all components of interest after each simulation timestep Δt, based on the various heat loads—both external and internal—that the ESS is subjected to. Each instance of AC storage system has its own system thermal model, and captures the thermal behavior of all components present in each AC storage system. The analysis applies the zero-dimensional lumped capacity approach, and the central assumption is that all the components are treated as lumped isotropic homogeneous objects with heat capacities and heat transfer coefficients. The internal air in the container is assumed to possess a uniform temperature throughout its volume, and flows are not considered. The temperatures of the storage technologies influence important parameters such as efficiency and voltage, as well as the rate at which they degrade. The component models used in **SimSES**, which are explained in the subsequent sections, take these temperature variations into account.

The system thermal model solves a system of first-order coupled differential equations to obtain the temperatures of the storage technologies, the internal air, and components such as the ACDC converter, if they are present within the same housing. This list of components, whose temperatures are of interest, can be expanded as required owing to the modular structure of the system thermal model. As the temperatures at the start of each timestep Δt are known, and the temperatures at the end of each timestep are of interest, an initial value problem can be formulated.

Within each DC storage system, for each instance of storage technology i with a mass m_{st} and specific heat c_p^{st}, a differential equation capturing the variation in its temperature T_{ST} under the combined effects of natural convection with the internal air (ia) P_{conv}^{st-ia} and the heat generation within itself on account of energy conversion losses P_{loss}^{st} can be formulated (see Fig. 9). For an AC storage system with a total of n storage technology instances within its DC storage systems, a total of n differential equations based on Eq. (14) can be formulated.

$$m_{st,i} \cdot c_p^{st,i} \cdot \frac{dT_{st,i}}{dt} = P_{loss}^{st,i} - P_{conv}^{st,i-ia} \tag{14}$$

Similarly, a heat balance equation with a form similar to Eq. (14) can be formulated for other components such as the ACDC converter, which also introduce heat into the housing due to the energy conversion losses (see Fig. 9).

For the internal air with a mass m_{ia} and specific heat c_p^{ia}, a heat balance can also be formulated to determine the variation in its temperature T_{ia}. The heat balance outlines its interaction via natural convection with each storage technology P_{conv}^{st-ia}, other components such as the ACDC converter (if present) $P_{conv}^{acdc-ia}$, and the innermost layer (il) of the housing walls P_{conv}^{il-ia}. The thermal power of the HVAC P_{hvac} is also accounted for in this balance (see Eq. (15)).

$$m_{ia} \cdot c_{p,ia} \cdot \frac{dT_{ia}}{dt} = \Sigma P_{conv}^{st,i-ia} + P_{conv}^{acdc-ia} - P_{hvac} - P_{conv}^{ia-il} \tag{15}$$

The innermost layer of the housing walls, in addition to the convective heat transfer with the internal air, also exchanges heat with the insulation layer adjacent to it via heat conduction, and a heat balance equation can be written.

The insulation layer interacts with both the innermost and outer layers via heat conduction, and a corresponding heat balance equation can be drafted as well. The outer layer exchanges heat with the adjacent insulation layer via conduction, and interacts with the ambient air via natural convection. The outer layer is also subjected to a heat load due to the direct and diffuse solar irradiation incident on its surfaces. A heat balance for the outer layer can be applied by taking into account the heat loads due to the incident solar irradiation, the conduction through the layers, and the natural convection with the ambient air.

Depending on the chosen simulation timestep Δt, the heat balance equations for all considered components are then solved simultaneously at least once, or in the case of very large Δt, the system of equations is solved multiple times in an attempt to obtain a greater degree of accuracy. The solution of this system of equations yields the values of the temperatures at the end of each simulation timestep, which influence the component models.

In case simpler simulations are to be conducted, the thermal model can also be disabled, in which case the storage technologies experience a constant (user-defined) ambient temperature, and the temperatures of the storage technologies and other components are also set to remain at this value and are not updated. **SimSES** currently only offers modeling of thermal behavior for LIB. Augmentation of these capabilities for other storage technologies is planned for future releases.

5.4. Analysis

Following the simulation of ESSs, an analysis of the simulation results is conducted automatically by **SimSES** providing Key Performance Indicators (KPIs) and plots that allow the user to gain insights of the configured ESS. Furthermore, the analysis can be used to compare simulation results of different scenarios quantitatively and qualitatively. While the *Data* subpackage provides relevant parsers and utility functions for processing the time series of simulation results, the *Evaluation* subpackage includes the actual methods for deriving the KPIs and creating plots. Which evaluations should be performed, as well as relevant input data (e.g., electricity prices and storage cost) can be specified by the user. In the following, the technical evaluation and economic evaluation will be explained in more detail.

5.4.1. Technical evaluation

Within the *Technical Evaluation* part of **SimSES**, technical KPIs are determined on the system and storage technology level. Depending on the storage technology used, the respective KPIs are exported at the end of the analysis. Automatically generated plots give the user an impression of the usage and performance of the simulated ESS like time variance of AC and DC power, SOC and capacity. More advanced users can also use the simulation results to calculate characteristic values beyond the displayed KPIs. The technical evaluation's KPIs on system, lithium-ion, redox flow and hydrogen level are summarized in Table 7. As an example, the calculation of two KPIs is shown below.

The Round-Trip Efficiency (RTE) is calculated on the system level using Eq. (17) deviated from Eq. (16). To calculate the RTE, the discharged energy (E_{out}) is divided by the charged energy (E_{in}), from which the change of energy by SOC rise or decrease (ΔE) is subtracted. For simulations over a longer period of time, the efficiency influence on the SOC change can be neglected because charged and discharged energy are substantially larger than the change in energy between the start and end SOC of the simulation. For shorter simulation periods, the influence of efficiency on the SOC change must be considered. For this purpose, the SOC change is divided by the root of the efficiency, since, for example, the additionally charged energy at SOC increase has already passed through the power electronics in one direction and was thus influenced by the efficiency. A symmetrical efficiency for charge and discharge is assumed here.

$$\eta_{RTE} = \frac{E_{out}}{E_{in} - \frac{\Delta E}{\sqrt{\eta_{RTE}}}} \tag{16}$$

with $\Delta E = SOC_{last} \cdot E_{last} - SOC_{initial} \cdot E_{initial}$. Solving Eq. (16) for η_{RTE} leads to:

$$\eta_{RTE} = \frac{E_{out}}{E_{in}} + \frac{\Delta E^2 + \Delta E\sqrt{4E_{out}E_{in} + \Delta E^2}}{2E_{in}^2} \tag{17}$$

Another KPI calculated in the technical analysis is the remaining energy content (e_{rem}) as a percentage of the initial energy (Eq. (18)). For this, the current energy (E_{act}) is divided by the initial energy (E_{nom}).

$$e_{rem} = \frac{E_{act}}{E_{nom}} \tag{18}$$

Table 7
Key Performance Indicators (KPIs) for technical evaluation and the level at which they are calculated. Crosses indicate for which level the respective KPI is calculated.

Selected key performance indicators (KPI)	System	Lithium-ion	Redox flow	Hydrogen
Round-trip efficiency (%)	x	x	x	x
Mean state of charge (%)	x	x	x	x
Number of changes of signs per day (#)	x	x	x	x
Avg. length of resting times (min)	x	x	x	x
Pos. energy between changes of sign (% of capacity)	x	x	x	x
Avg. fulfillment factor (%)	x	x	x	x
Remaining capacity (%)	x	x	x	x
Energy throughput (kWh)	x	x	x	x
Mean power electronics efficiency (%)	x			
Equivalent full cycles (#)		x	x	
Depth of discharges (%)		x	x	
Coulomb efficiency (%)			x	
State of health (%)				x
Energy for heating of water (kWh)				x
Energy for compression of hydrogen produced (kWh)				x
Total mass of hydrogen (kg)				x

5.4.2. Economic evaluation

The economic evaluation of **SimSES** allows assessing the overall profitability of an energy storage project through economic KPIs. These KPIs include the net present value (NPV), internal rate of return, profitability index, return on investment, and levelized cost of storage. Eq. (19) shows the calculation of the NPV as it is performed in **SimSES**.

$$\mathrm{NPV} = -\mathrm{I}_0 + \sum_{n=1}^{N} \frac{\mathrm{CF}_n}{(1+i)^n} \tag{19}$$

I_0 denotes the initial investment cost, i the discount rate, CF the cashflow, and n and N the current and total number of project years, respectively. All parameters apart from the cashflow are derived from the settings in the Configuration File. The cashflow itself is calculated from the time series of logged simulation results. Depending on the selected operation strategy, the cashflows of multiple revenue streams ($\mathrm{CF}_{n,r}$) may be added to obtain the cashflow for a single project year (CF_n), as shown in Eq. (20).

$$\mathrm{CF}_n = -\mathrm{OM}_n + \sum_{r\in R} \mathrm{CF}_{n,r} \tag{20}$$

Here, R denotes the set of applicable revenues streams r for the selected operation strategy and OM the operation and maintenance cost. Table 8 shows the matching of revenue streams and operation strategies, while the following list provides brief descriptions for all currently implemented revenue streams. For stacked operation strategies, such as *FCR* paired with *IDM*, all respective revenue streams will be considered in Eq. (20).

- *Energy Cost Reduction (ECR)*: Reduction of energy-based electricity costs, caused, for example, by increased self-consumption of PV-generated electricity. This is calculated based on the total site load for both with and without the BESS, the electricity purchase price, and the electricity sales price or feed-in tariff.
- *Demand Charge Reduction (DCR)*: Savings generated by a reduction in demand charges, calculated based on the maximum site load with and without the BESS, the applicable billing period, and the demand charge price per unit of power.
- *Frequency Containment Reserve (FCR)*: Revenue that is generated by participating in the FCR market, calculated based on the system's nominal power, the FCR price, and the power allocated to the FCR market.
- *Spot Market Trading (SMT)*: Revenue that is generated through spot market trading, based on the amount of energy traded and the specified time series of prices.

6. Case studies

The following section will focus on **SimSES** from a user perspective. Compared to other solutions and tools in the field of energy system simulation, **SimSES** provides detailed modeling of ESS and applications on a system level during the full investment period. Both the technical properties of different storage technologies and the economic modeling of the components and systems are mapped in detail.

In order to clarify the implementation and adaptability of the tool, two applications are discussed. First, Peak Shaving (PS) for an industrial application comparing a different set of storage technologies—LIB, RFB, and a hybrid system of both technologies. Second, Frequency Containment Reserve (FCR) including an Intraday Continuous Market (IDM) by considering various system topologies are discussed. The underlying system costs are discussed in Appendix D. These case studies can be downloaded and executed as described in Appendix E.

6.1. Case study 1: Peak shaving application

A commonly used application for ESS is Peak Shaving (PS). The tariff model with separate energy- and power-related prices plays an important role here. The PS application aims to cut high power demands from the distribution grid. Since the highest power peak per billing period (usually monthly or annually) is multiplied by the power-related price, it can be economical favorable to cap high demand peaks by using an ESS to provide the necessary power and energy [9].

In this case study, three different storage systems are simulated: a LIB system with 150 kWh, a RFB system with 200 kWh, and a hybrid system with 10 kWh LIB capacity and 180 kWh RFB capacity. More detail on the system configuration chosen for this case study is given in Fig. 10. When investing in a system the user may be interested in deciding upfront which of the three configurations will provide the best economic solution. All systems are dimensioned to provide the peak shaving power even after 20 years, including capacity degradation. In addition, the restriction of a usable SOC range of RFB systems from 20% to 80% is considered [36]. The power electronics is dimensioned with 40 kW rated power. The Sony LFP cell technology for LIB and a scaled *CellDataStack5550W* model (cf. Table 4) as an all-Vanadium RFB system is considered. The assumed system costs for the economic evaluation are provided in Table D.11. As a revenue for reducing the power peak a fixed price of 100 EUR/kW in a yearly billing period is assumed. As an input power profile for the PS application, the Cluster 1 PS power profile from Kucevic et al. [73] is used and scaled to an annual load of 347.55 MWh from which the peak power is reduced to 63.5 kW.

After the simulation has been executed, the analysis and evaluation include both detailed technical and economic evaluations. An extract of the evaluations and results can be seen in the following illustrations:

Table 8
Matching of revenue streams and operation strategies for the cashflow calculation within the economic evaluation.

	ECR	DCR	FCR	SMT
Residential PV Greedy	x			
Residential PV Feed in Damp	x			
Peak Shaving	x	x		
Peak Shaving Perfect Foresight	x	x		
Frequency Containment Reserve			x	
Intraday Continuous Market				x

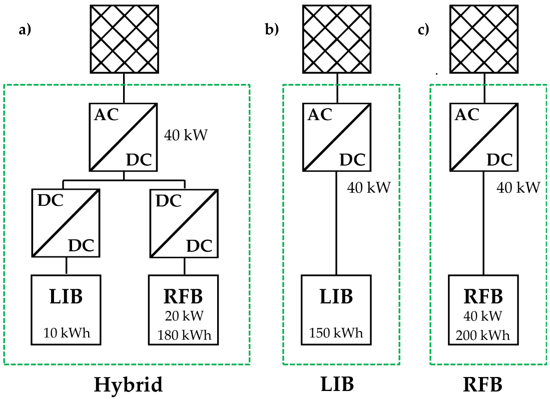

Fig. 10. Three different Energy Storage Systems (ESS) are investigated in the Peak Shaving (PS) case study: **(a)** A hybrid ESS consisting of a DC-coupled LIB and RFB system as well as single storage systems of **(b)** LIB and **(c)** RFB. All systems are dimensioned for providing the PS power even after 20 years of operation. A maximum Depth of Discharge (DOD) for RFB systems of 0.6 is considered. The Power Distribution Strategies (PDS) for the hybrid system performs according to the technology prioritization as described in Section 5.2.2. The DCDC converter is assumed with a fixed efficiency of 98%.

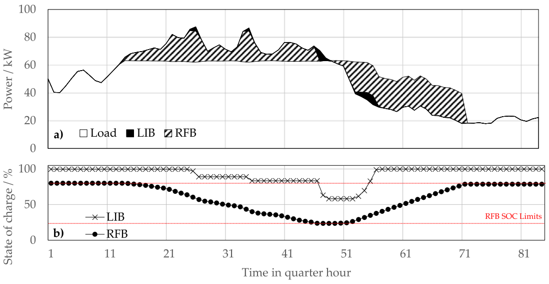

Fig. 11. Peak Shaving (PS) application on a hybrid Energy Storage System (ESS). **(a)** Residual load with and without the PS application with the delivered AC power of the installed ESS as well as the power distribution between the two DC-coupled storage systems. **(b)** State of Charge (SOC) development of the hybrid ESS. LIB systems takes over if target power exceed RFB stack power or if the RFB system hits its SOC limits.

Fig. 11 shows the characteristic curve of the power during the PS application for the hybrid storage system. The residual power can be seen with and without energy storage. It can be seen that the power drawn from the grid does not exceed the value of the PS threshold as was dictated by the operation strategy. Power demand values above the PS threshold are provided by the respective storage unit. This comes in line with charging and discharging power from the ESS and a simultaneous change in the storage-lumped SOC. According to the conditions set, recharging of the storage systems is executed only at times such that the PS threshold is never exceeded. In addition, the power distribution to the corresponding storage technologies of the hybrid system can be seen. The RFB system is prioritized to provide the bulk energy of the PS event while the LIB system covers high power peaks, especially if the RFB systems power capabilities are exhausted.

The remaining capacity (SOH) of the ESS can be seen in Fig. 12. The LIB capacity decreases to 70% during the 20-year simulation, while for the hybrid system as well as for the RFB system the capacity remains higher at 97% and 96%, respectively. Although the integrated degradation models consider both the calendar and the cycle degradation, it is noteworthy that the calendar degradation takes up the largest share in this operation of PS application [59].

In Fig. 12 the difference of the system round-trip efficiency can be observed. The LIB system demonstrates the highest efficiency with 88%, followed by the hybrid system with 68% and the RFB system with 62%. The energy losses of the RFB storage compartments are higher compared to LIB, attributed to a comparably low Coulomb efficiency and additional energy needed for electrolyte pumps.

In addition to the technical evaluation, **SimSES** also provides a comprehensive economic analysis of the simulated time series. In order to show a metric for overall costs, an alternative NPV considering capacity degradation as well is shown in Eq. (21), where c_{ST} represents energy-specific costs of the storage technology and C_{deg} the capacity degradation.

$$NPV_{CD} = NPV - c_{ST} \cdot C_{deg} \tag{21}$$

Fig. 12 shows the overall costs of the ESS operated with baseline cost set to 100% of the LIB system. For the evaluation of the system, not only real tariff models but also the investment costs for the ESS are integrated in the tool resulting in the NPV. In addition, the cost of capacity degradation is added to the NPV in order to take not only the system efficiency into account but also the capacity loss over 20 years (see Eq. (21)). It can be seen that the hybrid system is 5% more cost effective while the RFB system has 81% higher overall costs. The primary reason for these values are the cost of capacity degradation, which is 51% of the overall costs for the LIB system although the NPV for the LIB systems is lowest compared to the other systems. In conclusion, a hybrid system can deliver an overall better solution compared to single storage systems although only a small peak LIB ESS is added to an RFB system, combining the benefits of both techniques, i.e., a higher NPV compared to a single RFB system and a lower capacity degradation compared to a single LIB system. However, with the input parameters chosen herein, none of the three negative storage solutions were able to justify an investment as all resulted in negative NPV_{CD} values. The overall economics of this case study could potentially be improved if the ESS value generation was increased, e.g., by applying multi-use operation and dispatching storage in PS idle times [4,74]. Additionally, results with hybrid storage systems could be improved with optimization and machine learning techniques instead of applying a rule-based algorithm [75,76].

6.2. Case study 2: Frequency containment reserve application

A widely used application of utility-scale ESS is participation in the market for FCR. In this application, the ESS compensate for fluctuations

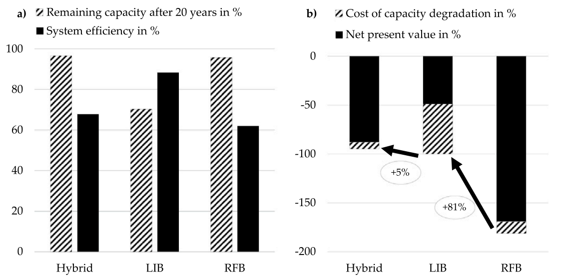

Fig. 12. Economic analysis of the three different Energy Storage Systems (ESS) serving the Peak Shaving (PS) application. **(a)** Comparison of remaining capacity and system efficiency of all simulated ESS after 20 years. **(b)** Overall costs consisting of the NPV and cost of capacity degradation using the LIB system as the baseline. The hybrid system could decrease overall cost by 5%, whereas the RFB system increased the cost by 81%.

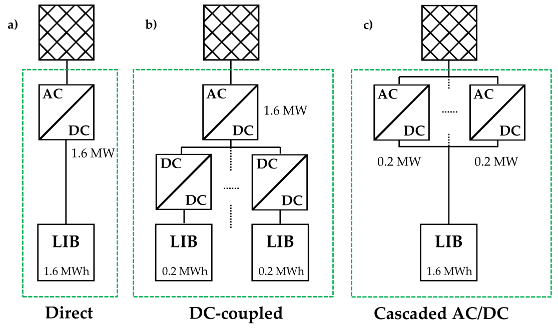

Fig. 13. Three different ESS topologies are investigated in the FCR case study, all with a LIB system of 1.6 MWh and an ACDC connection to the grid of 1.6 MW. The ACDC converter model is the *NottonAcDcConverter* (cf. Table 6). **(a)** A direct-coupled ESS with one ACDC converter. **(b)** Eight parallel DC-coupled systems with an assumed fixed DCDC efficiency of 98%. **(c)** Eight parallel connected ACDC converter with a cascaded activation: The first ACDC converter drives to its nominal power of 0.2 MW before the second ACDC converter is activated.

between consumption and generation in the power grid by reacting accordingly to changes in the grid frequency. The regulations and degrees of freedom for FCR application complying to German regulation criteria are taken into account and are described in detail in [4,8,62,73]. In this operation strategy of **SimSES** the SOC stabilization of the ESS is achieved by support of IDM. FCR and IDM are each basic operation strategies running in a stacked operation. For the simulation a grid frequency profile of 2014 is used to account for the provided stabilizing power [77]. It is assumed that the provided power of 1 MW does not affect the integrated network frequency.

In this case study, three different ESS topologies are simulated (cf. Fig. 13), each with a Sony LFP cell technology providing a capacity of 1.6 MWh and a grid-connection power of 1.6 MW. First, a simple direct approach of connecting a LIB to a grid-connected ACDC converter is investigated. Second, eight parallel DC-coupled systems with a LIB capacity of 0.2 MWh each are simulated. Third, eight parallel connected ACDC converters with a nominal power of 0.2 MW each are activated in a cascaded approach promising a higher efficiency [78]. The assumed system costs for the economic evaluation are provided in Table D.12. The revenue of FCR[12] is taken as a fixed price of 0.2 EUR per kW and day and the IDM[13] price is fixed to 0.04 EUR/kWh, corresponding to a price level of 2020.

The results of the 20-year simulations are displayed in Fig. 14. The cascaded ACDC converter approach shows the best efficiency with 92% compared to the direct approach with 78% and the least efficient topology with DC-coupled systems of 63%. FCR is an application with a high partial-load frequency below 30% of nominal power [55]. Hence, the cascaded ACDC converter are either under a high load compared to their nominal power or deactivated, leading to a higher overall efficiency compared to the direct system. The DC-coupled system shows an overproportional efficiency decrease compared to the direct system. The systems of the DC-coupled ESS are activated similar to the cascade of ACDC converter: one system is ramped up to full power before the second system is activated. Due to relatively high currents in addition to the losses of the DCDC converter, the DC-coupled system shows a comparatively low efficiency. This result suggests that the chosen PDS is inappropriate in terms of efficiency for a FCR application with the given system for the DC-coupled system. Comparing the remaining capacity of the three investigated systems, no large difference can be observed, with a remaining capacity of each system after 20 years of around 80%. One target of the chosen PDS for the DC-coupled system was to reduce the capacity degradation by cycling a few systems more often than other systems in order to get an overall better degradation behavior. However, it can be observed that the chosen strategy shows no improvement in terms of the degradation behavior for this application compared to the other systems.

Analyzing the economics, the high efficiency advantage of the cascaded system could be transferred to a slight monetary improvement compared to the other systems. The cascaded system shows a 4% increase of the NPV compared to the direct system. The DC-coupled system falls behind with a lower NPV of 5% in comparison to the direct system (cf. Fig. 14). This could be explained with IDM recharging cost over the simulation time period since the FCR revenue is the same for all investigated systems (cf. Table 9).

First, the IDM transaction costs are comparatively low: The direct system accounts for 36 kEUR, the DC-coupled system for 64 kEUR and the cascaded system for 14 kEUR, accumulated after 20 years of operation. In comparison, the FCR revenue compensates for around 1,218 kEUR. Second, the low efficiency of the DC-coupled system results in 231 MWh energy sold on the IDM whereas the direct system and the cascaded system could sell 347 MWh and 494 MWh, respectively. This is also reflected in the numbers of bought energy: the DC-coupled system had to buy most energy with 1,829 MWh while the cascaded system had to buy 851 MWh. Although large differences in terms of efficiency exist compared to the direct system (+14% for the cascaded system and -15% for the DC-coupled system) this could only be translated into a 4% increase of the NPV, respectively to a 5% decrease. The economic result of more efficient ESS could be improved by reducing the storage capacity and improving the IDM operation strategy. In conclusion, all three systems have a positive NPV, likely leading to a positive investment decision.

With these case studies a high variety of topologies as well as technology combinations could be investigated. Parameter variations, e.g., for the investment costs or sizing of individual components can easily be made by the user when adapting according initialization files of the case studies available as presented in Appendix E.

7. Conclusion and outlook

Within this work, the simulation and analysis tool for energy storage systems **SimSES** is presented. **SimSES** provides a library of state-of-the-art energy storage models by combining modularity of multiple topologies as well as the periphery of an ESS. This paper summarizes the structure as well as the capabilities of **SimSES**. Storage technology

---

[12] Prices for the German FCR market can be found at https://www.regelleistung.net.

[13] Prices for the European spot market can be found at https://www.epexspot.com.

Table 9
Overview of the IDM transaction costs for all three investigated ESS.

System	IDM transaction costs/EUR	Energy bought/MWh	Energy sold/MWh
Direct	35,772	1242	347
DC-coupled	63,894	1829	231
Cascaded	14,280	851	494

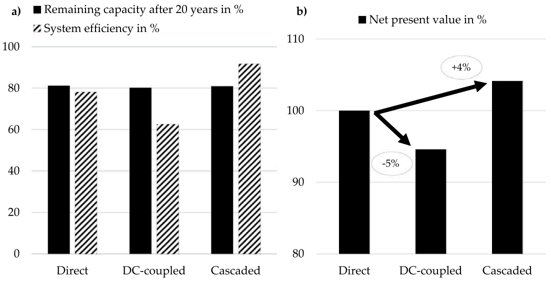

Fig. 14. Technical and economical analysis of the three different Energy Storage Systems (ESS) serving the Frequency Containment Reserve (FCR) application. **(a)** Comparison of remaining capacity after 20 years and system efficiency of all simulated ESSs. **(b)** Economic value consisting of the NPV using the direct system as baseline.

models based on current research for lithium-ion batteries, redox flow batteries, as well as hydrogen storage-based electrolysis and fuel cell are presented in detail. In addition, thermal models and their corresponding HVAC systems, housing, and ambient models are depicted. Power electronics are represented with ACDC and DCDC converters mapping the main losses of power electronics within a storage system. Additionally, auxiliary components like pumps, compressors, and HVAC are considered. Standard use cases like peak shaving, residential storage, and control reserve power provisions through dispatch of storage are discussed in this work, with the possibility to stack these applications in a multi-use scenario. The analysis is provided by technical and economic evaluations illustrated by KPIs.

SimSES' capabilities are demonstrated through the discussion of two case studies mapped to the applications of peak shaving and frequency containment reserve, respectively. It is demonstrated how different energy storage system topologies as well as various performance indicators can be investigated and analyzed with **SimSES**. For the specific cases discussed, the results underline that hybrid storage systems can lead in terms of overall cost and degradation behavior to a beneficial economic results. Special ESS topologies like the cascaded ACDC converter approach can lead to a substantial increase in system efficiency for the FCR application, although the economic benefits are comparatively low.

In the future, more detailed performance and aging models for all types of storage systems will be implemented. This will allow a more detailed cross-technology comparison. For instance, models for bidirectional thermal storage system could be implemented in future versions. Further operating strategies matching internationally renowned and national derivatives of application scenarios could also be investigated. This may allow assessing the value of storage deployment across different regions and convince internationally active investors to reveal best investment scenarios worldwide. **SimSES** has interfaces that can be easily integrated into physically derived and more accurate storage models as well as grid modeling and system analysis tools. While selected validation experiments have already been executed, the authors encourage others in the research community to conduct hardware validation experiments at their sites and contribute to the presented tool. The authors envision interlinking **SimSES** to the vast selection of open-source tools in order to expand on the value chain that storage simulations are capable of covering, e.g., **SimSES** is already a part of the *openMOD*[14] initiative. **SimSES** is open-source available, and the authors encourage users and developers to join in and assist in its further development.

CRediT authorship contribution statement

Marc Möller: Conceptualization, Methodology, Writing - original draft, Writing - review & editing, Software, Project administration, Visualization, Investigation. **Daniel Kucevic:** Writing - original draft, Writing - review & editing, Validation, Software, Methodology. **Nils Collath:** Writing - original draft, Writing - review & editing, Software, Methodology. **Anupam Parlikar:** Writing - original draft, Writing - review & editing, Software, Methodology. **Petra Dotzauer:** Writing - original draft, Writing - review & editing, Software, Methodology. **Benedikt Tepe:** Investigation, Validation, Writing - original draft, Writing - review & editing, Software. **Stefan Englberger:** Investigation, Validation, Writing - original draft, Writing - review & editing. **Andreas Jossen:** Writing - review & editing, Funding acquisition. **Holger Hesse:** Writing - original draft, Writing - review & editing, Supervision.

Declaration of competing interest

The authors declare that they have no known competing financial interests or personal relationships that could have appeared to influence the work reported in this paper.

Acknowledgments

This work was financially supported by the Federal Ministry for Economic Affairs and Energy within the open_BEA project (Grant No. 03ET4072) and the EffSkalBatt project (Grant No. 03ET6148). Both projects are supported by Project Management Juelich. The responsibility for this publication rests with the authors.

We thank Jacob Klinkenberg, Kareem Abo Gamra, and Benedikt Wiesend for their contribution with simulating and implementing models in the hydrogen package, Timo Sandner and Felix Müller for their implementations of ACDC converters, Dang The Phong for his work on the model for a RFB stack as well as Ni Chuanqin and Yuhui Geng for their implementations of two LIB degradation models.

Appendix A. Open circuit voltage curve fitting

The OCV for LIBs (see Section 4.1) is dependent on the cell type. The OCV data for all currently implemented cell types have been measured at the Institute for Electrical Energy Storage Technology at the Technical University of Munich. To improve the performance, the look-up tables of the voltage values are replaced with a mathematical function. These curve-fitting functions are based on the work of Weng et al. [79]. The parameters of this function for the OCV are estimated using the MATLAB® global optimization toolbox. Fig. A.15 shows the OCV in V for the measured data as well as the curve-fitted data and the difference between those in mV.

---

[14] https://openmod-initiative.org/

Table B.10
Physical parameters for modeling of thermal behavior of lithium-ion batteries (LIBs).

Manufacturer model	Mass (g)	Dimensions (mm)	Specific heat ($Jkg^{-1}K^{-1}$)	Convection coefficient ($Wm^{-2}K^{-1}$)	Source
Sony US26650FTC1	70	dia: 26 len: 65	1001	15	[55,80–89]
Panasonic NCR18650PD	44	dia: 18 len: 65	1048	15	[88–90]
E-One Moli Energy IHR18650A	45	dia: 18 len: 65	965	15	[83,86,89,91–94]
Sanyo UR18650E	46	dia: 18 len: 65	965	15	[83,86,89,92–95]

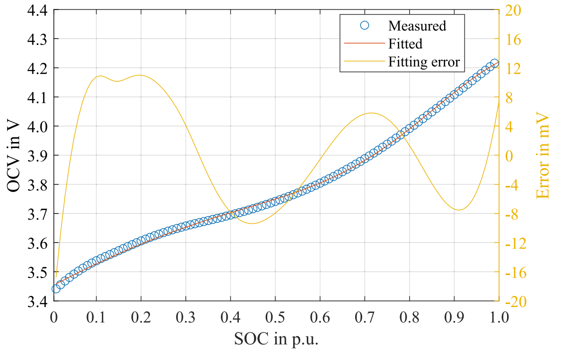

Fig. A.15. Open Circuit Voltage (OCV) curve fitting for the MolicelNMC lithium-ion battery (LIB). The figure shows the OCV in V for the measured data as well as the curve-fitted data and the difference between those in mV.

Appendix B. Thermal parameters

The geometrical and thermal parameters used for modeling the thermal behavior of LIBs are presented in Table B.10. Geometrical parameters such as the dimensions and the weight are obtained from datasheets of the cells. The thermal properties, such as the specific heat capacity for each cell type, are determined from the literature for each cell chemistry, and averaged over several values found in the literature. The value of the convection coefficient is known with the least accuracy, and a value of 15 $Wm^{-2}K^{-1}$ is selected as a "reasonable" value lying between typical values for purely natural convection and forced convection. This is assumed to emulate slow intermittent motion of air around the cells. It is expected that availability of better data in the future will increase the accuracy of the modeling process.

Appendix C. Stack data for a redox flow battery

The parameters are based on single-cell measurements carried out at ZAE Bayern of a cell with a technical representative cell area of 2160 cm^2. To obtain parameters for a stack, the measured values were scaled up with a number of 40 cells. Fig. C.16 shows the data of the internal resistance of the 40-cell stack for charge and discharge. The internal resistance is determined by applying a constant current and measuring the resulting change of voltage. The cell was operating in Vanadium electrolyte (1.6 mol/l V solved in 2 mol/l H_2SO_4) from GfE (Gesellschaft für Elektrometallurgie mbH). Temperature and flow rate were controlled during the procedure. The SOC was determined with an OCV-cell. Due to the relatively high ohmic resistance of the cell and the low possible operation current density (up to approx. 50 mA/cm^2), the cell resistance shows no significant current dependency. The cell resistance R_{cell} was scaled up with the number of cells n_{cell} to receive the stack resistance R_{stack} ($R_{stack} = n_{cell} \cdot R_{cell}$).

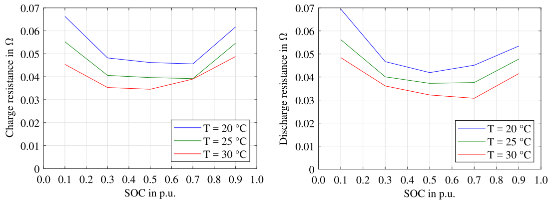

Fig. C.16. Charge and discharge resistance of a stack for a redox flow battery (cell area = 2160 cm^2) dependent on State of Charge (SOC) and temperature (T). The single-cell measurements were scaled up to a stack resistance with a cell number of 40.

Appendix D. Economics for case studies

Assumptions for economical analysis of the case studies are based on Tsiropoulos et al. Minke et al. Figgener et al. and Mongird et al. [96–99]. Challenges for determining energy-specific costs for ESS occur due to a wide range of technology costs as well as various system sizes and designs. In order to distinguish between power and energy system design, Tsiropoulos et al. takes the EPR as an indicator: If EPR is above one, the authors talk about an energy-driven design, otherwise about power-driven design [96]. In addition, it is not always clearly stated which costs for a system design are included, e.g., power electronics, housing, and grid connection [96,98]. For instance, utility scale system costs for LIB in 2017 ranged between 300 EUR/kWh and 1200 EUR/kWh with an average around 570 EUR/kWh [96]. Figgener et al. depicted a similar range for 2018 [98] as well as one reported system for 2019 with an EPR of 1 h and system costs of around 900 EUR/kWh. However, LIB systems with an EPR of 0.125 h show lowest cost with 300 EUR/kWh and costs increase with rising EPR [96]. Mongird et al. have presented system costs for LIB system with an EPR larger than 1 h with falling costs [99]. Interestingly, the system costs of [99] show a lower average system cost price than those of [96,98] representing European costs' levels (a USD to EUR conversion of 0.82 is assumed). In contrast, a broad cost database does not exist for RFB systems. However, Minke et al. investigated various RFB projects from 2004 to 2017 by determining system prices for different EPR, similar to Tsiropoulos et al. [97]. The authors also found an even broader range of system costs for RFB from 155 EUR/kWh to 1738 EUR/kWh, especially due to different electrolytes, stack modules, sizing, and system definition. RFB system costs decrease with a rising EPR with average system costs of 717 EUR/kWh for an EPR of 2 h and 166 EUR/kWh for a ratio of 15 h. These findings are also in agreement with the results of Mongird et al. [99].

For the following case studies, system cost curves depending on EPR are assumed for LIB and RFB systems with the prices and ratios

Table D.11
Economics for Case Study 1.

Storage technology	Power/kW	Capacity/kWh	EPR/h	Specific system cost/EUR kWh^{-1}	System cost/EUR	Overall system cost/EUR
LIB	40	10	0.25	584	5,839	
RFB	20	180	9.00	329	59,216	65,055
LIB only	40	150	3.75	367	55,089	55,089
RFB only	40	200	5.00	451	90,247	90,247

Table D.12
Economics for Case Study 2.

Storage technology	Power/kW	Capacity/kWh	EPR/h	Specific system cost/EUR kWh^{-1}	System cost/EUR
LIB	1,600	1,600	1	473	756,800

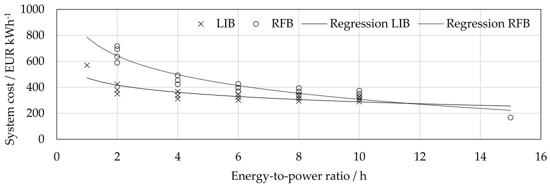

Fig. D.17. System costs curves depending on EPR for LIB and RFB systems based on [96,97,99].

given represented by regression curves in Eqs. (D.1) and (D.2). From an EPR of 1 h up to 15 h, this cost curve has a realistic cost range with decreasing cost over EPR. The system costs, however, have a high uncertainty attached, as shown in the previous analysis. The used price curves are shown in Fig. D.17. It is worth mentioning that the cost assumptions for RFB systems are based on a usable SOC range of 20% and 80%, which reduces the gross capacity configured by 40% [97].

$$c_{\text{LIB}} = -80 \cdot \ln(\text{EPR}) + 473 \quad \text{and} \tag{D.1}$$

$$c_{\text{RFB}} = -208 \cdot \ln(\text{EPR}) + 786, \tag{D.2}$$

where c represents the energy specific costs of LIB, respectively RFB.

Using Eqs. (D.1) and (D.2) the system costs for the two case studies discussed in Section 6 are calculated as provided in Tables D.11 and D.12.

Appendix E. Availability of SimSES

SimSES is available as open source[15] and is part of the open-source simulation and optimization toolchain of the Institute for Electrical Energy Storage Technology at the Technical University of Munich.[16] A *readme.md* helps with the first steps in order to get **SimSES** running. An installed Python environment is mandatory as well as the required packages installed automatically if you run *setup.py*. With executing *main.py*, a default configured simulation could be started directly. This file offers also all necessary interfaces in order to connect it to other simulation programs. The case studies presented within this paper are conducted with the open-source release version 1.0.4.

For configuring a simulation, there are two important configuration files: *simulation.ini* and *analysis.ini*. These configuration files are documented and offer all possible settings for setting up a simulation and the consequent evaluation. These config files follow a pattern for a *default* and *local* configuration. The *default* configuration inherits all possible settings, in the *local* file: only the changed settings are necessary. This allows a quick exchange of configuration settings between users.

The *Simulation* package allows multiple simultaneous simulations, which are also used for the presented case studies. In here, the configurations and code could be found with the case study configs in *case_studies*. In order to execute the case studies, the configuration needs to be copied to the config location and renamed to *simulation.local.ini*.

References

[1] V. Lauber, S. Jacobsson, The politics and economics of constructing, contesting and restricting socio-political space for renewables – the German renewable energy act, Environ. Innov. Soc. Transitions 18 (2016) 147–163, http://dx.doi.org/10.1016/j.eist.2015.06.005.

[2] H.E. Murdock, D. Gibb, T. André, F. Appavou, A. Brown, B. Epp, B. Kondev, A. McCrone, E. Musolino, L. Ranalder, Renewables 2019 global status report, REN21, https://www.ren21.net/wp-content/uploads/2019/05/gsr_2019_full_report_en.pdf.

[3] P. Denholm, E. Ela, B. Kirby, M. Milligan, The Role of Energy Storage with Renewable Electricity Generation, Technical Report NREL (2010), 2010, http://dx.doi.org/10.2172/972169.

[4] S. Englberger, A. Jossen, H. Hesse, Unlocking the potential of battery storage with the dynamic stacking of multiple applications, Cell Rep. Phys. Sci. 1 (11) (2020) http://dx.doi.org/10.1016/j.xcrp.2020.100238.

[5] A. Evans, V. Strezov, T.J. Evans, Assessment of utility energy storage options for increased renewable energy penetration, Renew. Sustain. Energy Rev. 16 (6) (2012) 4141–4147, http://dx.doi.org/10.1016/j.rser.2012.03.048.

[6] D. Zafirakis, K.J. Chalvatzis, G. Baiocchi, G. Daskalakis, The value of arbitrage for energy storage: Evidence from European electricity markets, Appl. Energy 184 (2016) 971–986, http://dx.doi.org/10.1016/j.apenergy.2016.05.047.

[7] R.H. Byrne, R.J. Concepcion, C.A. Silva-Monroy, Estimating potential revenue from electrical energy storage in PJM, in: IEEE Power and Energy Society General Meeting (2016), 2016, http://dx.doi.org/10.1109/PESGM.2016.7741915.

[8] T. Thien, D. Schweer, D. vom Stein, A. Moser, D.U. Sauer, Real-world operating strategy and sensitivity analysis of frequency containment reserve provision with battery energy storage systems in the german market, J. Energy Storage 13 (2017) 143–163, http://dx.doi.org/10.1016/j.est.2017.06.012.

[9] A. Oudalov, R. Cherkaoui, Sizing and optimal operation of battery energy storage system for peak shaving application: Lausanne, Switzerland, 1 - 5 july 2007, IEEE Lausanne Power Tech. (2007) http://dx.doi.org/10.1109/PCT.2007.4538388.

[10] J. Hoppmann, J. Volland, T.S. Schmidt, V.H. Hoffmann, The economic viability of battery storage for residential solar photovoltaic systems – A review and a simulation model, Renew. Sustain. Energy Rev. 39 (2014) 1101–1118, http://dx.doi.org/10.1016/j.rser.2014.07.068.

[11] H. Hesse, R. Martins, P. Musilek, M. Naumann, C. Truong, A. Jossen, Economic optimization of component sizing for residential battery storage systems, Energies 10 (7) (2017) 835, http://dx.doi.org/10.3390/en10070835.

[12] S. Englberger, H. Hesse, D. Kucevic, A. Jossen, A techno-economic analysis of vehicle-to-building: Battery degradation and efficiency analysis in the context of coordinated electric vehicle charging, Energies 12 (5) (2019) 955, http://dx.doi.org/10.3390/en12050955.

[13] O.M. Toledo, D. Oliveira Filho, A.S.A.C. Diniz, Distributed photovoltaic generation and energy storage systems: A review, Renew. Sustain. Energy Rev. 14 (1) (2010) 506–511, http://dx.doi.org/10.1016/j.rser.2009.08.007.

[14] H. Hesse, M. Schimpe, D. Kucevic, A. Jossen, Lithium-ion battery storage for the grid—A review of stationary battery storage system design tailored for applications in modern power grids, Energies 10 (12) (2017) 2107, http://dx.doi.org/10.3390/en10122107.

[15] B. Dunn, H. Kamath, J.-M. Tarascon, Electrical energy storage for the grid: A battery of choices, Science 334 (2011) http://dx.doi.org/10.1126/science.1212741.

---

[15] https://gitlab.lrz.de/open-ees-ses/simses

[16] http://www.simses.org

[16] J. Weniger, T. Tjaden, Performance-Simulationsmodell für AC-gekoppelte PV-Batteriesysteme (PerModAC): Dokumentation | Version 1.0, Hochschule für Technik und Wirtschaft H.T.W. Berlin, Berlin, 2017, URL https://pvspeicher.htw-berlin.de/wp-content/uploads/2017/03/PerModAC_doku.pdf.

[17] N.-K.C. Nair, N. Garimella, Battery energy storage systems: Assessment for small-scale renewable energy integration, Energy Build. 42 (11) (2010) 2124–2130, http://dx.doi.org/10.1016/j.enbuild.2010.07.002.

[18] U. Sureshkumar, P.S. Manoharan, A.P.S. Ramalakshmi, Economic cost analysis of hybrid renewable energy system using HOMER, in: IEEE-International Conference on Advances in Engineering, Science and Management, ICAESM -2012, 2012, pp. 94–99.

[19] J. Figgener, P. Stenzel, K.-P. Kairies, J. Linßen, D. Haberschusz, O. Wessels, G. Angenendt, M. Robinius, D. Stolten, D.U. Sauer, The development of stationary battery storage systems in Germany – A market review, J. Energy Storage 29 (2020) http://dx.doi.org/10.1016/j.est.2019.101153.

[20] E. Gamma, R. Helm, R. Johnson, J.M. Vlissides, Design Patterns: Elements of Reusable Object-Oriented Software, first ed., Addison-Wesley Professional, 1994.

[21] B. Nykvist, M. Nilsson, Rapidly falling costs of battery packs for electric vehicles, Nature Clim. Change 5 (4) (2015) 329–332, http://dx.doi.org/10.1038/nclimate2564.

[22] G. Zubi, R. Dufo-López, M. Carvalho, G. Pasaoglu, The lithium-ion battery: State of the art and future perspectives, Renew. Sustain. Energy Rev. 89 (2018) 292–308, http://dx.doi.org/10.1016/j.rser.2018.03.002.

[23] M. Yoshio, R.J. Brodd, A. Kozawa, Lithium-Ion Batteries, Springer New York, New York, NY, 2009, http://dx.doi.org/10.1007/978-0-387-34445-4.

[24] A.M. Divakaran, M. Minakshi, P.A. Bahri, S. Paul, P. Kumari, A.M. Divakaran, K.N. Manjunatha, Rational design on materials for developing next generation lithium-ion secondary battery, Prog. Solid State Chem. 62 (2021) 100298, http://dx.doi.org/10.1016/j.progsolidstchem.2020.100298.

[25] M. Naumann, F.B. Spingler, A. Jossen, Analysis and modeling of cycle aging of a commercial LiFePO4/graphite cell, J. Power Sources 451 (2020) 227666, http://dx.doi.org/10.1016/j.jpowsour.2019.227666.

[26] M. Naumann, M. Schimpe, P. Keil, H.C. Hesse, A. Jossen, Analysis and modeling of calendar aging of a commercial LiFePO4/graphite cell, J. Energy Storage 17 (2018) 153–169, http://dx.doi.org/10.1016/j.est.2018.01.019.

[27] P. Keil, S.F. Schuster, J. Wilhelm, J. Travi, A. Hauser, R.C. Karl, A. Jossen, Calendar aging of lithium-ion batteries, J. Electrochem. Soc. 163 (9) (2016) A1872–A1880, http://dx.doi.org/10.1149/2.0411609jes.

[28] S.F. Schuster, T. Bach, E. Fleder, J. Müller, M. Brand, G. Sextl, A. Jossen, Nonlinear aging characteristics of lithium-ion cells under different operational conditions, J. Energy Storage 1 (2015) 44–53, http://dx.doi.org/10.1016/j.est.2015.05.003.

[29] J. Schmalstieg, S. Käbitz, M. Ecker, D.U. Sauer, A holistic aging model for li(NiMnCo)o2 based 18650 lithium-ion batteries, J. Power Sources 257 (2014) 325–334, http://dx.doi.org/10.1016/j.jpowsour.2014.02.012.

[30] M.M. Rahman, A.O. Oni, E. Gemechu, A. Kumar, Assessment of energy storage technologies: A review, Energy Convers. Manage. 223 (2020) 113295, http://dx.doi.org/10.1016/j.enconman.2020.113295.

[31] G. Kear, A.A. Shah, F.C. Walsh, Development of the all-vanadium redox flow battery for energy storage: a review of technological, financial and policy aspects, Int. J. Energy Res. 36 (11) (2012) 1105–1120, http://dx.doi.org/10.1002/er.1863.

[32] A.Z. Weber, M.M. Mench, J.P. Meyers, P.N. Ross, J.T. Gostick, Q. Liu, Redox flow batteries: a review, J. Appl. Electrochem. 41 (10) (2011) 1137–1164, http://dx.doi.org/10.1007/s10800-011-0348-2.

[33] N. Hagedorn, M.A. Hoberecht, L.H. Thaller, NASA redox cell stack shunt current, pumping power, and cell performance tradeoffs, U.S. Department of Energy / NASA Technical Memorandum, 1982, URL https://ntrs.nasa.gov/citations/19820011459.

[34] R. Schweiss, A. Pritzl, C. Meiser, Parasitic hydrogen evolution at different carbon fiber electrodes in vanadium redox flow batteries, J. Electrochem. Soc. 163 (9) (2016) A2089–A2094, http://dx.doi.org/10.1149/2.1281609jes.

[35] A.H. Whitehead, M. Harrer, Investigation of a method to hinder charge imbalance in the vanadium redox flow battery, J. Power Sources 230 (2013) 271–276, http://dx.doi.org/10.1016/j.jpowsour.2012.11.148.

[36] M. Skyllas-Kazacos, L. Cao, M. Kazacos, N. Kausar, A. Mousa, Vanadium electrolyte studies for the vanadium redox battery-a review, ChemSusChem 9 (13) (2016) 1521–1543, http://dx.doi.org/10.1002/cssc.201600102.

[37] A. Tang, J. Bao, M. Skyllas-Kazacos, Studies on pressure losses and flow rate optimization in vanadium redox flow battery, J. Power Sources 248 (2014) 154–162, http://dx.doi.org/10.1016/j.jpowsour.2013.09.071.

[38] E.A. Kaminski, R.F. Savinell, A technique for calculating shunt leakage and cell currents in bipolar stacks having divided or undivided cells, J. Electrochem. Soc. 130 (5) (1983) 1103–1107.

[39] fumatech, in: fumatech (Ed.), Redox-Flow-Batteries: data sheet: fumasep® membrane types, URL https://www.fumatech.com/NR/rdonlyres/6E4FA7B9-0AAA-42B9-98E4-BF756C23F981/0/FUMATECH_BWT_GmbHRedoxFlowBatteries.pdf.

[40] C. Blanc, R. Alfred, Understanding the vanadium redox flow batteries, in: InTech (Ed.), Paths to Sustainable Energy, InTechOpen, 2010, pp. 333–358.

[41] M. Robinius, P. Markewitz, P. Lopion, D. Stolten, Cost-efficient and climate-friendly transformation strategies for the german energy system up to 2050, in: Forschungszentrum JÜLich: Energy & Environment, 499, 2019.

[42] R.P. O'Hayre, S.-W. Cha, W.G. Colella, F.B. Prinz, Fuel cell fundamentals, third ed., John Wiley & Sons Inc, Hoboken New Jersey, 2016.

[43] G. Tjarks, PEM-electrolysis-systems for the integration in power-to-gas applications, (Ph.D. thesis), Lehrstuhl für Brennstoffzellen, RWTH Aachen, Aachen, 2017, http://dx.doi.org/10.18154/RWTH-2017-04470.

[44] C. Rakousky, U. Reimer, K. Wippermann, M. Carmo, W. Lueke, D. Stolten, An analysis of degradation phenomena in polymer electrolyte membrane water electrolysis, J. Power Sources 326 (2016) 120–128, http://dx.doi.org/10.1016/j.jpowsour.2016.06.082.

[45] C. Rakousky, U. Reimer, K. Wippermann, S. Kuhri, M. Carmo, W. Lueke, D. Stolten, Polymer electrolyte membrane water electrolysis: Restraining degradation in the presence of fluctuating power, J. Power Sources 342 (2017) 38–47, http://dx.doi.org/10.1016/j.jpowsour.2016.11.118.

[46] F. Marangio, M. Santarelli, M. Cali, Theoretical model and experimental analysis of a high pressure pem water electrolyser for hydrogen production, Int. J. Hydrogen Energy 34 (3) (2009) 1143–1158, http://dx.doi.org/10.1016/j.ijhydene.2008.11.083.

[47] M. Hammoudi, C. Henao, K. Agbossou, Y. Dubé, M.L. Doumbia, New multi-physics approach for modelling and design of alkaline electrolyzers, Int. J. Hydrogen Energy 37 (19) (2012) 13895–13913, http://dx.doi.org/10.1016/j.ijhydene.2012.07.015.

[48] C. Henao, K. Agbossou, M. Hammoudi, Y. Dubé, A. Cardenas, Simulation tool based on a physics model and an electrical analogy for an alkaline electrolyser, J. Power Sources 250 (2014) 58–67, http://dx.doi.org/10.1016/j.jpowsour.2013.10.086.

[49] D. Feroldi, M.S. Basualdo, Description of PEM Fuel Cells Systems, Springer, London and New York, 2012, http://dx.doi.org/10.1007/978-1-84996-184-4_2.

[50] A. Buttler, H. Spliethoff, Current status of water electrolysis for energy storage, grid balancing and sector coupling via power-to-gas and power-to-liquids: A review, Renew. Sustain. Energy Rev. 82 (2018) 2440–2454, http://dx.doi.org/10.1016/j.rser.2017.09.003.

[51] Q. Feng, X.-Z. Yuan, G. Liu, B. Wei, Z. Zhang, H. Li, H. Wang, A review of proton exchange membrane water electrolysis on degradation mechanisms and mitigation strategies, J. Power Sources 366 (2017) 33–55, http://dx.doi.org/10.1016/j.jpowsour.2017.09.006.

[52] A. Ursúa, E.L. Barrios, J. Pascual, I. San Martín, P. Sanchis, Integration of commercial alkaline water electrolysers with renewable energies: Limitations and improvements, Int. J. Hydrogen Energy 41 (30) (2016) 12852–12861, http://dx.doi.org/10.1016/j.ijhydene.2016.06.071.

[53] M. Schimpe, N. Becker, T. Lahlou, H.C. Hesse, H.-G. Herzog, A. Jossen, Energy efficiency evaluation of grid connection scenarios for stationary battery energy storage systems, Energy Procedia 155 (2018) 77–101, http://dx.doi.org/10.1016/j.egypro.2018.11.065.

[54] G. Notton, V. Lazarov, L. Stoyanov, Optimal sizing of a grid-connected PV system for various PV module technologies and inclinations, inverter efficiency characteristics and locations, Renew. Energy 35 (2) (2010) 541–554, http://dx.doi.org/10.1016/j.renene.2009.07.013.

[55] M. Schimpe, M. Naumann, N. Truong, H.C. Hesse, S. Santhanagopalan, A. Saxon, A. Jossen, Energy efficiency evaluation of a stationary lithium-ion battery container storage system via electro-thermal modeling and detailed component analysis, Appl. Energy 210 (2018) 211–229, http://dx.doi.org/10.1016/j.apenergy.2017.10.129.

[56] M. Förstl, N. Truon, M. Möller, H. Hesse, A. Singer, T. Weyh, The efficiency and profitability of the modular multilevel battery for frequency containment reserve, Atlantis Highlights Eng. 6 (2020) 80–85, http://dx.doi.org/10.2991/ahe.k.210202.012.

[57] A. Zeh, R. Witzmann, Operational strategies for battery storage systems in low-voltage distribution grids to limit the feed-in power of roof-mounted solar power systems, Energy Procedia 46 (2014) 114–123, http://dx.doi.org/10.1016/j.egypro.2014.01.164.

[58] D. Kucevic, C.N. Truong, A. Jossen, H.C. Hesse, Lithium-ion battery storage design for buffering fast charging stations for battery electric vehicles and electric buses, in: D. Schulz (Ed.), NEIS 2018, VDE VERLAG GMBH, Berlin, 2019, pp. 1–6, URL http://ieeexplore.ieee.org/stamp/stamp.jsp?tp=&arnumber=8669466&isnumber=8669446.

[59] N. Collath, S. Englberger, A. Jossen, H. Hesse, Reduction of battery energy storage degradation in peak shaving operation through load forecast dependent energy management, in: D. Schulz (Ed.), NEIS 2020, VDE VERLAG GMBH, 2020, pp. 250–254, URL https://ieeexplore.ieee.org/stamp/stamp.jsp?tp=&arnumber=9273426.

[60] D. Übertragungsnetzbetreiber, Eckpunkte und Freiheitsgrade bei Erbringung von Primaerregelleistung (in German): Leitfaden für Anbieter von Primaerregelleistung, Berlin, Germany, 50Hertz Transmission GmbH and Amprion GmbH and TenneT TSO GmbH and TransnetBW GmbH, https://www.regelleistung.net/ext/download/eckpunktePRL.

[61] D. Übertragungsnetzbetreiber, Anforderungen an die Speicherkapazitaet bei Batterien für die Primaerregelleistung (in German), Berlin, Germany, 50Hertz Transmission GmbH and Amprion GmbH and TenneT TSO GmbH and TransnetBW GmbH, https://www.bves.de/wp-content/uploads/2015/08/2015_08_26_Anforderungen_Speicherkapazitaet_Batterien_PRL.pdf.

[62] A. Zeh, M. Müller, M. Naumann, H. Hesse, A. Jossen, R. Witzmann, Fundamentals of using battery energy storage systems to provide primary control reserves in Germany, Batteries 2 (3) (2016) 29, http://dx.doi.org/10.3390/batteries2030029.

[63] M. Mühlbauer, O. Bohlen, M.A. Danzer, Analysis of power flow control strategies in heterogeneous battery energy storage systems, J. Energy Storage 30 (2020) 101415, http://dx.doi.org/10.1016/j.est.2020.101415.

[64] M. Bauer, System Design and Power Flow of Stationary Energy Storage Systems, (Ph.D. thesis), ETH Zurich, 2019, http://dx.doi.org/10.3929/ETHZ-B-000374736.

[65] C.N. Truong, M. Naumann, R.C. Karl, M. Müller, A. Jossen, H.C. Hesse, Economics of residential photovoltaic battery systems in Germany: The case of teslas powerwall, Batteries 2 (2) (2016) 14, http://dx.doi.org/10.3390/batteries2020014.

[66] A.M. Divakaran, D. Hamilton, K.N. Manjunatha, M. Minakshi, Design, development and thermal analysis of reusable li-ion battery module for future mobile and stationary applications, Energies 13 (6) (2020) 1477, http://dx.doi.org/10.3390/en13061477.

[67] D. Wang, Y. Bao, J. Shi, Online lithium-ion battery internal resistance measurement application in state-of-charge estimation using the extended Kalman filter, Energies 10 (9) (2017) 1284, http://dx.doi.org/10.3390/en10091284.

[68] C.R. Birkl, M.R. Roberts, E. McTurk, P.G. Bruce, D.A. Howey, Degradation diagnostics for lithium ion cells, J. Power Sources 341 (2017) 373–386, http://dx.doi.org/10.1016/j.jpowsour.2016.12.011.

[69] T. Waldmann, M. Wilka, M. Kasper, M. Fleischhammer, M. Wohlfahrt-Mehrens, Temperature dependent ageing mechanisms in lithium-ion batteries – a post-mortem study, J. Power Sources 262 (2014) 129–135, http://dx.doi.org/10.1016/j.jpowsour.2014.03.112.

[70] S. Ma, M. Jiang, P. Tao, C. Song, J. Wu, J. Wang, T. Deng, W. Shang, Temperature effect and thermal impact in lithium-ion batteries: A review, Prog. Nat. Sci. Mater. Int. 28 (6) (2018) 653–666, http://dx.doi.org/10.1016/j.pnsc.2018.11.002.

[71] B. Shabani, M. Biju, Theoretical modelling methods for thermal management of batteries, Energies 8 (9) (2015) 10153–10177, http://dx.doi.org/10.3390/en80910153.

[72] Deutsches Zentrum für Luft- und Raumfahrt (DLR) / German Aerospace Centre, greenius: Green Energy System Analysis, Deutsches Zentrum für Luft- und Raumfahrt (DLR) / German Aerospace Centre, Köln, Germany, 2018, URL https://www.dlr.de/sf/en/desktopdefault.aspx/tabid-11688/20442_read-44865/.

[73] D. Kucevic, B. Tepe, S. Englberger, A. Parlikar, M. Mühlbauer, O. Bohlen, A. Jossen, H. Hesse, Standard battery energy storage system profiles: Analysis of various applications for stationary energy storage systems using a holistic simulation framework, J. Energy Storage 28 (2020) 101077, http://dx.doi.org/10.1016/j.est.2019.101077.

[74] S. Englberger, H. Hesse, N. Hanselmann, A. Jossen, SimSES multi-use: A simulation tool for multiple storage system applications, in: 2019 16th International Conference on the European Energy Market, EEM, 2019, pp. 1–5, http://dx.doi.org/10.1109/EEM.2019.8916568, URL https://ieeexplore.ieee.org/abstract/document/8916568/.

[75] L. Gerlach, T. Bocklisch, Experts versus algorithms? Optimized fuzzy logic energy management of autonomous PV hybrid systems with battery and H2 storage, Energies 14 (6) (2021) 1777, http://dx.doi.org/10.3390/en14061777.

[76] L. Desportes, I. Fijalkow, P. Andry, Deep reinforcement learning for hybrid energy storage systems: Balancing lead and hydrogen storage, Energies 14 (15) (2021) 4706, http://dx.doi.org/10.3390/en14154706.

[77] 50Hertz Transmission GmbH, Archive of mains frequency of ENTSO-e, 2021, URL https://www.50hertz.com/de/Transparenz/Kennzahlen/Regelenergie/ArchivNetzfrequenz.

[78] A. Parlikar, H. Hesse, A. Jossen, Topology and efficiency analysis of utility-scale battery energy storage systems, Atlantis Highlights Eng. 4 (2019) 119–131, http://dx.doi.org/10.2991/ires-19.2019.15.

[79] C. Weng, J. Sun, H. Peng, A unified open-circuit-voltage model of lithium-ion batteries for state-of-charge estimation and state-of-health monitoring, J. Power Sources 258 (2014) 228–237, http://dx.doi.org/10.1016/j.jpowsour.2014.02.026.

[80] Akkuplus.de, Panasonic - UR18650e - 3,7 volt 2150mah Li-Ion - EOL, 2020, URL https://akkuplus.de/Panasonic-UR18650E-37-Volt-2150mAh-Li-Ion-EOL.

[81] N. Damay, C. Forgez, M.-P. Bichat, G. Friedrich, Thermal modeling of large prismatic LiFePO 4 /graphite battery. Coupled thermal and heat generation models for characterization and simulation, J. Power Sources 283 (2015) 37–45, http://dx.doi.org/10.1016/j.jpowsour.2015.02.091.

[82] C. Forgez, D. Vinh Do, G. Friedrich, M. Morcrette, C. Delacourt, Thermal modeling of a cylindrical LiFePO4/graphite lithium-ion battery, J. Power Sources 195 (9) (2010) 2961–2968, http://dx.doi.org/10.1016/j.jpowsour.2009.10.105.

[83] B. Lei, W. Zhao, C. Ziebert, N. Uhlmann, M. Rohde, H. Seifert, Experimental analysis of thermal runaway in 18650 cylindrical li-ion cells using an accelerating rate calorimeter, Batteries 3 (4) (2017) 14, http://dx.doi.org/10.3390/batteries3020014.

[84] M.S. Rad, D.L. Danilov, M. Baghalha, M. Kazemeini, P.H.L. Notten, Thermal modeling of cylindrical LiFePO4 batteries, J. Mod. Phys. 04 (07) (2013) 1–7, http://dx.doi.org/10.4236/jmp.2013.47A2001.

[85] L.H. Saw, K. Somasundaram, Y. Ye, A. Tay, Electro-thermal analysis of lithium iron phosphate battery for electric vehicles, J. Power Sources 249 (2014) 231–238, http://dx.doi.org/10.1016/j.jpowsour.2013.10.052.

[86] A. Lidbeck, K.R. Syed, Experimental Characterization of Li-ion Battery cells for Thermal Management in Heavy Duty Hybrid Applications, (Ph.D. thesis), Department of Energy and Environment - Division of Electric Power Engineering, Chalmers University of Technology, 2017, URL http://publications.lib.chalmers.se/records/fulltext/252994/252994.pdf.

[87] K.K. Parsons, Design and Simulation of Passive Thermal Management System for Lithium-Ion Battery Packs on an Unmanned Ground Vehicle, (Ph.D. thesis), Faculty of California Polytechnic State University, 2012, URL https://digitalcommons.calpoly.edu/cgi/viewcontent.cgi?article=1961&context=theses.

[88] M.W. Tahir, Thermal characterization, multi-scale thermal modeling and experimental validation of lithium-ion batteries for automobile application, (Ph.D. thesis), University of Stuttgart, 2016, http://dx.doi.org/10.18419/OPUS-8775.

[89] A. Greco, Numerical and Analytical Modelling of Battery Thermal Management using Passive Cooling Systems, (Ph.D. thesis), Faculty of Science and Technology, Lancaster University, 2015, URL https://eprints.lancs.ac.uk/id/eprint/78600/1/2016AngeloGrecophd.pdf.

[90] akkuteile.de, Panasonic NCR18650 3,6v 2900mah (flat top) ungeschützt, 2020, URL https://www.akkuteile.de/lithium-ionen-akkus/18650/panasonic/panasonic-ncr18650_100605_1206.

[91] E-One Moli Energy, Molicel IHR18650c, 2020, URL https://www.custompower.com/documents/MOLICELIHR18650CDataSheetV1.0LC.pdf.

[92] A. Awarke, M. Jaeger, O. Oezdemir, S. Pischinger, Thermal analysis of a li-ion battery module under realistic EV operating conditions, Int. J. Energy Res. 37 (6) (2013) 617–630, http://dx.doi.org/10.1002/er.2884.

[93] A. Hales, L.B. Diaz, M.W. Marzook, Y. Zhao, Y. Patel, G. Offer, The cell cooling coefficient: A standard to define heat rejection from lithium-ion batteries, J. Electrochem. Soc. 166 (12) (2019) A2383–A2395, http://dx.doi.org/10.1149/2.0191912jes.

[94] P.E. Roth, Thermal Abuse Performance of MOLI, Panasonic and Sanyo 18650 Li-Ion Cells, Sandia National Laboratories, https://prod-ng.sandia.gov/techlib-noauth/access-control.cgi/2004/046721.pdf.

[95] Akkuplus.de, Sony - US26650FTC1 - 3,2 Volt 3000mah LiFePO4, 2020, URL https://akkuplus.de/Sony-US26650FTC1-32-Volt-3000mAh-LiFePO4.

[96] I. Tsiropoulos, D. Tarvydas., N. Lebedeva, Li-ion batteries for mobility and stationary storage applications - Scenarios for costs and market growth, JRC Science for Policy Report, 2018, http://dx.doi.org/10.2760/87175.

[97] C. Minke, T. Turek, Materials, system designs and modelling approaches in techno-economic assessment of all-vanadium redox flow batteries – A review, J. Power Sources 376 (2018) 66–81, http://dx.doi.org/10.1016/j.jpowsour.2017.11.058.

[98] J. Figgener, P. Stenzel, K.-P. Kairies, J. Linßen, D. Haberschusz, O. Wessels, M. Robinius, D. Stolten, D.U. Sauer, The development of stationary battery storage systems in Germany – status 2020, J. Energy Storage 33 (2021) 101982, http://dx.doi.org/10.1016/j.est.2020.101982.

[99] K. Mongird, V. Viswanathan, J. Alam, C. Vartanian, V. Sprenkle, Energy Storage Grand Challenge Cost and Performance Assessment 2020, U.S. Department of Energy / Pacific Northwest National Laboratory, 2020, DOE/PA-0204, URL https://www.pnnl.gov/sites/default/files/media/file/Final20-20ESGC20Cost20Performance20Report2012-11-2020.pdf.

B Machine-learning assisted identification of accurate battery lifetime models with uncertainty

Machine-Learning Assisted Identification of Accurate Battery Lifetime Models with Uncertainty

Paul Gasper, Nils Collath, Holger Hesse, Andreas Jossen, Kandler Smith

Journal of the Electrochemical Society 169, p. 80518, 2022

Permanent weblink:
https://doi.org/10.1149/1945-7111/ac86a8

Journal of The Electrochemical Society, 2022 **169** 080518

Machine-Learning Assisted Identification of Accurate Battery Lifetime Models with Uncertainty

Paul Gasper,[1,z] Nils Collath,[2] Holger C. Hesse,[2,3] Andreas Jossen,[2] and Kandler Smith[1]

[1] *Energy Conversion and Storage Systems Center, National Renewable Energy Laboratory, Golden, Colorado, United States of America*
[2] *School of Engineering and Design, Department of Energy and Process Engineering, Technical University of Munich, 80333 Munich, Germany*
[3] *Kempten University of Applied Sciences, 87435 Kempten, Germany*

Reduced-order battery lifetime models, which consist of algebraic expressions for various aging modes, are widely utilized for extrapolating degradation trends from accelerated aging tests to real-world aging scenarios. Identifying models with high accuracy and low uncertainty is crucial for ensuring that model extrapolations are believable, however, it is difficult to compose expressions that accurately predict multivariate data trends; a review of cycling degradation models from literature reveals a wide variety of functional relationships. Here, a machine-learning assisted model identification method is utilized to fit degradation in a stand-out LFP-Gr aging data set, with uncertainty quantified by bootstrap resampling. The model identified in this work results in approximately half the mean absolute error of a human expert model. Models are validated by converting to a state-equation form and comparing predictions against cells aging under varying loads. Parameter uncertainty is carried forward into an energy storage system simulation to estimate the impact of aging model uncertainty on system lifetime. The new model identification method used here reduces life-prediction uncertainty by more than a factor of three (86% ± 5% relative capacity at 10 years for human-expert model, 88.5% ± 1.5% for machine-learning assisted model), empowering more confident estimates of energy storage system lifetime.

Manuscript submitted April 19, 2022; revised manuscript received June 23, 2022. Published August 24, 2022.

Models of battery degradation provide guidance for energy storage system design, empower battery dispatch to be optimized to extend system lifetime, and enable prognostic maintenance, all of which are crucial for leveraging the large initial investment required for any given battery energy storage system.[1,2] Qualitative understanding of the calendar and cycle life of various lithium-ion battery technologies, from sources such as battery warranties or from literature review, helps to define overarching industry trends or to identify targets for improving system lifetime,[3] but does not provide enough detail for optimizing the design or dispatch of individual battery systems, as degradation trends vary dependent on cell format, electrode chemistry, and manufacturer.[4] To provide this detail, many researchers utilize battery lifetime models parameterized using accelerated aging test data. While a wide variety of battery degradation models with varying levels of computational or mathematical complexity exist,[5,6] ranging from simple linear "bucket" models,[7] empirical or "semi-empirical" non-linear models,[8–10] or physics-based models (single particle[7,10] or pseudo-2D[11]), empirically derived algebraic lifetime models, also referred to as reduced-order models, are used widely due to their relative accessibility, interpretability, and ease of implementation. Many systems level and technoeconomic analyses utilize reduced-order lifetime models, combining these degradation models with simulations of battery systems and financial models to optimize the sizing of home energy storage systems,[12] determine battery degradation costs with energy arbitrage,[10,13,14] or optimizing mixed battery use, such as application stacking of stationary systems or use of electric vehicle batteries for vehicle-to-grid services.[15–17]

Battery degradation models can also be used to extend system lifetime and increase revenue for any given application, by balancing the revenue/utilization of the energy storage system with the cost of the incurred degradation during that use.[7,14,18–20] Battery dispatch can be optimized either through the development of battery derating strategies derived from the battery lifetime model,[19,20] or by directly optimizing the battery dispatch considering revenue, system costs, and degradation costs. Various optimization approaches exist, depending on the complexity of the model and compute resources Linear degradation models or piecewise linear approximations of non-linear degradation model may be implemented into a mixed integer linear program,[21,22] which are computationally efficient Non-linear convex degradation models can be used within a mode predictive control framework.[14] Non-linear or physics-based model may be used to optimize dispatch using an algorithmic or gradient free approach.[10,23,24] Accessibility of battery degradation models and their use in applications such as those cited above, is improve by recent publication of open-access battery models, includin physics-based models such as SLIDE[25] and PyBAMM,[26] as wel as technoeconomic modeling tools using the reduced-order batter lifetime models studied in this work, such as SimSES developed b Technical University of Munich,[27] and the System Advisor Mode developed by the National Renewable Energy Lab.[28]

One of the primary challenges for utilizing battery lifetim models is the relationship between accelerated aging data and real world use. While battery lifetime in real-world use may be anywher from 10 to 20 years, it is not reasonable to wait 20 years befor making evaluations of system lifetime. Thus, accelerated agin experiments, where the rate of degradation is increased by operatin batteries aggressively, are common for evaluating battery lifetime These experiments usually require from 6 months to a few years o aging to reach battery end-of-life instead of 10–20 years. Howeve there are many factors to consider when when extrapolating model from accelerated aging data to real-world use:

- Separating time- and cycling-dependent degradation, as aggressively cycled cells can reach 10 000 cycles in 2 years (∼1 cycles per day)[29] while real world cells may not reach 10 000 cycle for 20+ years[30]
- Aging mechanisms driven by cell age may not appear durin accelerated aging, such as the onset of a "knee" in the capacit curve[31,32]
- Aging mechanisms driven by aggressive cycling or extrem temperatures may not appear during real-world use[33]
- Experimental noise and life model inaccuracy may result i substantial predictive uncertainty when predicting battery state a 10–20 years[34]

---

[z] E-mail: pauljgasper@gmail.com; paul.gasper@nrel.gov

- Accelerated aging is typically conducted at constant temperature or using a repeating cycle,[9,29,35,36] while real-world use and environment vary dynamically[30]

The complications above apply not only to cell performance metrics, such as capacity and internal resistance, but also to cell internal states, such as lithium inventory and electrode capacities, which may be diagnosed via incremental capacity analysis.[37] Thus, to extrapolate degradation trends observed during accelerated aging to real-world applications, four key considerations need to be made:

(i) Visualization of degradation trends and connection to physical mechanisms, qualitatively deconvoluting stress-dependent trends (e.g., degradation rate vs. temperature) from chemistry-/architecture-dependent parameters
(ii) Identification of modeling equations predicting degradation trends
iii) Optimization of model parameters and quantification of model uncertainty, deconvoluting the contributions of various degradation mechanisms
iv) Extrapolation to dynamic aging and validation using lab-based or real-world data

The most significant challenge in the above approach is step (ii): the identification of modeling equations. Degradation trends may be dependent on three or more experimental variables, making a trial-and-error search for an accurate model equation very difficult. This work aims to summarize prior efforts to address this challenge, then demonstrate a methodology to identify accurate models by combining human-expert judgement with machine-learning methods, and finally describe how these models can be used to simulate real-world aging. Thus, the main contributions of this work are:

- A review of cycling degradation models, which reveals a wide variety of equation forms and complexities, indicating the challenge researchers face when attempting to discover accurate models
- Demonstration of a machine-learning assisted model identification procedure on a stand-out data set of the degradation of $LiFePO_4$ (LFP) - graphite (Gr) batteries[8,29] (accessible at[38,39]), using bootstrap resampling and cross-validation to quantify the accuracy and uncertainty of human-expert[8,29] and machine-learning assisted models
- Comprehensive description of the procedure for deriving dynamic state equations from the optimized degradation model, which is used for model validation on dynamic aging data as well as simulation of real-world aging in a stationary energy storage system using SimSES[40]

Each of these contributions is detailed in sections throughout the paper. The degradation model described in this work is provided open-source via SimSES.[40]

Literature Review of Cycling Degradation Models

Approaches for separating degradation modes.—In contrast to calendar aging trajectories, which in Li-ion batteries is usually dominated by a single degradation mechanism, growth of the solid-electrolyte interface (SEI) layer on the graphite electrode, and a function of only one variable, time (assuming temperature and state-of-charge (SOC) are constant), degradation for cycling batteries often involves multiple degradation modes and requires consideration of both time and cumulative cycles (even assuming constant cycling protocol). There are many possible approaches for handling these challenges. To account for the overlapping influence of time- and cycle-dependent degradation, many studies consider overall degradation, D, as a superposition of the calendar- and cycling-induced degradation, $D_{Calendar}$ and $D_{Cycling}$:[8,29,32]

$$D = D_{Cycling} + D_{Calendar}$$ [1]

These equations can then be separated into "calendar degradation", which is dependent only on time, and "cycling degradation", which is dependent on time, cycle count, or charge/energy throughput Another possible approach is to multiply the time-dependent fade trajectory by calendar or cycling dependent stress parameters:

$$D = \beta_{Cycling} \cdot \beta_{Calendar} \cdot f(t)$$ [2

where $\beta_{Cycling}$ and $\beta_{Calendar}$ are stress parameters dependent on cycling and calendar test conditions, respectively. The calenda degradation component, $\beta_{Calendar} \cdot f(t)$ can be first optimized to calendar aging data, and then the cycling component optimized afterwards,[9] or $\beta_{Cycling}$ and $\beta_{Calendar}$ can be treated as a single stres parameter, optimized over both the calendar and cycling aging tes data simultaneously.[41] Degradation modes can also be combined logically, as in Smith et al.:[9]

$$D = \min(D_1, D_2, \ldots)$$ [3

where the degradation states represented the lithium inventory positive electrode capacity, and negative electrode capacity, connecting the degradation modes to the battery physics. Finally various degradation trends can simply be treated independently by breaking the aging data set into two or more independent groups identifying separate aging models for each group.[36,42,43] Fo example, Sarasketa-Zabala et al. develop two equations to describe capacity loss, one for cells cycling between 10% and 50% depth o discharge (DOD), and one for cells cycling outside of that range.[4

Note that empirical degradation models do not necessarily need to account for the separate contributions of time- and cycle dependent losses, however, models that do not account for both cannot extrapolate accurately to real-world uses that mix resting and cycling. Models with only time dependence assume that eithe calendar aging dominates all other aging effects,[44] or that the degradation of the battery will not vary substantially with time,[4 i.e., either battery use is unchanging or the degradation rate i constant regardless of how the battery is utilized. Models with only cycle dependence are making a similar assumption,[46,47] implying that the cells are constantly cycling at a consistent rate, or that no degradation is expected if the battery is at rest.

Time-/cycle-dependent egradation trajectory models.—Once degradation modes have been identified, each mode needs to be fit with trajectory model. A trajectory model is an equation that predicts the degradation of the cell as a function of a time-dependent variable, e.g. either time, cycle count, charge-throughput, or energy-throughput. Many trajectory equations for cycling degradation have been proposed, due to the wide variety of trends observed in cycle aging studies. Table I report several examples from literature. By far the most common type o trajectory equation in this literature review is a power law function o cumulative charge-throughput, which can be expressed in units of *Ah* o as equivalent full cycles (EFCs), which is equal to the charge-throughpu divided by twice the nominal battery capacity. The power law model i simple, with only two free parameters (the degradation rate β_1 and the power, β_2) while still being flexible enough to fit a wide variety o degradation trends, such as self-limiting, linear, or accelerating degradation. Cumulative charge-throughput is a convenient input variable, as i can be easily measured in real-world systems, inherently incorporates the impact of the magnitude of the current on the degradation rate, and doe not require a definition of the cycle count that is consistent between varied charge/discharge protocols or dynamic tests.

While the rate coefficient (β_1) can be easily optimized to each tes condition, the power (β_2) is often assumed to be cell-independent, and thus shared across cells with varying degradation rates, making optimization of either parameter non-trivial; the power and degradation rate are co-dependent, so changing the value of the power will affect the value of the rate coefficient and vice-versa. Many studies simply judge the curvature of the capacity fade trajectory by eye, assigning linea trajectories a power of 1[29,48–50] and sub-linear trajectories a power o 1/2,[29,36] or even provide no justification.[43] Some works propose severa possible values, selecting one based on fit metrics.[61] Others optimize the

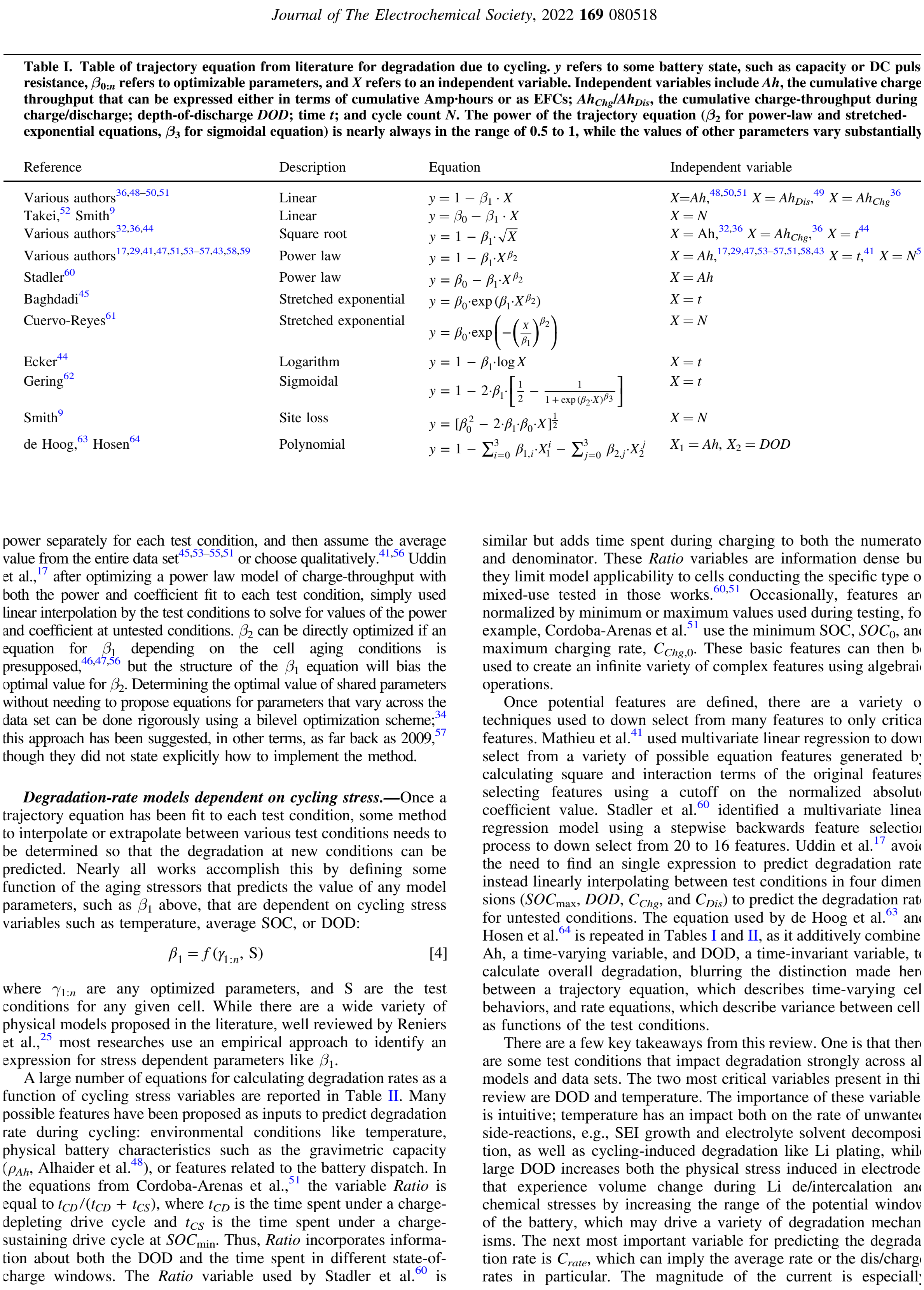

Table I. Table of trajectory equation from literature for degradation due to cycling. *y* refers to some battery state, such as capacity or DC puls resistance, $\beta_{0:n}$ refers to optimizable parameters, and *X* refers to an independent variable. Independent variables include *Ah*, the cumulative charge throughput that can be expressed either in terms of cumulative Amp·hours or as EFCs; Ah_{Chg}/Ah_{Dis}, the cumulative charge-throughput during charge/discharge; depth-of-discharge *DOD*; time *t*; and cycle count *N*. The power of the trajectory equation (β_2 for power-law and stretched-exponential equations, β_3 for sigmoidal equation) is nearly always in the range of 0.5 to 1, while the values of other parameters vary substantially

Reference	Description	Equation	Independent variable
Various authors[36,48–50,51]	Linear	$y = 1 - \beta_1 \cdot X$	$X{=}Ah$,[48,50,51] $X = Ah_{Dis}$,[49] $X = Ah_{Chg}$[36]
Takei,[52] Smith[9]	Linear	$y = \beta_0 - \beta_1 \cdot X$	$X = N$
Various authors[32,36,44]	Square root	$y = 1 - \beta_1 \cdot \sqrt{X}$	$X = \mathrm{Ah}$,[32,36] $X = Ah_{Chg}$,[36] $X = t$[44]
Various authors[17,29,41,47,51,53–57,43,58,59]	Power law	$y = 1 - \beta_1 \cdot X^{\beta_2}$	$X = Ah$,[17,29,47,53–57,51,58,43] $X = t$,[41] $X = N$[5
Stadler[60]	Power law	$y = \beta_0 - \beta_1 \cdot X^{\beta_2}$	$X = Ah$
Baghdadi[45]	Stretched exponential	$y = \beta_0 \cdot \exp(\beta_1 \cdot X^{\beta_2})$	$X = t$
Cuervo-Reyes[61]	Stretched exponential	$y = \beta_0 \cdot \exp\left(-\left(\frac{X}{\beta_1}\right)^{\beta_2}\right)$	$X = N$
Ecker[44]	Logarithm	$y = 1 - \beta_1 \cdot \log X$	$X = t$
Gering[62]	Sigmoidal	$y = 1 - 2 \cdot \beta_1 \cdot \left[\frac{1}{2} - \frac{1}{1 + \exp(\beta_2 \cdot X)^{\beta_3}}\right]$	$X = t$
Smith[9]	Site loss	$y = [\beta_0^2 - 2 \cdot \beta_1 \cdot \beta_0 \cdot X]^{\frac{1}{2}}$	$X = N$
de Hoog,[63] Hosen[64]	Polynomial	$y = 1 - \sum_{i=0}^{3} \beta_{1,i} \cdot X_1^i - \sum_{j=0}^{3} \beta_{2,j} \cdot X_2^j$	$X_1 = Ah$, $X_2 = DOD$

power separately for each test condition, and then assume the average value from the entire data set[45,53–55,51] or choose qualitatively.[41,56] Uddin et al.,[17] after optimizing a power law model of charge-throughput with both the power and coefficient fit to each test condition, simply used linear interpolation by the test conditions to solve for values of the power and coefficient at untested conditions. β_2 can be directly optimized if an equation for β_1 depending on the cell aging conditions is presupposed,[46,47,56] but the structure of the β_1 equation will bias the optimal value for β_2. Determining the optimal value of shared parameters without needing to propose equations for parameters that vary across the data set can be done rigorously using a bilevel optimization scheme;[34] this approach has been suggested, in other terms, as far back as 2009,[57] though they did not state explicitly how to implement the method.

Degradation-rate models dependent on cycling stress.—Once a trajectory equation has been fit to each test condition, some method to interpolate or extrapolate between various test conditions needs to be determined so that the degradation at new conditions can be predicted. Nearly all works accomplish this by defining some function of the aging stressors that predicts the value of any model parameters, such as β_1 above, that are dependent on cycling stress variables such as temperature, average SOC, or DOD:

$$\beta_1 = f(\gamma_{1:n}, \mathrm{S}) \qquad [4]$$

where $\gamma_{1:n}$ are any optimized parameters, and S are the test conditions for any given cell. While there are a wide variety of physical models proposed in the literature, well reviewed by Reniers et al.,[25] most researches use an empirical approach to identify an expression for stress dependent parameters like β_1.

A large number of equations for calculating degradation rates as a function of cycling stress variables are reported in Table II. Many possible features have been proposed as inputs to predict degradation rate during cycling: environmental conditions like temperature, physical battery characteristics such as the gravimetric capacity (ρ_{Ah}, Alhaider et al.[48]), or features related to the battery dispatch. In the equations from Cordoba-Arenas et al.,[51] the variable *Ratio* is equal to $t_{CD}/(t_{CD} + t_{CS})$, where t_{CD} is the time spent under a charge-depleting drive cycle and t_{CS} is the time spent under a charge-sustaining drive cycle at $SOC_{\min}$. Thus, *Ratio* incorporates information about both the DOD and the time spent in different state-of-charge windows. The *Ratio* variable used by Stadler et al.[60] is similar but adds time spent during charging to both the numerato and denominator. These *Ratio* variables are information dense bu they limit model applicability to cells conducting the specific type o mixed-use tested in those works.[60,51] Occasionally, features ar normalized by minimum or maximum values used during testing, fo example, Cordoba-Arenas et al.[51] use the minimum SOC, SOC_0, an maximum charging rate, $C_{Chg,0}$. These basic features can then b used to create an infinite variety of complex features using algebrai operations.

Once potential features are defined, there are a variety o techniques used to down select from many features to only critica features. Mathieu et al.[41] used multivariate linear regression to dow select from a variety of possible equation features generated b calculating square and interaction terms of the original features selecting features using a cutoff on the normalized absolut coefficient value. Stadler et al.[60] identified a multivariate linea regression model using a stepwise backwards feature selectio process to down select from 20 to 16 features. Uddin et al.[17] avoi the need to find an single expression to predict degradation rate instead linearly interpolating between test conditions in four dimensions ($SOC_{\max}$, DOD, C_{Chg}, and C_{Dis}) to predict the degradation rat for untested conditions. The equation used by de Hoog et al.[63] an Hosen et al.[64] is repeated in Tables I and II, as it additively combine Ah, a time-varying variable, and DOD, a time-invariant variable, t calculate overall degradation, blurring the distinction made her between a trajectory equation, which describes time-varying cel behaviors, and rate equations, which describe variance between cell as functions of the test conditions.

There are a few key takeaways from this review. One is that ther are some test conditions that impact degradation strongly across al models and data sets. The two most critical variables present in thi review are DOD and temperature. The importance of these variable is intuitive; temperature has an impact both on the rate of unwante side-reactions, e.g., SEI growth and electrolyte solvent decomposition, as well as cycling-induced degradation like Li plating, whil large DOD increases both the physical stress induced in electrode that experience volume change during Li de/intercalation an chemical stresses by increasing the range of the potential windo of the battery, which may drive a variety of degradation mechanisms. The next most important variable for predicting the degradation rate is C_{rate}, which can imply the average rate or the dis/charg rates in particular. The magnitude of the current is especiall

Table II. Table of cycling degradation rate equations from literature. Equations are predicting degradation rate coefficients, such as β_1 in the equation $y = \beta_1 \cdot x^{\beta_2}$, as a function of cycling stressors, such as DOD or C_{rate}, and environmental stressors like temperature. In some cases, such as for,[9,51,58] equations were reported for several degradation rate coefficients, usually for predicting multiple degradation states. There are two approaches that blur the distinction made in this work between trajectory equations, described in Table I, and degradation rate equations, described here. The approach by de Hoog[63] and Hosen[64] uses DOD as an input to directly predict lost capacity. Stadler[60] completely avoid predicting a trajectory, instead predicting the lost capacity at some specific amount of charge-throughput directly using the cycling stressors as input.

References	Equation
Alhaider[48]	$(\gamma_1 \cdot DOD + \lvert SOC - 0.5 \rvert \cdot \gamma_2) \cdot \exp(\rho_{Ah} \cdot C_{rate})$
Baghdadi[45]	$\exp\left(\exp\left(\frac{\gamma_1}{T} + \gamma_2\right) \cdot C_{rate}\right)$
Cordoba-Arenas[51]	$[\gamma_1 + \gamma_2 \cdot Ratio^{\gamma_3} + \gamma_4 \cdot (SOC_{\min} - SOC_0)^{\gamma_5}] \cdot \exp\left(\frac{\gamma_6}{T}\right)$ $[\gamma_1 + \gamma_2 \cdot (SOC_{\min} - SOC_0)^{\gamma_3} + \gamma_4$ $\cdot \exp(\gamma_5 \cdot (C_{Chg,0} - C_{Chg})) + \gamma_6 \cdot (SOC_{\min} - SOC_0)] \cdot \exp\left(\frac{\gamma_7}{T}\right)$
de Hoog,[63] Hosen[64]	$Q = 1 - \sum_{i=0}^{3} \beta_{1,i} \cdot Ah^i - \sum_{j=0}^{3} \beta_{2,j} \cdot DOD^j$
Diao[46]	$\exp(\gamma_1 \cdot T + \gamma_2)$ $\gamma_1 \cdot T + \gamma_2$
Ebbesen,[47] Schimpe[36]	$\gamma_1 \cdot \exp\left(\frac{\gamma_2}{T}\right)$
Mathieu[41]	$exp\left(\gamma_1 + \frac{\gamma_2}{T} + \gamma_3 \cdot SOC + \gamma_4 \cdot I + \gamma_5 \cdot \frac{I}{T} + \frac{\gamma_6}{T^2} + \gamma_7 \cdot SOC^2\right)$
Naumann[29]	$(\gamma_1 \cdot C_{rate} + \gamma_2) \cdot (\gamma_3 \cdot (DOD - 0.6)^3 + \gamma_4)$
Petit[58]	$\gamma_1 \cdot exp\left(\frac{\gamma_2 + \gamma_3 \cdot \lvert I \rvert}{T}\right)$
Sarasketa-Zabala[43]	$\gamma_1 \cdot DOD^2 + \gamma_2 \cdot DOD + \gamma_3$ $\gamma_1 \cdot \exp(\gamma_2 \cdot DOD) + \gamma_3 \cdot \exp(\gamma_4 \cdot DOD)$
Saxena[53]	$\gamma_1 \cdot SOC \cdot (1 + \gamma_2 \cdot DOD + \gamma_3 \cdot DOD^2)$
Schimpe[36]	$\gamma_1 \cdot \exp\left(\frac{\gamma_2}{T} + \gamma_3 \cdot C_{Chg}\right)$
Schmalsteig[32]	$\gamma_1 + \gamma_2 \cdot (V - \gamma_3)^2 + \gamma_4 \cdot DOD$ $exp(\gamma_2 \cdot DOD^{\gamma_3})$
Smith[9]	$1 + \gamma_1 \cdot DOD$ $\gamma_1 \cdot \exp\left(\frac{\gamma_2}{T}\right) \cdot DOD^{\gamma_3}$
Stadler[60]	$Q_{Loss@Ah} = \gamma_1 + \gamma_2 \cdot Ratio + \gamma_3 \cdot T^2 + \gamma_4 \cdot T + \gamma_5 \cdot Ratio^2 + \gamma_6 \cdot SOC_{\max}^2 + \gamma_7 \cdot SOC_{\min} + \gamma_8 \cdot SOC_{\min}^2 + \gamma_9 \cdot P_{Chg}^2 + \gamma_{10} \cdot SOC_{\max} \cdot Ratio$ $+ \gamma_{11} \cdot Ratio \cdot P_{Chg} + \gamma_{12} \cdot T \cdot SOC_{\max} + \gamma_{13} \cdot P_{Chg} + \gamma_{14} \cdot SOC_{\max} + \gamma_{15} \cdot T \cdot Ratio + \gamma_{16} \cdot SOC_{\max} \cdot SOC_{\min} + \gamma_{17} \cdot T \cdot P_{Chg}$
Suri[54]	$(\gamma_1 \cdot SOC + \gamma_2) \cdot \exp\left(\frac{\gamma_3 + \gamma_4 \cdot C_{rate}}{T}\right)$
Todeschini[55]	$\gamma_1 + \gamma_2 \cdot DOD + \gamma_3 \cdot \exp(C_{rate})$
Uddin[17]	Linear interpolation by $SOC_{\max}$, DOD, C_{Chg}, and C_{Dis} between test points
Wang 2011[56]	$\gamma_1 \cdot \exp\left(\frac{\gamma_2 + \gamma_3 \cdot C_{rate}}{T}\right)$
Wang 2014[50]	$(\gamma_1 \cdot T^2 + \gamma_2 \cdot T + \gamma_3) \cdot \exp((\gamma_4 \cdot T + \gamma_5) \cdot C_{rate})$

Table III. Algorithm for generating feature libraries used during symbolic regression. At each step, features from the prior step are kept, so th total number of descriptors is cumulative. Note that the procedure differs slightly when generating features for linear (additive) or multiplicativ equations. The example shown here uses temperature, SOC, and the anode-to-reference potential, U_a, as input features for generating features t model calendar aging behaviors. When generating features for cycle aging, only DOD and the average of the charge/discharge rate (C_{rate}) are used and step 3 is omitted to prevent division by 0 (DOD is set equal to 0 when evaluating calendar degradation), resulting in 48 features. Temperature i omitted when generating features for cycle aging because the aging test matrix does not have enough variance in the cycling temperature to identif any trends.

Step	Description	Formula	Example	# descriptors
1	Input features	$X_A(T)$, $X_B(SOC, U_a)$	T, SOC, U_a	3
2	Non-linearities	$X^{1/4}$, $X^{1/3}$, $X^{1/2}$, X^2, X^3, X^4	T^4, $SOC^{1/3}$	21
3	Inverse (calendar only)	X^{-1}	$1/T^2$, $1/U_a$	42
4	Multiplicative interactions	$X_1^{*}X_2$	$T^3{*}U_a^{1/4}$, SOC/T^3	434
5a	Exponential (linear eq. search)	e^X	$exp(U_a)$, $exp(SOC^2/T^4)$	868
5b	Natural log (multiplicative eq. search)	$log(X)$	$log(T)$, $log(T^{1/4}/U_a)$	868
6	Remove any infinities or NaNs			573 (linear), 553 (multiplicative

impactful in tests at low temperature, where high charging rates may lead to Li plating. Finally, some studies incorporate SOC variables into their degradation models. Perhaps one reason why SOC is not incorporated into more models is simply due to limited testing resources; creating a test matrix that varies temperature, DOD, dis/charging rates, and SOC windows requires a prohibitive number of batteries, forcing researchers to prioritize which experimental variables to explore.

A crucial takeaway from this review is that the range of possible input features, equation forms, and modeled variables used to predict cycling degradation is extremely wide, and there is little consistency between works. This is in contrast to a prior review of calendar degradation modeling,[34] which showed relatively uniformity in the features and equation forms, e.g., Arrhenius and Tafel type equations. Uniformity across works is somewhat expected, as degradation trajectories are often qualitatively similar between data sets, and most of the works cited here study Li-ion batteries from a narrow set of commercialized electrode and electrolyte chemistries. This qualitative similarity in the degradation trends between studies implies that most degradation is due to shared root causes, most commonly the growth of the SEI at the graphite electrode; but despite these shared trends, the features, equations, and model identification procedures reviewed here are widely disparate. This variety of approaches makes it difficult to compare modeling results, find useful models for new data sets by searching prior works, or to replicate the model identification procedure described in any given work. Thus, there is a clear need for identifying not only accurate equations, but also a replicable and repeatable model identification procedure, using automated methods when possible to assist the search for accurate and robust empirical degradation models.

Machine-Learning Assisted Model Identification Approach

In this work, model identification is done using a bilevel optimization and symbolic regression approach.[34] First, separate degradation modes are identified using expert-judgement; use of expert-judgement is required, as not all degradation mechanisms are electrochemically visible, and the connection of specific degradation mechanisms to degradation modes is complicated by mechanical, chemical, and electrochemical interactions.[65] After splitting the data into regimes dominated by individual modes, each mode is fit with the ML-assisted model identification method. Model identification has two key steps: defining a trajectory equation using expert-judgement aided by bilevel optimization, and identification of local parameter submodels using either intuition or symbolic regression. A graphical representation of this procedure can be seen in Fig. A·1 (Fig.1 of Ref. 34).

In the first step of identifying a model for a specific degradation mode, expert-judgement is used to select one or more potential trajectory equations for any given degradation mode, based on qualitative trends in the data or domain knowledge of the physical root cause. For instance, the calendar degradation mode, which i attributed to the SEI growth degradation mechanism, can b modeled well by a power law expression,[66] while a self-limitin reaction can be modeled by a sigmoidal expression.[62] Bileve optimization is used to separately optimize the values of loca (stress dependent) and global (cell independent) parameters. Globa parameters are optimized in an upper level optimization loop, wit multiple lower level optimization loops solving for the values o each local parameter for every data series. Each optimization loop i attempting to minimize the root mean square error between th model prediction and the data. Model fitness is reported using th adjusted coefficient of determination (R_{adj}^2) and the mean absolut error (MAE).

In the second step of identifying a model for a specific degradatio mode, local parameters are then modeled as functions of the agin conditions, such as constant temperature or constant average SOC Sometimes, well performing equations for these local paramete submodels can be identified by introspection or with domai knowledge,[9,34] but often, defining an equation that is robust is quit difficult; robust meaning a model that is accurate when trained on al the available data, cross-validates with low error, has narrow confidenc intervals, and extrapolates to extreme conditions without diverging Here, the ML method of symbolic regression is utilized to identif candidate submodels for local parameters. Symbolic regression i conducted by algorithmically generating a large library of possibl equation features, and then utilizing a regularization algorithm to searcl for an optimal linear combination of a small subset of features. Thi procedure can also be used to find multiplicative models by fitting th log of the response variable.[34]

Features for predicting locally fit parameter values are generated usin an algorithmic approach, which is decscribed in Table III. Possibl equations, which are constructed by linearly or multiplicative combinin these features, vary from simple, such as $\beta_1 = \gamma_0 + \gamma_1 \cdot DOD$, to mor complex, like $\beta_1 = \gamma_0 \cdot exp(\gamma_1 \cdot C_{rate}^{1/3}) \cdot \gamma_2 \cdot (DOD^2 \cdot C_{rate})^{\gamma_3}$. Because an subset of features could be a valid model, the search space of possibl equations has combinatorial complexity. For example, an exhaustiv search for the optimal equation using 6 features from a set of 1000 woul require calculating the results of $1.4 \cdot 10^{15}$ equations.

Searching for a parsimonious model in this large search space ca be done using many regularization or feature selection algorithms. I a prior work,[34] the LASSO regularization algorithm was used.[6 However, it was found that this algorithm did not perform well whe used on large feature libraries, approximately 10^2 features or greate as large feature libraries create wide matrices that have more feature (columns) than data points (rows). Here, the Sure-Independen Screening and Sparsifying Operator (SISSO) algorithm was used SISSO has been demonstrated to perform better than LASSO i similar cases.[68–70] SISSO also has several other advantages ove

LASSO. Rather than outputting a single model, SISSO outputs several candidate models of increasing complexity, which can then be manually screened to identify the best model. SISSO also is repeatable, outputting the same candidate models when re-run on the same inputs, which is not the case when using LASSO with wide input matrices. SISSO requires defining two hyperparameters: the maximum number of non-zero coefficients and the number of features selected per iteration (one iteration per non-zero coefficient). For searching for calendar degradation submodels, the maximum number of non-zero coefficients is set to 4, and the number of features per iteration is set to 40. Implementations of SISSO in Fortran,[71] MATLAB,[72] and Python with integration to the sklearn API[73] are available.

Local parameter submodels are then substituted into the trajectory equation, defining a global equation that predicts the behavior of all data series with a single expression. The global equation is then reoptimized on the entire data set, evenly weighting each data series so that the number of data points per series does not impact the optimal parameter values. This process is repeated each time a new degradation mode is added to the model, so that the values of all model parameters are optimized considering the cumulative effects of each degradation mode. Predictive uncertainty is estimated by training the model on a randomly resampled subset of the test groups using a bootstrap resampling approach,[34] and also using a leave-one-out cross-validation approach. Finally, the model is reformulated into a state model, enabling simulation of battery aging under dynamic environmental conditions or varying use, the procedure for which is described later.

Data

The data used for this study is LFP/Gr cell aging data, previously published in Naumann et al.[8,29] and available for download.[38,39] Data was provided at request from the original authors, and includes some data not reported in the prior works. The cells studied were commercial Sony/Murata US26650FTC1 LFP/Gr cells in the 26 650 cylindrical format. The manufacturer specified nominal discharge capacity of these cells is 2.85 Ah, however, the nominal discharge capacity is considered to be 3 Ah due to prior characterization work on over 1000 cells.[74] The aging study was conducted by aging cells in climate controlled chambers. Cell performance was monitored by routine performance checkups, conducted every week for the first three weeks, every other week for the following six weeks, and every four weeks for the rest of the study, approximately 900 d. Performance checkups consist of capacity checks and pulse resistance measurements. Capacity is measured using two repeated constant-current constant-voltage (CCCV) charge and discharg cycles (1C CC, 3.6V CV on charge with a C/30 cutoff on charge 2.0 V CV with a C/20 cutoff on discharge). DC pulse resistance i measured using 10 s charge and discharge pulses at 50% SOC an at 1/3C, 2/3C, and 1C rates, with 10 min of relaxation betwee each pulse. This work develops a model for the relative discharg capacity, which is defined as the mean of the discharged capacit from the two full CCCV discharge cycles (Eq. 5), divided by th initial discharge capacity recorded for each cell.

$$Q = \frac{1}{2}\left(Q_{CCCV_{discharge,1}} + Q_{CCCV_{discharge,2}}\right) \qquad [5$$

Table A·I reports the aging conditions of each test group. Th aging matrix consists of 17 static calendar aging test groups (group 1-17), 19 static cycle aging test groups (groups 18-36), 8 dynami calendar aging test groups (groups 37-44), and 5 dynamic cyclin aging test groups (groups 45-49), with three test replicates for mos groups. Static calendar aging tests varied storage temperature fron 0 °C to 60 °C and SOC from 0% to 100%. Static cycle aging test cycled cells using CC charge and discharge steps at only 25 °C an 45 °C, but widely varied DOD between 1% and 100%, varie average SOC between 25% and 75% at 20% DOD, varied discharg and charging rates (C_{rate}) between 0.2C and 2C, and cycled som cells using CCCV charging steps instead of CC charging steps. Mor detail is provided in the original works.[8,29] For modeling purposes the C_{rate} is considered as the average of the charging and dischargin rates, as a direct comparison of cells aging under asymmetri charging and discharge rates (groups 26, 27, 28, and 30) reveale no substantial difference in the capacity fade or resistance growt behavior.[29]

Visualizing prominent capacity fade trends.—The developmen of the capacity fade model begins with identifying major trends i the data, correlating those trends with the aging conditions, an determining an appropriate order in which to model individua mechanisms, which may combine additively[29,36] or competitively. Key calendar degradation trends are shown in Fig. 1, and cyclin degradation trends are shown in Fig. 2. The prominent trend observed during calendar aging are increasing degradation rat with respect to temperature (Fig. 1a) as well as with increasing SO (Fig. 1b). The time-dependent calendar aging behavior appears sublinear for most aging conditions, however, it can be seen in Fig. 1 that as the SOC approaches 0%, the degradation trajectory become almost linear. This behavior was also observed in a prior work.[34]

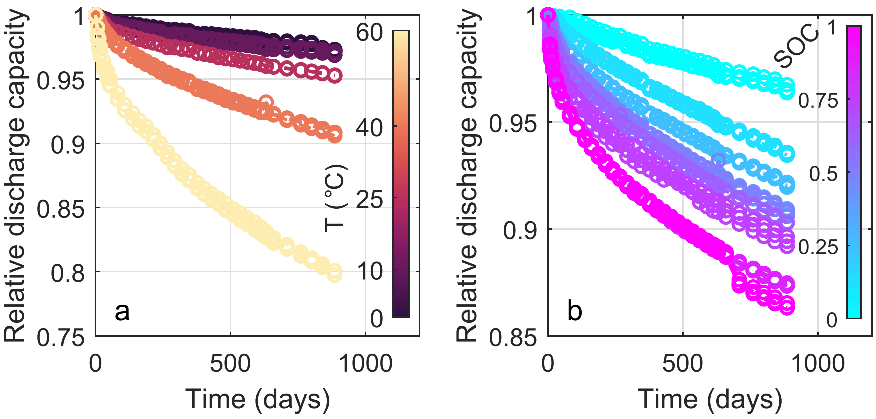

Figure 1. Capacity fade trends observed during calendar aging. (a) Impact of temperature variation at 50% SOC (groups 1, 2, 4, 10, 16). (b) Impact of SO variation at 40 °C (groups 6-14).

Figure 2 shows the dominant trends in the cycling data. Figures 2a–2b both show the impact of the average C_{rate} on the capacity fade, but with time on the x-axis in Fig. 2a and EFCs on the x-axis in Fig. 2b. While in Fig. 2a it seems clear that increasing C_{rate} increases the degradation rate, this is not accounting for the impact that increased charge-throughput may have on cell capacity over time. But when plotted vs EFCs in Fig. 2b, the apparent trend reverses, and it becomes unclear if the increased degradation at high C_{rate} is simply due to increased charge-throughput, or if there is an impact of C_{rate} on the degradation per EFC as well. these effects can be potentially deconvoluted by first subtracting the contribution of calendar fade, as described in Eq. 1; Naumann et al. identified a positive impact of C_{rate} on the degradation per EFC using this approach.[29] This simple example demonstrates why it is crucial to plot data vs both time and charge- or energy-throughput when considering the impact of C_{rate} on cell health metrics.

Figure 2c shows the impact of varying DOD on the capacity fade trajectory. The variation of DOD reveals that there are two additive degradation modes involved in the loss of discharge capacity during cycling: an initial sudden drop of capacity followed by a saturation period, i.e., break-in loss, and a nearly linear loss of capacity over the entire experiment, i.e., long-term loss. Break-in loss appears to always saturate within the first 300 d and 4000 EFCs. The magnitude of the break-in loss is a non-monotonic function of DOD and SOC. As seen in Figs. 2c–2d, the maximum break-in loss is observed at approximately 20% DOD and 50% SOC, decreasing in magnitude as both SOC and DOD vary from these values This break-in loss has been characterized in detail by prio work,[75] and is attributed to a uneven distribution of lithiu throughout that occurs when cycling at low DODs. While som of the break-in capacity loss is recoverable, by letting th lithium in the cell redistribute via relaxation or very slo cycling, the uneven utilization of the anode during low DO cycling also results in unrecoverable capacity loss. Thi physical explanation also implies that cells cycled with varyin DOD, or with suitably long rest periods between cycles, woul likely not experience this loss mechanism, which has implications for extrapolating the trends observed during the accelerated aging study to real-world use.

In contrast to the break-in fade, the long-term capacity los trends are relatively straightforward. The slope of the long-ter capacity loss appears to be a monotonic function of DOD, wit an increasing slope at increasing DODs. Figure 2d shows th impact of varying the average SOC on capacity fade. SOC seem to primarily impact the magnitude of the break-in loss, with maximum break-in loss at 50% SOC, and has no obvious impact on the slope of the long-term loss. Due to the complexity o these trends, prior work modeling the cycling degradation trend in this data set[29] neglected to fit the break-in loss. However, du to the additive nature of the break-in and long-term capacity los modes, and the large contribution of the break-in loss to many o the cells, accurately modeling the dependence of the long-ter loss rate on DOD without also modeling the break-in behavior i not possible.

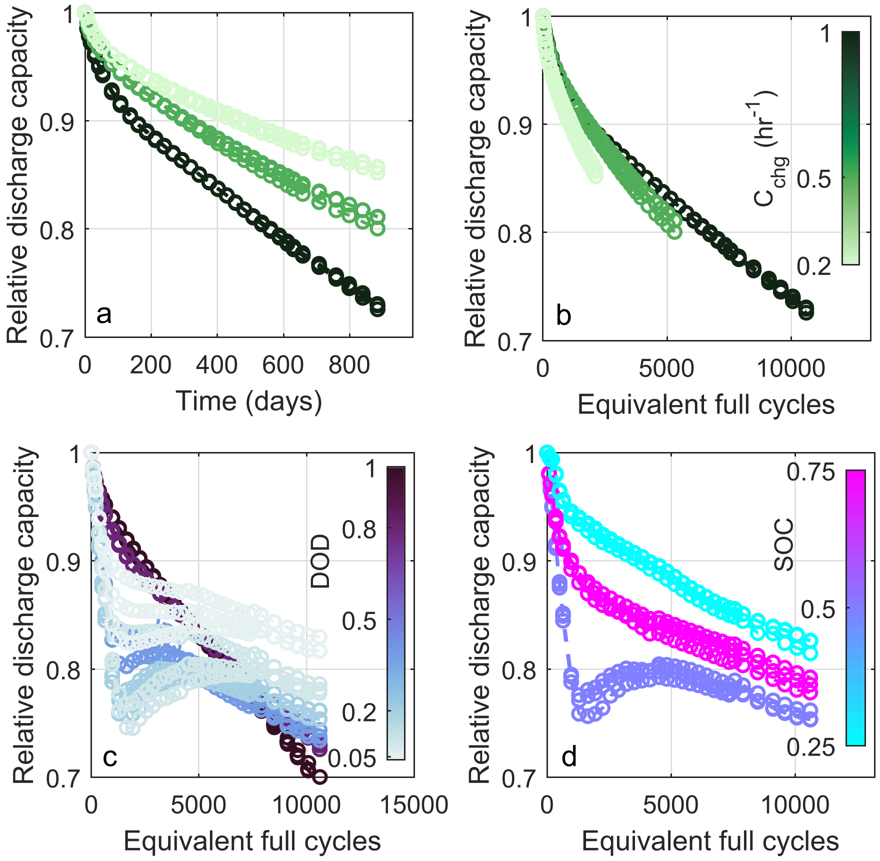

Figure 2. Capacity fade trends observed during cycling aging. (a), (b) Impact of C_{rate} variation vs (a) time and (b) EFC (groups 23-25). (c) Impact of DO variation (groups 22-23, 29, 31, 34). (d) Impact of SOC variation at 20% DOD (groups 31-33).

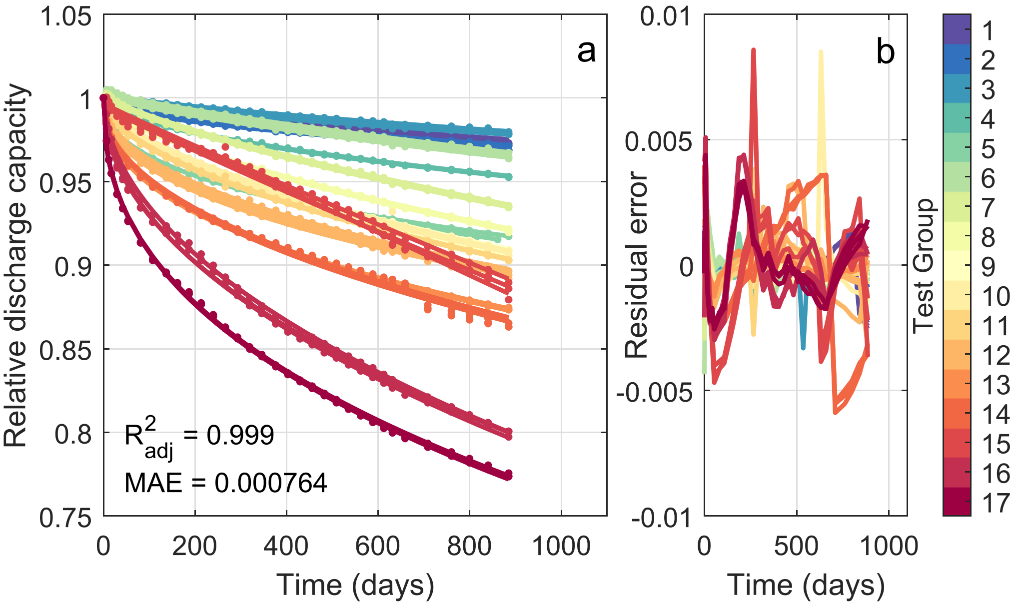

Figure 3. Calendar model local fit on all calendar aging cells.

Model Identification Using Static Aging Data

In this section, the identification of a capacity loss model using the bilevel optimization and symbolic regression approach and the test data from static aging tests (groups 1-36) is described in detail. Model identification begins by fitting the calendar degradation data (groups 1-17), and then this calendar degradation model is used to estimate the contribution of calendar degradation to the degradation observed during cycle aging (groups 8-36). As discussed in the previous section, capacity loss due to cycle aging is modeled using the additive combination of a break-in mode and a long-term degradation mode; the break-in mode is fit first, followed by fitting of the long-term degradation mode. After identifying the cycling degradation equations, all model parameters, including the calendar fade model parameters, are reoptimized over all of the static aging data.

Fitting calendar aging data.—Various different equation forms were considered for predicting the capacity loss due to calendar aging.[34] Comparing between square-root, linear, power-law, and sigmoidal equation forms, the sigmoidal equation results in the best overall model with regards to accuracy and uncertainty. This trajectory model is reported in Eq. 6:

$$q = 1 - q_{Loss,Cal}$$

$$q_{Loss,Cal} = 2\cdot q_1\cdot\left[\frac{1}{2} - \frac{1}{1 + exp((q_2\cdot t)^{q_3})}\right] \qquad [6]$$

where q_1, q_2, and q_3 are free parameters, and t is the time in days. The parameters q_1 and q_3 are fit locally to each cell, as both the extent of degradation and the curvature of the capacity fade trajectory differ across the various test conditions, while the parameter q_2 is optimized globally with a resulting value of $1.31 \cdot 10^{-4}$; fitting q_1 locally has a clear physical basis (the maximum extent of the reaction), while model errors are lower when allowing q_3 to be fit locally rather than q_2. Fitting all parameters locally results in chaotic trends for parameter values vs temperature and SOC, leading to a non-physical model. The result of this bilevel optimization is shown in Fig. 3. The model fits the data precisely, and there are no obvious trends observable in the residual errors indicating that the data is well fit.

Locally fit values of q_1 and q_3 are then modeled using th symbolic regression procedure. Locally fit values of q_1 and q_3 ar shown as circles in Figs. 4a–4b. q_1 varies primarily as an exponentia function of temperature, with little dependence on SOC until th SOC reaches 0%. q_3 seems to vary mostly as a function of SOC Considering both parameters, the behavior at 0% SOC across al temperatures differs substantially from cells tested at other SOCs this is because the capacity fade trajectory of cells at 0% SOC i much closer to linear than any of the other cells, leading to highe values of q_3, which then impacts the optimal value of q_1. Th symbolic regression procedure is able to find robust equations fo predicting the values of q_1 and q_3 as functions of temperature an SOC. The equation found for q_1 is reported below (Eq. 7), wher $q_{1,a-c}$ are free parameters, T is the temperature in Kelvin, and U_a i the anode-to-reference potential, calculated according to the equation defined by Safari and Delacourt[76] and parameterized for thi specific cell in Schimpe et al.[36] Model predictions are plotted as X' with 95% confidence intervals as determined by bootstrap resampling in Fig. 4a. The only test condition poorly predicted by th identified model is at 0 °C and 50% SOC, however, both th measured and predicted values are very small, resulting a lov predicted value for the capacity fade in Eq. 6, which matches th observed trends.

$$q_1 = q_{1,a}\cdot exp\left(q_{1,b}\cdot\frac{U_a^{0.5}}{T^2}\right)\cdot\exp\left(q_{1,c}\cdot\frac{U_a^{0.5}}{T}\right) \qquad [7$$

where U_a is a function of SOC, described in equation A·1 Equation 7 is then simulated between 0 °C–60 °C and 0%–100% SOC, to evaluate model trends over a wide range of conditions Model predictions at 0% SOC vary substantially from those at highe SOCs, which makes sense intuitively because the capacity fad trajectory of cells at 0% SOC is much different than those at large SOCs.

The equation found for q_3 is reported below (Eq. 8), where $q_{3,a-}$ are free parameters, with predictions plotted as X's in Fig. 4b. Th identified equation correctly captures all the trends of the locally fi

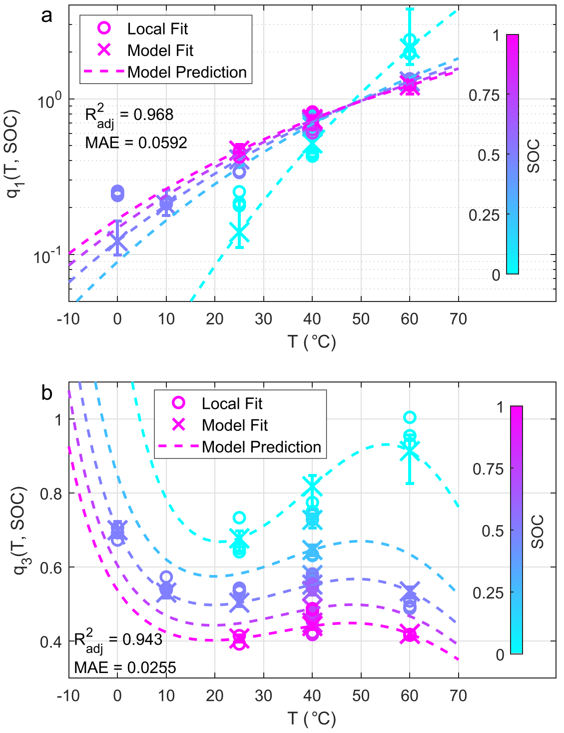

Figure 4. (a) Parameter q_1 values from local fits (circles), ML model (Eq. 7) fits with 95% confidence intervals (X's with error bars), and model predictions vs temperature at 0%, 25%, 50%, 75%, and 100% SOC. (b) Parameter q_3 values from local fits, ML model (Eq. 8) fits with 95% confidence intervals, and model predictions vs temperature at 0%, 25%, 50%, 75%, and 100% SOC.

q_3 values accurately. Simulation of the model shows that the model behaves sensibly across a large range of conditions. At 0% SOC and 5 °C, the value of q_3 becomes larger than 1, which results in faster than linear degradation, however, the value of q_1 is extremely small at this condition, so the predicted capacity fade (Eq. 6) will still conform to physical intuition.

$$q_3 = q_{3,a} \cdot exp\left(q_{3,b} \cdot \frac{U_a^{1/3}}{T^4}\right) \cdot exp\left(q_{3,c} \cdot T^3 \cdot U_a^{1/4}\right) \cdot exp\left(q_{3,d} \cdot \frac{U_a^{1/3}}{T^3}\right) \cdot exp\left(q_{3,e} \cdot T^2 \cdot U_a^{1/4}\right) \qquad [8]$$

The overall calendar fade model is then defined by substituting Eqs. 7 and 8 into Eq. 6.

Fitting cycling aging data.—For fitting the break-in and long-term cycling degradation modes, the data from static cycling cells was split into regions dominated by the break-in and long-term degradation behaviors. Splitting the data was done by defining logical conditions with respect to EFCs and the second derivative of the relative discharge capacity with respect to time in days; derivatives were calculated by element-wise division of the difference of capacity and the difference of time and then using the Matlab function *smoothdata*. The conditional statement for the break-in data mask is shown in Eq. 9, and the conditional statement for the long-term data mask is shown in Eq. 10.

$$q_{Break-in} \in q\left(0 < EFC < 4000 \;\&\; \frac{d^2q}{dt^2} > 3E-6\right)$$
$$OR$$
$$Test\ group\ == (20, 36) \qquad [9$$

$$q_{Long-term} \in q\left(EFC > 1000 \;\&\; \frac{d^2q}{dt^2} < 2.5E-7\right) \qquad [1$$

Modeling cycling break-in loss.—Because the capacity loss du to the break-in mechanism appears to saturate for all cases, sigmoidal equation was used to account for it (Eq. 11). Thi mechanism was additively combined with the existing equation fo the capacity loss due to calendar aging, optimizing the parameter q_4, q_5, and q_6; q_4 was optimized locally to each test group, while q and q_6 were optimized globally to the entire data set. The result o optimizing Eq. 11 to the masked off break-in data is shown in Fig. 5

$$q = 1 - q_{Loss,Cal} - q_{Loss,BreakIn}$$
$$q_{Loss,BreakIn} = 2 \cdot q_4 \cdot \left[\frac{1}{2} - \frac{1}{1 + exp\left((q_5 \cdot EFC)^{q_6}\right)}\right] \qquad [11$$

As shown in Figs. 2c–2d, the magnitude of the break-i mechanism is both a function of DOD and average SOC. Thi variation is captured by the locally optimized values of q_4, shown a circle markers in Fig. 6. The parameters q_5 and q_6 have optima values of $3.04 \cdot 10^{-3}$ and 1.43, respectively. Due to the lack of tes cases varying SOC, there is not enough data available to use th symbolic regression approach to learn a robust equation that predict the behavior of q_4 vs both SOC and DOD. Qualitative analysis of th trends of q_4 vs both DOD and average SOC led to the insight that two-dimensional skewed normal distribution describes the overal trend, while also ensuring the boundary conditions match physica expectations by multiplying by a sigmoid; there should be no break in if the DOD is equal to 0, or very near 0, and the experimenta results show no break-in at 100% DOD either. So, the data was fi with Eq. 12:

$$q_4 = q_{4,a} \cdot \phi_{skew}\left(SOC,\ q_{4,SOC,\mu},\ q_{4,SOC,\sigma},\ q_{4,SOC,\xi}\right) \cdot \phi_{skew}\left(DOD,\ q_{4,DOD,\mu},\ q_{4,DOD,\sigma},\ q_{4,DOD,\xi}\right) \cdot \left(2 \cdot \left[\frac{1}{2} - \frac{1}{1 + exp\left(q_{4,b} \cdot DOD\right)}\right]\right) \qquad [12$$

where SOC and DOD are inputs, $q_{4,a}$, $q_{4,b}$, $q_{4,SOC,\sigma}$, $q_{4,SOC,\xi}$ $q_{4,DOD,\sigma}$, and $q_{4,DOD,\xi}$ are fitting parameters, and $q_{4,SOC,\mu}$ an $q_{4,DOD,\mu}$ are set to 0.5 manually based on the qualitative trend observed in Figs. 2c–2d. ϕ_{skew} is defined here as:

$$\phi_{skew}(x) = 2 \cdot \phi\left(\frac{x - \mu}{\sigma}\right) \cdot \Phi\left(\xi \cdot \frac{x - \mu}{\sigma}\right) \qquad [13$$

where ϕ is the normal probability distribution function and Φ is th normal cumulative distribution function, both with mean μ an standard deviation σ, and a skew of ξ. Equation 12 fits the dat accurately, as seen in Fig. 6. The magnitude of the uncertainty a DOD less than 20% is quite large, which is sensible as q_4 grows ver quickly and there are only 3 available data points to train the mode in this regime.

Modeling long-term cycling loss.—After fitting the break-i behavior, the long-term cycling fade behavior was fit with a powe law model (Eq. 14), where the degradation rate parameter, q_7, was fi

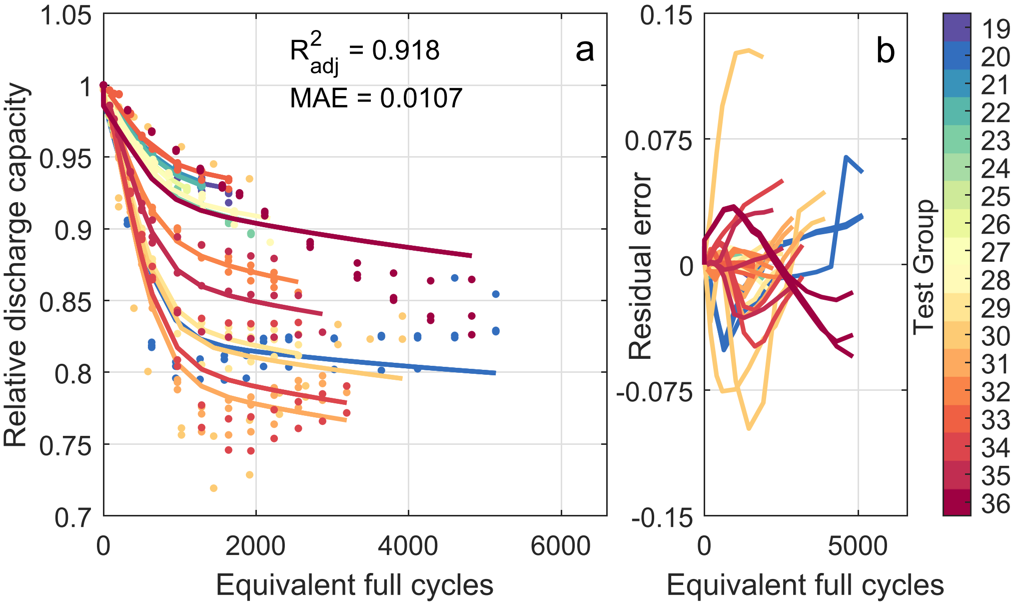

Figure 5. Local fitting of break-in cycling degradation behavior using Eq. 11.

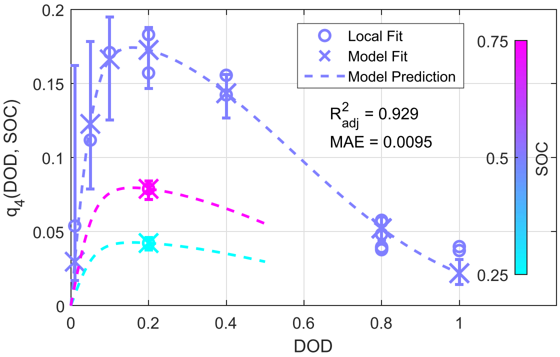

Figure 6. Parameter q_4 values vs DOD and SOC from local fits (circles), machine-learned model (Eq. 12) fits with 95% confidence intervals (X's with error bars), and model predictions vs DOD at 25%, 50%, and 75% SOC; only valid ranges of DOD and SOC are shown (maximum DOD at an average SOC of 75% is 50%).

locally to each test group, and the power, q_8, was fit to all of the data.

$$q = 1 - q_{Loss,Cal} - q_{Loss,BreakIn} - q_{Loss,LongTerm}$$
$$q_{Loss,LongTerm} = (q_7 \cdot EFC)^{q_8} \qquad [14]$$

The resulting fits can be seen in Fig. 7. Because the calendar and break-in losses are already accounted for, the contribution of just the long-term fade is deconvoluted from the overall capacity loss, and the data is fit well by a nearly linear model; the optimal value of q_8 is 1.13. The residual errors of the fit are small, with little apparent slope, excepting that from test group 30, which has very large cell-to-cell variance between the three cells in the test group due to the break-in loss. The locally fit values of q_7 are shown vs DOD and average C_{rate} in Fig. 8. The overall trend is relatively simple: degradation rate increases monotonically with DOD, and the impact of C_{rate} on q_7 increases with increasing DOD, indicating an interaction between DOD and C_{rate}. This data was fit by Eq. 15, which was identified via ML. Model uncertainty is relatively low except for the regime with high DOD and high C_{rate}, which has onl a single test group, resulting in high uncertainty.

$$q_7 = q_{7,a} + q_{7,b} \cdot DOD + q_{7,c} \cdot exp(DOD^2 \cdot C_{rate}^3) \qquad [15$$

Capacity Fade Model Results and Comparison to Prior Work

After identification of the capacity fade model using the ML assisted identification procedure, all parameters of the model ar reoptimized to all of the static aging data simultaneously t deconvolute the relative contributions of each degradation mod ($q_{Loss,Cal}$, $q_{Loss,BreakIn}$, and $q_{Loss,LongTerm}$) as accurately as possible Resulting optimal parameter values are reported in Table IV. Th model predictions on the entire data set are shown in Fig. 10. Al major trends in the data are clearly accounted for, resulting in lo model error: MAE for the calendar degradation data is only 0.4% and 1.2% for the cycling degradation data.

This model performance can be compared to that of the mode defined by Naumann et al. for this same data set.[8,29] The model i Naumann et al. incorporates a square-root of time calendar los equation and a square-root of EFC cycling loss equation. The value of the model parameters identified by Naumann et al. were fit using a iterative procedure, as described in the original publications;[8,29] to mak a like-for-like comparison, the parameters have been reoptimized on th same data as the ML-assisted model. The resulting predictions whe optimizing the model described by Naumann et al. to the entire data se are shown in Fig. 9. While most of the calendar aging trends ar predicted accurately, the degradation at 60 °C is fit poorly across th entire range of SOCs due to the deviation of the aging trajectory from square-root of time trend. Cycling degradation does not take int account the impact of break-in, and the square-root of EFC tren assumed by the model cannot accurately fit the cycling fade for severa cases, clearly seen by the systematic deviation of the residual errors i both positive and negative directions.

A comparison of the model errors from the Naumann model wit parameter values from prior work,[8,29] after refitting all parameters to th entire data set, and from the ML-assisted model defined here ar reported in Table V. Note that the simple act of optimizing all of th

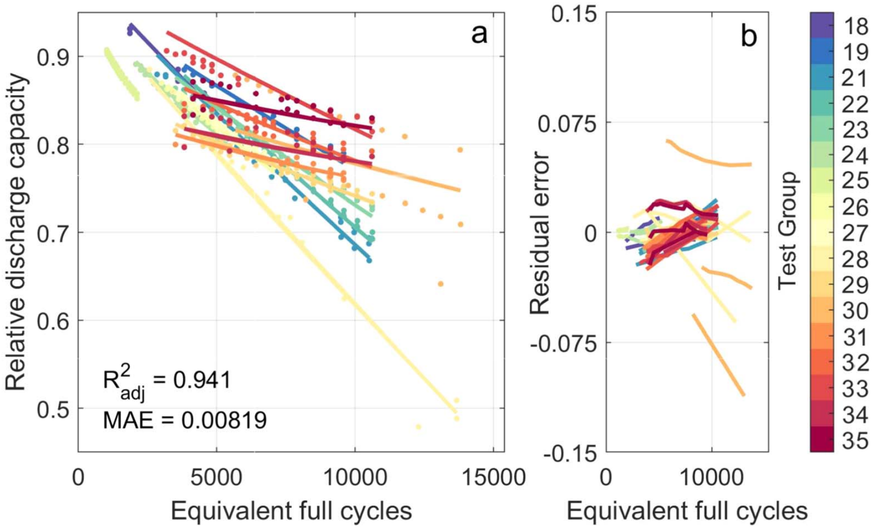

Figure 7. Local fitting of long-term cycling degradation behavior.

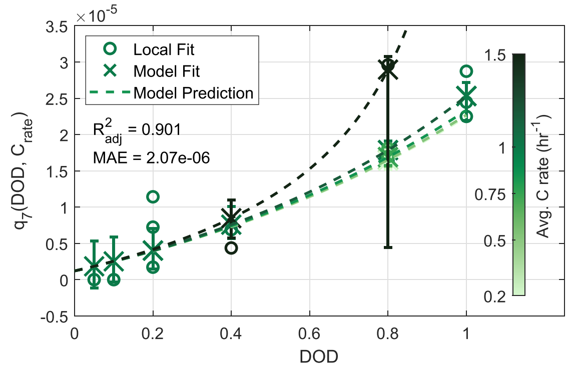

Figure 8. Parameter q_7 values from local fitting to the long-term cycling fade data (circles), fits by an ML equation (Eq. 15) with 95% confidence intervals (X's with error bars), and model predictions vs DOD at 0.2, 0.5, 0.75, 1, and 1.5 C_{rate}.

parameters in the Naumann model has resulted in approximately a 20% decrease of the model error. The ML-assisted model outperforms both the original and the refit Naumann model, with about 50% of the MAE as the refit Naumann model on all splits of the data. The uncertainty of the Naumann model and the ML-assisted model can also be compared using a cross-validation approach, where by each model is trained while leaving out one of the test groups, and a prediction made for this left out group, repeating across all groups. The ML-assisted model, overall, appears more robust than the refit Naumann model, with lower MAE_{CV}.

Uncertainty can be quantified more precisely utilizing a bootstrap resampling procedure. The predictive uncertainty for the ML-assisted and refit Naumann capacity fade models are shown in Figs. 11a–11e and 11f–11j, respectively, for 5 test groups from the overall data set. Bootstrap resampling for the "refit Naumann" model is done using a "sequential bootstrap" method, where for each bootstrap iteration the calendar fade model parameters are trained on a bootstrap resampled set of the calendar aging groups and the cycling fade model parameters trained on a bootstrap resampled set of the cycle aging groups, reflecting the model identification procedure outlined in the original works.[8,29] The ML-assisted model fits data trends more accurately for all cases. Confidence intervals for the ML-assisted model are also narrower than that of the refit Naumann model. Additionally, th variance of the uncertainty of the ML-assisted model is larger than tha of the refit Naumann model; uncertainty is extremely small for th calendar degradation data (test groups 13 and 22, Figs. 11a–11b) slightly larger for cycling degradation data at both low and high DOD (test groups 22 and 32, Figs. 11c, 11e), and very large for cyclin degradation at high DOD and high C_{rate} (test group 28, Fig. 11d). Th variance of the uncertainty highlights which degradation regimes ar difficult to predict accurately based on the available training data, and i crucial for helping distinguish between high-confidence and low confidence predictions, or for identifying potential new test cases tha may be useful for improving the performance of the aging model. Fo example, uncertainty is large for cells in test group 28 because this i the only cell at high DOD and high C_{rate}, resulting in a linea degradation trajectory with a much steeper slope than any other tes groups in the data set; this uncertainty can also be observed in the wid confidence interval for the data point at 80% DOD and 1.5 averag C_{rate} in Fig. 8. In comparison, the uncertainties of the refit Naumann model have low variance, with qualitatively similar trends across th entire data set, making it difficult to gain insights into model behavio

Dynamic Aging Validation and Simulation of Real-World Use

In order to simulate battery aging under varying load or environmental conditions, the identified aging model needs to be reformulate to be path independent, e.g. "memory-less".[77] Path independent agin depends not on the amount of time or cycles that have elapsed since th beginning of battery life, but rather, on the current state and the futur stress on the battery. For instance, consider the case of aging dominate by the loss of lithium inventory, which is primarily driven by SE growth: the growth rate of the SEI at any point depends not on th amount of time passed since beginning of life, but rather on the curren thickness of the SEI. This concept was first proposed by Thomas an Bloom,[77] and was likely independently applied by Serrao et al.[57] at th same time. Dynamic state models, as they are referred to here, hav been utilized in a wide variety of studies since.[8,29,35,36,41,44,58]

Deriving dynamic state models.—There have been several pas descriptions on deriving dynamic state models, using variou terminologies or definitions.[8,29,35,77,78] For any given degradatio equation, the dynamic model for each state (degradation mode) ca be derived using the following approach: (1) separate the overal model into several independent states, $y = f(x)$, each dependent o

Table IV. Optimal parameter values for the ML-assisted model identified here.

Parameter	$q_{1,a}$	$q_{1,b}$	$q_{1,c}$	q_2	$q_{1,a}$	$q_{3,b}$
Value	9.90E-01	−2.88E+06	8.74E+03	1.31E-04	3.33E-04	7.35E+11
Parameter	$q_{3,c}$	$q_{3,d}$	$q_{3,e}$	$q_{4,a}$	$q_{4,SOC,\xi}$	$q_{4,SOC,\sigma}$
Value	−2.82E-06	−3.28E+09	1.27E-03	5.82E-01	5.83E-02	2.09E-01
Parameter	$q_{4,DOD,\xi}$	$q_{4,DOD,\sigma}$	$q_{4,b}$	q_5	q_6	$q_{7,a}$
Value	−3.81E+00	1.16E+00	2.54E+01	3.04E-03	1.44E+00	−6.81E-0
Parameter	$q_{7,c}$	q_8				
Value	2.12E-06	1.13E+00				

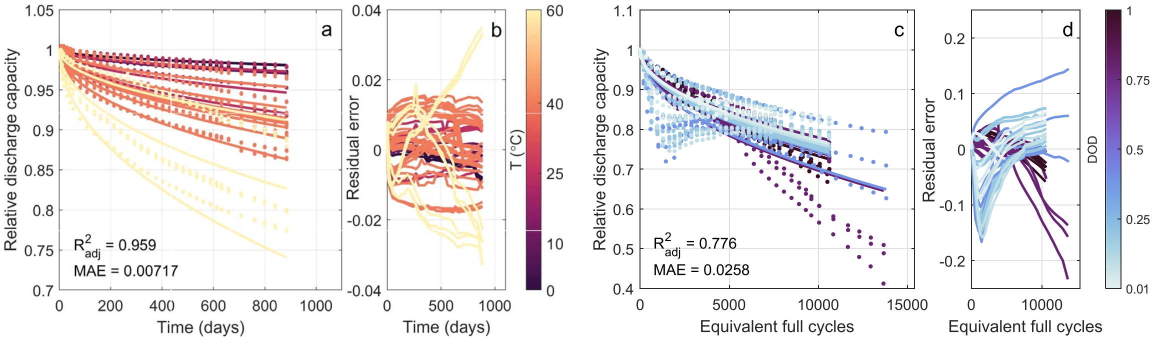

Figure 9. Refit Naumann capacity loss model. (a) Fit to calendar degradation data and (b) residual errors. (c) Fit to cycling degradation data and (d) residua errors. Axis limits are shared with Fig. 10 to assist comparison.

only one time-varying independent variable (e.g., calendar and cycle aging;[8,29] lithium loss, positive electrode capacity, and negative electrode capacity[9]); (2) solve the derivative of the equation with respect to the time-varying independent variable:

$$\frac{\mathrm{d}y}{\mathrm{d}x} = \frac{\mathrm{d}f(x,\,\mathrm{S})}{\mathrm{d}x} \qquad [16]$$

where x is the time-varying independent variable (e.g. time, charge-throughput, cycles, ...), and **S** is a vector of stressor values (temperature, average SOC, DOD, ...), which are assumed to be constant over the time step δx; (3) invert the equation to solve for x^*, referred to as the virtual-time or virtual-EFC in Naumann et al.[8,29] and in the next section, given the values of **S** for the current time step and the prior value of the state variable, y_{t-1}:

$$x^* = f^{-1}(y_{t-1},\,\mathrm{S}) \qquad [17]$$

(4) substitute x in the derivative (Eq. 16) with x^* to get the derivative for the current time step, dy_t/dx, dependent not on x, but on the prior value of the state:

$$\begin{aligned}\frac{\mathrm{d}y_t}{\mathrm{d}x} &= \frac{\mathrm{d}f(x^*,\,\mathrm{S})}{\mathrm{d}x}\\ &= \frac{\mathrm{d}f(f^{-1}(y_{t-1},\,\mathrm{S}),\,\mathrm{S})}{\mathrm{d}x}\end{aligned} \qquad [18]$$

(5) solve for the degradation in the current time step, δy_t, by multiplying Eq. 18 by δx:

$$\delta y_t = \frac{\mathrm{d}f(f^{-1}(y_{t-1},\,\mathrm{S}),\,\mathrm{S})}{\mathrm{d}x}\cdot\delta x \qquad [19]$$

or, as is done in SimSES and used in the following section, simply solve for δy by taking the difference between y_t and y_{t-1}:

$$\delta y_t = f(x^* + \delta x,\,\mathrm{S}) - f(x^*,\,\mathrm{S}) \qquad [20$$

This is equivalent to the above approach at small time steps bu may be more accurate if the time step is large, and thus th linearization described above is not valid; (6) enforce any initia conditions or special considerations (see Smith et al.,[35] Appendi A); (7) combine the dynamic models for each state additively (as i Refs. 8, 29) or logically (as in Ref. 9) to match the structure o overall degradation model. Derivations for a variety of degradatio equations are reported by Santhanagopalan et al.[78] and Smith et al.[3]

Even after deriving the dynamic equation forms for each state in th model, there are a several considerations for extracting the values o stress variables (temperature, C-rate, SOC, ...) from the varying load Note that only one variable in the degradation model can be treated a time-varying for any given state, therefore, the values of stressors suc as temperature, SOC, DOD, or others must be treated as constant withi any given time step. Thomas and Bloom[77] avoid this issue by solvin an integral where both time and the values of the stressors ar continuous variables (replacing the discrete calculation in Eq. 19), bu this approach only works for variables that smoothly vary with time such as temperature or SOC, and cannot account for variables such a DOD or cycle count, which do not smoothly vary and are difficult t define for complex battery loads. One approach is to break up the SO timeseries into discrete time steps by identifying turning points, usin techniques such as the rainflow algorithm[9,35,78] or the rising su envelope method;[79] DOD and cycle-count are then constant betwee each turning point. DOD can also be treated as a continuous variabl using a time-superposition approach.[35,80] A simpler approach, n requiring turning point identification, is to simply take the differenc between the maximum and minimum SOC in a predefined time step however, this requires setting the simulation time step to som appropriate value that captures the dynamics of the battery use. A fast Fourier transform of the battery load can be used to help determin an appropriate time step for simulating the battery degradation, bu there is still a risk of splitting a long duration charge or discharge int

Table V. MAE and cross-validation MAE (MAE$_{CV}$) of models on the static aging data used for model identification and optimization. The Nauman model uses the structure and the parameter values defined in prior work,[8,29] while the "Naumann (refit)" model reoptimizes the model parameter to all of the available aging data, and the "ML-assisted" model is the degradation model identified in this work. Storage error is calculated over dat from test groups 1–17. Cycling error is calculated over data from test groups 18–36.

	All data		Storage		Cycling	
Model description	MAE	MAE$_{CV}$	MAE	MAE$_{CV}$	MAE	MAE$_{C}$
Naumann	2.11%		1.01%		3.18%	
Naumann (refit)	1.66%	1.91%	0.72%	0.99%	2.58%	2.82%
ML-assisted	0.79%	0.83%	0.38%	0.47%	1.20%	1.43%

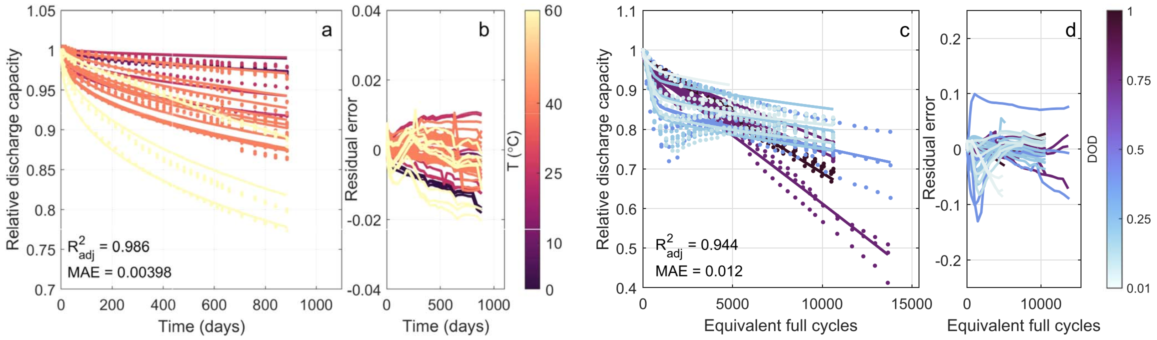

Figure 10. ML-assisted capacity loss model predictions. (a) Fit to calendar degradation data and (b) residual errors. (c) Fit to cycling degradation data and (d residual errors. Axis limits are shared with Fig. 9 to assist comparison.

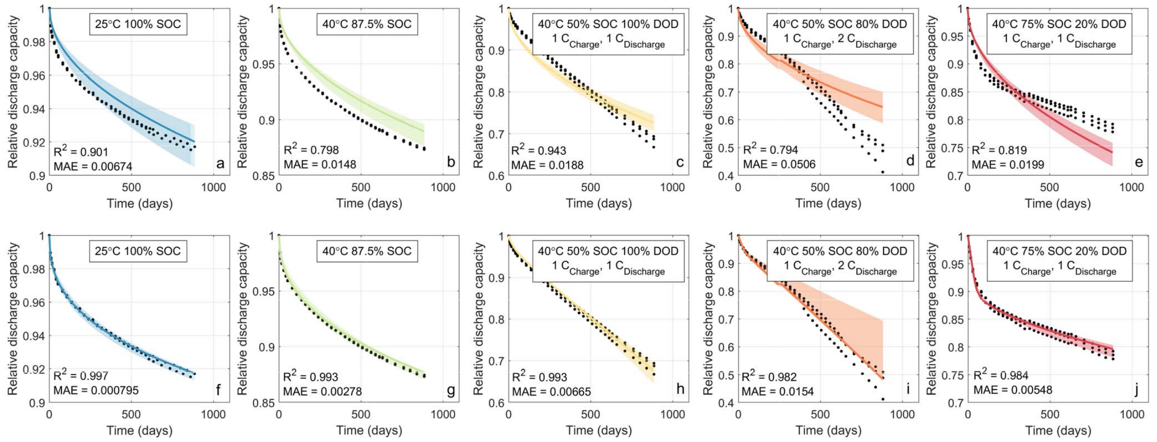

Figure 11. Comparison of model fits for groups 5 (a, f), 13 (b, g), 22 (c, h), 28 (d, i), and 32 (e, j) between the refit Naumann model (a)–(e) and the ML-assiste model identified in this work (f)–(j). Dots correspond to experimental data, solid lines are best-fit model predictions, and shaded regions denote 95% confidenc intervals from 1000 iterations of bootstrap resampling.

two different time steps, incurring some simulation error. SimSES, which is used in this work to simulate the lifetime of battery energy storage systems, avoids this issue by calculating degradation once per day, only calculating cycling degradation once at least a half-EFC of charge-throughput has occured.[27] Determining a "best-practice" approach from all of these options would require a huge variety of long-term aging data under dynamic use. Each of the approaches described above has demonstrated satisfactory results on available validation data.

Model validation on dynamic aging tests.—Comparisons of model predictions with 95% confidence intervals on a variety of dynamic aging tests are shown in Fig. 12. Qualitatively, both the human expert and ML-assisted models perform well on the validation test shown. The confidence intervals for the ML-assisted model identifie here are much narrower for both the calendar- and cycling-dependen degradation states. Prediction errors on the dynamic validation dat from each model are reported in Table VI. Corroborating the result from the model identification on the static testing data, the ML-assiste model identified here has the lowest average prediction erro. Thi improvement comes from substantially better accuracy on the dynami cycling cells. For duty cycles with less aggressive cycling, such as th PV-HESS and PV-PCR-BESS load profiles shown in Figs. 12c–12 (Naumann refit) and Figs. 12g–12h (ML-assisted), overall cyclin degradation is relatively low for both models. Where cyclin

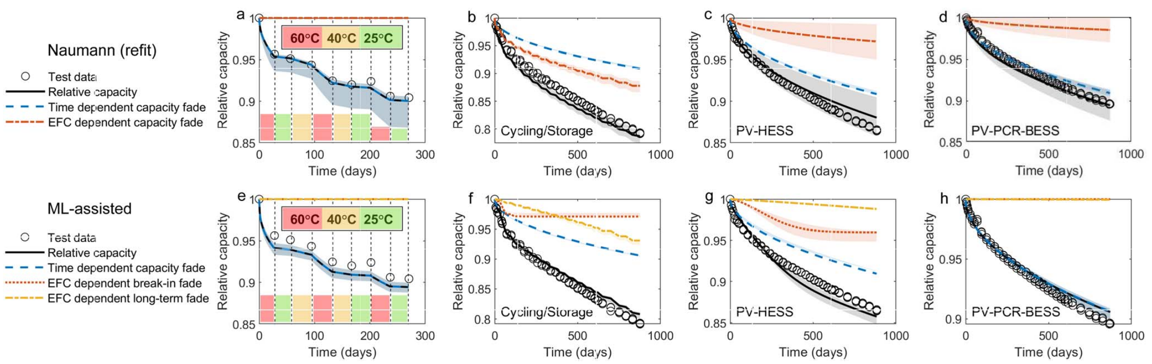

Figure 12. Model validation on dynamic aging tests. For each model, the overall capacity loss (black solid line) is the sum of the loss due to each state (dotte and/or dashed colored lines). (a)–(d) Human expert model described in Naumann et al.,[8,29] refit to the exact data used for ML-assisted model identification here (e)–(h) ML-assisted model identified in this work. The dynamic calendar fade test (Group 44 in Table A·I) data and model predictions plotted in (a, e) are show with colored regions denoting the aging temperature between capacity checks throughout the experiment.

degradation is incurred, the ML-assisted model predicts that it is dominated by the saturating break-in fade, which matches with the trends observed in the static aging data (Fig. 2c).

There is an additional assumption required for extrapolating the break-in fade to less aggressive cycling conditions that are more likely to be observed in real-world use: based on the aging data, and the known physics causing the break-in effect,[75] break-in is treated as unrecoverable, however, it should only occur during periods of high use, where lithium in the cell would not have a chance to redistribut during rest. For this work, "high-use" is assumed to be periods whe the battery is utilized at a rate of 2 EFCs/day or more. This is les strenuous than the accelerated aging tests, but more strenuous than mos real-world use cases, and thus break-in fade should only be expected t occur during short periods of very high-use in real-world applications

The approach shown here assumes that aging is path independent, however, there is experimental evidence that lithium-io

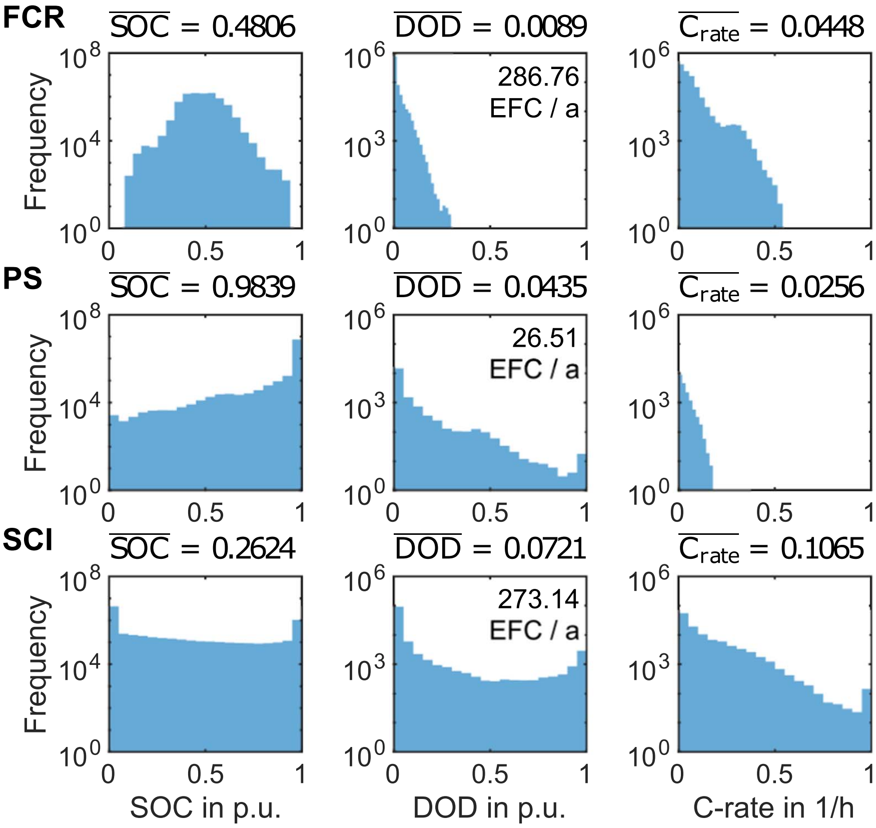

Figure 13. Distribution and mean values of the stress factors SOC, DOD and C_{rate} as well as average EFCs per annum (EFC/a) for the three applications Frequency Containment Reserve (FCR), Peak Shaving (PS), and Self Consumption Increase (SCI). Counts reported on y-axes are from 15 year simulations.

Table VI. MAE of models on dynamic aging data used for validation. Storage error is calculated over data from test groups 37–44. Cycling error i calculated over data from test groups 45–49.

Model description	MAE (All data)	MAE (Storage)	MAE (Cycling
Naumann	1.18%	0.78%	1.28%
Naumann (refit)	0.84%	0.71%	0.88%
ML-assisted	0.68%	1.29%	0.52%

battery degradation may sometimes be path dependent, e.g., not only does the number of cycles matter, but also the order in which those cycles occur, or how many cycles are conducted consecutively before rest periods.[81] Achieving accurate prediction of cell degradation in cases where path dependence is a clear factor is an open challenge for the battery degradation modeling community, but luckily, the assumption that degradation is path independent seems to hold true for many common real-world use cases, as is shown by the good performance of both the refit Naumann model and ML model when validated against dynamic aging dat presented here.

Simulation of realistic stationary energy storage applications.— Battery lifetime models may be utilized to estimate the lifetime of real world energy storage systems by incorporating them into systems-leve simulation tools such as SimSES. SimSES is a time-series based ope source tool that allows to perform holistic techno-economic simulation and analyses for battery energy storage systems.[27] Here, we conside

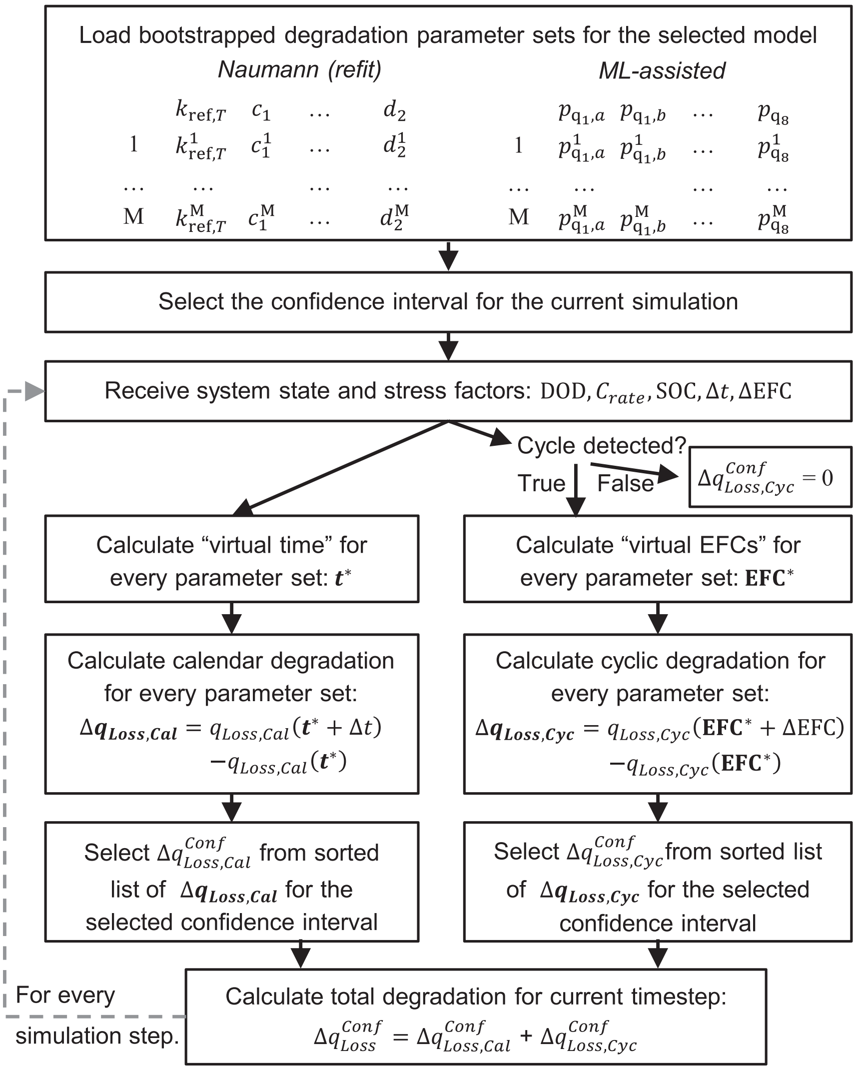

Figure 14. Schematic overview of how confidence intervals for the incremental capacity losses are calculated in the adapted version of the environment SimSE for each time step. The adapted version of SimSES has been made available open-access.[40]

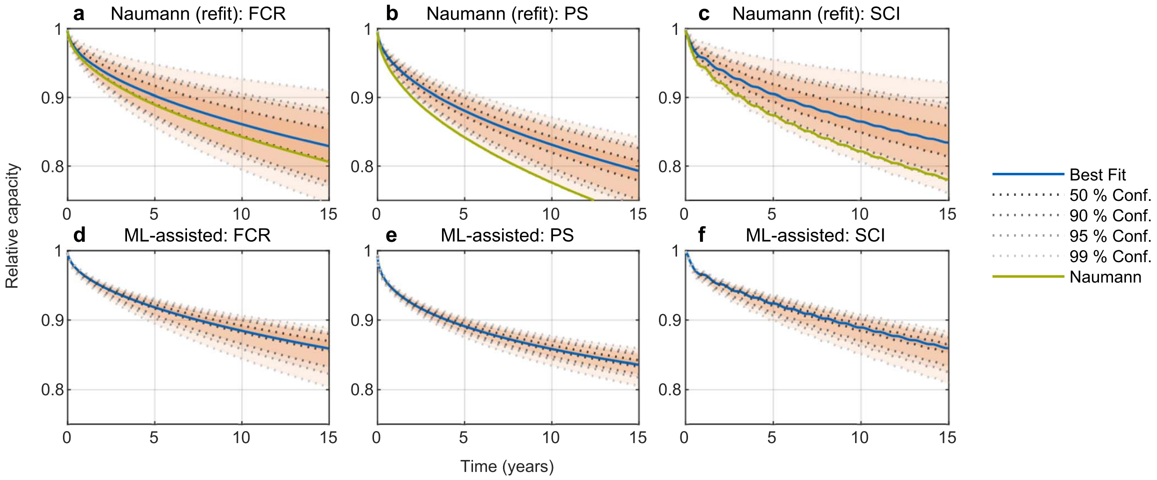

Figure 15. Relative discharge capacity for various realistic use-cases of battery energy storage systems over 15 years predicted by the degradation model identified by Naumann et al.[8,29] (a)–(c) and the degradation model identified in this work using ML (d)–(f). The green line in plots (a)–(c) uses the paramete values originally reported by Naumann et al.[8,29]

three applications: a commercial frequency containment reserve application (FCR), a commercial peak-shaving application (PS), and a residential PV-battery system performing a self-consumption increase service (SCI). These three applications are described in detail in previous work.[30] Battery load for each application is calculated using an energy management system based on realistic input profiles for the selected application and system parameterization. For FCR, a grid frequency profile serves as input, with the BESS discharging during underfrequency and charging during overfrequency. In PS, the BESS discharges when the used industrial load profile exceeds a predefined peak shaving limit and charges again afterwards. For SCI, a household load and PV generation profile serve as inputs. The BESS charges when PV power exceeds the household load and discharges when the household load exceeds PV power.

Histograms of the SOC, DOD, and C_{rate} stress factors throughout fifteen years of simulation are shown in Fig. 13. Each of the application cycles shows significantly different battery use: the FCR application operates around 50% SOC at low DOD with C_{rate} up to 0.5, the PS application spends a large amount of time at high SOC, even resting at 100% SOC for long periods, with an average DOD of approximately 40% but with low power demands (low C_{rate}), and the SCI application has the battery regularly being fully discharged, with little amount of time spent resting at high SOC, regular operation at high DOD, and relatively high C_{rate}. As the EFCs are less than 2 per day in all applications, the break-in loss model is not considered in this analysis. Furthermore, the BESS is assumed to be in a temperature controlled environment, kept at a constant temperature of 25 °C, to ensure comparability between applications.

In this work, uncertainty from the battery-level degradation is incorporated to estimate uncertainty at the system-level by resolving the degradation model using not only the best-fit parameter values for any given model, but also the bootstrapped parameter values. The process for calculating the capacity loss at each simulation time step with uncertainty in SimSES is shown in Fig. 14. For each model, there is a vector of the best-fit parameter values and $1{:}M$ vectors from M bootstrap resampling iterations. Incorporating degradation uncertainty into the system level simulation is challenging because the capacity loss in a given time step influences the requested power for the following time steps, i.e., the dispatch of the battery is dependent on its current health. For example, a home storage system that is degrading faster will see less charge-throughput over the same time frame, as it fills up quicker with surplus photovoltaic (PV) power at daytime and empties faster during nighttime. Estimating the impact of degradation uncertainty thus requires simulating th entire system lifetime for every set of M bootstrapped degradatio parameters, resulting in M system lifetime predictions. This is hov confidence intervals are calculated for Figs. 11 and 12, but with 100 sets of bootstrapped parameters used in this work, it is far to computationally expensive to run on a single workstation. To avoi this issue, the simulation can instead be run at a specified degradation percentile. This is conducted by calculating the incrementa change of each battery state (Eq. 20, for calendar loss and cyclin loss) for each bootstrapped parameter sets at each time step. Th 1000 values for the incremental change of each state are then sorte and the desired percentile output at each time step. The entire systen lifetime then only needs to be calculated once for each desire percentile, as well as for the best fit scenario.

The results from simulations of the FCR, PS, and SCI energ storage system applications for both the ML-assisted and refi Naumann degradation models are shown in Fig. 15. Immediatel clear is that the uncertainty of the model identified in Naumann e al.[8,29] is much larger than the uncertainty of the ML-assisted mode identified here, which reflects the results shown from the mode identification (Fig. 11) and validation (Fig. 12) steps reported prior This improved model confidence gives much narrower estimates fo the system lifetime: taking the lower-bound of the 99% confidenc interval as a prediction for the 'worst-case' lifetime of the energ storage system, the ML-assisted model predicts that the discharg capacity will remain >80% for at least 15 years in all of the agin scenarios, while the refit model from Naumann et al. gives minimum lifetime estimate of 9 years for the FCR application, years for the PS application, and 10 years for the SCI application Overall, the expected lifetime (best-fit line) does not vary hugel between the two models, with both models estimating 15 years o more of battery lifetime for all applications; this agreement i because calendar degradation dominates all applications, and in terms of the absolute error, the models differ more when predictin substantial cycling degradation than when predicting calenda degradation. An application with more aggressive battery use woul likely result in a larger disagreement between the two models tha the results shown here.

Conclusions

Battery degradation models play a key role in the planning development, and control of battery energy storage systems. Mos

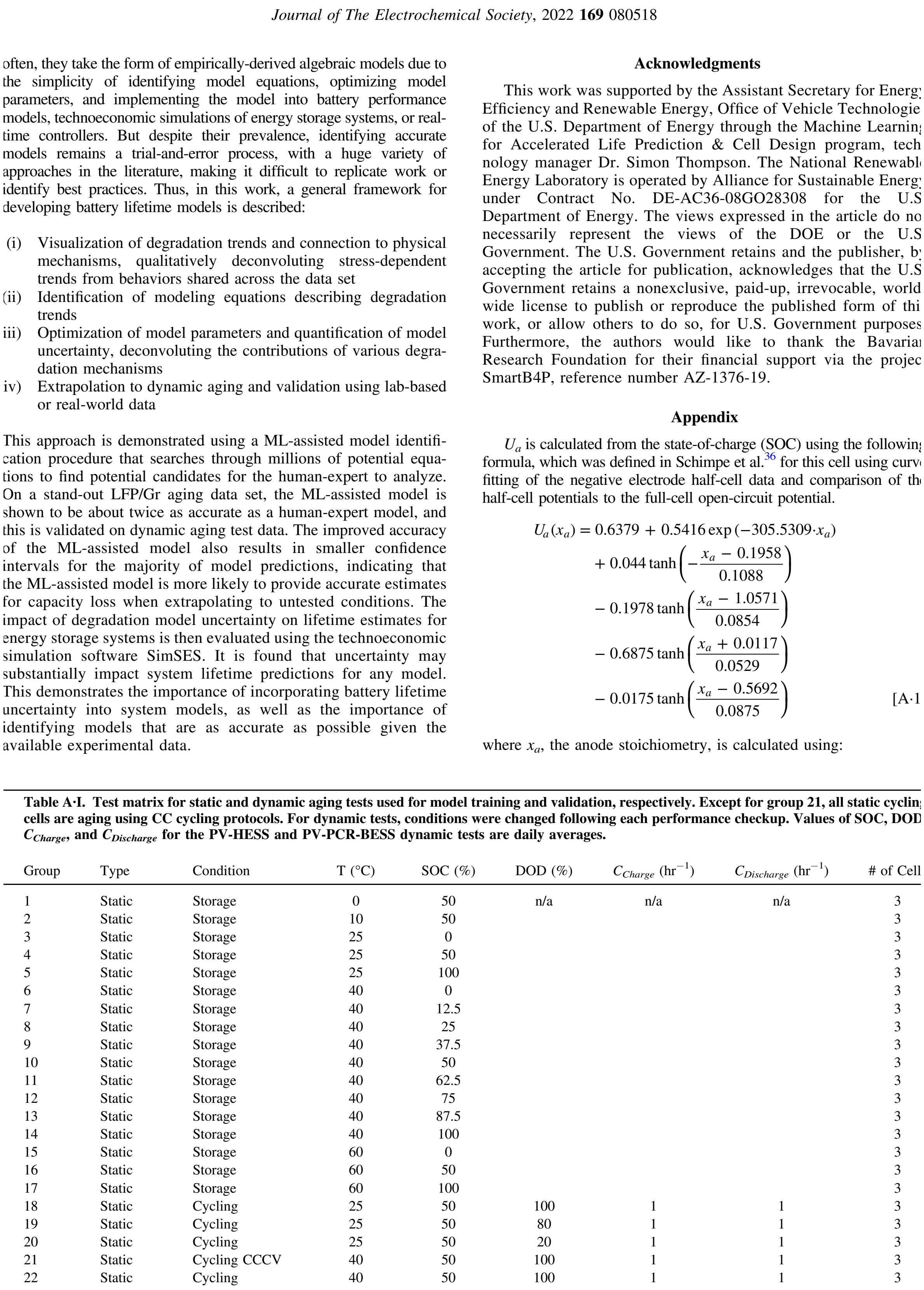

often, they take the form of empirically-derived algebraic models due to the simplicity of identifying model equations, optimizing model parameters, and implementing the model into battery performance models, technoeconomic simulations of energy storage systems, or real-time controllers. But despite their prevalence, identifying accurate models remains a trial-and-error process, with a huge variety of approaches in the literature, making it difficult to replicate work or identify best practices. Thus, in this work, a general framework for developing battery lifetime models is described:

(i) Visualization of degradation trends and connection to physical mechanisms, qualitatively deconvoluting stress-dependent trends from behaviors shared across the data set
(ii) Identification of modeling equations describing degradation trends
iii) Optimization of model parameters and quantification of model uncertainty, deconvoluting the contributions of various degradation mechanisms
iv) Extrapolation to dynamic aging and validation using lab-based or real-world data

This approach is demonstrated using a ML-assisted model identification procedure that searches through millions of potential equations to find potential candidates for the human-expert to analyze. On a stand-out LFP/Gr aging data set, the ML-assisted model is shown to be about twice as accurate as a human-expert model, and this is validated on dynamic aging test data. The improved accuracy of the ML-assisted model also results in smaller confidence intervals for the majority of model predictions, indicating that the ML-assisted model is more likely to provide accurate estimates for capacity loss when extrapolating to untested conditions. The impact of degradation model uncertainty on lifetime estimates for energy storage systems is then evaluated using the technoeconomic simulation software SimSES. It is found that uncertainty may substantially impact system lifetime predictions for any model. This demonstrates the importance of incorporating battery lifetime uncertainty into system models, as well as the importance of identifying models that are as accurate as possible given the available experimental data.

Acknowledgments

This work was supported by the Assistant Secretary for Energ Efficiency and Renewable Energy, Office of Vehicle Technologie of the U.S. Department of Energy through the Machine Learnin for Accelerated Life Prediction & Cell Design program, technology manager Dr. Simon Thompson. The National Renewabl Energy Laboratory is operated by Alliance for Sustainable Energ under Contract No. DE-AC36-08GO28308 for the U.S Department of Energy. The views expressed in the article do no necessarily represent the views of the DOE or the U.S Government. The U.S. Government retains and the publisher, b accepting the article for publication, acknowledges that the U.S Government retains a nonexclusive, paid-up, irrevocable, worldwide license to publish or reproduce the published form of thi work, or allow others to do so, for U.S. Government purposes Furthermore, the authors would like to thank the Bavaria Research Foundation for their financial support via the projec SmartB4P, reference number AZ-1376-19.

Appendix

U_a is calculated from the state-of-charge (SOC) using the followin formula, which was defined in Schimpe et al.[36] for this cell using curv fitting of the negative electrode half-cell data and comparison of th half-cell potentials to the full-cell open-circuit potential.

$$\begin{aligned} U_a(x_a) = {} & 0.6379 + 0.5416\exp(-305.5309{\cdot}x_a) \\ & + 0.044\tanh\left(-\frac{x_a - 0.1958}{0.1088}\right) \\ & - 0.1978\tanh\left(\frac{x_a - 1.0571}{0.0854}\right) \\ & - 0.6875\tanh\left(\frac{x_a + 0.0117}{0.0529}\right) \\ & - 0.0175\tanh\left(\frac{x_a - 0.5692}{0.0875}\right) \end{aligned}$$

[A·1

where x_a, the anode stoichiometry, is calculated using:

Table A·I. Test matrix for static and dynamic aging tests used for model training and validation, respectively. Except for group 21, all static cyclin cells are aging using CC cycling protocols. For dynamic tests, conditions were changed following each performance checkup. Values of SOC, DOD C_{Charge}, and $C_{Discharge}$ for the PV-HESS and PV-PCR-BESS dynamic tests are daily averages.

Group	Type	Condition	T (°C)	SOC (%)	DOD (%)	C_{Charge} (hr^{-1})	$C_{Discharge}$ (hr^{-1})	# of Cell
1	Static	Storage	0	50	n/a	n/a	n/a	3
2	Static	Storage	10	50				3
3	Static	Storage	25	0				3
4	Static	Storage	25	50				3
5	Static	Storage	25	100				3
6	Static	Storage	40	0				3
7	Static	Storage	40	12.5				3
8	Static	Storage	40	25				3
9	Static	Storage	40	37.5				3
10	Static	Storage	40	50				3
11	Static	Storage	40	62.5				3
12	Static	Storage	40	75				3
13	Static	Storage	40	87.5				3
14	Static	Storage	40	100				3
15	Static	Storage	60	0				3
16	Static	Storage	60	50				3
17	Static	Storage	60	100				3
18	Static	Cycling	25	50	100	1	1	3
19	Static	Cycling	25	50	80	1	1	3
20	Static	Cycling	25	50	20	1	1	3
21	Static	Cycling CCCV	40	50	100	1	1	3
22	Static	Cycling	40	50	100	1	1	3

Table A·I. (Continued).

Group	Type	Condition	T (°C)	SOC (%)	DOD (%)	C_{Charge} (hr^{-1})	$C_{Discharge}$ (hr^{-1})	# of Cell
23	Static	Cycling	40	50	80	1	1	3
24	Static	Cycling	40	50	80	0.5	0.5	3
25	Static	Cycling	40	50	80	0.2	0.2	3
26	Static	Cycling	40	50	80	0.5	1	3
27	Static	Cycling	40	50	80	1	0.5	3
28	Static	Cycling	40	50	80	1	2	3
29	Static	Cycling	40	50	40	1	1	3
30	Static	Cycling	40	50	40	1	2	3
31	Static	Cycling	40	50	20	1	1	3
32	Static	Cycling	40	75	20	1	1	3
33	Static	Cycling	40	25	20	1	1	3
34	Static	Cycling	40	50	10	1	1	3
35	Static	Cycling	40	50	5	1	1	3
36	Static	Cycling	40	50	1	1	1	3
37	Dynamic	Storage	25/40	100	n/a	n/a	n/a	2
38	Dynamic	Storage	25/60	100				2
39	Dynamic	Storage	40/60	100				2
40	Dynamic	Storage	0/60	100				2
41	Dynamic	Storage	60	0/50				2
42	Dynamic	Storage	60	0/100				2
43	Dynamic	Storage	60	50/100				2
44	Dynamic	Storage	25/40/60	100				1
45	Dynamic	Cycling/ Storage	40	50	80	1	1	3
46	Dynamic	Storage/ Cycling	40	50	80	1	1	3
47	Dynamic	Cycling	40	50	20/80	1	1	3
48	Dynamic	PV-HESS	40	51.4	74.6	0.243	0.172	3
49	Dynamic	PV-PCR-BESS	40	51.2	25.1	0.073	0.057	3

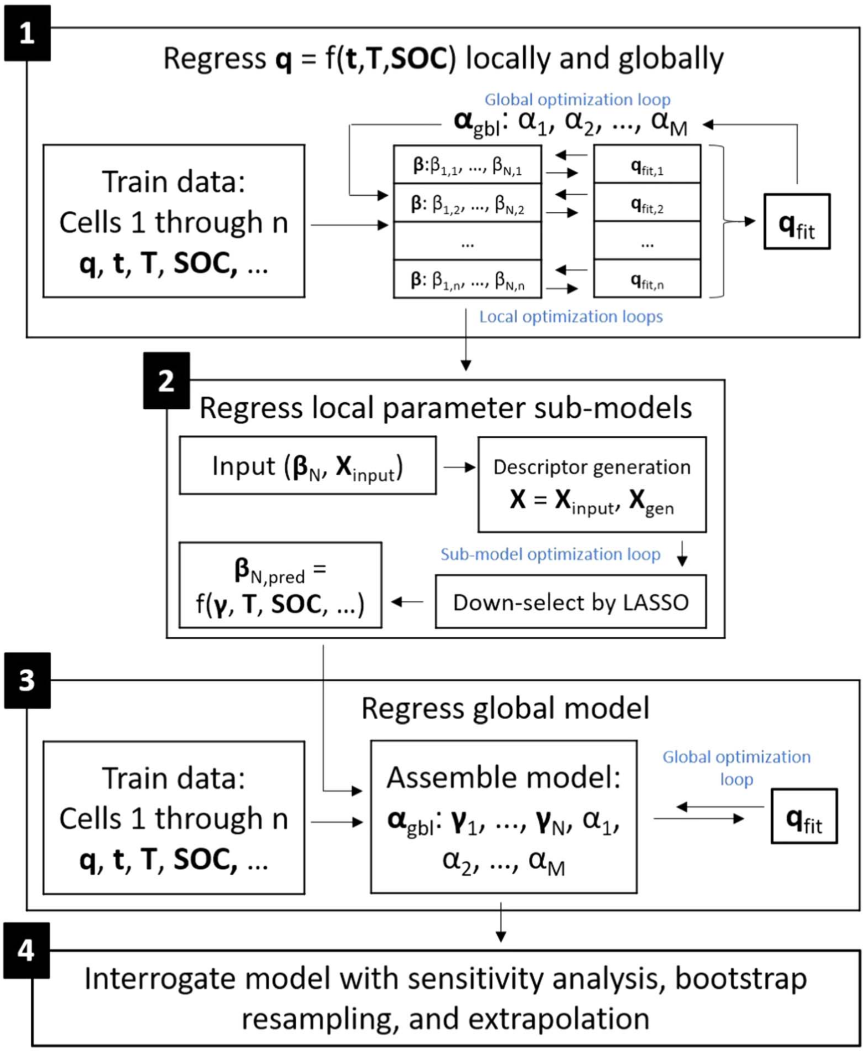

Figure A·1. Machine-learning assisted model identification procedure used here to identify model for each degradation mode. In this work, as Step 2, SISSO used rather than LASSO. Models for each degradation mode are then combined via superposition. Originally published in Ref. 34.

$$x_a(SOC) = 0.0085 + SOC\cdot(0.78 - 0.0085) \qquad [A\cdot 2]$$

ORCID

Paul Gasper https://orcid.org/0000-0001-8834-9458
Andreas Jossen https://orcid.org/0000-0003-0964-1405
Kandler Smith https://orcid.org/0000-0001-7011-0377

References

1. M. Woody, M. Arbabzadeh, G. M. Lewis, G. A. Keoleian, and A. Stefanopoulou, *Journal of Energy Storage*, **28**, 101231 (2020).
2. E. Minear, M. Simpson, and D. Long, *Electric Power Research Institute*, 3002020048 (2020).
3. K. Mongird, V. Viswanathan, J. Alam, C. Vartanian, V. Sprenkle, and R. Baxter, *U. S. Department of Energy, DOE/PA–0204* (2020).
4. D. Hill and M. Mills-Price, *DNV GL Energy*, 160620 (2019).
5. X. Hu, L. Xu, X. Lin, and M. Pecht, *Joule*, **4**, 310 (2020).
6. M. S. Hosen, J. Jaguemont, J. Van Mierlo, and M. Berecibar, *iScience*, **24**, 102060 (2021).
7. J. M. Reniers, G. Mulder, and D. A. Howey, *Journal of Power Sources*, **48** 229355 (2021).
8. M. Naumann, M. Schimpe, P. Keil, H. C. Hesse, and A. Jossen, *Journal of Energ Storage*, **17**, 153 (2018).
9. K. Smith, A. Saxon, M. Keyser, B. Lundstrom, Z. Cao, and A. Roc, *Proceedings the American Control Conference*, p. 4062 (2017).
10. A. Gailani, M. Al-Greer, M. Short, T. Crosbie, and N. Dawood, *Energies*, **13**, 281 (2020).
11. V. Sulzer, P. Mohtat, S. Pannala, J. B. Siegel, and A. G. Stefanopoulo *J. Electrochem. Soc.*, **168**, 120531 (2021).
12. M. Förstl, D. Azuatalam, A. Chapman, G. Verbič, A. Jossen, and H. Hess *International Journal of Energy Research*, **44**, 718 (2020).
13. A. Gailani, M. Al-Greer, M. Short, and T. Crosbie, *Electronics (Switzerland)*, **9**, 9 (2020).
14. J. Liu, C. Hu, and Z. Wang, *IEEE Transportation Electrification Conference Expo*, p. 863 (2020), https://doi.org/10.1109/itec48692.2020.9161750.
15. S. Englberger, S. Englberger, A. Jossen, and H. Hesse, *Cell Reports Physic Science*, **1**, 100238 (2020).
16. S. Englberger, K. A. Gamra, B. Tepe, M. Schreiber, A. Jossen, and H. Hess *Applied Energy*, **304**, 117862 (2021).
17. K. Uddin, T. Jackson, W. D. Widanage, G. Chouchelamane, P. A. Jennings, an J. Marco, *Energy*, **133**, 710 (2017).
18. V. Kumtepeli, H. C. Hesse, M. Schimpe, A. Tripathi, Y. Wang, and A. Josse *IEEE Access*, **8**, 204325 (2020).

19. M. Schimpe, J. V. Barreras, B. Wu, and G. J. Offer, *J. Electrochem. Soc.*, **168**, 060506 (2021).
20. J. Sowe, S. P. M. Few, M. Schimpe, B. Wu, C. Candelise, J. Nelson, and V. Barreras, *ECS PRiME*, **MA2020-02**, 3780 (2020).
21. B. Xu, J. Zhao, T. Zheng, E. Litvinov, and D. S. Kirschen, *IEEE Transactions on Power Systems*, **33**, 2248 (2017).
22. B. Xu, A. Oudalov, A. Ulbig, G. Andersson, and D. S. Kirschen, *IEEE Transactions on Smart Grid*, **9**, 1131 (2018).
23. B. T. Mirletz and D. L. Guittet, "Heuristic dispatch based on price signals for behind-the-meter pv-battery systems in the system advisor model." *2021 IEEE 48th Photovoltaic Specialists Conference (PVSC)* (IEEE, Piscataway, NJ) 1393 (2021), https://www.osti.gov/biblio/1798078.
24. S. Wang, D. Guo, X. Han, L. Lu, K. Sun, W. Li, D. U. Sauer, and M. Ouyang, *Energy*, **207**, 118228 (2020).
25. J. M. Reniers, G. Mulder, and D. A. Howey, *J. Electrochem. Soc.*, **166**, A3189 (2019).
26. V. Sulzer, S. G. Marquis, R. Timms, M. Robinson, and S. J. Chapman, *Journal of Open Research Software*, **9**, 14 (2021).
27. M. Möller, D. Kucevic, N. Collath, A. Parlikar, P. Dotzauer, B. Tepe, S. Englberger, A. Jossen, and H. Hesse, *Journal of Energy Storage*, **49**, 103743 (2022).
28. *2021 System advisor model version 2021.12.02 (sam 2021.12.02)*, https://sam.nrel.gov.
29. M. Naumann, F. Spingler, and A. Jossen, *Journal of Power Sources*, **451**, 227666 (2020).
30. D. Kucevic, B. Tepe, S. Englberger, A. Parlikar, M. Mühlbauer, O. Bohlen, A. Jossen, and H. Hesse, *Journal of Energy Storage*, **28**, 101077 (2020).
31. V. Sulzer et al., *Joule*, **5**, 1934 (2021).
32. J. Schmalstieg, S. Käbitz, M. Ecker, and D. U. Sauer, *Journal of Power Sources*, **257**, 325 (2014).
33. J. Vetter, P. Novák, M. R. Wagner, C. Veit, K. C. Möller, J. Besenhard, M. Winter, M. Wohlfahrt-Mehrens, C. Vogler, and A. Hammouche, *Journal of power sources*, **147**, 269 (2005).
34. P. Gasper, K. Gering, E. Dufek, and K. Smith, *J. Electrochem. Soc.*, **168**, 020502 (2021).
35. K. Smith, P. Gasper, A. M. Colclasure, Y. Shimonishi, and S. Yoshida, *J. Electrochem. Soc.*, **168**, 100530 (2021).
36. M. Schimpe, M. E. von Kuepach, M. Naumann, H. C. Hesse, K. Smith, and A. Jossen, *J. Electrochem. Soc.*, **165**, A181 (2018).
37. D. Anseán, M. Dubarry, A. Devie, B. Liaw, V. García, J. Viera, and M. González, *Journal of Power Sources*, **356**, 36 (2017).
38. M. Naumann, *Mendeley Data*, **V1** (2021), https://doi.org/10.17632/6hgyr25h8d.1.
39. M. Naumann, *Mendeley Data*, **V1** (2021), https://doi.org/10.17632/kxh42bfgtj.1.
40. mediaTUM, (2021), Techno-economic analysis results of bess use-cases considering battery degradation model confidence intervals 10.14459/2021mp1633017.
41. R. Mathieu, I. Baghdadi, O. Briat, P. Gyan, and J. M. Vinassa, *Energy*, **141**, 2108 (2017).
42. L. Tang, G. Rizzoni, and S. Onori, *IEEE Transactions on Transportation Electrification*, **1**, 211 (2015).
43. E. Sarasketa-Zabala, I. Gandiaga, E. Martinez-Laserna, L. M. Rodriguez-Martinez, and I. Villarreal, *Journal of Power Sources*, **275**, 573 (2015).
44. M. Ecker, J. B. Gerschler, J. Vogel, S. Käbitz, F. Hust, P. Dechent, and D. U. Sauer, *Journal of Power Sources*, **215**, 248 (2012).
45. I. Baghdadi, O. Briat, J. Y. Delétage, P. Gyan, and J. M. Vinassa, *Journal of Power Sources*, **325**, 273 (2016).
46. W. Diao, S. Saxena, and M. Pecht, *Journal of Power Sources*, **435**, 226830 (2019).
47. S. Ebbesen, P. Elbert, and L. Guzzella, *IEEE Transactions on Vehicular Technology*, **61**, 2893 (2012).
48. F. Alhaider, T. Klein, and S. Gerhard, *NEIS 2018—Conference on Sustainable Energy Supply and Energy Storage Systems*, p. 156 (2018), https://ieeexplore.ieee.org/document/8669467.
49. B. Bole, C. S. Kulkarni, and M. Daigle, *PHM 2014—Proceedings of the Annu Conference of the Prognostics and Health Management Society* **2014**, p. 50 (2014).
50. J. Wang, J. Purewal, P. Liu, J. Hicks-Garner, S. Soukazian, E. Sherma A. Sorenson, L. Vu, H. Tataria, and M. W. Verbrugge, *Journal of Powe Sources*, **269**, 937 (2014).
51. A. Cordoba-Arenas, S. Onori, Y. Guezennec, and G. Rizzoni, *Journal of Powe Sources*, **278**, 473 (2015).
52. K. Takei, K. Kumai, Y. Kobayashi, H. Miyashiro, N. Terada, T. Iwahori, an T. Tanaka, *Journal of Power Sources*, **97**, 697 (2001).
53. S. Saxena, C. Hendricks, and M. Pecht, *Journal of Power Sources*, **327**, 394 (2016
54. G. Suri and S. Onori, *Energy*, **96**, 644 (2016).
55. F. Todeschini, S. Onori, and G. Rizzoni, *IFAC Proceedings Volumes*, **45**, 45 (2012).
56. J. Wang, P. Liu, J. Hicks-garner, E. Sherman, S. Soukiazian, M. Verbrugge, H. Tatari J. Musser, and P. Finamore, *Journal of Power Sources*, **196**, 3942 (2011).
57. L. Serrao, S. Onori, G. Rizzoni, and Y. Guezennec, *IFAC Proceedings Volumes*, **4** 923 (2009).
58. M. Petit, E. Prada, and V. Sauvant-Moynot, *Applied Energy*, **172**, 398 (2016).
59. E. Sarasketa-Zabala, E. Martinez-Laserna, M. Berecibar, I. Gandiag L. M. Rodriguez-Martinez, and I. Villarreal, *Applied Energy*, **162**, 839 (2016).
60. J. Stadler, C. Krupp, M. Ecker, J. Bandlow, B. Spier, and A. Latz, (2021), https: doi.org/10.1016/j.jpowsour.2021.230952.
61. E. Cuervo-Reyes and R. Flückiger, *J. Electrochem. Soc.*, **166**, A1463 (2019).
62. K. L. Gering, *Electrochimica Acta*, **228**, 636 (2017).
63. J. de Hoog, J. M. Timmermans, D. Ioan-Stroe, M. Swierczynski, J. Jaguemon S. Goutam, N. Omar, J. Van Mierlo, and P. Van Den Bossche, *Applied Energy*, **20** 47 (2017).
64. M. S. Hosen, D. Karimi, T. Kalogiannis, A. Pirooz, J. Jaguemont, M. Berecibar, an J. Van Mierlo, *Journal of Energy Storage*, **28**, 101265 (2020).
65. P. M. Attia, A. Bills, and F. B. Planella, *J. Electrochem. Soc.*, **169**, 060517 (2022).
66. P. M. Attia, W. C. Chueh, and S. J. Harris, *J. Electrochem. Soc.*, **167**, 09053 (2020).
67. S. L. Kukreja, J. Löfberg, and M. J. Brenner, *IFAC Proceedings Volumes*, **39**, 81 (2006).
68. L. M. Ghiringhelli, J. Vybiral, S. V. Levchenko, C. Draxl, and M. Scheffler, *Phy Rev. Lett.*, **114**, 1 (2015), (Preprint 1411.7437).
69. L. M. Ghiringhelli, J. Vybiral, E. Ahmetcik, R. Ouyang, S. V. Levchenko, C. Drax and M. Scheffler, *New J. Phys.*, **19**, 023017 (2017).
70. R. Ouyang, S. Curtarolo, E. Ahmetcik, M. Scheffler, and L. M. Ghiringhelli, *Phy Rev. Mater.*, **2**, 1 (2018), (*Preprint* 1710.03319).
71. R. Ouyang, (2021), SISSO https://github.com/rouyang2017/SISSO.
72. P. Gasper, (2021), SISSORegressor_MATLAB https://github.com/NRE SISSORegressor_MATLAB.
73. D. Waroquiers, (2021), Matgenix pysisso https://github.com/Matgenix/pysisso.
74. K. Rumpf, M. Naumann, and A. Jossen, *Journal of Energy Storage*, **14**, 22 (2017).
75. F. B. Spingler, M. Naumann, and A. Jossen, *J. Electrochem. Soc.*, **167**, 040526 (2020
76. M. Safari and C. Delacourt, *J. Electrochem. Soc.*, **158**, A1123 (2011).
77. E. V. Thomas, I. Bloom, J. P. Christophersen, and V. S. Battaglia, *Journal of Powe Sources*, **184**, 312 (2008).
78. S. Santhanagopalan, K. Smith, J. Neubauer, G. H. Kim, M. Keyser, and A. Pesara *Design and analysis of large lithium-ion battery systems* (Artech House, Boston) (2015
79. R. Monteiro, I. Miyazato, and K. Takahashi, *The Journal of Physical Chemistry* **124**, 1754 (2020).
80. H. Cinco-Ley and V. F. Samaniego(OnePetro), *SPE Annual Technical Conferenc and Exhibition*, p. SPE-19817-MS (1989).
81. T. Raj, A. A. Wang, C. W. Monroe, and D. A. Howey, *Batteries & Supercaps*, 1377 (2020).

Supervised student theses

a Dönmez, A.: *Optimized power distribution for lithium-ion battery energy storage systems through particle swarm optimization*, Master's Thesis, 2023

b Abdullah, H.: *Validation of a battery thermal model*, Research Internship, 2023

c Senoner, F.: *Electrochemical aging modeling of lithium-ion cells with PyBaMM (German: Elektrochemische Alterungsmodellierung von Lithium-Ionen-Zellen mit PyBaMM)*, Research Internship, 2023

d Kohlmann, J.: *Energy arbitrage with battery storage on electricity markets (German: Energiearbitrage mit Batteriespeichern auf Strommärkten)*, Advanced Seminar, 2023

e Mumand, A.: *Optimized operation of battery energy storage systems at varying state-of-health (German: Optimierter Betrieb von Batteriespeichern mit variierenden Alterungszuständen)*, Master's Thesis, 2022

f Krammer, T.: *Electrochemical modelling of lithium-ion-cells in Python*, Research Internship, 2022

g Ren, D.: *Degradation modeling of lithium-ion cells (German: Alterungsmodellierung von Lithium-Ionen-Batterien)*, Research Internship, 2022

h Krammer, T.: *Modeling the non-linear aging of lithium-ion batteries (German: Modellierung der nichtlinearen Alterung von Lithium-Ionen-Batterien)*, Advanced Seminar, 2022

i Delseith, P.: *Influence of cell chemistry and cell design on the aging of lithium-ion batteries*, Advanced Seminar, 2022

j Velasquez, G.: *Analysis of battery energy storage systems integrated with EV fast charging stations*, Master's Thesis, 2021

k Selenić, K.: *Application-specific stochastic modelling of lithium-ion battery long-term capacity degradation*, Master's Thesis, 2021

l Engwerth, V.: *Peak shaving operation of battery energy storage systems through optimization (German: Peak Shaving-Betrieb stationärer Batteriespeicher durch Optimierung)*, Master's Thesis, 2021

m Natterer, J.: *Evaluation of deep reinforcement learning concepts for advanced energy management of battery storage systems (German: Erprobung von Deep Reinforcement Learning Konzepten für fortgeschrittenes Energiemanagement von Batteriespeichern)*, Semester Thesis, 2021 n Ramakrishnan, N.: *Implementation and assessment of non-linear aging models*, Research Internship, 2021

o Ponchev, N.: *Electrical characterization of large-format lithium-ion-cells (German: Elektrische Charakterisierung großformatiger Lithium-Ionen-Zellen)*, Research Internship, 2021

p Mayr, M.: *Comparison and evaluation of different lithium-ion cell types for stationary battery storage systems (German: Vergleich und Bewertung verschiedener Lithium-Ionen-Zelltypen für stationäre Batteriespeicher)*, Advanced Seminar, 2021

q Splawski, O.: *Operating strategies for stationary battery storage systems taking aging effects into account (German: Betriebsstrategien für stationäre Batteriespeicher unter Berücksichtigung von Alterungseffekten)*, Advanced Seminar, 2021

r Hörmann, S.: *Dynamic modeling and control of battery energy storage thermal behavior*, Bachelor's Thesis, 2020

s Engwerth, V.: *Operating strategies for stationary energy storage systems for peak shaving (German: Betriebsstrategien für stationäre Energiespeicher zum Peak Shaving)*, Advanced Seminar, 2020

t Thampi, G.: *Remaining useful life of lithium-ion batteries in stationary applications*, Advanced Seminar, 2020

Acknowledgment

This thesis originates from my time as a research associate at the Chair for Electrical Energy Storage Technology (EES) at the Technical University of Munich. Some said that going into academia to pursue a doctorate degree after having already worked in the industry is not an obvious choice. Next to the freedom and satisfaction that comes from being able to dive deep into a topic that one is passionate about, the people I met along the way made it a truly rewarding experience.

First and foremost, I want to thank my supervisor, Prof. Dr.-Ing. Andreas Jossen, for his continuous support and the great autonomy that he entrusted me with in following my research interests and later in my role as a team lead for the team Application and System Integration. In addition, I want to acknowledge my co-authors for the fruitful discussions and critical feedback that enabled this publication-based thesis. Gratitude also goes to the numerous master's and bachelor's thesis workers who supported me in exploring new research ideas and made me realize how fulfilling mentoring and teaching are.

Furthermore, I want to thank my colleagues, both my immediate team and the numerous people at the EES who I worked with in cross-team collaborations. I want to thank Daniel Kucevic, Stefan Englberger, and Holger Hesse, from whom I learned much in my early days at the chair. I also want to thank Benedikt Tepe and Martin Conejo for frequently acting as my sparing partners when it came to decisions and difficult topics during my time as the team lead. I especially want to thank those colleagues who turned into friends and made the time at the EES as fun as the shared adventures outside of working hours.

My doctorate mentor, Marcus Mueller, I want to thank for his ability to make me want to strive for more after just a short phone call. Furthermore, I would like to thank Cyril Daran-Daneau who has provided me with yet another Tesla adventure by convincing me to help him power up Gigafactory Berlin during the Corona lockdown days.

Most importantly, I want to thank my friends and family. I want to especially thank my parents for always having supported my life and career choices while making me feel that there is a second home waiting for me in my distant hometown of Sulingen.